The crystal structure and thermodynamic properties of titanite solid-solution Ca(Ti,Al)(O,F)SiO$_4$

by
Ulrike Troitzsch

A thesis submitted for the degree of
Doctor of Philosophy
of The Australian National University

Canberra
May 2000

The data, interpretations and conclusions presented in this thesis are my own unless stated otherwise. The contributions of co-authors are indicated in the acknowledgements.

Ulrike Troitzsch

Acknowledgements

Abstract

This is a study of binary titanite solid-solution $Ca(Ti,Al)(O,F)SiO_4$, which provides information about the crystal structure as well as thermodynamic properties of Al-rich titanite, including the previously unknown end-member $CaAlFSiO_4$. The investigation is predominantly based on synthetic samples that were equilibrated at high pressures and temperatures, using a piston-cylinder apparatus.

The crystal structure of titanite solid-solution was investigated with transmission electron microscopy (TEM), powder X-ray diffraction and Rietveld refinement for a range of monophase titanite samples of different compositions, covering the entire binary join $CaTiOSiO_4$ – $CaAlFSiO_4$. The end-member $CaAlFSiO_4$ crystallises in the titanite structure with space group $A2/a$, and has a unit-cell volume 7% smaller than that of titanite. The change in unit-cell dimensions along the binary join can be used to determine the Al-F content of synthetic binary titanite samples with an accuracy comparable to electron microprobe analyses. TEM investigations indicate that the change in space group from $P2_1/a$ (titanite) to $A2/a$ ($CaAlFSiO_4$) along the binary join occurs between $X_{Al} = 0.09$ and 0.18 [$X_{Al} = Al/(Al+Ti)$]. Non-linear changes of some of the bond-lengths indicate that the titanite structure undergoes a major atomic rearrangement at $X_{Al} > 0.4$. At Al-contents exceeding $X_{Al} = 0.6$, the Ca-site and O1-site become increasingly overbonded with Al-F substitution, demonstrating that the titanite structure is not well suited to accommodate large amounts of Al and F. The largest deviations from ideal bond valence sums occur in $CaAlFSiO_4$, suggesting the presence of a significant amount of structural stress, lattice energies of small magnitudes, and thus potential low thermodynamic stability of this end-member.

The heat capacity of $CaAlFSiO_4$ and titanite were measured with scanning differential calorimetry (DSC). Transition temperature measurements of titanite solid-solution samples with DSC allow to more narrowly constrain the $P2_1/a$ to $A2/a$ phase change to Al-contents between $X_{Al} = 0.15$ and 0.20 at room temperature, which is in good agreement with previous TEM observations.

The phase assemblage titanite - anorthite - fluorite was equilibrated at various pressures (5 to 20 kbar) and temperatures (800 to 1000°C). The displacement of the end-member forming reaction anorthite + fluorite = $CaAlFSiO_4$ in the presence of titanite allowed the determination of activity-composition relations of titanite solid-solution, as well as the extraction of thermodynamic properties (enthalpy of formation and standard state entropy) of $CaAlFSiO_4$.

IV

The results of the high-PT experiments indicate that titanite behaves like a non-ideal, symmetrical solid-solution. The application of a multi-site mixing (MM) model resulted in a slightly better fit to the data compared to a local-charge-balance (LCB) model, suggesting the independent distribution of Al^{3+} and F^- in the titanite structure. The MM model is consistent with positive deviation from ideality, and thus predicts a solvus, with a critical temperature between about 300 and 600°C, depending on the temperature dependence chosen for the Margules parameter (W_S), and the pressure. The existence of a solvus would be consistent with natural titanite samples equilibrated at various temperatures, which indicate that the extent of solid-solution increases with increasing temperature to a maximum of X_{Al} = 0.54. The absence of natural samples with higher Al-contents (below the critical temperature) suggests that, if a solvus is present in this system, it is possibly truncated by reactions stabilising other phase assemblages with respect to Al-rich titanite. The pressure dependence of the Margules parameter (W_V) was calculated from the excess volume of mixing based on the crystal structure data, as well as by data regression based on the experimental PTX-data set (MM model). Both W_V values agree remarkably well, suggesting internal consistency of the data presented in this study.

The thermodynamic data of the end-member $CaAlFSiO_4$ presented here open up a new field in composition space in which equilibria with Al-rich titanite can be modelled. The compositional area surrounding $CaAlFSiO_4$ was explored in this study by the construction of petrogenetic grids, predicting the Al-content of titanite in various F-rich assemblages. The thermodynamic calculations are in good qualitative agreement with the results of previous studies of natural as well as synthetic titanite, in that titanite with X_{Al} > 0.65 ± 0.15 is predicted to be absent from most phase assemblages. Titanite with higher concentrations of $CaAlFSiO_4$ is either metastable with respect to other phases, including minerals such as plagioclase, garnet, zoisite, calcite, kyanite, quartz and fluorite, or its stability field is restricted to extremely high pressures and low temperatures, not realised in natural rocks. The petrogenetic grids also predict that although titanite with Al-contents up to X_{Al} > 0.6 may be found at all metamorphic grades, the *most likely* occurrence of Al-rich titanite is at eclogite facies conditions. This is reflected in the numerous reports of Al-rich titanite from high-pressure and ultra-high pressure terrains, compared to only few yet significant finds at lower grades. Also, the generally low Al-contents of titanite in blueschist-facies rocks are consistent with the thermodynamic calculations based on $CaAlFSiO_4$.

The integration of the results from the crystal structure and thermodynamic part of this work, help to understand why titanite with more than 54 mol.% of the Al-end-member is rarely found in nature. It is proposed by this study that due to crystal structural stresses, the $CaAlFSiO_4$ end-member is thermodynamically less stable compared to other phases in natural assemblages. Therefore, an increasing amount of $CaAlFSiO_4$ in titanite causes crystal structural problems at about $X_{Al} > 0.6$, and at the same time is reflected in the breakdown of titanite with $X_{Al} > 0.65 \pm 0.15$ based on thermodynamic calculations. However, no activity-composition anomaly was detected in the experiments at $X_{Al} = 0.6$, which could be the direct thermodynamic expression of crystal structural problems beginning in a this point. Therefore, it may simply be the low stability of $CaAlFSiO_4$, manifested in its standard state thermodynamic properties, which causes the breakdown of titanite, as soon as the AlF-end-member starts to dominate the thermodynamic as well as structural properties of the solid-solution, that is at $X_{Al} > 0.5$.

The activity-composition relations of titanite solid-solution presented here will be of use for future studies, as they improve the accuracy of petrogenetic indicators based on titanite, such as equilibria used for geobarometry, the estimation of fluid-composition (X_{CO2}), or the determination of fluorine or oxygen fugacities. Based on the data presented here, the reliability of titanite as petrogenetic indicator can now be tested with natural assemblages by future studies. While previous studies were restricted to equilibria with the titanite end-member, it is now possible to use reactions with $CaAlFSiO_4$ in addition.

Contents

Chapter 1

Introduction

One of the main objectives of geological studies is to gain insight into the processes and conditions of formation that determine the chemical, textural and structural properties of a rock, as a first step towards understanding the system Earth. Metamorphic and igneous rocks, for example, contain information about the spatial variation of pressure, temperature and chemical composition inside the Earth, "frozen in" by the mineral assemblage at some interval during the rock's geological history. The prime tool with which to interpret mineral assemblages are thermodynamic calculations, which relate phase assemblages and/or compositions to pressure and temperature conditions via chemically balanced reactions. These equilibria, which are petrogenetic indicators such as geothermometers and geobarometers, may be based on any mineral assemblage, as long as the thermodynamic properties (i.e., enthalpy, entropy and heat capacity) and crystal structure (unit cell volume) of all phases are known, as well as the activity-composition relations of any solid-solution involved.

The mineral titanite [$CaTiOSiO_4$] is a common accessory phase in a large range of igneous, metamorphic, and even in some sedimentary rocks, and would be a very desirable candidate for such petrogenetic indicators because of their potential widespread use. The abundant occurrence of titanite is due to its ability to accommodate a large number of foreign atom species into its crystal lattice (e.g., Sahama, 1946; Cerny and Povondra, 1972; Cerny et al., 1995; Perseil and Smith, 1995), which allows it to adjust to very different geochemical environments and metamorphic conditions.

Numerous previous studies, based on natural assemblages, experiments, or thermodynamic modelling, have proposed the mineral titanite to be a potential indicator for a range of metamorphic conditions (Kowallis, 1997). For example, the studies by Essene and Bohlen (1985), Manning and Bohlen (1991), Mukhopadhyay et al. (1992) and Ghent and Stout (1994), investigated various net-transfer reactions with titanite that are pressure-sensitive, and can therefore be used as *geobarometers*. The experimental results reported by Hunt and Kerrick (1977) and Jacobs and Kerrick (1981), who studied the stability of titanite in the presence of an H_2O-CO_2 fluid, suggest that titanite can also serve as an indicator for metamorphic *fluid compositions* (see also, Valley and Essene, 1980; Aldahan and Morad, 1988; Itaya et al., 1985; Gieré, 1992). Moreover, Wones (1989) pointed out that the occurrence of titanite in granitic rocks could be used

to estimate *oxygen fugacities*. The dependence of the titanite stability on oxygen fugacity was also demonstrated in the experiments by Spear (1981), and the concept has since been used for the interpretation of natural mineral assemblages (Nakada, 1991; Piccoli and Candela, 1991). The fact that the formation of titanite can often be dated, based on its U-Pb content, opens the exciting possibility to date the above metamorphic conditions, using titanite as a *geochronometer* (Frost et al., 2000). Understanding the stability of titanite in igneous as well as metamorphic rocks is important, as it might play a dominant role in shaping their *rare earth element patterns* (Hellman and Green, 1979, Green and Pearson, 1986; Tribuzio et al., 1996; Paterson and Stephens, 1992; Dawson et al., 1994; Pan et al., 1995; Russell et al., 1994). Moreover, the presence or absence of titanite in felsic igneous rocks could be used as an indicator for *F-contents of magmas* (Price et al., 1999).

Thus, the occurrence and composition of titanite in natural mineral assemblages contain abundant petrogenetic information. The better our understanding of the thermodynamics and crystal structure of titanite solid-solution, the better will be the models underlying the thermodynamic calculations, and thus the more accurate our estimates of the petrogenetic conditions. Because titanite commonly occurs in solid-solution with other end-members, it is crucial to understand the activity-composition relations with the most important other end-members.

While the thermodynamic and crystal structure data of the end-member titanite [$CaTiOSiO_4$] are known, activity-composition relations of titanite solid-solution have never been determined, leaving previous studies no choice but to assume either ideal mixing behaviour (e.g., Manning and Bohlen, 1991; Ghent and Stout, 1994), or titanite to be pure (Mukhopadhyay et al., 1992). Mukhopadhyay et al. (1992) emphasized that these assumptions with respect to the activity of titanite "will undoubtedly affect the computed P values from the geobarometers. However, a rigorous assessment of the effect of … substitutions on $\log_{10}K_a$-T isopleths … is difficult because a − X relations for different solid-solution components in sphene are not known…".

The present study addresses this problem by investigating experimentally the activity-composition relations of Al-bearing titanite solid-solution along the binary join $CaTiOSiO_4$ - $CaAlFSiO_4$. Moreover, the crystal structure and thermodynamic properties of $CaAlFSiO_4$ are determined. The end-member $CaAlFSiO_4$ was chosen for several reasons. First, Al is one of the most common and abundant substituents for Ti in natural titanite, and thus most important for thermodynamic modelling of natural assemblages. Second, among the two main Al-end-members that occur in natural titanite, i.e. $CaAlOHSiO_4$ and $CaAlFSiO_4$, the latter always dominates in the most Al-rich titanites,

but never exceeds 54 mol.%. Although the reasons for this compositional limit were object of much discussion (e.g., Smith, 1981), there has been no previous attempt to synthesize more AlF-rich titanite in a mineralogically buffered assemblage. Third, the Al-content of titanite is pressure and temperature dependent, and thus is of special interest for geothermobarometry. $CaAlFSiO_4$ seems to play the most important role in high-pressure assemblages.

The potential of Al-bearing titanite to serve as a geobarometer has long been recognized (Smith, 1980; 1981). Many previous studies of natural (e.g., Franz and Spear, 1985; Krogh et al., 1990; Enami et al., 1993; Carswell et al., 1996) and synthetic Al-rich titanite (Smith, 1981) seemed to indicate a strong pressure and mild temperature dependence of the Al-content in titanite. However, the pressure-temperature-composition relationship was never quantified for any assemblage, mainly because of the strong dependence of the system on fluorine, which until more recently was difficult to analyze quantitatively with standard equipment (e.g., Jaffe, 1947). Significant improvement of the analytical equipment over the last decade with respect to fluorine analysis has now made the calibration of titanite as a petrogenetic indicator worth while, which was the prime motivation of this study.

Note that this study does not provide a 'ready-to-use' geobarometer of Al-titanite. Rather, it should be regarded as an investigation into the crystal structure and thermodynamics of titanite solid-solution, which helps to gain a more profound understanding of the characteristics and dynamics of this system. The data provided in this thesis will enable future studies to use titanite as petrogenetic indicator, and test its reliability, for example by thermodynamic modelling of natural assemblages, and comparison to other, well tested petrogenetic indicators. Future work on the water-bearing end-member $[CaAlOHSiO_4]$ is particularly desirable in order to extend the application of Al-titanite equilibria to a wider range of natural rocks.

1.1 Structure of study

Figure 1.1 shows a schematic overview of the structure of this study, and its organization into the chapters of this thesis. First of all, this study is based on the equilibration of titanite solid-solution at controlled pressures and temperatures, using the piston-cylinder apparatus, synthesising mono-phase titanite samples, as well as those with titanite in a buffered mineral assemblage. Thus, the material studied is of entirely synthetic origin. Besides the experimental calibration of the pressure and temperature dependence of Al and F in synthetic titanite, which is a rather 'macroscopical' and descriptive approach, this study also investigates - in a 'microscopical' approach - the crystal structure of the solid-solution along the binary join. The aim is to understand the properties of titanite solid-solution on each scale, and to integrate the results of both approaches to a larger picture.
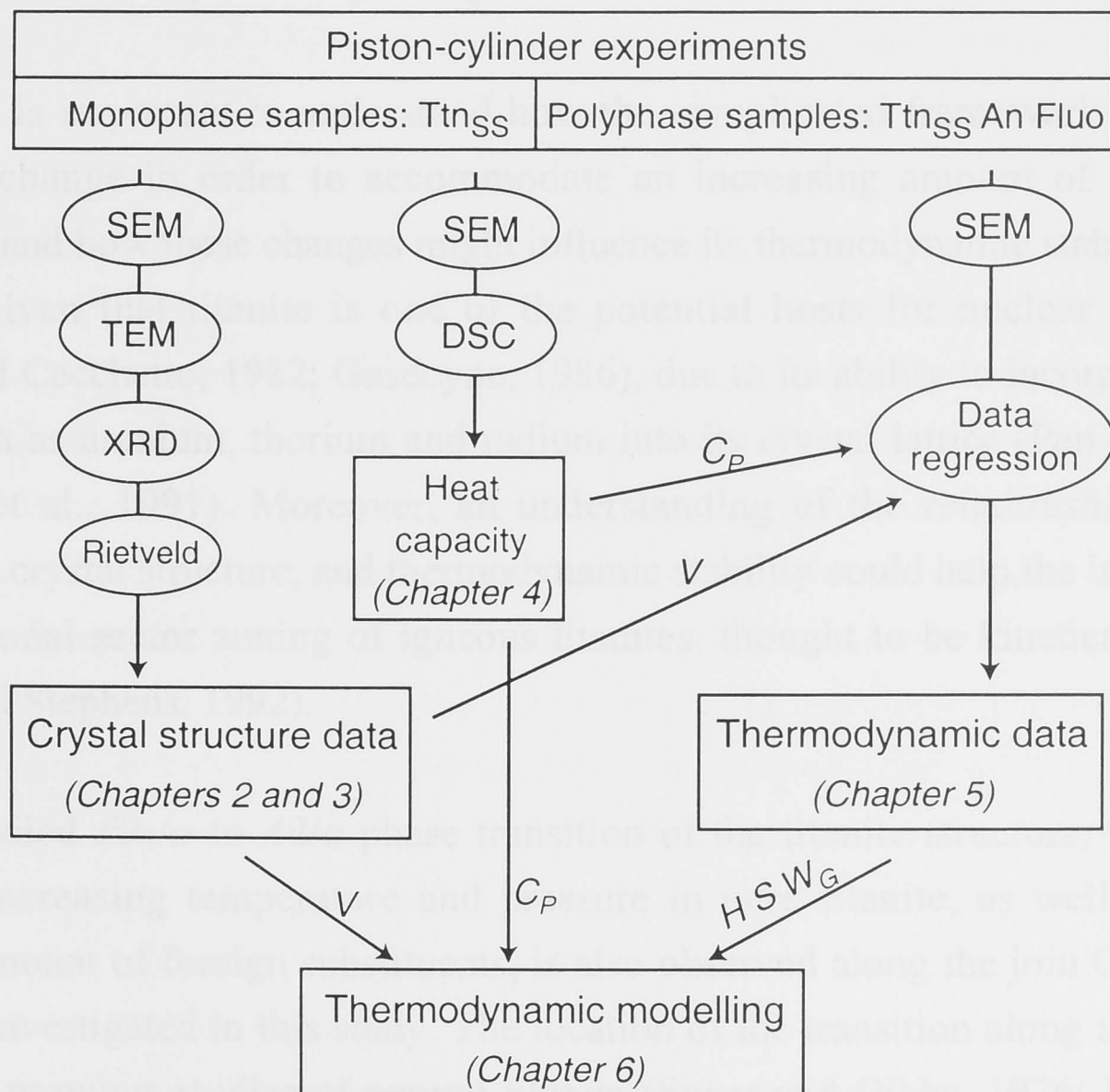
Figure 1.1 Schematic overview of the structure of this study, and organization of thesis. Abbreviations: Ttn$_{SS}$, titanite solid-solution; An, anorthite; Fluo, fluorite; SEM, scanning electron microscopy; TEM, transmission electron microscopy; XRD, X-ray diffraction; Rietveld, Rietveld refinement; DSC, differential scanning calorimetry; C_P, heat capacity; H, enthalpy of formation; S, standard state entropy; V, unit cell volume; W_G, Margules parameter (C_P, H, S refer to end-member CaAlFSiO$_4$, V and W_G to titanite solid solution).

1.1.1 Crystal structure investigations

The study of the crystal structure (Chapters 2 and 3) is based on transmission electron microscopy, powder X-ray diffraction, and Rietveld refinement (Figure 1.1). First of all, these investigations yield the unit-cell volume of the solid-solution and the end-member $CaAlFSiO_4$, values required for the thermodynamic calculations in the subsequent chapters. Besides this obvious reason, the crystal structure refinement was also motivated by the fact that previous studies of natural and synthetic titanites seemed to suggest that the amount of Al in the titanite structure is restricted to less than about X_{Al} = 0.54, possibly due to a crystal structural constraint (Smith, 1981; Oberti et al., 1991). This hypothesis could never be tested because the samples available were of course restricted to Al-contents below that value (Oberti et al., 1991). The synthesis of titanite with up to X_{Al} = 1.0 in this study (Chapter 2), although refuting the hypothesis of a hard crystal structural constraint, allowed for the first time the investigation of the structure of very Al-rich titanite, previously thought to be 'unstable'.

Moreover, it is important to understand how the complicated framework structure of titanite can change in order to accommodate an increasing amount of any foreign substituents, and how these changes might influence its thermodynamic stability. This is of interest given that titanite is one of the potential hosts for nuclear waste (e.g., Hayward and Cecchetto, 1982; Gascoyne, 1986), due to its ability to incorporate radio-nucleids such as uranium, thorium and radium into its crystal lattice (Pan et al., 1993; Hawthorne et al., 1991). Moreover, an understanding of the relationships between composition, crystal structure, and thermodynamic stability could help the interpretation of compositional sector zoning of igneous titanites, thought to be kinetically induced (Paterson and Stephens, 1992).

The well studied $P2_1/a$ to $A2/a$ phase transition of the titanite structure, which takes place with increasing temperature and pressure in pure titanite, as well as with an increasing amount of foreign substituents, is also observed along the join $CaTiOSiO_4$ - $CaAlFSiO_4$ investigated in this study. The location of the transition along this join will complement previous studies of natural titanite (Speer and Gibbs, 1976; Higgins and Ribbe, 1976) and synthetic samples (Kunz et al., 1997), and help to understand the effect of composition on crystal symmetry. Driven by the off-centering direction of the octahedral Ti atoms, this phase transition was studied by Kunz et al. (1997) along the binary join $CaTiOSiO_4$ - $CaSnOSiO_4$ [malayaite] (see also, Groat et al., 1996; Meyer et al., 1998) to gain insight into the interaction between the dipoles formed by the out-of-center distortion of neighbouring Ti atoms. This is of technical interest as the

structurally related $KTiOPO_4$ phase (KTP), in which, other than in titanite, all Ti atoms are off-centered in the same direction, has non-linear optical properties.

1.1.2 Thermodynamic investigations

The thermodynamic part of this study consists of three sections. First, the heat capacity of synthetic $CaAlFSiO_4$ was measured with differential scanning calorimetry (Chapter 4). Also, the change in $P2_1/a$ to $A2/a$ phase transition temperature with composition was calorimetrically determined. Second, a series of piston cylinder experiments were carried out with the assemblage anorthite – fluorite – titanite, which allowed the characterization of the activity-composition relationship of titanite solid-solution, as well as the indirect determination of the standard state entropy and enthalpy of formation of $CaAlFSiO_4$ (Chapter 5). Third, the thermodynamic data of $CaAlFSiO_4$ were used to calculate a range of equilibria with applicability to natural as well as synthetic assemblages (Chapter 6). The main focus of the thermodynamic modelling of natural rocks was on the maximum possible Al-content of titanite in various F-rich assemblages.

The activity-composition relations and mixing models discussed in this study will provide important data for future thermodynamic studies of titanite as petrogenetic indicator. Note that all previous studies focused on equilibria based on the end-member titanite, because it was the only important end-member of titanite solid-solution that was characterized thermodynamically. By providing thermodynamic data for the other end-member, $CaAlFSiO_4$, this study will open up a completely new field in composition space, in which equilibria with titanite solid-solution can be modeled (Chapter 6). For example, the fluorine fugacity of a rock has long been recognized to affect the Al-content of titanite, but the relationship could never be quantified (Markl and Piazolo, 1999). The end-member $CaAlFSiO_4$ is the thermodynamic link between these values.

1.1.3 Format of thesis

As most of the content of Chapters 2 and 3 has been published previously (Appendix 4 in back pocket), the format of the chapters was chosen to be similar to that of articles in scientific journals, containing abstract, introduction, results and discussion, etc.. However, the references of all chapters are listed together at the end of the thesis, before the appendix section. Although care was taken to minimize repetition especially in the introductions, some facts were stated more than once for the sake of clarity and ease of reading. A list of abbreviations and symbols used in this study is given in Appendix 3.

Chapter 2

The synthesis and crystal structure of CaAlFSiO$_4$, the AlF analog of titanite

2.1 Abstract

Aluminium-rich titanites [Ca(Ti,Al)(O,F)SiO$_4$] with $X_{Al} > 0.53$ [$X_{Al} = Al/(Ti+Al)$], including the pure end-member CaAlFSiO$_4$, were synthesised for the first time in a high-pressure experimental study. The crystal structure of CaAlFSiO$_4$ was determined by Rietveld analysis of an X-ray powder diffraction pattern. CaAlFSiO$_4$ is monoclinic, belongs to the space group $A2/a$, and has the unit cell dimensions $a = 6.916(1)$ Å, $b = 8.508(1)$ Å, $c = 6.439(1)$ Å and $\beta = 114.683(2)°$. The unit cell volume is more than 7% smaller than that of CaTiOSiO$_4$, which is consistent with the occurrence of Al-rich titanite predominantly in high-pressure rocks. Although previous studies suggested that titanite with $X_{Al} > 0.5$ is possibly not stable, this study demonstrates that complete solid-solution occurs between CaTiOSiO$_4$ and CaAlFSiO$_4$. The similarity of the crystal structures of titanite and CaAlFSiO$_4$ explains why, in very Al-rich natural titanite, the end-member CaAlFSiO$_4$ generally dominates over the hypothetical end-member CaAlOHSiO$_4$, which under geological conditions is stable in a different crystal structure. The end-member CaAlFSiO$_4$ could qualify as a new mineral (Nickel and Grice, 1998) given that natural titanite exceeding $X_{AlF} = 0.5$ has been found (Franz, 1987).

2.2 Introduction

Al-rich titanite [Ca(Ti,Al)(O,F,OH)SiO$_4$] has been the focus of many previous studies because Al is one of the most common and abundant substituents for Ti in natural titanite (e.g., Higgins and Ribbe, 1976; Smith, 1981; Franz and Spear, 1985; Oberti et al., 1991; Carswell et al., 1996). Moreover, the substitution appeared to be pressure and temperature dependent and thus could be of interest for geothermobarometry (Smith, 1981; Enami, 1993).

The two most important coupled substitution reactions which account for the formation of Al-bearing titanite are
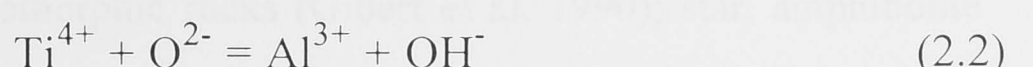
$$Ti^{4+} + O^{2-} = Al^{3+} + F^- \qquad (2.1)$$

and

$$Ti^{4+} + O^{2-} = Al^{3+} + OH^- \qquad (2.2)$$

Hence Al-rich titanite is made up of the three end-members $CaTiOSiO_4$ [titanite], $CaAlFSiO_4$ and $CaAlOHSiO_4$. The end-member titanite occurs in nature and its crystal structure and thermodynamic properties are known (Speer and Gibbs, 1976; Oberti et al, 1991; Berman, 1988). In contrast to this, $CaAlFSiO_4$ has never been found nor synthesized before, and neither has the pure $CaAlOHSiO_4$ end-member been reported. Although the mineral vuagnatite [$CaAlOHSiO_4$] (Sarp et al., 1976) is chemically equivalent to the AlOH-end member of Al-rich titanite, its crystal structure (McNear et al., 1976) is different to that of titanite. Therefore, vuagnatite does not represent the AlOH-component of titanite solid-solution. Throughout this thesis the terms 'AlOH end-member', 'AlOH component' and '$CaAlOHSiO_4$' refer to the hypothetical end-member with titanite structure, not to vuagnatite.

Figure 2.1 shows the compositional variation of natural titanites with respect to the above three end-members. Because the titanite analyses shown here are taken from high-Al titanite studies, they are strongly biased towards high Al-contents. It should be born in mind that the majority of natural titanite analyses, if shown, would plot more closely towards the titanite apex. However, the data shown in Figure 2.1 are representative for the *maximum extent* of solid-solution in natural, ternary Al-bearing titanite as reported by previous studies, which is to be discussed here.
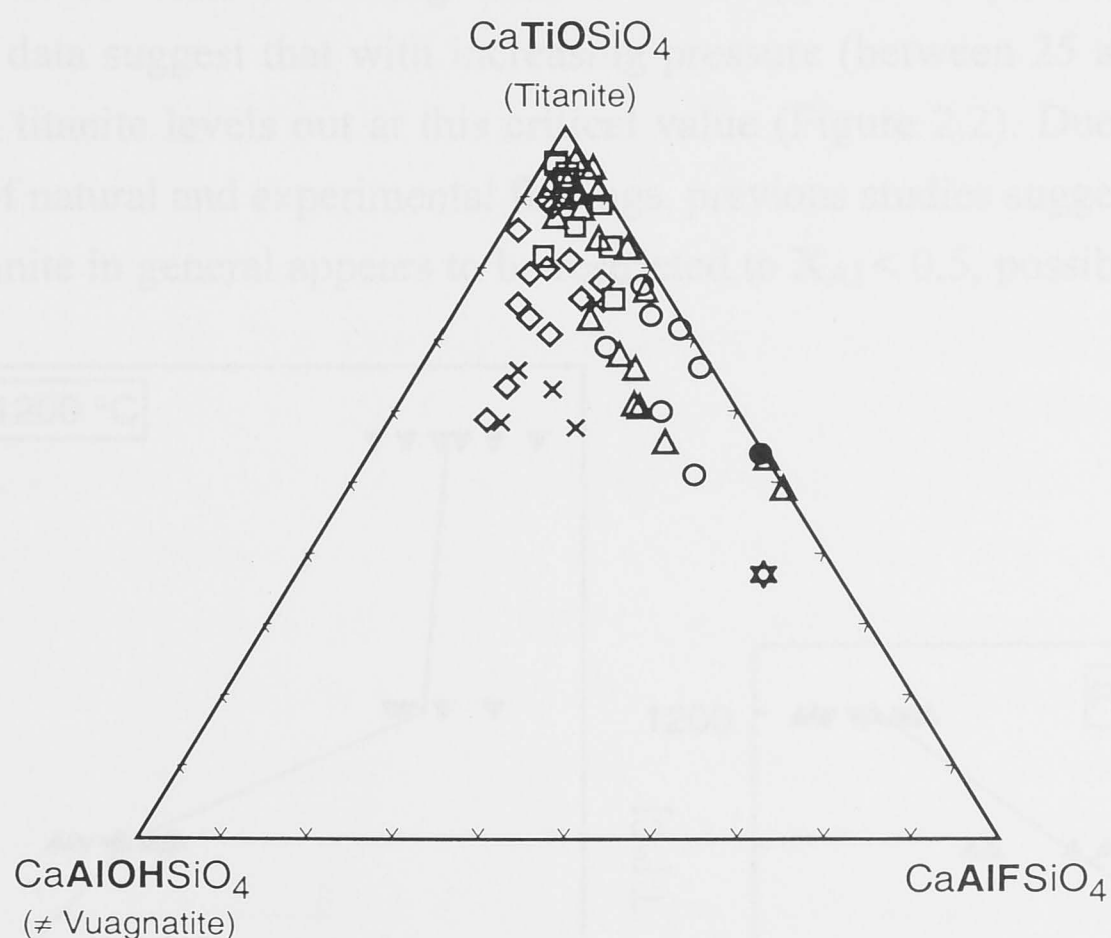
Figure 2.1 Ternary plot of compositional variation of natural titanites from various metamorphic grades, with respect to the three main end-members. Symbols: triangles, eclogite facies rocks (Franz and Spear 1985); open circles and squares, UHP rocks with peak metamorphic and retrograde titanite, respectively (Carswell et al. 1996); filled circle, UHP rock (Sobolev and Shatsky 1990); diamonds, low grade metamorphic rocks (Enami et al. 1993); crosses, low grade metamorphic rocks (Gibert et al. 1990); star, amphibolite facies rock (Franz 1987).

Figure 2.1 demonstrates that all natural titanites contain less than 54 mol.% of any of the Al-end-members. Only one titanite analysis reported by Franz (1987) exceeds this Al-content by about 8 mol.%. Because this analysis was overlooked, or not considered by most previous workers (e.g., Oberti et al., 1991; Markl and Piazolo, 1999), there was general agreement on the hypothesis that 50 to 54 mol.% represented the maximum Al-content of natural titanite. The most Al-rich titanites were predominantly reported from high pressure to ultra-high pressure rocks (Franz and Spear, 1985, Krogh et al., 1990, Carswell et al., 1996, Sobolev and Shatsky, 1990), or from low-T assemblages (Enami et al., 1993). Whereas high pressure and low temperature had always been regarded as promoting high Al-contents in titanite, reports of Al-rich titanite ($X_{Al} < 0.54$) from fluorite-bearing, low-P metamorphic assemblages indicate that also the fluorine fugacity of a system has a strong effect on Al-substitution in titanite (Gibert et al., 1990; Markl and Paizolo, 1999). The most Al-rich natural titanites are all dominated by the AlF-endmember (Franz and Spear, 1985; Carswell et al., 1996; Sobolev and Shatsky, 1990; Markl and Piazolo, 1999), indicating that the coupled substitution described by reaction 2.1 becomes more important towards high Al-contents compared to AlOH-substitution.

The maximum amount of Al-substitution reported from natural titanite is comparable to that of the first and only previous high-pressure and temperature experimental investigation of Al- and F-bearing titanite with $X_{Al} = 0.53$ (Smith, 1981). These experimental data suggest that with increasing pressure (between 25 and 35 kbar) the Al-content in titanite levels out at this critical value (Figure 2.2). Due to this striking coincidence of natural and experimental findings, previous studies suggested that the Al-content in titanite in general appears to be restricted to $X_{Al} < 0.5$, possibly due to some
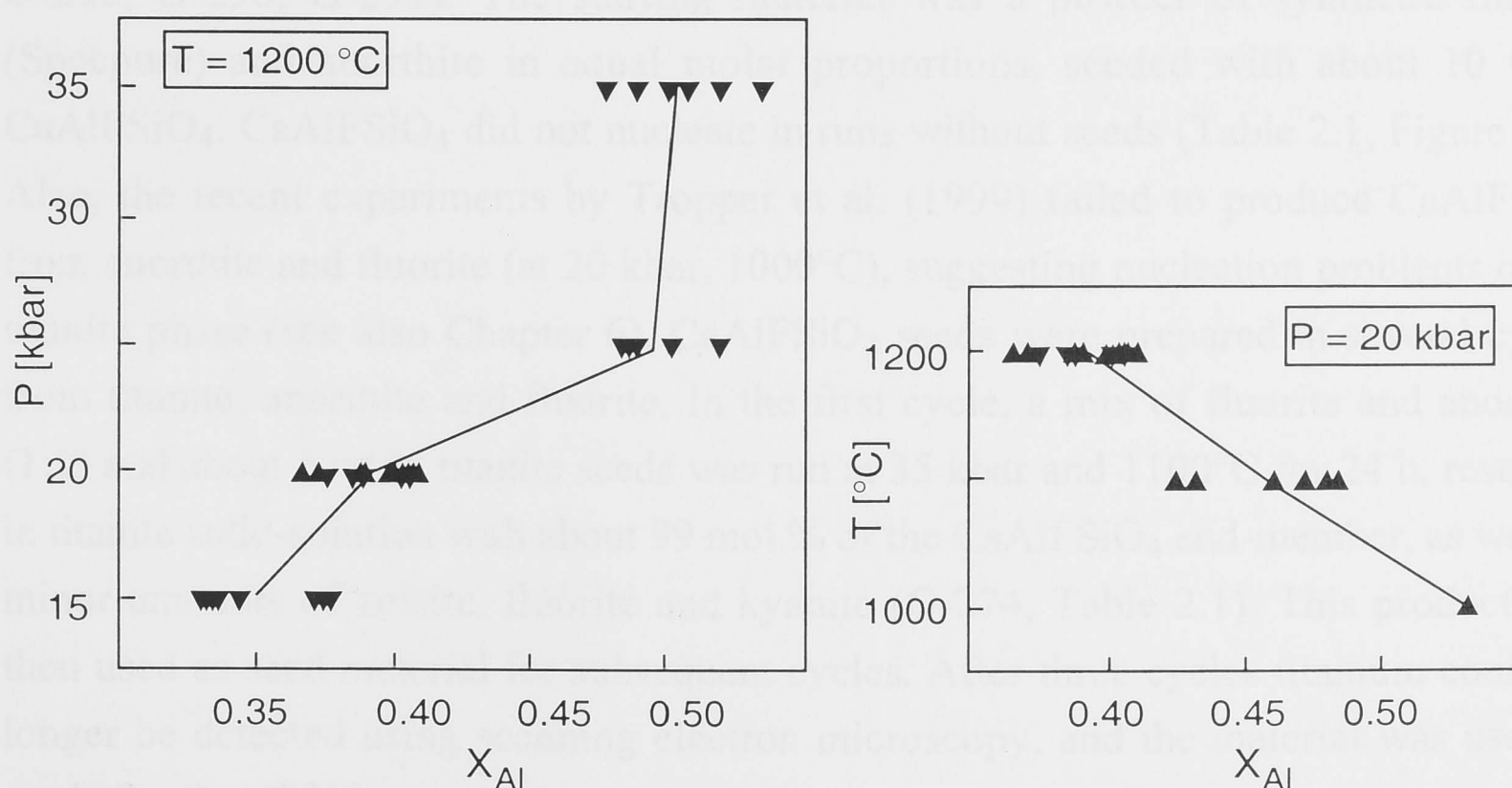
Figure 2.2 Experimental results of the pioneering study by Smith (1981) on the pressure and temperature dependence of Al in synthetic titanite in the system Ca-Ti-Al-Si-O-F. Note the maximum Al-content of $X_{Al} = 0.53$.

crystal structural constraint (note that earlier studies usually did not distinguish between the two aluminium-end-members due to lack of OH- and F-analyses). Oberti et al. (1991) investigated several natural Al-rich titanites ($X_{Al} < 0.37$), documenting changes in the crystal structure with increasing X_{Al}. They discussed various crystal structural features which might be responsible for the apparent compositional limit at $X_{Al} > 0.5$, but clear evidence for a crystal structural constraint was still missing.

The present study extends the information on Al-rich titanite summarized by Oberti et al. (1991) by presenting experimental evidence for complete solid-solution in the binary system CaTiOSiO$_4$ - CaAlFSiO$_4$, and by providing crystal structure data for the end-member CaAlFSiO$_4$. The crystallographic information presented in this chapter resulted from a new refinement of the sample previously investigated by Troitzsch and Ellis (1999). This time the preferred orientation correction for -111 was considered in the refinement, which probably represents a better model for this sample, as it improves the isotropic thermal parameters, and results in more even Si-O bonds (see also discussion in Chapter 3).

2.3 Experimental details

2.3.1 Synthesis of CaAlFSiO$_4$

The synthesis of CaAlFSiO$_4$ was carried out at 35 to 38 kbar and 1100°C using the piston-cylinder apparatus at the Geology Department, Australian National University. Run times varied from 21 to 24 h (see Table 2.1 for individual run conditions; samples G-295, G-296, G-297). The starting material was a powder of synthetic fluorite (Specpure) and anorthite in equal molar proportions, seeded with about 10 wt.% CaAlFSiO$_4$. CaAlFSiO$_4$ did not nucleate in runs without seeds (Table 2.1, Figure 2.3). Also, the recent experiments by Tropper et al. (1999) failed to produce CaAlFSiO$_4$ from anorthite and fluorite (at 20 kbar, 1000°C), suggesting nucleation problems of the titanite phase (see also Chapter 6). CaAlFSiO$_4$ seeds were prepared in several cycles from titanite, anorthite and fluorite. In the first cycle, a mix of fluorite and anorthite (1:1) and about 1 wt.% titanite seeds was run at 35 kbar and 1100°C for 24 h, resulting in titanite solid-solution with about 99 mol.% of the CaAlFSiO$_4$ end-member, as well as minor amounts of zoisite, fluorite and kyanite (G-274, Table 2.1). This product was then used as seed material for subsequent cycles. After three cycles titanium could no longer be detected using scanning electron microscopy, and the material was used as seeds for CaAlFSiO$_4$ synthesis.

Table 2.1 Experimental details. Chemical analyses of titanite in Appendix 1 and Table 2.2.

Exp. no.	T (°C)	P (kbar)	t* (h)	Mix†	Run result	X$_{Al}$-range in Ttn	Comments
G-312	1100	15	22	1:9	Ttn	0.01-0.24	Ttn zoned, X$_{Al}$ from core to rim
G-183	1100	30	21	1:1	Ttn	0.43-0.56	
G-184	1000	30	30	1:1	Ttn	0.44-0.50	
G-185	1200	30	22	1:1	Ttn	0.39-0.50	
G-186	1300	30	22	1:1	Ttn Melt	0.25-0.67	Ttn zoned, X$_{Al}$ from core to rim
G-187	1100	25	36	1:1	Ttn	0.46-0.47	
G-194	1100	25	25	2:1	Ttn	0.50-0.69	
G-197	1100	25	21	1:0	Zoi Fluo Ky	-	no seeds in starting mix
G-313	1100	25	23	3:1	Ttn Zoi Fluo	0.05-0.88	Ttn zoned, X$_{Al}$ from core to rim
G-198	1100	10	23	10:1	Ttn An Fluo Sill	0.34-0.36	
G-199	1100	25	26	10:1	Ttn Zoi Fluo Ky	0.85	
G-200	1100	25	21	20:1	Ttn Zoi Fluo Ky	0.87-0.90	
G-201	1100	25	20	99:1	Ttn Zoi Fluo Ky	0.90-0.95	
G-203	1100	25	80	99:1	Ttn Zoi Fluo Ky	0.85-0.90	
G-264	1100	22	21	99:1	Ttn Zoi Fluo Ky	0.87-0.96	
G-265	1100	15	23	99:1	Ttn An Fluo	0.54-0.57	
G-266	1100	35	20	99:1	Ttn Zoi Fluo Ky	0.97-1.00	
G-268	1050	35	47	99:1	Ttn Zoi Fluo Ky	0.95-1.00	
G-274	1100	35	16	99:1	Ttn Zoi Fluo Ky	0.97-1.00	
G-275	1100	35	22	99:1	Ttn Zoi Fluo Ky	0.96-0.99	starting material was G-274
G-276	1100	35	24	999:1	Ttn Zoi Fluo Ky	0.98-0.99	seed material was G-275
G-278	1100	35	21	1:0	Ttn Zoi Fluo Ky	0.98-1.00	seed material was G-276
G-280	1100	35	23	1:0	Ttn Zoi Fluo Ky	0.99-1.00	seed material was G-278
G-282	1100	35	39	1:0	Ttn Zoi Fluo Ky	0.98-1.00	seed material was G-280
G-295	1100	35	24	1:0	Ttn Zoi Fluo Ky	1.00	seed material was G-280
G-296	1100	38	21	1:0	Ttn Zoi Fluo Ky	1.00	seed material was G-280
G-297	1100	35	23	1:0	Ttn Zoi Fluo Ky	1.00	seed material: G-278 + G-280

Notes: Ttn = Titanite; An = anorthite; Zoi = F-rich zoisite; Fluo = fluorite; Sill = sillimanite; Ky = kyanite.
* Run duration
† Molar ratio of CaAlFSiO$_4$ to CaTiOSiO$_4$

Anorthite was crystallised from glass at 1000°C, 1 atm for 24 h with several cycles of crushing and heating. The glass was prepared by melting Al$_2$O$_3$, SiO$_2$ and CaCO$_3$ at 1600°C and 1 atm, and subsequent quenching in water. For each CaAlFSiO$_4$ synthesis run about 140 mg of mix was filled in 3 mm diameter silver-palladium capsules (Ag$_{75}$Pd$_{25}$), which were then dried at 110°C for 1 h before welding shut. The pressure medium enclosing the capsule was boron-nitride and a surrounding salt-sleeve, with zero friction correction (Figure 2.4). The pressure readings during the experiments are precise within 1%. The temperature was monitored by a Pt-Pt$_{90}$Rh$_{10}$ thermocouple, and was regulated automatically by a EUROTHERM controller. The accuracy of the temperature measurements was ±5°C.
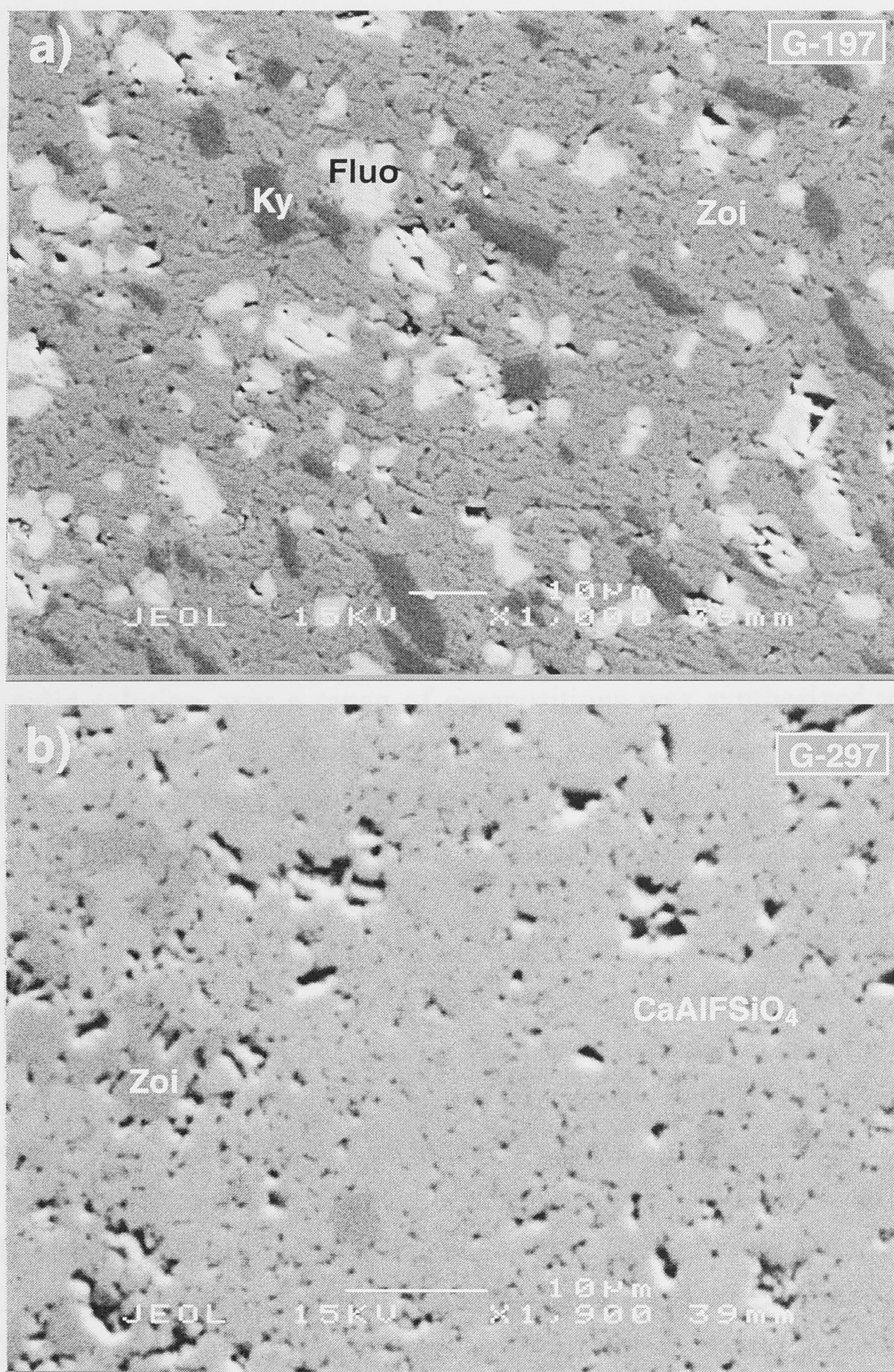
Figure 2.3 Backscattered electron images of two different piston-cylinder run products which resulted from the same starting composition (equivalent to CaAlFSiO₄) (run conditions as in Table 2.1). **a)** The starting mix was composed of anorthite and fluorite, CaAlFSiO₄ did not nucleate. **b)** The starting mix contained seeds of CaAlFSiO₄, besides anorthite and fluorite, facilitating the growth of CaAlFSiO₄. Abbreviations as in Table 2.1

Figure 2.4 Salt-only (left) and salt and pyrex (right) pressure assemblages, as used in the piston-cylinder experiments throughout this study (cross-section).

thermocouple leads
crushable alumina
boron-nitride
thermocouple
graphite sleeve
corundum disk
silver-palladium capsule with sample
pyrex sleeve
salt sleeve
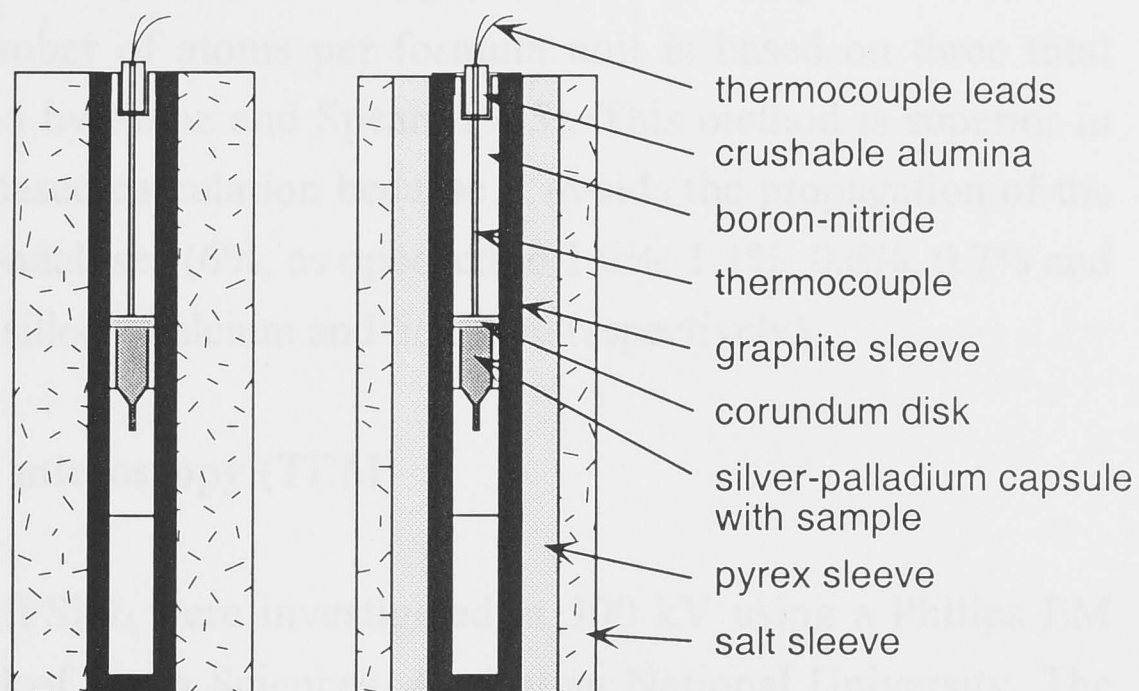
2.3.2 Synthesis of titanite solid-solution

Titanite solid-solution over a range of compositions was synthesized under various pressures and temperatures from two different starting mixes: Anorthite + fluorite (molar proportion 1:1) and grossular + quartz + kyanite + fluorite (molar proportion 1:1:2:3), both mixed with various amounts of titanite (Table 2.1). All starting mixes had the composition of binary titanite solid-solution. Synthetic fluorite (Specpure), SiO_2 (Aerosil, Degussa), natural kyanite (Northern Territory, Australia, $Fe_2O_3 < 0.4$ wt.%) and synthetic grossular, anorthite and titanite were used. Grossular was made from glass at 1200°C, 25 kbar for 26 hours, using the piston-cylinder apparatus. Titanite was crystallised from glass at 1100°C, 1 atm for four weeks, with several cycles of heating and crushing. Both the grossular and titanite glass were prepared from the oxides and $CaCO_3$ at 1450°C and 1 atm, and quenched in water. Silver-palladium capsules ($Ag_{75}Pd_{25}$) of 2 mm diameter were filled with about 10 mg of mix and thoroughly dried at 110°C before welding shut. Salt or salt and pyrex-sleeves were used as outer pressure media. The grain size of all run products was <10 μm. Each sample was investigated with transmitted and/or reflected light microscopy, with X-ray diffraction for phase identification, and with scanning electron microscopy for phase compositions.

2.3.3 Scanning electron microscopy (SEM)

A part of each sample was mounted in epoxy raisin, polished, and carbon coated. Quantitative analyses were obtained with a JEOL JSM-6400 scanning electron microscope with attached Si(Li) detector, Link ISIS EDS, at 15 kV and 1 nA, at the Electron Microscopy Unit, Australian National University. Analyses were calculated using ZAF-correction. Analysed elements were silicon (standard: SiO_2), titanium (TiO_2), aluminium (albite), calcium (diopside), fluorine (fluorite for titanite with

X_F>0.2, apatite for titanite with X_F<0.2) and oxygen (albite). Throughout this thesis the determination of the number of atoms per formula unit is based on three total cations, following the method by Franz and Spear (1985). This method is superior in this case to the usual anion-based calculation because it avoids the propagation of the large errors attached to the F-analyses (6%, as opposed to 1.0%, 1.1%, 0.6%, 0.7% and 1.3% for oxygen, aluminium, silicon, calcium and titanium, respectively).

2.3.4 Transmission electron microscopy (TEM)

Diffraction patterns of CaAlFSiO$_4$ were investigated at 300 kV using a Philips EM 430T at the Research School of Earth Sciences, Australian National University. The camera constant was calibrated against thallium chloride, the uncertainty of the measurements is 1%. The sample (G-297) was finely ground, dispersed on a carbon-coated copper grid, and mounted on a tilt-rotate holder.

2.3.5 X-ray diffraction (XRD)

Powder diffraction data were collected at room temperature with a Siemens D501 diffractometer at the Geology Department, Australian National University. The diffractometer was equipped with a curved graphite monochromator, a scintillation detector, and Cu$K\alpha$ radiation was used. Diffraction data collected for phase identification only were recorded in one pass over a range of 10 to 80°2θ, using a step width of 0.02° at a scan speed of 1° per minute. The diffraction data for Rietveld refinement of CaAlFSiO$_4$ were recorded in four passes over a range of 10 to 100°2θ, with a step width of 0.02° at a scan speed of 0.5° per minute. Due to the small amount of material the sample had to be dispersed with acetone onto a low-background holder (oriented quartz single crystal) with a pipette. This technique has the disadvantage of increasing the effect of preferred orientation, as demonstrated in Chapter 3.

2.3.6 Structure Refinement

Rietveld refinement using up to 50 parameters was performed on sample G-297 with the computer program RIETAN-94 (Izumi, 1993; Kim and Izumi, 1994) which uses the pseudo-Voigt function as profile-shape function, and the "International Tables for Crystallography" (Wilson et al., 1992) as the data base. All four phases present in the sample (85 wt.% CaAlFSiO$_4$, 10 wt.% zoisite, 2 wt.% fluorite, 3 wt.% kyanite) were accounted for in the refinement. The relic fluorite was used as an internal standard for zero correction. Neutral atom scattering factors were chosen for all atoms. Refined non-atomic parameters included one for specimen-displacement, scale factors, eight

background parameters, 12 profile-shape parameters, preferred orientation of all phases (see discussion in Chapter 3), and unit cell parameters of $CaAlFSiO_4$ and zoisite. One global isotropic thermal parameter was refined for all anions. The starting coordinates for the refinement process were those of a titanite with $X_{Al} = 0.09$ in space group $A2/a$ (Hollabaugh and Foit, 1984). For the $CaAlFSiO_4$ refinement the octahedral site was fully occupied with Al, and the O1-site with F. The occupation factors of all sites were set to 1, assuming ideal composition.

2.4 Results and discussion

2.4.1 Titanite solid-solution

All run products are dominated by titanite solid-solution, but may contain various amounts of additional phases such as fluorite, anorthite, kyanite, F-bearing zoisite and melt (Table 2.1). Fluorite and anorthite represent unreacted starting material, whereas the formation of kyanite is probably due to slight deviations of the starting mix from the binary join. The formation of F-bearing zoisite is discussed below. Figure 2.5 shows that the titanites synthesized in this experimental series span the entire range of possible Ti-Al exchange including the end-members titanite and $CaAlFSiO_4$ (Tables 2.1 and 2.2). This is the first time that titanite is reported with $X_{AlF} > 0.53$. Complete solid-solution between $CaTiOSiO_4$ and $CaAlFSiO_4$ is observed, suggesting that there is no crystal structural constraint in the titanite structure that precludes the occupation of more than 50% the octahedral sites with Al.
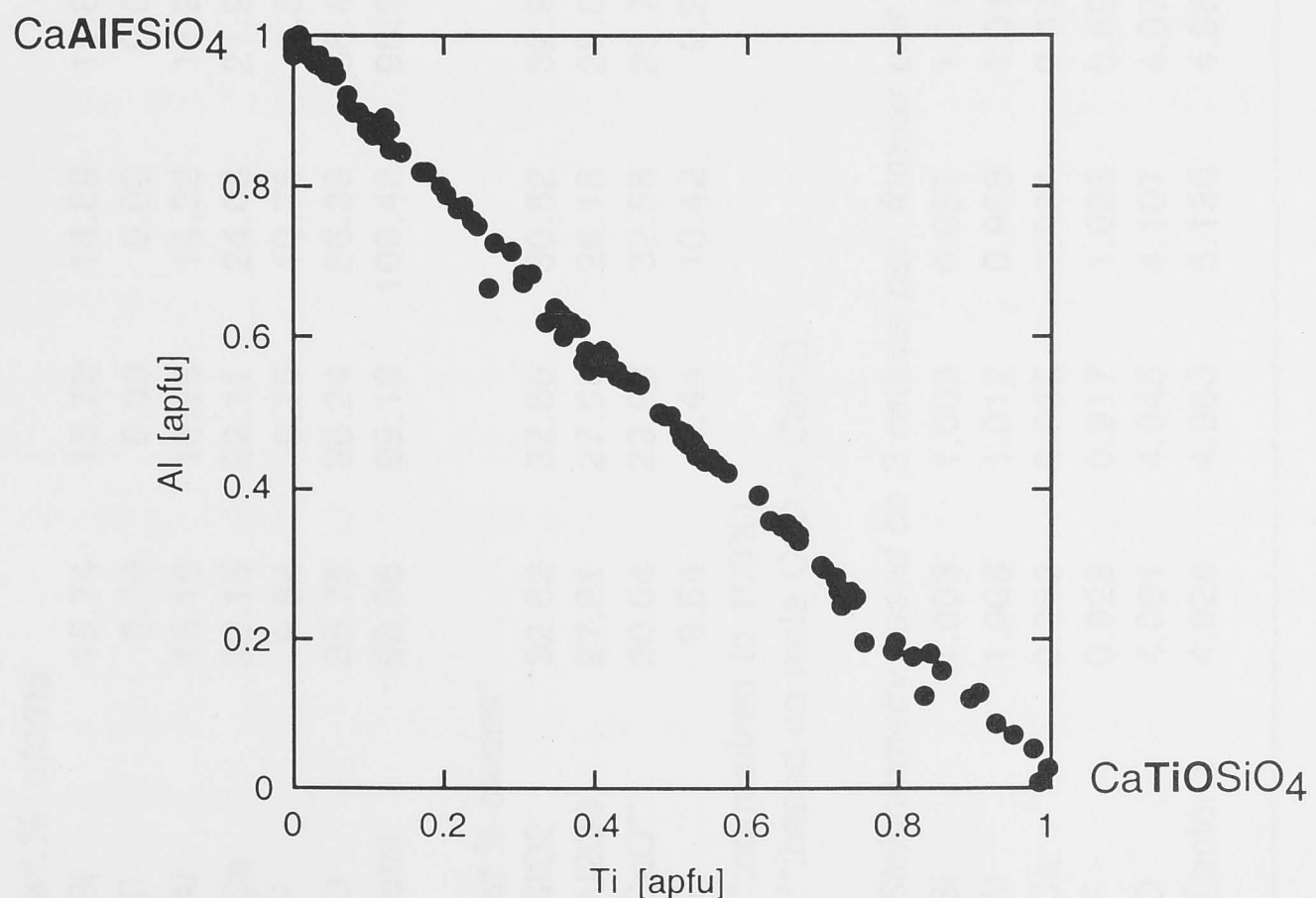
Figure 2.5 Compositional variation of synthetic binary titanite, $Ca(Ti,Al)(O,F)SiO_4$, with respect to the two end-members, based on experimental results of this study. Shown is the amount of Ti and Al atoms per formual unit (apfu).

Table 2.2 Representative selection of SEM analyses of CaAlFSiO$_4$ from sample G-297.

wt.% atoms

Si	15.74	15.78	14.89	15.88	15.76	15.78	15.75	15.56	15.59	15.92	15.74	15.37
Ti	0.00	0.00	0.00	0.00	0.00	0.00	0.00	0.00	0.00	0.00	0.00	0.00
Al	15.18	15.28	14.32	15.26	15.19	15.00	15.22	14.96	15.08	15.36	15.22	15.06
Ca	22.15	22.11	24.06	21.90	22.35	22.12	22.01	22.67	22.45	22.20	22.39	22.72
F	9.84	9.75	10.76	9.53	9.88	9.63	10.33	10.13	9.81	10.22	9.76	10.31
O	35.75	36.24	36.39	36.41	36.44	36.05	36.53	36.38	36.02	36.71	36.06	36.22
total	98.66	99.16	100.42	98.98	99.62	98.58	99.84	99.70	98.95	100.41	99.17	99.68

wt.% oxides*

SiO2	32.62	32.66	30.82	32.99	32.56	32.89	32.54	32.19	32.35	32.63	32.53	31.79
Al2O3	27.81	27.96	26.18	28.01	27.71	27.60	27.76	27.34	27.65	27.82	27.78	27.50
CaO**	30.04	29.93	32.58	29.75	30.19	30.14	29.74	30.68	30.49	29.75	30.27	30.74
F	9.54	9.44	10.42	9.26	9.54	9.37	9.97	9.79	9.52	9.79	9.43	9.97

(*:normalized to 100%)

(**:based on mole CaO + CaF2)

Stoichiometry based on 3 cations per fomuar unit

Si	1.003	1.003	0.957	1.011	1.001	1.010	1.005	0.993	0.994	1.006	0.999	0.982
Al	1.008	1.012	0.958	1.012	1.004	0.999	1.011	0.994	1.002	1.011	1.005	1.001
Ca	0.989	0.985	1.084	0.977	0.995	0.992	0.984	1.014	1.004	0.983	0.996	1.017
F	0.928	0.917	1.023	0.897	0.928	0.910	0.974	0.955	0.925	0.955	0.916	0.974
O	4.001	4.045	4.107	4.070	4.063	4.049	4.092	4.076	4.035	4.074	4.016	4.061
Σanions	4.928	4.963	5.130	4.967	4.990	4.959	5.066	5.031	4.960	5.028	4.932	5.034

2.4.2 CaAlFSiO₄ synthesis

The results of three experiments carried out under comparable run conditions (G-295 to G297, Table 2.1) are identical. They consist of a mixture of $CaAlFSiO_4$ (>70 wt.%), F-rich zoisite (<20 wt.%), fluorite (<10 wt.%) and traces of kyanite. The formation of $CaAlFSiO_4$ and F-rich zoisite in the experiments can be described by the reactions

$$CaF_2 + CaAl_2Si_2O_8 = 2\ CaAlFSiO_4 \tag{2.3}$$
$$\text{Fluorite} + \text{Anorthite} = CaAlFSiO_4$$

and

$$CaF_2 + 3\ CaAl_2Si_2O_8 = 2\ Ca_2Al_3Si_3O_{12}F \tag{2.4}$$
$$\text{Fluorite} + \text{Anorthite} = \text{Fluor-zoisite}$$

The composition of the synthetic $CaAlFSiO_4$ is close to ideal with a deviation of less than 0.05 apfu per cation of all analyses from the end-member composition (Table 2.2). The average chemical formula from 23 SEM analyses of $CaAlFSiO_4$ calculated on the basis of three cations is $Ca_{1.013}Al_{0.990}F_{0.986}Si_{0.996}O_{3.938}$.

The formation of zoisite under anhydrous conditions was unexpected, because to my knowledge the existence of F-rich zoisite has never previously been reported in the literature. The average structural formula for zoisite synthesised in this study is $Ca_{2.06}Al_{2.94}Si_{3.00}O_{12.48}F_{0.43}$. It was calculated from 17 SEM analyses on the basis of 8 cations. The surplus of O^{2-} and deficiency of F^- compared to the ideal formula as used in reaction 2.4, together with a charge unbalance of -0.46 for this chemical formula, suggests the presence of about 0.46 apfu H^+ in the form of OH^-. This changes the above formula to $Ca_{2.06}Al_{2.94}Si_{3.00}O_{12.02}F_{0.43}OH_{0.46}$. Water contamination of the supposedly dry experiments is possible. Even though the starting mix was dried inside the open capsules at 110°C before welding, water contamination cannot be excluded entirely during the subsequent welding process which involves cooling of the capsule using water-soaked tissue paper. Note that for 140 mg sample it requires only 0.00014 g of water contamination to account for 10% of the product to be the above zoisite composition. The formation of F-rich zoisite (reaction 2.4) instead of $CaAlFSiO_4$ (reaction 2.3) accounts for the presence of 'left-over' fluorite in the run product. The presence of kyanite in the reaction products indicates slight deviation of the starting mix from ideal composition.

It is possible that F-rich zoisite and fluorite in these experiments are metastable, and only persist because of nucleation problems of $CaAlFSiO_4$, or incomplete reaction due to slow diffusion rates. A high activation energy for nucleation of $CaAlFSiO_4$ is

suggested by the fact that mixes without seeds react to form F-rich zoisite and fluorite, whereas seeded mixes react to form up to 100% $CaAlFSiO_4$ (Figure 2.3a and b). Incomplete reaction could be suggested by the textures of the reaction products. Fluorite and F-rich zoisite are typically preserved as isolated grains surrounded by $CaAlFSiO_4$. The stability of F-rich zoisite is discussed in the light of thermodynamic data for $CaAlFSiO_4$ and fluor-zoisite in Chapter 6.

The intimate intergrowth of the individual $CaAlFSiO_4$ grains in the samples limits the development of crystal faces, which therefore cannot be used to gain insight into the symmetry or crystal structure of $CaAlFSiO_4$. Neither larger sample aggregates nor slightly crushed sample particles revealed clear crystal morphologies for $CaAlFSiO_4$ when investigated with SEM. Only two images were obtained from crystal fragments which display any faces (Figure 2.6). These $CaAlFSiO_4$ fragments, however, resemble titanite grains, thus suggesting related crystal structures.

2.4.3 $CaAlFSiO_4$ structure

2.4.3.1 Space group

The X-ray powder diffraction pattern of $CaAlFSiO_4$ (Figure 2.7) is comparable to that of titanite (space group $P2_1/a$) and Al-rich titanite (space group $A2/a$; Higgins and Ribbe, 1976), suggesting a similar structure. Space group $A2/a$ was confirmed for $CaAlFSiO_4$ by the absence of hkl, $k + l = 2n + 1$ reflections from the diffraction pattern of zone [102] (Figure 2.8a) (Higgins and Ribbe, 1976; Speer and Gibbs, 1976). Also, the absence of hkl, $k + l = 2n + 1$ reflections from the diffraction pattern of zone [102] is consistent with space group $A2/a$ (Figure 2.8b).

2.4.3.2 Crystal structure

The refinement result is shown in Figure 2.7, with $R_{wp} = 10.05$, $R_e = 6.62$, $S = 1.51$, and $R_B = 3.66$, as defined in Young (1993). The unit cell dimensions of $CaAlFSiO_4$, atom coordinates, bond-lengths and -angles and other structural information are summarised in Tables 2.3 to 2.5. In Table 2.6 the most intensive reflections are listed, and the calculated and observed intensities for Cu $K\alpha_1$ and Cu $K\alpha_2$ radiation compared. Note that in the diffraction pattern presented here (Figure 2.7) the Cu $K\alpha_1$ and Cu $K\alpha_2$ reflections are only resolved as seperate peaks for d-spacings smaller than ~1.9 Å.
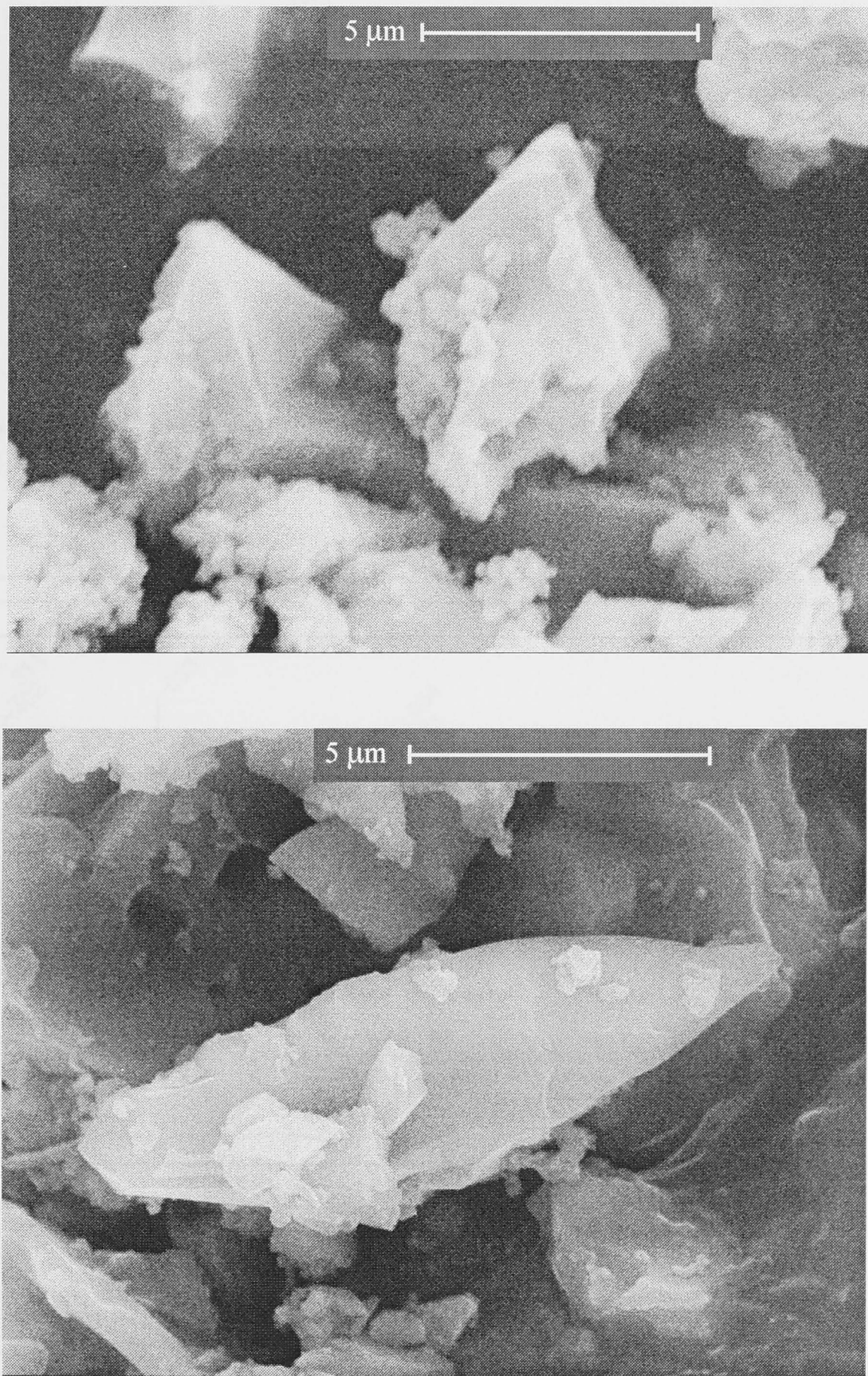
Figure 2.6 Scanning electron micrographs of CaAlFSiO₄ (sample G-297).
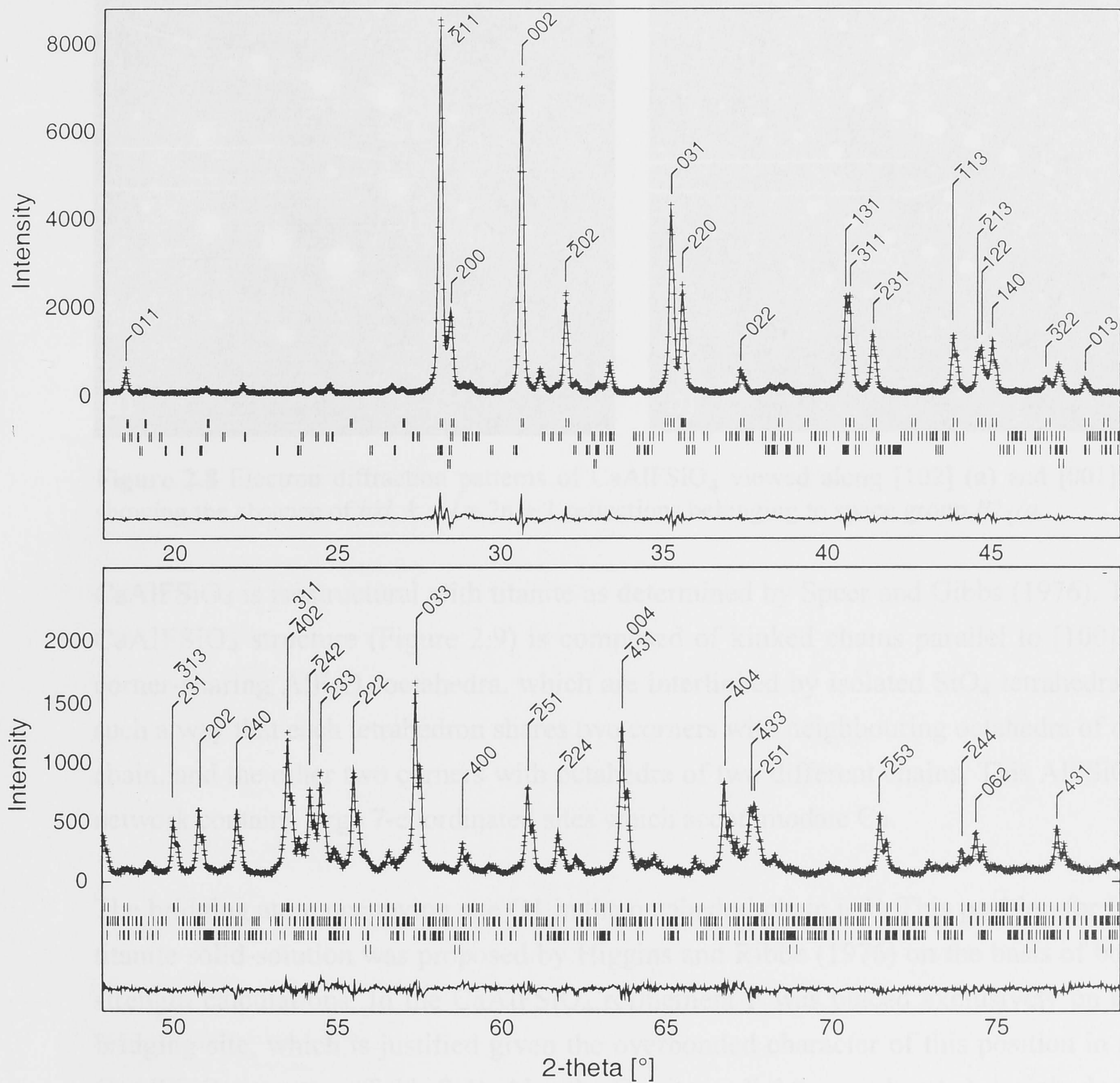
Figure 2.7 X-ray powder diffraction pattern and Rietveld refinement result of CaAlFSiO₄ with traces of zoisite, kyanite and fluorite (sample G-297). Crosses represent the raw diffraction data, the upper solid curve is the calculated trace, and the lower solid curve shows the difference between the two. Positions of all *hkl* reflections are indicated by vertical bars (four rows from top to bottom: CaAlFSiO₄, Zoisite, Kyanite, Fluorite), major reflections of CaAlFSiO₄ are indexed. Note the difference in scale between the two parts of the figure.
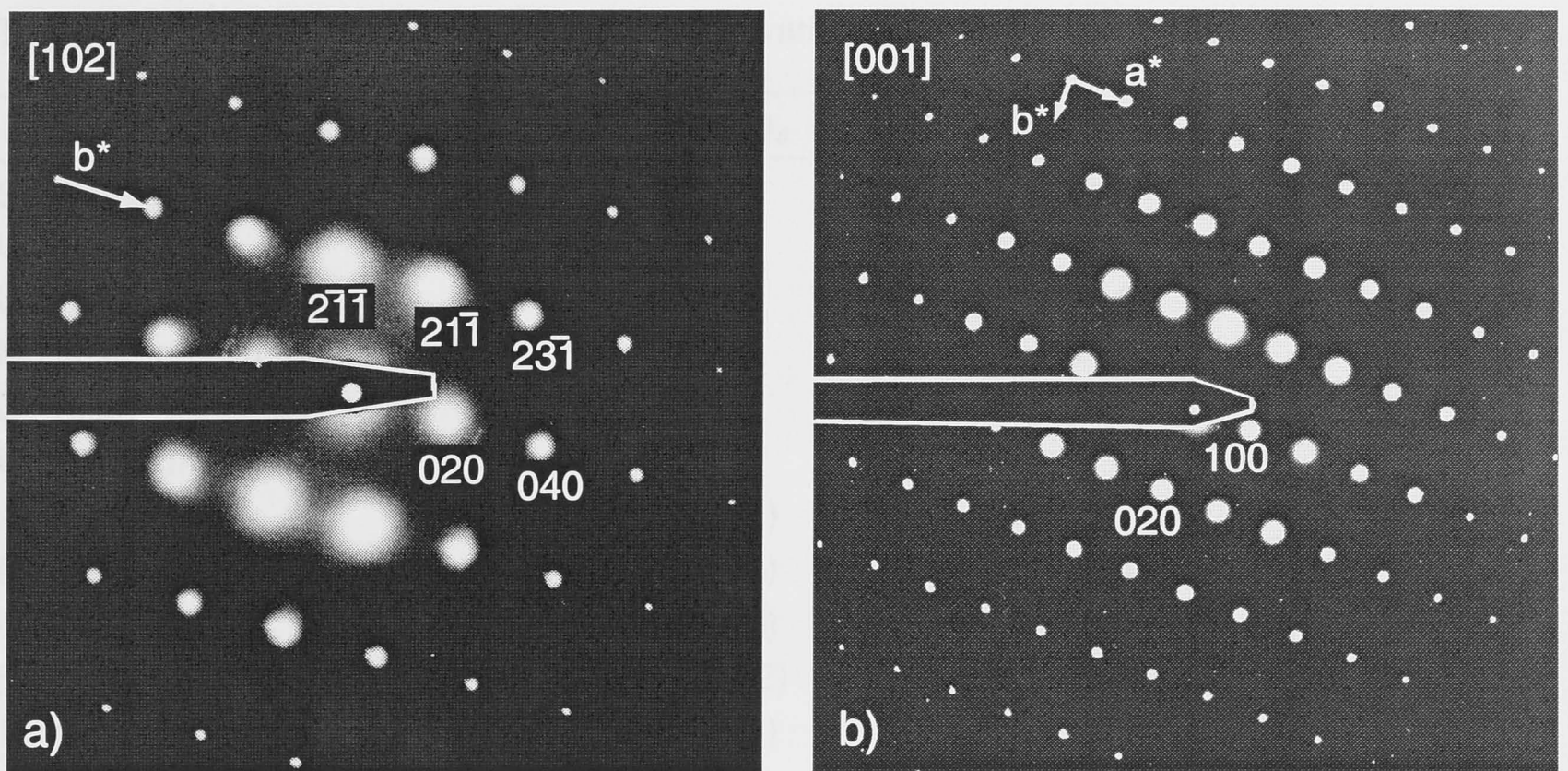
Figure 2.8 Electron diffraction patterns of $CaAlFSiO_4$ viewed along [102] **(a)** and [001] **(b)**, showing the absence of hkl, $k + l = 2n + 1$ reflections belonging to space group $P2_1/a$.

$CaAlFSiO_4$ is isostructural with titanite as determined by Speer and Gibbs (1976). The $CaAlFSiO_4$ structure (Figure 2.9) is composed of kinked chains parallel to [100] of corner-sharing AlF_2O_4 octahedra, which are interlinked by isolated SiO_4 tetrahedra in such a way that each tetrahedron shares two corners with neighbouring octahedra of one chain, and the other two corners with octahedra of two different chains. This $AlFSiO_4$-network contains large 7-coordinated sites which accommodate Ca.

The bridging atom occupying site O1 in the octahedral chain is F. This position for F in titanite solid-solution was proposed by Higgins and Ribbe (1976) on the basis of bond strength calculations. In the $CaAlFSiO_4$ refinement F was placed exclusively on this bridging-site, which is justified given the overbonded character of this position in the $CaAlFSiO_4$ structure (Table 2.4). Also the Ca-site is slightly overbonded, mainly due to shortening of the Ca-O2 bond (Table 2.5) by about 0.1 Å compared to those in titanite (Kek et al., 1997, Table 11). The bond valence sums for all other sites are close to ideal values, which supports our structural model.

The unit-cell volume of $CaAlFSiO_4$ is 7% smaller than that of titanite (Table 2.3), which is consistent with the smaller ionic raidus of Al compared to Ti, and in agreement with the predominant occurrence of Al-rich titanite in high-pressure and low-temperature rocks. The unit-cell volume and density of $CaAlFSiO_4$ are very similar to those of the mineral vuagnatite (342.5 $Å^3$ and 3.42 gcm^{-3}, respectively), which has the composition of the hypothetical AlOH-end-member, but a different crystal structure. A more detailed comparison and discussion of crystal structures of the two end-members $CaTiOSiO_4$ and $CaAlFSiO_4$, as well as intermediate compositions, is given in Chapter 3.

Table 2.3 Selected crystal structure data of synthetic $CaAlFSiO_4$ and titanite*.

	$CaAlFSiO_4$	$CaTiOSiO_4$
Space group	A2/a	$P2_1/a$
Unique axis	b†	b
Unit-cell content	Z = 4	Z = 4
Molar weight (gmol⁻¹)	178.14	196.02
D (gcm⁻³)	3.437	3.517
Unit cell dimensions		
a (Å)	6.9157(2)	7.0697(3)
b (Å)	8.5076(1)	8.7223(4)
c (Å)	6.4391(2)	6.5654(4)
β (°)	114.683(2)	113.853(4)
V (Å³)	344.24(2)	370.27(3)
Octahedron		
Mean oct-O bond (Å)	1.874	1.959
Mean O-O bond (Å)	2.651	2.768
V (Å³)	8.767	9.971
Quadratic elongation	1.0014	1.0058
Angle variance	2.149	-
Oct-O1-oct angle (°)	142.3	141.8‡
Tetrahedron		
Mean Si-O bond (Å)	1.623	1.647
Mean O-O bond (Å)	2.649	2.688
V (Å³)	2.175	2.282
Quadratic elongation	1.0064	1.0033
Angle variance	22.234	12.566

Notes: Sites occupied by fluorine or oxygen are represented by "O", the octahedral cation by "Oct". Bond lengths, angles, polyhedral volumes, quadratic elongation and angle variance were calculated with the program VOLCAL (Hazen and Finger 1982). Errors of unit cell parameters of $CaAlFSiO_4$ as given by the program RIETAN (Izumi, 1993; Kim and Izumi, 1994).
* Refined by Kek et al. (1997)
† Non-standard setting was chosen for comparison with titanite.
‡ Speer and Gibbs (1976)

Table 2.4 Fractional atomic coordinates, isotropic thermal parameters (B_{iso} in Å²) and bond-valence sums (BVS) of synthetic $CaAlFSiO_4$.

site	atom	x	y	z	B_{iso}	BVS*
Ca	Ca	1/4	0.1642(2)	0	1.34(7)	2.18
Al	Al	1/2	0	1/2	1.40(7)	2.99
Si	Si	3/4	0.1867(4)	0	1.03(7)	4.01
O1	F	3/4	0.0694(5)	1/2	0.56(6)	1.25
O2	O	0.9048(5)	0.0662(4)	0.1877(5)	0.56(6)	1.96
O3	O	0.3898(5)	0.2020(4)	0.4054(6)	0.56(6)	2.01

*Calculated with the program EUTAX (Brese and O'Keeffe, 1991)
Note: Errors as given by the program RIETAN (Izumi, 1993; Kim and Izumi, 1994), see text.
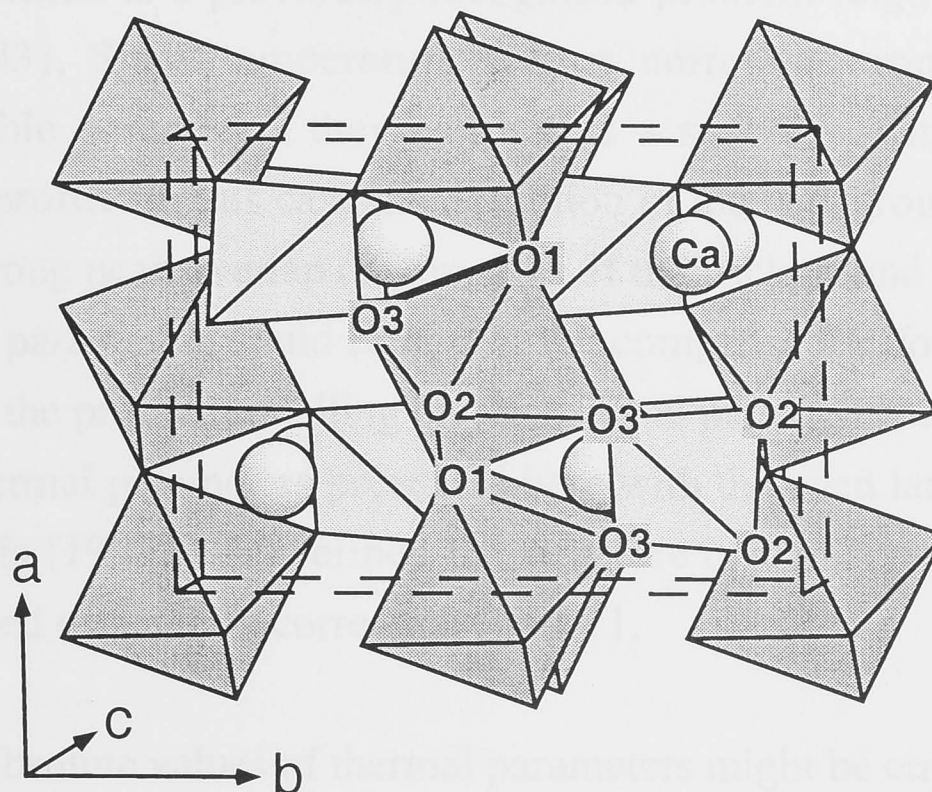
Figure 2.9 Polyhedral representation of a section of the crystal structure of CaAlFSiO₄. Stippled lines show unit-cell boundaries. Octahedra are occupied by Al, tetrahedra by Si, and the O1-site by F. Drawn with computer program ATOMS (Dowty, 1993).

Table 2.5 Selected bond lengths and angles of synthetic CaAlFSiO₄.

	bond lengths (Å)	angles on Al (°)		bond lengths (Å)	angles on Si (°)
Octahedron			Tetrahedron		
Al-O1 x2	1.827(1)		Si-O2 x2	1.605(4)	
Al-O2 x2	1.920(3)		Si-O3 x2	1.642(5)	
Al-O3 x2	1.876(4)		O2-O2'	2.471(6)	100.6
O1-O2 x2	2.643(3)	89.7	O2'-O3 x2	2.716(5)	113.5
O1-O2' x2	2.658(4)	90.3	O2-O3' x2	2.655(5)	109.7
O1-O3 x2	2.566(6)	87.7	O3-O3'	2.682(8)	109.6
O1-O3' x2	2.670(5)	92.3	Ca[7]-site		
O2-O3 x2	2.666(5)	89.2	Ca-O1	2.267(5)	
O2-O3' x2	2.703(5)	90.8	Ca-O2 x2	2.317(4)	
			Ca-O3 x2	2.397(3)	
			Ca-O3' x2	2.570(4)	

2.4.3.3 Thermal parameters

The large absolute values of the thermal parameters of the cations are unrealistic (Table 2.4). For comparison, isotropic atomic displacement parameters determined with single-crystal X-ray diffractometry for an Al-rich titanite $X_{Al}=0.36$ by Oberti et al. (1991, sample HEL697) are 1.15 (Ca), 1.00 (oct), 0.41 (Si), 0.66 (O1), 0.66 (O2), 0.59 (O3). Note that the errors obtained from the Rietveld refinement (Table 2.4) are probably

underestimated, which is a previously recognised problem (e.g., Sakata and Cooper, 1979; Scott, 1983). Since temperature factors correlate strongly with other 2θ-dependent refinable parameters they can act as a sink for systematic errors in the modelling of the profile. In this case the definition of the background at high angle was difficult due to strong peak overlap (Figure 2.7). If the background was chosen too high, the large thermal parameters could represent the compensation for this mismatch. The effect of errors in the profile modelling on the thermal parameters is demonstrated when comparing the thermal parameters presented here with the even larger ones reported by Troitzsch and Ellis (1999), who refined the structure of the same sample, but without applying a preferred orientation correction for -111.

Even though the absolute values of thermal parameters might be erroneous, their relative values are significant. While the relative magnitudes of the thermal parameters of Ca, O1, O2 and O3 in $CaAlFSiO_4$ are comparable to titanite, those of Al and Si seem too high. High thermal parameters for Al and Si could be caused by some disordering in the octahedral and tetrahedral sites, resulting in local distortion of the crystal lattice. Diffuse scattering in the electron diffraction patterns which could indicate such disorder, however, could not be observed. A single crystal diffraction study is necessary in order to obtain more reliable information about the thermal motion of the atoms and possible chemical and displacive disorder in the structure of $CaAlFSiO_4$.

2.4.3.4 Polyhedral distortion

While the AlF_2O_4 octahedron in $CaAlFSiO_4$ is quite regular, the SiO_4 tetrahedron is very distorted. It has one very short edge (O2-O2 = 2.478 Å), two short and two long Si-O bonds (Si-O2 = 1.605 Å, Si-O3 = 1.642 Å), a small O2-Si-O2 angle (100.6°), and large angle variance and quadratic elongation values (Hazen and Finger, 1982) (Table 2.3). This is surprising, because SiO_4 tetrahedra generally behave as rigid units which hardly deviate from ideal bond lengths and angles, whereas octahedra deform more easily. While a short O2-O2 edge and a small O2-Si-O2 angle of the tetrahedron is typical for most minerals in the titanite structure, uneven Si-O bonds as described above are unusual for this group. It should be noted that the Si-O bonds in $CaAlFSiO_4$ proved to be very sensitive to the addition of new parameters to the refinement, and therefore have large relative errors attached to them. For example, the consideration of the preferred orientation correction for -111 in the refinement presented in this chapter, changed the Si-O2 and Si-O3 bonds as originally presented by Troitzsch and Ellis (1999) without this correction [1.603(4) Å and 1.653(4) Å] to the corrected values of 1.605(4) Å and 1.642(5) Å. Thus the tetrahedral distortion in $CaAlFSiO_4$ is slightly less pronounced than described by Troitzsch and Ellis (1999).

Table 2.6 Observed (I_{obs}) and calculated (I_{calc}) intensities of the most important reflections of CaAlFSiO₄ for Cu Kα_1 and Cu Kα_2 radiation.

h	k	l	d [Å]	$I_{obs}\,\alpha_1$	$I_{calc}\,\alpha_1$	$I_{obs}\,\alpha_2$	$I_{calc}\,\alpha_2$
0	1	1	4.8208	4.2	4.4	2.1	2.2
-2	1	1	3.1799	100.0	97.8	49.8	48.7
2	0	0	3.1419	18.7	18.2	9.3	9.1
0	0	2	2.9254	83.6	81.3	41.6	40.4
-2	0	2	2.8029	25.8	26.6	12.7	13.2
0	3	1	2.5519	52.3	53.6	26.0	26.6
2	2	0	2.5273	29.1	29.8	14.5	14.8
0	2	2	2.4104	6.0	5.6	3.0	2.8
1	3	1	2.2272	27.3	27.9	13.6	13.9
-3	1	1	2.2206	15.8	16.1	7.8	8.0
-2	3	1	2.1852	19.2	19.5	9.5	9.7
-1	1	3	2.0677	16.1	15.1	7.9	7.5
-2	1	3	2.0339	12.6	12.0	6.3	6.0
1	2	2	2.0291	7.8	7.5	3.9	3.7
1	4	0	2.0146	17.3	16.6	8.5	8.2
-3	2	2	1.9472	4.5	4.4	2.2	2.2
0	1	3	1.9010	4.7	4.6	2.3	2.3
2	3	1	1.8249	5.9	6.4	2.9	3.2
2	0	2	1.7989	7.4	8.0	3.7	4.0
2	4	0	1.7613	7.6	8.0	3.8	4.0
3	1	1	1.7172	3.1	3.1	1.5	1.5
-4	0	2	1.7142	17.6	17.4	8.8	8.6
-1	3	3	1.7039	3.6	3.5	1.8	1.8
-2	4	2	1.6943	10.9	10.7	5.4	5.3
-2	3	3	1.6849	11.2	11.0	5.6	5.5
2	2	2	1.6568	15.1	14.3	7.5	7.1
0	3	3	1.6069	25.5	24.3	12.8	12.1
4	0	0	1.5710	4.2	3.8	2.1	1.9
-2	5	1	1.5241	14.1	13.2	6.9	6.6
-2	2	4	1.5037	5.8	5.6	2.9	2.8
0	0	4	1.4627	5.8	5.8	2.9	2.9
-4	3	1	1.4619	19.2	19.1	9.6	9.5
-4	0	4	1.4015	14.8	15.1	7.3	7.5
-4	3	3	1.3869	6.7	7.0	3.3	3.5
-2	5	3	1.3207	9.3	10.2	4.6	5.1
-2	4	4	1.2824	2.3	2.4	1.2	1.2
0	6	2	1.2760	6.0	6.3	3.0	3.1
4	3	1	1.2407	8.8	8.8	4.4	4.4
4	0	2	1.1920	4.7	4.0	2.4	2.0
-3	2	6	1.0392	3.1	2.6	1.5	1.3
-4	3	5	1.1142	3.4	3.2	1.7	1.6
-6	2	2	1.1103	4.2	4.0	2.1	2.0
2	7	1	1.0828	3.3	3.2	1.6	1.6
0	3	5	1.0817	5.1	4.9	2.6	2.5

In order to double-check the coordinates of our structure model, the refinement was repeated with hard constraints on the Si-O (1.624 Å) and O-O bond lengths (2.652 Å) of the tetrahedron. When the constraints were softened at the end of the refinement process, all atoms moved back to the positions forming the distorted tetrahedron. Since the overall fit (R_{wp}) improved by several percent after releasing the constraints, the distortion of the tetrahedron in $CaAlFSiO_4$ at room pressure and temperature seems to be real. Bond valence sums calculated for the same structure, but with Si located at the equidistant point of the tetrahedron, are 2.13 (Ca), 3.94 (Si), 1.88 (O2), 2.05 (O3), (those of the Al- and O1-site remain unchanged, Table 2.5). This shows that off-centring of Si improves the bond valence sums of all tetrahedral atoms, but slightly worsens that of Ca.

Hammonds et al. (1998) suggested that due to the absence of rigid unit modes from the titanite structure, formation of solid-solutions in this structure requires distortion of the polyhedra to accommodate cations of different size. This is consistent with the distortion of the tetrahedron in $CaAlFSiO_4$, but does not explain why in this case only the tetrahedra appear to take up the strain.

Kunz et al. (1997), who investigated crystal structural changes along the join $CaTiOSiO_4$ - $CaSnOSiO_4$ [malayaite], proposed that a considerable amount of steric strain exists in the titanite structure. This statement was partly based on the observation that the Si-O bonds in titanite are longer (~1.64 Å) than a typical Si-O bond for silicates, suggesting that "the otherwise very dominant Si-O bonds are not able to fully overcome the rigidness of the CaO_7-TiO_6 framework". This conclusion drawn by Kunz et al. (1997) is in good agreement with the distorted tetrahedron in $CaAlFSiO_4$ reported in this study.

2.5 Conclusions

The synthesis of the end-member $CaAlFSiO_4$ and titanite solid-solution with $X_{Al} \gg 0.5$ shows that these inorganic compounds are not 'impossible' structures, and thus that there is no crystal structural constraint which precludes their existence as such.

The data presented in this chapter help understanding the F and OH content of natural Al-rich titanites. While $CaAlFSiO_4$ has a very similar crystal structure to titanite, thus permitting solid-solution to any degree, the pure AlOH-component is stable in a different crystal structure represented by the mineral vuagnatite, indicating that the titanite structure can only accommodate a limited amount of $CaAlOHSiO_4$. Previous

studies of natural (Enami et al., 1993; Franz and Spear, 1985) and synthetic titanite (Hellman and Green, 1979) reported maximum contents of CaAlOHSiO$_4$ of about 30 mol%. Thus very Al-rich titanites have to be dominated by the AlF-component, whereas those with lower Al-contents can be dominated by either the AlOH- or the AlF-component. This is in agreement with previous studies of natural titanite as shown in Figure 2.1.

A number of questions arise from the synthesis of titanite along the entire binary join: Do the limits of X$_{Al}$ in most natural titanites and that of Smith's (1981) experiments coincide by accident, or are they due to an underlying physical reality? How does the stability of titanite change along the join TiO-AlF? Are there any crystal structural constraints which might have a negative effect on the thermodynamic stability of Al-rich titanite with respect to other phases? In the following chapters the attempt is made to address these questions in two ways: 1) The crystal structural changes in titanite along the join TiO-AlF are investigated, and 2) The thermodynamic properties and mixing behaviour of Al-bearing titanite are studied with high-pressure and -temperature experiments.

Chapter 3

Crystal structural changes in titanite along the join TiO-AlF

3.1 Abstract

The crystal structural changes in titanite solid-solution $Ca(Ti,Al)(O,F)SiO_4$ along the binary join TiO-AlF were investigated on the basis of X-ray powder data and Rietveld refinement of 13 synthetic titanites of intermediate compositions, as well as the end-members titanite and $CaAlFSiO_4$. Investigations with the transmission electron microscope allow to narrow down the space group transition from $P2_1/a$ (end-member $CaTiOSiO_4$) to $A2/a$ (end-member $CaAlFSiO_4$) to compositions between $X_{Al} = 0.09$ and $X_{Al} = 0.18$ [$X_{Al} = Al/(Al+Ti)$]. The changes in all unit-cell dimensions along the binary join are non-linear, resulting in a small excess volume of mixing with a maximum at $X_{Al} = 0.57$. The commonly observed trend of positive deviation of the excess volume of mixing near the large end-member, and negative deviation towards the small end-member (Newton and Wood, 1980) is reversed in this case. The a dimension shows unusual behaviour at very low Al-contents, as it increases with X_{Al} between $X_{Al} = 0.05$ and $X_{Al} = 0.10$, despite the increasing amount of smaller ions Al. This can probably be linked to the $P2_1/a$ - $A2/a$ phase transition. At AlF-contents larger than $X_{Al} = 0.6$, the Ca-site and the O1-site in the titanite structure become increasingly overbonded with Al-F substitution. At about $X_{Al} = 0.4$, the octahedral cation-oxygen distances change significantly, indicating that the titanite structure undergoes a major atomic rearrangement at high AlF-contents in order to accommodate the increasingly different ionic size and charge.

Generally, with increasing AlF content the polyhedra are being deformed rather than rotated. The changes in unit-cell dimensions, bond lengths and bond valence sums along the binary join suggest the presence of structural strain in AlF-rich titanite, especially at Al-F contents exceeding $X_{Al} = 0.4$. The structural problems are obviously not significant enough to prevent the formation of Al-rich titanite in simple chemical systems as in these experiments. However, the structural stresses may be significant enough to decrease the thermodynamic stability of Al-rich titanite in natural rocks compared to other Al- and F-bearing phases. This could partly explain the rare natural occurrence of titanite with $X_{Al} > 0.54$.

3.2 Introduction

It was demonstrated in Chapter 2 that the solubility of Al in natural titanite appears to be mostly restricted to $X_{Al} < 0.54$, which is consistent with the synthetic titanite reported by Smith (1981). This led to the suggestion by previous workers (e.g., Oberti et al., 1991) that the titanite structure cannot accomodate more than about 50 mol.% of any Al-end-member due to crystal structural limitations. Oberti et al. (1991) investigated the crystal structures of natural Al-rich titanites, and discussed the possibility of a crystal structural constraint in detail, but the potential structural problems in titanite with increasing Al-content could not be identified. Because their study relied on natural titanite samples restricted to lower Al-contents ($0.0 < X_{Al} < 0.36$), the interpretations by Oberti et al. (1991) regarding the crystal structural constraint was based on extrapolation of the data to higher Al-contents. In an earlier crystal structure study of natural titanites, Cerny and Sanseverino (1972) reported changes in unit cell dimensions of titanite with increasing Al and F/OH substitution. However, their titanite samples contained less than 11 mol.% of any Al-endmember, and various amounts of other substituents such as Fe and Mg, so that their data are not suited for an investigation of the structural changes along the binary join TiO-AlF. The samples investigated by Higgins and Ribbe (1976), with less than $X_{Al} = 0.21$, suffer similar drawbacks.

As stated in Chapter 2, the existence of complete solid-solution in synthetic binary° titanite along the join $CaTiOSiO_4$ - $CaAlFSiO_4$ (Troitzsch and Ellis, 1999) seems to refute the hypothesis of a crystal structural constraint. With the synthesis methods for Al-rich titanite described in the last chapter, the opportunity exists for the first time to study the crystal structural changes in titanite with increasing X_{Al} beyond 54 mol.%.

In this chapter crystal structure data are presented from synthetic samples covering the entire range of compositions of binary titanite solid-solution $Ca(Ti,Al)(O,F)SiO_4$. The samples are labeled AlF00, AlF09, AlF18, AlF29, etc. with respect to their Al-content ($X_{Al} = 0.00, 0.09, 0.18, 0.29$, etc., where $X_{Al} = Al/(Al+Ti)$). In addition to the samples which were discussed by Troitzsch et al. (1999), five additional samples with low Al-contents are included here, which were originally synthesised for calorimetric measurements (Chapter 4) during a later stage of this doctoral study. Only the unit cell dimensions of these samples were determined. These additional data significantly improve the resolution of the structural information at $X_{Al} < 0.25$ compared to Troitzsch et al. (1999), especially with respect to the changes of dimension a. The data from the end-member $CaAlFSiO_4$, which were already discussed in Chapter 2, are shown again to facilitate comparison.
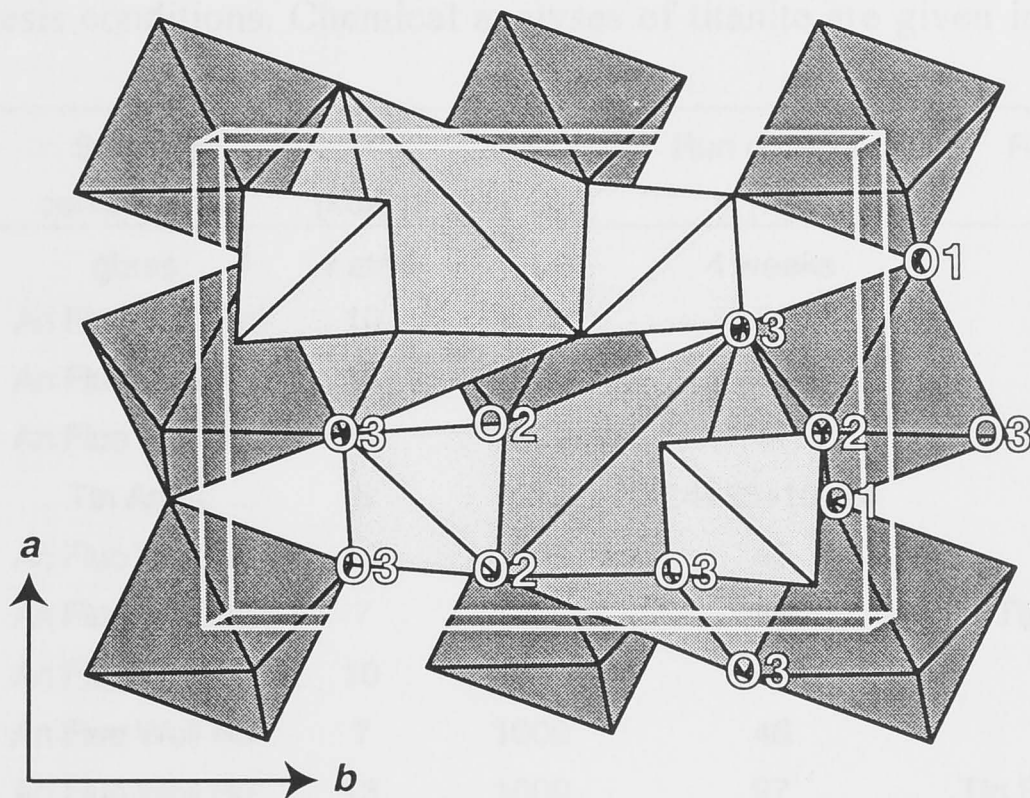
Figure 3.1 Polyhedral representation of a section of the titanite structure, showing the geometrical relationship between the Al/Ti-octahedra, Si-tetrahedra and $Ca^{[7]}$-polyhedra. O1 is occupied by oxygen or fluorine.

3.3 Crystal structure

The titanite structure (Figure 3.1) is composed of kinked chains of edge-sharing octahedra parallel to *a*, which are interlinked by isolated SiO_4-tetrahedra (Speer and Gibbs, 1976). This network encloses the $Ca^{[7]}$-sites, which form chains of edge-sharing polyhedra interlacing with the octahedral chain (Kunz et al., 1997). Along the binary join TiO-AlF, titanium in the octahedron together with the oxygen occupying the O1-site are replaced by aluminium and fluorine, respectively ($Ti^{4+} + O^{2-} = Al^{3+} + F^-$).

3.4 Experimental details

3.4.1 Synthesis

Since the substitution of Al and F in the titanite structure is facilitated by high pressures, the titanite samples used in this study were synthesised in the piston-cylinder apparatus at various pressures ranging from 5 to 35 kbar, depending on the Al-content of each sample. Temperatures were chosen to lie below the solidus (encountered in this study), and ranged from 1000°C to 1100°C. Individual run conditions are listed in Table 3.1. The starting mixes were composed of synthetic anorthite, fluorite (Specpure), and either synthetic wollastonite and TiO_2 (Degussa), or synthetic titanite. The preparation of anorthite and titanite (sample AlF00) from glasses is described in Chapter 2.

Table 3.1 Synthesis conditions. Chemical analyses of titanite are given in Appendix 1.

Sample	No. of runs	Starting components	P [kbar]	T [°C]	Run duration [h]	Result
AlF00	1	glass	1 atm	1100	4 weeks	Ttn
AlF05	1	An Fluo Woll Ru	10	1000	52	Ttn
AlF06	1	An Fluo Woll Ru	10	1000	45	Ttn
AlF09	1	An Fluo Woll Ru	10	1000	47	Ttn
AlF10	4	Ttn An Fl	5	1075	24+33+10+24	Ttn
AlF14	1	An Fluo Woll Ru	10	1000	45	Ttn
AlF18	1	An Fluo Woll Ru	7	1000	46	Ttn Fluo
AlF23	1	An Fluo Woll Ru	10	1000	47	Ttn
AlF29	1	An Fluo Woll Ru	7	1000	46	Ttn
AlF37	1	An Fluo Woll Ru	13	1000	27	Ttn Fluo ±Ha
AlF49	1	An Fluo Woll Ru	15	1000	46	Ttn Fluo
AlF67	1	Ttn An Fluo	23	1030	24	Ttn Fluo
AlF75	2	Ttn An Fluo	24	1000	28+41	Ttn Fluo Zoi
AlF82	1	An Fluo Woll Ru	30	1000	68	Ttn Fluo Zoi
AlF100	1	An Fluo seeds	35	1100	23	Ttn Fluo Zoi Ky

Abbreviations: Ru = rutile, Woll = wollastonite, Ha = halite, and as in Table 2.1.

The glass for wollastonite synthesis was prepared from $CaCO_3$ (Specpure) and SiO_2 (Aerosil, Degussa), which were dried prior to weighing at 400°C for 4 h, and 1000°C for 18 h, respectively. The mix was ground in acetone in an agate mortar for 2 h. It was then heated from 800°C to 1600°C over the course of 8 h, held at 1600°C for 1 h, and then quenched in water. Wollastonite was then crystallised from the glass at 1100°C for 13 h. Examination of the result with optical microscopy and X-ray diffraction confirmed that only wollastonite was present, and no glass remained.

Xirouchakis et al. (1997) pointed out that titanite prepared from glass has the potential to be non-stoichiometric due to Ca- and Si-vacancies together with Si-rich and Ca-Si-rich phase impurities, and could yield unit-cell dimensions larger than those of the ideal crystal. However, their unit-cell data for titanite synthesised at sub-solidus conditions ($a = 7.062(1)$, $b = 8.716(2)$, $c = 6.559(1)$, $\beta = 113.802(9)$, $V = 369.4(3)$, Xirouchakis et al., 1997) are in very good agreement with those obtained from the glass-derived titanite that was used for starting mixes in this study (Table 3.2). This shows that titanite prepared from a glass can yield accurate unit-cell data, and that the titanite used in this study is close to ideal stoichiometry. Since all Al-bearing titanite samples of this study were synthesised at sub-solidus conditions, their unit-cell volumes should be reliable, unless there is a significant effect of the potential non-stoichiometry of the glass-derived starting mix components anorthite and wollastonite on the titanite unit-cell dimensions.

Table 3.2 Rietveld refinement results and unit-cell dimensions of synthetic titanite solid-solution. Standard deviations of chemical analyses in column 2 are given in brackets. Third column specifies impurity phases which were considered in the refinement.

sample	X_{Al}	other phases	Ttn wt.%	R_{wp}	R_{Bragg}	a [Å]	b [Å]	c [Å]	β [°]	V [Å³]
AlF00[2]	0.000(0)	-	100	11.3	4.11	7.0613(3)	8.7158(2)	6.5588(2)	113.809(2)	369.31(2)
AlF05[1,2]	0.052(6)	Q	99	10.22	3.17	7.0525(2)	8.6985(2)	6.5483(2)	113.850(2)	367.40(2)
AlF06[1,2]	0.055(6)	-	100	10.78	3.34	7.0527(3)	8.6994(2)	6.5480(2)	113.850(3)	367.44(2)
AlF09[1,2]	0.094(8)	-	100	10.99	4.48	7.0539(3)	8.6900(2)	6.5433(2)	113.920(2)	366.66(2)
AlF10	0.099(40)	AgPd Q	95	10.27	4.88	7.0541(3)	8.6925(2)	6.5445(2)	113.903(2)	366.88(2)
AlF14[1,2]	0.138(9)	-	100	12.01	7.62	7.0527(4)	8.6813(3)	6.5379(3)	113.980(3)	365.75(3)
AlF18	0.182(4)	AgPd Fluo	98	9.42	3.71	7.0511(2)	8.6722(2)	6.5325(2)	114.026(2)	364.84(2)
AlF23[1,2]	0.234(4)	-	100	10.31	4.14	7.0481(2)	8.6626(2)	6.5274(2)	114.100(2)	363.84(2)
AlF29	0.291(12)	AgPd	99	10.03	4.23	7.0462(3)	8.6529(2)	6.5231(2)	114.143(1)	362.92(2)
AlF37	0.372(4)	Fluo Ha	96	9.47	2.97	7.0368(2)	8.6360(2)	6.5135(2)	114.232(2)	360.95(2)
AlF49	0.489(7)	Fluo	99	9.00	3.58	7.0229(3)	8.6130(2)	6.5023(2)	114.344(2)	358.34(2)
AlF67	0.672(18)	Fluo Q	97	9.46	3.84	6.9904(3)	8.5759(2)	6.4798(2)	114.480(2)	353.54(2)
AlF75[2]	0.753(19)	Fluo Q Zoi	76	10.77	3.93	6.9734(3)	8.5586(2)	6.4704(3)	114.539(2)	351.29(2)
AlF82	0.819(22)	Fluo Zoi	96	11.30	5.11	6.9580(3)	8.5445(2)	6.4612(3)	114.585(3)	349.35(2)
AlF100	1.000(0)	Fluo Q Zoi Ky	84	10.05	3.66	6.9157(2)	8.5076(1)	6.4391(1)	114.683(2)	344.24(1)

[1] Samples synthesised for calorimetry

[2] Unit cell dimensions determined only

Abbreviations: Q - quartz, and as in Table 3.1

The starting mixes for the Al-titanite syntheses were ground in acetone, and about 15 mg or 150 mg of mix were filled in silver-palladium capsules ($Ag_{0.75}Pd_{0.25}$) with a diameter of either 2 or 3 mm. The capsules were then dried at 110°C for at least 1 h before welding shut. The pressure medium enclosing the capsule was boron-nitride and a surrounding salt- or salt-pyrex sleeve, with zero friction correction (Figure 2.4). The pressure readings during the experiments are precise to within 2%. The temperature was monitored by a $Pt-Pt_{90}Rh_{10}$ thermocouple, and was regulated automatically by a EUROTHERM controller. The accuracy of the temperature measurements was 5°C.

Samples AlF10 and AlF75 were crushed and re-run at the same synthesis conditions more than once (Table 3.1) because of chemical inhomogeneity of the first run products. Generally, starting mixes containing wollastonite and TiO_2 resulted in chemically more homogeneous run products, compared to mixes containing titanite. Titanite from the starting mix tended to be preserved as Ti-rich cores in an otherwise Al-rich solid-solution.

The grain size of the run products ranged from 5 to 20 μm. Apart from titanite solid-solution, all run products contained a certain amount of additional phases, including fluorite, silver-palladium, F-bearing zoisite, kyanite, and quartz (Table 3.1). The formation of fluorite and kyanite is due to slight deviations of the starting mix from the binary join. F-bearing zoisite forms from anorthite and fluorite, and its presence in these types of experiments is discussed in Chapter 2. Contamination with the capsule material silver-palladium can occur both during the run as well as afterwards, when recovering the sample by cutting open the capsule. Contamination of the sample by diffusion during the run is suggested by the presence of small interstitial particles of silver-palladium which occur in the vicinity of the capsule-wall, but are clearly detached from it. Small amounts of quartz were detected with X-ray diffraction, but could not be confirmed with scanning electron microscopy. It is therefore likely that quartz contamination occurred during grinding of the samples in an agate mortar when preparing for X-ray diffraction. In addition, one sample contained a small amount of halite, which probably represents salt-sleeve material entering the sample through a rupture in the capsule wall. Since the titanite in this sample does not contain any sodium or chlorine, the sample was used for refinement. Sample AlF75 contained almost 20 wt.% zoisite, which made the crystal structure refinement of the titanite component difficult. Therefore this sample was only used to determine unit-cell parameters.

3.4.2 SEM

Sample preparation and instrumental details are as given in Chapter 2. Between 15 and 25 titanite grains were analysed per sample. All analyses were stoichiometric binary titanite solid-solution $Ca(Ti,Al)(O,F)SiO_4$ within a precision of 0.05 apfu with respect to the cations (Appendix 1).

3.4.3 TEM

Diffraction patterns of sample AlF18 were investigated at 300 kV using a Philips EM 430T, now located at the Electron Microscopy Unit, Australian National University. For calibration details and sample preparation see Chapter 2.

3.4.4 XRD

Instrument details as given in Chapter 2. The diffraction data were collected at room temperature in four or five passes over a range of 17 to 95°2-theta, using a step width of 0.02° at a scan speed of 0.5° per minute. Due to the small amount of material, the samples had to be dispersed with acetone onto a low-background holder (oriented quartz single crystal) with a pipette. This technique has the disadvantage of increasing the effect of preferred orientation in the mounted sample. For the sample AlF82, diffraction data were also collected using a Guinier-Hägg Camera XDC-700 (Junger Instrument Sweden), with Cu $K\alpha_1$ radiation, at 40 kV, 25 mA and 30 min exposure time. The sample was pressed down onto sticky tape to enhance preferred orientation (see discussion below).

3.4.5 Rietveld refinement

Refinement of the crystal structures using the Rietveld method was carried out with the computer program RIETAN (Izumi, 1993; Kim and Izumi, 1994), using a pseudo-Voigt profile-shape function, and the "International Tables for Crystallography" (Wilson et al., 1992) as the data base. Neutral-atom scattering factors were chosen for all sites. All phases shown in Table 3.2 were included in the profile fitting. Refined non-atomic parameters include one for specimen displacement, eight background parameters, scale factors, up to 6 peak shape parameters per phase, preferred orientation, and the unit-cell parameters of titanite and silver-palladium. The occupation factors of all sites were set to 1, with the mixed occupation of the octahedral and the O1-site fixed to values obtained from the chemical analyses. Fixing the occupations is justified given that chemical analyses with the microprobe yield more reliable data compared to occupation

factors refined from a complex multi-phase powder pattern. Due to significant peak overlap at high 2-theta angles, the background was fixed before the isotropic thermal parameters were refined in order to avoid correlation problems. One global isotropic thermal parameter was refined for all anions.

If no preferred orientation (March-Dollase function) was applied in the refinement, peak intensities could not be matched well in some of the samples (e.g. AlF10 and AlF82). In order to confirm that the intensity mismatch was related to preferred orientation of the sample on the low background holder, a Guinier experiment was carried out with sample AlF82, and the relative peak intensities of both patterns compared. While the reflection geometry in the X-ray diffractometer leads to preferred diffraction of those planes which are about parallel to the preferred cleavage plane, the transmission geometry of the Guinier Camera will result in preferred diffraction of those lattice planes that are oriented perpendicular to the cleavage.

Comparison of the relative peak intensities of the Guinier pattern with those obtained with Bragg-Brentano geometry showed that in the Guinier pattern peaks -211 and -202, for example, were significantly smaller, while reflection 140 was stronger (Figure 3.2). The fact that plane 140 is about perpendicular to -211 and -202 is consistent with the hypothesis that the intensity difference between the two patterns is indeed due to preferred orientation of the crystallites in the sample, with a cleavage plane sub-parallel to reflections -211 and -202. The prominent cleavage plane of titanite is -111 (Deer et al., 1962). Since this plane has a similar orientation to -211 and -202, -111 was chosen to represent the preferred orientation plane in the Rietveld refinement. The application of this preferred orientation correction improved the overall fit of the refinement of AlF82 significantly (R_{wp} decreased from 12.29 to 11.30, and R_{Bragg} of titanite from 7.16 to 5.11), and peak intensities of the main peaks could now be matched well. Preferred orientation correction was applied only to those other samples which showed an intensity mismatch of the same peaks compared to those observed in AlF82 before the correction.

It should be pointed out that the oxygen positions O2 and O3 in sample AlF82 correlated strongly with the preferred orientation correction. The resulting Si-O bonds were especially sensitive to preferred orientation, resulting in uneven tetrahedral Si-O bonds (1.620(7) Å and 1.660(8) Å) without correction, and more reasonable bond lengths (1.636(6) Å and 1.621(7) Å) when the correction was applied.

Figure 3.3 shows the X-ray diffraction patterns and Rietveld refinement results of those samples which were used to obtain atomic parameters.
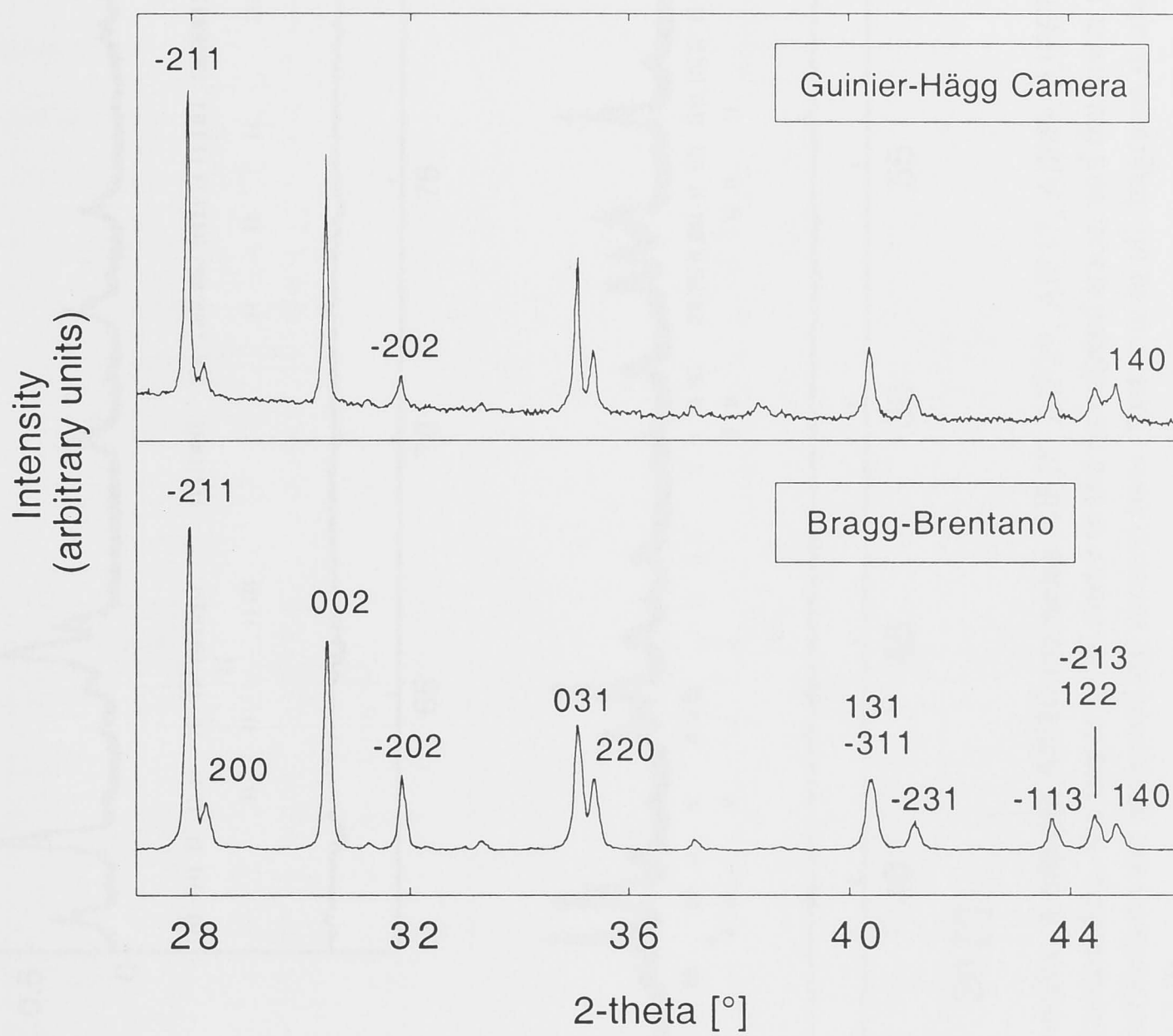
Figure 3.2   XRD profiles for sample AlF82 between 27°2-theta and 46°2-theta collected by Guinier-Hägg Camera and Bragg-Brentano geometry.
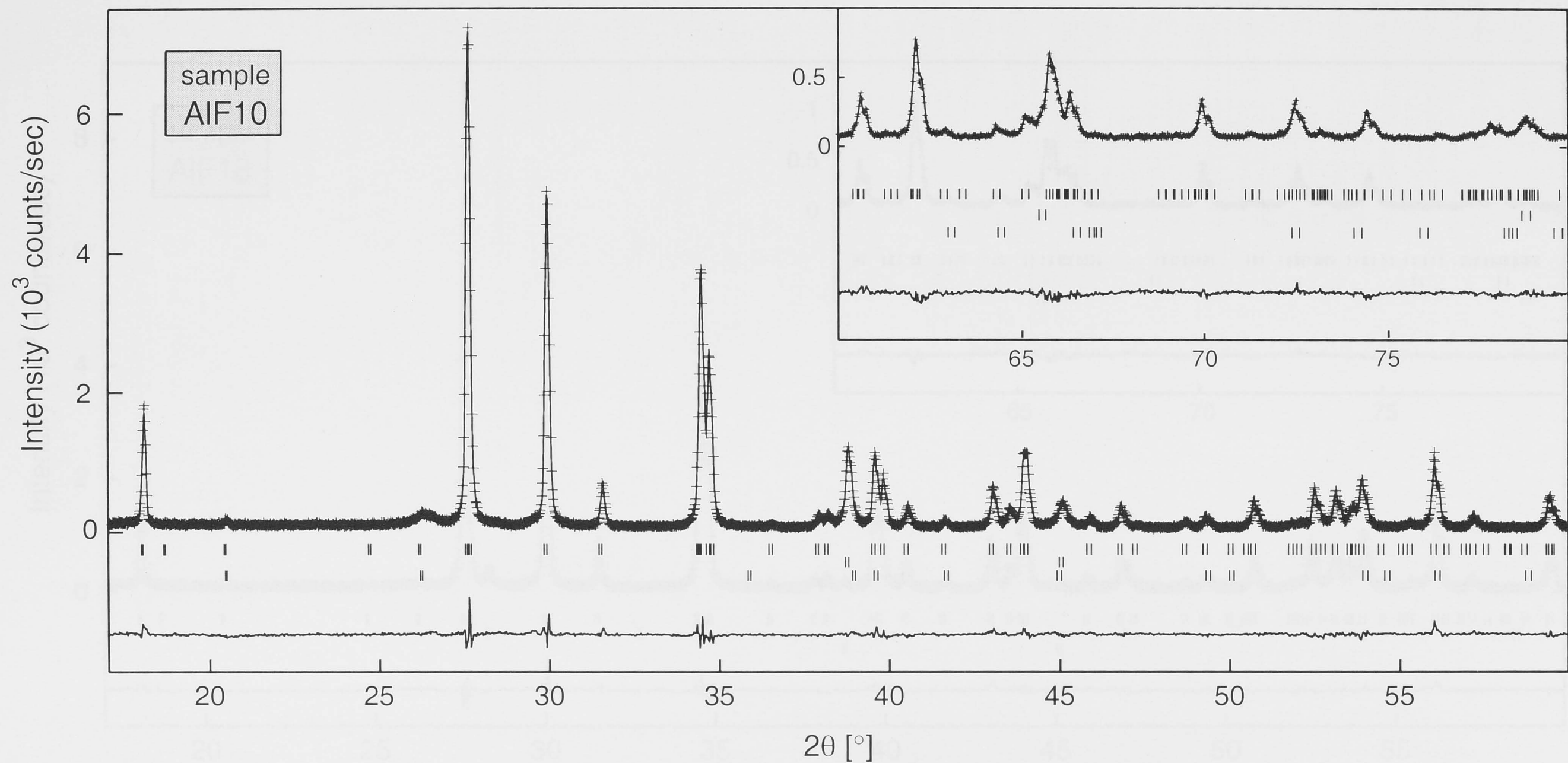
Figure 3.3 X-ray diffraction patterns and Rietveld refinement results of sample AlF10 (samples AlF18, AlF29, AlF37, AlF49, AlF67 and AlF82 in the following diagrams). Crosses represent the raw diffraction data, the upper solid curve is the calculated trace, and the lower solid curve shows the difference between the two. Positions of all *hkl* reflections are indicated by vertical bars (first row in all diagrams is titanite, the following rows are the respective impurities as listed in Table 3.2).
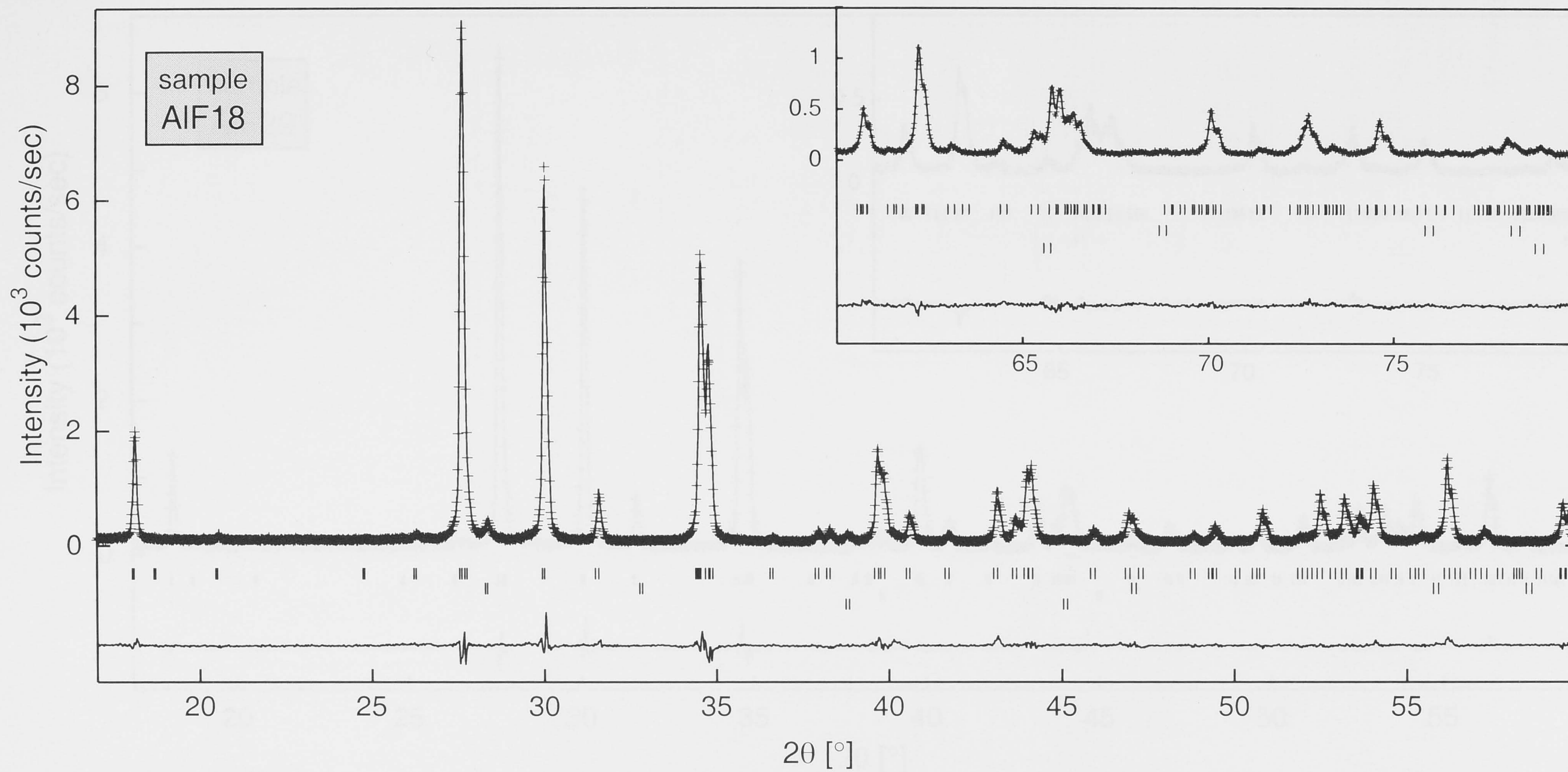
Figure 3.3 *continued.*
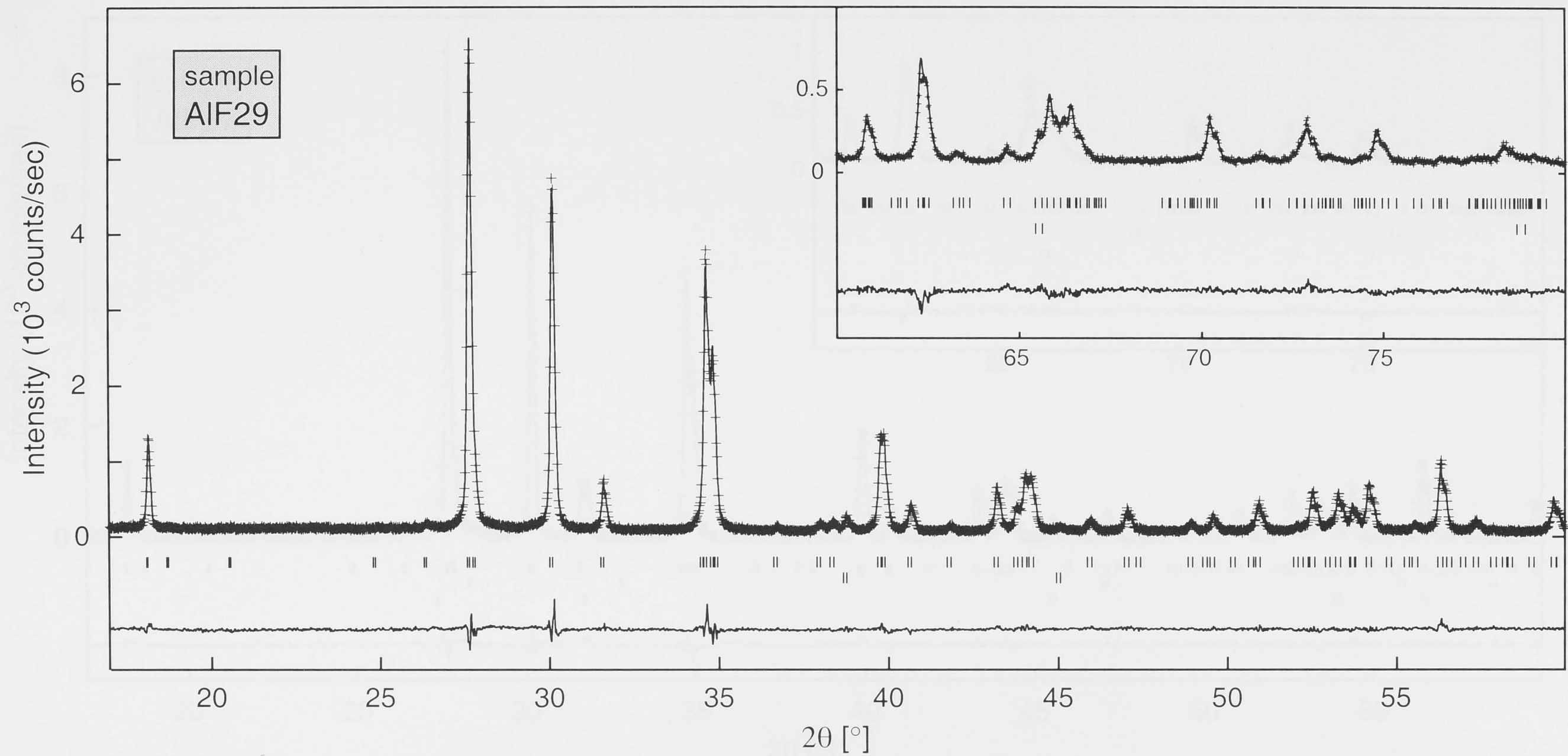
Figure 3.3 *continued.*
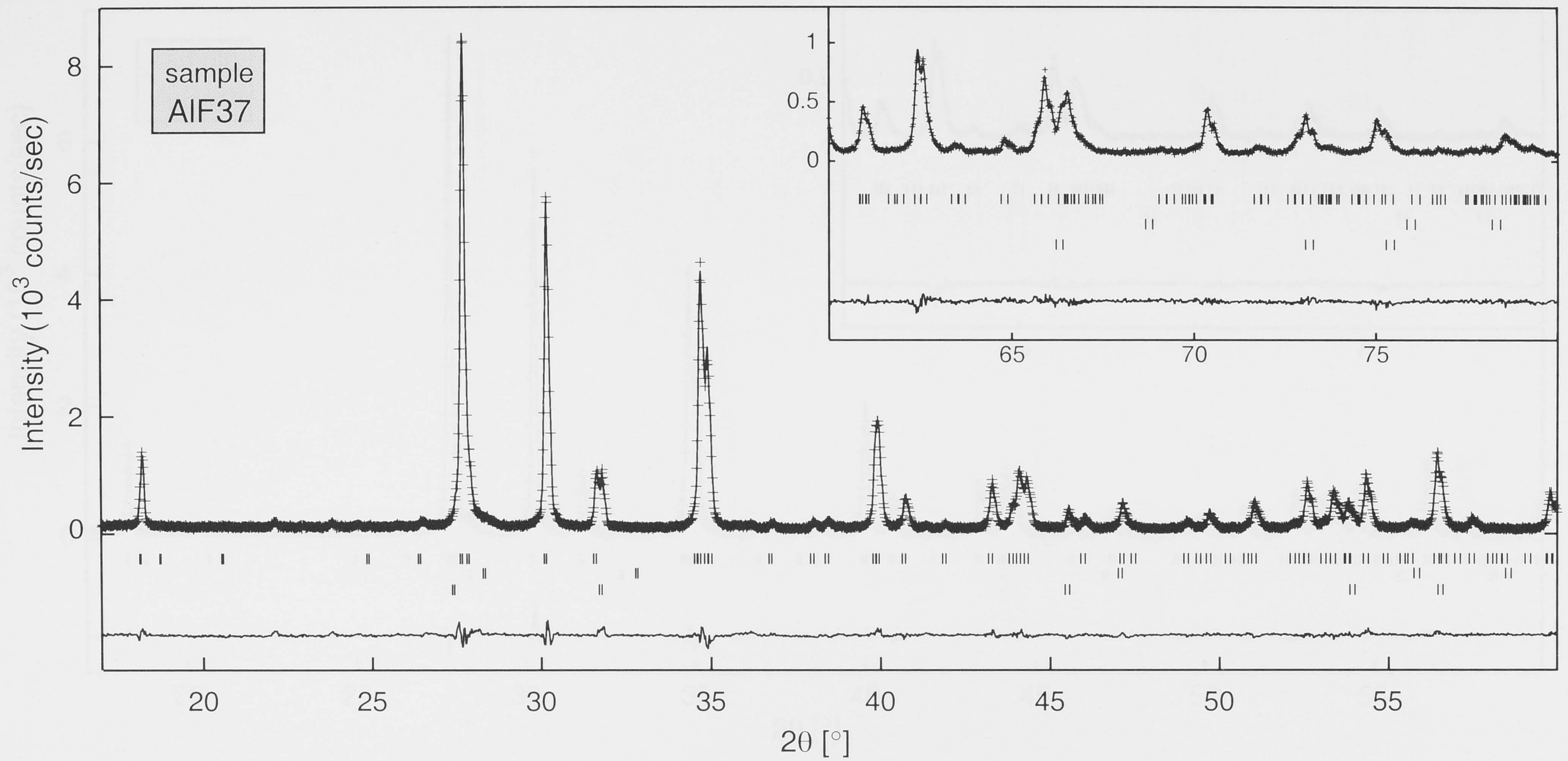
Figure 3.3 *continued.*
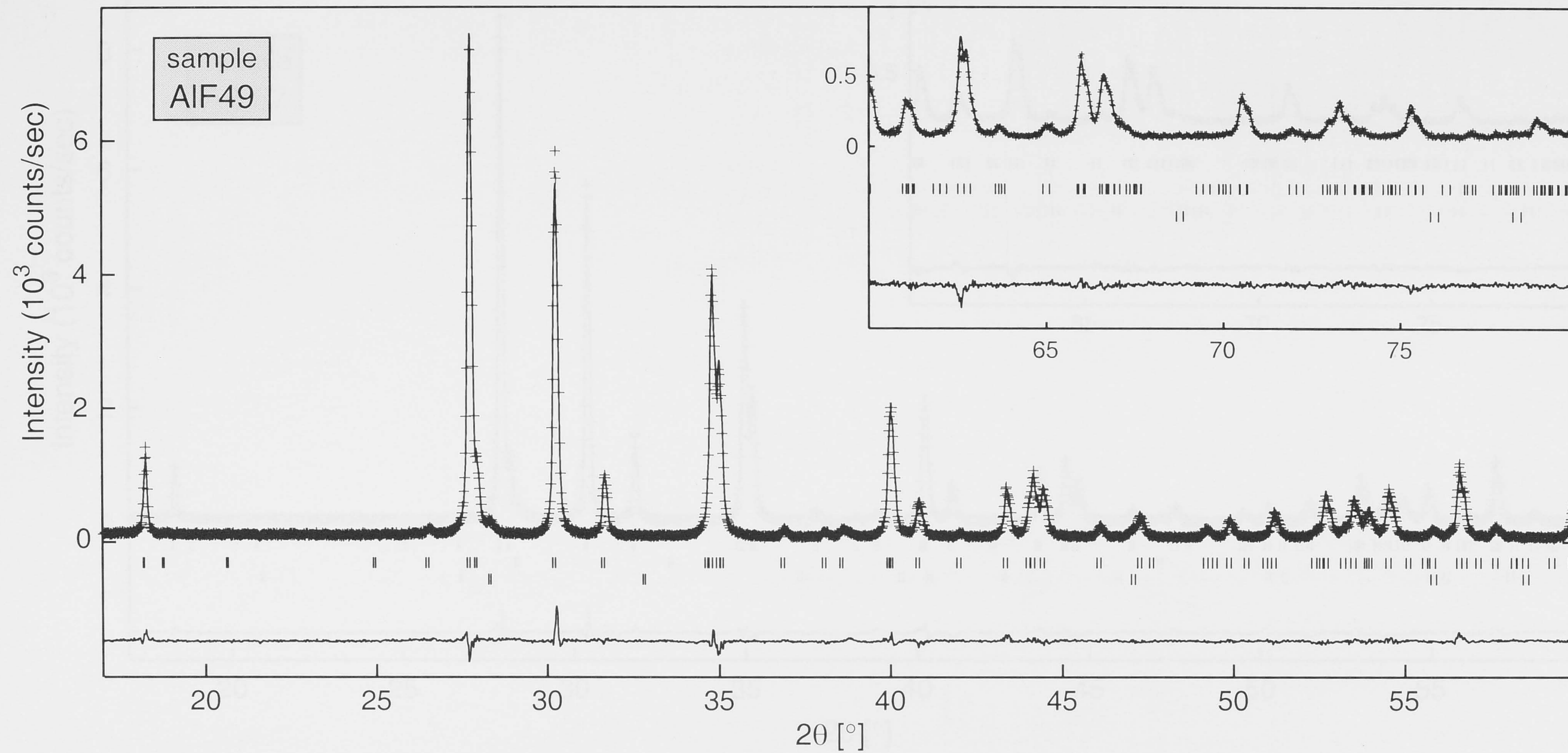
Figure 3.3 *continued.*
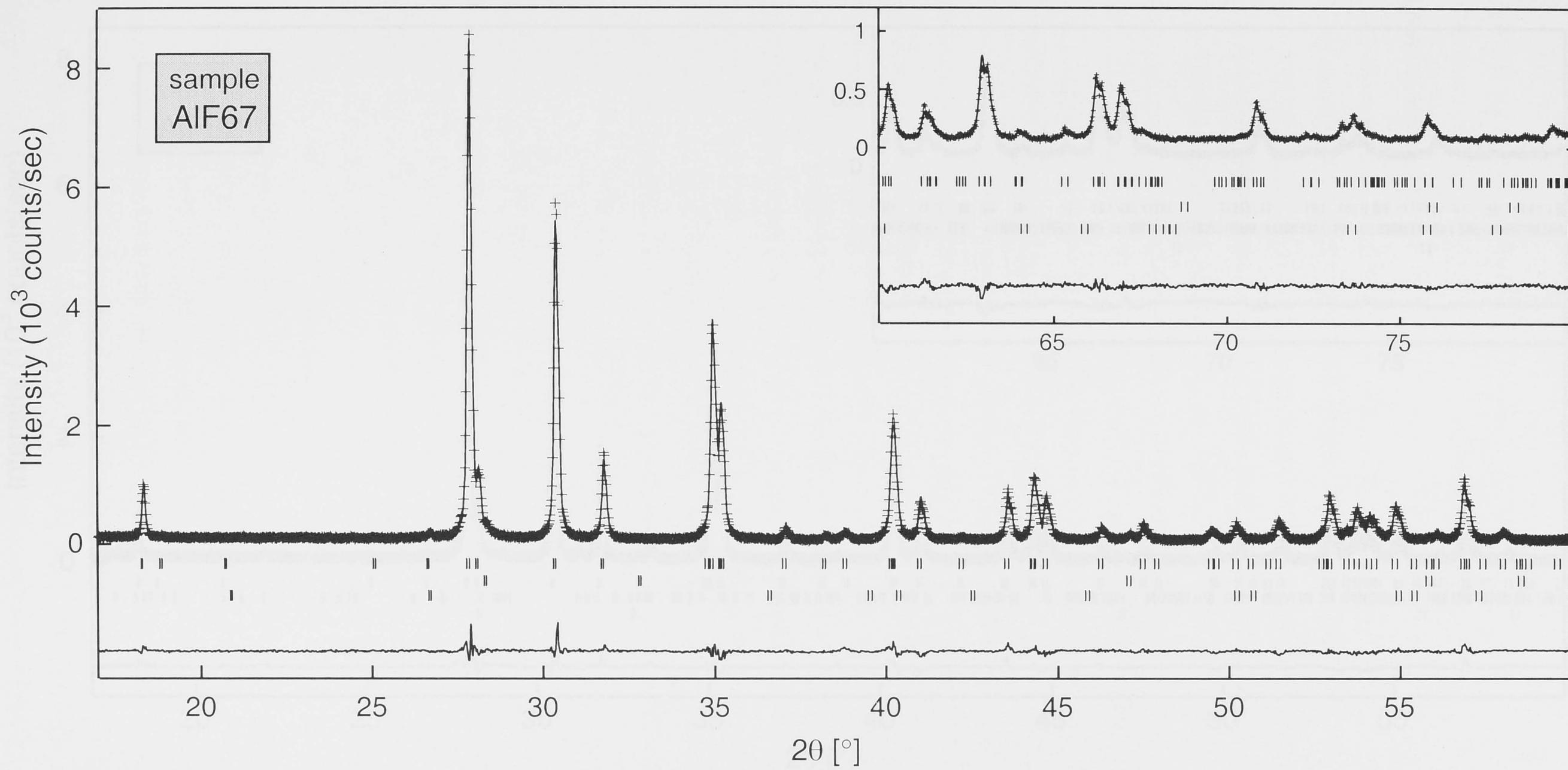
Figure 3.3 *continued.*
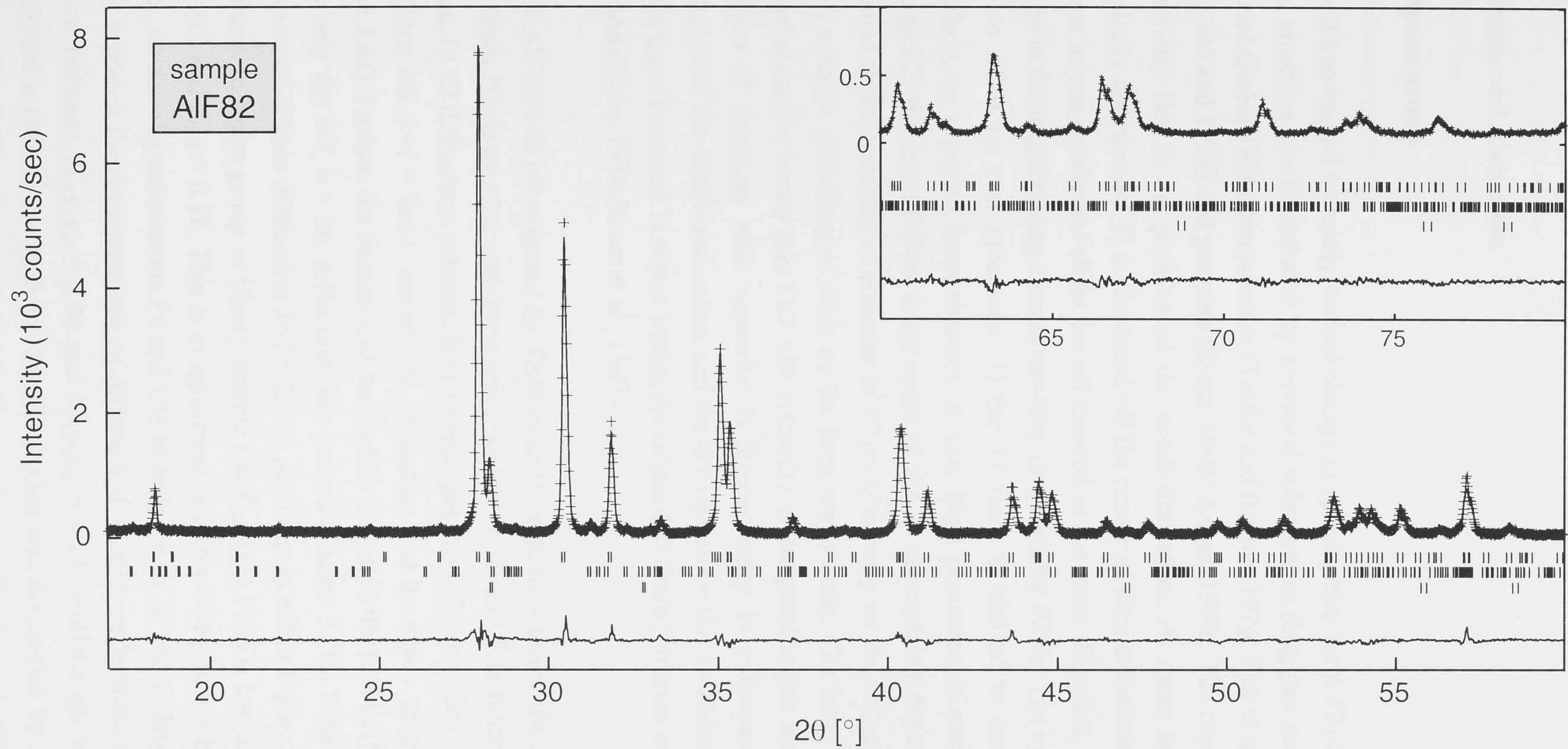
Figure 3.3 *continued.*

3.5 Results and discussion

3.5.1 Space group

The well known and intensely studied change in space group from $P2_1/a$ to $A2/a$ in the titanite structure can be induced by chemical substitution (Higgins and Ribbe, 1976; Speer and Gibbs, 1976), temperature (Taylor and Brown, 1976; Kek et al., 1997; Meyer et al., 1996 and 1998) and pressure (Kunz, 1996; Angel, 1999). The reason for the gain in symmetry lies in the position of the octahedral atom. At room temperature, the octahedrally coordinated Ti is displaced off the center of the octahedron. In titanite, all Ti atoms in one octahedral chain are off-centred in the same direction, but in opposite direction in the neighbouring chains, resulting in symmetry $P2_1/a$. The symmetry can be raised to $A2/a$ by two processes: 1) the Ti atom is shifted to the center of the octahedron, as reported from titanites at very high pressures (Kunz, 1996; Angel, 1999), and 2) the loss of short range order of the Ti off-centring direction within one octahedral chain, resulting in domains of $P2_1/a$ symmetry on the unit-cell scale, but an overall, average symmetry of $A2/a$ on the long-range scale. The latter process can be observed along the binary join TiO-AlF in titanite investigated in this study, because the formation of domains with opposite Ti-displacement is enhanced by chemical substitution of the octahedral cation and the O1 site, since this weakens the interaction between the off-centred Ti atoms within the octahedral chain (Higgins and Ribbe, 1976; Speer and Gibbs, 1976; Kunz et al., 1997).

Sample AlF18 was investigated by TEM in order to narrow down the change in space group from $P2_1/a$ to $A2/a$ with increasing content in Al and F in binary titanite solid-solution. In all diffraction patterns, for example that viewed along the [-12-1] zone axis, reflections hkl, $k+l = 2n+1$ are absent, indicating that the space group is A-centered (Figure 3.4a). Further, the existence of the a-glide is seen in the [010] diffraction pattern, where only the $h0l$, $h = 2n$ reflections are present (Figure 3.4b). Note that there is no trace even of diffuse diffraction $k+l = 2n+1$ positions in either Figure 3.4a or b. Thus the change in space group in binary titanite $Ca(Ti,Al)(O,F)SiO_4$ has to occur between $X_{Al} = 0.0$ and $X_{Al} = 0.18$. This is in agreement with previous studies based on natural titanite, containing substituents Fe and OH in addition to Al and F. Higgins and Ribbe (1976) reported the disappearance of diffuse $k+l = 2n+1$ reflections in titanite solid-solution between $X_{Al+Fe} = 0.08$ and $X_{Al+Fe} = 0.21$. Hollabaugh and Foit (1984) investigated a titanite in which the Ti-substitution was dominated by Al ($X_{Al} = 0.09$, $X_{Fe} = 0.01$). Diffraction patterns of this specimen still showed diffuse reflections belonging to space group $P2_1/a$. In contrast to this, the high-Al titanites ($X_{Al} > 0.25$)

investigated by Oberti et al. (1991) did not produce $k+l = 2n+1$ reflections. Combining the data of Hollabaugh and Foit (1984) and this study points to the $P2_1/a$ - $A2/a$ transition occurring between $X_{Al} = 0.09$ and $X_{Al} = 0.18$.

Sample AlF10 was unsuitable for space group investigations because of the large chemical variation this sample displays (Table 3.2). It probably covers the entire compositional range over which the space group conversion occurs, and contains both titanites belonging to space group $P2_1/a$ as well as those having $A2/a$ symmetry. I chose to refine the structure of this sample in space group $A2/a$, noting that this is possibly a simplification for some of the crystallites in the sample. While the unit-cell parameters resulting from this refinement should represent valid data corresponding to the average composition of the sample, it has to be born in mind that the atom positions and resulting bond lengths of sample AlF10 might only be an approximation.
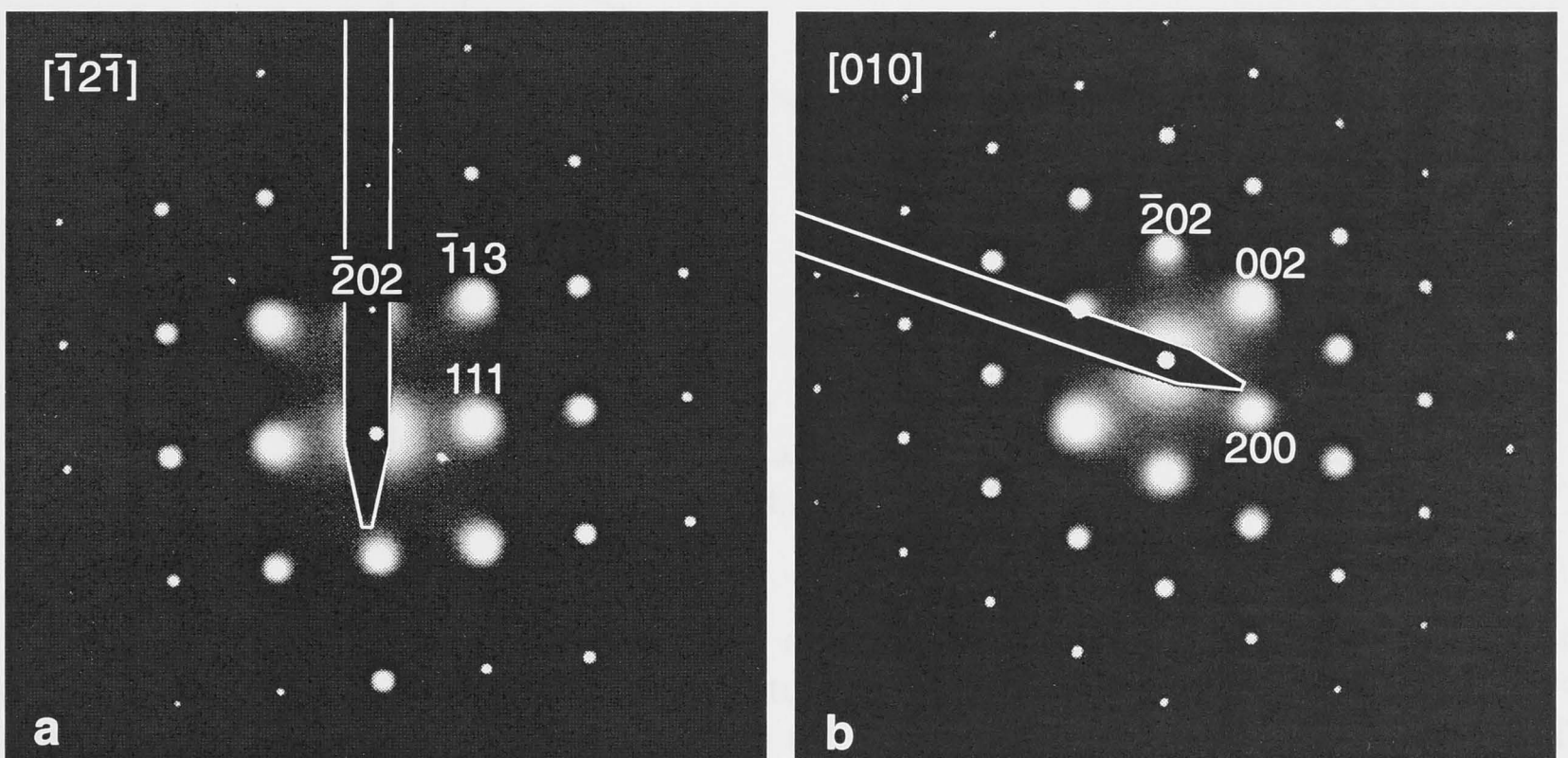
Figure 3.4 Electron diffraction patterns of titanite with $X_{Al} = 0.182$ (sample AlF18) viewed along [-12-1] **(a)** and along [010] **(b)**.

3.5.2 Unit-cell dimensions

The changes in unit-cell dimensions along the binary join TiO-AlF (Table 3.2) are shown in Figure 3.5. Good agreement exists between my data and those from the literature. The polynomial coefficients for Figure 3.5 are given in Table 5.3 (p. 96; for discussion of curve fitting methods and polynomial coefficients see Chapter 5). All dimensions change non-linearly, resulting in a small excess volume of mixing (Figure 3.5f). Thus this binary titanite represents a non-ideal solid-solution.
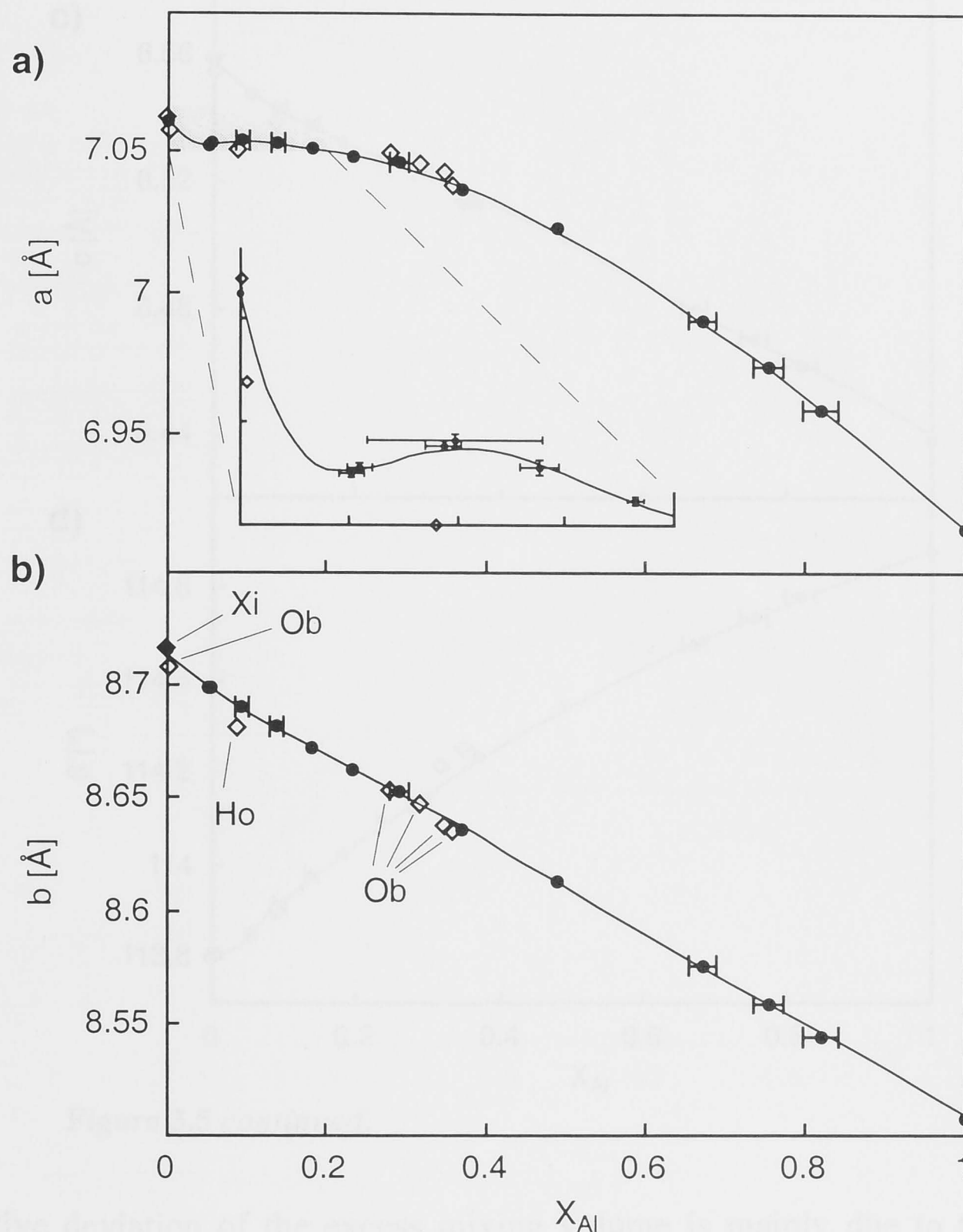
Figure 3.5 a), b), c), d) and **e)** Unit-cell dimensions of binary titanite solid-solution Ca(Ti,Al)(O,F)SiO$_4$. Full symbols, this study; open diamonds, previous studies: Xi = Xirouchakis et al. (1997b), Ho = Hollabaugh and Foit (1984), Ob = Oberti et al. (1991). **f)** The excess volume of mixing was calculated as the difference between the curve in Figure 3.5e and linear interpolation between the end-member volumes of titanite (AlF00) and CaAlFSiO$_4$ (AlF100). Horizontal bar shows the ideal volume. The curve fitting method of all curves shown in Figure 3.5 is discussed in Chapter 5. Polynomial coefficients are listed in Table 5.3, p. 96 (Approach 2 "fit by eye"). Errors are standard deviation of SEM analyses.

The excess volume of mixing reaches its maximum at about $X_{Al} = 0.57$ (± 0.10) (Figure 3.5f). It might just be coincidence that this value is very close to the maximum Al-content in titanite reported in many previous studies (Smith, 1981; Franz and Speer, 1985; Markl and Piazolo, 1999). However, it could also indicate that at this point along the binary join the crystal structure is undergoing major changes in order to accommodate an increasing amount of Al and F. Even though excess volumes of mixing have been reported for many solid-solutions, it should be noted that in this case the usual trend of positive deviation near the large end-member, and negative deviation towards the small end-member (Newton and Wood, 1980), is reversed.

c)

d)
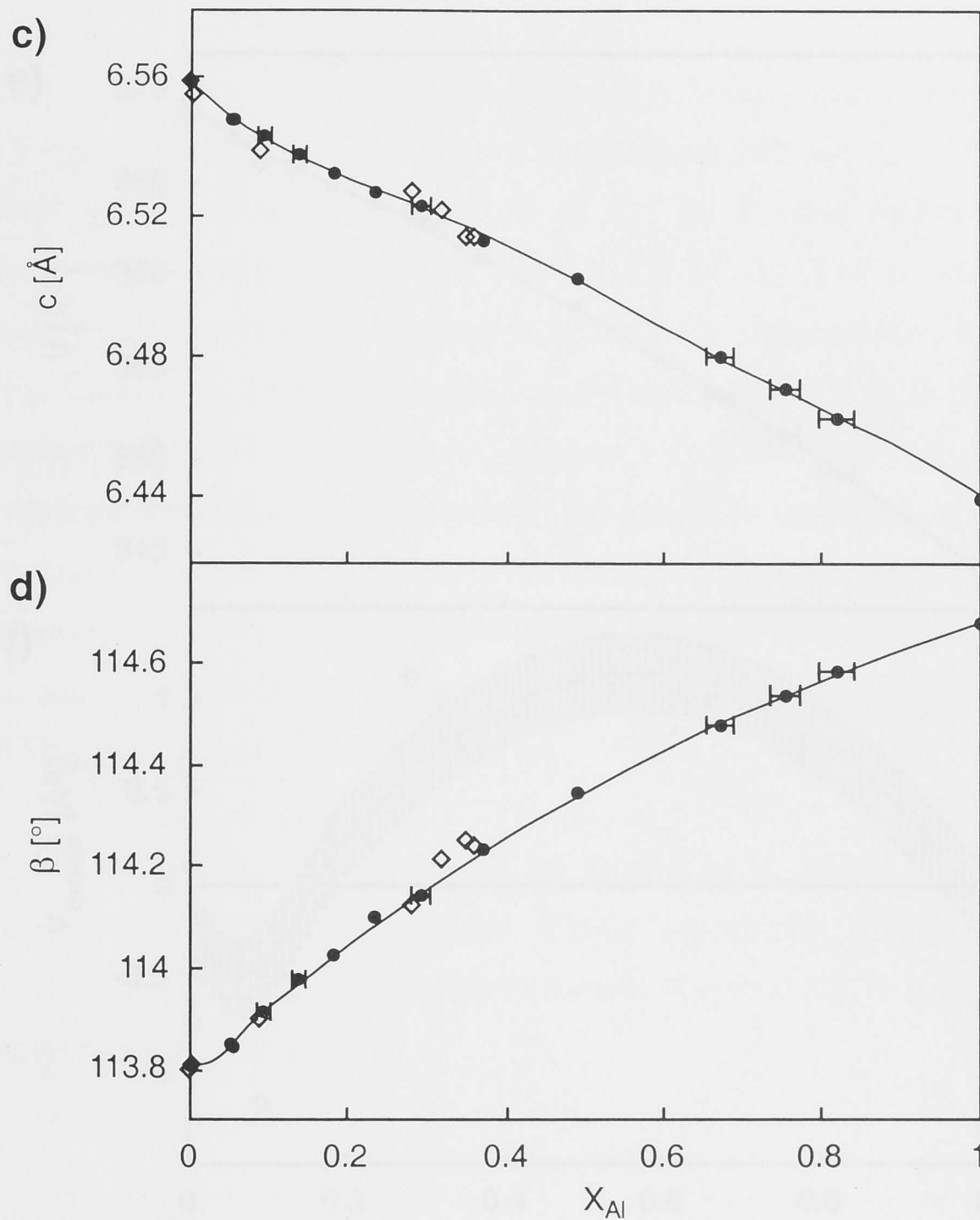
Figure 3.5 *continued.*

The negative deviation of the excess mixing volume is mainly due to the unusual behaviour of the a-dimension at very low Al-contents (Figure 3.5a). Initially, the *a* dimension decreases rapidly with X_{Al}, but then increases again between $X_{Al} = 0.05$ and $X_{Al} = 0.10$ before decreasing constantly towards the smaller end-member. The increase in *a* between $X_{Al} = 0.05$ and $X_{Al} = 0.10$ seems to be a real feature as it could be reproduced by two samples of each of the above compositions. A similar sigmoidal anomaly at very low Al-contents is also observed in β, although the sign of the slope remains the same in this case. The unusual behaviour of *a* could possibly be related to structural changes in the vicinity of the $P2_1/a$ - $A2/a$ phase transition, because the movement of the octahedral cation, which is the driving mechanism of the transition, is mostly in the *a* direction.

A correlation between changes in *a* and the $P2_1/a$ - $A2/a$ phase transition in pure titanite with increasing pressure was recently reported by Angel et al. (1999). They observed an increase in *a* as the structure changed from $A2/a$ to $P2_1/a$, and related this to the bond valence sum requirements for the Ti atoms. However, the results from Angel et al. (1999) cannot strictly be compared to the ones presented here, as the phase transition
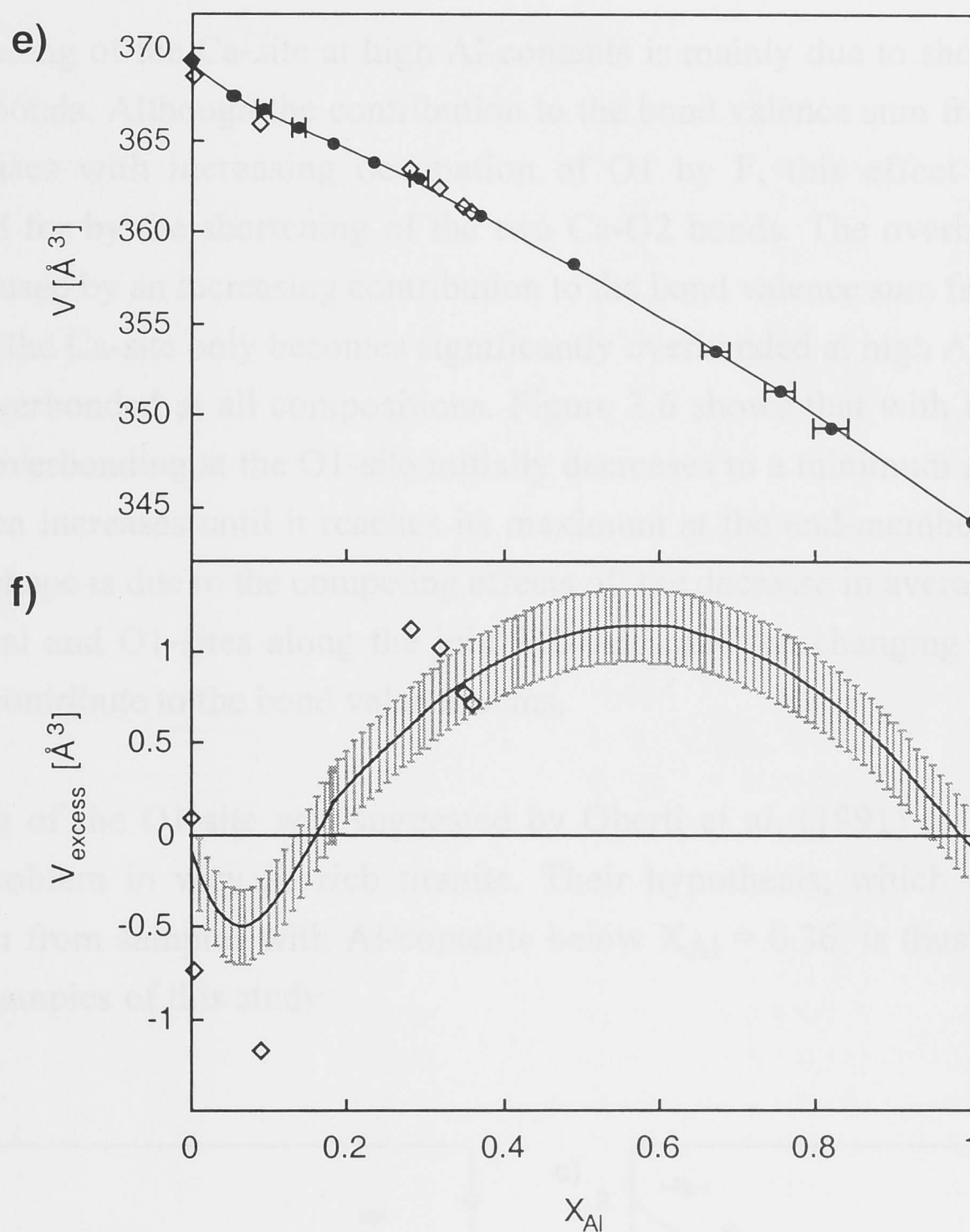
Figure 3.5 *continued*.

with pressure involves the movement of thé Ti-atom to the centre of the octahedron, whereas the transition observed with increasing X_{Al} is driven initially by the formation of anti phase domains, and thus by the movement of the Ti-atom to the opposite off-centred position in the octahedron, but not the centre. Nevertheless, the study by Angel et al. (1999) shows that the *a* dimension in the titanite structure is a sensitive indicator for the $P2_1/a$ - $A2/a$ phase transition, which could explain anomalous behaviour of *a* as shown in Figure 3.5a.

3.5.3 Bond valence sums

The atom positions, bond valence sums and bond lengths are listed in Tables 3.3 and 3.4. The bond valence sums, which were calculated with the computer program EUTAX (based on Brese and O'Keeffe, 1991), are close to ideal values for the octahedral site (Figure 3.6b), Si, O2 and O3. However, those for Ca and the O1 site clearly deviate from ideality (Figure 3.6a, c), indicating which parts of the titanite structure seem to have difficulties in adjusting to the increasing substitution of Al and F.

The overbonding of the Ca-site at high Al-contents is mainly due to shortening of the two Ca-O2 bonds. Although the contribution to the bond valence sum from the Ca-O1 bond decreases with increasing occupation of O1 by F, this effect is more than compensated for by the shortening of the two Ca-O2 bonds. The overbonding of the O1-site is caused by an increasing contribution to the bond valence sum from the Ca-O1 bond. While the Ca-site only becomes significantly overbonded at high Al-contents, the O1-site is overbonded at all compositions. Figure 3.6 shows that with increasing Al-content the overbonding at the O1-site initially decreases to a minimum at about $X_{Al} =$ 0.40, but then increases until it reaches its maximum at the end-member $CaAlFSiO_4$. The curved shape is due to the competing effects of the decrease in average valences of the octahedral and O1-sites along the join TiO-AlF, and the changing bond lengths, which both contribute to the bond valence sums.

Overbonding of the O1-site was suggested by Oberti et al. (1991) to be a potential structural problem in very Al-rich titanite. Their hypothesis, which was based on extrapolation from samples with Al-contents below $X_{Al} = 0.36$, is thus confirmed by the Al-rich samples of this study.
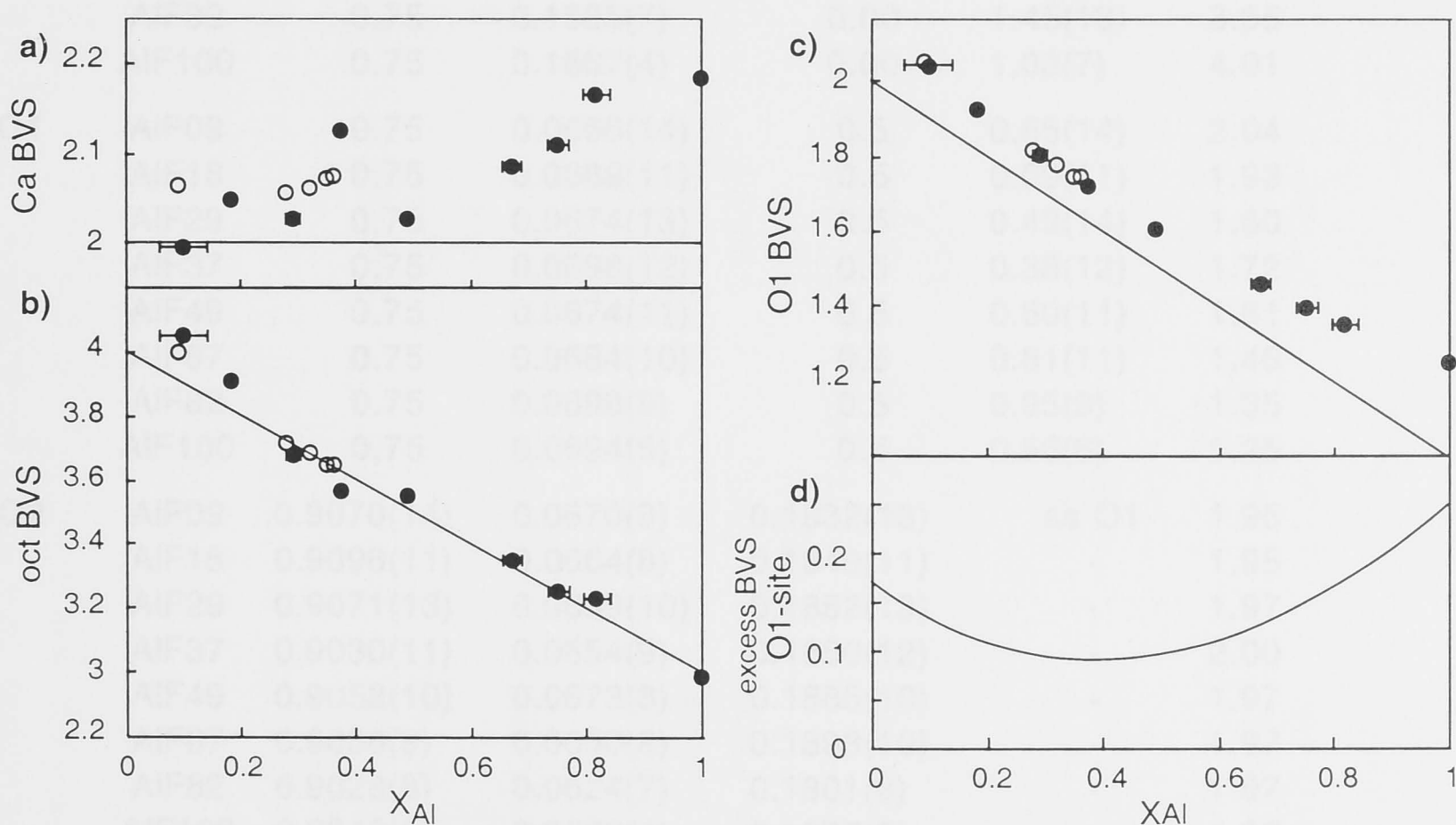
Figure 3.6 Bond valence sums (BVS) of the Ca-site **(a)**, the octahedral cation **(b)** and the O1-site **(c)**. Lines show the ideal valence sums for each site. The deviation from ideality of BVS of O1 **(d)** was calculated as the difference between function BVS and the ideal bond valence sum. Full symbols: this study, open symbols: previous studies, as given in Figure 3.5.

Table 3.3 Atom positions, isotropic thermal parameters (B_{iso} in $Å^2$) and bond valence sums (BVS) of synthetic titanite solid-solution.

	sample	x	y	z	B_{iso}	BVS
Ca	AlF09	0.25	0.1666(6)	0.00	1.94(18)	2.00
	AlF18	0.25	0.1659(5)	0.00	1.77(15)	2.05
	AlF29	0.25	0.1652(7)	0.00	1.85(19)	2.03
	AlF37	0.25	0.1651(6)	0.00	1.28(15)	2.13
	AlF49	0.25	0.1639(5)	0.00	1.64(14)	2.03
	AlF67	0.25	0.1632(5)	0.00	1.66(13)	2.09
	AlF82	0.25	0.1623(4)	0.00	1.87(11)	2.17
	AlF100	0.25	0.1642(2)	0.00	1.34(7)	2.18
oct	AlF09	0.50	0.00	0.50	1.98(13)	4.06
	AlF18	0.50	0.00	0.50	1.64(12)	3.91
	AlF29	0.50	0.00	0.50	1.75(14)	3.68
	AlF37	0.50	0.00	0.50	1.59(13)	3.56
	AlF49	0.50	0.00	0.50	1.52(12)	3.55
	AlF67	0.50	0.00	0.50	1.70(12)	3.35
	AlF82	0.50	0.00	0.50	2.20(11)	3.23
	AlF100	0.50	0.00	0.50	1.40(7)	2.99
Si	AlF09	0.75	0.1846(10)	0.00	1.62(21)	3.93
	AlF18	0.75	0.1833(8)	0.00	0.93(16)	3.83
	AlF29	0.75	0.1834(10)	0.00	1.59(21)	4.04
	AlF37	0.75	0.1837(9)	0.00	0.83(17)	4.00
	AlF49	0.75	0.1848(8)	0.00	1.19(16)	3.98
	AlF67	0.75	0.1856(8)	0.00	1.22(15)	4.00
	AlF82	0.75	0.1865(7)	0.00	1.45(13)	3.95
	AlF100	0.75	0.1867(4)	0.00	1.03(7)	4.01
O1	AlF09	0.75	0.0666(14)	0.5	0.65(14)	2.04
	AlF18	0.75	0.0689(11)	0.5	0.09(11)	1.93
	AlF29	0.75	0.0674(13)	0.5	0.49(14)	1.80
	AlF37	0.75	0.0698(12)	0.5	0.38(12)	1.72
	AlF49	0.75	0.0674(11)	0.5	0.50(11)	1.61
	AlF67	0.75	0.0684(10)	0.5	0.81(11)	1.46
	AlF82	0.75	0.0698(9)	0.5	0.95(9)	1.35
	AlF100	0.75	0.0694(5)	0.5	0.56(6)	1.25
O2	AlF09	0.9070(14)	0.0670(9)	0.1832(13)	as O1	1.95
	AlF18	0.9096(11)	0.0664(8)	0.1849(11)	-	1.95
	AlF29	0.9071(13)	0.0669(10)	0.1852(13)	-	1.97
	AlF37	0.9030(11)	0.0654(9)	0.1850(12)	-	2.00
	AlF49	0.9052(10)	0.0673(8)	0.1885(10)	-	1.97
	AlF67	0.9036(9)	0.0650(8)	0.1893(10)	-	1.97
	AlF82	0.9028(8)	0.0624(7)	0.1901(8)	-	1.97
	AlF100	0.9048(5)	0.0662(4)	0.1877(5)	-	1.96
O3	AlF09	0.3842(15)	0.2086(10)	0.4001(15)	as O1	2.02
	AlF18	0.3853(12)	0.2088(8)	0.3989(13)	-	1.98
	AlF29	0.3821(14)	0.2103(10)	0.3993(15)	-	2.00
	AlF37	0.3796(12)	0.2083(9)	0.3948(13)	-	1.98
	AlF49	0.3838(10)	0.2057(8)	0.4017(11)	-	2.00
	AlF67	0.3850(10)	0.2049(8)	0.4045(11)	-	2.02
	AlF82	0.3845(8)	0.2028(7)	0.4049(9)	-	2.03
	AlF100	0.3898(5)	0.2020(4)	0.4054(6)	-	2.01

Table 3.4 Selected bond lengths, bond angles and polyhedral volumes (V), quadratic elongation (QE) and angular variance (AV) of the octahedron and tetrahedron in titanite solid-solution.

		AlF09	AlF18	AlF29	AlF37	AlF49	AlF67	AlF82	AlF100
Ca[7]-site									
Ca-O1	[Å]	2.320(13)	2.300(11)	2.314(13)	2.290(12)	2.314(11)	2.301(10)	2.289(9)	2.267(5)
Ca-O2	[Å]	2.390(9)	2.383(7)	2.371(9)	2.347(8)	2.357(7)	2.323(7)	2.289(6)	2.317(4)
Ca-O3A	[Å]	2.424(9)	2.411(8)	2.412(9)	2.379(8)	2.410(7)	2.416(7)	2.409(5)	2.397(3)
Ca-O3B	[Å]	2.626(10)	2.617(8)	2.63(1)	2.644(9)	2.632(8)	2.620(7)	2.621(6)	2.570(4)
Ca-O mean	[Å]	2.457	2.446	2.449	2.433	2.445	2.431	2.418	2.405
V	[Å^3]	19.74(12)	19.382(95)	19.648(111)	19.263(96)	19.502(85)	19.233(80)	18.902(65)	18.401(41)
octahedron									
oct-O1	[Å]	1.856(4)	1.861(3)	1.856(4)	1.860(3)	1.849(3)	1.844(3)	1.839(2)	1.827(1)
oct-O2	[Å]	1.991(8)	1.977(7)	1.970(8)	1.961(7)	1.942(6)	1.922(6)	1.904(5)	1.920(3)
oct-O3	[Å]	1.988(8)	1.983(7)	1.997(8)	1.986(8)	1.945(7)	1.925(7)	1.901(6)	1.876(4)
oct-O mean	[Å]	1.945	1.941	1.941	1.936	1.912	1.897	1.881	1.874
V	[Å^3]	9.792(43)	9.723(36)	9.730(43)	9.652(38)	9.309(33)	9.089(32)	8.872(26)	8.767(16)
QE		1.0023(40)	1.0021(32)	1.0022(38)	1.0020(34)	1.0013(30)	1.0010(29)	1.0008(24)	1.0014(15)
AV		0.558	1.520	0.544	1.313	0.618	0.843	0.839	2.149
tetrahedron									
Si-O2	[Å]	1.623(9)	1.627(8)	1.615(9)	1.609(8)	1.617(7)	1.624(7)	1.636(6)	1.605(4)
Si-O3	[Å]	1.639(12)	1.654(10)	1.627(11)	1.639(10)	1.636(9)	1.625(9)	1.621(7)	1.642(5)
Si-O mean	[Å]	1.631	1.640	1.621	1.624	1.626	1.624	1.629	1.623
V	[Å^3]	2.210(17)	2.250(14)	2.172(17)	2.183(13)	2.195(13)	2.182(13)	2.194(10)	2.175(7)
QE		1.0049(133)	1.0044(107)	1.0036(131)	1.0048(99)	1.0037(102)	1.0051(99)	1.0071(84)	1.0064(52)
AV		17.806	15.259	13.180	16.372	13.380	19.645	27.634	22.234
oct-O1-oct	[°]	143.7	142.5	143.4	142.2	143.4	142.9	142.2	142.3

3.5.4 Cation polyhedra

The decrease in unit-cell volume with increasing X_{Al} (Figure 3.5) is mainly caused by the decreasing size of the $(Ti,Al)(O,F)_2O_4$ octahedron and the $Ca^{[7]}$ polyhedron (Figure 3.7, Table 3.4). In contrast, the SiO_4 tetrahedron remains constant in volume. The correlation between the octahedral- and Ca-sites in titanite solid-solution was pointed out by Oberti et al. (1991) and Kunz et al. (1997). Since the Ca-polyhedron is closely interlinked with the octahedral chain via two shared O1-O3 edges (Figure 3.1), it has to change shape and size together with the octahedron when this is occupied by ions of different size.
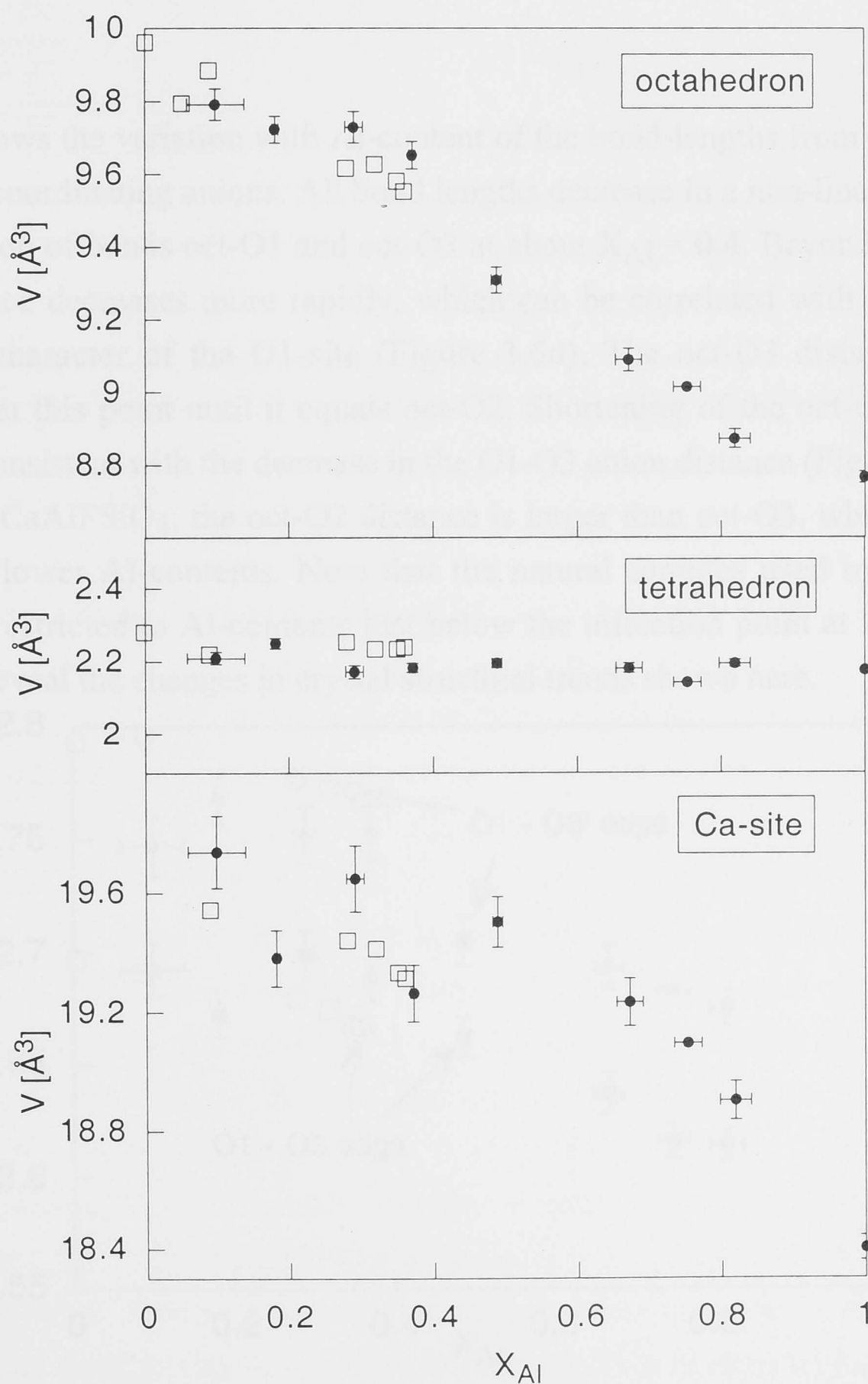
Figure 3.7 Polyhedral volumes of the octahedron, tetrahedron and the Ca-site in the titanite structure at various Al-contents. Open squares represent previous studies as defined in Figure 3.5.

With a remarkably constant oct-O1-oct angle of about 143°(±1°) (Table 3.4), the kinked oct-O1 chain is acting as a shrinking, but rigid skeleton which forces the rest of the structure to adjust. Since the SiO_4-tetrahedra represent fairly incompressible structural units, it is the large Ca-polyhedron which is forced to change shape and decrease in size, even though its occupying cation remains the same. This is the reason for the large bond valence sums of Ca at high Al-contents. Major atomic rearrangement taking place in this part of the structure is also indicated by the significant shortening (up to 5%) of both O1-O3 edges which are shared between octahedron and Ca-site (Figure 3.8). The competing relationship between the chain of corner-sharing octahedra and that of edge-sharing Ca-polyhedra in the titanite structure was previously demonstrated for the structurally related titanite-malayaite [$CaSnOSiO_4$] solid-solution by Kunz et al. (1997).

Figure 3.9 shows the variation with Al-content of the bond-lengths from the octahedral cation to the coordinating anions. All bond lengths decrease in a non-linear way, with a major inflection of bonds oct-O1 and oct-O3 at about $X_{Al} = 0.4$. Beyond this point the oct-O1 distance decreases more rapidly, which can be correlated with the increasing overbonded character of the O1-site (Figure 3.6d). The oct-O3 distance decreases significantly at this point until it equals oct-O2. Shortening of the oct-O1 and oct-O3 distances is consistent with the decrease in the O1-O3 anion distance (Figure 3.8). In the end-member $CaAlFSiO_4$, the oct-O2 distance is larger than oct-O3, which is reversed compared to lower Al-contents. Note that the natural samples used by Oberti et al. (1991) were restricted to Al-contents just below the inflection point at $X_{Al} = 0.4$, and thus did not reveal the changes in crystal structural trends shown here.
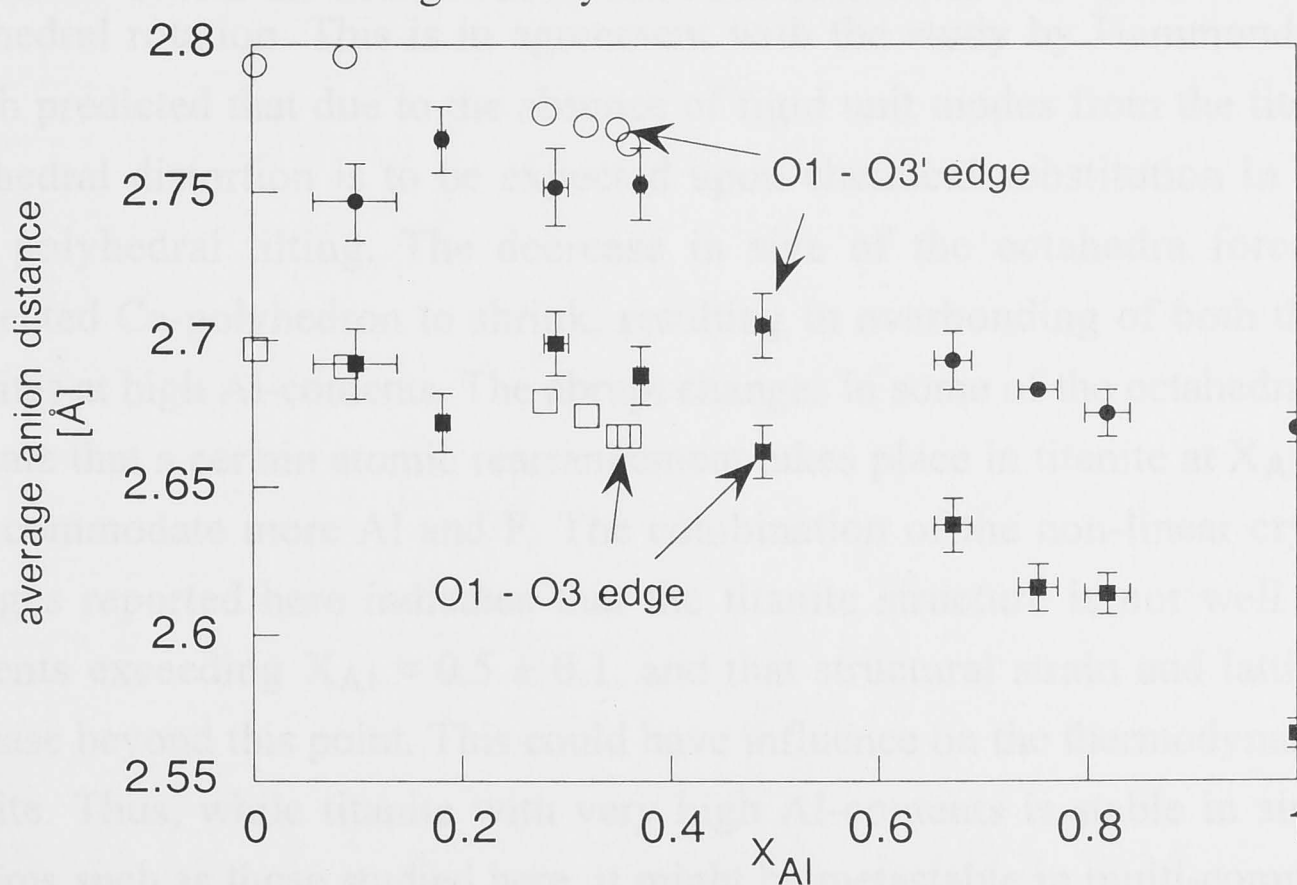
Figure 3.8 Average anion-anion distances of the two O1-O3 edges which are shared by the octahedra and Ca-polyhedra of the titanite structure. Full symbols: this study, open symbols: previous studies, as listed in Figure 3.5.
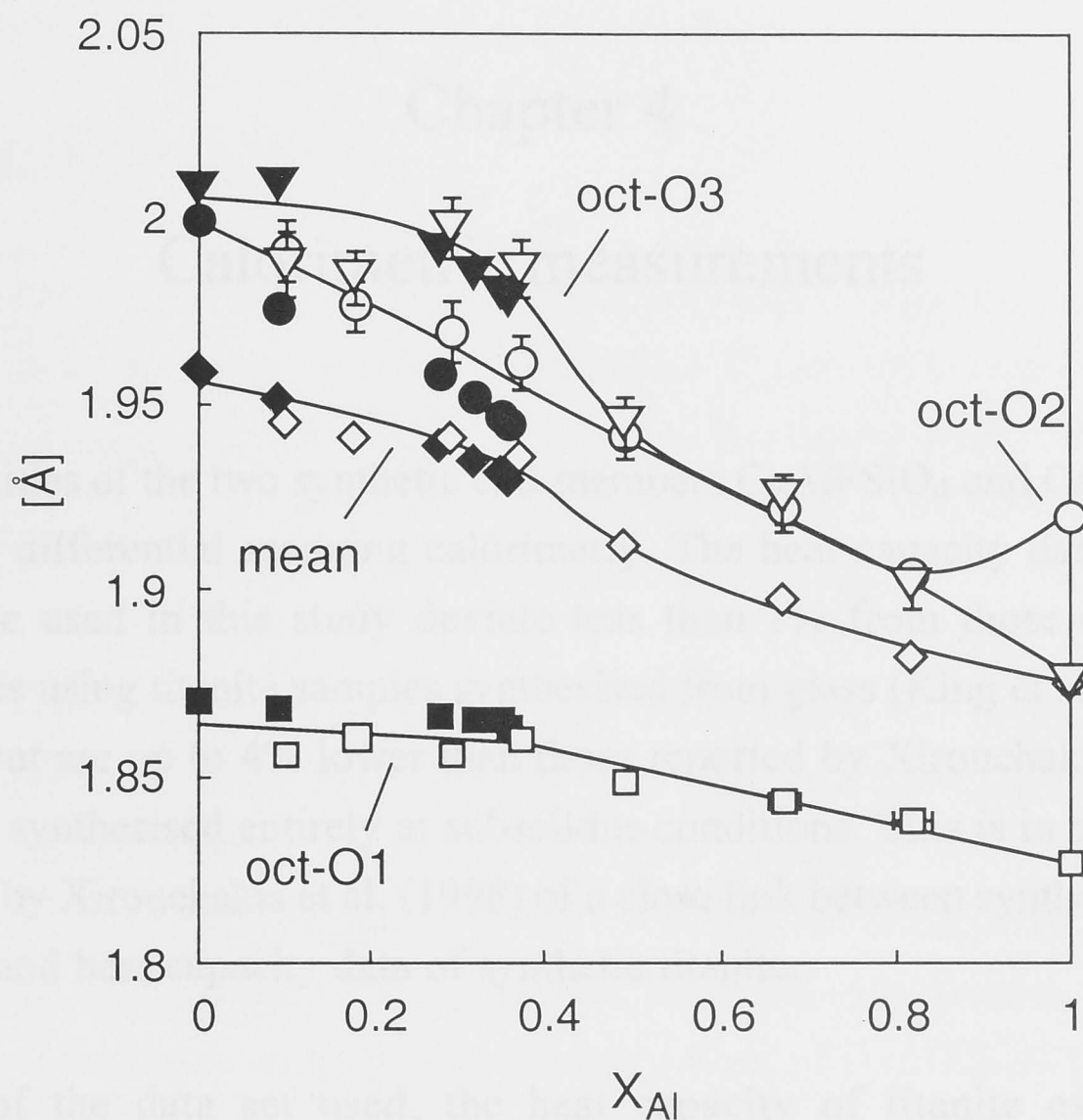
Figure 3.9 Average bond lengths from the octahedral cation to the coordinating anions O1, O2 and O3, and their mean. Open symbols: this study; full: previous studies (Figure 3.5).

3.6 Conclusions

The crystal structure of titanite accommodates the increasing amount of Al and F by changing the size and shape of all the cation polyhedra, rather than simply by polyhedral rotation. This is in agreement with the study by Hammonds et al. (1998) which predicted that due to the absence of rigid unit modes from the titanite structure, polyhedral distortion is to be expected upon chemical substitution in titanite, rather than polyhedral tilting. The decrease in size of the octahedra forces the closely connected Ca-polyhedron to shrink, resulting in overbonding of both the Ca- and the O1-sites at high Al-contents. The abrupt changes in some of the octahedral bond lengths indicate that a certain atomic rearrangement takes place in titanite at $X_{Al} > 0.4$ in order to accommodate more Al and F. The combination of the non-linear crystal structural changes reported here indicates that the titanite structure is not well suited for Al-contents exceeding $X_{Al} \approx 0.5 \pm 0.1$, and that structural strain and lattice energy will increase beyond this point. This could have influence on the thermodynamic stability of titanite. Thus, while titanite with very high Al-contents is stable in simple chemical systems such as those studied here, it might be metastable in multi-component systems like natural rocks. Here, other phases such as amphiboles, micas, epidote minerals and garnets might be more suited to accommodate Al and F. This would explain the rare occurrence of titanite with $X_{Al} > 0.54$ in real rocks.

Chapter 4

Calorimetric measurements

4.1 Abstract

The heat capacities of the two synthetic end-members $CaAlFSiO_4$ and $CaTiOSiO_4$ were determined by differential scanning calorimetry. The heat capacity data of the glass-derived titanite used in this study deviate less than 1% from those determined by previous studies using titanite samples synthesised from glass (King et al., 1954; Zhang et al., 1995), but are up to 4% lower than those reported by Xirouchakis et al. (1998) from a sample synthesised entirely at subsolidus conditions. This is in agreement with the suggestion by Xirouchakis et al. (1998) of a close link between synthesis conditions, sample purity and heat capacity data of synthetic titanite.

Independent of the data set used, the heat capacity of titanite exceeds that of $CaAlFSiO_4$ at low temperatures, indicating that in the case of the absence of low-temperature heat capacity anomalies, the standard state entropy of $CaAlFSiO_4$ can be expected to be smaller than that of titanite. At high temperatures the heat capacity of titanite is lower than (Robie and Hemingway, 1995) or equal to (Xirouchakis et al., 1998) that of $CaAlFSiO_4$.

The calorimetric contribution to the third law entropy of $CaAlFSiO_4$ was estimated by combining the calorimetric data with low-temperature heat capacity calculations based on lattice vibrational theory (Debye model). Two different extrapolation methods of the Debye temperature to zero K yielded calorimetric entropies $S^0{}_{298}$ of 104.7 $Jmol^{-1}K^{-1}$ and 118.1 $Jmol^{-1}K^{-1}$. The entropy estimated for $CaAlFSiO_4$ on the basis of the entropies of the components anorthite and fluorite, is 112.9 ± 0.3 $Jmol^{-1}K^{-1}$.

An attempt was made to measure the $P2_1/a$ to $A2/a$ phase transition temperature in three samples with $X_{Al} = 0.00$, $X_{Al} = 0.05$ and $X_{Al} = 0.09$. The detected signals are very weak and should only be interpreted in the light of other methods. The transition temperature seems to decrease at a rate of about 10 degrees per 1 mol.% of the end-member $CaAlFSiO_4$, narrowing down the transition composition at room temperature to the range of $X_{Al} = 0.151$ and $X_{Al} = 0.195$. This is in good agreement with previous investigations (Chapter 3), but is more tightly bracketed. Upon multiple heating and cooling the Al-bearing samples seem to unmix Al-free domains of the pure titanite end-member. Future TEM investigations are necessary to test the unmixing hypothesis.

4.2 Introduction

4.2.1 Heat capacity of CaAlFSiO₄

As a first step towards understanding the thermodynamic behaviour of titanite solid-solution, the heat capacity of the end-member $CaAlFSiO_4$ was determined by differential scanning calorimetry (DSC). This was measured from 170 to 850 K, the maximum temperature range accessible with the calorimeter, to allow the best possible extrapolation of the data to both lower and higher temperatures.

The extrapolation of the heat capacity to higher temperatures was performed in order to allow the combination of the heat capacity with the experimental results of a phase equilibrium study (Chapter 5), carried out at higher temperatures. The extrapolation to higher temperatures were constrained by the 'Dulong-Petit limit', as explained below. The combination of calorimetry and phase equilibrium experiments will permit the extraction of standard state enthalpy and entropy values of $CaAlFSiO_4$ (Chapter 5).

Extrapolation of the heat capacity to zero K can be performed on the basis of vibrational theory as discussed below, which yields estimates of the the standard state entropy of $CaAlFSiO_4$. The third law standard state entropy of a phase, $S^0_{3rd-law}$, represents the summation of various entropy contributions, such as the calorimetric entropy, the configurational entropy, and possible phase transition effects

$$S^0_{3rd-law} = \int_0^{298.15} \frac{C_p}{T} dT + S_{configurational} + \Delta S_{transition}$$ (4.1)

The main contribution to the third-law entropy usually stems from the calorimetric entropy, which can be calculated if the heat capacity of a phase is known between 0 and 298.15 K. The heat capacity data of $CaAlFSiO_4$ obtained with DSC are limited to temperatures above 170 K. However, these data can be combined with first principle calculations of low-temperature heat capacities, filling in the data gap from 170 to 0 K, thus allowing an approximation of the calorimetric entropy of the end-member $CaAlFSiO_4$. If $CaAlFSiO_4$ is perfectly ordered at 0 K, and if no phase change occurs between 0 and 298.15 K, then the configurational and phase transition entropy contributions equal 0, so that the calorimetric entropy is identical to the third-law standard state entropy. However, if there is any 'frozen in' disorder at 0 K, e.g. with respect to Si and Al, then a configurational entropy term has to be estimated to calculate the third-law entropy.

4.2.2 Heat capacity of CaTiOSiO$_4$

Besides the heat capacity of CaAlFSiO$_4$, that of the titanite sample synthesised for and used throughout this study, e.g. for X-ray diffraction (Chapter 3), and as starting material for piston-cylinder experiments (Chapters 2 and 5), was measured. The heat capacity of titanite was first determined by King et al. (1954) with low temperature adiabatic calorimetry from 51 to 298 K, and heat content measurements from 298 to 1811 K. The results of that study form the basis of most internally consistent thermodynamic data sets (e.g., Holland and Powell, 1985; Bermann 1988; Robie and Hemingway, 1995). The data of King et al. (1954) were reproduced within error with differential scanning calorimetry between 340 and 900 K by Zhang et al. (1995), as well as with drop-calorimetry measurements between 400 and 1800 K by Thiéblot et al. (1999) (Figures 4.1 and 4.2). All three studies used synthetic titanite samples which had been crystallized either from glass (King et al., 1954; Thiéblot et al., 1999) or melt (Zhang et al., 1995).

However, the thermodynamic properties of titanite were reinvestigated recently in a series of calorimetric measurements (Xirouchakis et al., 1997a; Xirouchakis and Tangeman, 1998), an experimental phase-equilibrium study (Xirouchakis and Lindsley, 1998), as well as one X-ray diffraction study (Xirouchakis et al., 1997b). The heat capacity, the enthalpy of formation and the unit-cell volume of titanite were determined by the above studies using a carefully prepared and well characterized titanite sample that was synthesised entirely at sub-solidus conditions (Xirouchakis et al., 1997b). At high temperatures (> 500 K) the heat capacity of this sample (Xirouchakis and Tangeman, 1998) exceeds that reported by all other studies (King et al., 1954, Zhang et al., 1995; Thiéblot et al., 1999) by up to 4% (Figure 4.1). Also, the enthalpy of formation of this sample differs significantly from previously determined values (e.g., King et al., 1954), being more negative by about 9 kJmol^{-1} (Xirouchakis et al., 1997a). The unit cell volume of the sub-solidus derived titanite sample by Xirouchakis et al. (1997b) is slightly smaller than that determined by previous crystallographic studies which used melt- or glass-derived samples (e.g., Speer and Gibbs, 1976; Tanaka et al., 1988).

The discrepancies in the thermochemical data and unit cell volume between the sub-solidus derived samples used in Xirouchakis' studies, and the super-solidus derived samples used by all other workers were interpreted by Xirouchakis et al. (1997a, 1997b) to reflect different degrees of purity and stoichiometry of the titanite samples.
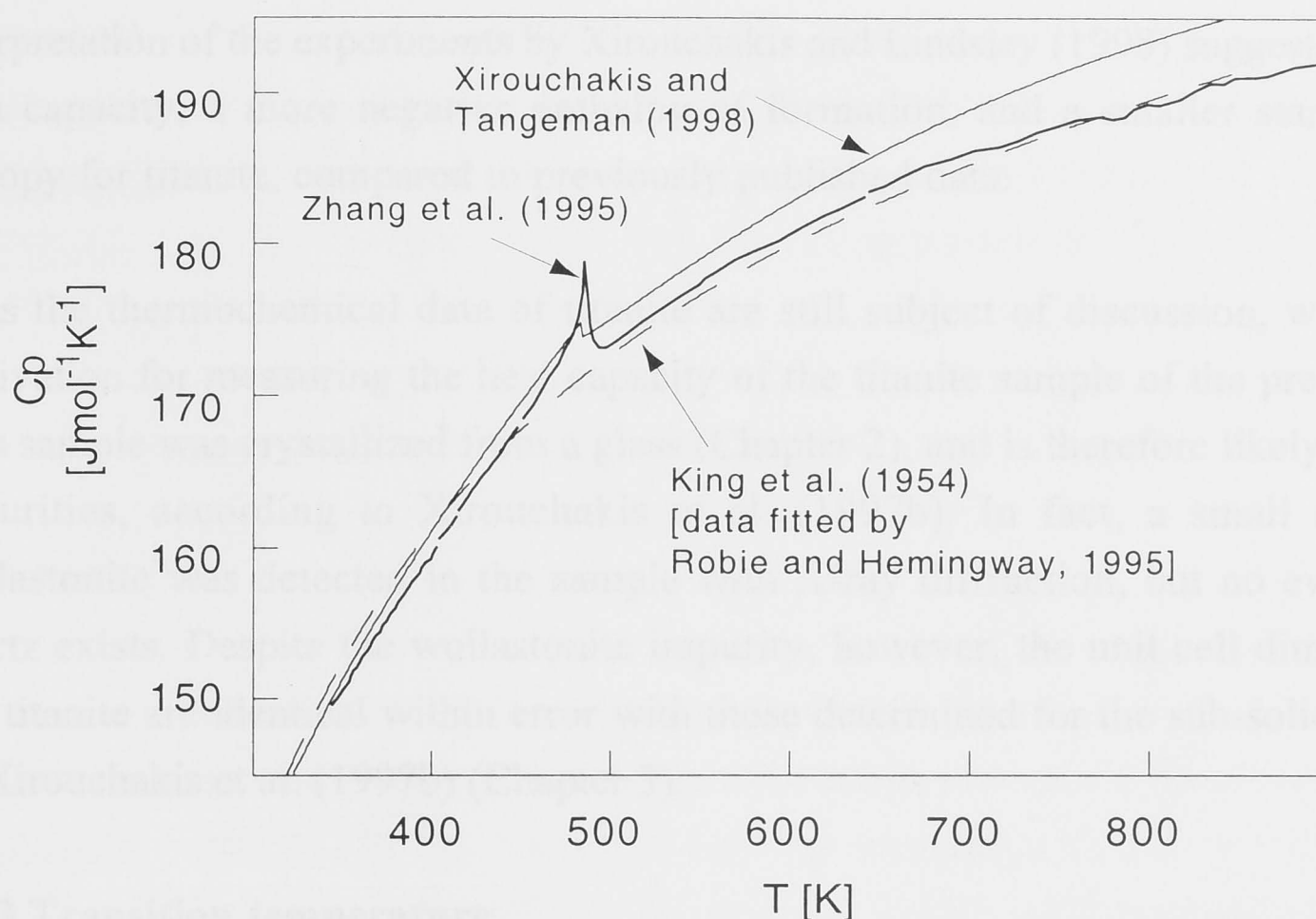
Figure 4.1 Specific heat of synthetic titanite determined by previous studies (see text).
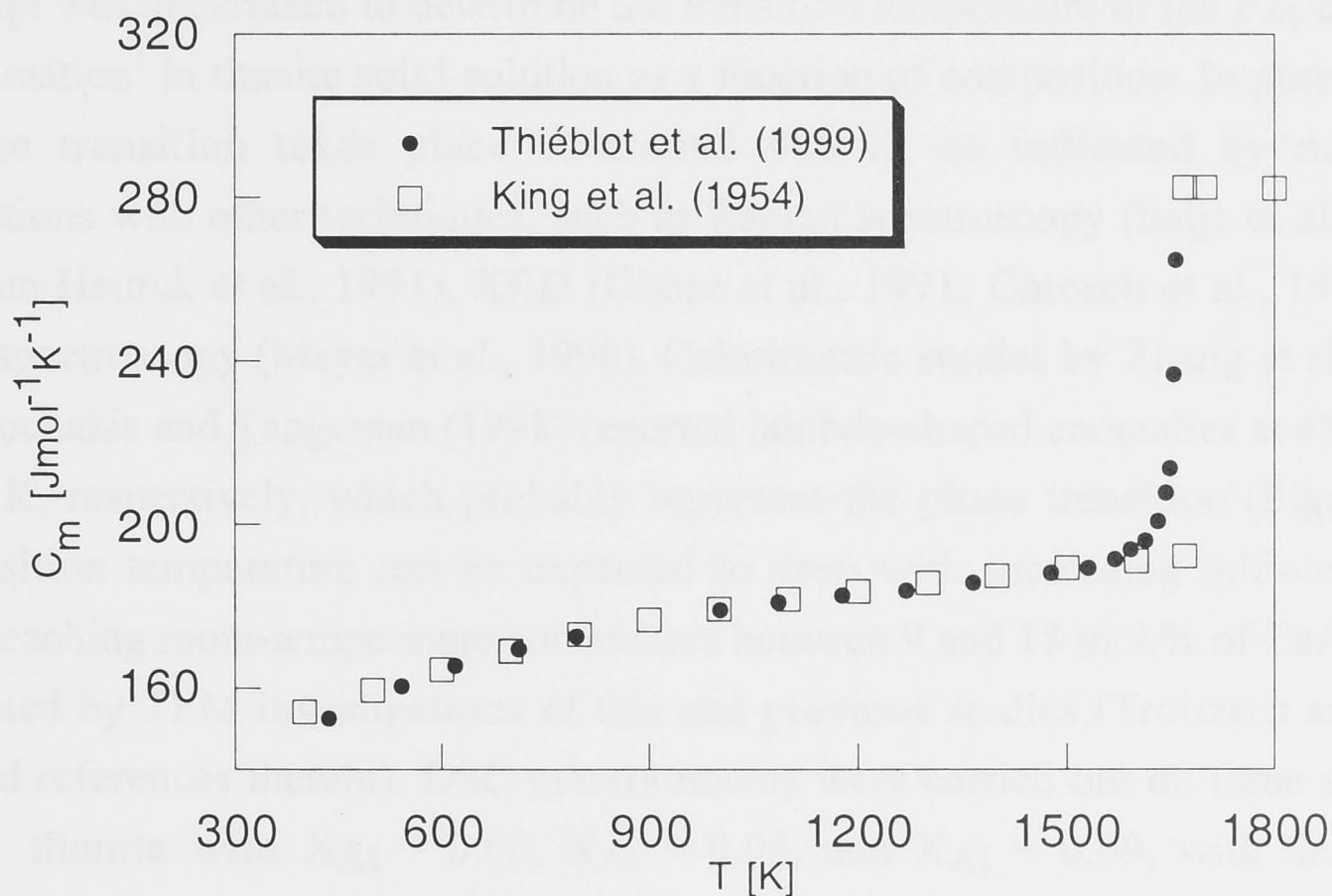
Figure 4.2 Specific heat of synthetic titanite determined by previous studies (see text).

Xirouchakis et al. (1997b) suggested that only the synthesis performed entirely at sub-solidus conditions is likely to produce phase-pure titanite, and that melt- or glass-derived titanite samples are prone to contain impurities such as glass, quartz or wollastonite. This interpretation was independently supported by the results of Xirouchakis and Lindsley's (1998) phase-equilibrium study of titanite-bearing assemblages, which allowed the refinement of thermochemical standard state data for end-member titanite. Based on the QUIlF data base (Frost et al., 1988; Lindsley and Frost, 1992; Frost and Lindsley, 1992; Andersen et al., 1993), the thermodynamic

interpretation of the experiments by Xirouchakis and Lindsley (1998) suggested a higher heat capacity, a more negative enthalpy of formation, and a smaller standard state entropy for titanite, compared to previously published data.

Thus the thermochemical data of titanite are still subject of discussion, which is the motivation for measuring the heat capacity of the titanite sample of the present study. This sample was crystallized from a glass (Chapter 2), and is therefore likely to contain impurities, according to Xirouchakis et al. (1997b). In fact, a small amount of wollastonite was detected in the sample with X-ray diffraction, but no evidence for quartz exists. Despite the wollastonite impurity, however, the unit cell dimensions of this titanite are identical within error with those determined for the sub-solidus sample by Xirouchakis et al. (1997b) (Chapter 3).

4.2.3 Transition temperature

An attempt was undertaken to determine the transition temperature of the $P2_1/a$ to $A2/a$ phase transition[1] in titanite solid-solution as a function of composition. In pure titanite, the phase transition takes place at around 496 K, as indicated by numerous investigations with other techniques, such as Raman spectroscopy (Salje et al., 1993), TEM (Van Heurck et al., 1991), XRD (Ghose et al., 1991; Chrosch et al., 1997), and infrared spectroscopy (Meyer et al., 1998). Calorimetric studies by Zhang et al. (1995) and Xirouchakis and Tangeman (1998) reported lambda-shaped anomalies at 486 K and 483 ± 5 K, respectively, which probably represent the phase transition (Figure 4.1). The transition temperature can be expected to drop with increasing AlF-content in titanite, reaching room-temperature somewhere between 9 and 18 mol.% of $CaAlFSiO_4$, as indicated by TEM investigations of this and previous studies (Troitzsch and Ellis, 1999, and references therein). DSC measurements were carried out on three synthetic samples: titanite with $X_{Al} = 0.00$, $X_{Al} = 0.05$, and $X_{Al} = 0.09$, with the aim to extrapolate the 'transition composition' of the binary join $CaTiOSiO_4$-$CaAlFSiO_4$ to room temperature. This project was testing the detection limit of the calorimeter,

[1] Because this phase change appears to take place in several steps over a certain temperature interval (Kek et al., 1996), it is necessary to define which part of the transition is determined here. According to Kek et al. (1996), the onset of the phase transition in pure titanite at 496 K is characterized by the displacement of the Ti atom. This causes the formation of anti-phase domains, and thus the loss of long-range order within each octahedral chain, which characterizes the low-temperature phase α with space group $P2_1/a$ (see also discussion in Chapter 3). Kek et al. (1996) proposed that an intermediate phase β is stable between 495 and 825 K, which is characterized by a split-position of the Ca atom. According to these authors titanite with true $A2/a$ symmetry, phase γ, only exists above 825 K, where the Ca atom oscillates between two possible positions. The most energetic part of this stepwise phase change is represented by its onset at around 496 K, as this is detectable with various different methods, including scanning differential calorimetry (see discussion in text). It is this *onset* of the phase change that will be determined in this study. For simplicity, and for the sake of consistency with most previous studies, this onset will be termed the $P2_1/a$ to $A2/a$ 'phase transition', or 'phase change', bearing in mind that it probably does not strictly represent the entire $P2_1/a$ to $A2/a$ transformation.

because the transition enthalpy of the titanite phase transition is known to be very small (~80 Jmol^{-1}, as estimated by Thiéblot et al., 1999). Moreover, the well-defined lambda-shaped anomaly in the heat capacity of pure titanite (Zhang et al., 1995) can be expected to broaden and 'smear out' with increasing amount of 'impurities' (Meyer et al., 1998) such as Al^{3+}.

4.3 Experimental details

4.3.1 Samples

The synthesis of pure titanite from glass (sample AlF00) was described in Chapter 2. This sample contains a small amount of wollastonite as indicated by weak reflections (< 3% relative intensity) in the XRD pattern. The samples with X_{Al} = 0.052 ± 0.006 (sample AlF05) and X_{Al} = 0.094 ± 0.008 (sample AlF09) were synthesised at 1000°C and 10 kbar from synthetic wollastonite, rutile, anorthite and fluorite using the piston-cylinder apparatus, as described in Chapter 3. Chemical analyses of all four samples are listed in Appendix 1. The sample size was about 150 mg. Both AlF-bearing samples were investigated with SEM and XRD to ensure that only homogeneous titanite was present.

4.3.2 DSC

All measurements were carried out using a differential scanning calorimeter DSC 2920 (TA Instruments) located at the Research School of Chemistry at the Australian National University. Temperature calibrations performed on phase transitions of indium, tin, zinc and $C_{10}H_8$ indicate an accuracy of ± 1.5 degrees over the temperature range of 353 to 670 K. Non-hermetically sealing aluminium pans were used for all samples. The calorimetric precision of the instrument is given as 1% by the manufacturer (DSC 2920 instruction, 1994). However, multiple scans of this study indicate that heat capacities can only be reproduced to within 2%. Problems encountered during a second set of heat capacity measurements are described in Appendix 2.

4.3.2.1 Heat capacity measurements

The titanite and $CaAlFSiO_4$ samples were finely ground and dried. Between 40 and 50 mg of the powders was filled into the pans. The lid was inverted in order to press down the powder firmly in the pan. Compacting the powder improved the contact of the sample with the pan bottom and thus with the thermocouple, and facilitated heat

transfer in the sample. The samples were annealed at temperatures above 800 K for about 30 minutes to avoid strain-release and recrystallization effects during the run. Before each sample-run, the heat capacity of a standard sapphire disk was determined over the entire temperature range (170 to 851 K), which yielded a calibration factor E (see DSC 2920 instruction, 1994). This was subsequently used to convert the measured heat flow of the sample runs to the heat capacity of each sample. The standard and sample runs were performed at a heating rate of 20 degrees per minute. Two scans were performed for each substance, and their mean was taken as the final value.

4.3.2.2 Phase transition temperature

The samples were finely ground and dried. About 20 mg of each sample was filled into the pans, with the lid inverted. Pressing down the powder was especially important in this case because this significantly smoothened and straightened the signal, probably by limiting movement of grains within the sample during heating. The weak signals of the phase transition would otherwise not stand up from the background noise. A heating and cooling rate of 5°/min, which was a trade-off between producing a large signal and smooth background (fast heating rate) and a sharp peak (slow), proved to be the most sensitive for this sample size, and was applied to all samples. The temperature ranges scanned were 323 to 673 K for samples AlF00 and AlF05, and 273 to 573 K for the sample AlF09. Both heating and cooling ramps were recorded. One larger sample of AlF09 (30 mg) was scanned at a heating rate of 20°/min between 170 and 850 K.

4.4 Results and discussion

4.4.1 CaAlFSiO$_4$

4.4.1.1 Experimental specific heat of CaAlFSiO$_4$

The specific heat of CaAlFSiO$_4$, which was calculated as the mean of two scans of the same sample, increases smoothly over the investigated temperature range (Table 4.1, Figure 4.3). The experimental data can be reproduced within 1% by the heat capacity equation based on Haas and Fisher (1976), as used in the data base of Robie and Hemingway (1995)

$$C_P = a + bT + cT^{-2} + dT^{-0.5} + eT^2 \tag{4.2}$$

as well as by the equation proposed by Berman and Brown (1985)

$$C_P = a + cT^{-2} + dT^{-0.5} + fT^{-3} \tag{4.3}$$

Table 4.1 Experimental specific heats of $CaAlFSiO_4$ and $CaTiOSiO_4$, based on two scans for each substance.

	CaAlFSiO$_4$		CaTiOSiO$_4$			CaAlFSiO$_4$		CaTiOSiO$_4$			CaAlFSiO$_4$		CaTiOSiO$_4$	
T	C_P	1σ	C_P	1σ	T	C_P	1σ	C_P	1σ	T	C_P	1σ	C_P	1σ
[K]	[Jmol^{-1}K^{-1}]		[Jmol^{-1}K^{-1}]		[K]	[Jmol^{-1}K^{-1}]		[Jmol^{-1}K^{-1}]		[K]	[Jmol^{-1}K^{-1}]		[Jmol^{-1}K^{-1}]	
170	86.81	0.10	92.62	1.12	400	162.83	0.86	162.52	1.32	630	184.86	0.48	180.97	0.56
180	92.21	0.84	97.32	1.05	410	164.45	0.91	163.94	0.95	640	185.99	0.26	181.43	0.82
190	97.14	0.87	101.64	1.74	420	165.77	0.89	165.17	0.95	650	185.91	0.38	181.80	0.74
200	101.80	0.52	105.95	1.21	430	166.97	1.10	166.73	0.99	660	186.51	0.22	182.50	1.03
210	106.15	0.45	110.49	0.92	440	168.65	1.24	168.09	0.41	670	187.50	0.44	182.92	0.70
220	110.45	0.63	114.48	1.35	450	170.00	1.30	169.55	0.35	680	187.78	0.22	183.08	0.45
230	114.35	0.64	117.65	1.10	460	170.93	1.26	170.99	0.36	690	188.69	0.09	183.42	0.55
240	118.08	0.26	121.37	1.14	470	172.11	1.38	172.82	0.22	700	189.15	0.26	183.81	0.03
250	121.63	0.13	124.90	1.34	480	173.21	1.39	174.11	0.41	710	189.84	0.19	184.34	0.42
260	124.89	0.59	127.69	1.58	490	174.26	1.35	174.27	0.32	720	190.29	0.14	184.86	0.06
270	128.25	0.37	130.74	1.27	500	174.94	0.99	173.89	0.27	730	190.77	0.14	185.77	0.85
280	131.50	0.27	133.55	1.15	510	175.94	1.22	174.42	0.42	740	191.02	0.29	185.76	0.58
290	134.80	0.51	136.27	1.01	520	176.84	1.31	175.15	0.30	750	191.27	0.04	186.35	0.49
300	137.41	0.22	139.07	0.88	530	177.47	1.44	175.58	0.39	760	191.82	0.48	186.53	0.52
310	140.40	0.27	141.54	0.61	540	178.24	1.39	176.45	0.48	770	192.53	0.14	186.90	0.22
320	143.04	0.18	143.80	0.69	550	178.80	1.96	176.74	0.50	780	192.93	0.33	187.19	0.47
330	145.81	0.31	146.63	1.07	560	179.73	1.29	177.45	0.42	790	193.10	0.26	187.71	0.73
340	148.61	0.34	149.03	0.88	570	180.85	1.07	177.93	0.39	800	193.05	0.30	187.81	0.59
350	151.08	0.89	151.52	0.78	580	181.48	1.49	178.52	0.31	810	193.79	0.09	188.04	0.34
360	153.92	0.70	153.93	1.13	590	182.04	1.27	179.09	0.59	820	194.48	0.15	188.32	0.58
370	156.66	0.76	156.76	1.40	600	182.55	0.93	179.26	0.53	830	194.60	0.09	188.31	0.62
380	158.97	0.52	159.16	1.20	610	183.31	1.00	180.24	0.62	840	195.08	0.21	188.34	0.45
390	160.98	0.80	160.93	1.30	620	184.39	0.61	180.62	0.71	850	194.82	0.48	188.57	0.56
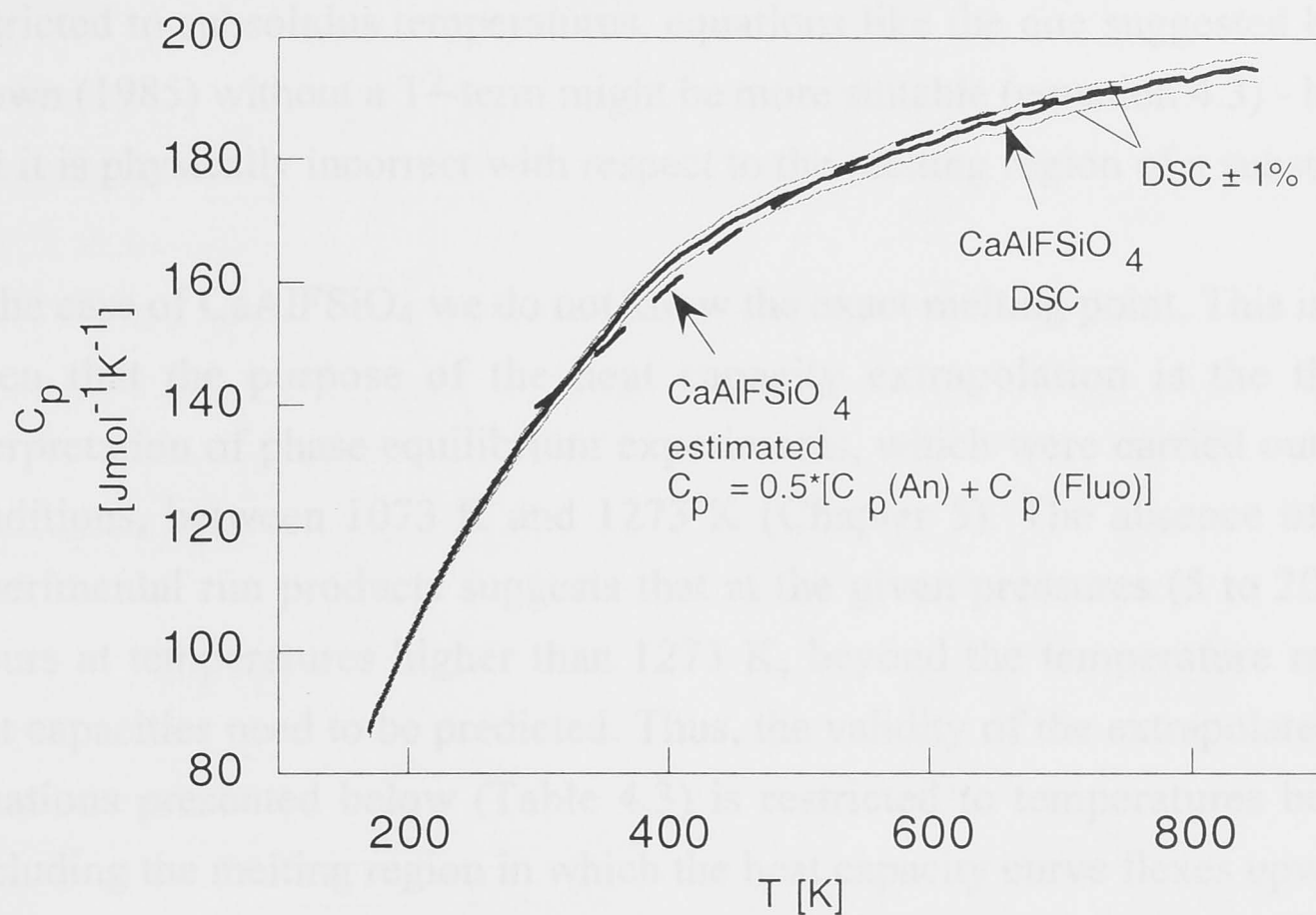
Figure 4.3 Heat capacity of synthetic $CaAlFSiO_4$, determined by differential scanning calorimetry (solid line), and estimated from the component heat capacities (stippled line, see text). Solid line represents the average of two scans deviating less than 1% from the mean value.

The equation suggested by Maier and Kelley (1932)

$$C_P = a + bT + cT^{-2} \qquad (4.4)$$

does not reproduce the experimental results satisfactorily, with deviations up to 5 % from the calorimetric data. The coefficients for all equations are given in Table 4.2. The experimental heat capacity data presented here are in good agreement with the heat capacity estimate for $CaAlFSiO_4$, calculated as the sum of the heat capacities of anorthite and fluorite, as given in the data base of Robie and Hemingway (1995) (Figure 4.3; see also Figure A2.7b in Appendix 2).

4.4.1.2 Extrapolation to higher temperatures

When extrapolating experimental heat capacity data to higher temperatures, it has to be decided up to which temperature the prediction would be reasonable, what shape the heat capacity curve is likely to have, and thus which heat capacity equation would represent the data most accurately. The suitability of various equations to predict high-temperature heat capacities, has been the subject of many previous studies (see discussion and references in Berman and Brown, 1985). Essentially, if the extrapolation exceeds the melting point of a substance, the equations have to be able to describe the sudden increase of the heat capacity in the melting region, as is that by Haas and Fisher

(1976) due to the T^2-term it includes (equation 4.2). However, if the extrapolation is restricted to subsolidus temperatures, equations like the one suggested by Berman and Brown (1985) without a T^2-term might be more suitable (equation 4.3) - bearing in mind that it is physically incorrect with respect to the melting region of a substance.

In the case of $CaAlFSiO_4$ we do not know the exact melting point. This is not a problem given that the purpose of the heat capacity extrapolation is the thermodynamic interpretation of phase equilibrium experiments, which were carried out at sub-solidus conditions, between 1073 K and 1273 K (Chapter 5). The absence of melt from all experimental run products suggests that at the given pressures (5 to 20 kbar) melting occurs at temperatures higher than 1273 K, beyond the temperature range for which heat capacities need to be predicted. Thus, the validity of the extrapolated heat capacity equations presented below (Table 4.3) is restricted to temperatures below ~1300 K. Excluding the melting region in which the heat capacity curve flexes upwards simplifies the data extrapolation, which is now only constrained by the so-called 'Dulong-Petit limit' (Gopal, 1966), besides the obvious criterion of a good fit to the data.

The Dulong-Petit limit defines the maximum possible heat capacity at constant volume C_V of a substance to be equal to $3nR$, where n is the number of atoms per formula unit, and R the gas constant. This limit was initially determined by Dulong and Petit in 1819 in an empirical study on solid elements, and was later explained theoretically by Boltzman in 1871 on the basis of classical kinetic theory (Gopal, 1966; Berman and Brown, 1985). Because the Dulong-Petit limit is approached by the specific heats only at high temperatures, as was justified by Einstein with quantum theory in 1907 (Gopal, 1966), the extrapolation of the data of $CaAlFSiO_4$ performed here simply requires that the heat capacity curve approaches the limit smoothly with increasing temperature without exceeding it. As the relation between the heat capacity at constant pressure C_P and that at constant volume C_V is described by equation

$$C_P = C_V + \frac{\alpha^2 VT}{\beta} \tag{4.5}$$

the Dulong-Petit limit is defined with respect to the heat capacity at constant pressure as

$$C_P = 3nR + \frac{\alpha^2 VT}{\beta} \tag{4.6}$$

Table 4.2 Coefficients for various heat capacity equations fitted to the calorimetric data of CaAlFSiO$_4$ [Jmol^{-1}K^{-1}].

Valid over the temperature range of 170 to 850 K.

T-term in equation coefficients	T^2 e [*10^4]	T^1 b	T^0 a	T$^{-0.5}$ d	T^{-2} c	T^{-3} f [*10^{-8}]	ARD* [%]
Haas and Fisher (1976)	1.6179 ±0.0527	-0.38647 ±0.01043	689.96 ±9.69	-8356.1 ±135.8	2911300 ±71388		0.33
Haas and Fisher (1976)		-0.067365 ±0.001553	398.02 ±2.97	-4315.5 ±52.1	886610 ±42492		0.48
Berman and Brown (1985)			226.14 ±0.83	-661.41 ±26.15	-6958600 ±106230	7.6173 ±0.1307	0.40
Maier and Kelley* (1932)		0.058447 ±0.001065	153.13 ±0.73		-2556700 ±29146		1.75

* ARD is the average relative deviation of the fitted from the experimental data, calcualted at intervals of 1 K.

Table 4.3 Coefficients for various heat capacity equations fitted to the calorimetric data of CaAlFSiO$_4$ [Jmol^{-1}K^{-1}], and extrapolated to higher temperatures.

Valid over the temperature range of 250 to 1300 K.

T-term in equation coefficients	T^2 e [*10^6]	T^1 b	T^0 a	T$^{-0.5}$ d	T^{-2} c	T^{-3} f [*10^{-8}]	ARD** [%]
Haas and Fisher* (1976)	4.5652 ±1.1852	-0.03067 ±0.00459	301.83 ±7.99	-2390.2 ±150.2	-1482900 175080		0.33
Haas and Fisher* (1976)		-0.01319 ±0.00067	272.54 ±2.46	-1854.4 ±56.567	-2055700 ±92437		0.33
Berman and Brown (1985)			224.36 ±1.57	-617.76 ±54.37	-6789800 ±313060	6.7774 ±0.51071	0.31
Berman and Brown* (1985)			211.27 ±0.75	-153.77 ±33.05	-9549900 ±294890	11.2780 ±0.56551	0.32
Maier and Kelley (1932)		0.02244 ±0.00059	181.94 ±0.46		-4491900 ±30927		0.44

* 'Dummy points' were added to the experimental data set (1500 K/202.32 Jmol^{-1}K^{-1} and 1800 K/202.87 Jmol^{-1}K^{-1})
** ARD as in Table 4.2., calculated between 250 and 850 K

Thermal expansion α and compressibility β are defined as

$$\alpha = V^{-1}\left(\frac{\delta V}{\delta T}\right)_P \tag{4.7}$$

and

$$\beta = -V^{-1}\left(\frac{\delta V}{\delta P}\right)_T \tag{4.8}$$

Due to lack of high-pressure and high-temperature XRD-data of $CaAlFSiO_4$, the thermal expansion α and isothermal compressibility β have to be estimated. They were chosen to be identical to those of the structurally related titanite end-member.

The thermal expansion of titanite was estimated by fitting straight lines through the high-temperature crystal structure data by Ghose et al. (1991) and Taylor and Brown (1976), yielding $1.68*10^{-5}$ K^{-1} and $1.96*10^{-5}$ K^{-1}, respectively (Figure 4.4). The mean of these values, $1.82*10^{-5}$ K^{-1}, was used for $CaAlFSiO_4$. The isothermal compressibility of titanite was estimated with a polynomial fit to the high-pressure data by Angel et al. (1999) and the volume of titanite at 1 bar (Table 3.2, p. 32), resulting in values for β as shown in Figure 4.5.

Figure 4.6 shows the Dulong-Petit limit for $CaAlFSiO_4$ which was calculated with equation (4.6), substituting the above values for expansion and compressibility, the unit-cell volume of 344.24(1) $Å^3$ (Chapter 2), and $n = 8$. All four equations which were fitted to the calorimetric data between 170 and 850 K (Figure 4.3, Table 4.2) were extrapolated to 1300 K (Figure 4.6, Table 4.3). To ensure that the curves approach the Dulong-Petit limit, two 'dummy points' at 1500 K (202.32 $Jmol^{-1}K^{-1}$) and 1800 K (202.87 $Jmol^{-1}K^{-1}$), placed exactly on the limit, were included in the fitting process. Note that these two data points are theoretically impossible as they probably lie above the melting temperature, where the heat capacity should be much higher than the Dulong-Petit limit. Consistent with this they lie outside the temperature range over which the equations are defined to be valid (Table 4.3). The equation by Berman and Brown (1985) was fitted with and without dummy points.

Again, the Maier and Kelley (1932) equation is not well suited to represent the heat capacity of $CaAlFSiO_4$. It either matches the experimental data well, but fails to approach the Dulong-Petit limit (Figure 4.6), or it fits the dummy points satisfactorily, but not the data. Although all other curves slightly exceed the Dulong-Petit limit above 1150 K as well in order to obtain a satisfactory fit to the data, they deviate less than 1.5 $Jmol^{-1}K^{-1}$ at 1273 K, for example, as opposed to 7 $Jmol^{-1}K^{-1}$ for Maier and Kelley (1932), and are therefore favoured by this study.
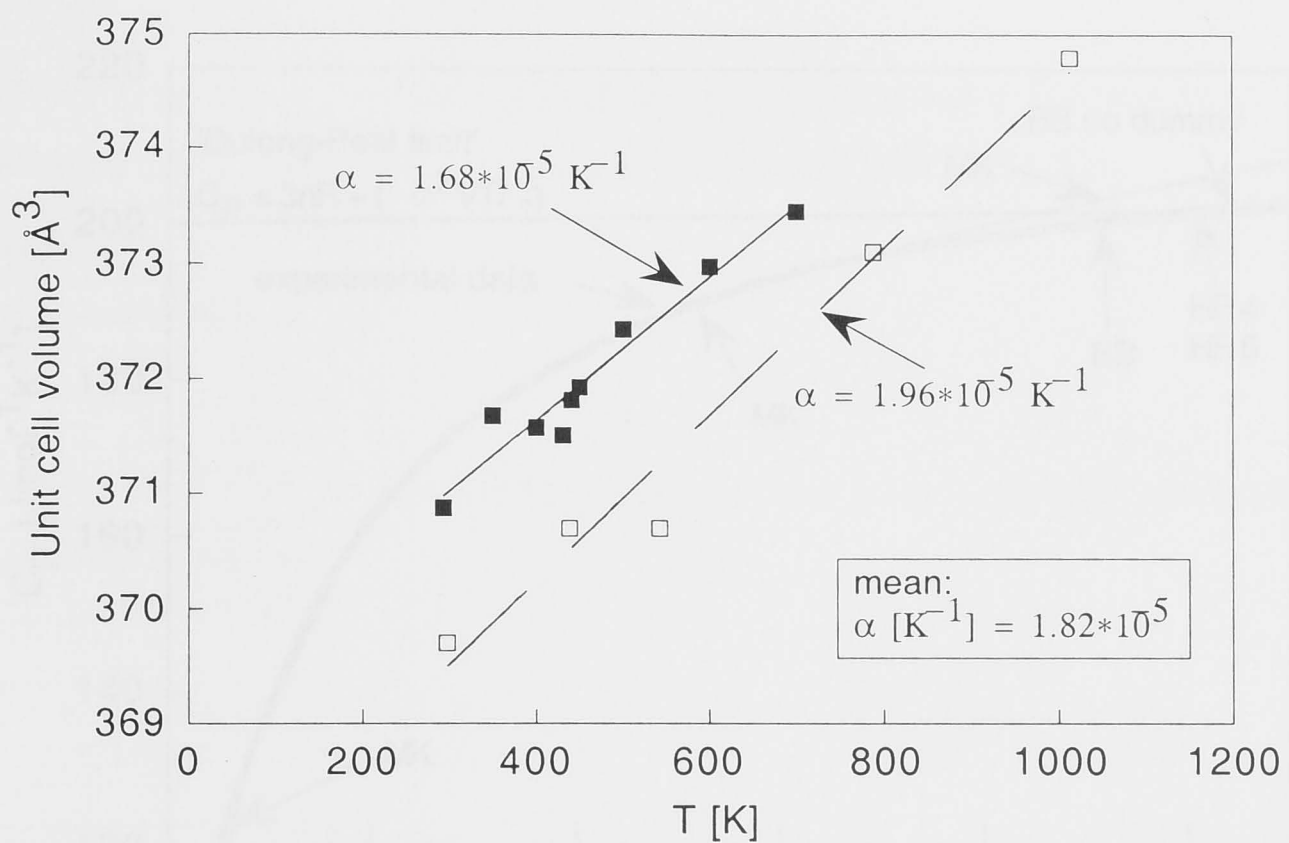
Figure 4.4 Estimation of thermal expansion α of titanite, based on high-temperature XRD data of Taylor and Brown (1976) (open symbols) and Ghose et al. (1991) (filled symbols).
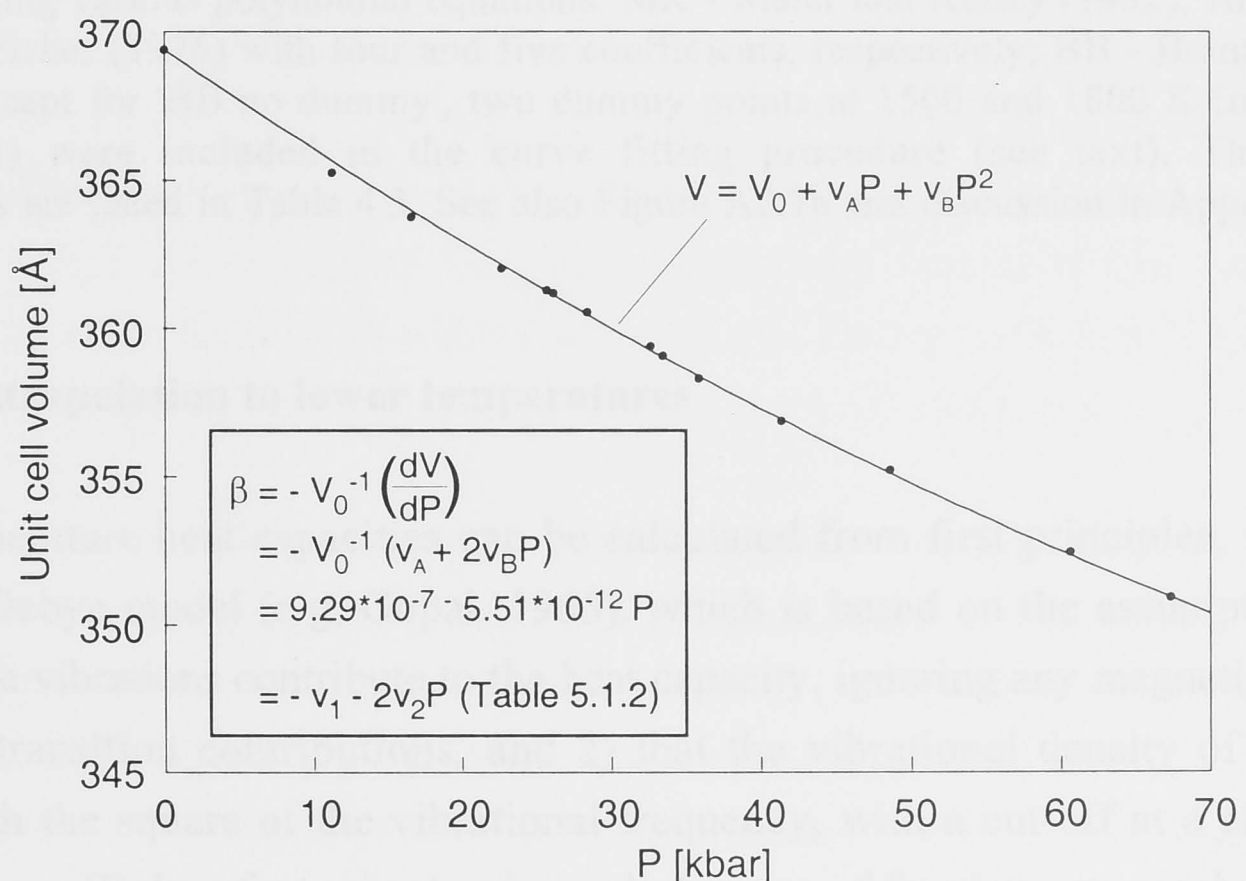
Figure 4.5 Estimation of isothermal compressibility β of titanite from high-pressure (room temperature) XRD data by Angel et al. (1999). The relationship between the compressibility and the coefficients v_1 and v_2 (compare Table 5.1.2, p. 92) is shown in box.

The fact that a good fit to the $CaAlFSiO_4$ data always requires that the Dulong-Petit limit is exceeded at higher temperatures (Figure 4.6), could either indicate inaccurate (too high) experimental data are at high temperatures, or that the Dulong-Petit limit is slightly underestimated, based on errors in the thermal expansion or compressibility of $CaAlFSiO_4$. For example, the Dulong-Petit limit would increase by 1.5 $Jmol^{-1}K^{-1}$, if the thermal expansion was dependent on temperature ($\alpha = a + bT$) with $b = 40*10^{-10}$ K^{-1}, a value similar to other silicates (compare parameter v_4 in Berman, 1988). An error in the compresssibility of $3.6*10^{-7}$ bar^{-1} would have the same effect.
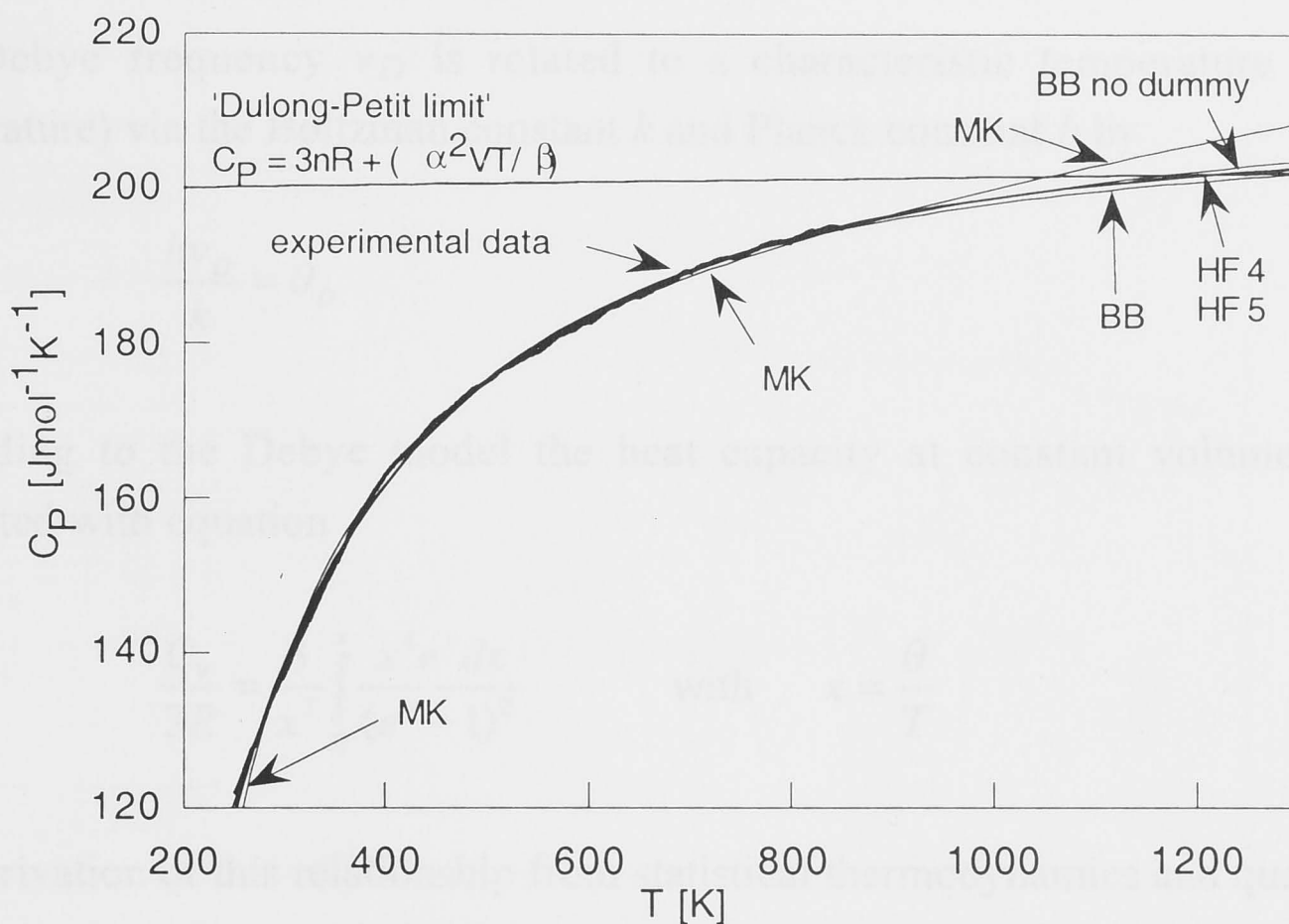
Figure 4.6 Extrapolation of the experimentally determined heat capacity of CaAlFSiO₄ to 1300 K, using various polynomial equations: MK - Maier and Kelley (1932); HF 4 and HF 5 - Haas and Fisher (1976) with four and five coefficients, respectively; BB - Berman and Brown (1985). Except for 'BB no dummy', two dummy points at 1500 and 1800 K (on the Dulong-Petit limit) were included in the curve fitting procedure (see text). The polynomial coefficients are listed in Table 4.3. See also Figure A2.7b and discussion in Appendix 2.

4.4.1.3 Extrapolation to lower temperatures

Low-temperature heat capacities can be calculated from first principles, for example with the Debye model (e.g, Gopal, 1966), which is based on the assumptions that 1) only lattice vibrations contribute to the heat capacity, ignoring any magnetic, electronic or phase transition contributions, and 2) that the vibrational density of states, g(v) varies with the square of the vibrational frequency, with a cut-off at a characteristic frequency v_D (Debye frequency), where all degrees of freedom are reached (equation 4.9). By allowing a range of different frequencies up to v_D the Debye model represents a significant improvement of the pioneering Einstein model, which was based on the assumption that all atoms in the crystal vibrate with the same frequency. Excluding the very low frequencies, the Einstein model failed to reproduce heat capacities at lower temperature satisfactorily.

The frequency distribution assumed by the Debye model is formulated as (Gopal, 1966)

$$g(v) = \frac{3v^2}{v_D} \quad \text{for } v \leq v_D \tag{4.9}$$

$$= 0 \qquad\qquad \text{for } v > v_D$$

The Debye frequency v_D is related to a characteristic temperature θ_D (Debye temperature) via the Boltzman constant k and Planck constant h by

$$\frac{h v_D}{k} = \theta_D \tag{4.10}$$

According to the Debye model the heat capacity at constant volume C_V can be computed with equation

$$\frac{C_V}{3R} = \frac{3}{x^3} \int_0^x \frac{x^4 e^x dx}{(e^x - 1)^2} \qquad \text{with} \qquad x = \frac{\theta}{T} \tag{4.11}$$

The derivation of this relationship from statistical thermodynamics and quantum theory is described in Gopal (1966). Equation 4.11 demonstrates that the heat capacity is a function of the ratio of the Debye temperature to the actual temperature. Thus, for any known heat capacity of a substance the Debye temperature can be calculated at each temperature, and vice versa. As the relationship between the heat capacity at constant volume and that at constant pressure C_p (measured by DSC) is known (equation 4.5), the Debye temperature for $CaAlFSiO_4$ can be calculated over the temperature interval of the DSC measurements. The extrapolation of the Debye to 0 K will then allow to calculate heat capacity values for temperatures between 0 and 170 K.

If the Debye model was an ideal model for the atomic vibrations and the resulting heat capacity, the Debye temperature calculated from calorimetric data should be a constant value over the entire temperature interval. However, it is found that for most substances the Debye temperature changes with temperature, especially for solids with more complex crystal structures, such as silicates (Kieffer, 1980). The Debye temperature calculated from the DSC data for $CaAlFSiO_4$ is shown in Figure 4.7. It is not constant, as expected, and shows a drop-off towards lower temperature, as observed in many silicates (Kieffer, 1980). Typically, the Debye temperature rises again as 0 K is approached, but since DSC data of this area are unavailable, this point remains unknown for $CaAlFSiO_4$ and cannot be modelled. Therefore two alternative extrapolations of the Debye temperature were performed with the intent to cover the entire possible range for entropy values. The first model assumes that the Debye temperature of 763.2 K, which was calculated for the lowest temperature data point, remains constant between 0 and 170 K. Model two extrapolates the drop-off of the Debye temperature with a 2nd degree polynomial function, fitted to DSC data between 170 and 300 K (Figure 4.7).
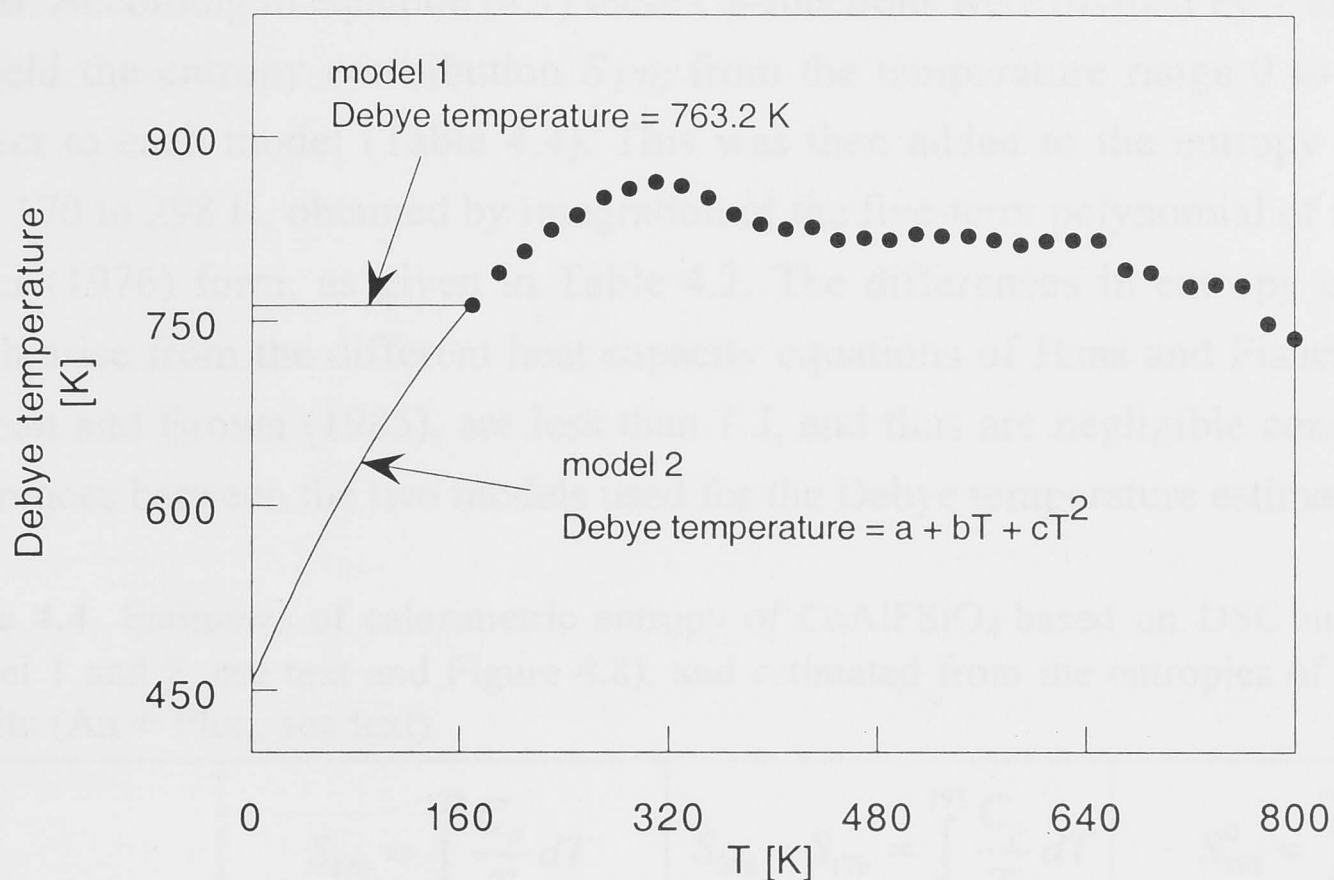
Figure 4.7 Variation of the Debye temperature of CaAlFSiO$_4$ with temperature. Debye temperatures calculated from calorimetric data above 170 K (dots) were extrapolated to absolute zero with two methods (solid lines), which are discussed in the text. Polynomial coefficients of model 2: a = 456.25, b = 2.4175, c = -3.5535*10^{-3}.
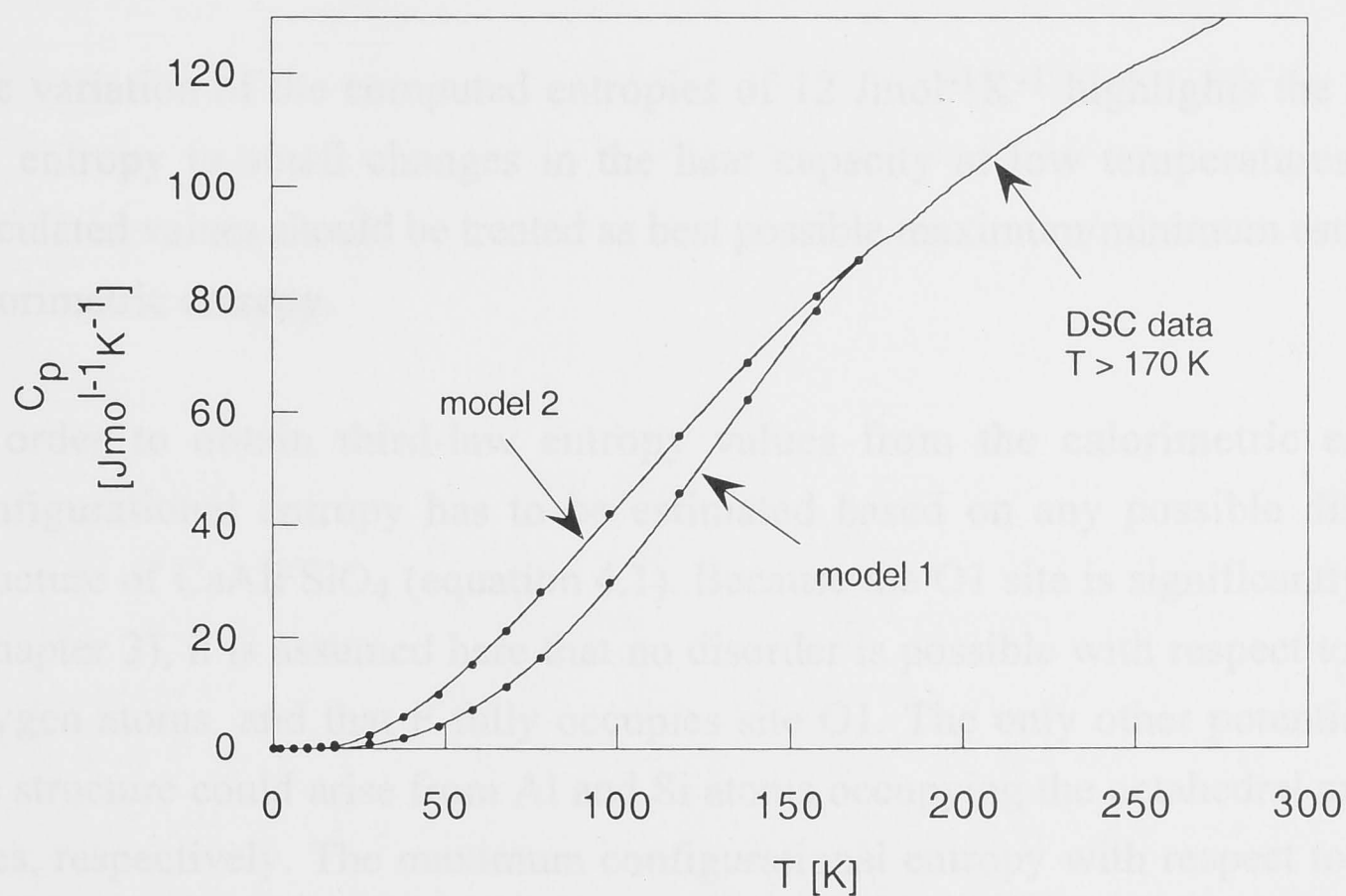
Figure 4.8 Low-temperature heat capacity of CaAlFSiO$_4$ (dots, T < 170 K), calculated with the extrapolated Debye temperatures shown in Figure 4.7, and experimentally determined heat capacity (solid line, T > 170 K). Polynomial functions y = a + bT + cT^2 + dT^3 + eT^4 were fitted to the data points between 0 and 170 K (solid lines). Coefficients: a=0.17013, b=-0.028054, c=0.00042239, d=4.8116*10^{-5}, e=-1.885*10^{-7} (model 1); a=0.50414, b=-0.15768, c=0.0091496, d=-3.6691*10^{-5}, e=3.4537*10^{-8} (model 2).

Figure 4.8 shows the low-temperature heat capacities which were calculated with these two models. Polynomial functions were fitted to 16 data points calculated with each model. According to equation (4.1) these C_P-functions were divided by T and integrated to yield the entropy contribution S_{170} from the temperature range 0 to 170 K with respect to each model (Table 4.4). This was then added to the entropy contribution from 170 to 298 K, obtained by integration of the five-term polynomial of the Haas and Fisher (1976) form, as given in Table 4.2. The differences in entropy contributions which arise from the different heat capacity equations of Haas and Fisher (1976) and Berman and Brown (1985), are less than 1 J, and thus are negligible compared to the differences between the two models used for the Debye temperature estimates.

Table 4.4 Estimates of calorimetric entropy of $CaAlFSiO_4$ based on DSC measuremenets (model 1 and 2, see text and Figure 4.8), and estimated from the entropies of anorthite and fluorite (An + Fluo, see text).

	$S_{170} = \int\limits_{0}^{170} \dfrac{C_p}{T} dT$	$S_{298} - S_{170} = \int\limits_{170}^{298} \dfrac{C_p}{T} dT$	$S_{298}^{0} = \int\limits_{0}^{298} \dfrac{C_p}{T} dT$
method	Debye model	calorimetry	
	[Jmol^{-1}K^{-1}]	[Jmol^{-1}K^{-1}]	[Jmol^{-1}K^{-1}]
model 1	41.7	63.0	104.7
model 2	55.1	63.0	118.1
An + Fluo			112.9

The variation of the computed entropies of 12 Jmol^{-1}K^{-1} highlights the sensitivity of the entropy to small changes in the heat capacity at low temperatures. Thus these calculated values should be treated as best possible maximum/minimum estimates for the calorimetric entropy.

In order to obtain third-law entropy values from the calorimetric entropies, the configurational entropy has to be estimated based on any possible disorder in the structure of $CaAlFSiO_4$ (equation 4.1). Because the O1 site is significantly overbonded (Chapter 3), it is assumed here that no disorder is possible with respect to fluorine and oxygen atoms, and that F fully occupies site O1. The only other potential disorder in the structure could arise from Al and Si atoms occupying the octahedral and tetrahedral sites, respectively. The maximum configurational entropy with respect to this disorder can be estimated following the method described in Ulbrich and Waldbaum (1976) based on the equation

$$S_{configurational} = -R \sum_{j} m_{j} \sum_{i} X_{i,j} \ln X_{i,j} \qquad (4.12)$$

where R is the gas constant, i the atom species on a site j, m_j the ratio of site multiplicity to number of formula units per unit cell, and $X_{i,j}$ the molar ratio of an atom species on a site. For complete Al-Si disorder on two sites in $CaAlFSiO_4$ m_j and $X_{i,j}$ are 1 and 0.5, respectively, which results in a maximum possible configurational entropy of

$$S_{configurational} = -2R(0.5\ln 0.5 + 0.5\ln 0.5) = 11.53 \text{ Jmol}^{-1}\text{K}^{-1} \qquad (4.13)$$

Given that the real amount of disorder is unknown, the third-law entropy can only be estimated to range between 104.7 and 116.2 $\text{Jmol}^{-1}\text{K}^{-1}$ with respect to model 1, and between 118.1 and 129.6 $\text{Jmol}^{-1}\text{K}^{-1}$ with respect to model 2. However, based on the different sizes of Al and Si it is proposed here that only little, if any disorder exists between the tetrahedral and octahedral sites in $CaAlFSiO_4$, and that the third-law entropy is best approached by values close to the calorimetric entropy, as given in Table 4.4.

4.4.1.4 Sum of component entropies

An alternative way to estimate the standard state entropy of an unknown substance is to sum up the entropies of all constituting components, and to apply a volume correction for any volume difference between the substance and its components, as described in Fyfe et al. (1958). Based on the data base by Robie and Hemingway (1995) the sum of the component entropies anorthite and fluorite is 268.2 ± 0.6 $\text{Jmol}^{-1}\text{bar}^{-1}$, and thus 134.1 ± 0.3 Jbar^{-1} per mole $CaAlFSiO_4$. The volume correction is essential because the entropy of any substance depends on volume due to the relationship

$$\frac{\partial S}{\partial V} = \frac{\alpha}{\beta} \qquad (4.14)$$

As the volume difference between dense high-pressure phase $CaAlFSiO_4$ compared to anorthite and fluorite is known (-1.084 $\text{Jmol}^{-1}\text{bar}^{-1}$), and α and β are assumed to be equal to those of titanite as calculated above, the volume correction of the entropy at 1 bar amounts to -21.24 $\text{Jmol}^{-1}\text{K}^{-1}$. Thus the entropy of $CaAlFSiO_4$ is 134.1 - 21.24 = 112.9 ± 0.3 $\text{Jmol}^{-1}\text{K}^{-1}$. This value lies within the entropy range estimated from combined DSC and first principle calculations (Table 4.4). Note that these calculations, similar to those with the Debye model, estimate the *calorimetric entropy*, which is only identical to the *standard state entropy* under the assumption that there is neither a low-temperature heat-capacity anomaly, e.g. due to a phase transition, nor a configurational entropy contribution.

4.4.2 Heat capacity of Titanite

Figure 4.9 shows the experimental heat capacity of titanite, determined in two scans using the synthetic sample of this study (Table 4.1). The position of the positive heat capacity anomaly at 485 ± 3 K shown by the data of this study, compares very well to that of the lambda-shaped anomalies reported from the DSC studies by Zhang et al. (1995) at 486 K, and Xirouchakis et al. (1998) at 483 ± 5 K (Figure 4.1). This anomaly can be ascribed to the $P2_1/a$ to $A2/a$ phase transition in titanite. As in the study by Xirouchakis and Tangeman (1998), the potential second anomaly above 800 K (Zhang et al., 1995 and 1997; Kek et al., 1996) could not be confirmed with the present data.

Below 450 K the data of this study reproduce the heat capacity data of the studies by King et al. (1954) and Xirouchakis and Tangeman (1998) within error (Figure 4.9). At higher temperatures, the data presented here are comparable to those reported by King et al. (1954) with mean deviations of 0.82 % and 0.66 % of all data points from literature values (Robie and Hemingway, 1995, based on King et al., 1954). These values are probably even slightly overestimated, because the maximum deviation of 2.2 % occurs at the phase transition near 484 K. This transition, however, was not detected by the heat content measurements of King et al. (1954), and therefore was not considered in the curve fitting of their data by Robie and Hemingway (1995) (Figure 4.9).
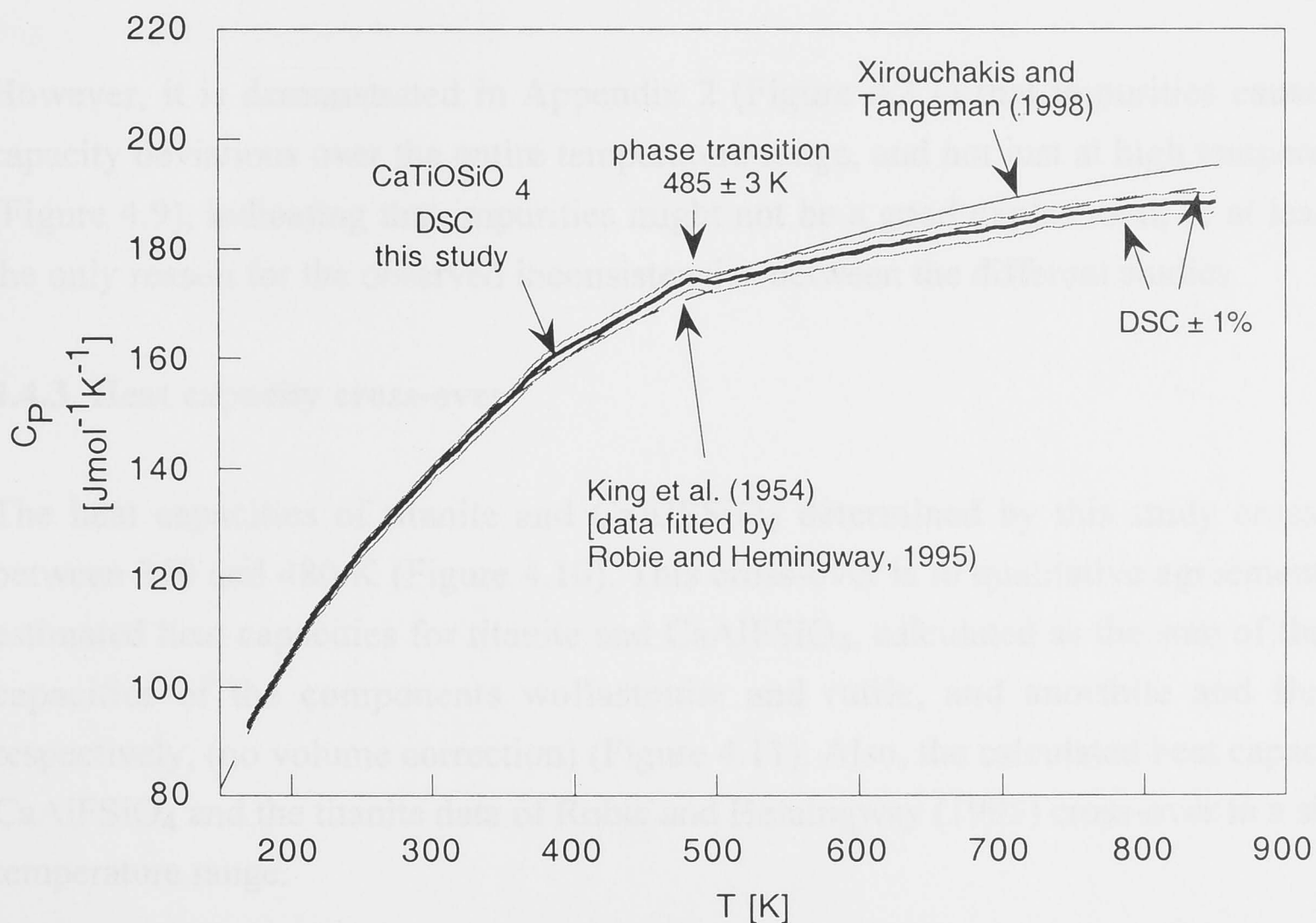
Figure 4.9 Heat capacity of synthetic titanite determined by differential scanning calorimetry. Solid line (this study) represents the average of two scans deviating less than 1% from the mean value. Some previous studies are shown for comparison. See also Figure A2.7a and discussion in Appendix 2.

In contrast to the good agreement of the data presented here and those of King et al. (1954), the specific heats reported by Xirouchakis and Tangeman (1998) exceed the ones of this study significantly, with deviations of up to 4 % at high temperatures (Figure 4.9; Note the discussion of potential errors attached to the calorimetric measurements in Appendix 2, and compare Figure A2.7a).

This allows two interpretations. First, it is possible that the measurements of Xirouchakis and Tangeman (1998) are inaccurate due to unaccounted analytical difficulties, in which case the data presented here, together with all other previous studies, would reflect more realistic heat capacity data of titanite. Alternatively, the hypothesis put forward by Xirouchakis et al. (1997a, 1997b) regarding the effect of synthesis condidtions on the purity of the sample as well as its thermochemical properties, as discussed in section 4.2.2, could be correct. In this case the heat capacity of titanite determined by Xirouchakis and Tangeman (1998) using a well characterized and stoichiometric sample, would be the most appropriate, whereas all other studies, including the present one, would suffer inadequacies based on sample impurity. The latter interpretation is supported by small amounts of wollastonite which were detected with XRD in the sample of this study. Also, the careful preparation and characterization of the synthetic titanite samples by Xirouchakis et al. (1997a, 1997b), and their detailed investigation with respect to unit cell volume and thermodynamic properties, suggests that they report high quality data.

However, it is demonstrated in Appendix 2 (Figure A2.1) that impurities cause heat capacity deviations over the entire temperature range, and not just at high temperatures (Figure 4.9), indicating that impurities might not be a good explanation, or at least not the only reason for the observed inconsistencies between the different studies.

4.4.3 Heat capacity cross-over

The heat capacities of titanite and $CaAlFSiO_4$ determined by this study cross over between 350 and 480 K (Figure 4.10). This cross-over is in qualitative agreement with estimated heat capacities for titanite and $CaAlFSiO_4$, calculated as the sum of the heat capacities of the components wollastonite and rutile, and anorthite and fluorite, respectively, (no volume correction) (Figure 4.11). Also, the calculated heat capacity of $CaAlFSiO_4$ and the titanite data of Robie and Hemingway (1995) cross-over in a similar temperature range.

Such a cross-over of heat capacities of two isostructural end-members has been reported previously, e.g. for grossular and pyrope (Kieffer, 1980). The fact that the heat capacity

of pyrope exceeds that of grossular at low temperatures, but is lower at temperatures above 400 K, was explained with low-frequency optical vibrations of the Mg atom in the eight-fold coordinated site of the garnet structure, which results in an anomalously high entropy for pyrope (Kieffer, 1980, Navrotsky, 1994). Such high vibrational contributions to heat capacity and entropy were found in several other high-pressure phases.

However, this concept cannot be applied to the cross-over observed in the titanite structure (Figure 4.10), because in this case the cross-over is reversed. The heat capacity of the high-pressure end-member $CaAlFSiO_4$ exceeds that of titanite at high temperatures, but is lower at low temperatures. Thus an excess entropy of the high-pressure phase does not exist. The fact that the cross-over in the titanite structure is predicted simply by summing up the component heat capacities of each end-member (Figure 4.11) also indicates that the cross-over should not be linked to the typical low-frequency vibrations found in other high-pressure phases. Alternatively, it could be speculated that vibrational changes linked to the $P2_1/a$ to $A2/a$ phase transition in the titanite end-member could possibly be the reason for a smaller increase in heat capacity at higher temperatures, and thus be the reason for the cross-over. Although this hypothesis is tempting because the cross-over is observed in the vicinity of the transition, it can be refuted on the grounds of the above argument that the calculated heat capacities show the same cross-over without considering any crystal structural features of the titanite structure.
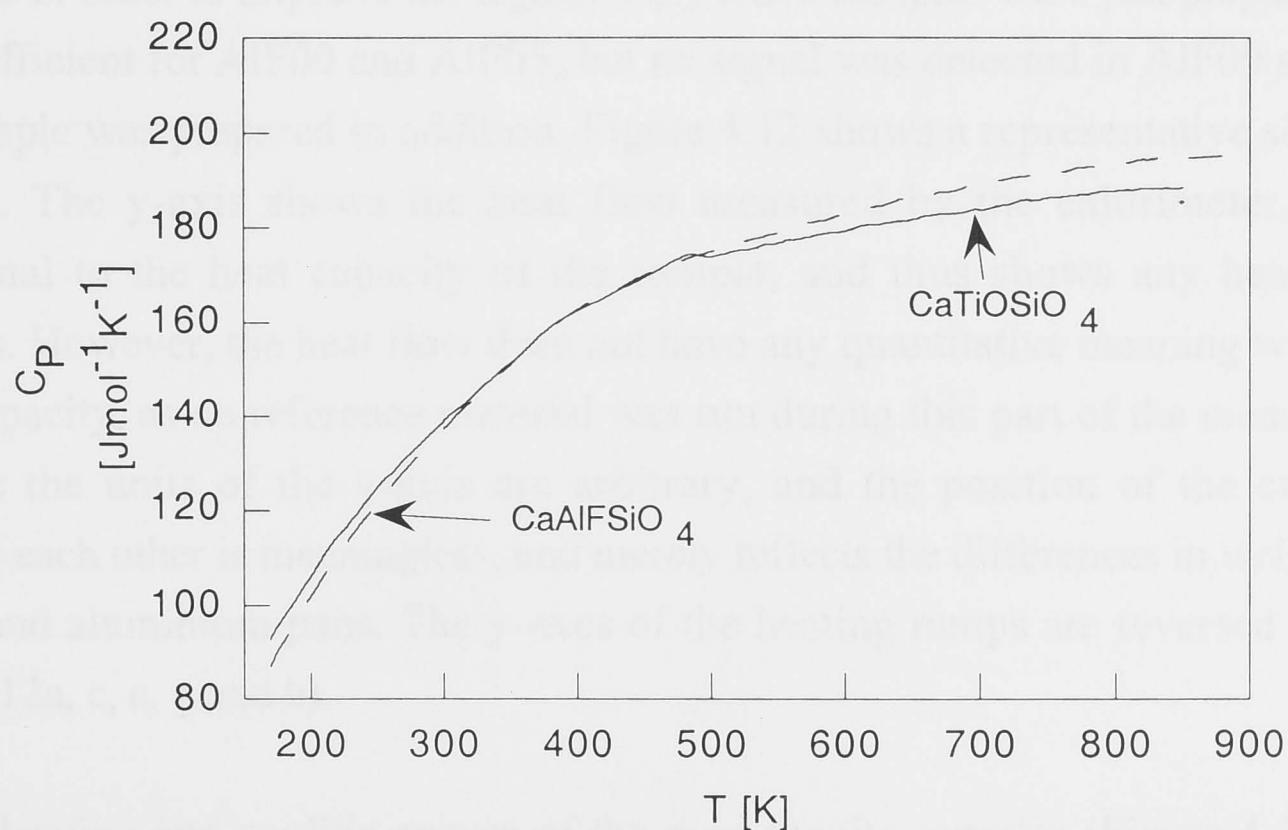
Figure 4.10 Experimental heat capacities of synthetic titanite and $CaAlFSiO_4$.
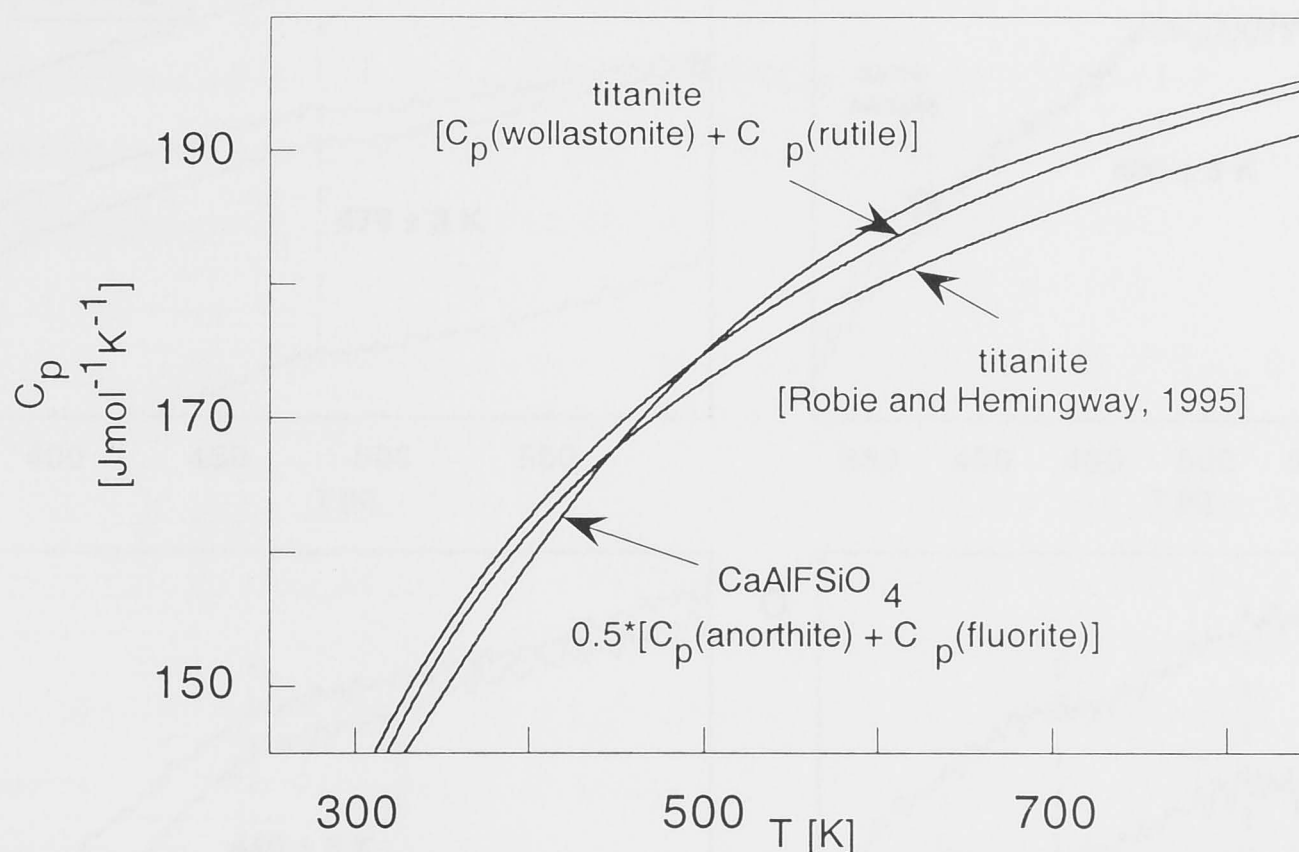
Figure 4.11 Heat capacity of CaAlFSiO$_4$, estimated by summing up the heat capacities of its components anorthite and fluorite, crosses over with that of titanite. This holds for both, titanite data estimated from the heat capacities of the components wollastonite and rutile, as well as titanite data based on calorimetry.

4.4.4 Transition temperature

The signal of the phase transition proved to be very weak, as expected, and could not be distinguished from the background in many scans. Being limited to small sample sizes for those samples synthesised in the piston-cylinder, the choice had to be made either to run several small samples of the same material in order to ensure reproducibility, or one big sample in order to improve the signal. Only small samples were just prepared, which proved sufficient for AlF00 and AlF05, but no signal was detected in AlF09 so that one larger sample was prepared in addition. Figure 4.12 shows a representative selection of the scans. The y-axis shows the heat flow measured by the calorimeter, which is proportional to the heat capacity of the sample, and thus shows any heat capacity anomalies. However, the heat flow does not have any quantitative meaning with respect to heat capacity, as no reference material was run during this part of the measurements. Therefore the units of the y-axis are arbitrary, and the position of the curves in y relative to each other is meaningless, and merely reflects the differences in weights of the samples and aluminium pans. The y-axes of the heating ramps are reversed for clarity (Figure 4.12a, c, e, g and h).

Both the heating and cooling curves of the pure titanite samples (Figure 4.12a and b) show a clear, reproducible signal at about 480 K, consistent with those shown in Figures 4.1 and 4.9. The heating curves stem from three individual titanite samples (from the same titanite batch), one of which was run twice.
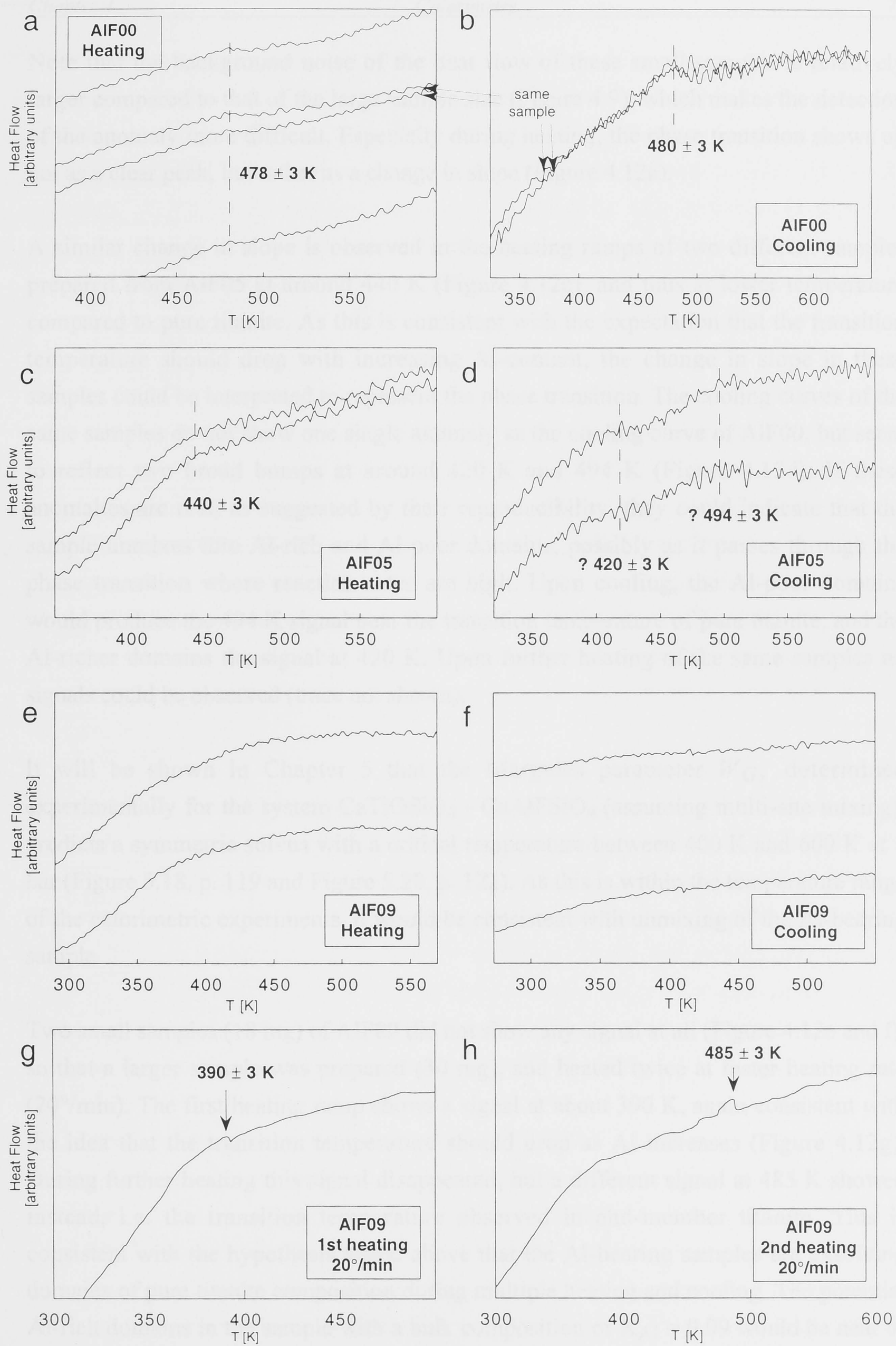
Figure 4.12 Heat flow measurements during heating and cooling of synthetic titanite samples with different Al-contents (X_{Al} = 0.00, 0.05, 0.09). Potential heat capacity anomalies are indicated. The traces in g) and h) were collected at a faster heating rate of 20°C/min (see text).

Note that the background noise of the heat flow of these small samples is relatively larger compared to that of the large sample size (Figure 4.9), which makes the detection of the anomaly more difficult. Especially during heating, the phase transition shows up not as a clear peak, but rather as a change in slope (Figure 4.12a).

A similar change in slope is observed in the heating ramps of two different samples prepared from AlF05 at around 440 K (Figure 4.12c), and thus at lower temperature compared to pure titanite. As this is consistent with the expectation that the transition temperature should drop with increasing Al-content, the change in slope in these samples could be interpreted to represent the phase transition. The cooling curves of the same samples do not show one single anomaly as the cooling curve of AlF00, but seem to reflect two broad bumps at around 420 K and 494 K (Figure 4.12d). If these anomalies are real, as suggested by their reproducibility, they could indicate that the sample unmixes into Al-rich and Al-poor domains, possibly as it passes through the phase transition where reaction rates are high. Upon cooling, the Al-poor domains would produce the 494 K signal near the transition temperature of pure titanite, and the Al-richer domains the signal at 420 K. Upon further heating of the same samples no signals could be observed (trace not shown).

It will be shown in Chapter 5 that the Margules parameter W_G, determined experimentally for the system $CaTiOSiO_4$ - $CaAlFSiO_4$ (assuming multi-site mixing), predicts a symmetric solvus with a critical temperature between 400 K and 600 K at 1 bar (Figure 5.18, p. 119 and Figure 5.20, p. 122). As this is within the temperature range of the calorimetric experiments, it would be consistent with unmixing of the Al-bearing sample.

Two small samples (18 mg) of AlF09 did not show any signal at all (Figure 4.12e and f), so that a larger sample was prepared (30 mg), and heated twice at faster heating rate (20°/min). The first heating ramp shows a signal at about 390 K, again consistent with the idea that the transition temperature should drop as Al increases (Figure 4.12g). During further heating this signal disappeared, but a different signal at 485 K showed instead, i.e. the transition temperature observed in end-member titanite. This is consistent with the hypothesis stated above that the Al-bearing samples are exsolving domains of pure titanite composition during multiple heating and cooling. The potential Al-rich domains in the sample with a bulk composition of $X_{Al} = 0.09$ would be near or even beyond the 'phase transition composition' at room temperature, and therefore belong to space group $A2/a$, not showing any signal, as suggested by Figure 4.12h. Alternatively, the small amounts of Al could be expelled from the titanite structure, and crystallize in a different phase, leaving behind pure titanite.

Although compositional *zoning* of titanite (Paterson and Stephens, 1992; Piccoli and Candela, 1991; Franz and Spear, 1985; Giére, 1992; Perseil and Smith, 1995), as well as *twinning* (Ribbe, 1980; Borg, 1970; Borg and Heard, 1972; Stephenson and Cook, 1997) are frequently observed, *unmixing textures* of titanites into Al-poor and Al-rich titanite domains, which would support the above hypothesis, have never been reported. Instead, Carswell et al. (1996) reported the breakdown of primary Al-rich titanite to a symplectite of secondary Al-poor titanite and anorthite (see also discussions in Chapters 5 and 6).

To test for unmixing into two titanites of different composition, the sample which produced Figure 4.12h was re-investigated with XRD after the calorimetric experiments. However, split peaks or peak broadening, which would suggest unmixing into Al-rich and Al-poor titanite domains, was not observed. It is possible, that the compositional differences between the potential domains are too small to be detected with XRD, or that the volumetric quantity of Al-rich domains is too small in such a Ti-rich titanite (X_{Al} = 0.09) to produce detectable titanite peaks in the diffraction pattern. Alternatively, the exsolved Al-rich phase is not titanite. Future investigation of this sample with TEM could provide more reliable information about unmixing of this sample.

Figure 4.13 is a summary plot of all heat capacity anomalies detected in the three samples, which were interpreted to represent the phase transition. This includes the heating and cooling ramps of AlF00, and the first heating ramps of AlF05 and AlF09. The extrapolation of the data to room temperature results in 'transition compositions' of X_{Al} = 0.196 ± 0.001 and X_{Al} = 0.151 ± 0.001 for linear and polynomial curve fit functions, respectively (Table 4.5). This compositional range is in agreement with the TEM investigations of this and previous work, which narrowed down the transition compositions to X_{Al} = 0.09 - 0.18 (Troitzsch and Ellis, 1999).

The extrapolation of the phase boundary shown in Figure 4.13 to absolute zero suggests that the $P2_1/a$ - $A2/a$ phase transition does not occur in the pure $CaAlFSiO_4$ end-member. At 0 K the phase boundary intersects the abcissa at compositions between X_{Al} = 0.27 and 0.51 (Table 4.5), so that $CaAlFSiO_4$ lies in the $A2/a$ stability field at all temperatures. Therefore, a low-temperature heat capacity anomaly due to the $P2_1/a$ - $A2/a$ phase transition, is not expected in pure $CaAlFSiO_4$. This is consistent with the above assumption, made in the Debye model calculations and entropy estimates, of the absence of any low-temperature heat capacity anomalies.
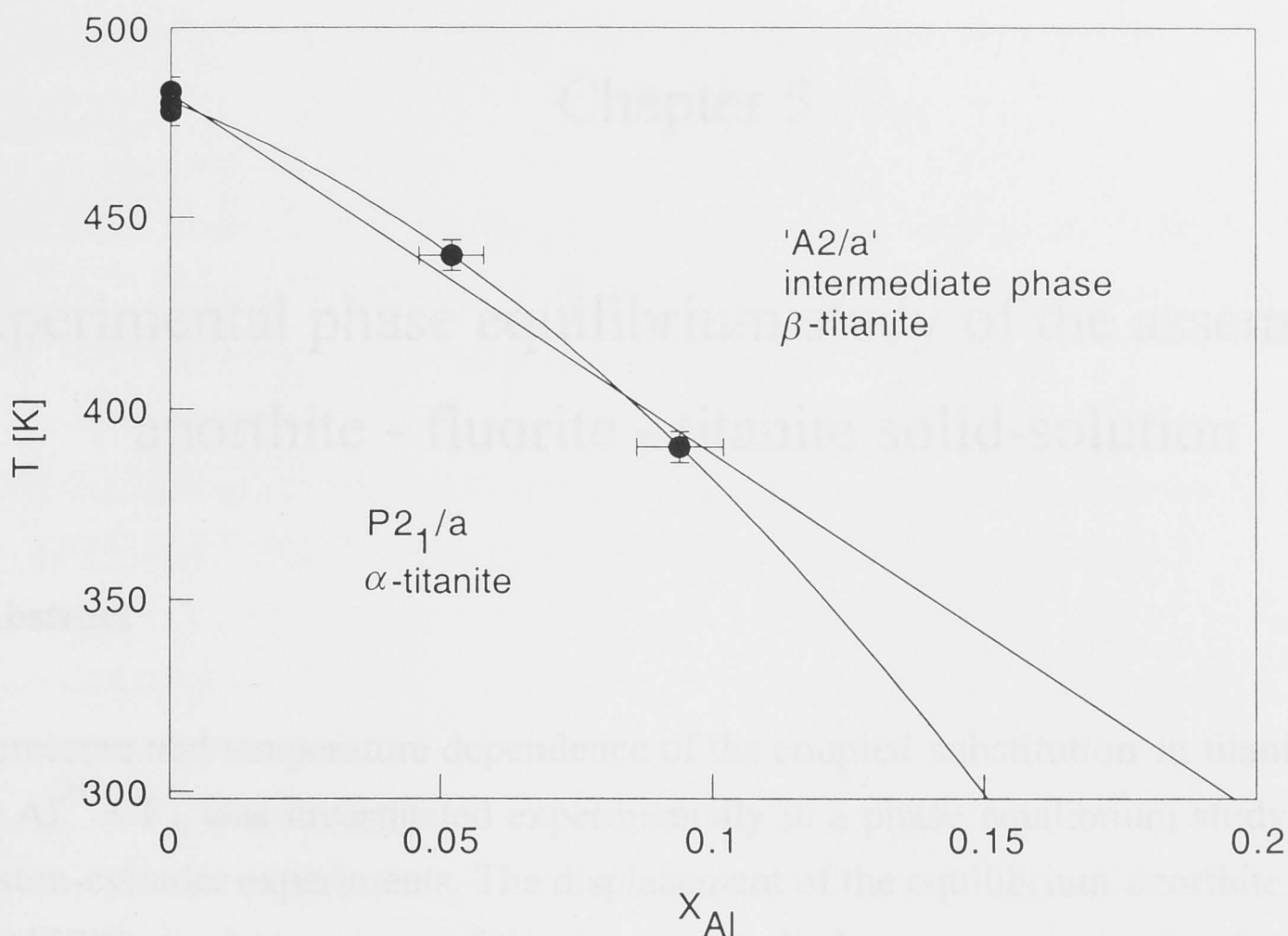
Figure 4.13 Section of the phase diagram of binary titanite solid-solution $CaTiOSiO_4$ - $CaAlFSiO_4$, which covers the T-X_{Al} range of the $P2_1/a$ - $A2/a$ phase transition (compare footnote in text for terminology). The construction of the phase diagram is based on thermal anomalies (data points) that were detected with heat flow measurements shown in Figure 4.12. Curve fit coefficients are listed in Table 4.5.

Table 4.5 Coefficients of linear and polynomial curve fit of Figure 4.13, relating the phase transition temperature (T) to the Al-content (X_{Al}) of titanite. $X_{Al}^{298.15}$ and X_{Al}^{0} are the phase transition compositions at room temperature and absolute zero.

Equation	$T\,[K] = a + bX_{Al}$	$T\,[K] = a + bX_{Al} + cX_{Al}^2$
a	482.33 ± 2.93	480.33 ± 5.96
b	-942.8 ± 51.0	-546.16 ± 1.4*10⁻⁴
c	-	-4413.1 ± 6.7*10⁻⁴
$X_{Al}^{298.15}$	0.195 ± 0.150	0.151 ± 0.015
X_{Al}^{0}	0.512 ± 0.030	0.274 ± 0.027

Given the weakness and therefore potential ambiguity of the heat capacity anomalies reported in this chapter, heat capacity measurements do not seem to be suitable to better resolve this area of the phase diagram of binary titanite solid-solution (Figure 4.13) compared to TEM and XRD investigations. They should be regarded as further evidence consistent with other methods, but their quality is not good enough to justify rigorous interpretation. The difficulty in determining the phase boundary more precisely with any method probably lies in the transitional nature of the phase change in the investigated temperature range, which proceeds as an increasing number of antiphase domains of essentially the same structure are formed.

Chapter 5

Experimental phase equilibrium study of the assemblage anorthite - fluorite - titanite solid-solution

5.1 Abstract

The pressure and temperature dependence of the coupled substitution in titanite, $Ti^{4+} + O^{2-} = Al^{3+} + F^-$, was investigated experimentally in a phase equilibrium study based on 25 piston-cylinder experiments. The displacement of the equilibrium anorthite + fluorite = $CaAlFSiO_4$ in the presence of titanite was studied at pressures ranging from 5 to 20 kbar, and temperatures between 800 and 1000°C. The Al-content of titanite increases with pressure and decreases with temperature, which is in qualitative agreement with the pioneering study by Smith (1981). The compositional range spanned by titanite of this study is large ($0.28 < X_{Al} < 0.92$), and exceeds the maximum Al-content of $X_{Al} = 0.54$ reported from synthetic titanite by Smith (1981). There is very good agreement of the pressure-temperature-composition data presented here with the recent experimental study of the same assemblage by Tropper et al. (1999, 2000), indicating good reproducibility.

The experimental results indicate that this binary titanite [$Ca(Ti,Al)(O,F)SiO_4$] behaves like a non-ideal, symmetrical solid-solution. The crystal structural problems, identified in very Al-rich titanite in Chapter 3, are not reflected in the experimentally determined activity-composition relations, which are simple and without any significant anomaly.

The enthalpy of formation from the elements, and third-law entropy of $CaAlFSiO_4$ were determined by least-squares regression of the experimental data. The agreement of the entropy determined here with the calorimetric entropy (Chapter 4) indicates that the configurational entropy, or any entropy contribution from a potential low-temperature phase transition, are either small or non-existent. The application of a mixing-on-sites model resulted in a slightly better fit to the data compared to a local-charge-balance model. While the latter predicts the excess free energy and the Margules parameter to be negative, which indicates compound formation, multi-site mixing is consistent with positive deviation from ideality and the existence of a solvus in this binary system between 300 and 600°C. The composition of natural Al-rich titanite seems to suggest

the existence of a solvus in titanite at these temperatures, thus supporting the multi-site mixing model.

The pressure dependent Margules parameter W_V was determined independently from the excess volume of mixing, as well as refined in the data regression for multi-site mixing. Both values coincide exceptionally well.

The AlF-content of titanite can be determined via the unit cell dimensions obtained with X-ray diffraction, with an accuracy comparable to microprobe analyses.

5.2 Introduction

Although it is known at least since the early eighties that Al-bearing titanite $Ca(Ti,Al)(O,OH,F)SiO_4$ is a potential geothermobarometer (Smith, 1980; Franz and Speer, 1985), no attempt has been made to rigorously calibrate the pressure and temperature dependence of this ternary solid-solution through experiments. To my knowledge the only previous experimental investigation of Al-titanite which is available in the literature is that by Smith (1981)[1], who conducted a series of preliminary isobaric and isothermal experiments in the binary system $CaTiOSiO_4$-$CaAlFSiO_4$. Although Smith's study determined the pressure and temperature dependence of aluminium in titanite qualitatively (Figure 2.2, p. 9), the phase assemblage equilibrated in these experiments contained melt, and thus was not chemically buffered, preventing a thorough thermodynamic interpretation of the results.

One of the reasons why the Al-titanite system had never been tackled thermodynamically, was probably the lack of knowledge regarding the two Al-bearing end-members $CaAlOHSiO_4$ and $CaAlFSiO_4$, i.e. their existence, crystal structures and thermodynamic properties. The pure OH-end-member was found to be stable in a different crystal structure than titanite, as the mineral vuagnatite, which shows only very limited solution with titanite (McNear et al., 1976; Oberti et al., 1991). Together with the complete absence of any reports of the F-end-member until recently (Troitzsch and Ellis, 1998), this led to the suggestion that the Al-end-members in the titanite structure are possibly not stable, thus adding another complication to this system. The biggest drawback of the Al-titanite geothermobarometer for a long time was its dependency on fluorine, because reliable quantitative fluorine analyses were difficult to obtain by standard methods such as the electron mircoprobe, until about 10 to 15 years ago. Therefore, even though an experimental pressure and temperature calibration of the

---

[1] Note, however, the two recent abstracts by Tropper et al. (1999, 2000), describing experiments similar to the ones conducted here.

F-free binary titanite system could have been possible, the application of such a geothermobarometer would have been questionable due to the abundance of fluorine in many natural Al-rich titanites.

The technical improvement of analytical equipment over the last 15 years with respect to fluorine analyses, which can now be carried out with most standard electron microprobes, have finally made it worthwhile to study the Al-titanite system experimentally, which was the prime motivation of this study. Moreover, it was shown recently that one of the Al-bearing end-members, $CaAlFSiO_4$, is stable in the titanite structure, and that complete solid-solution exists between it and titanite (Troitzsch and Ellis, 1999). Thus at least the binary system $CaTiOSiO_4$ - $CaAlFSiO_4$ is less complicated than previously thought, making the calibration a much easier task than expected, especially since the unit cell volume of $CaAlFSiO_4$ is now known (Troitzsch et al., 1999). The determination of thermodynamic properties of the AlF-end-member is the first step towards the calibration of Al-rich titanite as petrogenetic indicator. The thermodynamic investigation of the OH-end-member has to follow to allow the application of this system to a large variety of natural rocks.

In this chapter results are presented of one isothermal and two isobaric series of piston-cylinder experiments, carried out with samples of a composition equivalent to binary titanite solid-solution $CaTiOSiO_4$-$CaAlFSiO_4$. In contrast to the study by Smith (1981), which was performed in the same chemical system (although with starting compositions off the binary join), the present experiments were conducted at sub-solidus conditions in order to avoid a melt phase. The aim of this project was the investigation of the activity-composition relations, and the determination of the thermodynamic properties of $CaAlFSiO_4$, i.e. standard enthalpy and third law entropy.

The displacement of the reaction

$$0.5 \ CaAl_2Si_2O_8 + 0.5 \ CaF_2 = CaAlFSiO_4 \qquad (5.1)$$
$$\text{Anorthite} + \text{Fluorite} = CaAlFSiO_4$$

in the presence of titanite solid-solution was studied in the system Ca-Ti-Al-Si-O-F. As all coexisting phases (anorthite, fluorite and titanite solid-solution) can be described in terms of the three components anorthite, fluorite, and pure titanite, the system is ternary (Figure 5.1). According to the Gibbs phase rule, the number of degrees of freedom of a three-phase assemblage in a ternary system is two. Thus, if pressure and temperature are known, as in the experiments, the titanite composition is buffered at a specific Al-content in the assemblage anorthite - fluorite - titanite solid-solution.

Titanite
CaTiOSiO$_4$

CaAl$_2$Si$_2$O$_8$
Anorthite

CaF$_2$
Fluorite
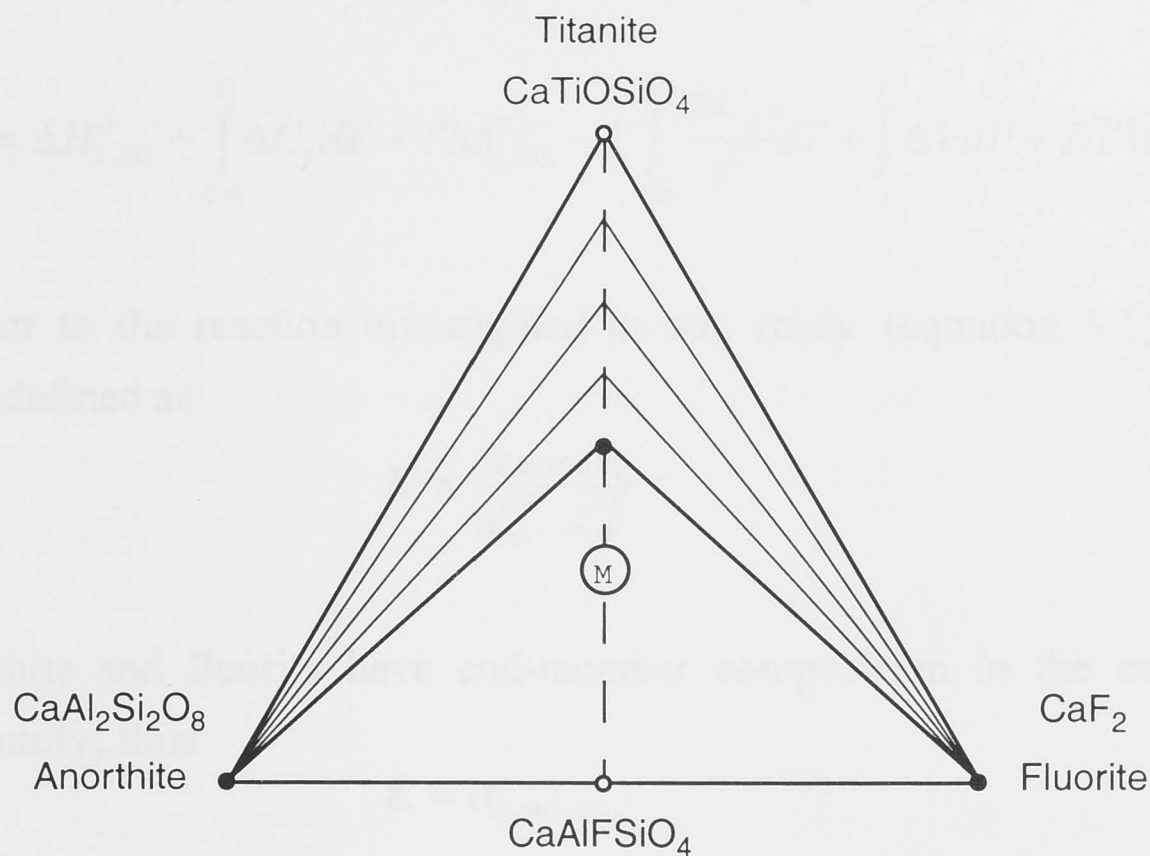
CaAlFSiO$_4$

Figure 5.1 Ternary plot of the phase relationships in the system CaTiOSiO$_4$ - CaAlFSiO$_4$ in molecular proportions (M is an example of a starting mix composition, as referred to in text).

To ensure the stability of this chemically buffered ternary assemblage, the starting mixes (Figure 5.1, M) were chosen to be of the composition of binary titanite solid-solution (Figure 5.1, dashed line) with a higher Al-content than the equilibrium titanite composition expected at a given pressure and temperature. The pressure-temperature-composition data triplets obtained from the experiments were then used to determine the activity-composition relations, and to compute the thermodynamic properties of CaAlFSiO$_4$.

5.3 Thermodynamic theory

The change in Gibbs free energy G of a reaction at any given pressure P and temperature T can be described by

$$\Delta G_{P,T} = \Delta H_{1,298}^0 + \int_{298}^{T} \Delta C_p dT - T\Delta S_{1,298}^0 - T\int_{298}^{T} \frac{\Delta C_p}{T} dT + \int_{1}^{P} \Delta V dP + RT \ln K \qquad (5.2)$$

where ΔH, ΔS, ΔC_P and ΔV are the differences in enthalpy of formation, third-law entropy, heat capacity and unit cell volume between reaction products and reactants, respectively. The standard state is 1 bar and 298.15 K. R is the gas constant, and K the equilibrium constant of the specific reaction.

If the system is at equilibrium, as proposed for the experiments presented here, then

$$\Delta G_{P,T} = 0 = \Delta H^0_{1,298} + \int_{298}^{T} \Delta C_p dT - T\Delta S^0_{1,298} - T\int_{298}^{T} \frac{\Delta C_p}{T} dT + \int_{1}^{P} \Delta V dP + RT \ln K \qquad (5.3)$$

With respect to the reaction investigated in this study (equation 5.1) the equilibrium constant is defined as

$$K = \frac{a_{CaAlFSiO_4}}{a_{An}^{0.5} \cdot a_{Fl}^{0.5}} \qquad (5.4)$$

Since anorthite and fluorite have end-member composition in the experiments, their activity is unity, thus

$$K = a_{CaAlFSiO_4} \qquad (5.5)$$

The reaction volume was considered to be dependent on pressure and temperature. Isothermal compressibility and thermal expansion of the phases (see below) were included in the form of the equation used by Berman (1988)

$$V_{P,T} = V_{1,298}[1 + v_1(P - P_r) + v_2(P - P_r)^2 + v_3(T - T_r) + v_4(T - T_r)^2] \qquad (5.6)$$

with P_r and T_r referring to the pressure and temperature of the reference state of 1 bar and 298.14 K, respectively. Thus the volume term in equation (5.3) becomes

$$\int_{1}^{P} \Delta V dP = \Delta V_{1,298}[(1 - \Delta v_1 P_r - \Delta v_2 P_r P + \Delta v_3(T - T_r) + \Delta v_4(T - T_r)^2)(P - P_r)$$
$$+ \frac{\Delta v_2}{3}(P^3 - P_r^3) + \frac{\Delta v_1}{2}(P^2 - P_r^2)] \qquad (5.7)$$

Note that the coefficients Δv_1 to Δv_4 of the reaction (equation 5.7) are not simply the difference between the coefficients v_1 to v_4 of the product and reactant phases, but have to be calculated as

$$\Delta V_x = \frac{\sum n v_{xj} V_j^0}{\Delta V^0} \qquad (5.8)$$

where n is the stoichiometric coefficient for each phase j.

5.3.1 Ideal activity models

The type of activity-composition relation in titanite is dependent on the choice of mixing model. The coupled substitution $Ti^{2+} + O^{2-} = Al^{3+} + F^-$ involves the distribution of two different atoms, Al and F, on two different sites, i.e. the octahedral and the O1-site, respectively. The multi-site mixing model (MM model) assumes random and independent distribution of Al and F, in which case the composition of the titanite solid-solution and the activity of the Al-end-member are related by

$$a_{CaAlFSiO_4} = [X_{Al}] \cdot [X_F] = [X_{Al}]^2 \qquad (5.9)$$

assuming ideal behaviour[2].

Because the coupled substitution involves two ion pairs of different charge, one could expect that Al and F are more likely to occupy adjacent sites in the crystal lattice to maintain local charge balance (LCB model). In this case their contribution to the configurational or mixing entropy and activity-composition relations would be like that of a single molecule, with

$$a_{CaAlFSiO_4} = X_{Al} \qquad (5.10)$$

again assuming ideal behaviour. As the behaviour of the solid-solution is possibly a combination of the two models, the thermodynamic properties of $CaAlFSiO_4$ were calculated for both models (non-ideal) to cover the entire possible data range.

5.3.2 Activity models used in previous studies

Both ideal models were used in different previous studies investigating equilibria with titanite solid-solution. For example, in their geobarometry study of low-temperature eclogites, Ghent and Stout (1994) calculated the activity of the titanite component based on Ca and Ti atoms with

$$a^{Ttn}_{CaTiOSiO_4} = X_{Ca} X_{Ti} \qquad (5.11)$$

thus assuming molecular mixing of Ti and O according to the LCB model.

---

[2] Strictly speaking, the multi-site mixing model defines the activity of $CaAlFSiO_4$ by

$$a_{CaAlFSiO_4} = [X_{Ca}] \cdot [X_{Al}] \cdot [X_F] \cdot [X_{Si}] \cdot [X_O]^4$$

However, it is shown below that the composition of the titanites in the experiments is near stoichiometric. Therefore, with respect to the thermodynamic models discussed here, it is assumed that the Ca-site is fully occupied with Ca, the Si-site with Si, and the four oxygen-sites different to O1 with O. This limits the substitutions to the octahedral and O1-site, and simplifies the above expression to equation (5.9).

In contrast to this, Manning and Bohlen (1991), who investigated several titanite-rutile equilibria for barometry in eclogites, computed the activity of titanite based on all atom species with

$$a^{Ttn}_{CaTiOSiO_4} = X_{Ca} X_{Ti} X_{Si} X_O^5 \text{ with } X_O = (5 - X_{Al})/5 \qquad (5.12)$$

Besides assuming independent mixing of Ti and O according to the MM model, their model also implies that F (and OH) can enter all five oxygen sites in titanite. Because this is unlikely due to the overbonded character of the O1-site along the entire binary join $CaTiOSiO_4$-$CaAlFSiO_4$, as demonstrated in Chapter 3 (Figure 3.6, p. 49), the present study prefers to consider the O1-site only for the calculation of X_O and X_F, as for example in equation (5.9) ($X_F = X_{Al}$).

5.3.3 Non-ideal activity models used in the present study

It is already known from the excess volume of mixing of binary titanite (Figure 3.5 f, p. 48) that the solid-solution under investigation does not behave ideally. Thus the activity coefficient γ is not unity, which modifies the activity expression for the MM model (5.9) to

$$a_{CaAlFSiO_4} = [X_{Al} \cdot \gamma_{Al}]^2 \qquad (5.13)$$

and that for the LCB model (5.10) to

$$a_{CaAlFSiO_4} = X_{Al} \cdot \gamma_{Al} \qquad (5.14)$$

If the Gibbs free energy of the solid-solution is symmetrical with respect to the composition, then the activity coefficient is defined with one Margules parameter W_G according to

$$RT \ln \gamma_{Al} = (1 - X_{Al})^2 W_G \qquad (5.15)$$

5.3.4 Margules parameters

Margules parameters are generally pressure as well as temperature dependent, and thus can be split into the parameters W_H, W_S and W_V, which describe the non-idealities with respect to enthalpy, entropy, and volume, respectively (Thompson, 1967; Ganguly and Saxena, 1967)

$$W_G(P,T) = W_H(1,T) - TW_S(1,T) + \int_1^P W_V(T)dP \qquad (5.16)$$

The relationship of the Margules parameters to the excess enthalpy, excess entropy and excess volume of mixing of a binary solid-solution with components 1 and 2 is defined as (e. g., Wood, 1976)

$$H^{exc} = W_H X_1 X_2$$

$$S^{exc} = W_S X_1 X_2 \qquad (5.17\text{-}19)$$

$$V^{exc} = W_V X_1 X_2$$

While the experimental data presented here allow the refinement of the *term* $(W_H - TW_S)$ with least squares regression, the narrow temperature range spanned by the experiments (800 to 1000°C) does not permit the determination of the temperature dependence of W_G, i.e. W_S. An attempt to refine W_S resulted in unreasonably large errors for the refined parameters, indicating overfitting. Therefore, in this study it is initially assumed that W_G is independent of temperature, bearing in mind that this may restrict the application of the derived W_G to temperatures near the experimental range.

In contrast to this, it is possible to estimate the pressure-dependent component of the Margules parameter, W_V, using the non-ideality in unit-cell volume (equation 5.19), already determined with X-ray diffraction (Chapter 3). Note that the calculation of the excess volume of mixing shown in Figure 3.5 (p. 48) is based on the ideal volume change between titanite with space group $P2_1/a$ (369.39 Å^3), and the end-member CaAlFSiO$_4$ with space group $A2/a$ (344.24 Å^3), measured at room conditions (Figure 5.2).

In contrast to this, the titanites equilibrated in the high-PT experiments all refer to the same space group $A2/a$, because of their high Al-contents ($X_{Al} > 0.28$), as well as the high temperatures at the time of equilibration (compare Figure 4.13, p. 80). Therefore, when determining the excess volume of mixing to be used for the thermodynamic interpretation of the experimental data, it is justified to exclude all volume data points with $P2_1/a$-titanite from the volume-composition curve fit, to assure consistency with respect to the space group (Figure 5.2). Although the phase change is of transitional nature, and occurs somewhere between $X_{Al} = 0.1$ and $X_{Al} = 0.2$, only data with $X_{Al} < 0.09$ were excluded. Data points between $X_{Al} = 0.09$ and 0.2 had a negligible effect on the curve fit.

Figure 5.2 shows the extrapolated end-member volume for a fictitious titanite with space group $A2/a$. (368.19 Å^3), which was used to calculate the excess volume of mixing in this chapter.
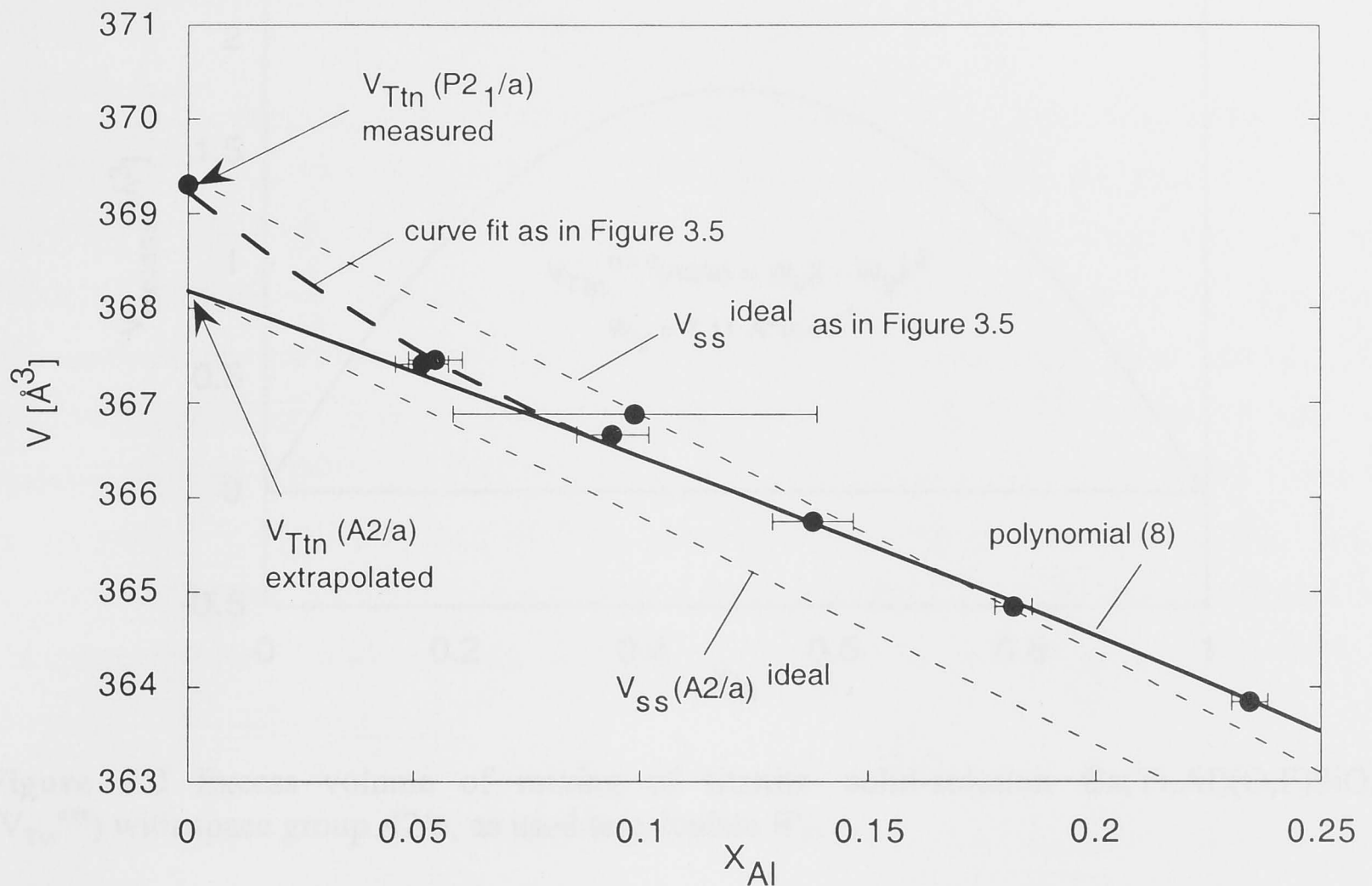
Figure 5.2 Unit-cell volume of titanite at low Al-contents; different curve fits and ideal volume (V_{ss}^{ideal}), depending on end-member volume (V_{Ttn}) chosen (see text). Polynomial (8) (Table 5.3) was fitted to data points with $X_{Al} > 0.09$, and extrapolated to $X_{Al} = 0$. Error bars show the standard deviation in composition (Table 5.2).

The polynomial (no. (8) in Table 5.3) describing the unit-cell volume of titanite with space group $A2/a$ is

$$V(\text{Å}^3) = M_0 + M_1 X_{Al} + M_2 X_{Al}^2$$
$$= 368.19 - 16.85 X_{Al} - 7.11 X_{Al}^2$$

(5.20)

Subtracting the ideal unit-cell volume for space group $A2/a$

$$V^{ideal} (\text{Å}^3) = 368.19(X_{Al} - 1) + 344.24 X_{Al}$$

(5.21)

from equation (5.20) yields the excess volume of mixing (Figure 5.3), and thus the Margules parameter

$$W_V = -M_2$$
$$= 7.11 \pm 0.59 \ \text{Å}^3$$
$$= 0.10704 \pm 0.00888 \ Jbar^{-1}$$

(5.22)
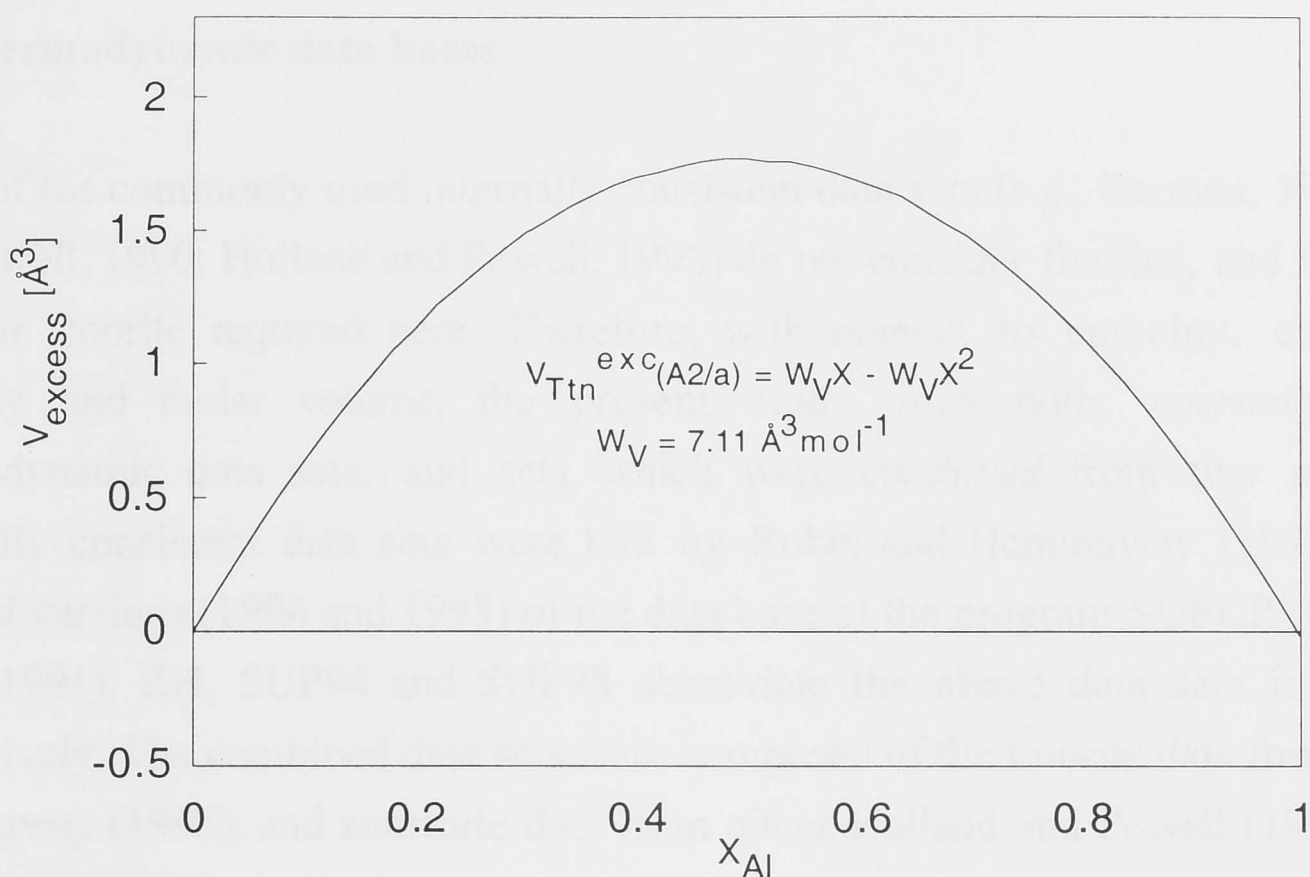
Figure 5.3 Excess volume of mixing of titanite solid-solution $Ca(Ti,Al)(O,F)SiO_4$ (V_{Ttn}^{exc}) with space group $A2/a$, as used to calculate W_V.

Thus, instead of being asymmetrical with respect to composition, as suggested in Figure 3.5 (p. 48), the excess volume of mixing of titanite with space group $A2/a$ is symmetrical (Figure 5.3).

5.3.5 Regression equation

The experimental pressure - temperature - composition data triplets were fitted to the following combinations of equations (5.3), (5.5), and (5.13) to (5.16) for the MM model

$$0 = \Delta H_{1,298}^0 + \int_{298}^{T} \Delta C_P dT - T\Delta S_{1,298}^0 - T\int_{298}^{T} \frac{\Delta C_P}{T} dT + \int_{1}^{P} \Delta V dP$$
$$+2RT\ln X_{Al} + 2(W_H - W_S T + W_V P)(1 - X_{Al})^2 \tag{5.23}$$

and the LCB model

$$0 = \Delta H_{1,298}^0 + \int_{298}^{T} \Delta C_P dT - T\Delta S_{1,298}^0 - T\int_{298}^{T} \frac{\Delta C_P}{T} dT + \int_{1}^{P} \Delta V dP$$
$$+RT\ln X_{Al} + (W_H - W_S T + W_V P)(1 - X_{Al})^2 \tag{5.24}$$

Knowing the thermodynamic data of anorthite and fluorite, as well as the unit cell volume and heat capacity of $CaAlFSiO_4$, and the Margules parameter W_V, this allowed the determination of the standard state enthalpy and entropy of reaction (5.1), and thus of $CaAlFSiO_4$, and the Margules parameter term (W_H-$W_S T$).

5.4 Thermodynamic data bases

Some of the commonly used internally consistent data sets (e.g., Berman, 1988; Holland and Powell, 1990; Holland and Powell, 1998) do not consider fluorine, and thus lack the data for fluorite required here. Therefore, with respect to enthalpy, entropy, heat capacity and molar volume, the present study uses both, *internally consistent* thermodynamic data sets, and sets which were *combined* from two sources. The internally consistent data sets were that by Robie and Hemingway (1995), and two updated versions (1994 and 1998) of the data base of the program SUPCRT92 (Johnson et al., 1991). RH, SUP94 and SUP98 abbreviate the above data sets in this study, respectively. The combined data sets were composed of the fluorite data from Robie and Hemingway (1995), and anorthite data from either Holland and Powell (1998) (HP), or Berman (1988) (B).

The thermodynamic data of anorthite and fluorite in the above data compilations differ from each other mainly in the form of the heat capacity equation (equation (4.2) used by RH and HP, equation (4.3) by B, and equation (4.4) by SUP94 and SUP98), and in the enthalpy and entropy of anorthite (Table 5.1). The entropy of anorthite, as given in both SUPCRT92 versions, exceeds those of most other data bases, including RH, B and HP, by several kilo-joules. According to Berman (1988), the significantly larger entropy of anorthite in Helgeson et al. (1978) (used in SUPCRT92) compared to the other data bases could be "the result of their overestimation of the high temperature C_P of grossular using the Maier-Kelley function (see Berman & Brown, 1985)" when fitting experimental phase equilibrium data. This is quite possible given that the present study itself has experienced the limitations of the Maier-Kelley equation when fitting and extrapolating experimental heat capacity data (Table 4.2, p. 65, Figure 4.6, p. 68). While the enthalpy of formation of anorthite from RH, HP, B and SUP94 are comparable, that of SUP98 is significantly less negative.

Regarding $CaAlFSiO_4$, all of the heat capacity equations listed in Table 4.3 (p. 65) were used, except for that of Maier and Kelley (1932) (see Chapter 4 and discussion therein). Because the choice of heat capacity equation had a negligible effect on the results when using the data base RH (see below), the subsequent regressions with the data from SUP94, SUP98, RH/HP, and RH/B were performed with only one heat capacity equation for $CaAlFSiO_4$. The equation of Haas and Fisher (1976) with four coefficients (a to d, compare Table 4.3, p. 65) was chosen, as it represents the experimental data well, and is simpler than the five term polynomial, which does not fit the data any better (Table 4.3). The standard state reaction volume for reaction (5.1) was calculated using the molar volume of 5.183 Jbar^{-1} (Table 2.3, p. 22) of the end-member $CaAlFSiO_4$.

Table 5.1.1 Thermodynamic properties of anorthite and fluorite, as used in this study, from the data bases of Robie and Hemingway (1995) (RH), two updated versions of the program SUPCRT by Johnson et al. (1991) (SUP94 and SUP98), Holland and Powell (1998) (HP), and Berman (1988) (B). From top to bottom: Gibbs energy of formation from the elements, enthalpy of formation from the elements, standard state entropy, molar volume, and coefficients a to e of heat capacity equations as defined in Table 4.2 (p. 65), and equations 4.2 to 4.4. The standard state is 298.15 K and 1 bar.

| Data base | Anorthite | | | | |
	RH	SUP94	SUP98	HP	B
$d_f G^0$ [kJmol^{-1}]	-4007.9	-4007.8	-3993.8	-4007.51	-4003.221
$d_f H^0$ [kJmol^{-1}]	-4234.0	-4231.8	-4217.6	-4233.48	-4228.730
S^0 [Jmol^{-1}K^{-1}]	199.3	205.5	#	200.0	200.186
V^0 [Jmol^{-1}bar^{-1}]	10.079	10.079	#	10.079	10.075
a	$5.168*10^2$	$2.650*10^2$	#	$3.716*10^2$	$4.3937*10^2$
b	$-9.249*10^{-2}$	$6.193*10^{-2}$	#	$1.2615*10^{-2}$	0
c	$-1.408*10^6$	$-6.463*10^6$	#	$-4.1102*10^6$	0
d	$-4.589*10^3$	0	#	$-2.0384*10^3$	$-3.7341*10^{-3}$
e	$4.188*10^{-5}$	0	#	0	0
f	0	0	#	0	$-3.1702*10^8$

| Data base | Fluorite | | |
	RH	SUP94	SUP98
$d_f G^0$ [kJmol^{-1}]	-1175.3	-1174.1	#
$d_f H^0$ [kJmol^{-1}]	-1228.0	-1226.5	#
S^0 [Jmol^{-1}K^{-1}]	68.9	68.6	#
V^0 [Jmol^{-1}bar^{-1}]	2.454	2.454	#
a	$2.033*10^3$	$5.986*10^1$	#
b	-1.436	$3.047*10^{-2}$	#
c	$2.988*10^7$	$1.967*10^5$	#
d	$-3.312*10^4$	0	#
e	$5.040*10^{-4}$	0	#
f	0	0	#

Data identical to SUP94

Table 5.1.2 Coefficients for isothermal compressibility (v_1, v_2) and thermal expansion (v_3, v_4) for equation (5.6), as used in this study.

	v_1 (10^7) [bar^{-1}]	v_2 (10^{12}) [bar^{-2}]	v_3 (10^5) [K^{-1}]	v_4 (10^9) [K^{-2}]	Reference
Titanite/CaAlFSiO$_4$[1]	-9.29	2.754			this study
Titanite/CaAlFSiO$_4$[1]			1.820	0	this study
Anorthite	-12.72	3.176	1.0918	4.1985	Berman (1988)
Fluorite	-12.10	3.950			Birch (1966)[2]
Fluorite			6.331	0	Carmichael (1984)[2]
ΔV_x of reaction[3]	-28.43	6.071	3.541	19.528	

[1] Coefficients determined with XRD data of titanite (see text). They are used in this study as an approximation for CaAlFSiO$_4$ because neither high-pressure nor high-temperature XRD data are available for this substance yet.
[2] Coefficients modified to suit equation (5.6)
[3] ΔV_x of reaction calculated with equation (5.8)

Isothermal compressibility and thermal expansion coefficients for anorthite were taken from Berman (1988), and those for fluorite from Birch (1966) and Carmichael (1984), respectively. The values of the latter two had to be transformed to suit equation (5.6) (Table 5.1). Because compressibility and expansion of the end-member $CaAlFSiO_4$ are unknown, they had to be estimated, based on the hypothesis that the volumes of compounds with similar crystal structure change at a similar rate with pressure and temperature (e.g., Powell and Holland, 1985). As in Chapter 4, it was assumed that the compressibility and expansion of $CaAlFSiO_4$ are identical to that of titanite, and were estimated on the basis of the high-temperature studies by Ghose et al. (1985), Taylor and Brown (1976), and the high-pressure investigations of Angel et al. (1999) (Table 5.1).

5.5 Experimental details

5.5.1 Piston-cylinder experiments: Main runs

Eighteen polybaric and isothermal runs (1000°C) and two sets of polythermal and isobaric runs (four at 7 kbar, five at 10 kbar) were carried out to equilibrate binary titanite solid-solution over a large compositional range in the assemblage titanite solid-solution - anorthite - fluorite. The individual run-conditions are listed in Table 5.2. Chemical analyses of titanite are given in Appendix 1. The starting mixes were of binary titanite composition, ranging from $X_{Al} = 0.60$ to $X_{Al} = 0.96$, and were composed of synthetic anorthite, wollastonite, fluorite (Specpure), and TiO_2 (Degussa).

The presence of any titanite in the starting mixes was deliberately avoided, as previous experiments, such as the synthesis runs presented in Chapter 3, have shown that once titanite is formed, it changes its composition only very slowly, and mostly along the rims, if attempted to be re-equilibrated at new pressure and temperature conditions. The synthesis of anorthite and wollastonite from glass was described in Chapters 2 and 3, respectively. For all runs 2 mm diameter silver-palladium capsules were filled with the starting powder, dried for at least 2 h at 110°C, and then welded shut. The pressure assemblage is identical to that described in Chapter 2. An error of ±0.2 kbar of all pressure readings, and ±5°C with respect to temperature, was assumed in the curve fitting procedure.

Table 5.2 Run conditions and results of piston-cylinder experiments.

Exp. No.	T (°C)	P (kbar)	t[+] (h)	X_{Al} of mix =Al/(Al+Ti)	Run products	X_{Al} in Ttn	sd X_{Al}
G-391	1000	5	70	0.60	Ttn$_{ss}$ An Fluo	0.282	0.007
G-396	1000	5	71	0.60	Ttn$_{ss}$ An Fluo	0.282*	0.004
G-392	1000	6	70	0.60	Ttn$_{ss}$ An Fluo	0.290*	0.004
G-444	800	7	504	0.60	Ttn$_{ss}$ An Fluo	0.393*	0.004
G-416	850	7	192	0.80	Ttn$_{ss}$ An Fluo	0.371*	0.004
G-422	950	7	72	0.60	Ttn$_{ss}$ An Fluo	0.330*	0.004
G-402	1000	7	58	0.60	Ttn$_{ss}$ An Fluo	0.309*	0.004
G-398	1000	8	50	0.60	Ttn$_{ss}$ An Fluo	0.340	0.011
G-389	1000	9	70	0.60	Ttn$_{ss}$ An Fluo	0.367	0.005
G-400	1000	10	50	0.60	Ttn$_{ss}$ An Fluo	0.394	0.012
G-383	850	10	480	0.60	Ttn$_{ss}$ An Fluo	0.471	0.005
G-409	900	10	71	0.60	Ttn$_{ss}$ An Fluo	0.460*	0.004
G-404	950	10	71	0.60	Ttn$_{ss}$ An Fluo	0.417	0.014
G-382	800	10	480	0.60	Ttn$_{ss}$ An Fluo Gro#	0.519*	0.004
G-388	1000	11	70	0.60	Ttn$_{ss}$ An Fluo	0.422	0.009
G-397	1000	11	71	0.60	Ttn$_{ss}$ An Fluo	0.427	0.019
G-395	1000	12	36	0.60	Ttn$_{ss}$ An Fluo	0.464	0.016
G-386	1000	13	68	0.60	Ttn$_{ss}$ An Fluo	0.487	0.013
G-411	1000	14	44	0.84	Ttn$_{ss}$ An Fluo	0.563	0.014
G-413	1000	15	79	0.84	Ttn$_{ss}$ An Fluo Zoi#	0.605	0.012
G-412	1000	15.5	44	0.84	Ttn$_{ss}$ An Fluo	0.612	0.011
G-403	1000	16	58	0.80	Ttn$_{ss}$ An Fluo Zoi#	0.632	0.014
G-407	1000	17	51	0.84	Ttn$_{ss}$ An Fluo	0.679	0.013
G-418	1000	20	67	0.96	Ttn$_{ss}$ An Fluo	0.816*	0.020
G-443	1000	21	69	0.96	Ttn$_{ss}$ An Fluo Zoi#	0.914*	0.004

Notes: Abbreviations as in Table 2.1; Gro = grossular
[+] Run duration
* Al-content determined only with XRD via unit cell dimensions. 'Standard deviations' of these values as given in the last column represent the estimated mean error of this method (Exception: X_{Al} of sample G-418 was determined with both XRD and SEM, here 'sd' is actual standard deviation).
# Trace amounts

5.5.2 Piston-cylinder experiments: Reversals

In order to test whether equilibrium was attained during the runs, two sets of reversal experiments were carried out at two different pressures. In the first set, the run products of samples G-395 and G-398, previously equilibrated at 12 and 8 kbar, respectively, were re-run at 10 kbar. Each sample was reground, filled in a 2 mm diameter silver-palladium capsule, dried and welded shut. Both capsules were then placed next to each other in the same pressure assemblage and run in one experiment to ensure identical pressure and temperature conditions. The second set of reversals consisted of samples

G-407 and G-411, formerly equilibrated at 17 and 14 kbar, which were re-run at 15.5 kbar in the same experiment.

5.5.3 Sample investigation

The run products were investigated optically (reflected light microscopy), with X-ray diffraction, and scanning electron microscopy. In high-temperature runs (> 900°C) the grain-size of the run products (< 10 μm) was large enough to allow the determination of the titanite composition with the electron microprobe. However, titanites equilibrated at lower temperatures were much finer-grained (< 2 μm), thus approaching the resolution limit of the microprobe. Potential grain-overlap of the neighbouring phases, in this case anorthite and fluorite, under the electron beam could lead to an overestimation of X_{Al} in titanite. Therefore the Al- and F-content of titanite in these fine-grained samples, as well as that of some of the high-temperature runs, was determined indirectly via the unit-cell dimensions a, b and c of titanite, which were obtained using X-ray diffraction.

5.5.3.1 Determination of AlF-content of titanite with XRD

Because of severe overlap of the numerous reflections of anorthite with those of titanite, it was not possible to rely on the position of an individual peak in the X-ray spectrum. Instead, the unit cell dimensions a, b and c of titanite in each sample were refined from the XRD powder pattern of each sample using the program RIETAN (Izumi, 1993; Kim and Izumi, 1994). Each of the dimensions was then converted to a value X_{Al} with selected polynomial functions presented in Table 5.3, and the mean was taken. Although this method only requires the determination of a, b and c, for the sake of completeness the other two dimensions, β and V are also included in the curve fitting discussion below.

Because the quality of the X_{Al} values determined with this method is strongly dependent on the quality of the curve fit to the unit cell data, two different approaches were taken to fit polynomial functions. The first approach was based on statistical considerations, the other based on judging the fit by eye. The reproducibility of X_{Al} by both methods was then tested on several high-temperature run products, which were coarse-grained and thus yielded reliable microprobe analyses.

Table 5.3 Coefficients of curve fit polynomials which represent the unit cell dimensions a, b, c, β and V in Figure 3.5, p. 46 (Approach 2 "fit by eye") and in Figure 5.4 (Approach 1 "statistics"). The two different approaches are discussed in the text. The polynomials are defined as

$$Y_{a,b,c,\beta,V,BVS} = \sum (M_n)_{a,b,c,\beta,V,BVS} X^n \quad \text{with } n = 0, 1, ..., 5.$$

In all polynomials X represents the independent variable X_{Al}, Y is the dependent variable a, b, c, or β, and M_n are the polynomial coefficients.

Approach 1 "statistics"

Polynom. no.	(1)	(2)	(3)	(4)
Unit cell dim.	a [Å]	a [Å]	b [Å]	c [Å]
X_{Al} range	0.05 - 1.00	0.09 - 1.00	0.05 - 1.00	0.05 - 1.00
M_0	7.0506 ± 0.0005	7.0545 ± 0.0006	8.7096 ± 0.0006	6.5542 ± 0.0003
M_1	0.0556 ± 0.0084	0.0076 ± 0.0043	-0.2020 ± 0.0006	-0.1150 ± 0.0004
M_2	-0.2997 ± 0.0352	-0.1464 ± 0.0038		
M_3	0.1092 ± 0.0275			
χ^2	1.55	0.13	0.28	0.60

Polynom. no.	(5)	(6)	(7)	(8)
Unit cell dim.	β [°]	β [°]	V [Å³]	V [Å³]
X_{Al} range	0.05 - 1.00	0.09 - 1.00	0.05 - 1.00	0.09 - 1.00
M_0	113.775 ± 0.009	113.816 ± 0.007	368.33 ± 0.08	368.19 ± 0.14
M_1	1.574 ± 0.074	1.272 ± 0.028	-17.46 ± 0.49	-16.85 ± 0.72
M_2	-1.044 ± 0.178	-0.408 ± 0.022	-6.63 ± 0.42	-7.11 ± 0.59
M_3	0.375 ± 0.113			
χ^2	1.07	0.98	0.4	0.31

Approach 2 "fit by eye"

Polynom. no.	(9)	(10)	(11)	(12)
Unit cell dim.	a [Å]	a [Å]	b [Å]	c [Å]
X_{Al} range	0.00 - 0.182	0.182 - 1.00	0.00 - 1.00	0.00 - 1.00
M_0	7.0612 ± 0.0003	7.0477 ± 0.0030	8.7135 ± 0.0015	6.5583 ± 0.0009
M_1	-0.4906 ± 0.0204	0.0675 ± 0.0203	-0.3005 ± 0.0310	-0.2159 ± 0.0183
M_2	9.8272 ± 0.5714	-0.2876 ± 0.0377	0.6571 ± 0.1996	0.6507 ± 0.1177
M_3	-84.343 ± 6.3601	0.0886 ± 0.0209	-1.6357 ± 0.5196	-1.5301 ± 0.3064
M_4	322.67 ± 30.000		1.727 ± 0.5820	1.5398 ± 0.3435
M_5	-460.46 ± 50.250		-0.6529 ± 0.2345	-0.5628 ± 0.1383
χ^2	5×10^{-6}	1×10^{-3}	1×10^{-3}	4×10^{-4}

Polynom. no.	(13)	(14)	(15)	(16)
Unit cell dim.	β [°]	β [°]	V [Å³]	V [Å³]
X_{Al} range	0.00 - 0.105	0.105 - 1.00	0.00 - 0.19	0.19 - 1.00
M_0	113.810 ± 0.0040	113.79 ± 0.0060	369.23 ± 0.060	368.35 ± 0.110
M_1	-0.2045 ± 0.2199	1.3885 ± 0.0448	-39.57 ± 1.890	-17.619 ± 0.510
M_2	22.483 ± 3.9730	-0.6062 ± 0.0910	146.25 ± 18.35	-6.571 ± 0.489
M_3	-88.812 ± 18.526	0.1066 ± 0.0538	-324.87 ± 50.63	
χ^2	4×10^{-3}	0.015	1.61	18.24

Except for dimensions b and c, it turned out that polynomial functions are not well suited to represent the entire data set at covering $X_{Al} = 0.0$ to $X_{Al} = 1.0$, because polynomial wiggle occurs before all data points are matched well. Especially data points at low Al-contents ($X_{Al} < 18.2$) seem to behave differently to the rest of the data set, which could be due to the fact that the symmetry of the titanite structure changes somewhere between $X_{Al} = 0.09$ and $X_{Al} = 0.182$ (Chapter 3). Given that there might be an underlying physical reason for different behaviour, the high-Al data were fitted separately to those of very low Al-contents.

In the first curve fit approach ('statistical') only data with $X_{Al} > 0.09$ were included, and the polynomial degree was increased until χ^2 was reasonable, considering the standard deviation in X_{Al}, and the error in the unit cell dimensions. The same procedure was carried out extending the data set to $X_{Al} = 0.05$. The resulting polynomial coefficients are shown in Table 5.3. While the visual fit of these statistically correct functions to the data for b, β and V is acceptable, that for dimensions a and c is unsatisfactory at higher Al-contents (Figure 5.4).

The second approach ('fit by eye') was to increase the polynomial degree until all data points were fitted satisfactorily judging by eye. For dimensions a, β and V, low-Al and high-Al data were fitted separately, with some samples being included in both data sub-sets to allow the curves to join smoothly. The resulting polynomial degrees for all curve fits are higher compared to the statistical approach, which indicates significant 'overfitting' of the data in a statistical sense. However, the reproducibility of X_{Al} of this second approach of 'fitting by eye' is excellent, whereas that of the statistical approach yields X_{Al} values systematically offset from the ideal 1:1 correlation (Figure 5.5). Apart from producing larger errors in X_{Al}, the X_{Al} values obtained from a, b and c for each sample spread much more in the statistical approach (standard deviation sd < 0.024) compared to the 'fitting by eye' method (sd < 0.011) (Table 5.4).

Therefore, despite significant overfitting, the polynomial functions 'fit by eye' are preferred in this study for obtaining X_{Al} for small-grained titanite of unknown composition. The mean error in X_{Al} determined with this method is ± 0.0034, plus the uncertainty of the microprobe analyses, upon which the calibration of this method relies. The polynomial functions 'fit by eye' are shown together with the data points in Figure 3.5 (p. 46).
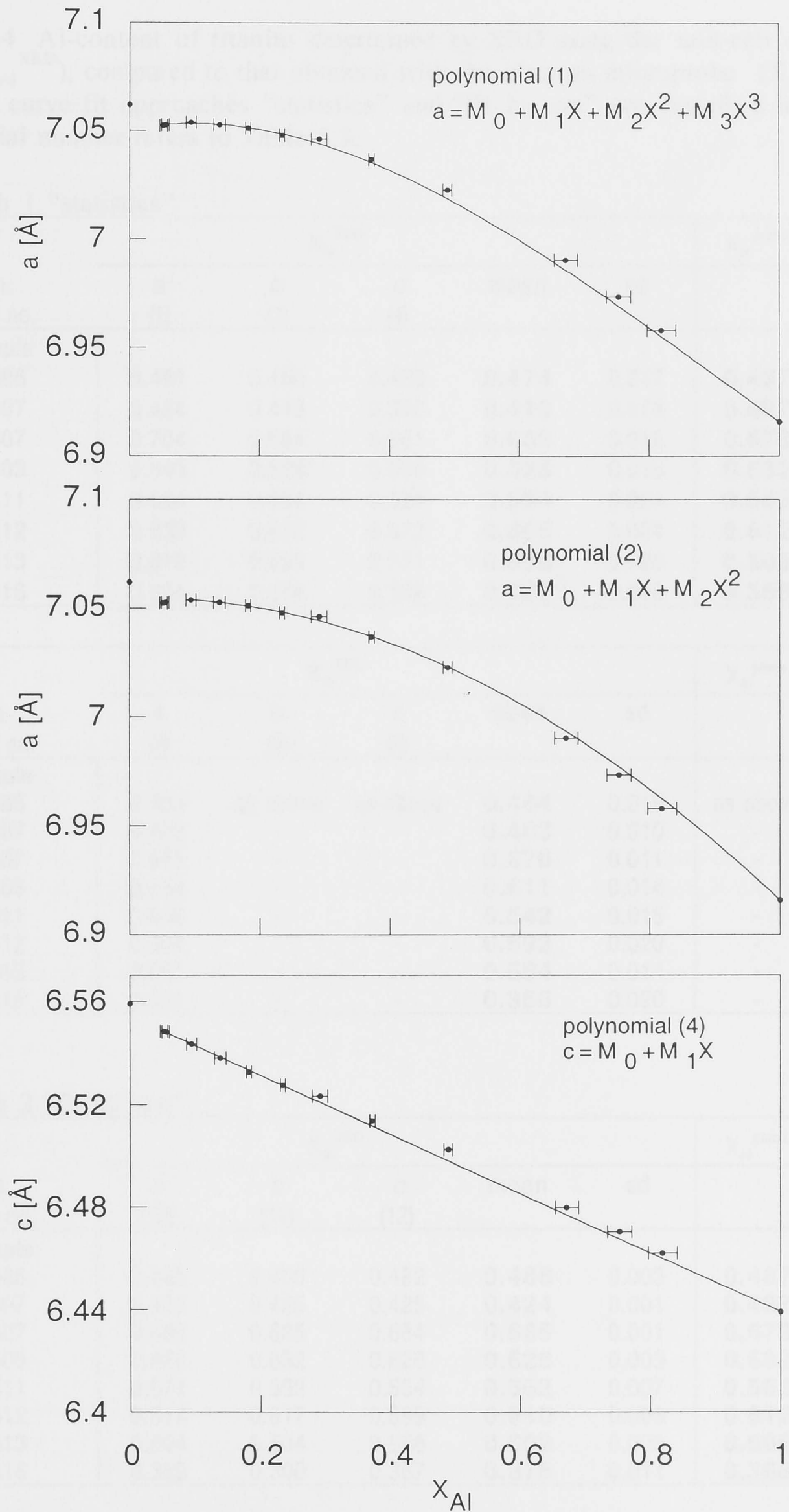
Figure 5.4 Unit cell dimensions a and c versus composition of binary titanite solid-solution Ca(Ti,Al)(O,F)SiO$_4$ (from Chapter 3, Figure 3.5, p. 46), and their representation by the polynomials, based on 'statistical' fit (Table 5.3). Note that the 'statistical' fit is not satisfactory at high Al-contents

Table 5.4 Al-content of titanite determined by XRD using the unit-cell dimensions a, b and c (X_{Al}^{XRD}), compared to that obtained with the electron microprobe (X_{Al}^{probe}). The two different curve fit approaches "statistics" and "fit by eye" are described in the text. The polynomial number refers to Table 5.3.

Approach 1 "statistics"

Unit cell dim. Polynomial no.	X_{Al}^{XRD} a (1)	b (3)	c (4)	mean	sd	X_{Al}^{probe}	X_{Al}^{XRD} - X_{Al}^{probe}
Sample							
G-386	0.491	0.480	0.450	**0.474**	0.017	**0.487**	-0.013
G-397	0.424	0.413	0.393	**0.410**	0.013	**0.427**	-0.017
G-407	0.704	0.684	0.661	**0.683**	0.018	**0.679**	0.004
G-403	0.643	0.628	0.600	**0.623**	0.018	**0.632**	-0.009
G-411	0.584	0.554	0.524	**0.554**	0.024	**0.563**	-0.009
G-412	0.630	0.612	0.572	**0.605**	0.024	**0.612**	-0.007
G-413	0.619	0.599	0.571	**0.596**	0.020	**0.605**	-0.009
G-416	0.364	0.378	0.339	**0.360**	0.016	**0.368**	-0.008

Unit cell dim. Polynomial no.	X_{Al}^{XRD} a (2)	b (3)	c (4)	mean	sd	X_{Al}^{probe}	X_{Al}^{XRD} - X_{Al}^{probe}
Sample							
G-386	0.463	as above	as above	**0.464**	0.015	as above	-0.023
G-397	0.403	-	-	**0.403**	0.010	-	-0.024
G-407	0.665	-	-	**0.670**	0.011	-	-0.009
G-403	0.604	-	-	**0.611**	0.014	-	-0.022
G-411	0.548	-	-	**0.542**	0.015	-	-0.021
G-412	0.591	-	-	**0.592**	0.020	-	-0.020
G-413	0.581	-	-	**0.584**	0.014	-	-0.021
G-416	0.351	-	-	**0.356**	0.020	-	-0.012

Approach 2 "fit by eye"

Unit cell dim. Polynomial no.	X_{Al}^{XRD} a (10)	b (11)	c (12)	mean	sd	X_{Al}^{probe}	X_{Al}^{XRD} - X_{Al}^{probe}
Sample							
G-386	0.485	0.490	0.482	**0.486**	0.003	**0.487**	-0.001
G-397	0.423	0.425	0.425	**0.424**	0.001	**0.427**	-0.003
G-407	0.686	0.685	0.684	**0.685**	0.001	**0.679**	0.006
G-403	0.626	0.632	0.626	**0.628**	0.003	**0.632**	-0.004
G-411	0.571	0.562	0.554	**0.562**	0.007	**0.563**	-0.001
G-412	0.614	0.617	0.599	**0.610**	0.008	**0.612**	-0.002
G-413	0.604	0.604	0.598	**0.602**	0.003	**0.605**	-0.003
G-416	0.369	0.390	0.367	**0.375**	0.011	**0.368**	0.007
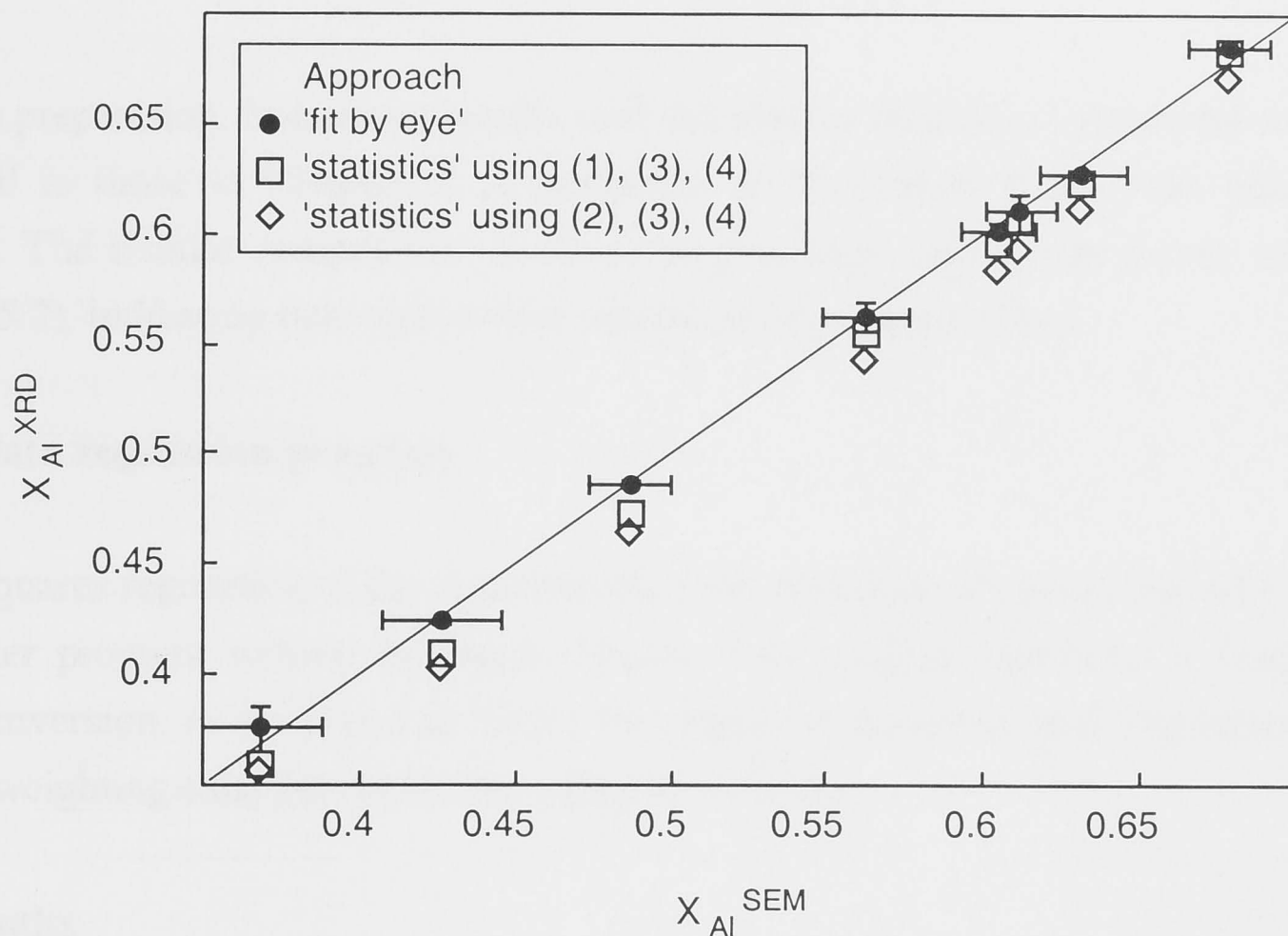
Figure 5.5 The Al-content of synthetic titanite determined via the unit cell dimensions with X-ray diffraction (X_{Al}^{XRD}), compared to electron microprobe data (X_{Al}^{SEM}) of the same samples. Three different combinations of polynomials for the cell dimensions a, b and c were used (see Table 5.3 and text for description of the different approaches). Solid line represents ideal correlation. Error bars in X_{Al}^{SEM} are the standard deviation of the microprobe data. They are valid for all three data sets, but are omitted on the open symbols for clarity.

5.5.3.2 XRD and 'Rietveld refinement'

The samples were prepared for X-ray diffraction as described in Chapter 3. The diffraction data were recorded in one pass over a range of 17 to $65°2\theta$, using a step width of $0.02°$ at a scan speed of $0.5°$ per minute. The three main phases, anorthite, fluorite and titanite were considered in the refinement. Starting values for atom coordinates and unit cell dimensions of titanite were guessed on the basis of microprobe analyses and the crystal structure data presented in Chapter 3. Parameters refined included background (8 parameters), specimen displacement (1), peak shape (up to 6 per phase), preferred orientation (1 per phase), unit cell dimensions (4) and an overall isotropic displacement parameter for titanite. Special attention was paid to matching the two main fluorite peaks to ensure proper zero correction. With R_{Bragg} values for titanite ranging from 5 to 9, these refinements are poor and should certainly not be regarded as proper crystal structure refinements. However, they yield reliable unit cell dimensions, which produce very good estimates for X_{Al} in titanite (Figure 5.5).

5.5.3.4 SEM

Sample preparation, instrument details, and calculation method of structural formula are identical to those in Chapter 2. A minimum of 10 titanite grains was analysed per sample. The titanite composition in most samples only varied over a very small range (Table 5.2), indicating that equilibrium conditions were approached.

5.5.4 Data regression program

Least squares regression of the experimental data-triplets was carried out with a BASIC computer program written by Hugh O'Neill. This program performs a Gauss-Jordan matrix inversion, as described in "Basic Programs for Scientists and Engineers" (Miller, 1981), weighting each data point according to its error.

5.6 Results

All run products were composed of the phases anorthite, fluorite and titanite solid-solution (Figure 5.6). Some samples also contained trace amounts of grossular or zoisite (Table 5.2). The composition of the three main phases is close to ideal, with anorthite and fluorite of pure end-member composition, and titanite as binary solid-solution.
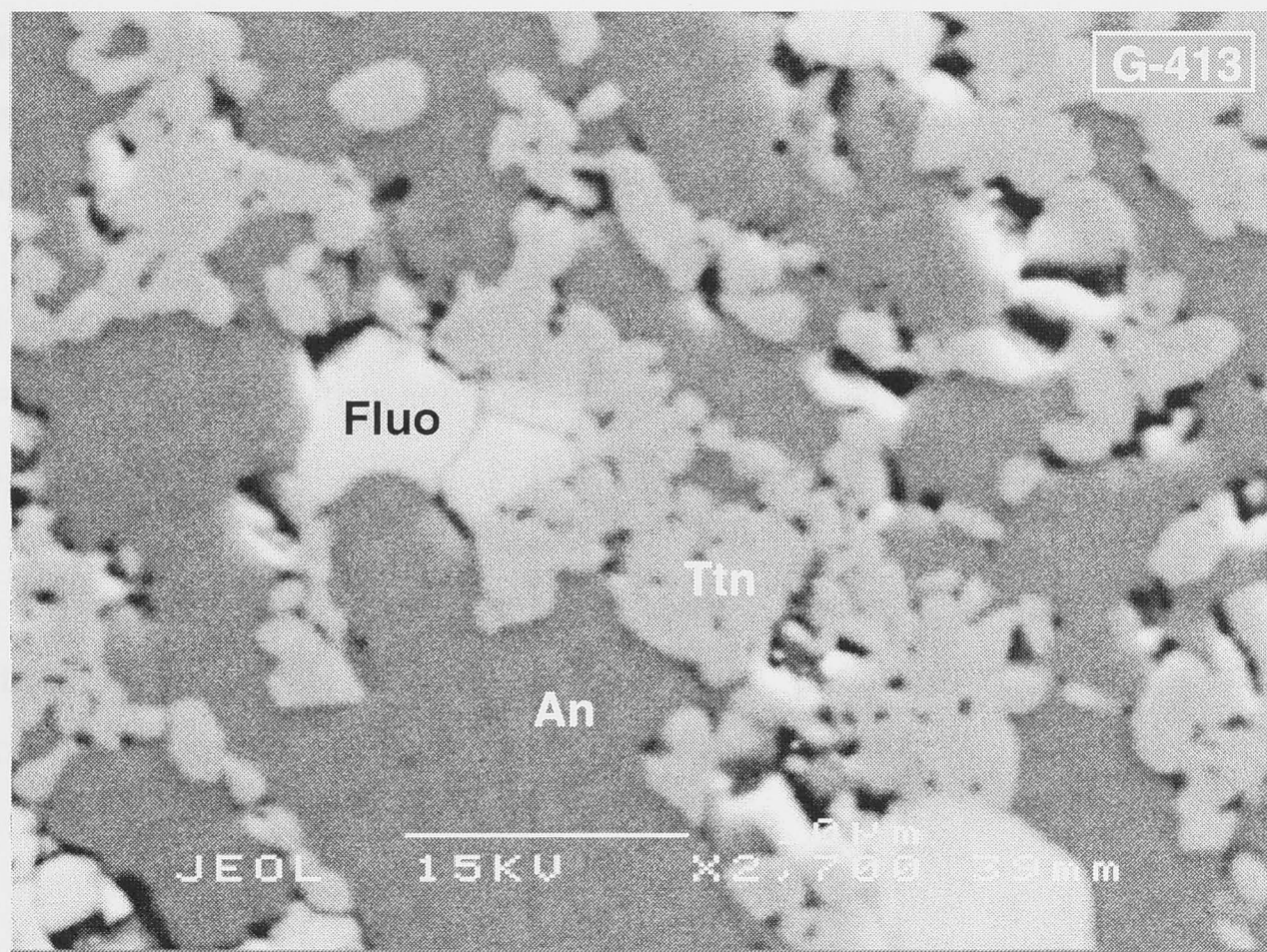
Figure 5.6 Backscattered electron image of the run product of piston cylinder experiment G-413 (compare Table 5.2). Fluorite (Fluo), anorthite (An), and titanite solid solution (Ttn) are coexisting. Black areas are cavities in the sample.

5.6.1 Titanite composition

Figures 5.7a and b show that the correlation between Al and Ti, and between Al and F of most titanite analyses is ideal within error, confirming that the coupled substitution observed is accurately described with $Ti^{2+} + O^{2-} = Al^{3+} + F^-$. The sum of the octahedral atoms Al and Ti is concentrated around the ideal value of 1 apfu (Figure 5.7c), but a slight Si-deficiency and a small Ca-surplus exist in most analyses (Figure 5.7d).

The Si-deficiency could possibly be explained by vacancies, or by partial substitution of Si by Ti or Al (Hollabaugh and Rosenberg, 1983). As there is no correlation between any excess Ti [with $Ti^{excess} = Ti - (1 - Al)$] and Si (Figure 5.7e), or between excess Al [with $Al^{excess} = Al - (1 - Ti)$] and Si (plot identical to Figure 5.7e), vacancies are the preferred explanation. The presence of Si vacancies was reported by previous studies from both synthetic as well as natural titanites (Rosenberg, 1974; Markl and Piazolo, 1999).

A surplus in Ca atoms in the titanite structure exceeding 1 apfu could be due to limited substitution into the octahedral site, as suggested by a weak negative correlation between Ca and Ti (Figure 5.7f). Alternatively, the Ca-surplus might be an artificial feature due to the calculation method of the structural formula, which is based on the assumption that the total number of cations is exactly 3. If there were any cation vacancies, e.g. in Si, in the analysed crystal, then the number of those cations with full occupation would falsely be calculated to exceed one.

Since all deviations of titanite analyses from the ideal cation occupations (Ca = 1, Si = 1, Al + Ti = 1) discussed in this section are small compared to the X_{Al} range investigated in this chapter, ideal occupation in the binary solid-solution $Ca(Ti,Al)(O,F)SiO_4$ is adopted in the thermodynamic calculations below. Note that this assumption is only valid for the experimental phase assemblage investigated here, in which the composition of titanite is tightly constrained by the Gibbs phase rule. See Appendix 2 for the discussion of an experiment that was carried out with excess TiO_2 in the starting mix.
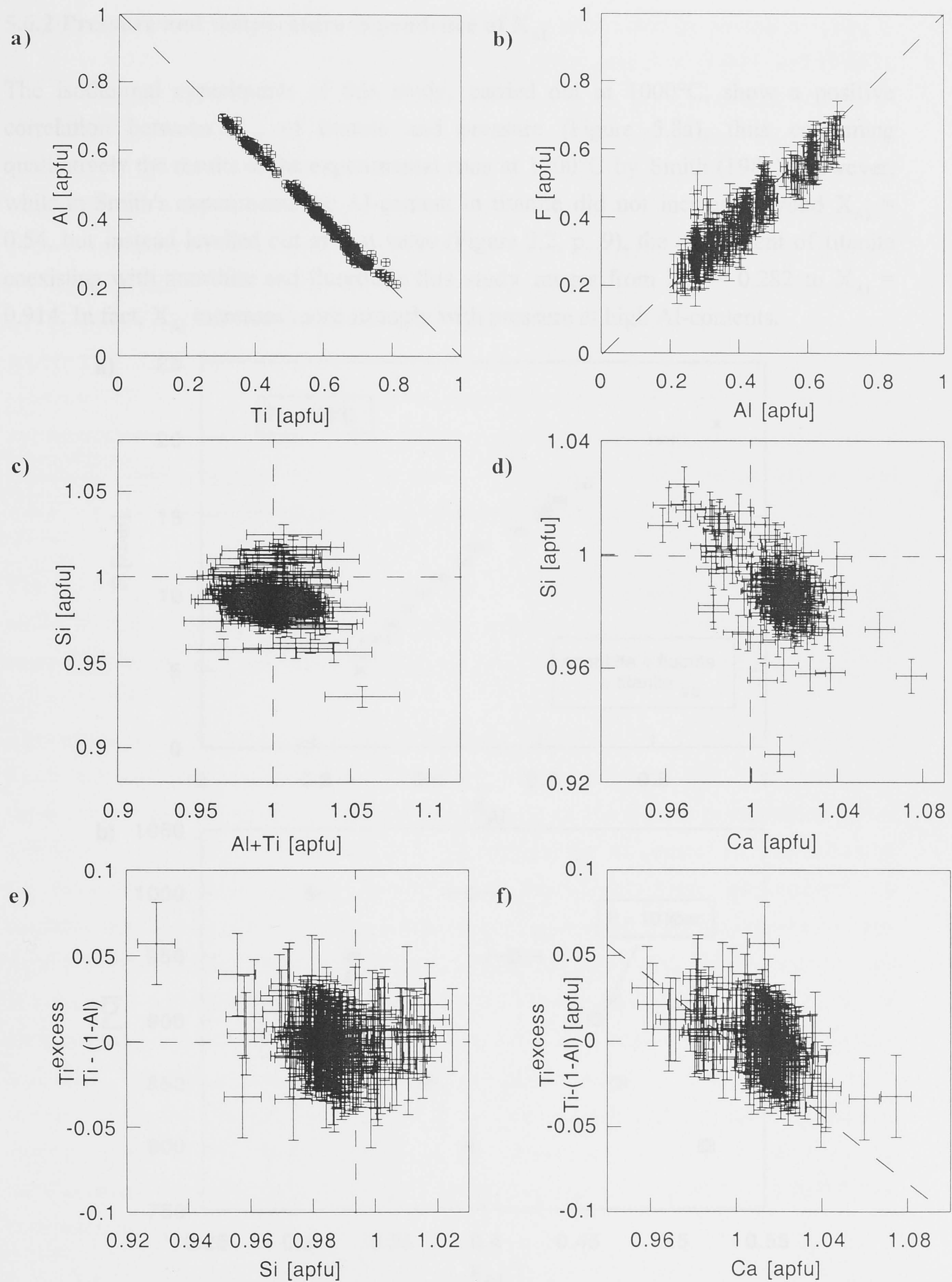
Figure 5.7 Chemical composition of synthetic titanite solid-solution [Ca(Ti,Al)(O,F)SiO$_4$], based on electron microprobe analyses of the samples listed in Table 5.2. Shown are selected cations and anions in atoms per formula unit (apfu). Dashed lines represent ideal occupation of the sites in the titanite structure.

5.6.2 Pressure and temperature dependence of X_{Al}

The isothermal experiments of this study, carried out at 1000°C, show a positive correlation between X_{Al} of titanite and pressure (Figure 5.8a), thus confirming qualitatively the results of the experimental runs at 1200°C by Smith (1981). However, while in Smith's experiments the Al-content in titanite did not increase beyond X_{Al} = 0.54, but instead levelled out at that value (Figure 2.2, p. 9), the Al-content of titanite coexisting with anorthite and fluorite in this study ranges from X_{Al} = 0.282 to X_{Al} = 0.914. In fact, X_{Al} increases more strongly with pressure at high Al-contents.
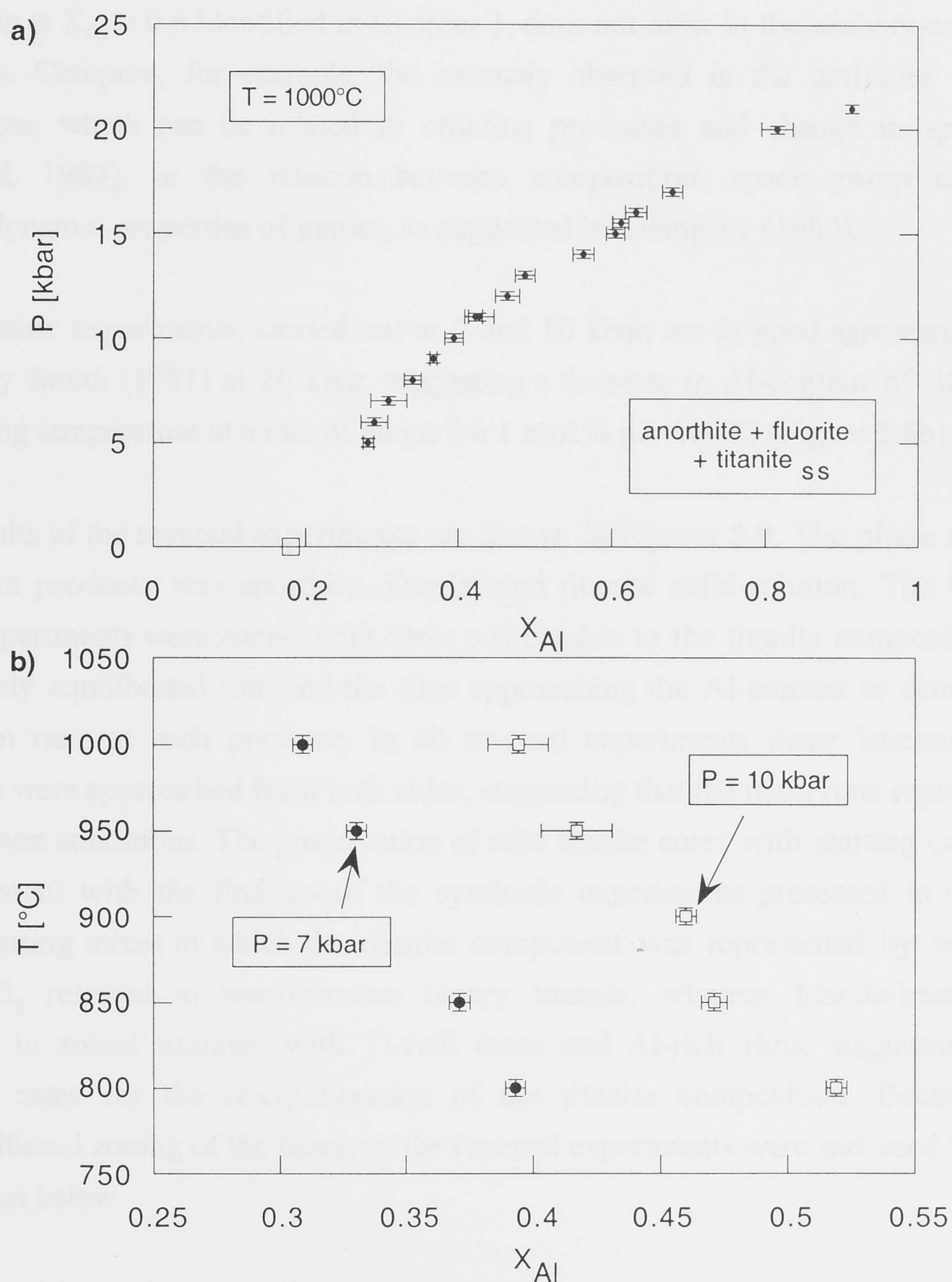
Figure 5.8 Pressure **(a)** and temperature dependence **(b)** of the Al-content [X_{Al}] of synthetic titanite solid-solution, coexisting with anorthite and fluorite in piston-cylinder experiments. Open square in figure a) represents an experimental run that was not considered in the thermodynamic interpretation, as it failed due to capsule rupture. However, it is shown here because the run product contained the assemblage titanite, anorthite and fluorite, amongst other phases which are not discussed here.

The generally smooth increase of X_{Al} with pressure is interrupted by a small irregularity at Al-contents between $X_{Al} = 0.49$ and $X_{Al} = 0.61$. Here (samples G-411 and G-413), the Al-content of titanite is slightly higher for the given pressures than would be expected from smooth interpolation between the adjacent data points. This anomaly could well be the reflection of underlying crystal structural processes, such as the atomic rearrangement in titanite at this composition (Chapter 3) with its potential effect on the activity-composition relations of titanite solid-solution. However, the anomaly is within the range of experimental error, and thus should be noted, but not over-interpreted. It can be concluded that a significant thermodynamic expression of the crystal structural problems at $X_{Al} > 0.6$ identified in Chapter 3, does not exist in the activity-composition relations. Compare, for example, the anomaly observed in the activities of jadeitic pyroxenes, which can be related to ordering processes and change in space group (Holland, 1983), or the relation between composition, space group change and thermodynamic properties of garnet, as suggested by Dempsey (1980).

The isobaric experiments, carried out at 7 and 10 kbar, are in good agreement with the study by Smith (1981) at 20 kbar, suggesting a decrease in Al-content of titanite with increasing temperature at a rate of about 5 ± 1 mol.% per 100°C (Figure 5.8b).

The results of the reversal experiments are shown in Figures 5.9. The phase assemblage in all run products was anorthite, fluorite and titanite solid-solution. The titanites in these experiments were zoned, with cores comparable to the titanite composition of the previously equilibrated run, and the rims approaching the Al-content as determined by the main runs at each pressure. In all reversal experiments these 'intermediate' Al-contents were approached from both sides, suggesting that the main runs represent near-equilibrium conditions. The preservation of relic titanite cores with starting composition is consistent with the findings of the synthesis experiments presented in Chapter 3. Only starting mixes in which the titanite component was represented by wollastonite and TiO_2 resulted in homogeneous binary titanite, whereas titanite-bearing mixes resulted in zoned titanites with Ti-rich cores and Al-rich rims, suggesting sluggish reaction rates for the re-equilibration of the titanite composition. Because of the compositional zoning of the titanites, the reversal experiments were not used in the data regression below.
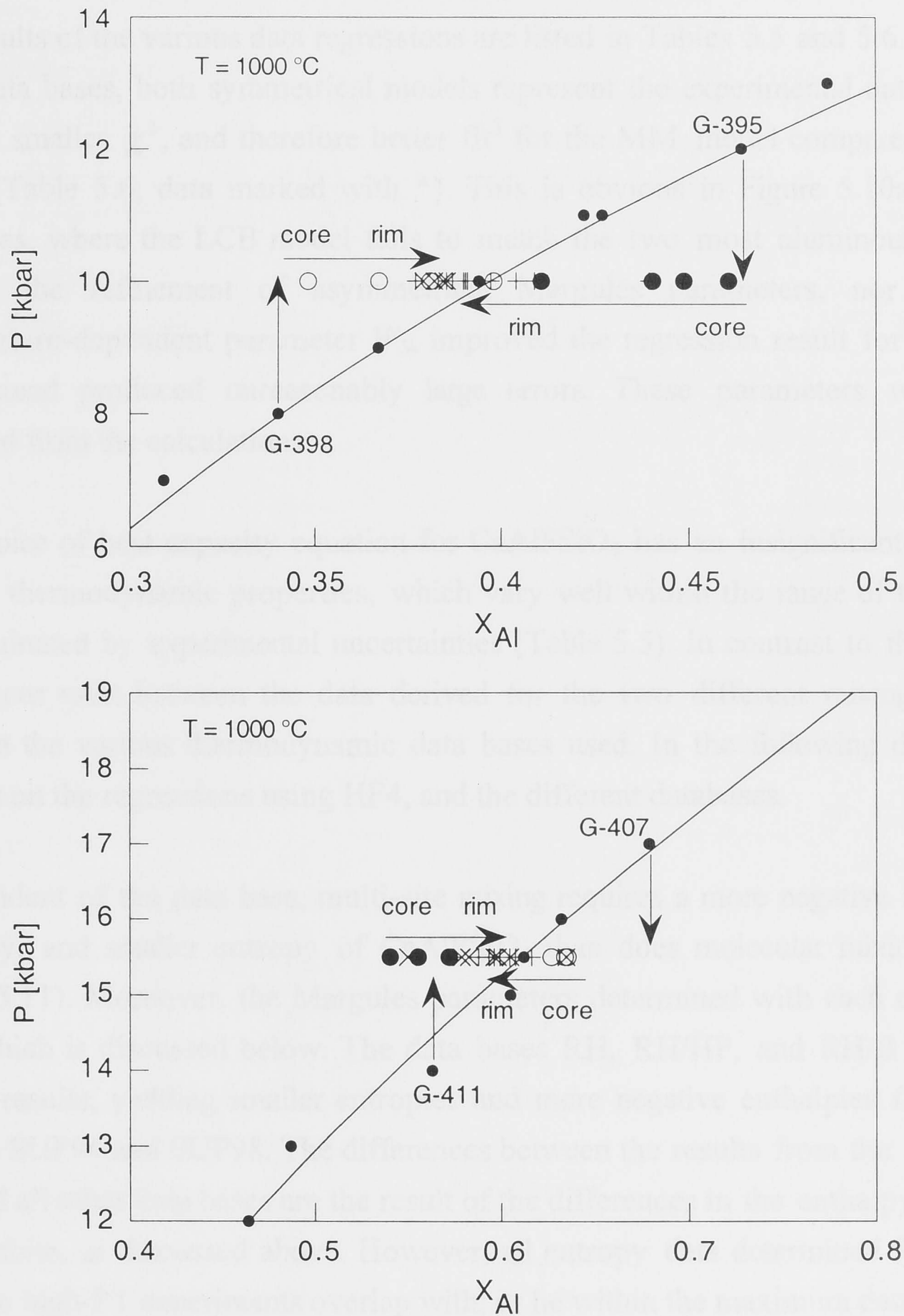
Figure 5.9 Titanite composition of four reversal experiments (large symbols) compared to previous runs (small symbols, and interpolated solid line). Starting materials of the reversals are characterised by their run number (e.g., G-395) as shown in Table 5.2. Vertical arrows indicate pressure difference between previous and reversed runs. Horizontal arrows indicate changes in composition from core (circles) to rim (crosses) of the titanite grains of the reversal runs. Reversals with samples G-395 and G-411 are shown as solid circles and upright crosses, those with samples G-398 and G-407 as open circles and diagonal crosses.

5.6.3 Thermodynamic properties of CaAlFSiO$_4$

The results of the various data regressions are listed in Tables 5.5 and 5.6. With respect to all data bases, both symmetrical models represent the experimental data well, with a slightly smaller χ^2, and therefore better fit[3] for the MM model compared to the LCB model (Table 5.6, data marked with *). This is obvious in Figure 5.10a only at high pressures, where the LCB model fails to match the two most aluminous data points. Neither the refinement of asymmetrical Margules parameters, nor that of the temperature-dependent parameter W_S, improved the regression result for either model, but instead produced unreasonably large errors. These parameters were therefore excluded from the calculations.

The choice of heat capacity equation for CaAlFSiO$_4$ has an insignificant effect on the derived thermodynamic properties, which vary well within the range of the errors that are dominated by experimental uncertainties (Table 5.5). In contrast to this, significant differences exist between the data derived for the two different mixing models, and between the various thermodynamic data bases used. In the following discussion, the focus is on the regressions using HF4, and the different databases.

Independent of the data base, multi-site mixing requires a more negative standard state enthalpy, and smaller entropy of CaAlFSiO$_4$ than does molecular mixing (Table 5.5, Figure 5.11). Moreover, the Margules parameters determined with each model differ in sign, which is discussed below. The data bases RH, RH/HP, and RH/B produce very similar results, yielding smaller entropies and more negative enthalpies for CaAlFSiO$_4$ than do SUP94 and SUP98. The differences between the results from the two SUP data sets and all other data bases are the result of the differences in the enthalpy and entropy of anorthite, as discussed above. However, all entropy data determined for CaAlFSiO$_4$ from the high-PT experiments overlap with, or lie within the maximum data range for the entropy as estimated from calorimetric data, and their extrapolation to absolute zero (Figure 5.11a).

---

[3] The fact that χ^2 is generally smaller than one for the MM model indicates that some of the errors used in the data regression are possibly overestimated. The uncertainty of the temperature readings of $\pm$ 5°C is unlikely to be any smaller. However, if the error of the pressure readings was only half of that assumed here ($\pm$ 0.2 kbar), then χ^2 would result in values close to unity for the MM model, and respectively higher for the LCB model. Also, it is likely that some of the errors of X_{Al} are overestimated (sd, Table 5.2), especially those that are represented by the standard deviation of X_{Al} based on microprobe analyses of each sample. If these errors did not refer to the chemical variation of titanite in each sample, but were based only on the accuracy of the microprobe analyses (Al $\pm$ 1.1 wt.%, Ti $\pm$ 1.3 wt.%), and applied to the average X_{Al} of each sample (i.e., $X_{Al} \pm$ 0.06), then χ^2 would approach unity for the MM model, and be respectively larger for the LCB model. In any case, the fit to the data using the MM model is always better than that of the LCB model.

Table 5.5 Enthalpy of formation from the elements (d_fH^0) and the third-law entropy (S^0) of CaAlFSiO$_4$, and Margules parameter at experimental temperature $(W_H\text{-}TW_S)$. The calculation of the Gibb's energy of formation (d_fG^0) was based on the data for the elements by Robie and Hemingway (1995). The standard state is 298.15 K and 1 bar. Heat capacity equations for CaAlFSiO$_4$: Haas and Fisher (1976) with 4 and 5 coefficients (HF4, HF5), Berman and Brown (1985) with and without dummy (BBd, BBnd) (compare Table 4.3, p. 65). Data for anorthite (Anor) and fluorite (Fluo) from data bases: Robie and Hemingway (1995) (RH), two updates of the program SUPCRT (Johnson et al., 1992) (SUP94 and SUP98), Holland and Powell (1998) (HP), Berman (1988) (B). Statistical results are given in Table 5.6.

C_P equation for CaAlFSiO$_4$	data Anor	data Fluo	MM model	LCB model
			d_fH^0 [kJmol^{-1}]	d_fH^0 [kJmol^{-1}]
HF5	RH	RH	-2743.721 ± 3.026	-2736.722 ± 3.077
HF4	RH	RH	-2743.733 ± 3.026	-2736.735 ± 3.077
BBnd	RH	RH	-2743.800 ± 3.026	-2736.802 ± 3.078
BBd	RH	RH	-2743.600 ± 3.025	-2736.563 ± 3.076
HF4	HP	RH	-2744.327 ± 2.031	-2737.325 ± 2.082
HF4	B	RH	-2740.837 ± 3.025	-2733.841 ± 3.076
HF4	SUP94	SUP94	-2741.138 ± 3.020	-2734.147 ± 3.072
HF4	SUP98	SUP98	-2734.028 ± 3.020	-2727.037 ± 3.072
			S^0 [kJmol^{-1}]	S^0 [kJmol^{-1}]
HF5	RH	RH	104.200 ± 1.130	110.676 ± 1.169
HF4	RH	RH	104.159 ± 1.130	110.635 ± 1.169
BBnd	RH	RH	104.111 ± 1.130	110.587 ± 1.169
BBd	RH	RH	104.359 ± 1.130	110.835 ± 1.168
HF4	HP	RH	103.690 ± 1.134	110.169 ± 1.173
HF4	B	RH	104.861 ± 1.129	111.335 ± 1.168
HF4	SUP	SUP	108.186 ± 1.125	114.655 ± 1.164
			$W_H - TW_S$ [Jmol^{-1}]	$W_H - TW_S$ [Jmol^{-1}]
HF5	RH	RH	6798 ± 225	-9111 ± 439
HF4	RH	RH	6798 ± 225	-9111 ± 439
BBnd	RH	RH	6797 ± 225	-9112 ± 440
BBd	RH	RH	6798 ± 225	-9110 ± 439
HF4	HP	RH	6795 ± 226	-9114 ± 441
HF4	B	RH	6797 ± 225	-9112 ± 439
HF4	SUP	SUP	6798 ± 224	-9114 ± 437
			d_fG^0 [kJmol^{-1}]	d_fG^0 [kJmol^{-1}]
HF5	RH	RH	-2595.4 ± 2.8	-2590.3 ± 2.8
HF4	RH	RH	-2595.4 ± 2.8	-2590.3 ± 2.8
BBnd	RH	RH	-2595.5 ± 2.8	-2590.4 ± 2.8
BBd	RH	RH	-2595.3 ± 2.8	-2590.2 ± 2.8
HF4	HP	RH	-2595.8 ± 1.8	-2590.8 ± 1.8
HF4	B	RH	-2592.9 ± 1.8	-2587.8 ± 1.8
HF4	SUP94	SUP94	-2594.3 ± 3.0	-2589.3 ± 3.0
HF4	SUP98	SUP98	-2587.0 ± 3.0	-2581.9 ± 3.0

Table 5.6 Statistical results of data regressions, considering different combinations of refined parameters (+), i.e. reaction enthalpy dH, entropy dS, and Margules parameters $[W_H\text{-}TW_S]$ and W_V, as well as independently determined constants (o), i.e. thermal expansion α, isothermal compressibility β, and Margules parameter W_V. Heat capacity equations and data bases as in Table 5.5.

C_P equation for CaAlFSiO$_4$	data Anor	data Fluo	dH	dS	W_H -TW_S	α, β	W_V	X^2 MM model	X^2 LCB model
HF4	RH	RH	+	+	+			0.76	1.01
HF4	RH	RH	+	+	+	o		0.79	1.00
HF4	RH	RH	+	+	+		o	0.70	1.13
HF4	RH	RH	+	+	+		+[#]	0.72	-
HF4*	RH	RH	+	+	+	o	o	0.67	1.10
HF4	RH	RH	+	+	+	o	+[†]	0.71	-

Preferred results

C_P equation for CaAlFSiO$_4$	data Anor	data Fluo	dH	dS	W_H -TW_S	α, β	W_V	X^2 MM model	X^2 LCB model
HF5*	RH	RH	+	+	+	o	o	0.67	1.10
HF4*	RH	RH	+	+	+	o	o	0.67	1.10
BBnd*	RH	RH	+	+	+	o	o	0.67	1.10
BBd*	RH	RH	+	+	+	o	o	0.67	1.10
HF4*	HP	RH	+	+	+	o	o	0.67	1.09
HF4*	B	RH	+	+	+	o	o	0.67	1.10
HF4*	SUP	SUP	+	+	+	o	o	0.68	1.11

* These values pertain to the data shown in Table 5.5.
[#] $W_V = 118 \pm 57$ [Jmol^{-1}bar^{-1}]
[†] $W_V = 99 \pm 57$ [Jmol^{-1}bar^{-1}]

The good agreement between the entropy derived from the experiments with that determined with calorimetry, as well as that estimated from anorthite and fluorite (Figure 5.11a), suggests that there are no significant additional entropy contributions, such as configurational entropy, or excess entropy based on a low-T phase transition.

The main features of both models are summarised in G-X and activity-composition plots in Figures 5.12 and 5.13, respectively. Figure 5.14 shows the Al-content in titanite in the divariant assemblage anorthite – fluorite – titanite. These plots, which were constructed using the values for enthalpy, entropy and interaction parameters based on the regression with RH and HF4 (Table 5.5), are qualitatively representative for the results of all other regressions. Note the good agreement of the Al-contents predicted in Figure 5.14, and the recent experimental results by Tropper et al. (1999, 2000), demonstrating reproducibility of the experiments presented here.

a)

b)
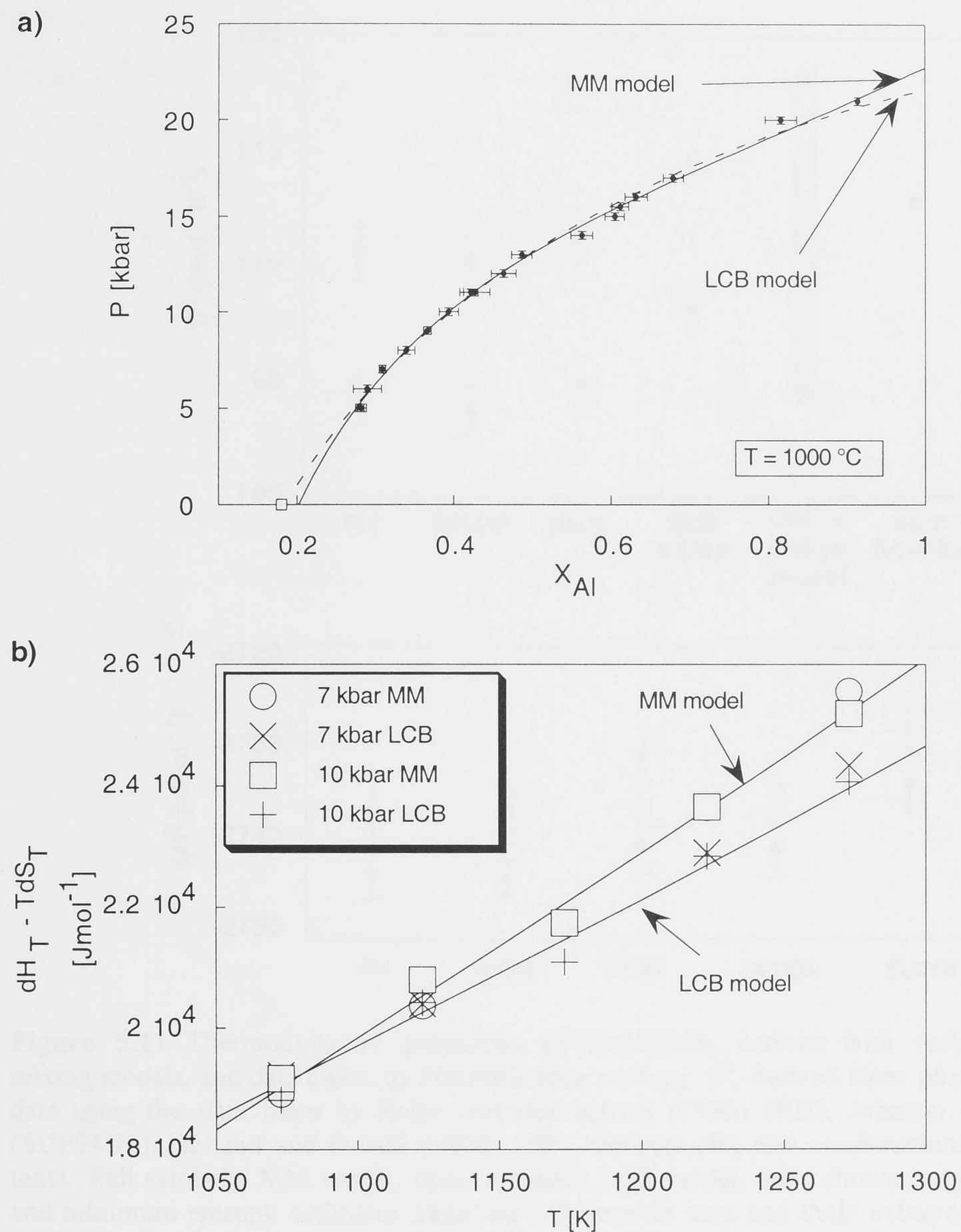
Figure 5.10 Data regression results for the MM and LCB model (compare Table 5.5). **a)** Isothermal and polybaric experiments. **b)** Isobaric and polythermal experiments. Errors in T are as large as the symbols, errors in dH_T - TdS_T are all less than 2200 Jmol^{-1}. Solid lines in b) were calculated as $y = \Delta H_T - T\Delta S_T$, experimental data points as $y = -RT \ln K - \int \Delta V dP$ (LCB model) and $y = -2RT \ln K - \int \Delta V dP$ (MM model).
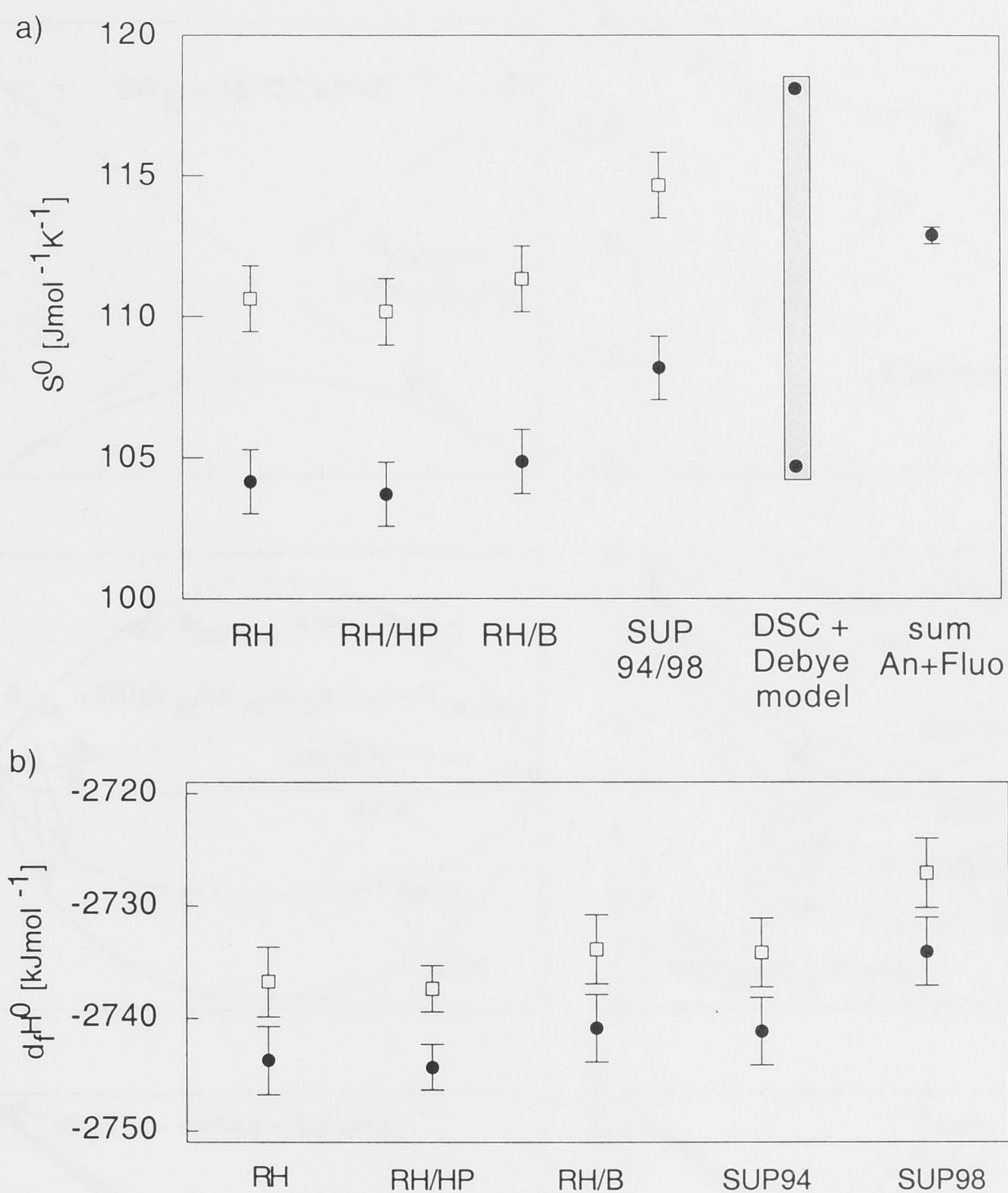
Figure 5.11 Thermodynamic properties of CaAlFSiO$_4$, derived with various methods, mixing models, and data bases. **a)** Standard state entropy S^0, derived from phase equilibrium data using the data bases by Robie and Hemingway (1995) (RH), Johnson et al. (1992) (SUP94/98), Holland and Powell (1998) (HP), Berman (B), and combinations thereof (see text). Full symbols: MM model, open symbols: LCB model. Also shown are the maximum and minimum entropy estimates based on calorimetric data and their extrapolation to 0 K (DSC+Debye model) (Chapter 4), and estimated from the component entropies of anorthite and fluorite (sum An+Fluo) (Chapter 4). **b)** Enthalpy of formation from the elements d$_f$H^0, derived from phase equilibrium data (this chapter). Models and data bases as above. Note that the differences between the values determined with SUP, and those calculated with the other data bases, can be traced back to the differences in entropy and enthalpy values for anorthite between these data bases.

MM model   **LCB model**
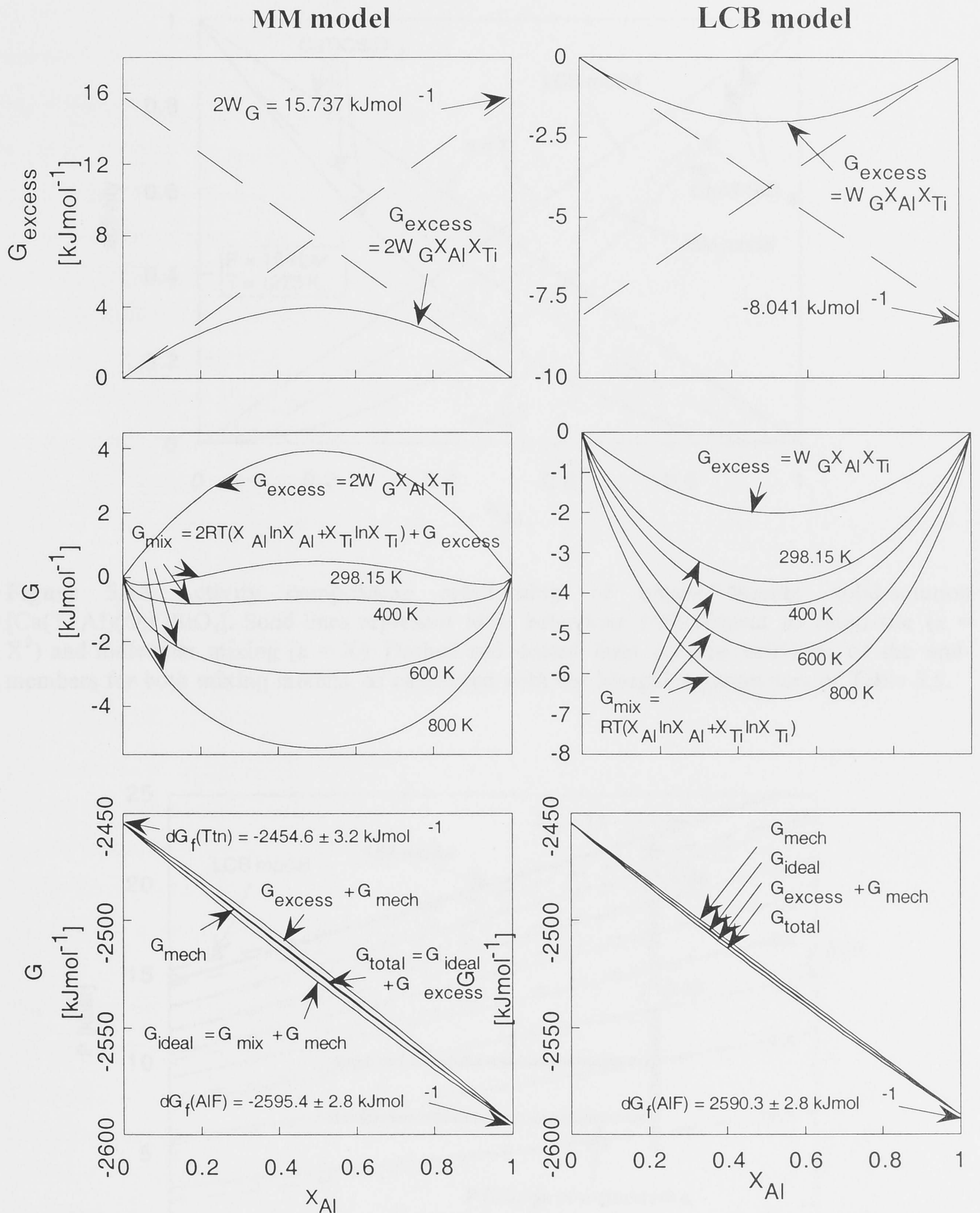
Figure 5.12 Gibb's free energy versus composition of binary titanite solid-solution [Ca(Ti,Al)(O,F)SiO$_4$] with respect to both mixing models (see text), based on the thermodynamic data presented in Table 5.5 (RH, HF4). The calculation methods of the different parts of the total Gibb's free energy (G$_{total}$), i.e. energy of mixing (G$_{mix}$), mechanical (G$_{mech}$), ideal (G$_{ideal}$), and excess (G$_{excess}$) (e.g., Speer, 1993) are given in the respective figures. Bottom figures: intermediate lines represent two curves, but cannot be resolved at this scale. W_G refers to 10 kbar.
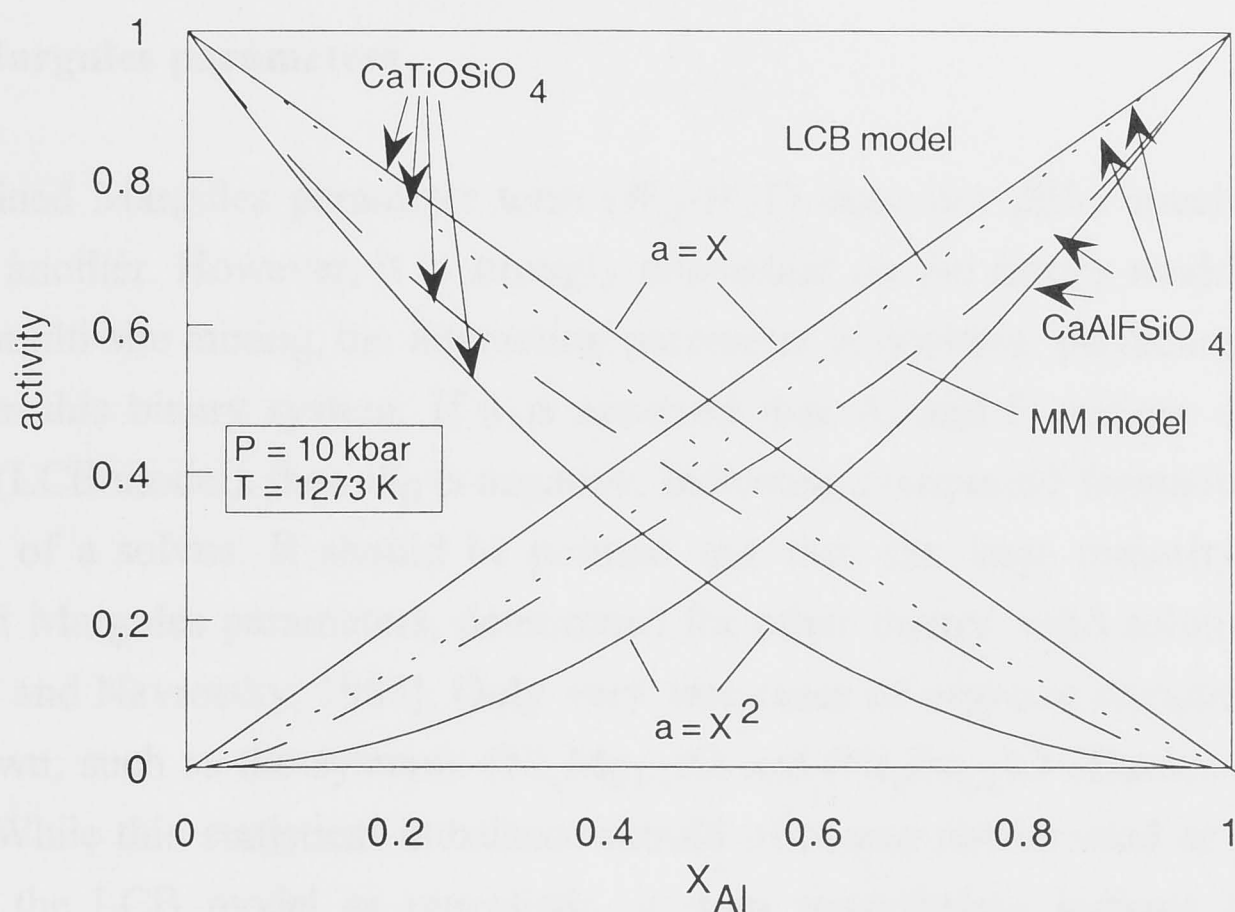
Figure 5.13 Activity composition relationship of binary titanite solid-solution [Ca(Ti,Al)(O,F)SiO$_4$]. Solid lines represent ideal behaviour with respect to multi-site (a = X^2) and molecular mixing (a = X). Dashed and dotted lines are the activities of the end-members for both mixing models, as calculated with the Margules parameters of Table 5.5.
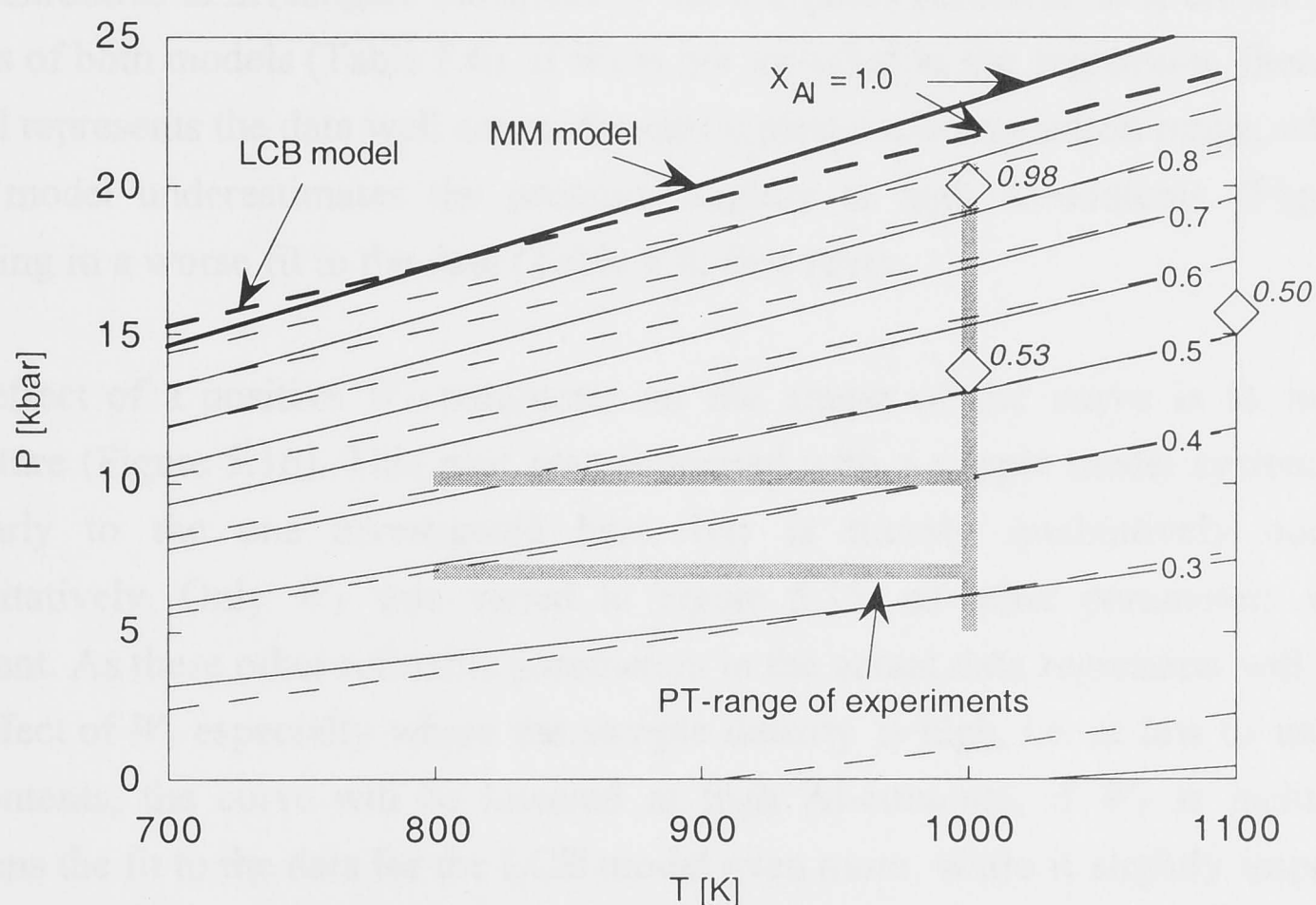
Figure 5.14 Al-content of titanite [X$_{Al}$] in the divariant assemblage anorthite – fluorite – titanite solid-solution, as described by the MM and LCB models. Open diamonds are recent experimental results by Tropper et al. (1999, 2000), indicating the run conditions at which they equilibrated titanite with anorthite and fluorite, with or without rutile. The titanite composition they reported is shown in italics next to the symbol.

5.6.4 Margules parameters

The refined Margules parameter term $(W_H-W_S T)$ does not differ much from one data base to another. However, it is strongly dependent on the mixing model chosen. In the case of multi-site mixing, the interaction parameter is positive, predicting a symmetrical solvus in this binary system. If it is assumed that Al and F occupy adjacent sites in titanite (LCB model), then W_G is negative, indicating compound formation, and thus the absence of a solvus. It should be pointed out that the large majority of previously reported Margules parameters, determined for other binary solid-solutions, is positive (Davies and Navrotsky, 1983). Only very rare cases of negative deviation from ideality are known, such as the systems $(Ni_x Mg_{1-x})O$ and $(Ni_x Zn_{1-x})O$ (Davies and Navrotsky, 1981). While this statistical imbalance should of course not be used as an argument to dismiss the LCB model as unrealistic, it does nevertheless indicate that the results obtained with this model should be treated with caution. It is surprising that the local charge balance model, which at the first glance seems more appropriate for a mixed-charge coupled substitution, seems less likely with its negative deviation from ideality, and a slightly worse fit to the data, compared to the MM model (Table 5.6).

It is instructive to investigate the effect of the Margules parameter W_V, on the regression results of both models (Table 5.6). If W_V is not included in the regression, then the M M model represents the data well across the entire pressure/composition range, whereas the LCB model underestimates the pressure slightly at high Al-contents (Figure 5.15), resulting in a worse fit to the data (Table 5.6, first row).

The effect of a positive W_V parameter on the shape of the curve is to increase its curvature (Figure 5.16). This plot was generated with a simple model system behaving similarly to the one investigated here, but is merely qualitatively correct, not quantitatively. Only W_V was varied in Figure 5.15, all other parameters were kept constant. As these other refinable parameters in the actual data regression will adjust for the effect of W_V especially where the sample density is high, i.e. at low to intermediate Al-contents, the curve will be lowered at high Al-contents, if W_V is included. This worsens the fit to the data for the LCB model even more, while it slightly improves that of the MM model (Table 5.6, third row). Thus the independently determined positive value of W_V, which of course should be considered in the final data regression, seems to be consistent with the MM model rather than the LCB model.
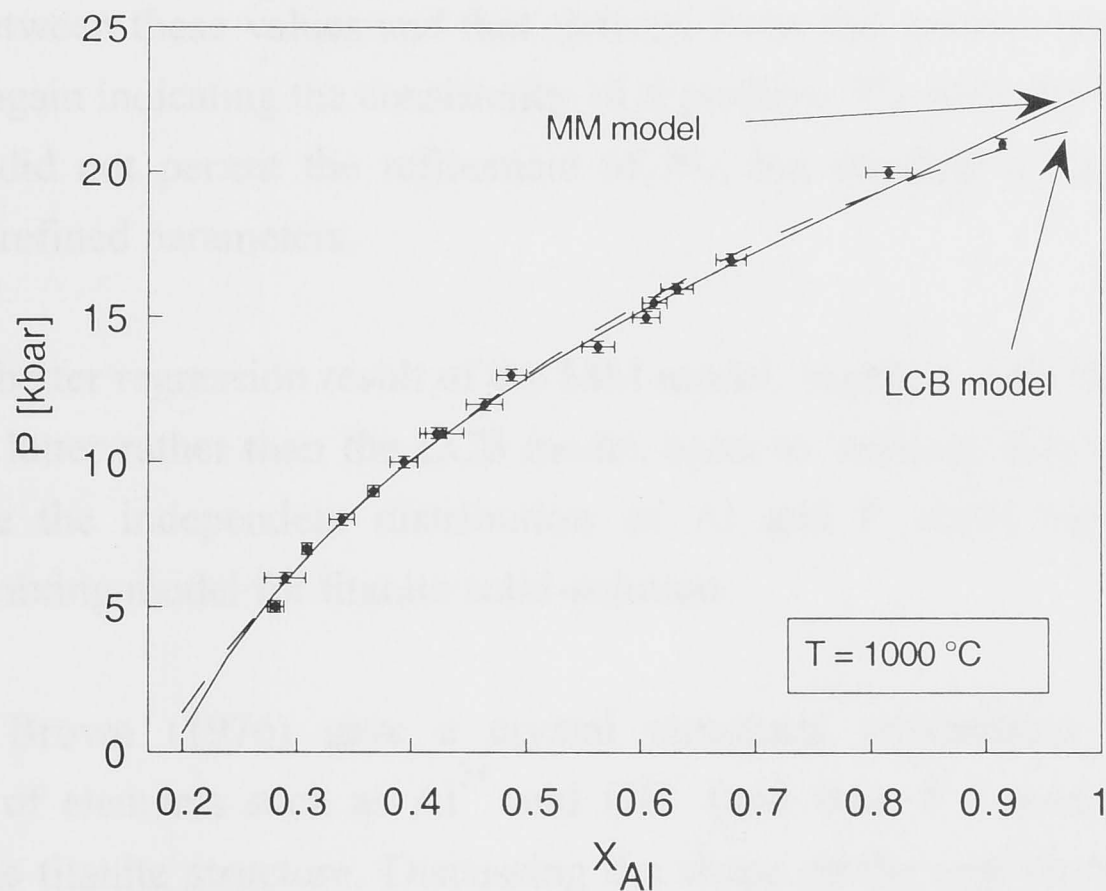
Figure 5.15 Data regression results for the MM and LCB models, without considering Margules parameter W_V in the calculations. Data bases used: RH and HF4, as defined in Table 5.5. Results for MM/LCB: dH = -12492±1080/-5604±1104 Jmol^{-1}, dS = -29.969±0.873/-23.468±0.890 Jmol^{-1}K^{-1}, W_G = 7267±234/-8640±448 Jmol^{-1}, X^2 = 0.79/1.00.
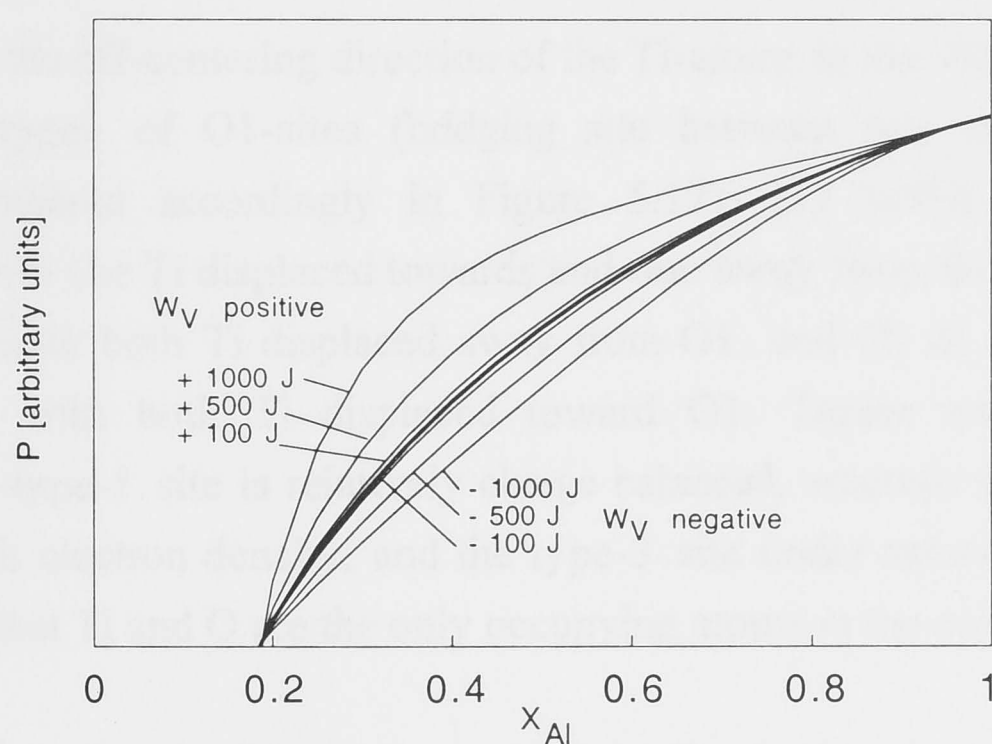
Figure 5.16 Qualitative effect of Margules parameter W_V, and its sign, on the curve fit (compare Figure 5.15).

In order to test the value for W_V (107.04 ± 8.88 Jkbar^{-1}) that was derived from unit-cell volume data above, the attempt was made to refine W_V from the experimental data set. This was possible with respect to the MM model, which in fact yielded W_V values very similar to the one calculated from the excess volume of mixing, namely 99 ± 57 Jkbar^{-1} and 118 ± 57 Jkbar^{-1}, with and without the consideration of compression and expansion terms, respectively (Table 5.6). Although the errors of W_V are admittedly large, the

agreement between these values and that derived from the excess volume of mixing is remarkable, again indicating the consistency of a positive W_V with the MM model. The LCB model did not permit the refinement of W_V, but resulted in unreasonably large errors for all refined parameters.

The slightly better regression result of the MM model, together with the consistency of W_V with the latter rather than the LCB model, seem to indicate that multi-site mixing, and therefore the independent distribution of Al and F could represent the more appropriate mixing model for titanite solid-solution.

Taylor and Brown (1976) gave a crystal structural explanation as to why the substitution of elements such as Al^{3+} and OH^- (and thus F^-) need not be spatially coupled in the titanite structure. Discussing the shape of the anti-phase domains in the titanite structure, they suggested that the opposite displacement of the Ti-atoms at the anti-phase boundaries might compensate for any local charge imbalance caused by an individual anion or cation of different charge. The formation of anti-phase domains in titanite by substitution of impurities such as Al and F was discussed in Chapter 3.

Figure 5.17 shows the off-centering direction of the Ti-atoms in the vicinity of a domain boundary. Three types of O1-sites (bridging site between two octahedra) can be distinguished (numbered accordingly in Figure 5.17): (1) within an undisturbed octahedral chain with one Ti displaced towards and one away from the O1-site, (2) at a domain boundary with both Ti displaced away from O1, and (3) at a second type of domain boundary with both Ti displaced toward O1. Taylor and Brown (1976) suggested that the type-1 site is relatively charge balanced, whereas the type-2 site is over-saturated with electron density, and the type-3 site under-saturated with negative charge (assuming that Ti and O are the only occupying atoms in the octahedral chains).

They concluded that the number of energetically unfavourable type-2 and 3 sites in titanite would be minimised, and that the domain boundaries would preferably run parallel to the octahedral chains. Thus, one can imagine the type-2 and 3 sites to be located at the opposite ends of anti-phase domains elongated along the crystallographic direction *a*. Taylor and Brown (1976) pointed out that the charge imbalance at the type-2 and 3 sites could be compensated for by the substitution of F for O in a type-2 site, as well as the location of Al next to a type-3 site. They "emphasised that the substitution of Fe, Al, and OH need not be spatially coupled since the structure at a domain boundary could provide the necessary charge balance".
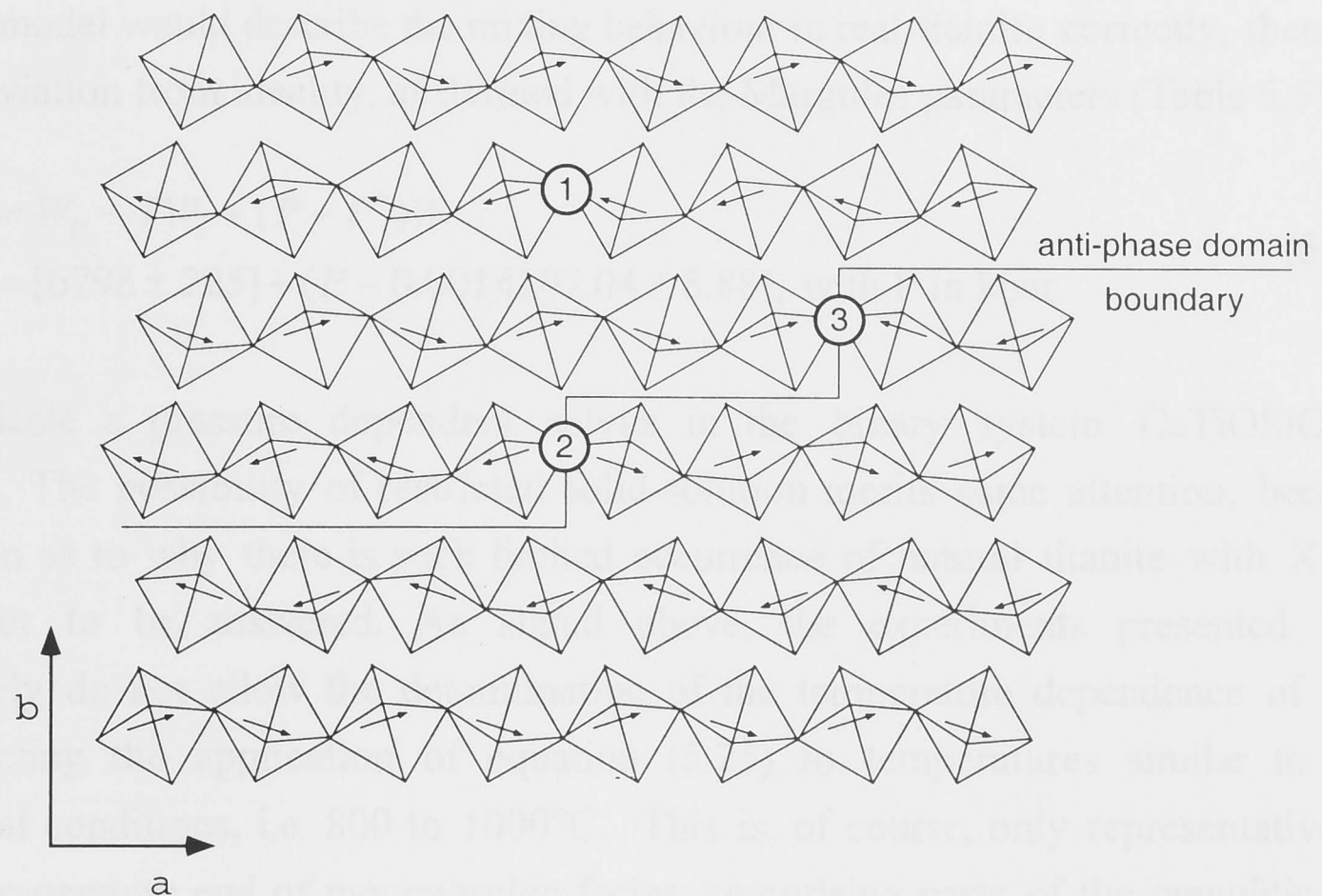
Figure 5.17 Chains of TiO$_6$-octahedra in the titanite structure. Arrows show the off-centering direction of the Ti atom in each octahedron, which changes at anti-phase boundaries, thus creating three different types of bridging oxygen sites O1 (lables 1 to 3, see text) (adapted from Taylor and Brown, 1976).

Hughes et al. (1997) extended this concept of charge balance between different types of domain boundaries and substituting atoms in titanite to the coupled substitution of Ca^{2+} and Ti^{4+} by REE^{3+} and Al^{3+}, respectively. According to that study, REE^{3+} on the Ca-site charge balances type 2 boundaries, and Al^{3+} stabilises type-3 sites. Hughes et al. (1997) agreed with Taylor and Brown (1976) that the two substituents do not have to occupy adjacent sites in the crystal lattice.

While this argument of charge balance along the domain boundaries might be valid for temperatures below the $P2_1/a - A2/a$ phase transition (T < 825 K, Kek et al., 1997), where Ti is off-centred and domain formation occurs, it may not be applicable to the temperature range covered by the experiments of this study (1073 to 1273 K).

5.6.5 Potential solvus

If the MM model would describe the mixing behaviour in real titanite correctly, then the positive deviation from ideality, as defined with the Margules parameters (Table 5.5)

$$W_G \ (J) = W_H - TW_S + (P - P^0)W_V$$
$$= [6798 \pm 225] + (P - 0.001)[107.04 \pm 8.88], \text{ with P in kbar} \tag{5.25}$$

would indicate a pressure dependent solvus in the binary system $CaTiOSiO_4$ – $CaAlFSiO_4$. The possibility of restricted solid-solution merits some attention, because the question as to why there is such limited occurrence of natural titanite with $X_{Al} > 0.54$, is yet to be answered. As stated above, the experiments presented here unfortunately do not allow the determination of the temperature dependence of W_G, thus restricting the application of equation (5.25) to temperatures similar to the experimental conditions, i.e. 800 to 1000°C. This is, of course, only representative of the high-temperature end of metamorphic facies, comprising parts of the granulitic and eclogitic rocks. Figure 5.18 shows solvi calculated with W_G from equation (5.25), and the relation (modified after Powell, 1978)

$$T = \frac{W_G(2X - 1)}{R \ln\left(\dfrac{X}{1 - X}\right)} \tag{5.26}$$

The solvi in Figure 5.18 lie well below 800°C for all pressures possibly realised in metamorphic rocks, and therefore would not affect the Al-content of natural titanites in rocks equilibrated at or above that temperature.

Even the ultrahigh-pressure gneisses from the Kokchetav Massiv (Sobolev and Shatsky, 1990), containing garnets with both diamond as well as titanite ($X_{Al} < 0.46$) inclusions, which presumably were equilibrated at > 40 kbar and 900 – 1000°C, would plot well above the solvus in Figure 5.18. A pressure of 111 kbar would be necessary in order to raise the critical temperature of the solvus to 900°C, which is clearly unrealistic. However, the Kokchetav Massiv rocks are the only natural example of high-Al titanite at such high temperatures, and might not be the most reliable candidate to test the above hypothesis, because of the uncertainty with respect to the formation conditions of the titanite inclusions. Although the maximum equilibrium conditions of the Kokchetav Massiv are constrained by the stability of diamond, the formation of titanite may have occurred later, during the uplift of these rocks from more than 140 km depth (Manning and Bohlen, 1991).
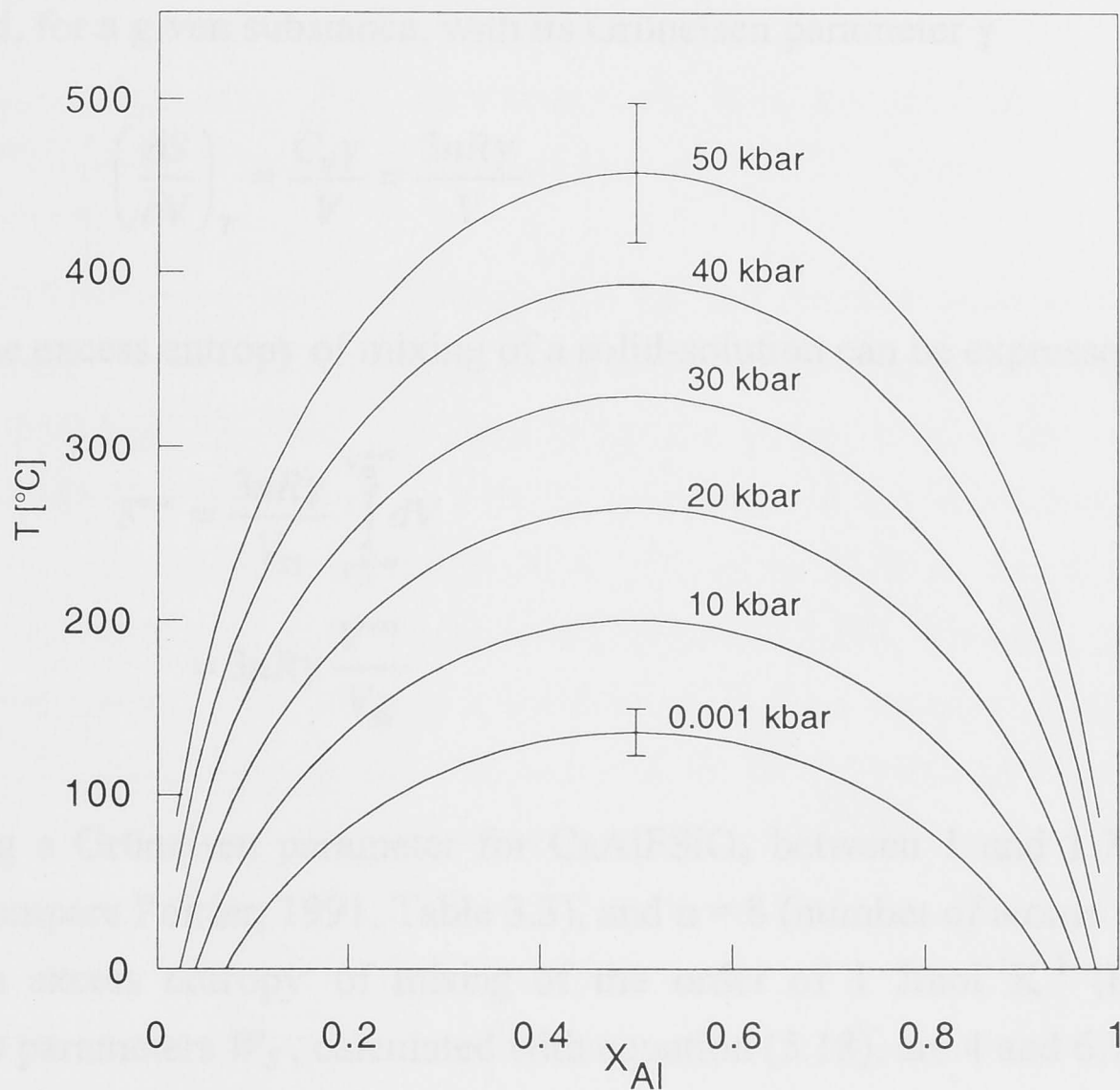
Figure 5.18 Solvi at various pressures in the binary system $CaTiOSiO_4$ - $CaAlFSiO_4$, as predicted by the multi-site mixing model, calculated with equation (5.26) and the Margules parameters $[W_H\text{-}TW_S]$ = 6798 ± 225 $Jmol^{-1}$ and W_V = 107.04 ± 8.88 $Jkbar^{-1}$. Valid at temperatures between 800 and 1000°C.

In order to test whether the presence of a solvus could have affected the formation of Al-bearing titanite in other, and partly better constrained, natural examples with equilibrium conditions below 800°C (e.g. Franz and Spear; 1985, Carswell et al., 1996), the change of the Margules parameter with decreasing temperature has to be estimated. In general, the non-ideality of a system can be expected to increase with decreasing temperature, because the contraction of the crystal structure due to cooling will make the system less tolerable towards the accommodation of ions of different size and charge. Thus, W_S should be positive (equation 5.16), and the critical temperature should be higher compared to the solvi in Figure 5.18. Two different approaches were taken to estimate the dimension of W_S, one based on theoretical reasoning, the other on empirical observations.

The first approach is based on the close relation between excess volume and excess entropy, as proposed by Newton and Wood (1980), and discussed in Pownceby and O'Neill (1994).

According to the latter authors, the relationship between volume and entropy can be described, for a given substance, with its Grüneisen parameter γ

$$\left(\frac{\delta S}{\delta V}\right)_T = \frac{C_V \gamma}{V} = \frac{3nR\gamma}{V} \tag{5.27}$$

so that the excess entropy of mixing of a solid-solution can be expressed as

$$S^{exc} = \frac{3nR\gamma}{V_{SS}} \int_{V_{SS}^{ideal}}^{V_{SS}^{real}} dV \tag{5.28}$$

$$= 3nR\gamma \frac{V^{exc}}{V_{SS}}$$

Assuming a Grüneisen parameter for $CaAlFSiO_4$ between 1 and 1.7, similar to other solids (compare Poirier, 1991, Table 3.3), and n = 8 (number of atoms per formula unit), yields an excess entropy of mixing of the order of 1 $Jmol^{-1}K^{-1}$ (Figure 5.19). The Margules parameters W_S, calculated with equation (5.18), are 4 and 6.7 $Jmol^{-1}K^{-1}$.
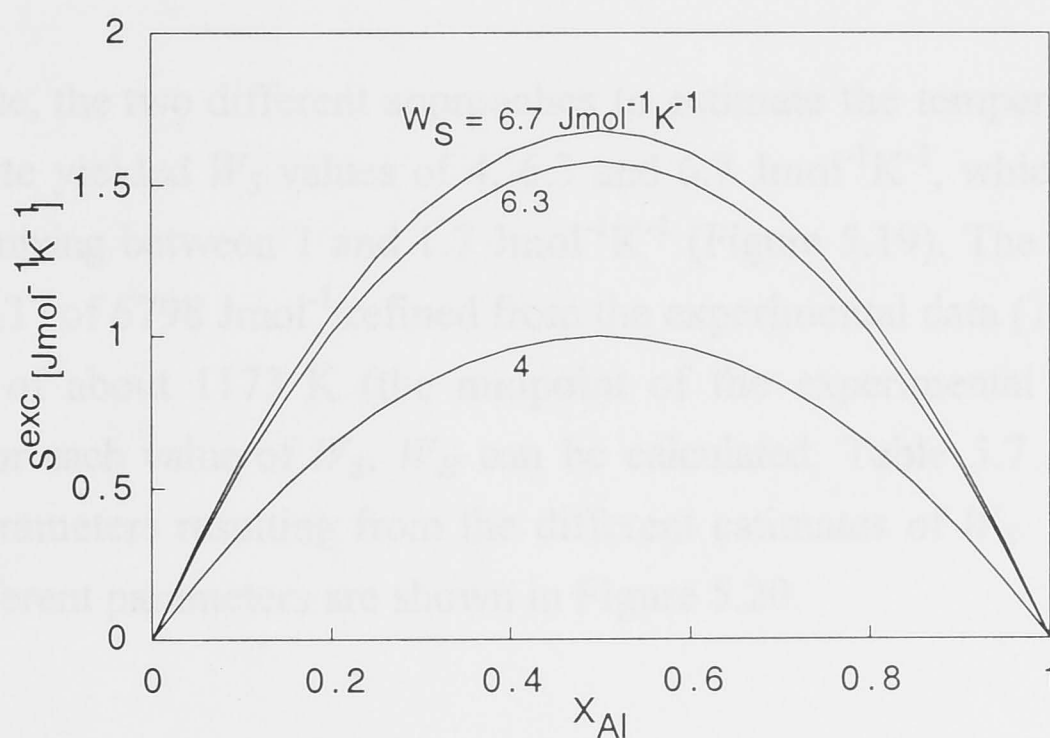
Figure 5.19 Excess volume of mixing of binary titanite, calculated with different Margules parameters W_S (see text).

Because this theoretical approach led to excess entropy values half of the actual value in the example chosen by Pownceby and O'Neill (1994), an alternative method to estimate W_S was followed in addition. This second approach is based on the observation that the non-ideality of different solid-solutions is generally comparable if the volume differences between the end-members are similar (Davies and Navrotsky, 1983). While the study by

Davies and Navrotsky (1983) derived this concept for W_G independent of pressure and temperature, the present study extends this concept of similarity to the temperature dependence. Thus, as a first approximation, it is assumed here that silicates with comparable end-member size differences have similar W_S values.

The grossular-pyrope solid-solution, with an end-member volume difference of about 10%, is taken as a model system for titanite solid-solution, where the end-member volumes differ by 7%. The non-ideality for the garnet solid-solution was investigated experimentally by Hensen et al. (1975), who derived the relationship W_G (Jmol^{-1}) = $31205 - 18T(K)$, so that $W_S = 18$ Jmol^{-1}K^{-1}. Thus, at 1273 K, which is the temperature to which W_G of titanite in this study refers (equation 5.25), W_G of garnet is 8308 Jmol-1. This is comparable to W_G of titanite solid-solution, thus supporting the choice of garnet as a model system for titanite. Newton and Wood (1980) and Haselton and Newton (1980) reinterpreted the data of Hensen et al. (1975), taking into account the excess volume of mixing of garnet, and corrected the value for W_S to 6.3 Jmol^{-1}K^{-1} (Newton and Haselton, 1981). This value for W_S is preferred by the present study, because it is independent of the excess volume of mixing, and therefore comparable to the W_S to be estimated for titanite (equation 5.16 and 5.25).

To summarise, the two different approaches to estimate the temperature dependence of W_G for titanite yielded W_S values of 4, 6.3 and 6.7 Jmol^{-1}K^{-1}, which describe an excess entropy of mixing between 1 and 1.7 Jmol^{-1}K^{-1} (Figure 5.19). The Margules parameter term (W_H-W_ST) of 6798 Jmol^{-1} refined from the experimental data (Table 5.5) refers to a temperature of about 1173 K (the midpoint of the experimental temperature range). Therefore, for each value of W_S, W_H can be calculated. Table 5.7 shows three sets of Margules parameters resulting from the different estimates of W_S. The solvi calculated from the different parameters are shown in Figure 5.20.

Table 5.7 Different sets of Margules parameters for titanite, depending on the choice of W_S.

W_H*	W_S	W_V
[Jmol^{-1}]	[Jmol^{-1}K^{-1}]	[Jmol^{-1}kbar^{-1}]
11490	4.0	107.04
14188	6.3	107.04
14657	6.7	107.04

* calculated as W_H = 6798 + 1173W_S (compare Table 5.5)
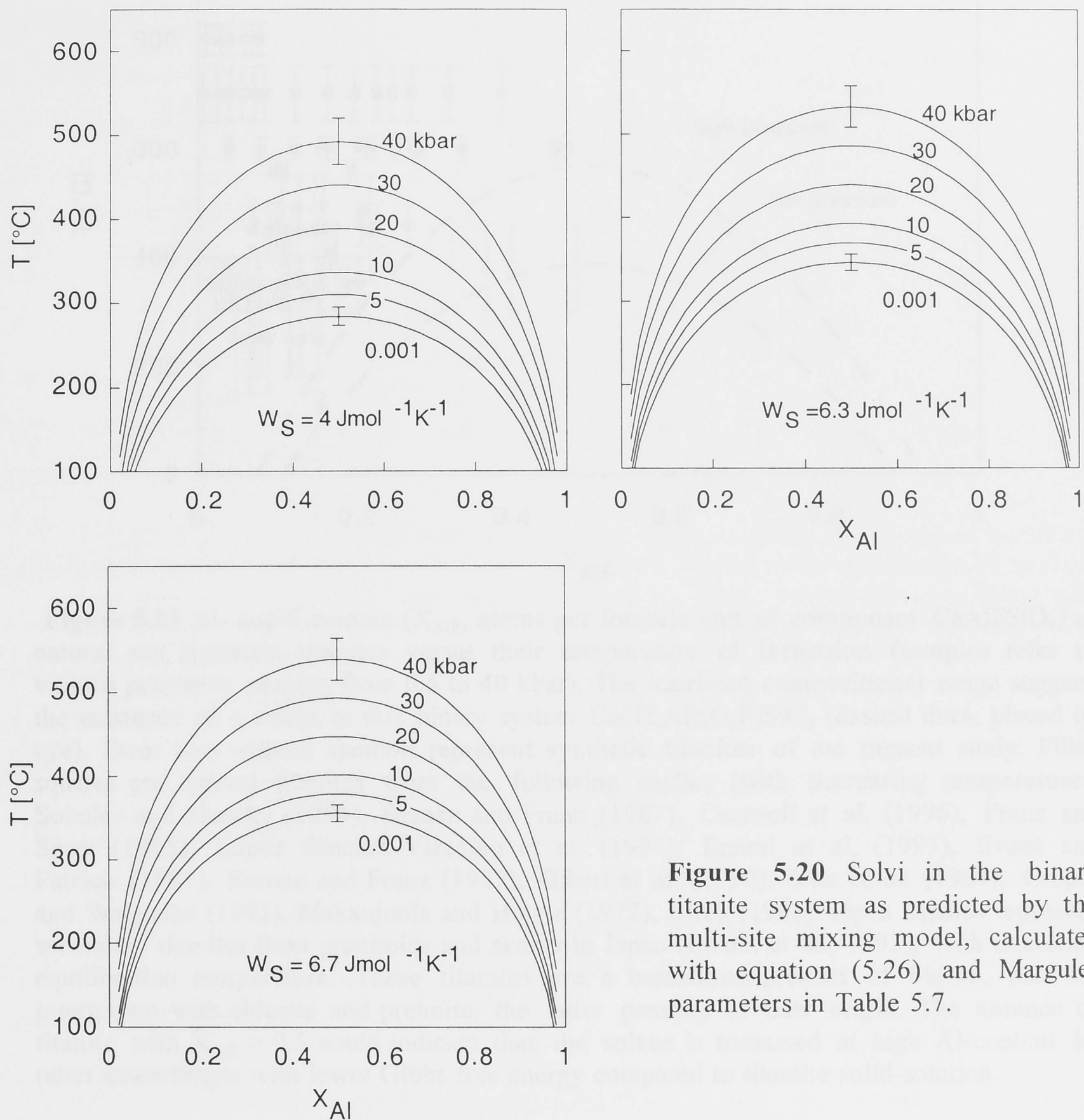
Figure 5.20 Solvi in the binary titanite system as predicted by the multi-site mixing model, calculated with equation (5.26) and Margules parameters in Table 5.7.
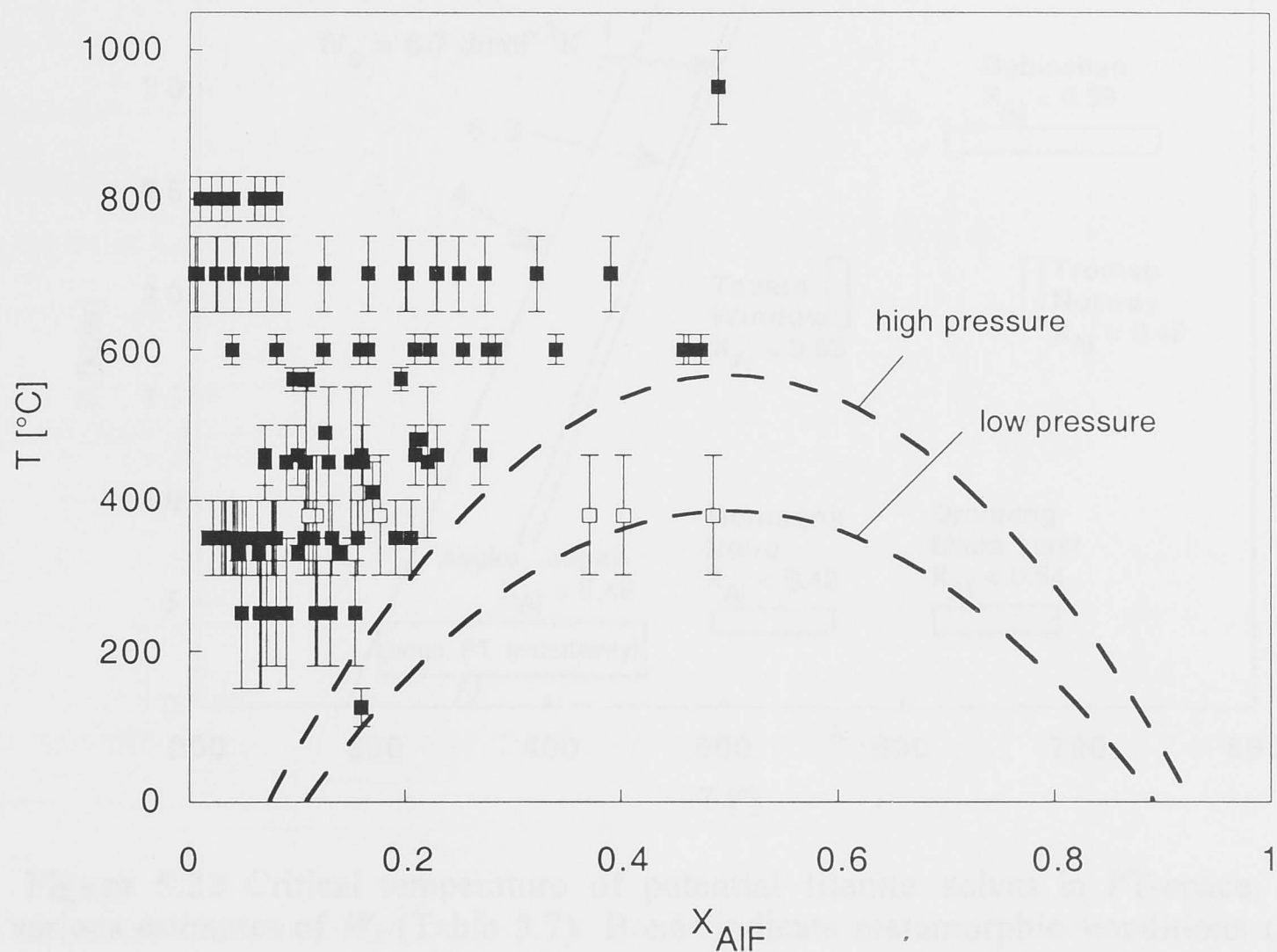
Figure 5.21 Al- and F content (X_{AlF}, atoms per formula unit of component $CaAlFSiO_4$) of natural and synthetic titanites versus their temperature of formation (samples refer to various pressures, ranging from 0.5 to 40 kbar). The restricted compositional range suggests the existence of a solvus in this binary system $Ca(Ti,Al)(O,F)SiO_4$ (dashed lines, placed by eye). Error bars without symbols represent synthetic titanites of the present study. Filled squares are natural titanites from the following studies (with decreasing temperature): Sobolev and Shatsky (1990), Bernau and Franz (1987), Carswell et al. (1996), Franz and Spear (1985), López Sánchez-Vizcaíno et al. (1997), Enami et al, (1993), Evans and Patrick (1987), Bernau and Franz (1987), Gibert et al. (1990), Yau et al. (1984), Grapes and Watanabe (1992), Makanjuola and Howie (1972), Birch (1983). Open squares represent secondary titanites from granitoids and skarns in Japan (Enami et al., 1993), with uncertain equilibration temperature. These titanites are a breakdown-product of biotite, and are intergrown with chlorite and prehnite, the latter possibly of later origin. The absence of titanite with $X_{AlF} > 0.5$ could indicate that the solvus is truncated at high Al-content by other assemblages with lower Gibbs free energy compared to titantite solid-solution.

Figure 5.21 shows a T-X_{Al} plot of the binary system $CaTiOSiO_4$–$CaAlFSiO_4$, based on all analyses of natural titanite available to the author that included fluorine, and for which estimates of the equilibration temperatures of titanite were given. Although the samples refer to different pressures ranging from 2 to 40 kbar, the general increase of the maximum X_{Al} with increasing temperature (up to $X_{Al} \approx 0.5$) would be consistent with the presence of a solvus in this system, with a critical temperature between 400°C and 600°C. This temperature range is in good agreement with the calculated solvi in Figure 6.20. Figure 5.22 shows that the most Al-rich titanite samples all plot above the predicted critical temperature in PT-space, consistent with the existence of a solvus.
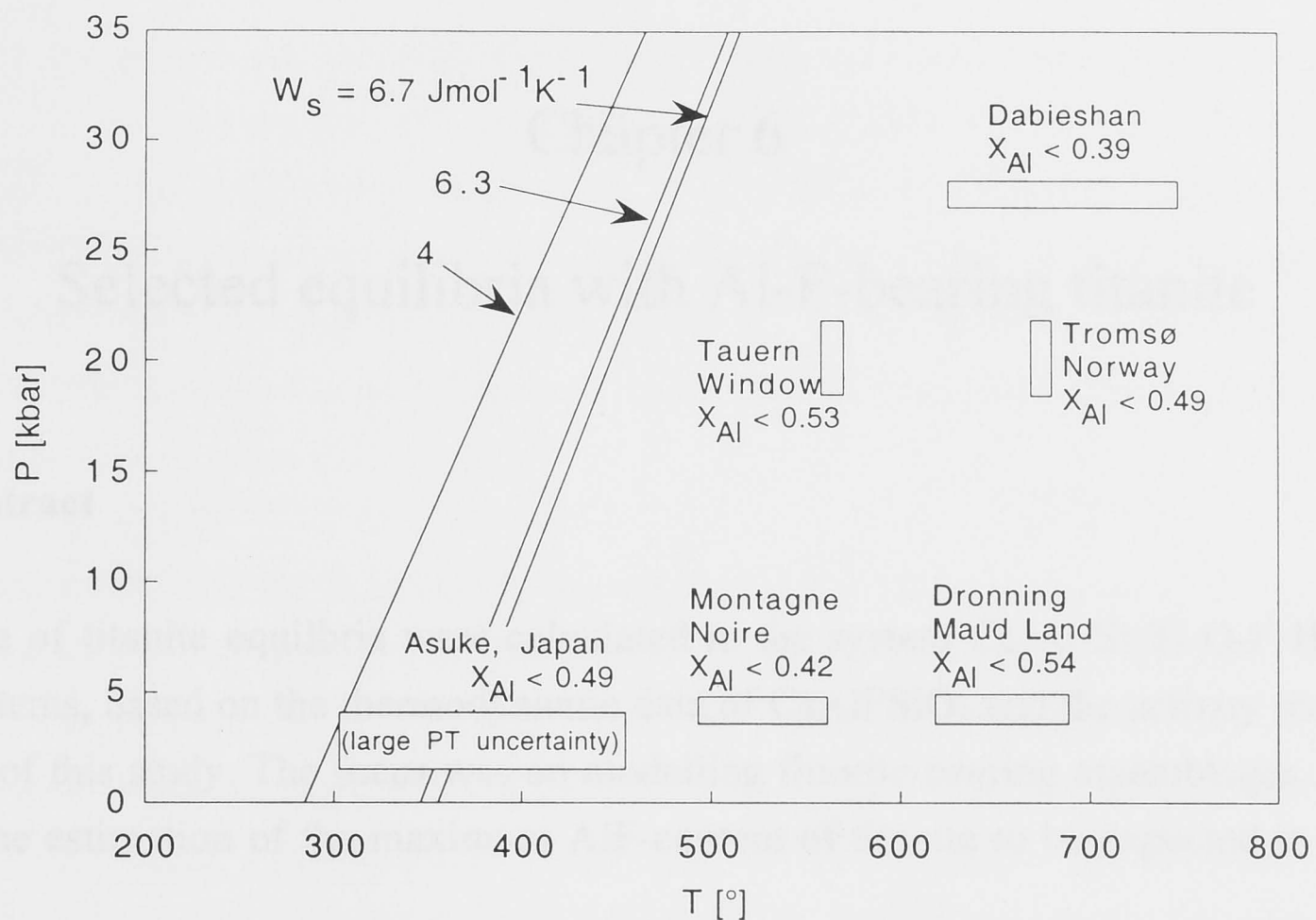
Figure 5.22 Critical temperature of potential titanite solvus in PT-space, based on various estimates of W_S (Table 5.7). Boxes indicate metamorphic conditions of various Al-titanite bearing rocks (Dabieshan: Carswell et al., 1996; Tauern Window: Franz and Spear, 1985; Montagne Noire: Gibert et al., 1990; Dronning Maud Land: Markl and Piazolo, 1999; Asuke, Japan: Enami et al., 1993; Norway: Krogh et al., 1990).

Although the thermodynamic properties of titanite solid-solution discussed in this chapter, and the composition of natural titanite (Figure 6.21) suggest the presence of a solvus, unmixing textures, such as an intergrowth of Al-rich and A-poor titanite, have never been reported from natural samples. Instead, Al-rich titanite is observed to break down to a vermicular intergrowth of Al-poor titanite and anorthite, for example (Carswell et al., 1996).

It will be demonstrated in the following chapter that the potential solvus of the system $CaTiOSiO_4 - CaAlFSiO_4$ is likely to be truncated by other reactions, which destabilise very Al-rich titanite with respect to other Ca-Al phases. This would explain the absence of titanite with $X_{Al} > 0.54$ from Figure 5.21.

Chapter 6

Selected equilibria with Al-F-bearing titanite

6.1 Abstract

A range of titanite equilbria were calculated in the system Ca-Al-Si-Ti-O-F-H-C and sub-systems, based on the thermodynamic data of $CaAlFSiO_4$ and the activity model for titanite of this study. The focus was on modelling fluorite-bearing assemblages, as they allow the estimation of the maximum AlF-content of titanite to be expected in natural rocks.

The resulting petrogenetic grids are in good agreement with natural mineral assemblages, in that very Al-rich titanite ($X_{Al} > 0.65 \pm 0.15$) is generally absent, because it is either unstable with respect to other phases, or its stability field lies outside the pressure-temperature conditions realised on Earth. Although titanite with Al-contents up to $X_{Al} = 0.6$ can be stable in all metamorphic facies, the petrogenetic grids predict that the most likely occurrence Al-rich titanite is at high metamorphic grade, predominantly at eclogite facies conditions. In contrast to this, blueschist facies rocks are predicted to contain titanite with low Al-contents, which is in agreement with natural rocks. The most Al-rich titanite can be expected in the absence of any fluid, as H_2O and CO_2 destabilise the $CaAlFSiO_4$ component with respect to hydrous Ca-Al phases and calcite assemblages, respectively. The isopleths of many equilibria, especially of high-grade assemblages, have very widely spaced Al-isopleths, which prevents their use as geobarometers or thermometers.

Good agreement exists also between the thermodynamic calculations and recent experimental results by Tropper et al. (1999, 2000), indicating both the reproducibility of the experimental results presented in Chapter 5, as well as high quality of the thermodynamic data for $CaAlFSiO_4$ that were extracted from them.

The end-member $CaAlFSiO_4$ is unstable with respect to other phases in almost all investigated assemblages. This is consistent with the hypothesis based on crystal structure data (Chapters 2 and 3), that the presence of structural stresses in the crystal lattice of $CaAlFSiO_4$ might influence its thermodynamic stability. The fact that the titanite structure is not well suited to accommodate Al and F instead of Ti and O is

probably the reason for the high Gibbs free energy of $CaAlFSiO_4$ compared to other phases. The increasing amount of the less stable $CaAlFSiO_4$ end-member along the binary join is the reason why titanite with $X_{Al} > 0.65 \pm 0.15$ becomes unstable in most petrogenetic grids presented here. Thus the compositional limit of natural titanite ($X_{Al} \approx 0.54$) is probably reflecting the point beyond which the less stable end-member begins to dominate the solid-solution, affecting both crystal structure and thermodynamic properties.

Thermodynamic data for fluor-zoisite were estimated in order to model its occurrence in the experimental run products of this study. These calculations are consistent with the synthetic run results, and help to understand the stability of $CaAlFSiO_4$ with respect to fluor-zoisite. The computed equilibria indicate that fluor-zoisite formed as a stable phase in all experiments, not metastably, and that $CaAlFSiO_4$ does not necessarily have difficulties to nucleate in the absence of seeds, as was suggested in Chapter 2. The calculations show that the end-member fluor-zoisite is unstable with respect to grossular, kyanite, quartz and fluorite at any pressure and temperature, and can only be stabilised in small concentrations (about < 5 mol%). This is consistent with the low F-contents of natural zoisites.

Part I   The stability of titanite in fluorine-rich assemblages

6.2 Introduction

In the previous chapter, the Al-content of titanite was investigated experimentally in a simple, fluid-absent assemblage, which was chemically well constrained, and thus permitted the extraction of thermodynamic data for the end-member $CaAlFSiO_4$. These data are now used to calculate phase equilibria as a function of the Al-content of titanite in more complex chemical systems. In order to model more realistic mineral assemblages, most importantly, one has to allow for the presence of a fluid phase. Four types of reactions with Al-rich titanite will be dealt with here. These are (non-stoichiometric, and with unspecified additional product and reactant phases):

Fluid-absent: 1. reactants + fluorite = products + $CaAlFSiO_4$

Fluid-present: 2. reactants + hydrous phase + fluorite = products + $CaAlFSiO_4$ + H_2O

3. reactants + carbonate + fluorite = products + $CaAlFSiO_4$ + CO_2

4. reactants + F_2 = products + $CaAlFSiO_4$ + O_2

Metamorphic fluids are generally dominated by the fluid species of the C-O-H system, especially H_2O, CO_2, and CH_4, compared to which the amounts of CO, H_2 and O_2 are negligible (Ohmoto and Kerrick, 1977). Because CH_4 is a dominant species only at very reducing conditions, thermodynamic modelling of metamorphic phase assemblages or mineral solubilities is frequently based on the assumption that the fluid is a binary mixture of H_2O and CO_2 ($P_{fluid} = P_{H2O} + P_{CO2}$) (Eugster and Baumgartner, 1987).

Since the equilibria discussed in the following involve fluorine-bearing as well as hydrous phases, the role of the fluid species HF and F_2 has to be evaluated. Munoz and Eugster (1969) calculated the composition of a C-O-H-F fluid, coexisting with various buffer assemblages at 2 kbar, over a range of temperatures and different oxygen fugacities. That study demonstrated that the amount of HF in the fluid is restricted to fugacities less than 10^2 bar, and the component F_2 to even lower fugacities of less than 10^{-23} bar. Thus the concentrations of HF and F_2 in a C-O-H-F fluid are similar to those of H_2 and O_2, respectively. Based on an experimental investigation of fluor-phlogopite exchange equilibria, Munoz and Eugster (1969) suggested "that a common range for igneous and metamorphic fluids would be 0.001 – 0.005 mol.% HF". These orders of magnitude for the amounts of HF and F_2 in metamorphic fluids were subsequently confirmed by several experimental studies of various phase assemblages, such as Droll and Seck (1984), Aksyuk and Zhukovskaya (1994), Munoz and Ludington (1974), Webster and Holloway (1990), and Haselton et al. (1988), and by the thermodynamic modelling of phase assemblages of metamorphic rocks, such as the studies by Bohlen and Essene (1978), Valley et al. (1982), and Rice (1980).

Given the low concentrations of HF and F_2, this study assumes the fluid to be a pure H_2O or CO_2 fluid, or a binary H_2O-CO_2 fluid mixture ($P_{fluid} = P_{H2O} + P_{CO2}$), for reactions of the above types 2 and 3. Ignoring HF and F_2 in such equilibria is common practice (e. g., Rice, 1980; Barton, 1982), and is justified because the small amounts of HF and F_2 would have a negligible effect on the calculation of the fugacity of the main fluid species H_2O and CO_2.

Although HF and F_2 can be safely ignored when calculating fugacities of major fluid components, these fluid species do affect the stability of assemblages with F-bearing phases (e.g., Bohlen and Essene, 1978), by analogy to the strong effect oxygen has on many phase equilibria despite its extreme dilution (fugacities between 10^{-5} to 10^{-50} bar; e.g., Frost, 1991). The effect of F_2 on the stability of AlF-bearing titanite is investigated with reactions of the above type 4.

Because the rare occurrence of titanite with $X_{Al} > 0.5$ in natural rocks is yet to be understood, the following investigation of phase equilibria (reaction types 1 to 3) in the system $CaO - CaF_2 - Al_2O_3 - SiO_2 \pm TiO_2 \pm H_2O \pm CO_2$ is focussed on the *maximum possible extent of solid-solution in binary titanite* $Ca(Ti,Al)(O,F)SiO_4$ in various assemblages. The stability of $CaAlFSiO_4$ was calculated for a hypothetical rock that should represent an ideal medium for the crystallisation of AlF-rich titanite, as it is composed of fluorite, kyanite, quartz, and at least one Ca-phase (anorthite, grossular, lawsonite, zoisite, margarite, calcite, depending on fluid species and metamorphic grade), besides titanite solid-solution. All phases considered in the following are shown in a quarternary phase diagram in Figure 6.1.

The investigation will proceed from fluid-absent equilibria to those involving a pure H_2O fluid, a CO_2 fluid, and a H_2O-CO_2 mixture. Then TiO_2 will be added, and finally the effect of F_2 evaluated.
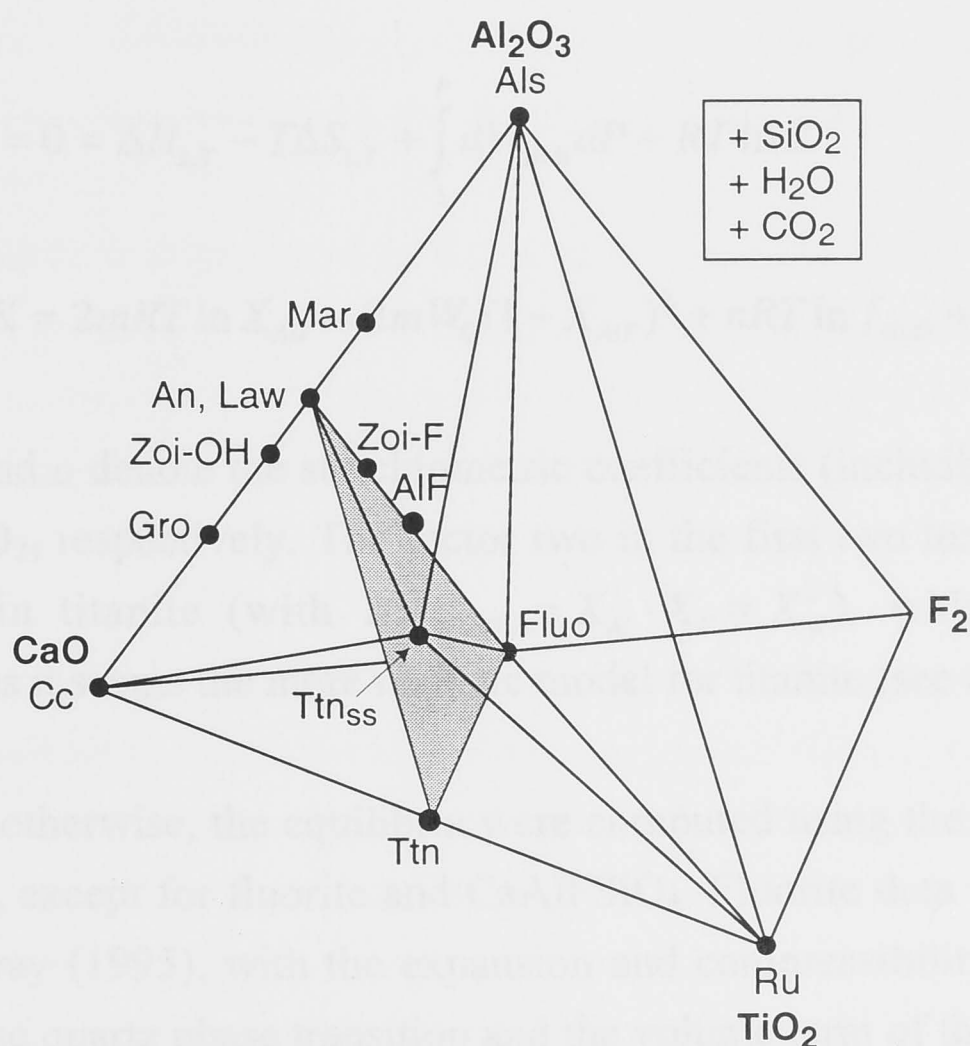
Figure 6.1 Tetrahedral phase diagram $CaO - Al_2O_3 - TiO_2 - F_2$, projected from SiO_2, H_2O, and CO_2, showing all phases considered in this section. The grey plane represents the ternary system of the experiments of this study. As an example, stability lines are shown for assemblages with anorthite – fluorite – titanite solid-solution plus one additional phase. Abbreviations in this and the following figures: AlF – $CaAlFSiO_4$, Als – aluminosilicate, An – anorthite, Cc – calcite, Fa – fayalite, Fluo – fluorite, Gro – grossular, Ky – kyanite, Law – lawsonite, M – magnetite, Mar – margarite, Q – quartz, Ru – rutile, Ttn – titanite, Ttn_{ss} – titanite solid-solution, V – vapour, Woll – wollastonite, Zoi – zoisite, Zoi-OH – hydroxy-zoisite, Zoi-F – fluor-zoisite, Zoi_{ss} – zoisite solid-solution.

Note that this first thermodynamic investigation of the maximum possible Al-content of titanite focuses on solid-solution along the binary join TiO-AlF, so that the values of X_{Al} throughout this chapter represent the amount of aluminium that is substituted with fluorine ($Ti^{4+} + O^{2-} = Al^{3+} + F^-$). It has to be born in mind that in the hydrous model assemblages considered below, titanite would also contain a certain amount of water (Hammer et al., 1996), so that the total Al-content would be the sum of aluminium coupled to fluorine, and that coupled to water. Ignoring the Al-OH end-member in this chapter is justified given that the most Al-rich natural titanites, which are to be modelled primarily, are dominated by the Al-F end-member, and only contain up to 10 mol.% $CaAlOHSiO_4$ (Figure 2.1, p. 8).

6.3   Calculation details

The equilibria and X_{Al} contours were calculated by free energy minimisation with the equation

$$\Delta G_{reac} = 0 = \Delta H_{1,T} - T\Delta S_{1,T} + \int_1^P dV_{solids} dP + RT \ln K \qquad (6.1)$$

with

$$RT \ln K = 2mRT \ln X_{AlF} + 2mW_G(1 - X_{AlF})^2 + nRT \ln f_{H_2O} + oRT \ln f_{CO_2} \qquad (6.2)$$

where m, n, and o denote the stoichiometric coefficients (including sign) of $CaAlFSiO_4$, water, and CO_2, respectively. The factor two in the first two terms accounts for multi-site mixing in titanite (with $a_{CaAlFSiO_4} = X_{Al} \cdot X_F = X_{Al}^2$), which is assumed in all calculations, as it seems the more realistic model for titanite (see Chapter 5).

Unless stated otherwise, the equilibria were computed using the data of Berman (1988) for all phases, except for fluorite and $CaAlFSiO_4$. Fluorite data were taken from Robie and Hemingway (1995), with the expansion and compressibility terms given in Table 5.1 (p. 92). The quartz phase transition and the volume term of the solids were treated as described in Berman (1988). The activity of grossular was calculated with the model of Berman (1990). To estimate the effect that different data bases might have on the results, some calculations were performed with the data by Robie and Hemingway (1995). In this case, expansion and compressibility terms, which are absent from their tables, were taken from Berman (1988).

To maintain internal consistency as much as possible, the thermodynamic data for $CaAlFSiO_4$ were derived specifically for each data base (Table 5.5, p. 108). The heat

capacity equation of Haas and Fisher (1976) with four terms was used for $CaAlFSiO_4$ (Table 4.3, p. 65). The Margules parameter W_G for titanite was assumed to be independent of temperature ($W_S = 0$), with $W_V = 107.041$ Jkbar^{-1}, and W_H as given in Table 5.5 (p. 108) for each data base.

Fugacities of CO_2 (at all pressures) and H_2O (above 10 kbar) were calculated as in Berman (1988), using the Modified Redlich-Kwong equation proposed by Kerrick and Jacobs (1981), and the empirical equation from Delany and Helgeson (1978), respectively. The equation of state of water proposed by Haar et al. (1984), which Berman (1988) uses for pressures below 10 kbar, was avoided in this study, because the computational complications and the risk of making undetected mistakes when working with a polynomial of more than 40 terms, did not seem justified. Instead, water fugacities below 10 kbar were computed with the Modified Redlich-Kwong equation of Kerrick and Jacobs (1981). It will be demonstrated below that the uncertainties in the calculations are dominated by other factors, compared to which the differences arising from the choice of different equations of state for water are small. Fugacities in H_2O-CO_2 mixtures were computed with the equations of Kerrick and Jacobs (1981).

The fluid pressure was assumed to equal total pressure. Of course, this is a rigorous simplification compared to natural metamorphic conditions, where the fluid pressure can be less than the total pressure, especially at high metamorphic grades. However, any forward modelling should start in a simple system, in order to understand the basic phase relationships, and more details can be added at a later stage.

The substitution of F$^-$ for OH$^-$ in hydrous minerals was not considered in the calculations, and all phases were assumed to represent the respective OH-end-member. Although zoisite in the experiments of this study contained considerable amounts of fluorine, the assumption that it is F-free in this model system is justified, given that natural zoisite does not seem to incorporate much fluorine even in very fluorine-rich rocks. Equilibria with fluor-zoisite are investigated in Part II of this chapter.

6.4 Fluid-absent equilibria: The system $CaO - CaF_2 - Al_2O_3 - SiO_2$

As a starting point, phase relations in the fluid-absent system are investigated. Figure 6.2 shows the variation of the Al-content of titanite in the system $CaO - CaF_2 - Al_2O_3 - SiO_2$, which is well constrained for the anorthite assemblage by the experiments of this study.
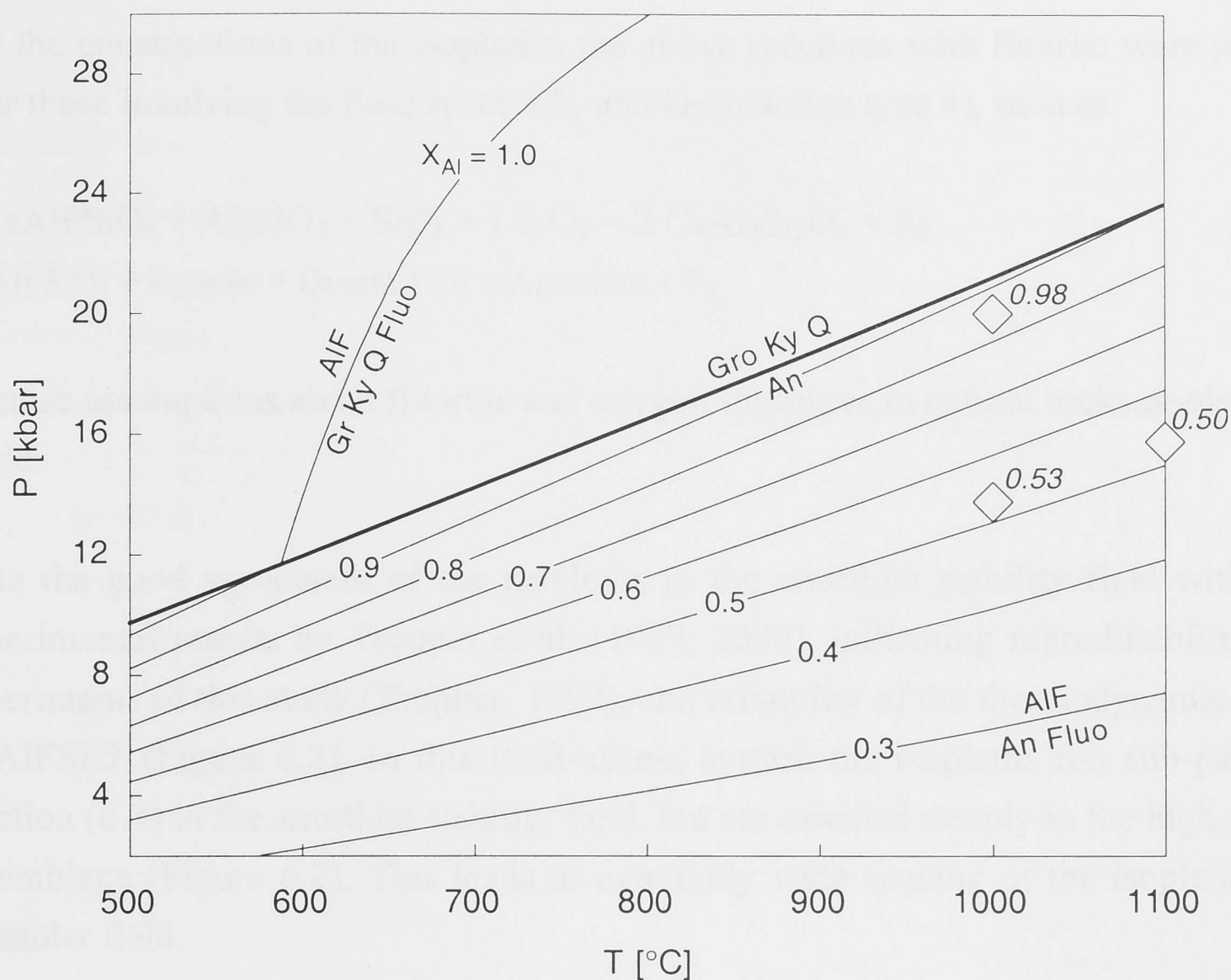
Figure 6.2 Al-content of titanite [Ca(Ti,Al)(O,F)SiO$_4$], coexisting with fluorite and either anorthite, or grossular, kyanite and quartz, in the fluid-absent pseudo-system CaO-CaF$_2$-Al$_2$O$_3$-SiO$_2$. Numbers on isopleths refer to X$_{Al}$ in titanite. All phases except titanite are of pure end-member composition. Diamonds show experimental conditions at which Tropper et al. (1999, 2000) equilibrated titanite with anorthite and fluorite, with or without rutile. The titanite composition (X$_{Al}$) they report is shown in italics next to the symbol. Abbreviations as in Fig. 6.1.

The stability fields of grossular and anorthite are given by

$$Ca_3Al_2Si_3O_{12} + 2 \ Al_2SiO_5 + SiO_2 = 3 \ CaAl_2Si_2O_8 \qquad (6.3)$$

Grossular + Kyanite + Quartz = Anorthite
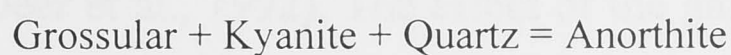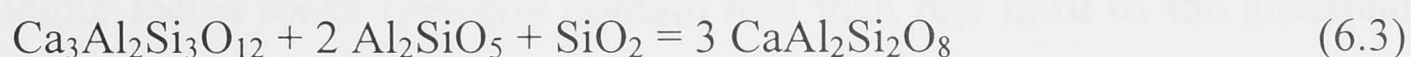
The X$_{Al}$-isopleths of titanite solid-solution, coexisting with fluorite and either anorthite, or grossular, kyanite and quartz, were determined with equations 6.1 and 6.2, for the equilibria

$$2 \ CaAlFSiO_4 = CaAl_2Si_2O_8 + CaF_2 \qquad (6.4)$$

CaAlFSiO$_4$ = Anorthite + Fluorite

and

$$6 \ CaAlFSiO_4 = Ca_3Al_2Si_3O_{12} + 2 \ Al_2SiO_5 + SiO_2 + 3 \ CaF_2 \qquad (6.5)$$

CaAlFSiO$_4$ = Grossular + Kyanite + Quartz + Fluorite

For the constructions of the isopleths, the above reactions with fluorite were preferred over those involving the fluid species F_2 and O_2 (reaction type 4), such as

$$2\ CaAlFSiO_4 + Al_2SiO_5 + SiO_2 + 1/2\ O_2 = 2\ CaAl_2Si_2O_8 + F_2 \qquad (6.6)$$

$CaAlFSiO_4$ + Kyanite + Quartz + O_2 = Anorthite + F_2
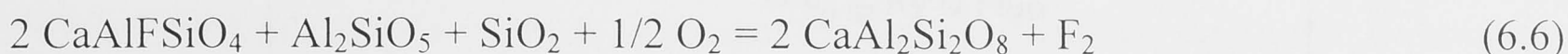
because assumptions about fluorine and oxygen fugacities in natural rocks needed not be made.

Note the good agreement of the isopleths in the anorthite stability field with recent experimental results by Tropper et al. (1999, 2000), indicating reproducibility of the experiments of this study (Tropper, 1999), and reliability of the thermodynamic data for $CaAlFSiO_4$ (Figure 6.2). In this fluid-absent system the isopleths run sub-parallel to reaction (6.3) in the anorthite stability field, but are oriented steeply in the high-pressure assemblage (Figure 6.2). This leads to extremely wide spacing of the isopleths in the grossular field.

Figure 6.2 predicts that titanite with $X_{Al} > 0.9$, including the $CaAlFSiO_4$ end-member, should be stable at eclogite facies conditions. The reason why $CaAlFSiO_4$ has not been reported from natural rocks might be that the complete absence of any fluid is an unrealistic assumption, and that anorthite and grossular usually exist in solid-solution. Both the dilution of anorthite by albite, and that of grossular by other garnet components, would lower the Al-content of titanite at a given pressure and temperature.

Garnets of eclogite facies rocks typically contain less than one third of the grossular component (Deer et al., 1992). The effect of the garnet composition on Al in titanite is shown in Figure 6.3, which was constructed using the garnet composition (32 mol.% grossular) from titanite-bearing eclogites of the Tauern Window (Franz and Spear, 1985). Figure 6.3 demonstrates that the dilution of the grossular component to values representative of natural rocks restricts the Al-content in titanite to less than about $X_{Al} = 0.7$ for typical pressures of crustal metamorphism. Large parts of the stability field of titanite with $X_{Al} > 0.7$ lie beyond the geotherm of 5°C/km, which is generally regarded to approximate the limit of pressure and temperature conditions realised on Earth (Schreyer, 1988). According to Figure 6.3, the pure $CaAlFSiO_4$ end-member would be stable only above 55 kbar, well within the 'forbidden zone', which is in agreement with its absence from natural assemblages.
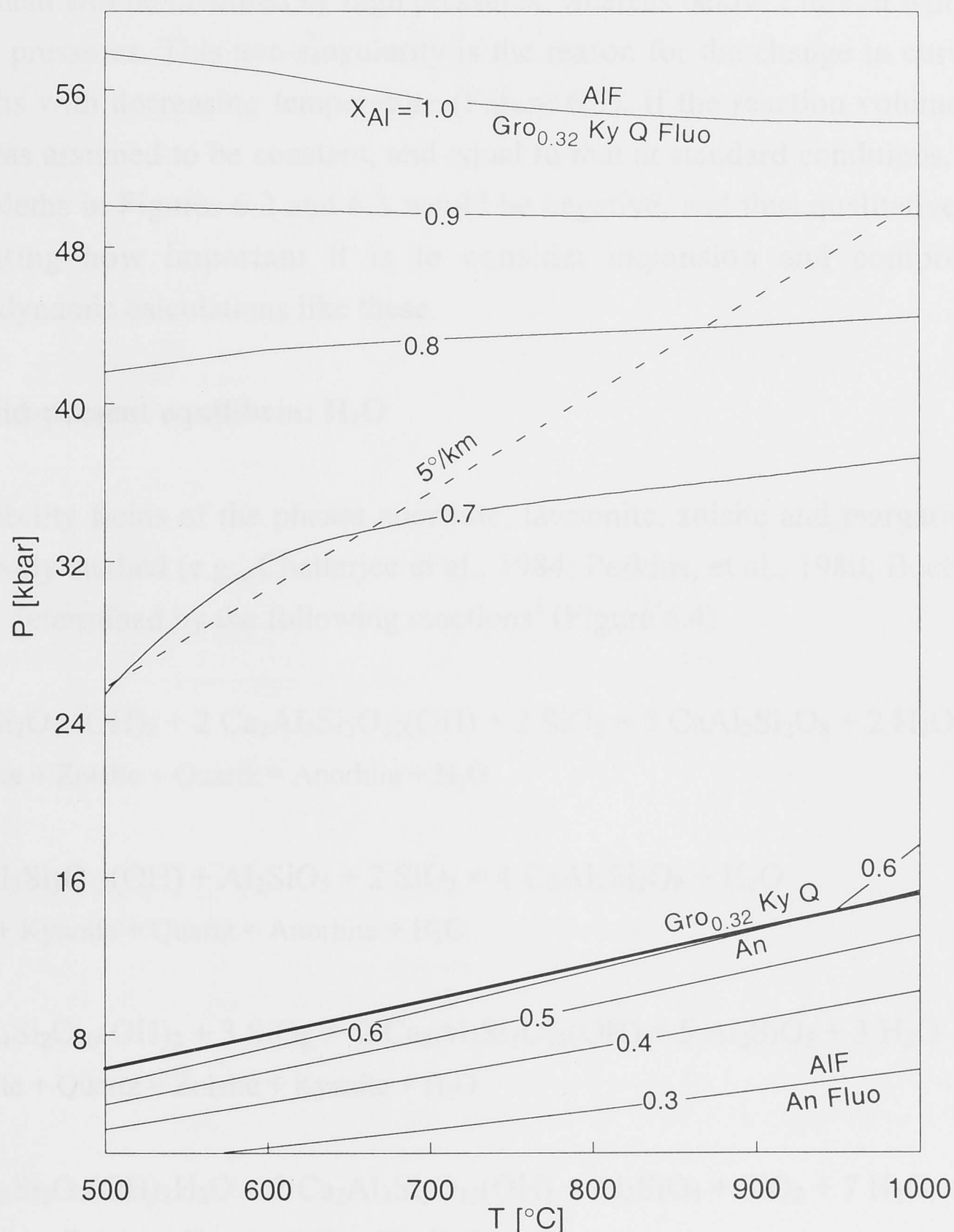
Figure 6.3 Al-content of titanite as in Figure 6.2, but with garnet composed of 32 mol% grossular, 57 mol% almandine, and 6 mol% pyrope (Tauern Window eclogite sample; Franz and Spear, 1985). Garnet activities were calculated with the mixing model of Berman (1990). Dashed line shows the 5°/km geotherm, which approximates the limit of pressure and temperature conditions realised on Earth (Schreyer, 1988). Abbreviations as given in Figure 6.1.

The wide spacing of the isopleths with respect to pressure in the garnet stability field is due to the small reaction volume of reaction (6.5). In fact, with a value of only 0.105 $Jbar^{-1}K^{-1}$ at standard conditions, the reaction volume is so small that the different thermal expansions of the product and reactant phases change the reaction volume from positive to negative at about 250°C. This is primarily due to the large thermal expansion of fluorite compared to all other phases. The sign change of the reaction volume leads to a non-singularity of the isotherms, because above this temperature the $CaAlFSiO_4$

component will be favoured by high pressures, whereas below 250°C it will be favoured by low pressures. This non-singularity is the reason for the change in curvature of the isopleths with decreasing temperature (Figure 6.3). If the reaction volume of reaction (6.5) was assumed to be constant, and equal to that at standard conditions, the slope of all isopleths in Figures 6.2 and 6.3 would be negative, and thus qualitatively incorrect, illustrating how important it is to consider expansion and compressibility in thermodynamic calculations like these.

6.5 Fluid-present equilibria: H_2O

The stability fields of the phases anorthite, lawsonite, zoisite and margarite have been extensively studied (e.g., Chatterjee et al., 1984; Perkins, et al., 1980; Boettcher, 1970), and are determined by the following reactions[1] (Figure 6.4)

$$CaAl_4Si_2O_{10}(OH)_2 + 2\ Ca_2Al_3Si_3O_{12}(OH) + 2\ SiO_2 = 5\ CaAl_2Si_2O_8 + 2\ H_2O \qquad (6.7)$$
Margarite + Zoisite + Quartz = Anorhite + H_2O

$$2\ Ca_2Al_3Si_3O_{12}(OH) + Al_2SiO_5 + 2\ SiO_2 = 4\ CaAl_2Si_2O_8 + H_2O \qquad (6.8)$$
Zoisite + Kyanite + Quartz = Anorhite + H_2O

$$4\ CaAl_4Si_2O_{10}(OH)_2 + 3\ SiO_2 = 2\ Ca_2Al_3Si_3O_{12}(OH) + 5\ Al_2SiO_5 + 3\ H_2O \qquad (6.9)$$
Margarite + Quartz = Zoisite + Kyanite + H_2O

$$4\ CaAl_2Si_2O_7(OH)_2H_2O = 2\ Ca_2Al_3Si_3O_{12}(OH) + Al_2SiO_5 + SiO_2 + 7\ H_2O \qquad (6.10)$$
Lawsonite = Zoisite + Kyanite + Quartz + H_2O

$$5\ CaAl_2Si_2O_7(OH)_2H_2O =$$
$$CaAl_4Si_2O_{10}(OH)_2 + 2\ CaAl_4Si_2O_{10}(OH)_2 + 2\ SiO_2 + 8\ H_2O \quad (6.11)$$
Lawsonite = Margarite + Zoisite + Quartz + H_2O

---

[1] Several other reactions describing the breakdown of margarite with increasing pressure lie near reaction (6.9) and run subparallel to it (Chatterjee et al., 1984). These reactions are omitted in this discussion and the diagrams, for the sake of clarity and simplicity. For a similar reason, the breakdown of margarite and quartz to anorthite, kyanite and vapour with increasing temperature (Chatterjee et al., 1984) was omitted. As all of these reactions produce relatively small divariant fields, in which the gradients of the X_{Al}-isopleths change only slightly, their effect on the Al-content in titanite, is negligible.
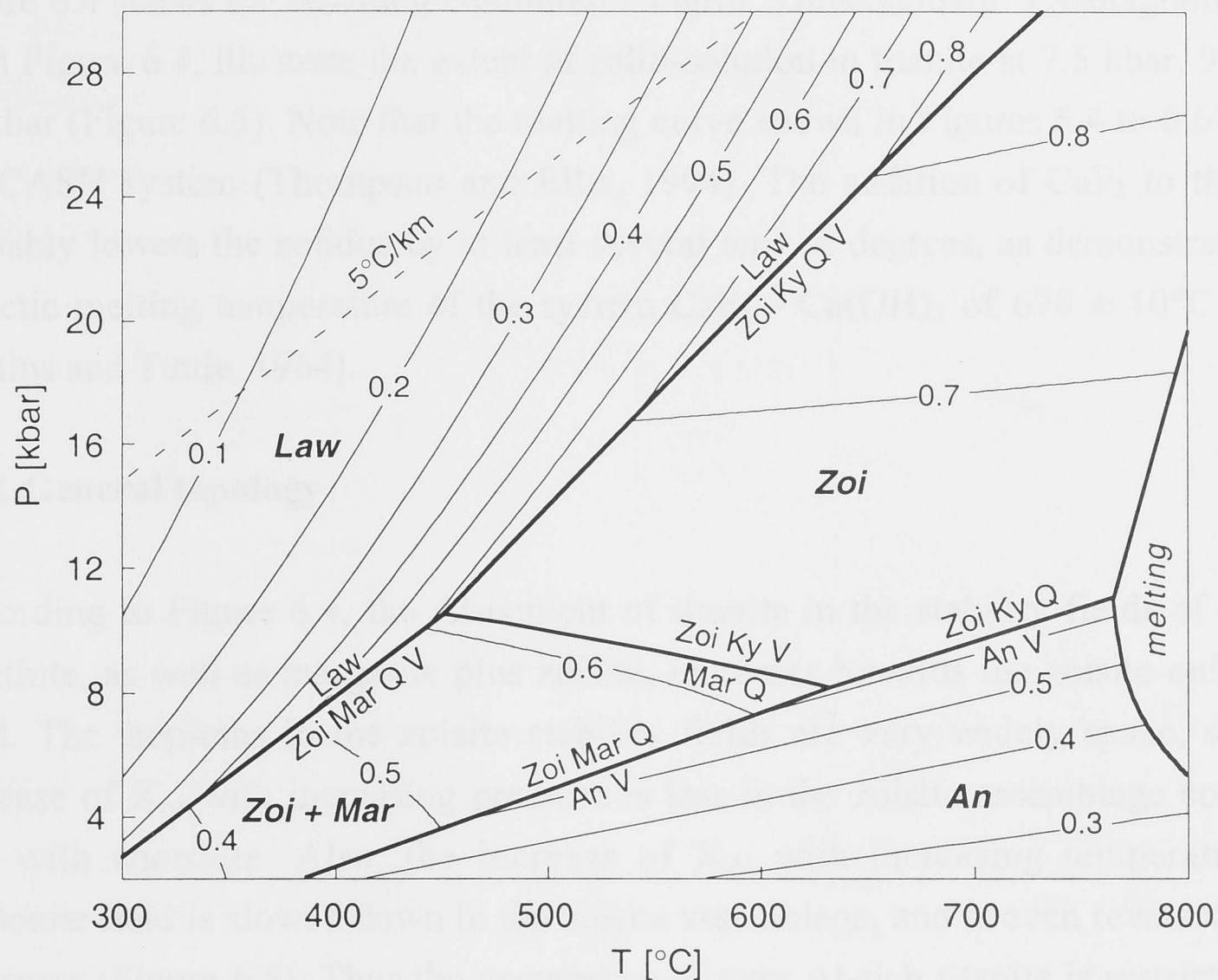
Figure 6.4 Al-content of titanite [Ca(Ti,Al)(O,F)SiO$_4$] in the fluid-present pseudo-system CaO-CaF$_2$-Al$_2$O$_3$-SiO$_2$-H$_2$O (P$_{H2O}$ = P$_{total}$). Bold lines: fluorite-absent reactions (6.7) to (6.11), with the stability fields of the different Ca-Al phases labeled in bold. Thin lines: X$_{Al}$-isopleths based on reactions (6.4), (6.12), (6.13), and (6.14) in the stability fields **An**, **Zoi + Mar**, **Law**, and **Zoi**, respectively. Numbers on isopleths refer to X$_{Al}$ in titanite. Dashed line is 5°C/km geotherm (Schreyer, 1988). All phases except titanite are of pure end-member composition (Zoi is hydroxy-zoisite). The solidus refers to the pure CASH system (Thompson and Ellis, 1994), and can be expected to plot at slightly lower temperatures in the presence of fluorite (see text). Abbreviations as given in Figure 6.1.

The concentration of the AlF-component in titanite at various pressures and temperatures was calculated using reaction (6.4), as well as the following equilibria, which describe the breakdown of CaAlFSiO$_4$ to fluorite and the Ca-Al phase stable at the respective metamorphic conditions:

10 CaAlFSiO$_4$ + 2 H$_2$O = CaAl$_4$Si$_2$O$_{10}$(OH)$_2$ + 5 CaF$_2$ + 2 Ca$_2$Al$_3$Si$_3$O$_{12}$(OH) + 2 SiO$_2$

CaAlFSiO$_4$ + H$_2$O = Margarite + Fluorite + Zoisite + Quartz   (6.12)

2 CaAlFSiO$_4$ + 2 H$_2$O = CaAl$_2$Si$_2$O$_7$(OH)$_2$H$_2$O + CaF$_2$ (6.13)

CaAlFSiO$_4$ + H$_2$O = Lawsonite + Fluorite

8 CaAlFSiO$_4$ + H$_2$O = 2 Ca$_2$Al$_3$Si$_3$O$_{12}$(OH) + 4 CaF$_2$ + Al$_2$SiO$_5$ + SiO$_2$ (6.14)

CaAlFSiO$_4$ + H$_2$O = Zoisite + Fluorite + Kyanite + Quartz
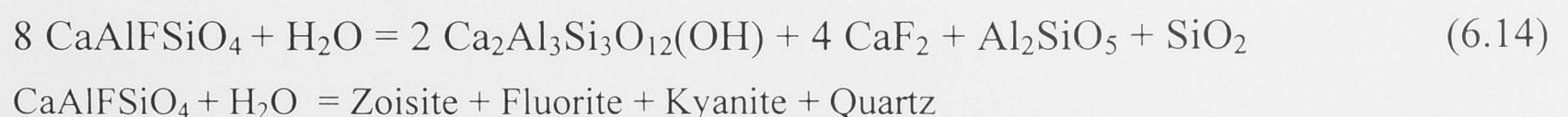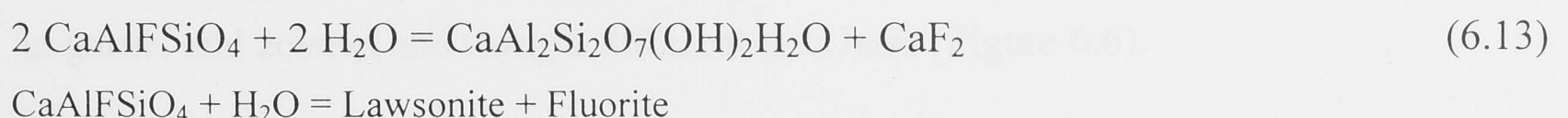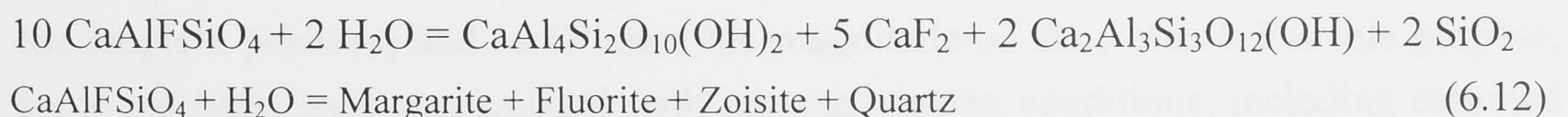
Figure 6.4 shows the resulting contoured PT-grid. Three isobaric TX-diagrams, derived from Figure 6.4, illustrate the extent of solid-solution in titanite at 7.5 kbar, 9 kbar, and 24 kbar (Figure 6.5). Note that the melting curve shown in Figures 6.4 to 6.6 is that for the CASH system (Thompson and Ellis, 1994). The addition of CaF_2 to this system probably lowers the solidus by at least several tens of degrees, as demonstrated by the eutectic melting temperature of the system CaF_2 - $Ca(OH)_2$ of $670 \pm 10°C$ at 1 kbar (Gittins and Tuttle, 1964).

6.5.1 General topology

According to Figure 6.4, the Al-content of titanite in the stability fields of lawsonite, anorthite, as well as margarite plus zoisite, increases towards the zoisite-only stability field. The isopleths in the zoisite stability fields are very widely space, so that the increase of X_{Al} with increasing pressure is less in the zoisite assemblage compared to that with anorthite. Also, the increase of X_{Al} with increasing temperature in the lawsonite field is slowed down in the zoisite assemblage, and is even reversed at higher pressures (Figure 6.5). Thus the occurrence of very Al-rich titanite is restricted to high metamorphic grades. For example, titanite with $X_{Al} > 0.6$ predominantly occurs at eclogite facies conditions, and Al-contents of $X_{Al} > 0.8$ are restricted to a small wedge-shaped PT-window at very high grade, which might even be limited by melting reactions at higher pressures before the stability of the $CaAlFSiO_4$ end-member is reached. Note that melting in the fluorite-bearing system probably sets in at even lower temperatures than indicated by the solidus of the CASH system (Thompson and Ellis, 1994) (Figures 6.4 to 6.6), as discussed above.

Due to the topology of the PT-grid at high pressures near the melting region, the maximum possible X_{Al} in the water-saturated system is predominantly controlled by the position of the isopleths in the zoisite stability field. The location of these widely spaced isopleths in PT-space, however, is extremely sensitive to variations in the thermodynamic data used. Therefore it is crucial to understand which factors may affect the isopleth position, and to estimate the magnitude of their effect. For this purpose, some isopleths were recalculated with varying starting conditions, including assumed errors in the thermodynamic data, variations in the titanite mixing model, solid-solution in garnet and zoisite, and using a different data base (Figure 6.6).
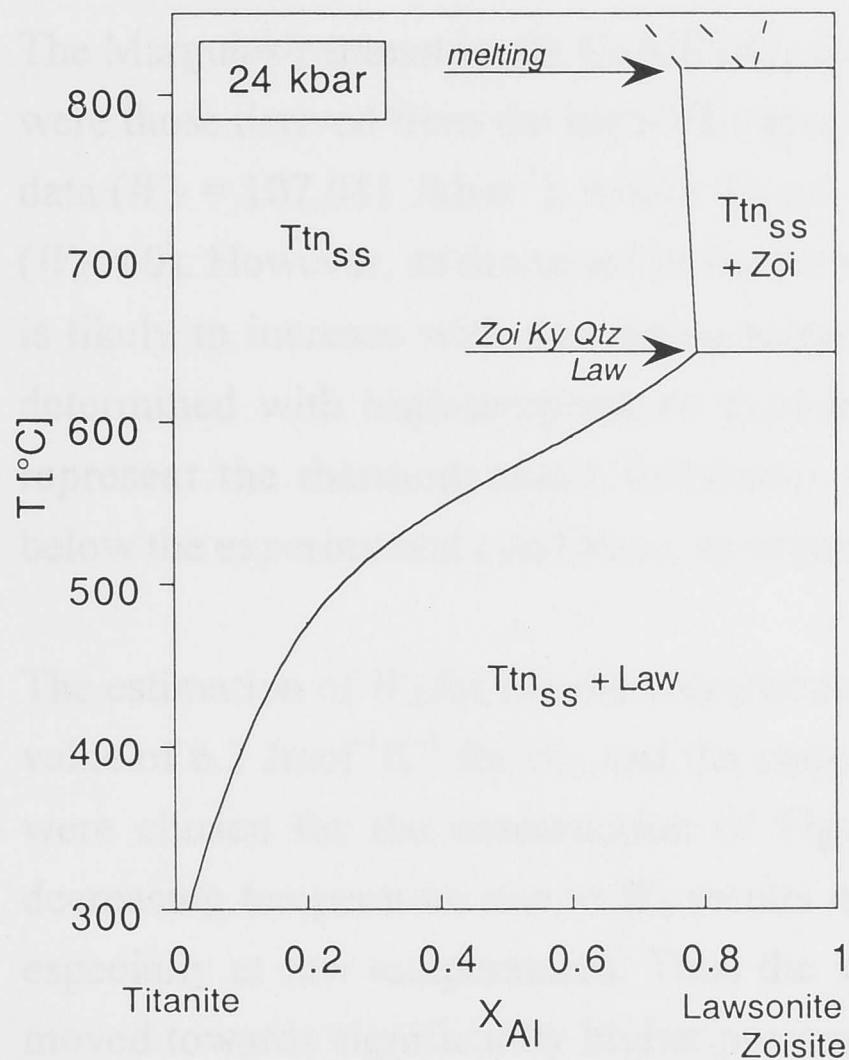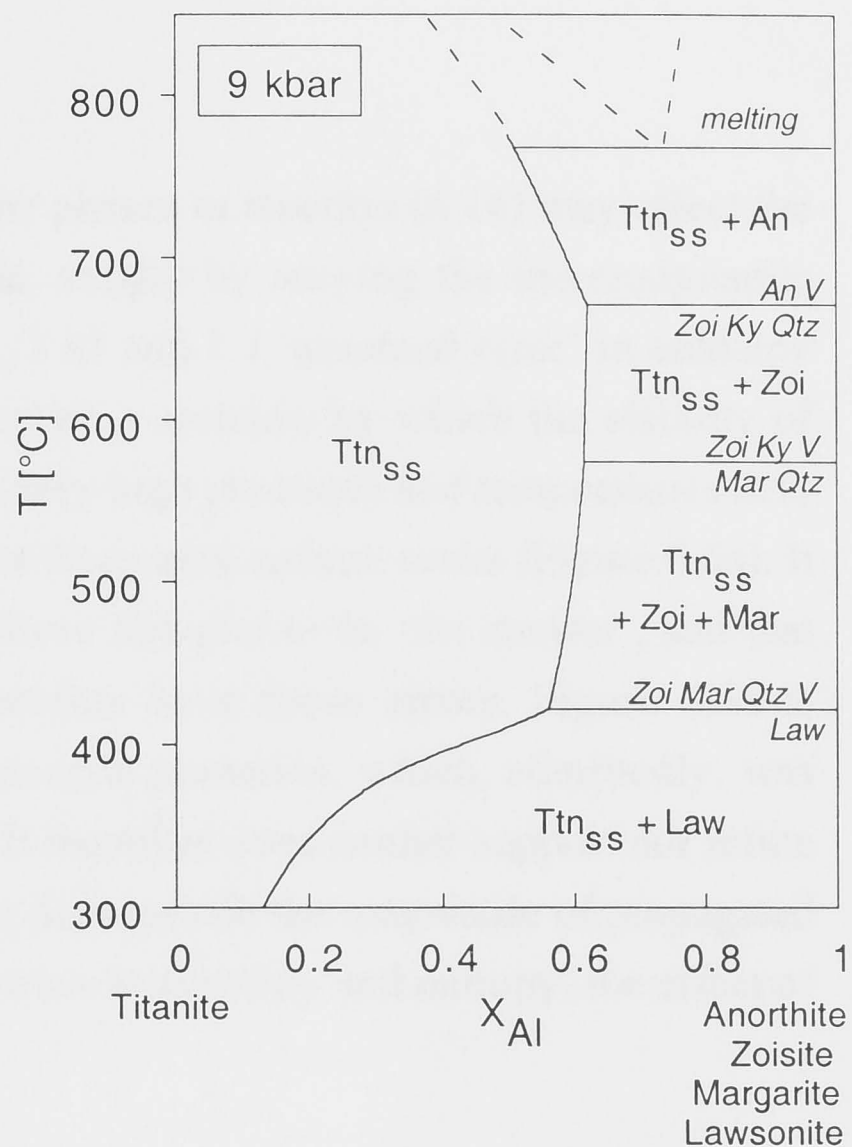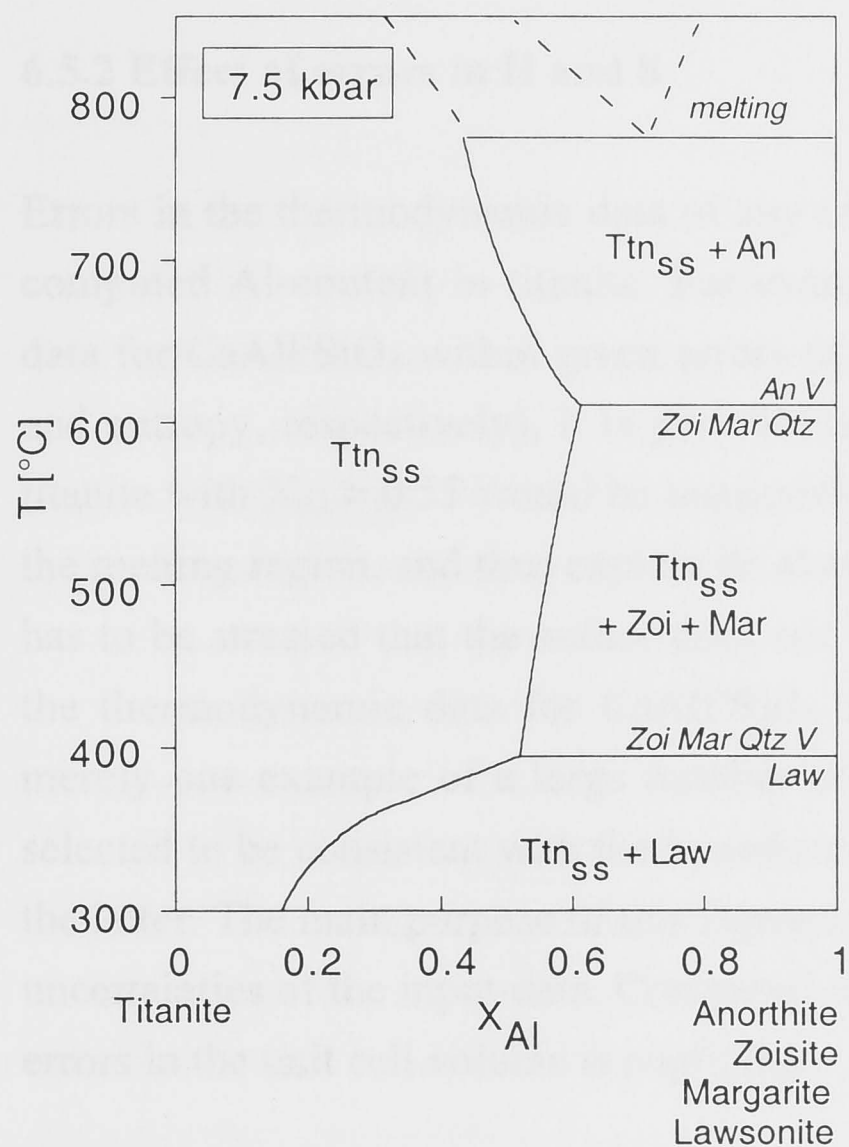
Figure 6.5 Isobaric T-X_{Al} plots (P_{H2O} = P_{total}) of the pseudo-binary system TiO_2 – $AlO_{1.5}$, (based on Figure 6.4), illustrating the limited extent of solid solution of titanite in various assemblages. Phase compositions in the melting region are semi-quantitative estimates. Abbreviations as given in Figure 6.1. Zoi is hydroxy-zoisite.

6.5.2 Effect of errors in H and S

Errors in the thermodynamic data of any of the phases in reaction (6.14) may effect the computed Al-content in titanite. For example, simply by varying the thermodynamic data for $CaAlFSiO_4$ within given errors (e.g., 2 kJ and 1 J 'assumed error' in enthalpy and entropy, respectively), it is possible to create a scenario by which the stability of titanite with $X_{Al} > 0.55$ would be restricted to very high pressures and temperatures near the melting region, and thus explain its absence from most natural rocks (Figure 6.6a). It has to be stressed that the author does not believe this plot to be 'the answer', and that the thermodynamic data for $CaAlFSiO_4$ therefore have these errors. Figure 6.6a is merely one example of a large number of possible scenarios, which, admittedly, was selected to be consistent with the hypothesis. It therefore does neither support nor refute the latter. The main purpose of this figure is to demonstrate the magnitude of propagated uncertainties of the input-data. Compared to errors in enthalpy and entropy, the effect of errors in the unit cell volume is negligible.

6.5.3 Effect of W_S

The Margules parameters for $CaAlFSiO_4$ used for the construction of Figures 6.4 and 6.5 were those derived from the high-PT experiments (Table 5.5, p. 108), and X-ray volume data ($W_V = 107.041$ Jkbar^{-1}), which do not account for changes of W_G with temperature ($W_S = 0$). However, as discussed in the previous chapter, non-ideality in a solid-solution is likely to increase with decreasing temperature. Therefore, the Margules parameters determined with high-temperature experiments between 800 and 1000°C might not represent the thermodynamic behaviour of titanite adequately at temperatures well below the experimental conditions, as required for the PT-grid in Figure 6.4.

The estimation of W_S for titanite was discussed in the previous chapter. The intermediate value of 6.3 Jmol^{-1}K^{-1} for W_S, and the respective W_H of 14724 Jmol^{-1} (Table 5.7, p. 121) were chosen for the construction of Figure 6.6b. The increasing non-ideality with decreasing temperature due to W_S results in lower Al-contents compared to Figure 6.4, especially at low temperatures. Thus the stability field of titanite with $X_{Al} > 0.55$ has moved towards significantly higher pressures and temperatures, but the topology of the PT-grid at high temperatures remains comparable to Figure 6.4.

6.5.4 Effect of garnet composition

The applicability of Figure 6.4 to natural rocks can be significantly improved by allowing for solid-solution in the Ca-Al phases. The assumption of end-member composition of all phases except titanite is the reason why the breakdown of zoisite and lawsonite to grossular with reactions

$$6\ Ca_2Al_3Si_3O_{12}(OH) = 4\ Ca_3Al_2Si_3O_{12} + 5\ Al_2SiO_5 + SiO_2 + H_2O \tag{6.15}$$

Zoisite = Grossular + Kyanite + Quartz + H_2O

$$4\ CaAl_2Si_2O_7(OH)_2H_2O = Ca_3Al_2Si_3O_{12} + 2\ Al_2SiO_5 + SiO_2 + 6\ H_2O \tag{6.16}$$

Lawsonite = Grossular + Kyanite + Quartz + H_2O

is located at very high pressures and temperatures, beyond the PT-range of Figure 6.4. This is unrealistic, as the grossular component in garnet in eclogites typically amounts to only about 30% (Deer et al, 1992), thus expanding the grossular stability field to lower metamorphic conditions compared to the pure end-member. Again, the rocks of the Tauern Window (Franz and Spear, 1985) were used as a representative example for an eclogite facies rock with titanite. The activity of the phases were calculated according to the study by Manning and Bohlen (1991), who determined the activity of zoisite of these rocks to be $a_{Zoi} = 0.833$, and calculated the grossular activity with the mixing model of Berman (1990).

Figure 6.6c shows that the dilution of grossular expands the garnet stability down to about 13 kbar, thus limiting the stability of zoisite. The titanite Al-isopleths in the zoisite stability field move to slightly higher pressures due to the dilution of zoisite. More importantly, the zoisite stability field is cut off by grossular before the Al-contents of $X_{Al} = 0.7$ are reached (compare Figure 6.4). Since the isopleths in the grossular stability field are even more widely spaced compared to those in the zoisite field (isopleth for $X_{Al} = 0.7$ lies outside PT-range show here), the stability of titanite with $X_{Al} > 0.7$ is restricted to significantly higher pressures and temperatures compared to the pure end-member calculations (Figure 6.4).

The topology of Figure 6.6c is in good general agreement with the natural occurrence of aluminous titanite. For example, Figure 6.6c suggests that titanite with Al-contents up to about $X_{Al} = 0.6$ can be stabilised at pressures and temperatures covering many metamorphic facies, but that the *most likely* occurrence of Al-rich titanite is at the high pressures and temperatures of the eclogite facies. This is reflected by the numerous

reports of Al-rich titanite from eclogite terrains (e.g., Smith, 1980; Franz and Spear, 1985, Sobolev and Shatsky, 1990; Krogh et al., 1990; Hirajima et al., 1992; Carswell et al., 1996; Ye and Hirajima, 1996), and the less abundant, yet important finds of Al-rich titanite in rocks formed at lower pressure and/or temperature (e.g., zeolite facies: Boles and Coombs, 1977; greenschist facies: Franz (1987), Enami et al. (1993); amphibolite facies: Markl and Paizolo, 1999) (compare Figure 5.22 for PT-conditions of some of these rocks, p. 124). At temperatures below 450°C, titanite does not incorporate more than $X_{Al} = 0.55$ at any pressure. Especially the blueschist facies, according to Figure 6.6c, is dominated by lower Al-contents. This is in good agreement with natural titanites from such high-pressure, low-temperature terrains, which typically contain less than $X_{Al} = 0.20$ (e.g., Itaya et al., 1985; Makanjuola and Howie, 1972).

Remember that titanite in the assemblages investigated here approaches the *maximum possible* Al-content of titanite, because the presence of fluorite buffers the fluorine fugacity to high values. Any assemblage containing the silicates described here, but lacking fluorite, must result in lower Al-contents of titanite compared to the values presented here.
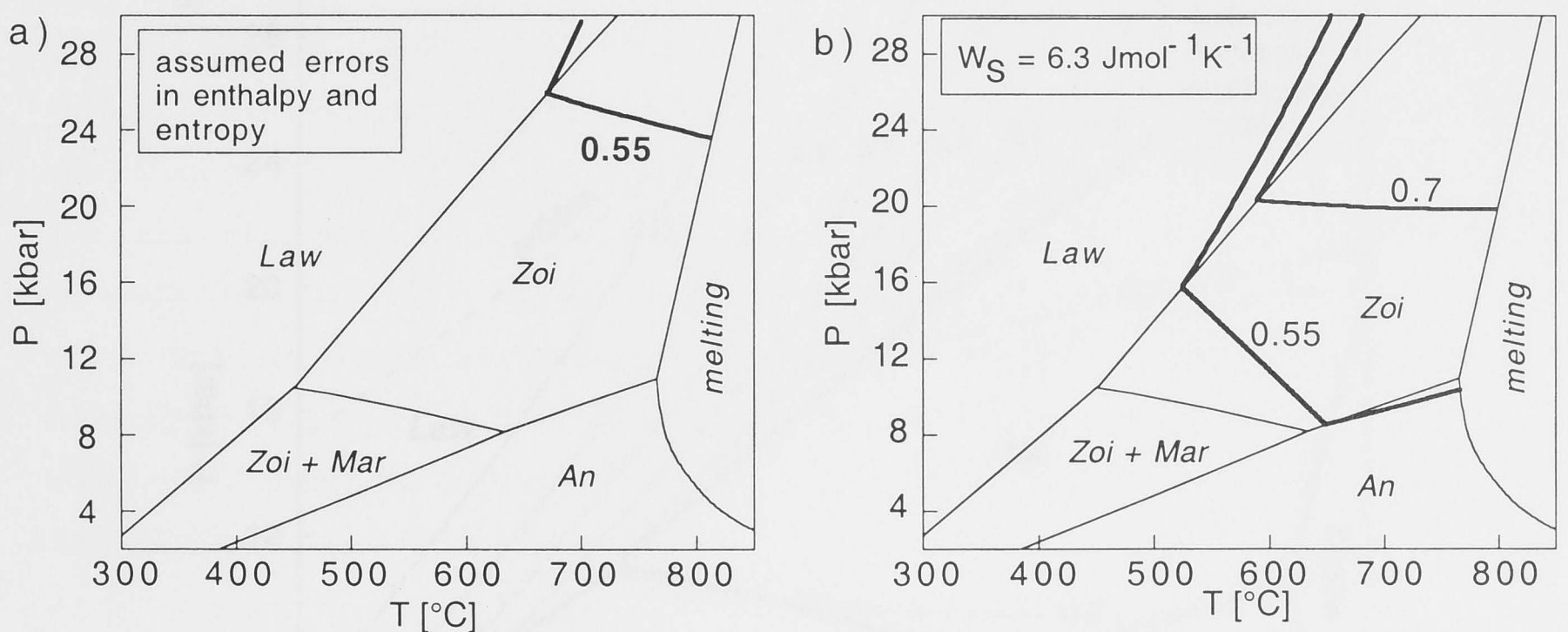
Figure 6.6 Different versions of the PT-grid shown in Figure 6.4, illustrating the effects of various factors on the isopleth position: **a)** Assumed errors in enthalpy of formation (+2 kJmol^{-1}) and standard state entropy (-1 Jmol^{-1}K^{-1}) of phase CaAlFSiO$_4$. **b)** Introduction of temperature dependence of the Margules parameter ($W_G = W_H - TW_S + PW_V$) to the model. **c)** Reduced grossular and zoisite activites due to solid solution (grossular as in Figure 6.3; activity of zoisite = 0.833, as determined for Tauern Window rocks by Manning and Bohlen, 1991). **d)** Using a different data base (Robie and Hemingway, 1995) and fugacity model for H$_2$O (Kerrick and Jacobs, 1981, at all pressures). Dashed line without label in d) represents isopleth $X_{Al} = 0.7$ calculated with the fugacity model for H$_2$O of Delany and Helgeson (1978). Reactions as in Figure 6.4, except indicated otherwise.
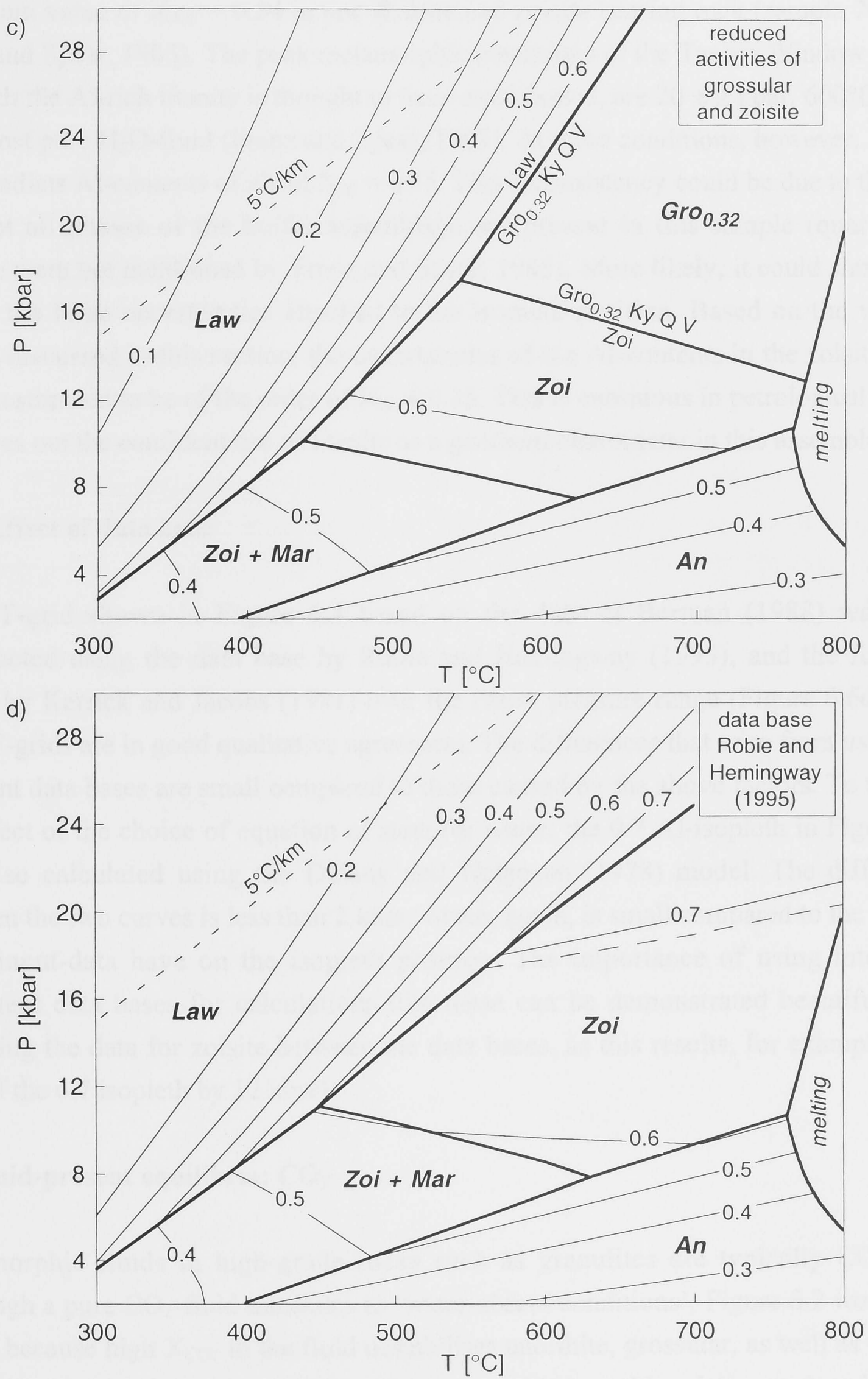
Figure 6.6 *continued*

The Al and F-contents of titanite in the Tauern Window rocks span a large range, with a maximum value of $X_{AlF} = 0.54$ in one fluorite and zoisite bearing rock (sample 79-102; Franz and Spear, 1985). The peak metamorphic conditions of the Tauern Window rocks, at which the Al-rich titanite is thought to have equilibrated, are 20 ± 2 kbar, 600°C, with an almost pure H_2O-fluid (Franz and Spear, 1983). At these conditions, however, Figure 6.6c predicts Al-contents of about $X_{Al} = 0.65$. This inconsistency could be due to the fact that not all phases of the buffer assemblage are present in this sample (quartz and kyanite were not mentioned by Franz and Spear, 1985). More likely, it could simply be due to the large uncertainties attached to the isopleth position. Based on the various factors discussed in this section, the uncertainties of the Al-contents in the zoisite field can be estimated to be of the order of $X_{Al} \pm 0.25$. This is enormous in petrological terms, and rules out the confident use of titanite as a geothermobarometer in this assemblage.

6.5.5 Effect of data base

The PT-grid shown in Figure 6.4 based on the data of Berman (1988) was also constructed using the data base by Robie and Hemingway (1995), and the fugacity model by Kerrick and Jacobs (1981) over the entire pressure range (Figure 6.6d). The two PT-grids are in good qualitative agreement. The differences that arise from using the different data bases are small compared to those caused by the above factors. To test for the effect of the choice of equation of state for water, the 0.7 Al-isopleth in Figure 6.4 was also calculated using the Delany and Helgeson (1978) model. The difference between the two curves is less than 2 kbar, which, again, is small compared to the effects other input-data have on the isopleth position. The importance of using internally consistent data bases for calculations like these can be demonstrated beautifully by swapping the data for zoisite between the data bases, as this results, for example, in a shift of the 0.7 isopleth by 12 kbar!

6.6 Fluid-present equilibria: CO_2

Metamorphic fluids in high-grade rocks such as granulites are typically CO_2-rich. Although a pure CO_2-fluid translates to 'water-absent conditions', Figure 6.2 would not apply, because high X_{CO2} in the fluid destabilises anorthite, grossular, as well as the Al-component in titanite with respect to phase assemblages with calcite, as described by reactions

$$CaCO_3 + Al_2SiO_5 + SiO_2 = CaAl_2Si_2O_8 + CO_2 \qquad (6.17)$$

Calcite + Kyanite + Quartz = Anorthite + CO_2

$$3\ CaCO_3 + Al_2SiO_5 + 2\ SiO_2 = CaAl_2Si_2O_8 + 3\ CO_2 \tag{6.18}$$

Calcite + Kyanite + Quartz = Grossular + CO_2

$$CaCO_3 + Al_2SiO_5 + SiO_2 + CaF_2 = 2\ CaAlFSiO_4 + CO_2 \tag{6.19}$$

Calcite + Kyanite + Quartz + Fluorite = $CaAlFSiO_4$ + CO_2

In contrast to the fluid-absent system (Figure 6.2), pure grossular does not exist in the presence of a CO_2 fluid, as it becomes unstable with respect to calcite, kyanite and quartz at low pressures well within the anorthite stability field. Thus, reaction (6.18) is metastable (Figure 6.7). In natural assemblages, however, garnet can be stabilised by dilution of the grossular component with other garnet end-members.

Figure 6.7 demonstrates that the presence of a pure CO_2 fluid with $P_{CO_2} = P_{total}$ restricts the Al-content of titanite, yet again, to less than about $X_{Al} = 0.75$, at crustal conditions. Although at higher pressure the isopleths of decarbonation reaction (6.19) swing back to lower temperatures, titanite with $X_{Al} > 0.7$ is only stabilised again at extremely high pressures (for example, 55 kbar at 750°C).
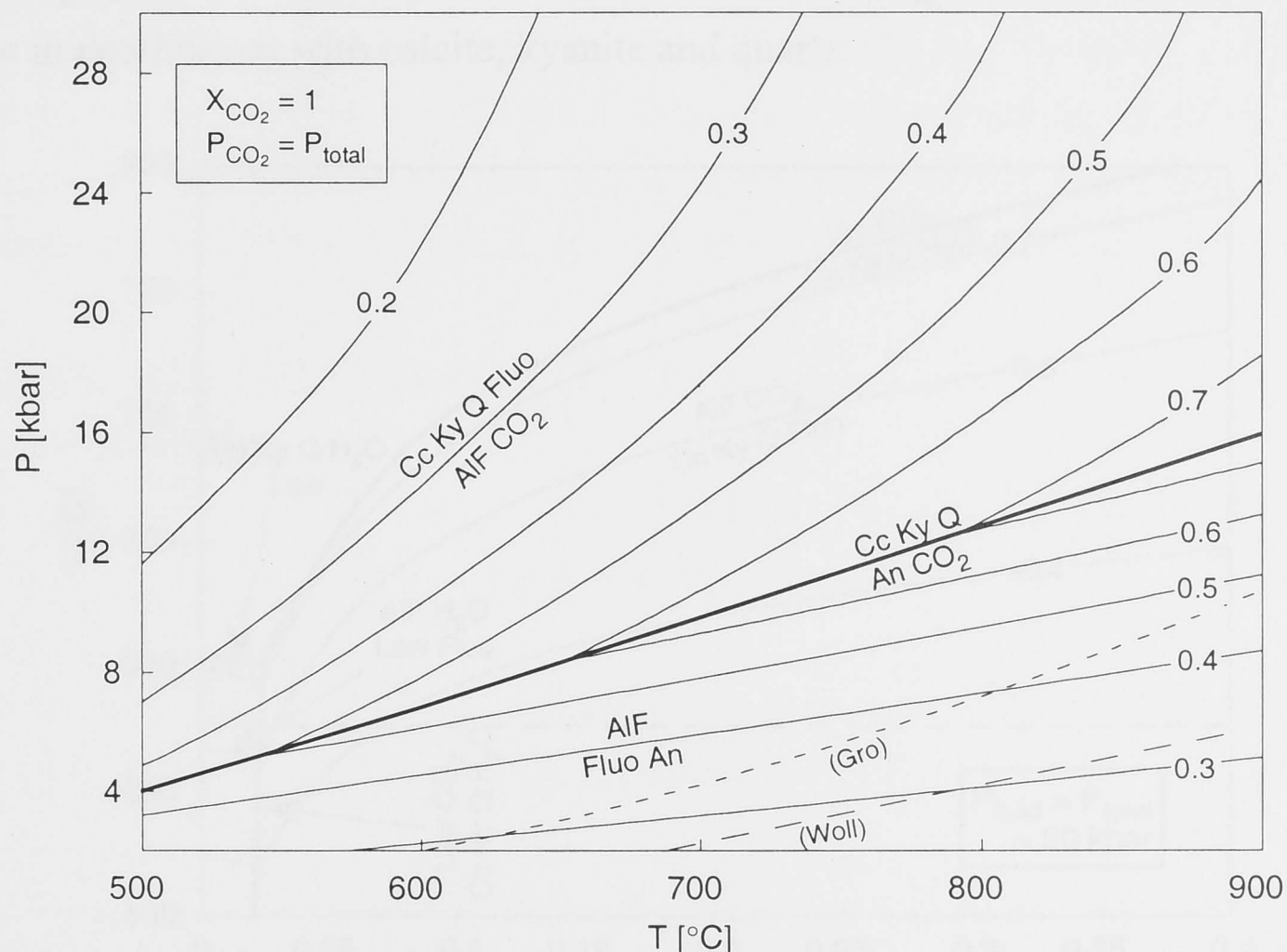
Figure 6.7 Al-content of titanite, coexisting with a pure CO_2-fluid in the pseudo system CaO-CaF_2-Al_2O_3-SiO_2-CO_2. Reaction (6.18) (Gro) is metastable. Also shown is reaction Calcite + Kyanite = Wollastonite + CO_2 (Woll). Melting can be expected in this system at or below 880 ± 10°C, which is the eutectic temperature in the binary system $CaF_2 - CaCO_3$ at 1 kbar (Gittins and Tuttle (1964). Abbreviations as in Figure 6.1.

6.7 Fluid-present equilibria: $CO_2 - H_2O$

Both the dilution of the pure H_2O-fluid with CO_2, and the pure CO_2-fluid with H_2O in the above systems (Figures 6.4 and 6.7), would result in an increase of the Al-content of titanite at a given pressure and temperature. Therefore, the effect of composition of a binary H_2O–CO_2 fluid on the above reactions has to be considered when investigating the maximum possible Al-content of titanite.

Figure 6.8 shows the changes in phase relationships with fluid composition at 20 kbar, thus representing the link between Figures 6.4 and 6.7. As expected, at a given temperature the Al-content of titanite increases with the dilution of a pure H_2O fluid with CO_2, and vice versa. The maximum X_{Al} at each temperature, which corresponds to the minimum of the isopleths in Figure 6.8, lies at extremely low CO_2 contents (X_{CO2} = 0.02) at reaction

$$CaCO_3 + Al_2SiO_5 + SiO_2 + 2\ H_2O = CaAl_2Si_2O_7(OH)_2H_2O + CO_2 \qquad (6.20)$$
Calcite + Kyanite + Quartz + H_2O = Lawsonite + CO_2

which separates the stability fields of titanite coexisting with lawsonite, from that of titanite in equilibrium with calcite, kyanite and quartz.
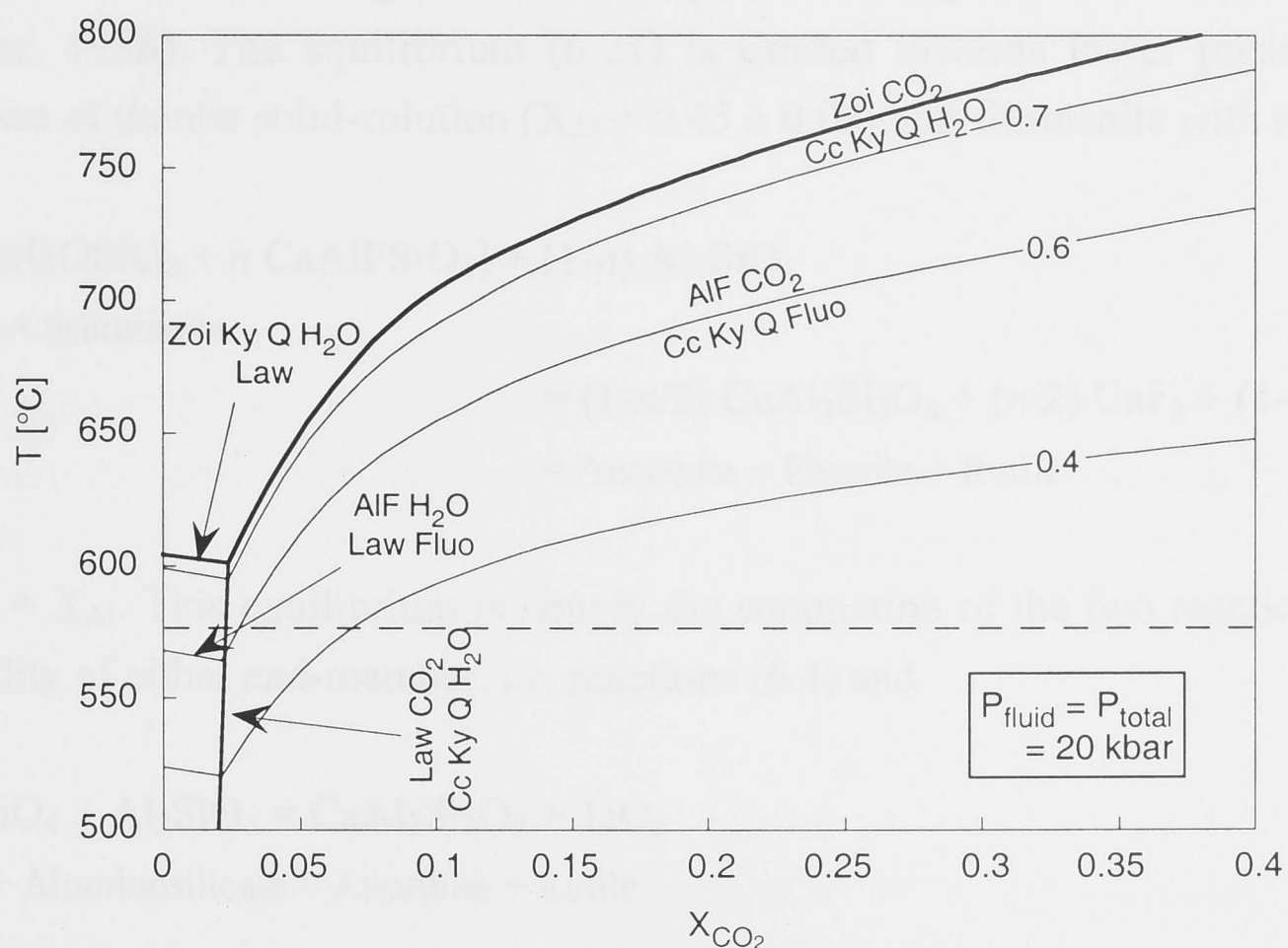
Figure 6.8 Al-content in titanite coexisting with an H_2O-CO_2 fluid in the pseudo-system CaO - CaF_2 - Al_2O_3 - SiO_2 - H_2O - CO_2 at 20 kbar. Numbers on isopleths refer to X_{Al} in titanite, calculated with reactions (6.13), (6.14), and (6.19). Dashed line represents eutectic melting point in the system CaF_2 – $CaCO_3$ – $Ca(OH)_2$ (Gittins and Tuttle, 1964). Abbreviations as in Figure 6.1.

Due to the breakdown of lawsonite at such low CO_2 contents, the maximum possible X_{Al} in the mixed fluid system hardly differs from that of the pure H_2O system, but is significantly higher compared to that with a pure CO_2 fluid. In this system with fluorite, H_2O and CO_2, melting probably sets in at temperatures as low as $575°C$ (dashed line), as indicated by the eutectic temperature of the system $CaF_2 - CaCO_3 - Ca(OH)_2$ of $575°C$ (Gittins and Tuttle, 1964). Thus, large parts of Figure 6.8 are probably metastable, restricting the maximum possible Al-content of titanite coexisting with a binary H_2O-CO_2 fluid to $X_{Al} < 0.6$.

6.8 Addition of TiO$_2$

Allowing for titanium in this chemical system adds the important phases rutile and the $CaTiOSiO_4$ end-member to the above assemblages. One of the most basic, fluid-absent reactions that relates the two titanite end-members in this system is

$$2\ CaAlFSiO_4 + TiO_2 = CaTiOSiO_4 + Al_2SiO_5 + CaF_2 \hspace{2cm} (6.21)$$
CaAlFSiO$_4$ + Rutile = Titanite + Aluminosilicate + Fluorite

Figure 6.9 shows the Al-content of titanite buffered by this equilibrium. Again, titanite with extremely high Al-contents, and the $CaAlFSiO_4$ end-member, are not to be expected in this assemblage, as their isopleths lie beyond the $5°C/km$ geotherm (Schreyer, 1988). The equilibrium (6.21) is limited towards lower pressure by the breakdown of titanite solid-solution ($X_{Al} = 0.45 \pm 0.03$) and sillimanite with reaction

$$[(1\text{-}n)\ CaTiOSiO_5 + n\ CaAlFSiO_4] + (1\text{-}n)\ Al_2SiO_5 \hspace{2cm} (6.22)$$
Titanite$_{ss}$ + Sillimanite

$$= (1\text{-}n/2)\ CaAl_2Si_2O_8 + (n/2)\ CaF_2 + (1\text{-}n)\ TiO_2$$
$$= \text{Anorthite} + \text{Fluorite} + \text{Rutile}$$
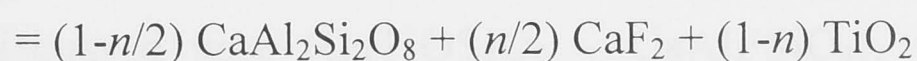
where $n = X_{Al}$. This equilibrium is simply the summation of the two reactions limiting the stability of either end-member, i.e. reactions (6.4) and

$$CaTiOSiO_4 + Al_2SiO_5 = CaAl_2Si_2O_8 + TiO_2 \hspace{2cm} (6.23)$$
Titanite + Aluminosilicate = Anorthite + Rutile
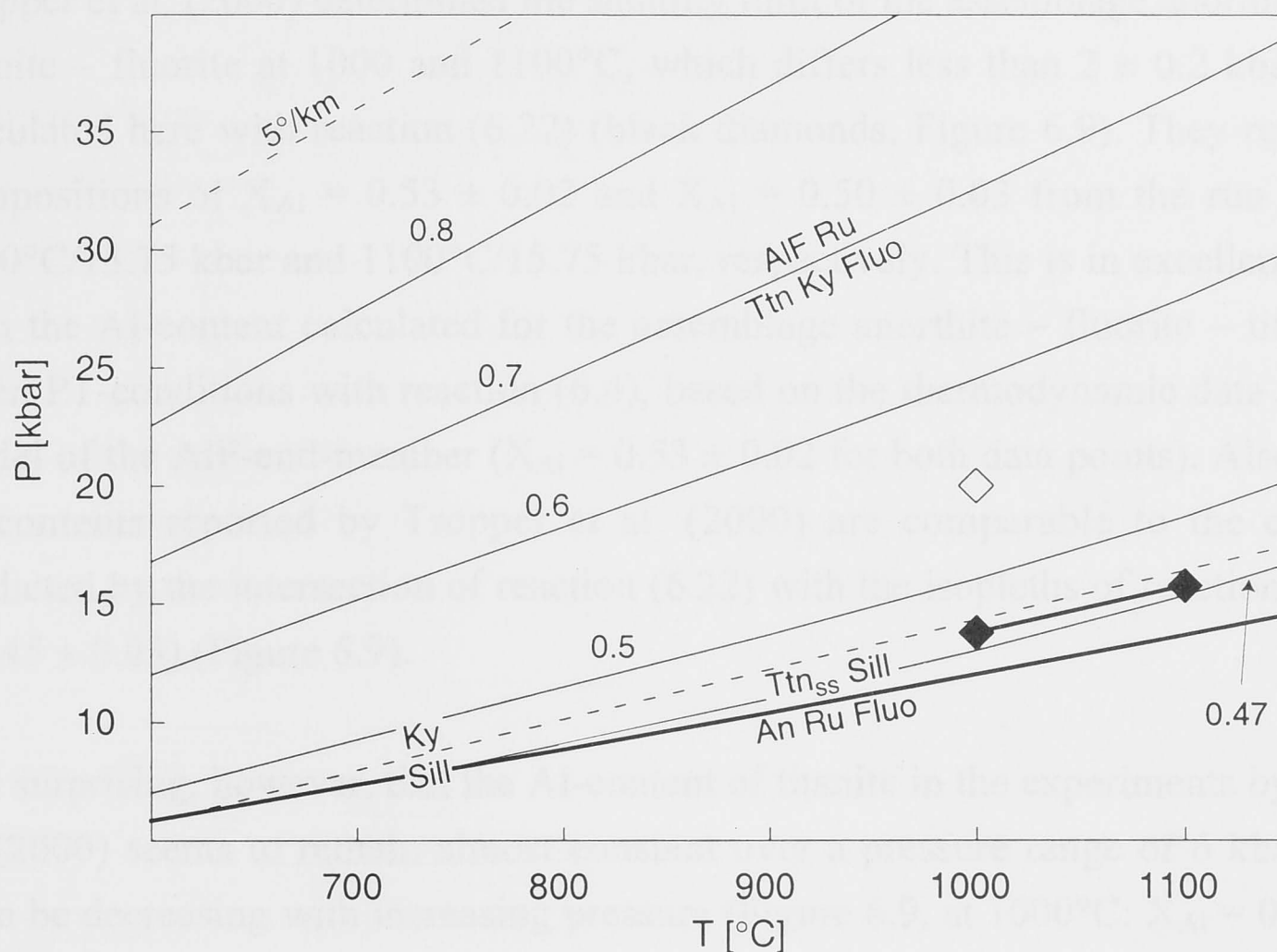
Figure 6.9 Al-content in titanite coexisting with rutile, kyanite and fluorite (reaction 6.21). Numbers on isopleths refer to X_{Al} of titanite. Upper dashed line shows the 5°C/km geotherm, which approximates the limit of pressure and temperature conditions realised on Earth (Schreyer, 1988). Also shown is the breakdown of titanite solid-solution and sillimanite to anorthite, rutile and fluorite, referring to $X_{Al} = 0.45 \pm 0.03$ (reaction (6.22)). Open diamond shows experimental conditions at which Tropper et al. (1999) synthesised titanite with $X_{AlF} = 0.5$ in the assemblage titanite – fluorite – kyanite – rutile. Black diamonds represent experimentally determined stability limit of the assemblage anorthite – rutile – titanite – fluorite by Tropper et al. (2000) (1000°C, 13.75 kbar, $X_{Al} = 0.53$; 1100°C, 15.75 kbar, $X_{Al} = 0.50$). Abbreviations as given in Figure 6.1.

Reaction (6.23) was studied experimentally by Manning and Bohlen (1991). The displacement of this reaction in the presence of fluorite, which allows for titanite solid-solution along the binary join discussed here ($CaTiOSiO_4$ – $CaAlFSiO_4$), was investigated recently with piston cylinder experiments by Tropper et al. (1999, 2000). Although these two conference abstracts only contain limited information, the data by Tropper et al. (1999, 2000) are briefly discussed here, as they represent the only other experimental study of AlF-bearing titanite in this assemblage.

Tropper et al. (1999) reported titanite with $X_{Al} = 0.50$ from the synthetic assemblage titanite – fluorite – kyanite – rutile at 20 kbar and 1000°C (open diamond, Figure 6.9). This is comparable to the value of $X_{Al} = 0.55$ as indicated by the isopleths of equilibrium (6.23).

Tropper et al. (2000) determined the stability limit of the assemblage anorthite – rutile – titanite – fluorite at 1000 and 1100°C, which differs less than 2 ± 0.2 kbar from that calculated here with reaction (6.22) (black diamonds, Figure 6.9). They report titanite compositions of $X_{Al} = 0.53 \pm 0.02$ and $X_{Al} = 0.50 \pm 0.03$ from the run products at 1000°C/13.75 kbar and 1100°C/15.75 kbar, respectively. This is in excellent agreement with the Al-content calculated for the assemblage anorthite – fluorite – titanite at the given PT-conditions with reaction (6.4), based on the thermodynamic data and activity model of the AlF-end-member ($X_{Al} = 0.53 \pm 0.02$ for both data points). Also, the above Al-contents reported by Tropper et al. (2000) are comparable to the composition predicted by the intersection of reaction (6.22) with the isopleths of reaction (6.21) ($X_{Al} = 0.45 \pm 0.03$) (Figure 6.9).

It is surprising, however, that the Al-content of titanite in the experiments by Tropper et al. (2000) seems to remain almost constant over a pressure range of 6 kbar, or might even be decreasing with increasing pressure (Figure 6.9, at 1000°C: $X_{Al} = 0.53$ at 13.75 kbar, $X_{Al} = 0.50$ at 20 kbar). A more detailed description of their experiments and product assemblages has to be awaited for further interpretation.

Two equilibria controlling the stability of the titanite end-members in the presence of CO_2-rich fluids are reactions (6.19) and

$$CaCO_3 + SiO_2 + TiO_2 = CaTiOSiO_4 + CO_2 \hspace{2cm} (6.24)$$
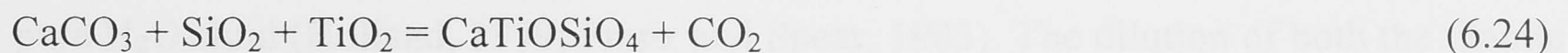
Calcite + Quartz/Coesite + Rutile = Titanite + CO_2

This reaction, which is well determined experimentally (Hunt and Kerrick, 1977; Jacobs and Kerrick, 1981), controlls the stability of titanite in calcareous rocks (Frost et al., 2000). In the presence of a pure CO_2-fluid, this reaction restricts the occurrence of titanite to low pressures and high temperatures (Figure 6.10). However, many calcareous rocks equilibrated at eclogite facies conditions contain titanite, typically Al-rich, such as the carbonate-bearing eclogites reported from central China, Dabieshan (Carswell et al., 1996), siliceous dolomites in eclogite facies rocks of the Tauern Window (Franz and Spear, 1985), and the intensely folded schistose calc-silicate rocks and marbles in the eclogite complex Tromsø, Northern Norway (Krogh et al. 1990). As pointed out in previous studies (Carswell et al., 1996; Frost et al., 2000) the stability of titanite in these assemblages can be extended to higher pressures by diluting the CO_2 content of the fluid, as well as by diluting the titanite component with other end-members in titanite solid-solution, thus explaining the presence of titanite in calcareous eclogite-facies rocks.
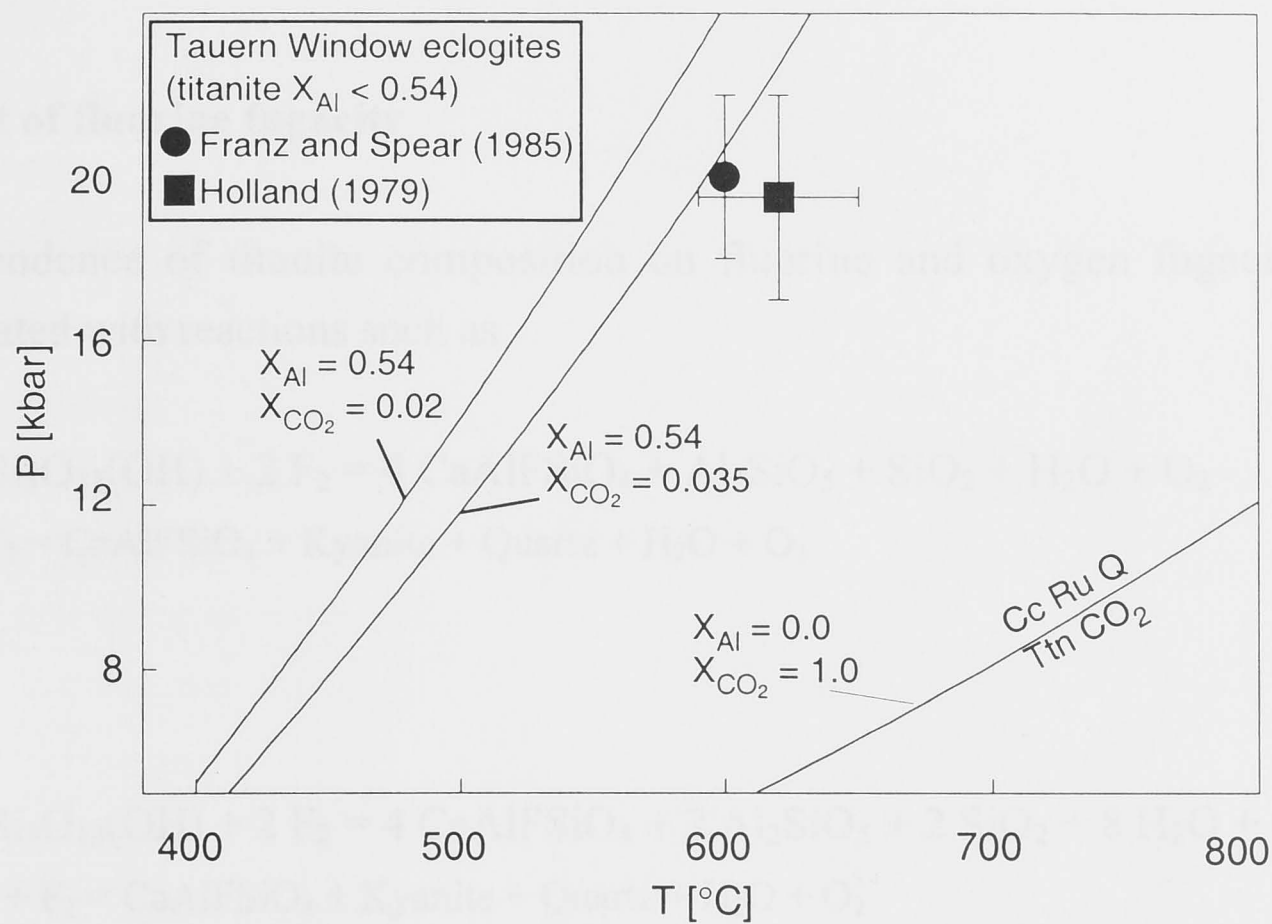
Figure 6.10 Three different positions of reaction (6.20), depending on the Al-content of titanite (X_{Al}) and the Xco_2 in the coexisting H_2O-CO_2 fluid ($P_{fluid} = P_{total}$). Data points represent peak-metamorphic conditions for titanite-bearing eclogites from the Tauern Window (with $X_{Al} <$ 0.54), as estimated by Holland (1979) and Franz and Spear (1985). The fluid composition for peak-metamorphism was estimated to be Xco_2 = 0.02 and Xco_2 = 0.035 by Holland (1979), and Franz and Spear (1983), respectively.

This is demonstrated in Figure 6.10 with the rocks from the Tauern Window, which equilibrated at 600°C, 20 ± 2 kbar (Franz and Spear, 1985), in the presence of an almost pure H_2O-fluid (Holland, 1979; Franz and Spear, 1983). The dilution of both the titanite component with $CaAlFSiO_4$ ($X_{Al} <$ 0.54, Franz and Spear, 1985), and the CO_2 fluid with H_2O, shifts the reaction to pressures high enough to stabilise titanite at the given metamorphic conditions.

The good agreement between the thermodynamic calculations and the independently determined metamorphic conditions, suggests that reaction (6.24) can be confidently used to estimate fluid compositions, if titanite composition, and equilibrium pressure and temperature of a metamorphic assemblage are known. For example, the coesite and carbonate-bearing eclogites at Shuanghe in Dabieshan, which were equilibrated at 700 ± 50°C, and minimum pressures between 27 and 28 kbar, contain titanite with a maximum $CaAlFSiO_4$ content of 39.3 mol.% (Carswell et al., 1996; Cong et al., 1995). Based on this titanite composition, the titanite activity model proposed by this study, and the given metamorphic conditions (P = 28 kbar), the maximum CO_2-content of the fluid was determined, resulting in Xco_2 = 0.032 at 700°C (and Xco_2 = 0.017 and 0.063 at 650°C and 750°C, respectively) ($P_{fluid} = P_{total}$). Low CO_2-pressures seem to be typical for such ultra-high pressure marble-eclogite assemblages (e.g., Kato et al., 1997).

6.9 Effect of fluorine fugacity

The dependence of titanite composition on fluorine and oxygen fugacities can be demonstrated with reactions such as

$$2\ Ca_2Al_3Si_3O_{12}(OH) + 2\ F_2 = 4\ CaAlFSiO_4 + Al_2SiO_5 + SiO_2 + H_2O + O_2 \qquad (6.25)$$
Zoisite + F_2 = CaAlFSiO$_4$ + Kyanite + Quartz + H$_2$O + O$_2$

and

$$4\ Ca_2Al_3Si_3O_{12}(OH) + 2\ F_2 = 4\ CaAlFSiO_4 + 2\ Al_2SiO_5 + 2\ SiO_2 + 8\ H_2O + O_2 \qquad (6.26)$$
Lawsonite + F_2 = CaAlFSiO$_4$ + Kyanite + Quartz + H$_2$O + O$_2$
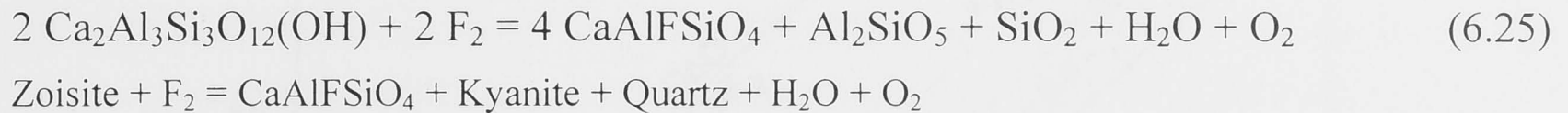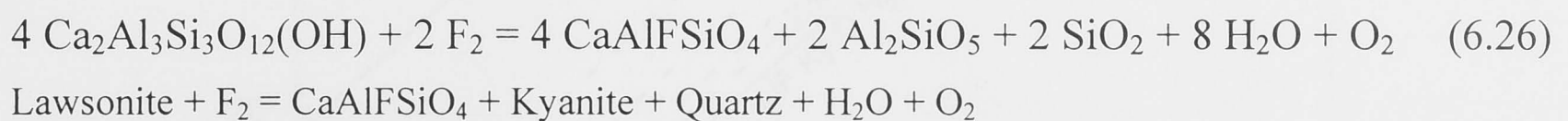
Figure 6.11 shows these reactions in $\log fO_2$-$\log fF_2$ space, as well as in a T-$\log fF_2$ diagram, which demonstrates the relationship of these reactions with those independent of oxygen and fluorine fugacities (e.g., reaction 6.10, Figure 6.11b). Assemblages like these can be used to estimate fluorine fugacities of a rock, if phase compositions, pressure, temperature, and oxygen fugacity of the metamorphic assemblage are known.

For example, Bohlen and Essene (1978) investigated fluorine-rich assemblages from several locations in the Adirondacks, U.S.A., and their buffering effect on fluorine and oxygen fugacities. While most of the observed assemblages are represented correctly by their $\log fO_2$-$\log fF_2$ petrogenetic grids, one titanite-bearing assemblage was found to be inconsistent with the titanite stability field.

Based on the calculations by Bohlen and Essene (1978), the stability of titanite is restricted to low fluorine fugacities with reaction

$$2\ CaTiOSiO_4 + 2\ F_2 = 2\ CaF_2 + 2\ TiO_2 + 2\ SiO_2 + O_2 \qquad (6.27)$$
Titanite + F_2 = Fluorite + Rutile + Quartz + O$_2$
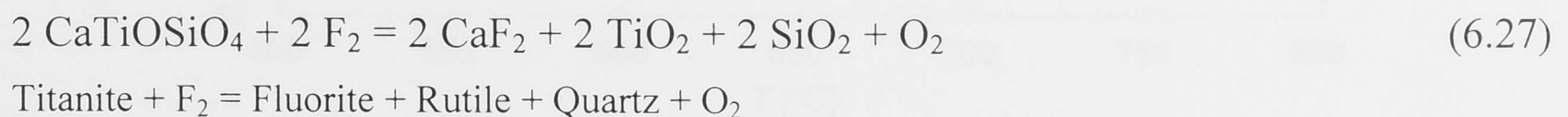
whereas the assemblage hedenbergite-quartz-fluorite-fayalite occurs at higher fF_2 due to reaction

$$2\ CaFeSi_2O_6 + 2\ F_2 = 2\ CaF_2 + Fe_2SiO_4 + 3\ SiO_2 + O_2 \qquad (6.28)$$
Hedenbergite + F_2 = Fluorite + Fayalite + Quartz + O$_2$
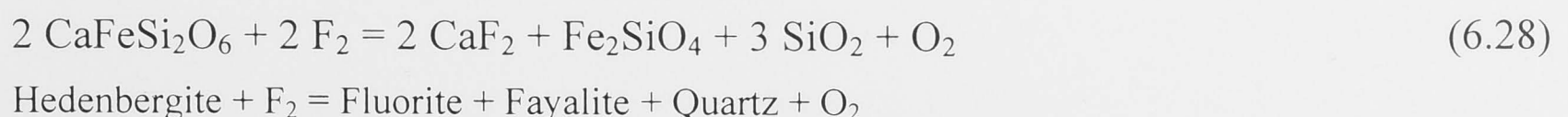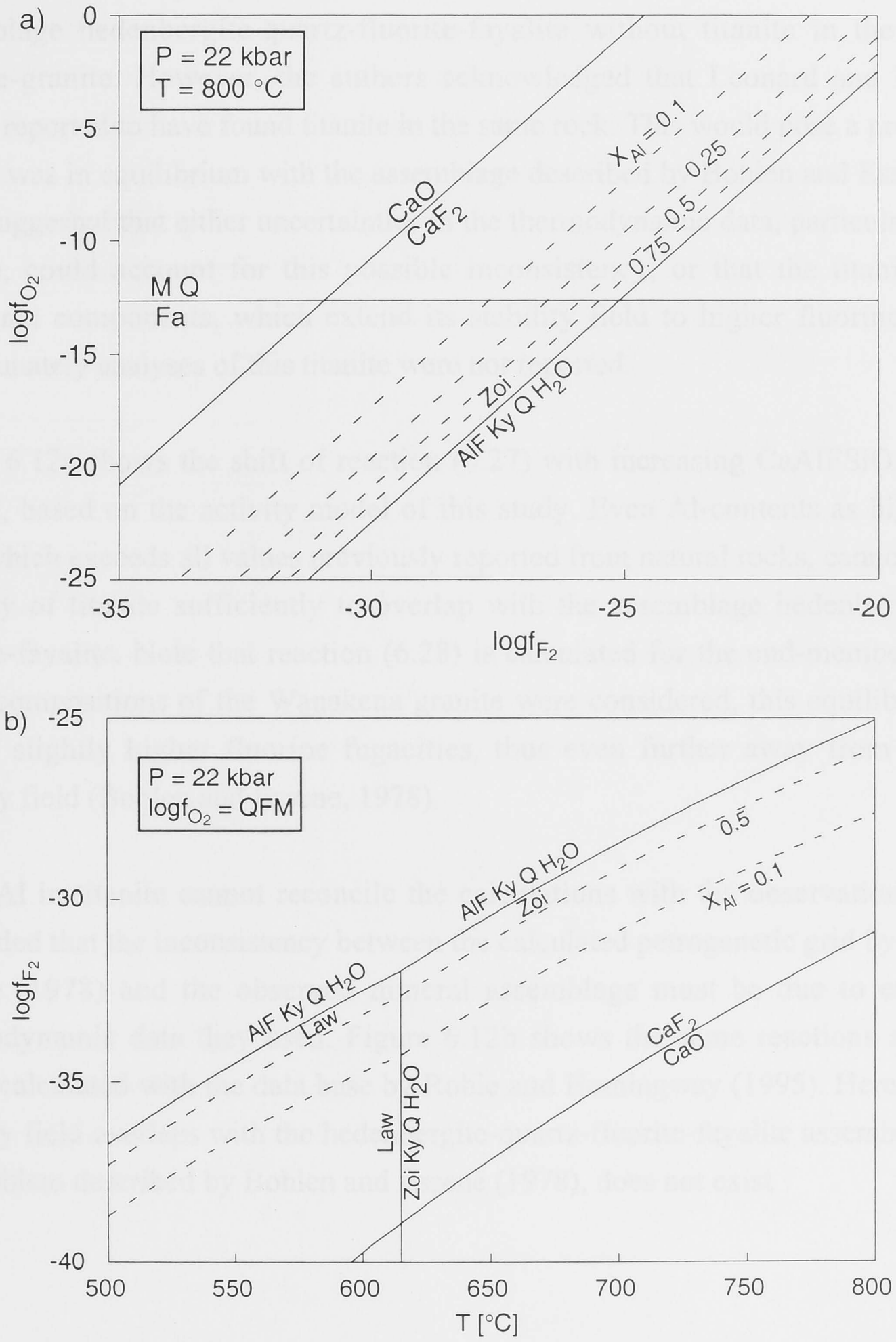
Figure 6.11 Reactions (6.25) **(a)**, (6.26) and (6.10) **(b)**, calculated at 22 kbar and 800°C. Al-isopleths are dashed. Also shown is stability limit of fluorite. Abbreviations as in Figure 6.1.

These reactions are shown in Figure 6.12a, which was constructed with the data used by Bohlen and Essene (1978). In agreement with this, Bohlen and Essene (1978) found the assemblage hedenbergite-quartz-fluorite-fayalite without titanite in the Wanakena fayalite-granite. However, the authors acknowledged that Leonard and Buddington (1964) reported to have found titanite in the same rock. This would pose a problem if the titanite was in equilibrium with the assemblage described by Bohlen and Essene (1978). They suggested that either uncertainties in the thermodynamic data, particularly those of titanite, could account for this possible inconsistency, or that the titanite contains additional components, which extend its stability field to higher fluorine fugacities. Unfortunately analyses of this titanite were not reported.

Figure 6.12a shows the shift of reaction (6.27) with increasing $CaAlFSiO_4$ content of titanite, based on the activity model of this study. Even Al-contents as high as $X_{Al} = 0.75$, which exceeds all values previously reported from natural rocks, cannot extend the stability of titanite sufficiently to overlap with the assemblage hedenbergite-quartz-fluorite-fayalite. Note that reaction (6.28) is calculated for the end-member phases. If phase compositions of the Wanakena granite were considered, this equilibrium would plot at slightly higher fluorine fugacities, thus even further away from the titanite stability field (Bohlen and Essene, 1978).

Since Al in titanite cannot reconcile the calculations with the observations, it can be concluded that the inconsistency between the calculated petrogenetic grid by Bohlen and Essene (1978) and the observed mineral assemblage must be due to errors in the thermodynamic data they used. Figure 6.12b shows the same reactions as in Figure 6.12a, calculated with the data base by Robie and Hemingway (1995). Here, the titanite stability field overlaps with the hedenbergite-quartz-fluorite-fayalite assemblage, so that the problem described by Bohlen and Essene (1978), does not exist.
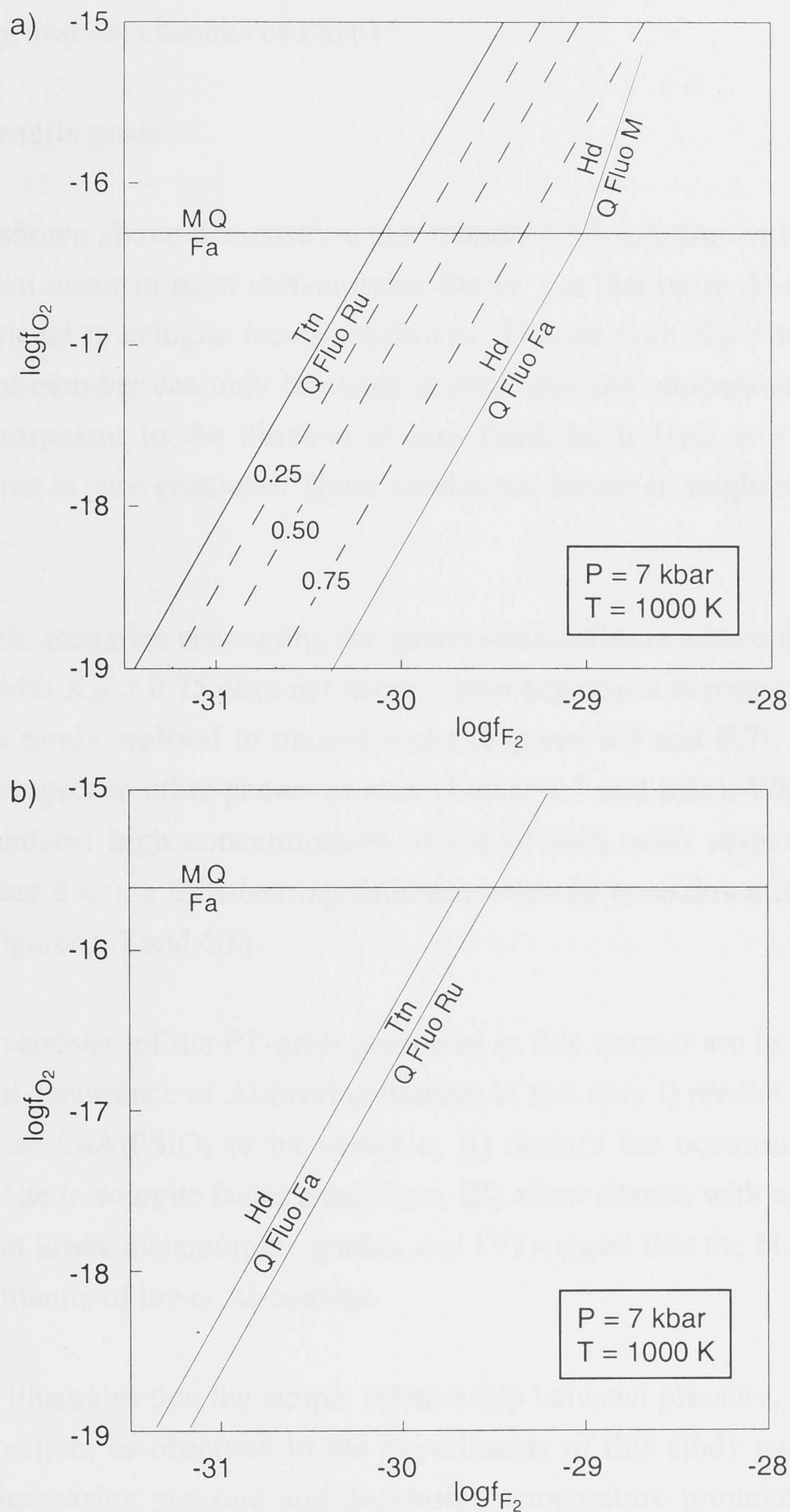
Figure 6.12 Reactions (6.27) and (6.28), calculated at 7 kbar and 1000 K (peak meatamorphic conditions of Adirondack rocks, see text), using the thermodynamic data as given in Bohlen and Essene (1978) **(a)**, and Robie and Hemingway (1995) **(b)**. Dashed lines are Al-isopleths. Note reversed position of the two reactions in a) and b). Abbreviations as in Figure 6.1.

6.10 Summary and conclusions of Part I

6.10.1 Petrogenetic grids

The PT-grids shown above demonstrate that titanite solid-solution with Al-contents up to $X_{Al} = 0.6$ can occur in most metamorphic facies, but that more Al-rich titanites are generally restricted to eclogite facies conditions. Titanite with $X_{Al} > 0.8$, and the pure $CaAlFSiO_4$ end-member can only be stable at pressures and temperatures accessible to crustal metamorphism in the absence of any fluid, be it H_2O or CO_2, and if the coexisting garnet is pure grossular. These conditions, however, might never be realised in nature.

In more realistic scenarios accounting for garnet solid-solution and/or the presence of a fluid, titanite with $X_{Al} > 0.75$ does not occur, either because it is restricted to extremely high pressures rarely realised in natural rocks (Figures 6.3 and 6.7), or because it is unstable with respect to other phases or melt (Figure 6.5 and 6.6c). While the presence of H_2O destabilises high concentrations of $CaAlFSiO_4$ with respect to zoisite or grossular (Figure 6.6c), a CO_2-bearing fluid promotes its breakdown to an assemblage with calcite (Figures 6.7 and 6.8).

The 'realistic versions' of the PT-grids presented in this chapter are in good agreement with the natural occurrence of Al-bearing titanite, in that they I) predict titanite with $X_{Al} > 0.75$ and pure $CaAlFSiO_4$ to be unstable, II) restrict the occurrence of the most aluminous titanite to eclogite facies conditions, III) allow titanite with up to $X_{Al} = 0.6$ to be stable also at lower metamorphic grades, and IV) suggest that the blueschist facies is dominated by titanite of lower Al-content.

The last point illustrates that the simple relationship between pressure, temperature and titanite composition, as observed in the experiments of this study and that by Smith (1981), (i.e., increasing pressure and decreasing temperature promote Al in titanite), cannot be used as a 'rule of thumb', but depends on the buffering effect of the specific mineral assemblage. The Al-content of titanite equilibrated with lawsonite and fluorite, for example, behaves inversely, increasing with increasing temperature and decreasing pressure (Figures 6.4 and 6.5). The general rule that the smaller end-member of a solid-solution is favoured by high pressures, does not hold for reactions involving a fluid phase, as the volume of the latter dominates the reaction volume.

The dependence of X_{Al} on the phase assemblage is also reflected in the experimental results of Tropper et al. (1999), who equilibrated titanite at 20 kbar and 1000°C in the two different assemblages titanite - anorthite - fluorite, and titanite - rutile - kyanite - fluorite. The resulting titanite compositions of $X_{Al} = 0.98$ and $X_{Al} = 0.50$, respectively, differ significantly from each other, but are in fairly good agreement with the Al-contents predicted by this study for these assemblages (open diamonds in Figures 6.2 and 6.9).

The extremely widely spaced X_{Al}-isopleths in high pressure assemblages with zoisite and grossular, are very sensitive to changes or errors in the input data. Thus, the uncertainties attached to the Al-content computed with these equilibria are very large, of the order of ±0.25 (X_{Al}), and do not allow the use of Al in titanite as a reliable geothermoarometer at high pressures. Although, for this reason, some of the PT-grids shown in this chapter should be regarded as semi-quantitative only, their topology and general trends are still instructive, and they agree with natural rock data.

In fact, the 'levelling out' of the Al-contents in titanite at about $X_{Al} = 0.53$ between 25 and 35 kbar in the experiments by Smith (1981) might well be due to such widely spaced isopleths also in that system. This is suggested by the striking similarity between the P-X_{Al} plot by Smith (1981), and that, for example, based on Figure 6.3 of this study (Figure 6.13).
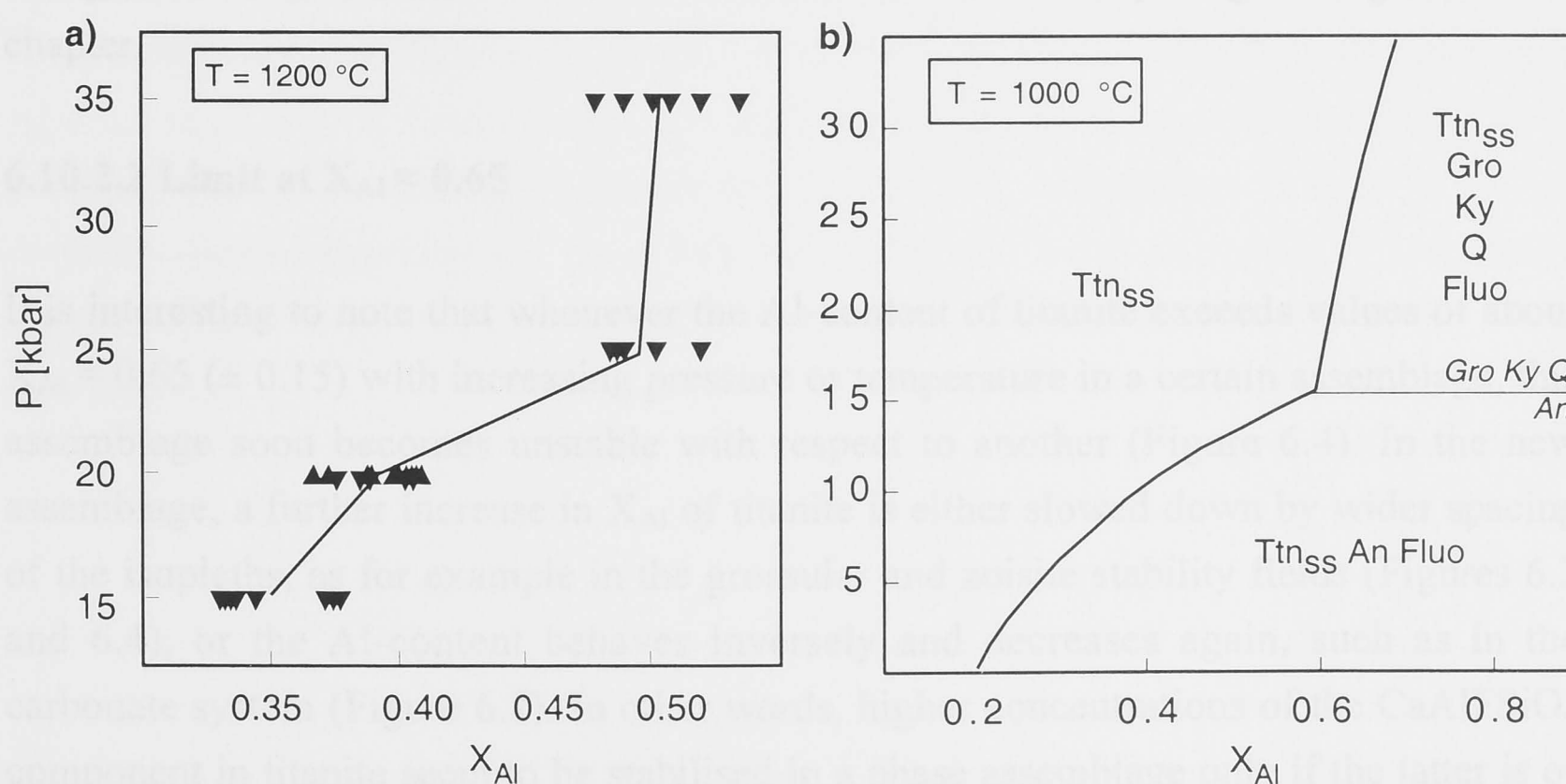
Figure 6.13 Pressure dependence of Al in titanite based on (a) experimental results from the assemblage titanite - rutile - corundum - melt ± kyanite ± quartz ± fluorite by Smith (1981), and (b) based on thermodynamic modelling in the system shown Figure 6.4. Note the similarity of the topologies of the two P-X_{Al} plots.

According to Smith (1981) various phase assemblages occur in his experiments (titanite – rutile – corundum – melt with either kyanite, or quartz, or fluorite), thus allowing for a potential reaction between 20 and 25 kbar, which would explain the change in slope (Figure 6.13a). Unfortunately, this system cannot be modelled in detail because the assemblages for individual experiments were not given by Smith (1981). Moreover, the presence of melt prevents straightforward thermodynamic modelling.

In contrast to the reactions with very widely spaced isopleths, reactions such as (6.18) seem to be good indicators for pressure-temperature-fluid composition relationships (Figure 6.10).

6.10.2 Linking thermodynamics and crystal structure

6.10.2.1 End-member $CaAlFSiO_4$

The instability of the $CaAlFSiO_4$ end-member with respect to other phases in almost all assemblages investigated above is in very good agreement with the crystal structure data (Chapters 2 and 3), which indicate that the titanite structure is not well suited to accommodate Al and F instead of Ti and O. High bond valence sums at the Ca and O1-site, and polyhedral distortion, indicate structural stresses, lattice energies of small magnitudes, and thus low thermodynamic stability of $CaAlFSiO_4$ (i.e., high Gibbs free energy), which is well reflected in its absence from almost all petrogenetic grids in this chapter.

6.10.2.2 Limit at $X_{Al} \approx 0.65$

It is interesting to note that whenever the Al-content of titanite exceeds values of about $X_{Al} = 0.65$ (± 0.15) with increasing pressure or temperature in a certain assemblage, this assemblage soon becomes unstable with respect to another (Figure 6.4). In the new assemblage, a further increase in X_{Al} of titanite is either slowed down by wider spacing of the isopleths, as for example in the grossular and zoisite stability fields (Figures 6.3 and 6.4), or the Al-content behaves inversely and decreases again, such as in the carbonate system (Figure 6.7). In other words, higher concentrations of the $CaAlFSiO_4$ component in titanite seem to be stabilised in a phase assemblage only if the latter is of low stability itself as it approaches its own stability limit.

This limiting value of about $X_{Al} = 0.65$ (± 0.15) is in agreement with the previously stated hypothesis based on crystal structure data, that the titanite stability decreases when X_{Al} exceeds 0.6 significantly (Chapter 3; Troitzsch et al., 1999). Note, however, that the activity-composition relations determined in Chapter 5 are simple, without any significant anomaly at high Al-contents (Figure 5.10, p. 110, and Figure 5.13, p.113) that could be the thermodynamic expression of the crystal structural problems setting in at about $X_{Al} = 0.65$ (Figure 3.6, p. 49). Thus, the limiting composition of titanite in the petrogenetic grids of this chapter cannot be linked directly to the crystal structural problems observed at these Al-contents *via the activity of titanite*. There does not seem to be a particular '*catastrophic*' crystal structural process, such as the collapse of the octahedral bonds at $X_{Al} = 0.40$ (Figure 3.9, oct-O3, p. 54), which could act as an energy-barrier, preventing high Al-titanite to form, as this would show in the activity of titanite. Rather, it seem to be *continuous* crystal structural changes that have an effect on the thermodynamic stability of titanite, such as the smooth change in bond valence sums from one end-member to the other (Figure 3.6, p. 49), as these might not stand out as anomalies in activity composition-relations.

Thus the structural problems at around $X_{Al} = 0.60$ and beyond, and the limiting composition in the petrogenetic grids have the same *cause*, i.e. the incorporation of an increasing amount of a component with a less suited structure and thus lower thermodynamic stability. Of course, these problems become most significant, both in the structure as well as with respect to thermodynamic stability, when the less stable component starts to dominate the phase, i.e. exceeds 50 mol.%. Therefore, the maximum Al-content of natural titanites of $X_{Al} \approx 0.54$, which has been speculated about a lot in previous studies (including Troitzsch and Ellis, 1999; and Troitzsch et al., 1999) is probably simply marking the point beyond which the thermodynamically less stable aluminium end-member starts to dominate over the titanite end-member in the solid-solution.

Part II The stability of fluorine-bearing zoisite

6.11 Introduction

Many experiments of this study that were carried out at pressures above 15 kbar, have run products that contain F-rich zoisite as an accessory phase (Tables 2.1 (p. 11), 3.1 (p. 31), and 5.2 (p. 94)). In one $CaAlFSiO_4$ synthesis run, which failed to produce the Al-titanite end-member, F-rich zoisite is even the most abundant component (G-197, Figure 2.3a, p. 12). Electron microprobe analyses suggest that zoisite in the above experiments represents a binary solid-solution between the end-members $Ca_2Al_3Si_3O_{12}F$ ('fluor-zoisite') and $Ca_2Al_3Si_3O_{12}OH$ ('hydroxy-zoisite'), although the presence of water in the experimental runs could only be confirmed qualitatively with IR and RAMAN spectroscopy (Troitzsch and Ellis, 1999). The F-content of the synthetic zoisite ranges from $X_F = 0.30$ to $X_F = 0.70$ [$X_F = F/(F+OH)$], depending on phase assemblage, pressure and temperature.

Two reasons were given in the previous chapters to account for the presence of zoisite in the supposedly dry experiments. These are 1) water-contamination of the starting-mix, which would explain the formation of hydroxy-zoisite instead of grossular, and 2) the metastable existence of fluoro-zoisite instead of $CaAlFSiO_4$, if the latter does not nucleate in the absence of titanite seeds. The two possibilities are tested in the following with thermodynamic modelling of the experimental assemblages.

In contrast to synthetic phases, the fluorine content of natural zoisite and epidote seems to be limited to very small amounts even in F-rich rocks (e.g., López Sánchez-Vizcaíno et al., 1997; Makanjuola and Howie, 1972), so that the results of the following investigation will be of interest mostly to experimental petrologists. The synthesis of F-rich zoisite in similar experiments was reported by Tropper (personal communication, 1999).

6.12 Calculation details

All calculations of this section were based on the data of Robie and Hemingway (1995). This data base was chosen instead of Berman (1988) because five out of seven phases considered below (fluorite, $CaAlFSiO_4$, fluor-zoisite, fluor-pargasite and hydroxy-pargasite) are not included in the latter. In contrast to this, the former data compilation contains fluorite, hydroxy-pargasite and fluor-pargasite, which were used for the

estimation of fluor-zoisite data. Only compressibility and expansion data were taken from Berman (1988).

Since zoisite with such high F-contents has never been reported before from natural or synthetic assemblages, thermodynamic data for fluor-zoisite are not available, and had to be estimated. Enthalpy of formation, standard state entropy and unit-cell volume were estimated based on hydroxy-zoisite data, which were modified according to differences between the OH- and F-end-members of pargasite. Pargasite was chosen as a model solid-solution, because the respective end-members contain amounts of OH and F that are similar to zoisite (about 2 wt%). Compared to hydroxy-pargasite, the enthalpy of fluor-pargasite is 0.63% more negative, its entropy 0.17% larger, and the unit cell volume 0.51% smaller. These values were used to adjust the zoisite data for the fluorine end-member. The heat capacity of fluor-zoisite was estimated by adding the heat capacities of anorthite and fluorite in the ratio 3:1. The compressibility and thermal expansion of fluor-zoisite were assumed to be identical to those of hydroxy-zoisite (Berman, 1988). The estimated data for fluor-zoisite are listed in Table 6.1. Zoisite solid-solution was assumed to behave ideally.

Table 6.1 Thermodynamic data for fluor-zoisite, estimated as described the text.

Enthalpy of formation dH_f^0	[kJmol^{-1}]	-6944.884
Standard state entropy S^0	[Jmol^{-1}K^{-1}]	296.4
Unit cell volume	[Jmol^{-1}bar^{-1}]	13.580
Heat capacity*		
a [J]		1791.7
b [JK^{-1}]		-0.856735
c [JK^2]		12828000
d [JK$^{0.5}$]		-23443.5
e [JK^{-2}]		0.00031482
Compressibility/expansion$^{\#}$		
v_1 [b^{-1}]		-5.15*10^{-07}
v_2 [b^{-2}]		1.288*10^{-12}
v_3 [K^{-1}]		0.00003467
v_4 [K^{-2}]		0

*Coefficients as in Robie and Hemingway (1995)
$^{\#}$ Coefficients as in Berman (1988)

6.13 Results and discussion

6.13.1 Hydroxy-zoisite versus grossular

In the experiments, fluor-zoisite commonly coexists with fluorite and titanite solid-solution, with or without kyanite and anorthite. Grossular is generally absent. The stability of the hydroxy-zoisite component with respect to grossular is investigated first. These two phases are related by reaction

$$6 \ Ca_2Al_3Si_3O_{12}(OH) = 4 \ Ca_3Al_2Si_3O_{12} + 5 \ Al_2SiO_5 + SiO_2 + 3 \ H_2O \qquad (6.29)$$

Zoisite = Grossular + Kyanite + Quartz + H_2O

Zoisite in the synthesis runs at 1100°C and 35 kbar (Table 2.1, p. 11) typically contains about $X_{OH} = 0.55 \pm 0.1$ [$X_{OH} = OH/(OH + F)$]. Assuming all other phases of reaction (6.15) to be pure, it can be calculated with equations (6.1) and (6.2) that fluid pressures as low as 4 % of the total pressure already stabilise hydroxy-zoisite with respect to grossular at these pressures and temperatures. From the molar volume of water at these conditions (16.64 cm^3mol^{-1}; Kerrick and Jacobs, 1981), the minimum amount of H_2O was estimated that would be needed to establish this or higher fluid pressures in the experiments. Assuming a sample volume of 1 mm^3 at run conditions (small capsule), a pore-space of 10 % in the sample, the presence of about 0.1 mg of H_2O in the sample is sufficient to maintain $P_{fluid} = 0.04 \ P_{total}$. A large capsule with a volume of about 10 mm^3 at run conditions, would require about 1 mg H_2O. These estimates are of the same order of magnitude as those in section 2.4.2 (minimum of 0.14 mg H_2O), that were based on the amount of zoisite present in the samples. The contamination with such small amounts of water during sample preparation is possible. Thus the absence of grossular from the experiments is in good agreement with the thermodynamic calculations. Grossular will therefore be excluded from the modelling of the F-bearing system below.

6.13.2 Fluoro-zoisite versus CaAlFSiO$_4$

Although the stability of zoisite is critically dependent on the fluid pressure, the thermodynamic modelling focuses on the pseudo-binary, fluid-absent system anorthite – fluorite, with the phases zoisite, anorthite, fluorite and titanite solid-solution (Figures 6.14, 6.15), in order to avoid uncertainties attached to fluid pressure estimates.
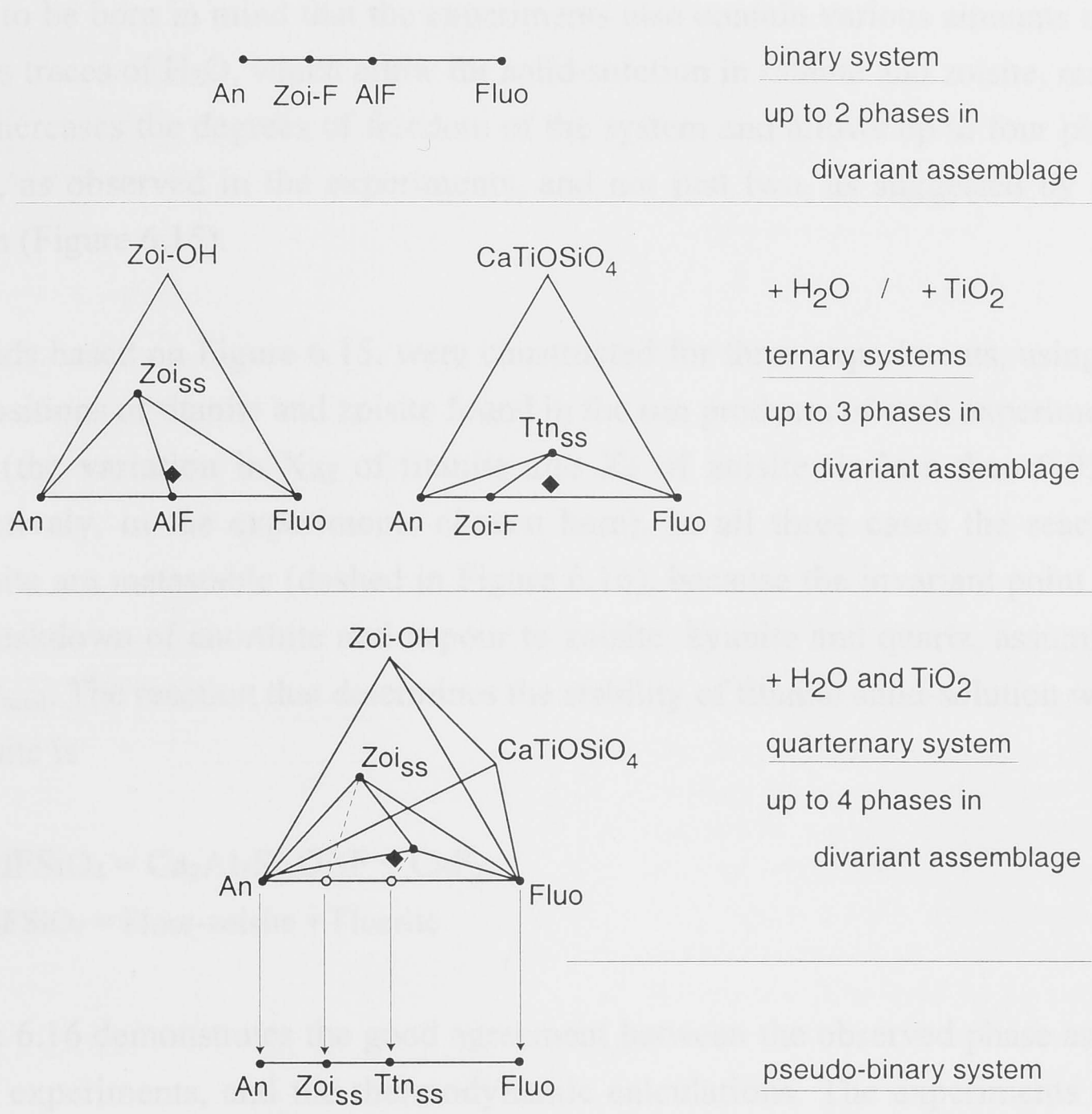
Figure 6.14 Derivation of pseudo-binary system anorthite – fluorite (+ H_2O + TiO_2). Diamonds are examples for starting mix compositions. Abbreviations as in Figure 6.1.
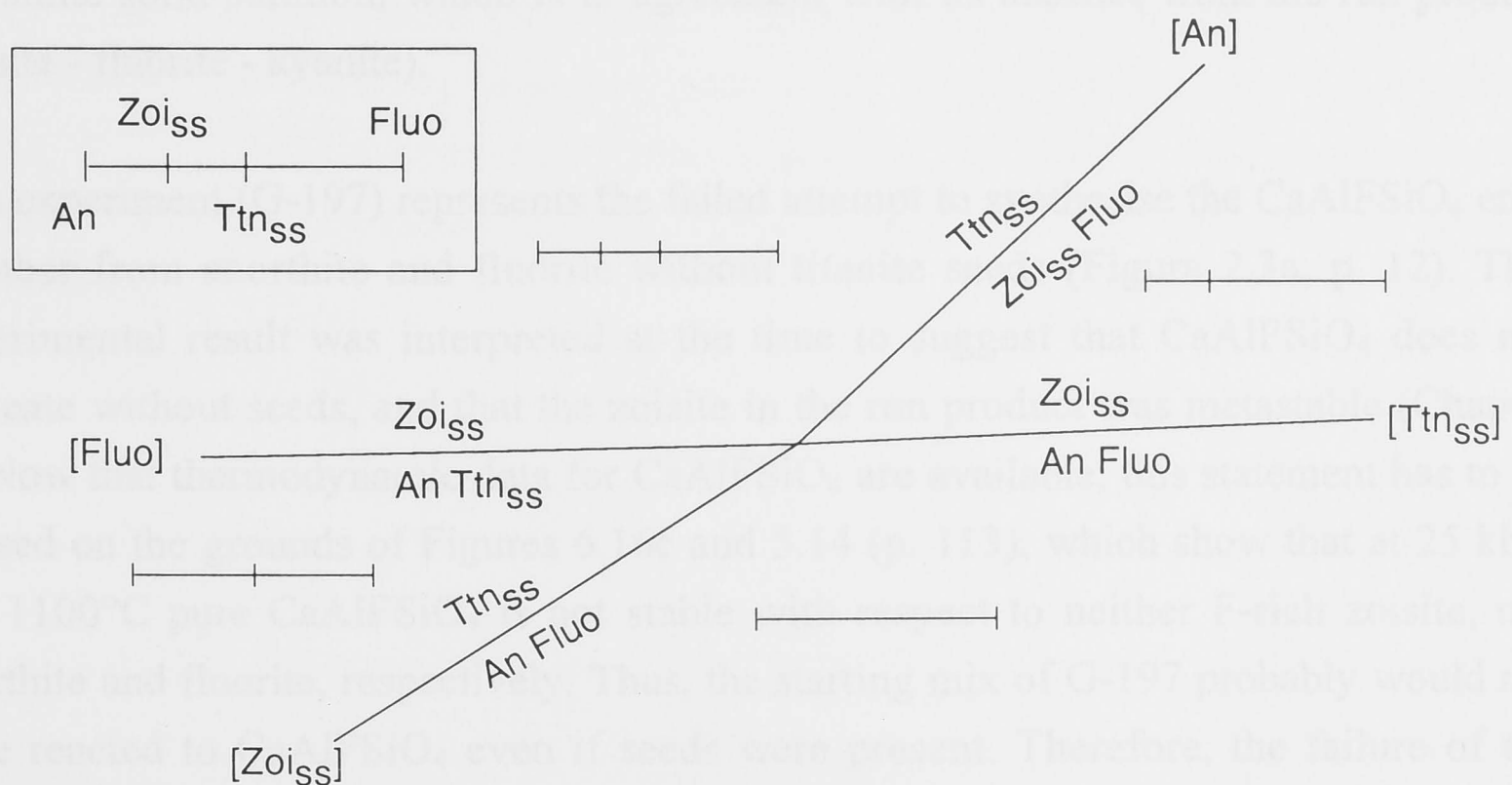
Figure 6.15 Petrogenetic grid for the pseudo-binary system anorthite – fluorite (+ H_2O + TiO_2) which is used to analyse the piston cylinder experiments presented in the earlier chapters. Abbreviations as in Figure 6.1.

It has to be born in mind that the experiments also contain various amounts of TiO_2, as well as traces of H_2O, which allow for solid-solution in titanite and zoisite, respectively. This increases the degrees of freedom of the system and allows up to four phases to be stable, as observed in the experiments, and not just two, as suggested by the binary system (Figure 6.15).

PT-grids based on Figure 6.15, were constructed for three experiments, using the mean compositions of titanite and zoisite found in the run products of each experiment (Figure 6.16) (the variation in X_{Al} of titanite and X_F of zoisite, is less than 0.05 and 0.1, respectively, in the experiments chosen here). In all three cases the reactions with anorthite are metastable (dashed in Figure 6.16), because the invariant point lies above the breakdown of anorthite and vapour to zoisite, kyanite and quartz, assuming $P_{fluid} = 0.04\ P_{total}$. The reaction that determines the stability of titanite solid-solution with respect to zoisite is

$$3\ CaAlFSiO_4 = Ca_2Al_3Si_3O_{12}F + CaF_2 \qquad\qquad (6.30)$$
$$3\ CaAlFSiO_4 = \text{Fluor-zoisite} + \text{Fluorite}$$

Figure 6.16 demonstrates the good agreement between the observed phase assemblages in the experiments, and the thermodynamic calculations. The experiments in Figures 6.16a and 6.16b, with the product assemblage titanite – fluorite – zoisite (+ kyanite), both plot in the field of coexisting titanite and zoisite solid-solutions (compare Figure 6.15). In contrast to this, the experiment in Figure 6.16c plots outside the stability field of titanite solid-solution, which is in agreement with its absence from the run product (zoisite - fluorite - kyanite).

This experiment (G-197) represents the failed attempt to synthesise the $CaAlFSiO_4$ end-member from anorthite and fluorite without titanite seeds (Figure 2.3a, p. 12). This experimental result was interpreted at the time to suggest that $CaAlFSiO_4$ does not nucleate without seeds, and that the zoisite in the run product was metastable (Chapter 2). Now that thermodynamic data for $CaAlFSiO_4$ are available, this statement has to be revised on the grounds of Figures 6.16c and 5.14 (p. 113), which show that at 25 kbar and 1100°C pure $CaAlFSiO_4$ is not stable with respect to neither F-rich zoisite, nor anorthite and fluorite, respectively. Thus, the starting mix of G-197 probably would not have reacted to $CaAlFSiO_4$ even if seeds were present. Therefore, the failure of the $CaAlFSiO_4$ synthesis of run G-197 was due to significant water-contamination of the sample, which stabilised zoisite instead of anorthite and fluorite, or $CaAlFSiO_4$, at the given run conditions.

a)

b)

c)
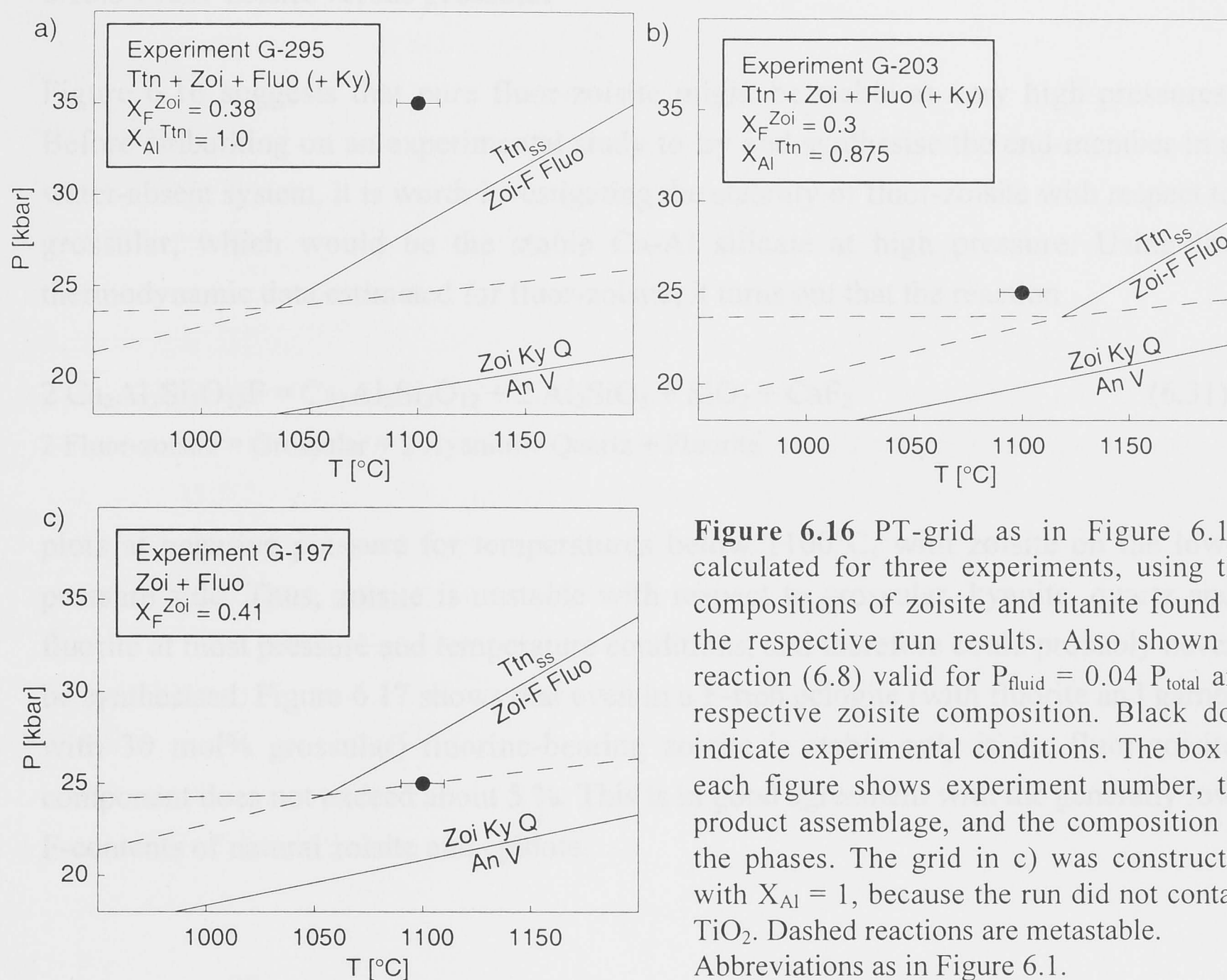
Figure 6.16 PT-grid as in Figure 6.15, calculated for three experiments, using the compositions of zoisite and titanite found in the respective run results. Also shown is reaction (6.8) valid for $P_{fluid} = 0.04 \ P_{total}$ and respective zoisite composition. Black dots indicate experimental conditions. The box in each figure shows experiment number, the product assemblage, and the composition of the phases. The grid in c) was constructed with $X_{Al} = 1$, because the run did not contain TiO_2. Dashed reactions are metastable. Abbreviations as in Figure 6.1.

The study by Tropper et al. (1999) did not succeed in the synthesis of $CaAlFSiO_4$ from anorthite and fluorite without seeds either. This is because the run conditions chosen by them (1000°C and 20 kbar) stabilise anorthite and fluorite with respect to $CaAlFSiO_4$ (Figure 5.14, p. 113), and probably also zoisite and fluorite, if water-contamination occurred. Unfortunately the abstract by Tropper et al. (1999) does not report the product assemblages.

6.13.3 Fluor-zoisite versus grossular

Figure 6.16 suggests that pure fluor-zoisite might be stable at very high pressures. Before embarking on an experimental study to try and synthesise the end-member in a water-absent system, it is worth investigating the stability of fluor-zoisite with respect to grossular, which would be the stable Ca-Al silicate at high pressure. Using the thermodynamic data estimated for fluor-zoisite, it turns out that the reaction

$$2\ Ca_2Al_3Si_3O_{12}F = Ca_3Al_2Si_3O_{12} + 2\ Al_2SiO_5 + SiO_2 + CaF_2 \qquad (6.31)$$

2 Fluor-zoisite = Grossular + 2 Kyanite + Quartz + Fluorite
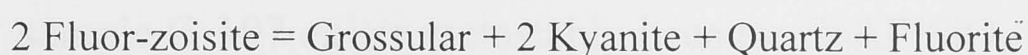
plots at negative pressure for temperatures below 1100°C, with zoisite on the low-pressure side. Thus, zoisite is unstable with respect to grossular, kyanite, quartz and fluorite at most pressure and temperature conditions, and therefore could probably never be synthesised. Figure 6.17 shows that even in a F-rich eclogite (with fluorite and garnet with 30 mol% grossular) fluorine-bearing zoisite is stable only if the fluor-zoisite component does not exceed about 5 %. This is in good agreement with the generally low F-contents of natural zoisite and epidote.
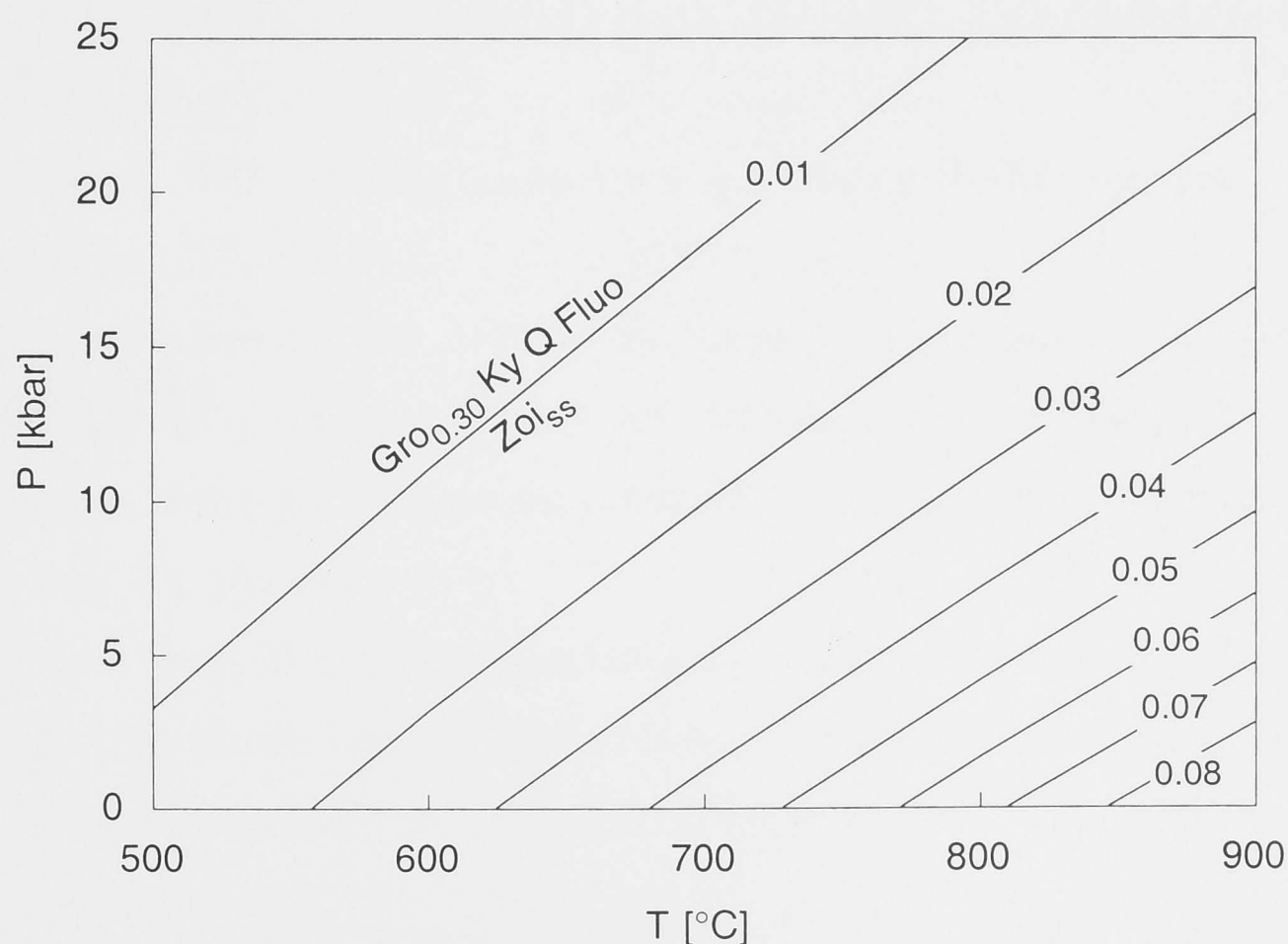
Figure 6.17 F-content of zoisite solid-solution, coexisting with garnet (30 mol% grossular component), kyanite, quartz and fluorite (reaction 6.31 in text). Numbers on isopleths represent $X_F = [F/(F + OH)]$ in zoisite.

6.14 Summary and conlusions – Part II

The thermodynamic calculations with titanite and zoisite solid-solution represent the experimental observations well, giving faith in the thermodynamic data for $CaAlFSiO_4$ and fluor-zoisite, as well as indicating that equilibrium was attained during the runs.

It is suggested by the calculations that F-rich zoisite in all experiments formed as a stable phase due to water contamination. The earlier stated hypothesis, that zoisite in sample G-197 exists metastably because $CaAlFSiO_4$ could not nucleate without seeds, is not supported by the thermodynamic modelling. It is still possible that $CaAlFSiO_4$ has difficulties to nucleate in the absence of seeds, but future experiments at higher pressure or lower temperature are needed to clarify this point.

The end-member fluor-zoisite is not stable with respect to the assemblage grossular, kyanite, quartz and fluorite at most pressures and temperatures. Fluor-zoisite can be stabilised only as solid-solution in significant dilution, which probably explains the generally low F-contents in natural zoisites.

References

Aksyuk, A.M., and Zhukovskaya, T.N. (1994) Experimental calibration of the phlogopite fluorimeter at 500-700°C and 1-4 kbar, and estimated HF concentrations of fluids associated with marble: Some examples. Geochimica et Cosmochimica Acta, 58, 4305-4315.

Aldahan, A.A., and Morad, S. (1988) Some remarks on the stability of sphene in diagenetic environments. Chemical Geology, 70, 249-255.

Andersen, D.J., Lindsley, D.H., and Davidson, P.M. (1993) QUILF: A PASCAL program to assess equilibria among Fe-Mg-Mn-Ti oxides, pyroxenes, olivine, and quartz. Computers and Geosciences, 19 (9), 1333-1350.

Angel, R.J., Kunz, M., Miletich, R., Woodland, A.B., Koch, M., and Xirouchakis, D. (1999) High-pressure phase transition in $CaTiOSiO_4$ titanite. Phase Transitions, 68 (3 Part B), 533-543.

Barton, M.D. (1982) The thermodynamic properties of topaz solid solutions and some petrologic applications. American Mineralogist, 67, 956-974.

Berman, R.G. (1988) Internally-consistent thermodynamic data for minerals in the system Na_2O-K_2O-CaO-MgO-FeO-Fe_2O_3-Al_2O_3-SiO_2-TiO_2-H_2O-CO_2. Journal of Petrology, 29, 445-522.

Berman, R.G. (1990) Mixing properties of Ca-Mg-Fe-Mn garnets. American Mineralogist, 75, 328-344.

Berman, R.G., and Brown, T.H. (1985) Heat capacity of minerals in the system Na_2O-K_2O-CaO-MgO-FeO-Fe_2O_3-Al_2O_3-SiO_2-TiO_2-H_2O-CO_2: representation, estimation, and high temperature extrapolation. Contributions to Mineralogy and Petrology, 89, 168-183.

Bernau, R., and Franz, G. (1987) Crystal chemistry and genesis of Nb-, V-, and Al-rich metamorphic titanite from Egypt and Greece. Canadian Mineralogist, 25, 695-705.

Birch, F. (1966) Compressibility; Elastic Constants. In S.P.J. Clark, Ed. Handbook of Physical Constants.

Birch, W.D. (1983) Babingtonite, fluorapophyllite and sphene from Harcourt, Victoria, Australia. Mineralogical Magazine, 47, 377-380.

Boettcher, A.L. (1970) The system CaO-Al_2O_3-SiO_2-H_2O at high pressures and temperatures. Journal of Petrology, 11, 337-79.

Bohlen, S.R., and Essene, E.J. (1978) The significance of metamorphic fluorite in the Adirondacks. Geochimica et Cosmochimica Acta, 42, 1669-1678.

Boles, J.R., and Coombs, D.S. (1977) Zeolite facies alteration of sandstones in the southland syncline, New Zealand. American Journal of Science, 277, 982-1012.

Borg, I.Y. (1970) Mechanical <110> twinning in shocked sphene. American Mineralogist, 55, 1876-1888.

Borg, I.Y., and Heard, H.C. (1972) Mechanical twinning in sphene at 8 kbar, 25° to 500°C. The Geological Society of America, Inc., Memoir, 132, 585-591.

Brese, N.E., and O'Keeffe, M. (1991) Bond-valence parameters for solids. Acta Crystallographica, B47, 192-197.

Carmichael, R.S. (1984) CRC Handbook of Physical Properties of Rocks. CRC Press Inc., Boca Raton Florida.

Carswell, D.A., Wilson, R.N., and Zhai, M. (1996) Ultra-high pressure aluminous titanites in carbonate-bearing eclogites at Shuanghe in Dabieshan, Central China. Mineralogical Magazine, 60, 461-471.

Cerny, P., Novák, M., and Chapman, R. (1995) The Al(Nb, Ta)Ti$_{-2}$ substitution in titanite: the emergence of a new species? Mineralogy and Petrology, 52, 61-73.

Cerny, P., and Povondra, P. (1972) An Al,F-rich metamict titanite from Czechoslovakia. Neues Jahrbuch für Mineralogie Monatshefte, 9, 400-406.

Cerny, P., and Riva di Sanseverino, L. (1972) Comments on crystal chemistry of titanite. Neues Jahrbuch für Mineralogie Monatshefte, 97-103.

Chatterjee, N.D., Johannes, W., and Leistner, H. (1984) The system CaO – Al$_2$O$_3$ – SiO$_2$ – H$_2$O: new phase equilibria data, some calculated phase relations, and their petrological applications. Contributions to Mineralogy and Petrology, 88, 1-13.

Chrosch, J., Bismayer, U., and Salje, E.K.H. (1997) Anti-phase boundaries and phase transitions in titanite: An X-ray diffraction study. American Mineralogist, 82, 677-681.

Cong, B., Zhai, M., Carswell, D.A., Wilson, R.N., Wang, Q., Zhao, Z., and Windley, B.F. (1995) Petrogenesis of ultrahigh-pressure rocks and their country rocks at Shuanghe in Dabieshan, Central China. European Journal of Mineralogy, 7, 119-138.

Davies, P.K., and Navrotsky, A. (1981) Thermodynamics of solid solution formation in NiO-MgO and NiO-ZnO. Journal of Solid State Chemistry, 38, 264-276.

Davies, P.K., and Navrotsky, A. (1983) Quantitative correlations of deviations from ideality in binary and pseudo-binary solid solutions. Journal of Solid State Chemistry, 46, 1-22.

Dawson, J.B., Smith, J.V., and Steele, I.M. (1994) Trace-element distribution between coexisting perovskite, apatite and titanite from Oldoinyo Lengai, Tanzania. Chemical Geology, 117, 285-290.

Deer, W.A., Howie, R.A., and Zussman, J. (1992) An Introduction to the Rock-Forming Minerals. 696 p. Longman Scientific & Technical, Hong Kong.

Delany, J.M., and Helgeson, H.C. (1978) Calculation of the thermodynamic consequences of dehydration in subducting oceanic crust to 100 kb and > 800°C. American Journal of Science, 278, 638-686.

Dempsey, M.J. (1980) Evidence for structural changes in garnet caused by calcium substitution. Contributions to Mineralogy and Petrology, 71, 281-282.

Dowty, E. (1993) ATOMS. A computer program for displaying atomic structures, Kingsport, Tennessee, USA.

Droll, K., and Seck, H.A. (1984) A new sampling technique for fluid phases in hydrothermal experiments applied to the determination of the HF-fugacities of the WFQ-buffer. Contributions to Mineralogy and Petrology, 88, 276-279.

Enami, M., Suzuki, K., Liou, J.G., and Bird, D.K. (1993) Al-Fe^{3+} and F-OH substitutions in titanite and constraints on their P-T dependence. European Journal of Mineralogy, 5, 219-231.

Essene, E.J., and Bohlen, S.R. (1985) New garnet barometers in the system CaO-FeO-Al$_2$O$_3$-SiO$_2$-TiO$_2$ (CFAST). EOS Trans. Amer. Geophys. Union, 66, 386.

Eugster, H.P., and Baumgartner, L. (1987) Mineral solubilities and speciation in supercritical metamorphic fluids. In I.S.E. Carmichael, and H.P. Eugster, Eds. Thermodynamic Modelling of Geological Materials: Minerals, Fluids and Melts; Reviews in Mineralogy 17, p. 367-403.

Evans, B.W., and Patrick, B.E. (1987) Phengite-3T in high-pressure metamorphosed granitic orthogneisses, Seward Peninsula, Alaska. Canadian Mineralogist, 25, 141-158.

Franz, G. (1987) Breakdown of amphibole and the formation of Al-titanite - an example from the polymetamorphic "Chephren-Diorite" (Gebl el Asr, SW Egypt). Publication Occasionelle, Centre International pour la formation et les échanges géologiques, Paris, 14th Colloquium African Geology, TU Berlin.

Franz, G., and Spear, F.S. (1983) High pressure metamorphism of siliceous dolomites from the central Tauern Window, Austria. American Journal of Science, 283 (A), 396-413.

Franz, G., and Spear, F.S. (1985) Aluminous titanite (sphene) from the Eclogite Zone, south-central Tauern Window, Austria. Chemical Geology, 50, 33-46.

Frost, B.R., Camberlain, K.R., and Schumacher, J.C. (2000) Sphene (titanite): Phase relations and role as a geochronometer. Chemical Geology, *in press.*

Frost, B.R., and Lindsley, D.H. (1992) Equilibria among Fe-Ti oxides, pyroxenes, olivine, and quartz: Part II. Application. American Mineralogist, 77, 1004-1020.

Frost, B.R., Lindsley, D.H., and Andersen, D.J. (1988) Fe-Ti oxide-silicate equilibria: Assemblages with fayalitic olivine. American Mineralogist, 73, 727-740.

Frost, R.B. (1991) Introduction to oxygen fugacity and its petrologic importance. In D.H. Lindsley, Ed. Oxide Minerals: Petrologic and magnetic significance; Reviews in Mineralogy 25, p. 1-9.

Fyfe, W.S., Turner, F.J., and Verhoogen, J. (1958) Metamorphic reactions and metamorphic facies. Waverly Press Inc., Baltimore.

Ganguly, J., and Saxena, S.K. (1987) Mixtures and Mineral Reactions. 291 p. Springer Verlag, Heidelberg.

Gascoyne, M. (1986) Evidence for the stability of the potential nuclear waste host, sphene, over geological time, from uranium-lead ages and uranium-series measurements. Applied Geochemistry, 1, 199-210.

Ghent, E.D., and Stout, M.Z. (1994) Geobarometry of low-temperature eclogites: applications of isothermal pressure-activity calculations. Contributions to Mineralogy and Petrology, 116, 500-507.

Ghose, S., Yoshiaki, I., and Hatch, D.M. (1991) Paraelectric-antiferroelectric phase transition in titanite, $CaTiSiO_5$. II. A high temperature X-ray diffraction study of the order parameter and transition mechanism. Physics and Chemistry of Minerals, 17, 591-603.

Gibert, F., Moine, B., and Gibert, P. (1990) Aluminous titanite (sphene) crystallized under low/medium pressure in the calc-silicate gneisses of the Montagne Noire. Comptes Rendus de l'Académie des Sciences, Série II, t. 311, 657-663.

Gieré, R. (1992) Compositional variation of metasomatic titanite from Adamello (Italy). Schweizer Mineralogisch Petrographische Mitteilungen, 72, 167-177.

Gittins, J., and Tuttle, O.F. (1964) The system CaF_2 - $Ca(OH)_2$ - $CaCO_3$. American Journal of Science, 262, 66-75.

Gopal, E.S.R. (1966) Specific Heats at low Temperatures. 240 p. Heywood Books, London.

Grapes, R., and Watanabe, T. (1992) Paragenesis of titanite in metagreywackes of the Franz Josef-Fox Glacier area, Southern Alps, New Zealand. European Journal of Mineralogy, 4, 547-555.

Green, T.H., and Pearson, N.J. (1986) Ti-rich accessory phase saturation in hydrous mafic-felsic compositions at high P,T. Chemical Geology, 54, 185-201.

Groat, L.A., Kek, S., Bismayer, U., Schmidt, C., Krane, H.G., Meyer, H., Nistor, L., and Van Tendeloo, G. (1996) A synchroton radiation, HRTEM, X-ray powder diffraction, and Raman spectroscopic study of malayaite, $CaSnSiO_5$. American Mineralogist, 81, 595-602.

Haar, L., Gallagher, J.S., and Kell, G.S. (1984) NBS/NRC Steam Tables. Thermodynamic and Transport Properties and Computer Programs for Vapor and Liquid States of Water in SI Units. 320 p. Hemisphere Publishing Corporation, Washington.

Haas, J.L., Jr., and Fisher, J.R. (1976) Simultaneous evaluation and correlation of thermodynamic data. American Journal of Science, 276, 525-545.

Hammer, V.M.F., Beran, A., Endisch, D., and Rauch, F. (1996) OH concentrations in natural titanites determined by FTIR spectroscopy and nuclear reaction analysis. European Journal of Mineralogy, 8, 281-288.

Hammonds, K.D., Bosenick, A., Dove, M.T., and Heine, V. (1998) Rigid unit modes in crystal structures with octahedrally coordinated atoms. American Mineralogist, 83, 476-479.

Haselton, H.T., and Newton, R.C. (1980) Thermodynamics of pyrope-grossular garnets and their stabilities at high temperatures and high pressures. Journal of Geophysical Research, 85, 6973-6982.

Haselton, H.T.J., Cygan, G.L., and D'Angelo, W.M. (1988) Chemistry of aqueous solutions coexisting with fluoride buffers in the system K_2O-Al_2O_3-SiO_2-H_2O-F_2O (1 kbar, 400°-700°C). Economic Geology, 83, 163-173.

Hawthorne, F.C., Groat, L.A., Raudsepp, M., Ball, N.A., Kimata, M., Spike, F.D., Gaba, R., Halden, N.M., Lumpkin, G.R., Ewing, R.C., Greegor, R.B., Lytle, F.W., Ercit, T.S., Rossman, G.R., Wicks, F.J., Ramik, R.A., Sherrif, B.L., Fleet, M.E., and McCammon, C. (1991) Alpha-decay damage in titanite. American Mineralogist, 75, 370-396.

Hayward, P.J., and Cecchetto, E.V. (1982) Development of sphene-based glass ceramics tailored for canadian waste disposal conditions. In V. Topp, Ed. The scientific basis for nuclear waste management, 3, p. 91-98. Elsevier, Boston.

Hazen, R.M., and Finger, L.W. (1982) Comparative Crystal Chemistry. John Wiley & Sons, New York.

Helgeson, H.C., Delany, J.M., Nesbitt, H.W., and Bird, D.K. (1978) Summary and critique of the thermodynamic properties of rock-forming minerals. American Journal of Science, 278A, 221.

Hellman, P.L., and Green, T.H. (1979) The role of sphene as an accessory phase in high-pressure partial melting of hydrous mafic compositions. Earth and Planetary Science Letters, 42, 191-201.

Hensen, B.J., Schmidt, R., and Wood, B.J. (1975) Activity-composition relationships for pyrope-grossular garnet. Contributions to Mineralogy and Petrology, 51, 161-166.

Higgins, J.B., and Ribbe, P.H. (1976) The crystal chemistry and space groups of natural and synthetic titanites. American Mineralogist, 61, 878-888.

Hirajima, T., Zhang, R., Li, J., and Cong, B. (1992) Petrology of the nyböite-bearing eclogite in the Donghai area, Jiangsu Province, eastern China. Mineralogical Magazine, 56, 37-46.

Hollabaugh, C.L., and Foit, F.F. (1984) The crystal structure of an Al-rich titanite from Grisons, Switzerland. American Mineralogist, 69, 725-732.

Hollabaugh, C.L., and Rosenberg, P.E. (1983) Substitution of Ti for Si in titanite and new end-member cell dimensions for titanite. American Mineralogist, 68, 177-180.

Holland, T.J.B. (1979) High water activities in the generation of high pressure kyanite eclogites of the Tauern Window. Journal of Geology, 87, 1-27.

Holland, T.J.B. (1983) The experimental determination of activities in disordered and short-range ordered jadeitic pyroxenes. Contributions to Mineralogy and Petrology, 82, 214-220.

Holland, T.J.B., and Powell, R. (1985) An internally consistent thermodynamic dataset with uncertainties and correlations: 2. Data and results. Journal of Metamorphic Geology, 3, 343-370.

Holland, T.J.B., and Powell, R. (1990) An enlarged and updated internally consistent thermodynamic dataset with uncertainties and correlations: the system $K_2O-Na_2O-CaO-MgO-MnO-FeO-Fe_2O_3-Al_2O_3-TiO_2-SiO_2-C-H_2-O_2$. Journal of Metamorphic Geology, 8, 89-124.

Holland, T.J.B., and Powell, R. (1998) An internally consistent thermodynamic data set for phases of petrological interest. Journal of Metamorphic Geology, 16, 309-343.

Hughes, J.M., Bloodaxe, E.S., Hanchar, J.M., and Foord, E.E. (1997) Incorporation of rare earth elements in titanite: Stabilization of the $A2/a$ dimorph by creation of antiphase boundaries. American Mineralogist, 82, 512-516.

Hunt, J.A., and Kerrick, D.M. (1977) The stability of sphene: experimental redetermination and geologic implications. Geochimica et Cosmochimica Acta, 41, 279-288.

Itaya, T., Brothers, R.N., and Black, P.M. (1985) Sulfides, oxides and sphene in high-pressure schist from New Caledonia. Contributions to Mineralogy and Petrology, 91, 151-162.

Izumi, F. (1993) Rietveld analysis programs RIETAN and PREMOS and special applications. In R.A. Young, Ed. The Rietveld Method. Oxford University Press, Oxford, 236-253.

Jacobs, G.K., and Kerrick, D.M. (1981) Devolatilization equilibria in H_2O-CO_2 and H_2O-CO_2-NaCl fluids: an experimental and thermodynamic evaluation at elevated pressures and temperatures. American Mineralogist, 66, 1135-1153.

Jaffe, H.W. (1947) Reexamination of sphene (titanite). American Mineralogist, 32, 637-642.

Johnson, J.W., Oelkers, R.H., and Helgeson, H.C. (1991) SUPCRT92: A software package for calculating the standard molal thermodynamic properties of minerals, gases, aqueous species, and reactions from 1 to 5000 bars and 0° to 1000°C. Short course manual presented at the Annual Meeting of the Geological Society of America, 1991, 151 p.

Kato, T., Enami, M., and Zhai, M. (1997) Ultra-high-pressure (UHP) marble and eclogite in the Su-Lu UHP terrane, eastern China. Journal of Metamorphic Geology, 15, 169-182.

Kek, S., Aroyo, M., Bismayer, U., Schmidt, C., Eichhorn, K., and Krane, H.G. (1997) The two-step phase transition of titanite, $CaTiSiO_5$: a synchrotron radiation study. Zeitschrift für Kristallographie, 212, 9-19.

Kerrick, D.M., and Jacobs, G.K. (1981) A modified Redlich-Kwong equation for H_2O, CO_2, and H_2O-CO_2 mixtures at elevated pressures and temperatures. American Journal of Science, 281, 735-767.

Kieffer, S.W. (1980) Thermodynamics and lattice vibrations of minerals: 4. Application to chain and sheet silicates and orthosilicates. Reviews of Geophysics and Space Physics, 18 (4), 862-886.

Kim, Y.-I., and Izumi, F. (1994) Structure refinement with a new version of the Rietveld-refinement program RIETAN. Journal of the Ceramic Society of Japan, 102, 401-404.

King, E.G., Orr, R.L., and Bonnickson, K.R. (1954) Low temperature heat capacity, entropy at 287.16°K, and high temperature heat content of sphene ($CaTiSiO_5$). Journal of the American Chemical Society, 76, 4320-4321.

Kowallis, B.J., Christiansen, E.H., and Griffin, D.T. (1997) Compositional variations in titanite. Geological Society of America, 1997 Annual Meeting, Abstracts with Programs, 29 (6), 402.

Krogh, E.J., Andresen, A., Bryhni, I., Broks, T.M., and Kristensen, S.E. (1990) Eclogites and polyphase P-T cycling in the Caledonian Uppermost Allochthon in Troms, northern Norway. Journal of Metamorphic Geology, 8, 289-309.

Kunz, M., Xirouchakis, D., Lindsley, D.H., and Häusermann, D. (1996) High-pressure phase transition in titanite ($CaTiOSiO_4$). American Mineralogist, 81, 1527-1530.

Kunz, M., Xirouchakis, D., Wang, Y., Parise, J.B., and Lindsley, D.H. (1997) Structural investigations along the join $CaTiOSiO_4$-$CaSnOSiO_4$. Schweizerische Mineralogische und Petrographische Mitteilungen, 77, 1-11.

Leonard, B.F., and Buddington, A.F. (1964) Ore deposits of the St. Lawrence Co. Magnetite district, N. W. Adirondacks, NY. U. S. Geological Survey Professional Paper, 377, 1-259.

Lindsley, D.H., and Frost, B.R. (1992) Equilibria among Fe-Ti oxides, pyroxenes, olivine, and quartz: Part I. Theory. American Mineralogist, 77, 987-1003.

López Sánchez-Vizcaíno, V., Connolly, J.A.D., and Gómez-Pugnaire, M.T. (1997) Metamorphism and phase relations in carbonate rocks from the Nevado-Filábride Complex (Cordilleras Béticas, Spain): application of the Ttn + Rt + Cal + Qtz + Gr buffer. Contributions to Mineralogy and Petrology, 126, 292-302.

Maier, C.G., and Kelley, K.K. (1932) An equation for the representation of high temperature heat content data. Journal of the American Chemical Society, 54, 3243-3246.

Makanjuola, A.A., and Howie, R.A. (1972) The mineralogy of the glaucophane schists and associated rocks from Île de Groix, Brittany, France. Contributions to Mineralogy and Petrology, 35, 83-118.

Manning, C.E., and Bohlen, S.R. (1991) The reaction titanite + kyanite = anorthite + rutile and titanite-rutile barometry in eclogites. Contributions to Mineralogy and Petrology, 109, 1-9.

Markl, G., and Piazolo, S. (1999) Stability of high-Al titanite from low-pressure calcsilicates in light of fluid and host-rock composition. American Mineralogist, 84, 37-47.

McNear, E., Vincent, M.G., and Parthé, E. (1976) The crystal structure of vuagnatite, $CaAl(OH)SiO_4$. American Mineralogist, 61, 831-838.

Meyer, H.-W., Bismayer, U., Adiwidjaja, G., Zhang, M., Nistor, L., and Van Tendeloo, G. (1998) Natural titanite and malayaite: Structural invesitgations and the 500 K anomaly. Phase Transitions, 67, 27-49.

Meyer, H.W., Zhang, M., Bismayer, U., Salje, E.K.H., Schmidt, C., Kek, S., Morgenroth, W., and Bleser, T. (1996) Phase transformation of natural titanite: an infrared, Raman spectroscopic, optical birefringence and X-ray diffraction study. Phase Transitions, 59, 39-60.

Miller, A.R. (1981) BASIC Programs for Scientists and Engineers. SYBEX Inc., Berkeley, 318 p.

Mukhopadhyay, A., Bhattacharya, A., and Mohanty, L. (1992) Geobarometers involving clinopyroxene, garnet, plagioclase, ilmenite, rutile, sphene and quartz: estimation of pressure in quartz-absent assemblages. Contributions to Mineralogy and Petrology, 110, 346-354.

Munoz, J.L., and Eugster, H.P. (1969) Experimental control of fluorine reactions in hydrothermal systems. American Mineralogist, 54, 943-959.

Munoz, J.L., and Ludington, S.D. (1974) Fluoride-hydroxyl exchange in biotite. American Journal of Science, 274, 396-413.

Nakada, S. (1991) Magmatic processes in titanite-bearing dacites, central Andes of Chile and Bolivia. American Mineralogist, 76, 548-560.

Navrotsky, A. (1994) Physics and chemistry of earth materials. 417 p. Cambridge University Press, New York.

Newton, R.C., and Haselton, H.T. (1981) Thermodynamics of the garnet-plagioclase-Al_2SiO_5-quartz geobarometer. In R.C. Newton, A. Navrotsky, and B.J. Wood, Eds. Thermodynamics of Minerals and Melts, p. 131-148. Springer Verlag, New York.

Newton, R.C., and Wood, B.J. (1980) Volume behavior of silicate solid solutions. American Mineralogist, 65, 733-745.

Nickel, E.H., and Grice, J.D. (1998) The IMA commission on new minerals and mineral names: procedures and guidelines on mineral nomenclature, 1998. The Canadian Mineralogist, 36, 913-926.

Oberti, R., Smith, D.C., Rossi, G., and Caucia, F. (1991) The crystal-chemistry of high-aluminium titanites. European Journal of Mineralogy, 3, 777-792.

Ohmoto, H., and Kerrick, D. (1977) Devolatilization equilibria in graphitic systems. American Journal of Science, 277, 1013-1044.

Pan, Y., Fleet, M.E., and MacRae, N.D. (1993) Late alteration in titanite ($CaTiSiO_5$): Redistribution and remobilization of rare earth elements and implications for U/Pb and Th/Pb geochronology and nuclear waste disposal. Geochimica et Cosmochimica Acta, 57, 355-367.

Pan, Y., Fleet, M.E., and Williams, H.R. (1995) Rare earth element mobility during prograde granulite-facies metamorphism: Significance of halogens. Programs and Abstracts Geological Association of Canada, 20, 79.

Paterson, B.A., and Stephens, W.E. (1992) Kinetically induced compositional zoning in titanite: implications for accessory-phase/melt partitioning of trace elements. Contributions to Mineralogy and Petrology, 109, 373-385.

Perkins, D., Westrum Jr., E.F., and Essene, E.J. (1980) The thermodynamic properties and phase relations of some minerals in the system CaO-Al$_2$O$_3$-SiO$_2$-H$_2$O. Geochimica et Cosmochimica Acta, 44, 61-84.

Perseil, E.-A., and Smith, D.C. (1995) Sb-rich titanite in the manganese concentrations at St. Marcel-Praborna, Aosta Valley, Italy: petrography and crystal-chemistry. Mineralogical Magazine, 59, 717-734.

Piccoli, P.M., and Candela, P.A. (1991) Zoning in titanite and f(O$_2$) history. Abstracts with Programs Geological Society of America, 23 (1), 115.

Poirer, J.-P. (1991) Introduction to the Physics of the Earth's Interior. 264 p. Cambridge University Press.

Powell, R. (1978) Equilibrium Thermodynamics in Petrology. 284 p. Harper & Row Ltd, London.

Powell, R., and Holland, T.J.B. (1985) An internally consistent thermodynamic dataset with uncertainties and correlations: 1. Methods and a worked example. Journal of Metamorphic Geology, 3, 327-342.

Pownceby, M.I., and O'Neill, H.S.C. (1994) Thermodynamic data from redox reactions at high temperatures. III. Activity-composition relations in Ni-Pd alloys from EMF measurements at 850-1250 K, and calibration of the NiO+Ni-Pd assemblage as a redox sensor. Contributions to Mineralogy and Petrology, 116, 327-339.

Price, J.D., Hogan, J.P., Gilbert, M.C., and IV, M.G.B. (1999) Experimental study of titanite-fluorite equilibria in the A-type Mount Scott Granite: Implications for assessing F contents of felsic magmas. Geology, 27 (10), 951-954.

Ribbe, P.H. (1980) Titanite. In P.H. Ribbe, Ed. Orthosilicates; Reviews in Mineralogy 5, p. 137-154.

Rice, J.M. (1980) Phase equilibria involving humite minerals in impure limestones, Part I. Calculated stability of clinohumite. Contributions to Mineralogy and Petrology, 71, 219-235.

Richet, P., Bottinga, Y., Denielou, L., Petitet, J.P., and Tequi, C. (1982) Thermodynamic properties of quartz, cristobalite and amorphous SiO_2: drop calorimetry measurements between 1000 and 1800 K and a review from 0 to 2000 K. Geochimica et Cosmochimica Acta, 46, 2639-2658.

Robie, R.A., and Hemingway, B.S. (1995) Thermodynamic properties of minerals and related substances at 298.15 K and 1 bar (10^5 Pascals) pressure and at higher higher temperatures. 461 p.

Rosenberg, P.E. (1974) Compositional variations in synthetic sphene. Abstracts with Programs Geological Society of America, 6, 1060.

Russell, J.K., Groat, L.A., and Halleran, A.D. (1994) LREE-rich niobian titanite from Mount Bisson, British Columbia: Chemistry and exchange mechanisms. Canadian Mineralogist, 32, 575-587.

Sahama, T.G. (1946) On the chemistry of the mineral titanite. C. R. Soc. Geol. Finlande, 19 (138), 88-120.

Sakata, M., and Cooper, M.J. (1979) An analysis of the Rietveld profile refinement method. Journal of Applied Crystallography, 12, 554-563.

Salje, E., Schmidt, C., and Bismayer, U. (1993) Structural phase transition in titanite, $CaTiSiO_5$: A Ramanspectroscopic Study. Physics and Chemistry of Minerals, 19, 502-506.

Sarp, H., Bertrand, J., and Mc Near, E. (1976) Vuagnatite, $CaAl(OH)SiO_4$, a new natural calcium aluminium nesosilicate. American Mineralogist, 61, 825-830.

Schreyer, W. (1988) Experimental studies on metamorphism of crustal rocks under mantle pressures. Mineralogical Magazine, 52, 1-26.

Scott, H.G. (1983) The estimation of standard deviations in powder diffraction Rietveld refinements. Journal of Applied Crystallography, 16, 159-163.

Smith, D.C. (1980) Highly aluminous sphene (titanite) in natural high-pressure hydrous-eclogite-facies rocks from Norway and Italy, and in experimental runs at high pressure. 26th International Geological Congress, Paris, France (abstract), section 02.3.1, 145.

Smith, D.C. (1981) The pressure and temperature dependence of Al-solubility in sphene in the system Ti-Al-Ca-Si-O-F. Progress in Experimental Petrology N.E.R.C. Publication Series, D-18, 193-197.

Sobolev, N.V., and Shatsky, V.S. (1990) Diamond inclusions in garnets from metamorphic rocks: a new environment for diamond formation. Nature, 343, 742-746.

Spear, F.S (1993) Metamorphic Phase Equilibria and Pressure-Temperature-Time Paths. 799 p. Mineralogical Society of America, Washington.

Spear, F.S. (1981) An experimental study of hornblende stability and compositional variability in amphibolite. American Journal of Science, 281, 697-734.

Speer, J.A., and Gibbs, G.V. (1976) The crystal structure of synthetic titanite $CaTiOSiO_4$, and the domain textures of natural titanites. American Mineralogist, 61, 238-247.

Stephenson, N.C.N., and Cook, N.D.J. (1997) Metamorphic evolution of calcsilicate granulites near Battye Glacier, northern Prince Charles Mountains, East Antarctica. Journal of Metamorphic Geology, 15, 361-378.

Tanaka, I., Obuchi, T., and Kojima, H. (1988) Growth and characterization of titanite $(CaTiSiO_5)$ single crystals by the floating zone method. Journal of Crystal Growth, 87, 169-174.

Taylor, M., and Brown, G.E. (1976) High-temperature structural study of the $P2_1/a$ <-> $A2/a$ phase transition in synthetic titanite, $CaTiSiO_5$. American Mineralogist, 61, 435-447.

Thiéblot, L., Téqui, C., and Richet, P. (1999) High-temperature heat capacity of grossular $(Ca_3Al_2Si_3O_{12})$, enstatite $(MgSiO_3)$ and titanite $(CaTiSiO_5)$. American Mineralogist, 84, 848-855.

Thompson, A.B., and Ellis, D.J. (1994) $CaO + MgO + Al_2O_3 + SiO_2 + H_2O$ to 35 KB: Amphibole, talc, and zoisite dehydration and melting reactions in the silica-excess part of the system and their possible significance in subduction zones, amphibolite melting, and magma fractionation. American Journal of Science, 294, 1229-1289.

Thompson, J.B.J. (1967) Thermodynamic properties of simple solid solutions. In P.H. Abelson, Ed. Researches in Geochemistry, 2, p. 340-361. Wiley.

Tribuzio, R., Messiga, B., Vannucci, R., and Bottazzi, P. (1996) Rare earth element redistribution during high-pressure-low-temperature metamorphism in ophiolitic Fe-gabbros (Liguria, northwestern Italy): Implications for light REE mobility in subduction zones. Geology, 24 (8), 711-714.

Troitzsch, U., and Ellis, D.J. (1998) The first synthesis of Al-rich titanite ($X_{Al} > 0.5$) including the new end-member $CaAlFSiO_4$. AGU abstract, EOS transactions, 70 (45), 972.

Troitzsch, U., and Ellis, D.J. (1999) The synthesis and crystal structure of $CaAlFSiO_4$, the Al-F analog of titanite. American Mineralogist, 84, 1162-1169.

Troitzsch, U., Ellis, D.J., Thompson, J., and Fitz-Gerald, J. (1999) Crystal structural changes in titanite along the join TiO-AlF. European Journal of Mineralogy, 6, 955-965.

Tropper, P., Manning, C., and Essene, E. (2000) Activity-composition relations of titanite in the system $CaTiOSiO_4O$-$CaAlSiO_4F$ at 1000-1100°C. Journal of Conference Abstracts, 5 (1), 104.

Tropper, P., Manning, C.E., and Essene, E.J. (1999) The synthesis and stability of Al-F-rich titanites between 900 and 1100°C and 11 to 40 kbar. Berichte der Deutschen Mineralogischen Gesellschaft, 1, 230.

Ulbrich, H.H., and Waldbaum, D.R. (1976) Structural and other contributions to the third-law entropies of silicates. Geochimica et Cosmochimica Acta, 40, 1-24.

Valley, J.W., and Essene, E.J. (1980) Calc-silicate reactions in Adirondack marbles: The role of fluids and solid solutions: Summary. Geological Society of America Bulletin, 91 (1), 114-117.

Valley, J.W., Petersen, E.U., Essene, E.J., and Bowman, J.R. (1982) Fluorphlogopite and fluortremolite in Adirondack marbles and calculated C-O-H-F fluid compositions. American Mineralogist, 67, 545-557.

Van Heurck, C., Van Tendeloo, G., Ghose, S., and Amelinckx, S. (1991) Paraelectric-antiferroelectric phase transition in titanite, $CaTiSiO_5$. II. Electron diffraction and electron microscopic studies of the transition dynamics. Physics and Chemistry of Minerals, 17, 604-610.

Webster, L.D., and Holloway, J.R. (1990) Partitioning of F and Cl between magmatic hydrothermal fluids and highly evolved granitic magmas. In H.J. Stein, and J.L. Hannah, Eds. Ore-bearing granite systems; Petrogenesis and mineralizing processes, Geol. Soc. Amer. Special Paper 246, p. 21-34.

Wilson, A.J.C., Shmuelli, U., and Hahn, T. (1992) International Tables for Crystallography. D. Reidel Pub. Co., Dordrecht.

Wones, D.R. (1989) Significance of the assemblage titanite + magnetite + quartz in granitic rocks. American Mineralogist, 74, 744-749.

Wood, B.J. (1978) Elementary Thermodynamics for Geologists. 303 p. Oxford University Press, Oxford.

Xirouchakis, D., Fritsch, S., Putnam, R.L., Navrotsky, A., and Lindsley, D.H. (1997a) Thermochemistry and the enthalpy of formation of synthetic end-member ($CaTiSiO_5$) titanite. American Mineralogist, 82, 754-759.

Xirouchakis, D., Kunz, M., Parise, J.B., and Lindsley, D.H. (1997b) Synthesis methods and unit-cell volume of end-member titanite ($CaTiOSiO_4$). American Mineralogist, 82, 748-753.

Xirouchakis, D., and Lindsley, D.H. (1998) Equilibria among titanite, hedenbergite, fayalite, quartz, ilmenite, and magnetite: Experiments and internally consistent thermodynamic data for titanite. American Mineralogist, 83, 712-725.

Xirouchakis, D., and Tangeman, J.A. (1998) Thermochemistry of end-member titanite ($CaTiSiO_5$). EOS, Transactions, AGU Fall Meeting Abstract, 79 (45), 880.

Yau, Y.-C., Anovitz, L.M., Essene, E.J., and Peacor, D.R. (1984) Phlogopite-chlorite reaction mechanisms and physical conditions during retrograde reactions in the Marble Formation, Franklin, New Jersey. Contributions to Mineralogy and Petrology, 88, 299-306.

Ye, K., and Hirajima, T. (1996) High-pressure marble at Yangguantun, Rongcheng County, eastern China. Mineralogy and Petrology, 57, 151-156.

Zhang, M., Salje, E., and Bismayer, U. (1997) Structural phase transition near 825 K in titanite: Evidence from infrared spectroscopic observations. American Mineralogist, 82, 30-35.

Zhang, M., Salje, E.K.H., Bismayer, U., Unruh, H.-G., Wruck, B., and Schmidt, C. (1995) Phase transition(s) in titanite $CaTiSiO_5$: An infrared spectroscopic, dielectric response and heat capacity study. Physics and Chemistry of Minerals, 22, 41-49.

Electron microprobe analyses (representative selection): Titanite

exp. no	G-312	G-312	G-312	G-312	G-183	G-183	G-183	G-183	G-183	G-184	G-184	G-185	G-185	G-185	G-185	G-185
phase	titanite	titanite	titanite	titanite	titanite	titanite	titanite	titanite	titanite	titanite	titanite	titanite	titanite	titanite	titanite	titanite
wt.% atoms																
Si	14.11	14.46	14.07	14.68	14.59	14.87	14.57	14.68	14.65	14.67	14.77	14.58	14.74	14.63	14.63	14.58
Ti	23.89	21.33	20.60	18.43	12.94	10.90	13.39	12.97	14.14	13.76	12.39	15.61	12.98	13.52	13.91	13.45
Al	0.10	2.21	2.52	2.68	6.73	7.99	6.47	6.70	6.12	6.21	7.21	5.60	6.82	6.40	6.26	6.37
Ca	20.71	20.79	20.46	21.01	21.42	21.80	21.54	21.55	21.30	21.80	22.01	21.30	21.67	21.62	21.44	21.65
F	0.32	2.53	3.11	2.35	4.31	5.55	4.12	4.41	4.22	3.89	4.54	3.65	4.50	4.09	3.94	4.24
O	39.04	38.96	38.33	39.19	38.13	38.73	39.09	38.62	39.17	38.80	38.88	39.54	38.84	38.91	38.75	38.74
total	98.17	100.28	99.09	98.34	98.12	99.84	99.18	98.93	99.60	99.13	99.80	100.28	99.55	99.17	98.93	99.03
wt.% oxides (normalized to 100%)																
SiO_2	30.33	30.24	29.80	31.74	31.28	31.45	31.18	31.32	31.19	31.24	31.22	30.81	31.26	31.20	31.22	31.13
TiO_2	40.04	34.76	34.05	31.06	21.63	17.98	22.33	21.58	23.45	22.85	20.42	25.71	21.45	22.49	23.14	22.38
Al_2O_3	0.18	4.07	4.71	5.12	12.74	14.93	12.22	12.63	11.50	11.67	13.46	10.44	12.77	12.06	11.79	12.01
CaO*	29.12	28.45	28.36	29.72	30.04	30.17	30.15	30.08	29.66	30.36	30.42	29.44	30.05	30.16	29.92	30.24
F	0.32	2.48	3.07	2.37	4.32	5.48	4.12	4.39	4.20	3.87	4.49	3.61	4.46	4.08	3.93	4.23
sum	100	100	100	100	100	100	100	100	100	100	100	100	100	100	100	100
(*:based on mole CaO + CaF2)																
stoichiometry based on 3 cations																
Si	0.991	0.990	0.979	1.024	0.990	0.994	0.988	0.993	0.994	0.990	0.986	0.983	0.991	0.989	0.990	0.988
Ti	0.984	0.856	0.841	0.754	0.515	0.428	0.532	0.514	0.562	0.544	0.485	0.617	0.512	0.536	0.552	0.534
Al	0.007	0.157	0.182	0.195	0.475	0.556	0.456	0.472	0.432	0.436	0.501	0.393	0.477	0.450	0.441	0.449
Ca	1.019	0.998	0.998	1.027	1.019	1.022	1.023	1.021	1.012	1.030	1.029	1.007	1.021	1.024	1.017	1.028
F	0.033	0.256	0.319	0.242	0.432	0.548	0.413	0.440	0.423	0.388	0.448	0.365	0.447	0.409	0.394	0.425
O	4.811	4.680	4.683	4.802	4.527	4.426	4.542	4.522	4.560	4.558	4.497	4.615	4.517	4.546	4.566	4.535
Al+Ti	0.991	1.013	1.023	0.949	0.990	0.984	0.989	0.986	0.994	0.980	0.986	1.010	0.988	0.987	0.993	0.983
sum an	4.844	4.937	5.002	5.044	4.959	4.974	4.955	4.963	4.983	4.946	4.945	4.979	4.965	4.955	4.960	4.960
X_{Al}	0.007	0.155	0.178	0.205	0.480	0.565	0.462	0.478	0.434	0.445	0.508	0.389	0.483	0.456	0.444	0.457

Appendix 1

Electron microprobe analyses (representative selection): Titanite

exp. no	G-186	G-186	G-186	G-186	G-186	G-186	G-187	G-187	G-194	G-194	G-194	G-194	G-194	G-313	G-313	G-313
phase	titanite	titanite	titanite	titanite	titanite	titanite	titanite	titanite	titanite	titanite	titanite	titanite	titanite	titanite	titanite	titanite
wt.% atoms																
Si	14.22	15.18	15.06	15.25	14.43	14.35	14.84	14.69	15.00	15.12	15.14	14.95	15.04	14.60	15.45	15.33
Ti	18.29	9.86	9.85	8.54	18.48	17.50	13.10	13.35	9.49	7.93	7.80	10.22	9.18	18.54	7.56	8.24
Al	3.68	8.29	8.39	8.89	3.53	4.11	6.68	6.63	9.01	10.02	9.77	8.16	9.23	3.60	10.49	10.03
Ca	21.34	21.94	21.84	21.66	21.32	21.28	21.72	21.47	22.10	21.99	22.01	22.13	22.31	20.90	21.65	21.75
F	2.65	5.05	5.30	5.40	2.36	2.72	4.18	4.06	5.77	7.00	6.62	5.81	6.17	2.79	7.58	7.02
O	38.72	39.20	37.90	36.82	38.85	39.09	38.58	38.00	37.85	37.50	37.91	38.47	38.26	38.64	36.95	37.33
total	98.90	99.52	98.34	96.56	98.97	99.05	99.10	98.20	99.22	99.56	99.25	99.74	100.19	99.07	99.68	99.70
wt.% oxides (normalized to 100%)																
SiO_2	30.30	32.36	32.09	32.82	30.71	30.65	31.49	31.33	12.45	12.42	12.44	12.35	12.33	30.93	31.98	31.85
TiO_2	30.40	16.39	16.38	14.33	30.63	29.14	21.69	22.19	4.62	3.82	3.76	4.95	4.41	30.59	12.19	13.35
Al_2O_3	6.92	15.62	15.80	16.90	6.63	7.75	12.52	12.49	7.79	8.56	8.36	7.01	7.88	6.74	19.18	18.42
CaO*	29.74	30.60	30.45	30.50	29.68	29.75	30.15	29.95	12.86	12.65	12.68	12.81	12.82	28.97	29.31	29.56
F	2.64	5.03	5.28	5.44	2.35	2.72	4.15	4.05	7.09	8.50	8.04	7.10	7.48	2.76	7.33	6.82
sum	100	100	100	100	100	100	100	100	55	54	55	56	55	100	100	100

(*:based on mole CaO + CaF2)

stoichiometry based on 3 cations

	G-186	G-186	G-186	G-186	G-186	G-186	G-187	G-187	G-194	G-194	G-194	G-194	G-194	G-313	G-313	G-313
Si	0.976	1.013	1.006	1.024	0.987	0.983	0.996	0.991	0.990	0.995	1.002	0.998	0.988	0.999	1.008	1.003
Ti	0.736	0.386	0.386	0.336	0.740	0.703	0.516	0.528	0.367	0.306	0.303	0.400	0.353	0.743	0.289	0.316
Al	0.263	0.576	0.584	0.621	0.251	0.293	0.467	0.466	0.620	0.686	0.673	0.567	0.631	0.257	0.713	0.683
Ca	1.026	1.026	1.023	1.019	1.022	1.022	1.021	1.015	1.023	1.013	1.021	1.035	1.027	1.002	0.990	0.997
F	0.269	0.497	0.524	0.536	0.239	0.276	0.415	0.405	0.564	0.681	0.648	0.574	0.599	0.282	0.731	0.679
O	4.709	4.438	4.423	4.402	4.733	4.694	4.538	4.550	4.385	4.303	4.318	4.395	4.357	4.638	4.232	4.287
Al+Ti	0.999	0.962	0.971	0.957	0.992	0.995	0.982	0.994	0.987	0.992	0.976	0.967	0.985	0.999	1.002	1.000
sum an	4.978	4.935	4.947	4.939	4.972	4.970	4.953	4.955	4.949	4.984	4.966	4.968	4.957	4.920	4.963	4.966
X_{Al}	0.263	0.599	0.602	0.649	0.253	0.294	0.475	0.469	0.628	0.691	0.690	0.586	0.641	0.257	0.711	0.684

Electron microprobe analyses (representative selection): Titanite

exp. no	G-313	G-313	G-198	G-198	G-198	G-198	G-198	G-199	G-200	G-200	G-200	G-201	G-201	G-201	G-203	G-203
phase	titanite	titanite	titanite	titanite	titanite	titanite	titanite	titanite	titanite	titanite	titanite	titanite	titanite	titanite	titanite	titanite
wt.% atoms																
Si	15.73	15.72	14.10	14.19	14.22	14.21	14.13	15.06	15.35	15.36	15.26	15.66	15.97	15.51	15.54	15.47
Ti	6.28	6.49	16.35	16.64	16.53	16.11	16.24	3.69	2.62	2.81	2.61	1.89	1.20	2.09	2.66	2.65
Al	11.24	11.23	4.75	4.74	4.86	4.94	4.95	12.32	13.05	12.86	13.07	13.56	14.38	13.41	13.05	13.21
Ca	22.00	22.29	21.25	21.26	21.34	21.20	21.05	22.00	22.63	22.65	22.27	22.77	22.18	22.68	22.70	22.79
F	8.20	8.07	3.42	2.99	3.25	3.46	3.34	7.93	8.61	8.28	8.50	8.79	9.03	8.81	8.69	8.97
O	36.98	37.33	38.64	38.70	38.83	38.84	38.47	35.88	35.83	36.14	36.61	36.75	35.65	35.95	36.82	37.14
total	100.43	101.13	98.51	98.52	99.03	98.76	98.18	96.88	98.09	98.10	98.32	99.42	98.41	98.45	99.46	100.23
wt.% oxides (normalized to 100%)																
SiO_2	32.25	32.04	30.29	30.42	30.32	30.48	30.40	32.10	32.15	32.29	32.21	32.54	33.06	32.36	32.34	32.03
TiO_2	10.04	10.31	27.40	27.80	27.48	26.95	27.24	6.13	4.28	4.60	4.28	3.06	1.93	3.40	4.32	4.27
Al_2O_3	20.35	20.22	9.02	8.98	9.16	9.37	9.40	23.19	24.14	23.86	24.36	24.91	26.26	24.70	23.98	24.17
CaO*	29.51	29.74	29.86	29.81	29.79	29.74	29.61	30.68	31.01	31.12	30.77	30.95	30.02	30.95	30.89	30.84
F	7.86	7.69	3.43	3.00	3.24	3.47	3.35	7.90	8.43	8.13	8.39	8.54	8.73	8.59	8.46	8.68
sum	100	100	100	100	100	100	100	100	100	100	100	100	100	100	100	100
(*:based on mole CaO + CaF2)																
stoichiometry based on 3 cations																
Si	1.014	1.007	0.972	0.972	0.971	0.976	0.973	0.994	0.994	0.997	0.995	1.003	1.016	0.999	1.001	0.993
Ti	0.237	0.244	0.661	0.668	0.662	0.649	0.656	0.143	0.099	0.107	0.099	0.071	0.045	0.079	0.101	0.100
Al	0.754	0.749	0.341	0.338	0.346	0.354	0.355	0.846	0.879	0.868	0.887	0.905	0.951	0.899	0.875	0.883
Ca	0.994	1.001	1.026	1.021	1.022	1.021	1.016	1.017	1.027	1.029	1.018	1.022	0.989	1.023	1.024	1.024
F	0.781	0.765	0.348	0.303	0.328	0.351	0.340	0.773	0.824	0.793	0.820	0.832	0.848	0.839	0.827	0.851
O	4.185	4.199	4.629	4.658	4.641	4.627	4.637	4.173	4.121	4.141	4.128	4.110	4.112	4.108	4.125	4.109
Al+Ti	0.992	0.992	1.002	1.007	1.007	1.003	1.011	0.989	0.979	0.974	0.986	0.976	0.996	0.978	0.975	0.983
sum an	4.966	4.963	4.977	4.962	4.969	4.978	4.977	4.946	4.945	4.934	4.948	4.942	4.960	4.947	4.952	4.960
X_{Al}	0.761	0.754	0.340	0.336	0.343	0.353	0.351	0.850	0.898	0.890	0.899	0.927	0.955	0.919	0.897	0.899

Electron microprobe analyses (representative selection): Titanite

exp. no	G-203	G-203	G-203	G-264	G-264	G-264	G-264	G-265	G-265	G-266	G-268	G-268	G-268	G-274	G-274	G-274
phase	titanite	titanite	titanite	titanite	titanite	titanite	titanite	titanite	titanite	titanite	titanite	titanite	titanite	titanite	titanite	titanite
wt.% atoms																
Si	15.55	15.28	15.56	16.50	15.83	15.89	15.67	15.00	15.15	15.82	15.80	15.81	15.59	16.19	15.91	15.91
Ti	3.41	3.06	2.62	1.40	1.57	1.90	3.36	11.86	11.70	0.32	1.22	1.41	0.54	0.44	0.68	0.31
Al	12.74	12.91	13.10	14.69	14.48	14.01	13.15	7.79	7.90	15.16	14.68	14.46	14.73	15.85	14.93	15.28
Ca	22.86	22.69	22.75	21.63	22.63	22.57	22.25	21.81	21.73	22.97	22.89	22.49	22.74	22.44	23.20	23.05
F	8.41	8.49	9.07	10.81	11.45	10.80	10.48	6.89	6.75	11.87	11.43	11.55	12.32	10.25	10.06	10.51
O	37.26	37.07	37.23	36.10	35.79	35.64	36.23	38.05	38.05	35.77	35.98	36.13	35.91	35.29	35.65	35.79
total	100.23	99.50	100.33	101.13	101.75	100.81	101.14	101.40	101.28	101.91	102.00	101.85	101.83	100.46	100.43	100.85
wt.% oxides (normalized to 100%)																
SiO_2	32.16	31.92	32.21	33.13	31.67	32.07	31.75	30.85	31.15	31.62	31.59	31.73	31.39	32.38	32.13	32.06
TiO_2	5.49	4.96	4.25	2.21	2.44	2.97	5.33	19.04	18.75	0.51	1.90	2.22	0.86	0.67	1.08	0.47
Al_2O_3	23.28	23.83	23.96	26.08	25.57	24.97	23.52	14.16	14.36	26.76	25.92	25.66	26.20	28.01	26.64	27.19
CaO*	30.93	31.00	30.82	28.42	29.61	29.79	29.47	29.33	29.24	30.02	29.92	29.55	29.95	29.36	30.65	30.38
F	8.14	8.29	8.77	10.15	10.71	10.19	9.93	6.63	6.50	11.09	10.68	10.84	11.59	9.59	9.49	9.90
sum	100	100	100	100	100	100	100	100	100	100	100	100	100	100	100	100
(*:based on mole CaO + CaF2)																
stoichiometry based on 3 cations																
Si	0.996	0.988	1.000	1.036	0.996	1.006	1.002	0.992	0.999	0.991	0.991	0.999	0.991	0.998	0.992	0.992
Ti	0.128	0.115	0.099	0.052	0.058	0.070	0.126	0.460	0.453	0.012	0.045	0.053	0.020	0.016	0.025	0.011
Al	0.850	0.869	0.876	0.961	0.948	0.923	0.875	0.537	0.543	0.989	0.958	0.952	0.975	1.017	0.969	0.991
Ca	1.026	1.028	1.025	0.952	0.998	1.001	0.997	1.011	1.005	1.008	1.006	0.996	1.013	0.969	1.014	1.007
F	0.797	0.811	0.861	1.004	1.065	1.011	0.991	0.674	0.659	1.100	1.059	1.079	1.158	0.934	0.927	0.968
O	4.150	4.132	4.107	4.066	3.995	4.032	4.071	4.384	4.394	3.948	3.986	3.988	3.920	4.055	4.038	4.014
Al+Ti	0.978	0.985	0.976	1.013	1.006	0.993	1.001	0.997	0.995	1.001	1.003	1.005	0.995	1.033	0.994	1.002
sum an	4.947	4.943	4.968	5.070	5.061	5.043	5.061	5.058	5.053	5.047	5.045	5.067	5.078	4.989	4.965	4.982
X_{Al}	0.869	0.883	0.898	0.949	0.943	0.929	0.874	0.538	0.545	0.988	0.955	0.948	0.979	0.985	0.975	0.989

Electron microprobe analyses (representative selection): Titanite

exp. no	G-275	G-275	G-275	G-275	G-275	G-275	G-275	G-276	G-276	G-278	G-278	G-278	G-278	G-280	G-280	G-280
phase	titanite	titanite	titanite	titanite	titanite	titanite	titanite	titanite	titanite	titanite	titanite	titanite	titanite	titanite	titanite	titanite
wt.% atoms																
Si	15.61	15.89	15.91	15.98	15.99	15.87	15.92	15.95	15.98	15.87	15.96	16.03	15.81	15.99	15.85	16.00
Ti	0.94	0.68	0.36	0.24	0.98	0.81	0.68	-0.02	-0.03	0.05	0.04	0.00	0.03	0.03	-0.04	-0.07
Al	14.70	14.92	15.25	15.32	14.65	14.84	14.91	14.84	15.20	15.35	15.15	15.27	15.13	15.22	15.10	15.22
Ca	22.40	22.94	23.08	23.12	22.64	23.00	23.23	23.00	22.94	23.06	23.39	23.12	22.79	23.20	23.20	23.00
F	10.29	10.42	10.57	10.56	10.12	10.59	10.74	10.14	10.77	10.82	10.92	10.82	10.66	10.41	10.52	10.82
O	35.36	35.56	34.87	35.76	35.60	35.60	35.40	35.75	35.73	36.08	35.81	36.08	35.80	35.64	35.72	35.31
total	99.30	100.41	100.04	100.98	99.98	100.71	100.88	99.66	100.59	101.23	101.27	101.32	100.22	100.49	100.35	100.28
wt.% oxides (normalized to 100%)																
SiO_2	31.99	32.12	32.01	32.12	32.48	32.00	31.93	32.66	32.33	31.99	32.05	32.24	32.20	32.29	32.17	32.33
TiO_2	1.49	1.08	0.57	0.37	1.55	1.25	1.08	-0.03	-0.07	0.07	0.07	0.00	0.03	0.07	-0.07	-0.10
Al_2O_3	26.63	26.63	27.10	27.19	26.28	26.44	26.43	26.84	27.18	27.32	26.89	27.14	27.24	27.16	27.08	27.17
CaO*	30.03	30.33	30.38	30.39	30.08	30.32	30.49	30.82	30.37	30.42	30.73	30.43	30.37	30.64	30.82	30.39
F	9.86	9.84	9.94	9.92	9.61	9.98	10.07	9.71	10.18	10.20	10.26	10.18	10.15	9.83	9.99	10.21
sum	100	100	100	100	100	100	100	100	100	100	100	100	100	100	100	100
(*:based on mole CaO + CaF2)																
stoichiometry based on 3 cations																
Si	0.993	0.995	0.991	0.993	1.006	0.994	0.992	1.007	1.002	0.991	0.994	0.999	0.997	0.997	0.994	1.002
Ti	0.035	0.025	0.013	0.009	0.036	0.029	0.025	-0.001	-0.002	0.002	0.002	0.000	0.001	0.002	-0.002	-0.002
Al	0.974	0.972	0.989	0.991	0.960	0.968	0.968	0.975	0.992	0.998	0.983	0.991	0.994	0.988	0.987	0.992
Ca	0.998	1.007	1.007	1.007	0.998	1.009	1.015	1.018	1.008	1.010	1.021	1.010	1.008	1.013	1.021	1.009
F	0.968	0.965	0.973	0.971	0.941	0.981	0.990	0.947	0.998	0.999	1.006	0.997	0.994	0.960	0.976	1.001
O	4.031	4.024	4.012	4.012	4.051	4.017	4.006	4.021	3.997	3.992	3.984	3.996	3.998	4.013	3.998	3.995
Al+Ti	1.009	0.998	1.002	1.000	0.996	0.997	0.993	0.975	0.990	0.999	0.985	0.991	0.995	0.990	0.985	0.990
sum an	4.998	4.989	4.985	4.983	4.993	4.997	4.996	4.968	4.995	4.991	4.990	4.993	4.992	4.972	4.974	4.996
X_{Al}	0.965	0.975	0.987	0.991	0.964	0.971	0.975	1.001	1.002	0.998	0.998	1.000	0.999	0.998	1.002	1.002

Electron microprobe analyses (representative selection): Titanite

exp. no	G-280	G-280	G-282	G-282	G-282	G-282	G-282	G-295	G-295	G-295	G-296	G-296	G-297	G-297	G-297	G-297
phase	titanite	titanite	titanite	titanite	titanite	titanite	titanite	titanite	titanite	titanite	titanite	titanite	titanite	titanite	titanite	titanite
wt.% atoms																
Si	15.82	15.82	15.83	15.81	15.87	15.98	15.82	15.86	16.11	15.79	16.41	16.67	15.56	15.59	15.92	15.74
Ti	-0.02	0.02	0.00	-0.04	-0.07	0.03	0.01	0.02	0.10	0.09	-0.04	-0.01	0.00	0.00	0.00	0.00
Al	15.11	15.14	15.04	15.00	15.08	15.25	15.10	15.32	15.42	15.34	15.73	15.93	14.96	15.08	15.36	15.22
Ca	22.97	23.23	23.18	22.99	23.09	23.11	23.13	23.21	23.25	23.11	23.49	23.73	22.67	22.45	22.20	22.39
F	10.90	10.70	10.53	10.40	10.29	10.77	10.79	10.83	10.78	10.58	10.75	11.12	10.13	9.81	10.22	9.76
O	35.20	35.03	34.52	34.68	34.44	34.44	34.84	35.96	36.06	35.15	36.19	37.11	36.38	36.02	36.71	36.06
total	99.98	99.94	99.10	98.84	98.70	99.58	99.69	101.20	101.72	100.06	102.53	104.55	99.70	98.95	100.41	99.17
wt.% oxides (normalized to 100%)																
SiO$_2$	32.11	32.03	32.16	32.28	32.31	32.19	32.07	31.95	32.19	31.93	32.36	32.40	32.19	32.35	32.63	32.53
TiO$_2$	-0.03	0.03	0.00	0.00	0.00	0.07	0.00	0.03	0.17	0.13	0.00	0.00	0.00	0.00	0.00	0.00
Al$_2$O$_3$	27.09	27.07	27.01	27.07	27.12	27.15	27.04	27.24	27.20	27.39	27.41	27.34	27.34	27.65	27.82	27.78
CaO*	30.49	30.75	30.82	30.72	30.77	30.45	30.67	30.57	30.38	30.56	30.32	30.17	30.68	30.49	29.75	30.27
F	10.34	10.13	10.01	9.94	9.80	10.14	10.22	10.20	10.06	9.99	9.91	10.10	9.79	9.52	9.79	9.43
sum	100	100	100	100	100	100	100	100	100	100	100.00	100.00	100	100	100	100
(*:based on mole CaO + CaF2)																
stoichiometry based on 3 cations																
Si	0.996	0.992	0.995	0.997	0.997	0.997	0.994	0.990	0.996	0.987	0.999	1.003	0.993	0.994	1.006	0.999
Ti	-0.001	0.001	0.000	0.000	0.000	0.002	0.000	0.001	0.004	0.003	0.000	0.000	0.000	0.000	0.000	0.000
Al	0.991	0.988	0.984	0.986	0.986	0.991	0.988	0.995	0.992	0.998	0.998	0.997	0.994	1.002	1.011	1.005
Ca	1.014	1.020	1.021	1.017	1.017	1.010	1.018	1.015	1.007	1.012	1.003	1.000	1.014	1.004	0.983	0.996
F	1.014	0.992	0.979	0.971	0.956	0.993	1.002	0.999	0.985	0.977	0.968	0.988	0.955	0.925	0.955	0.916
O	3.984	3.990	3.809	3.842	3.798	3.773	3.843	3.939	3.916	3.855	3.870	3.919	4.076	4.035	4.074	4.016
Al+Ti	0.990	0.988	0.984	0.986	0.986	0.992	0.988	0.996	0.996	1.001	0.998	0.997	0.994	1.002	1.011	1.005
sum an	4.998	4.982	4.788	4.813	4.754	4.766	4.844	4.939	4.901	4.832	4.838	4.907	5.031	4.960	5.028	4.932
X$_{Al}$	1.001	0.999	1.000	1.000	1.000	0.998	1.000	0.999	0.996	0.997	1.000	1.000	1.000	1.000	1.000	1.000

Electron microprobe analyses (representative selection): Titanite

name		AlF00	AlF00	AlF00	AlF00	AlF00	AlF00	AlF00
exp. no	G-297							
phase	titanite	titanite	titanite	titanite	titanite	titanite	titanite	titanite

wt.% atoms

Si	15.37	14.53	14.23	14.11	14.36	14.23	14.39	14.07
Ti	0.00	23.91	24.07	23.92	24.38	25.00	24.64	24.35
Al	15.06	-	-	-	-	-	-	-
Ca	22.72	20.74	20.15	20.38	20.26	20.39	20.44	20.58
F	10.31	-	-	-	-	-	-	-
O	36.22	40.81	40.33	40.20	40.74	41.05	41.01	40.51
total	99.68	99.99	98.78	98.61	99.74	100.67	100.48	99.51

wt.% oxides (normalized to 100%)

SiO_2	31.79	31.10	30.81	30.62	30.81	30.24	30.62	30.26
TiO_2	0.00	39.88	40.64	40.45	40.77	41.41	40.91	40.81
Al_2O_3	27.50	0.00	0.00	0.00	0.00	0.00	0.00	0.00
CaO*	30.74	29.03	28.55	28.93	28.42	28.34	28.47	28.93
F	9.97	0.00	0.00	0.00	0.00	0.00	0.00	0.00
sum	100	100	100	100	100	100	100	100

(*:based on mole CaO + CaF2)

stoichiometry based on 3 cations

Si	0.982	1.012	1.005	0.998	1.006	0.989	1.000	0.987
Ti	0.000	0.976	0.997	0.992	1.001	1.018	1.005	1.002
Al	1.001	-	-	-	-	-	-	-
Ca	1.017	1.012	0.998	1.010	0.994	0.993	0.996	1.011
F	0.974	-	-	-	-	-	-	-
O	4.061	4.987	5.002	4.991	5.006	5.006	5.004	4.988
Al+Ti	1.001							
sum an	5.034							
X_{Al}	1.000							

Electron microprobe analyses (representative selection): Titanite

name	AlF05	AlF05	AlF05	AlF05	AlF05	AlF06	AlF06	AlF06	AlF06	AlF06	AlF06	AlF09	AlF09	AlF09	AlF09	AlF09
exp. no	G-428	G-428	G-428	G-428	G-428	G-432	G-432	G-432	G-432	G-432	G-432	G-430	G-430	G-430	G-430	G-430
phase	titanite	titanite	titanite	titanite	titanite	titanite	titanite	titanite	titanite	titanite	titanite	titanite	titanite	titanite	titanite	titanite
wt.% atoms																
Si	14.31	14.20	14.21	14.29	14.38	14.02	14.18	14.15	14.07	14.23	14.20	14.14	13.99	14.00	13.96	13.93
Ti	23.03	23.44	23.82	22.88	23.06	23.31	23.10	23.24	23.23	23.18	23.63	22.45	22.41	21.86	22.29	22.01
Al	0.86	0.76	0.60	0.76	0.84	0.63	0.82	0.83	0.88	0.87	0.63	1.26	1.24	1.51	1.16	1.30
Ca	19.89	19.92	20.25	19.99	20.03	20.01	19.99	20.09	20.04	19.89	20.14	19.94	19.96	20.18	19.91	19.74
F	0.65	0.69	0.28	0.71	0.31	0.60	0.77	0.72	0.58	0.77	0.43	1.07	1.05	1.12	0.86	0.93
O	40.58	40.23	40.98	40.80	40.36	40.88	40.56	40.73	40.33	40.56	40.50	40.86	40.56	40.92	41.31	41.13
total	99.32	99.24	100.14	99.43	98.98	99.45	99.42	99.76	99.13	99.50	99.53	99.72	99.21	99.59	99.49	99.04
wt.% oxides (normalized to 100%)																
SiO_2	30.88	30.54	30.44	30.91	31.03	30.41	30.59	30.44	30.37	30.66	30.50	30.54	30.35	30.37	30.50	30.56
TiO_2	38.75	39.30	39.78	38.61	38.80	39.40	38.86	38.99	39.07	38.92	39.57	37.81	37.89	36.97	37.95	37.63
Al_2O_3	1.64	1.44	1.13	1.46	1.59	1.21	1.56	1.58	1.67	1.64	1.19	2.40	2.37	2.88	2.24	2.52
CaO*	28.06	28.02	28.37	28.30	28.27	28.38	28.21	28.27	28.30	28.01	28.31	28.16	28.33	28.63	28.44	28.34
F	0.66	0.70	0.28	0.72	0.31	0.61	0.78	0.72	0.59	0.78	0.44	1.08	1.07	1.14	0.87	0.95
sum	100	100	100	100	100	100	100	100	100	100	100	100	100	100	100	100
(*:based on mole CaO + CaF2)																
stoichiometry based on 3 cations																
Si	1.007	0.998	0.992	1.008	1.008	0.993	0.999	0.994	0.990	1.001	0.995	0.996	0.990	0.988	0.993	0.994
Ti	0.950	0.966	0.975	0.947	0.948	0.968	0.954	0.957	0.958	0.956	0.971	0.928	0.929	0.904	0.929	0.921
Al	0.063	0.055	0.043	0.056	0.061	0.046	0.060	0.061	0.064	0.063	0.046	0.092	0.091	0.110	0.086	0.097
Ca	0.980	0.981	0.990	0.989	0.984	0.993	0.987	0.989	0.988	0.980	0.989	0.984	0.990	0.998	0.992	0.988
F	0.068	0.072	0.029	0.074	0.032	0.063	0.080	0.074	0.060	0.080	0.045	0.112	0.110	0.117	0.090	0.098
O	5.012	4.962	5.021	5.055	4.966	5.083	5.015	5.022	4.980	5.006	4.982	5.054	5.036	5.067	5.156	5.155
Al+Ti	1.013	1.021	1.018	1.003	1.009	1.014	1.014	1.018	1.022	1.019	1.016	1.020	1.021	1.015	1.015	1.018
sum an	5.080	5.034	5.050	5.129	4.998	5.146	5.095	5.096	5.041	5.086	5.027	5.165	5.146	5.184	5.246	5.253
X_{Al}	0.062	0.054	0.043	0.056	0.060	0.046	0.059	0.060	0.063	0.062	0.045	0.090	0.089	0.109	0.084	0.095

48

Electron microprobe analyses (representative selection): Titanite

name	AlF14	AlF14	AlF14	AlF14	AlF14	AlF18	AlF18	AlF18	AlF18	AlF18	AlF23	AlF23	AlF23	AlF23	AlF23	AlF29
exp. no	G-433	G-433	G-433	G-433	G-433	G-379	G-379	G-379	G-379	G-379	G-431	G-431	G-431	G-431	G-431	G-401
phase	titanite	titanite	titanite	titanite	titanite	titanite	titanite	titanite	titanite	titanite	titanite	titanite	titanite	titanite	titanite	titanite
wt.% atoms																
Si	14.06	14.28	14.31	14.28	14.08	14.61	14.58	14.69	14.67	14.47	14.30	14.32	14.32	14.44	14.27	14.46
Ti	21.96	21.52	21.68	21.70	21.42	20.92	20.76	20.81	20.66	20.66	19.18	19.01	19.06	19.17	19.38	17.67
Al	1.97	1.99	2.02	1.81	1.88	2.66	2.56	2.56	2.66	2.57	3.29	3.37	3.19	3.31	3.18	4.07
Ca	20.26	20.17	20.32	20.19	20.32	20.40	20.25	20.58	20.42	20.47	20.55	20.33	20.18	20.54	20.35	21.34
F	1.45	1.35	1.41	1.30	1.52	1.62	1.87	1.77	1.82	1.74	2.17	2.32	1.74	2.09	2.25	3.01
O	40.46	40.07	40.75	40.18	40.40	39.87	39.54	39.80	40.22	39.87	40.53	40.53	39.64	40.74	40.40	40.74
total	100.16	99.38	100.49	99.46	99.62	100.08	99.56	100.21	100.45	99.78	100.02	99.88	98.13	100.29	99.83	101.29
wt.% oxides (normalized to 100%)																
SiO_2	30.00	30.62	30.48	30.64	30.33	30.84	30.92	30.94	31.00	30.74	30.67	30.80	31.12	30.90	30.65	30.63
TiO_2	36.56	35.97	36.02	36.30	35.94	34.44	34.32	34.19	34.03	34.24	32.08	31.86	32.30	31.97	32.47	29.20
Al_2O_3	3.71	3.76	3.79	3.43	3.56	4.96	4.81	4.77	4.96	4.82	6.24	6.40	6.13	6.26	6.04	7.61
CaO*	28.28	28.30	28.31	28.33	28.64	28.17	28.10	28.35	28.22	28.47	28.84	28.61	28.68	28.77	28.58	29.58
F	1.45	1.35	1.40	1.31	1.53	1.59	1.85	1.75	1.79	1.73	2.18	2.33	1.77	2.09	2.27	2.98
sum	100	100	100	100	100	100	100	100	100	100	100	100	100	100	100	100
(*:based on mole CaO + CaF2)																
stoichiometry based on 3 cations																
Si	0.977	0.994	0.990	0.996	0.986	0.997	1.003	1.002	1.003	0.995	0.989	0.994	1.000	0.995	0.991	0.985
Ti	0.895	0.878	0.880	0.887	0.879	0.838	0.837	0.833	0.829	0.834	0.778	0.773	0.781	0.774	0.789	0.706
Al	0.142	0.144	0.145	0.131	0.137	0.189	0.184	0.182	0.189	0.184	0.237	0.244	0.232	0.238	0.230	0.289
Ca	0.986	0.984	0.985	0.986	0.998	0.976	0.976	0.984	0.979	0.987	0.996	0.989	0.987	0.993	0.990	1.020
F	0.149	0.139	0.144	0.134	0.158	0.163	0.189	0.179	0.184	0.177	0.222	0.238	0.180	0.213	0.232	0.303
O	4.935	4.895	4.951	4.917	4.968	4.778	4.775	4.766	4.830	4.815	4.923	4.937	4.859	4.930	4.924	4.874
Al+Ti	1.037	1.022	1.025	1.018	1.016	1.027	1.021	1.015	1.018	1.018	1.015	1.017	1.013	1.012	1.019	0.995
sum an	5.083	5.034	5.095	5.051	5.126	4.941	4.964	4.945	5.014	4.992	5.146	5.175	5.039	5.143	5.155	5.177
X_{Al}	0.137	0.141	0.141	0.129	0.134	0.184	0.180	0.179	0.186	0.181	0.234	0.240	0.229	0.235	0.226	0.290

Electron microprobe analyses (representative selection): Titanite

name	AlF29	AlF29	AlF29	AlF29	AlF37	AlF37	AlF37	AlF49	AlF49	AlF49	AlF49	AlF49	AlF67	AlF67	AlF67	AlF67
exp. no	G-401	G-401	G-401	G-401	G-381	G-381	G-381	G-380	G-380	G-380	G-380	G-380	G-360	G-360	G-360	G-360
phase	titanite	titanite	titanite	titanite	titanite	titanite	titanite	titanite	titanite	titanite	titanite	titanite	titanite	titanite	titanite	titanite
wt.% atoms																
Si	14.07	14.45	14.44	14.39	15.01	14.83	14.65	15.05	15.14	15.12	14.98	15.07	15.20	15.08	15.13	15.46
Ti	18.84	17.62	17.81	17.67	15.83	15.88	16.27	13.23	13.17	13.11	13.44	13.15	9.03	8.49	8.20	6.92
Al	3.89	4.45	4.02	4.04	5.39	5.30	5.30	6.98	7.01	7.10	6.94	7.06	9.75	9.76	9.99	10.82
Ca	21.05	21.32	21.12	21.06	20.49	20.45	20.43	20.69	20.92	20.95	21.02	20.75	21.33	21.34	21.03	21.72
F	2.21	3.15	2.77	2.68	3.25	3.47	3.29	4.41	4.23	4.29	4.40	4.64	7.76	7.41	7.04	7.87
O	40.31	40.24	40.29	40.13	38.52	39.01	38.60	38.29	38.55	38.49	38.57	38.23	37.36	37.55	37.61	37.71
total	100.37	101.23	100.45	99.97	98.49	98.94	98.54	98.65	99.02	99.06	99.35	98.90	100.43	99.63	99.00	100.50
wt.% oxides (normalized to 100%)																
SiO_2	29.94	30.40	30.74	30.77	31.92	31.64	31.22	31.93	32.03	31.95	31.60	31.86	31.38	31.59	31.91	31.99
TiO_2	31.26	28.91	29.55	29.46	26.23	26.39	27.02	21.89	21.73	21.60	22.11	21.68	14.55	13.86	13.50	11.18
Al_2O_3	7.30	8.26	7.56	7.63	10.12	9.98	9.99	13.08	13.10	13.26	12.94	13.18	17.77	18.07	18.62	19.80
CaO*	29.30	29.34	29.40	29.45	28.50	28.52	28.49	28.73	28.96	28.95	29.01	28.69	28.80	29.22	29.02	29.41
F	2.20	3.10	2.76	2.68	3.23	3.46	3.27	4.37	4.19	4.24	4.34	4.59	7.50	7.26	6.95	7.62
sum	100	100	100	100	100	100	100	100	100	100	100	100	100	100	100	100
(*:based on mole CaO + CaF2)																
stoichiometry based on 3 cations																
Si	0.961	0.977	0.988	0.988	1.018	1.012	0.998	1.013	1.013	1.011	1.003	1.012	1.000	1.002	1.007	1.008
Ti	0.755	0.699	0.714	0.711	0.629	0.635	0.650	0.522	0.517	0.514	0.528	0.518	0.349	0.331	0.320	0.265
Al	0.276	0.313	0.286	0.289	0.380	0.376	0.376	0.489	0.488	0.494	0.484	0.493	0.668	0.675	0.692	0.735
Ca	1.008	1.011	1.012	1.013	0.973	0.977	0.976	0.976	0.981	0.981	0.986	0.976	0.983	0.993	0.981	0.992
F	0.223	0.315	0.280	0.272	0.326	0.350	0.331	0.439	0.419	0.424	0.435	0.461	0.756	0.728	0.693	0.759
O	4.834	4.777	4.835	4.835	4.585	4.670	4.617	4.525	4.531	4.516	4.532	4.507	4.317	4.377	4.394	4.317
Al+Ti	1.031	1.012	1.001	1.000	1.009	1.011	1.026	1.011	1.005	1.008	1.011	1.011	1.016	1.006	1.012	1.000
sum an	5.057	5.091	5.115	5.107	4.910	5.020	4.948	4.964	4.950	4.940	4.967	4.969	5.072	5.105	5.087	5.076
X_{Al}	0.268	0.309	0.286	0.289	0.377	0.372	0.367	0.483	0.486	0.490	0.478	0.488	0.657	0.671	0.684	0.735

Electron microprobe analyses (representative selection): Titanite

name	AlF67	AlF75	AlF75	AlF75	AlF75	AlF75	AlF82	AlF82	AlF82	AlF82	AlF82
exp. no	G-360	G-368	G-368	G-368	G-368	G-368	G-387	G-387	G-387	G-387	G-387
phase	titanite	titanite	titanite	titanite	titanite	titanite	titanite	titanite	titanite	titanite	titanite

wt.% atoms

Si	15.05	15.47	15.44	15.27	15.38	15.32	15.46	15.28	15.28	15.38	15.48
Ti	8.41	6.96	6.10	6.05	5.94	6.76	3.92	4.82	4.74	4.77	5.40
Al	9.86	10.84	11.39	11.17	11.43	10.94	12.83	12.12	12.16	12.11	11.72
Ca	21.45	21.76	21.78	21.54	21.64	21.80	22.67	22.54	22.41	22.70	22.00
F	7.35	7.28	7.56	7.77	8.06	7.65	8.52	7.84	8.35	8.22	7.96
O	37.34	37.48	37.61	37.26	37.44	37.60	37.09	36.53	36.96	36.36	36.58
total	99.46	99.79	99.88	99.06	99.89	100.07	100.49	99.13	99.90	99.54	99.14

wt.% oxides (normalized to 100%)

SiO_2	31.51	32.16	32.14	32.09	32.03	31.87	31.77	31.74	31.63	31.73	32.14
TiO_2	13.72	11.28	9.90	9.92	9.65	10.94	6.30	7.80	7.66	7.67	8.74
Al_2O_3	18.22	19.89	20.94	20.74	21.02	20.10	23.28	22.23	22.25	22.07	21.50
CaO*	29.36	29.59	29.67	29.62	29.46	29.65	30.47	30.62	30.36	30.61	29.89
F	7.19	7.08	7.36	7.63	7.84	7.44	8.18	7.61	8.09	7.92	7.72
sum	100	100	100	100	100	100	100	100	100	100	100

(*:based on mole $CaO + CaF_2$)

stoichiometry based on 3 cations

Si	0.998	1.007	1.004	1.006	1.005	1.001	0.987	0.986	0.987	0.988	1.004
Ti	0.327	0.266	0.233	0.234	0.228	0.258	0.147	0.182	0.180	0.180	0.205
Al	0.680	0.734	0.771	0.766	0.777	0.744	0.852	0.814	0.818	0.810	0.791
Ca	0.996	0.993	0.993	0.994	0.990	0.997	1.014	1.019	1.015	1.022	1.000
F	0.720	0.701	0.727	0.756	0.778	0.739	0.804	0.747	0.798	0.780	0.763
O	4.344	4.281	4.293	4.309	4.293	4.310	4.155	4.137	4.193	4.102	4.165
Al+Ti	1.006	1.000	1.003	1.000	1.005	1.002	0.999	0.996	0.998	0.990	0.997
sum an	5.064	4.982	5.019	5.065	5.071	5.049	4.958	4.884	4.991	4.882	4.927
X_{Al}	0.675	0.734	0.768	0.766	0.773	0.742	0.853	0.817	0.820	0.818	0.794

Electron microprobe analyses (representative selection): Titanite

exp. no	G-391	G-391	G-391	G-391	G-391	G-398	G-398	G-398	G-398	G-398	G-389	G-389	G-389	G-389	G-389	G-400	G-400	G-400
phase	titanite	titanite	titanite	titanite	titanite	titanite	titanite	titanite	titanite	titanite	titanite	titanite	titanite	titanite	titanite	titanite	titanite	titanite
wt.% atoms																		
Si	14.47	14.47	14.24	14.47	14.28	14.28	14.47	14.42	14.58	14.27	14.60	14.66	14.66	14.57	14.61	14.46	14.91	14.59
Ti	17.84	17.84	17.88	17.63	18.27	16.85	15.87	17.24	15.94	15.56	15.78	16.03	16.06	15.89	16.01	15.13	14.48	15.34
Al	4.03	4.03	3.89	3.93	3.82	4.76	4.83	4.60	5.00	4.79	5.31	5.26	5.25	5.18	5.32	5.62	5.88	5.51
Ca	21.31	21.31	21.65	21.48	21.27	21.41	21.28	21.32	21.30	21.23	21.47	21.48	21.59	21.71	21.74	21.57	21.04	21.48
F	2.68	2.68	2.66	2.63	2.64	3.00	3.09	2.73	3.38	3.22	3.51	3.15	3.47	3.58	3.21	3.95	4.06	3.82
O	39.89	39.89	40.30	39.22	39.85	39.60	39.13	39.18	39.81	39.46	40.00	39.88	39.86	39.21	39.64	39.01	38.90	39.14
total	100.22	100.22	100.62	99.36	100.13	99.90	98.67	99.49	100.01	98.53	100.67	100.46	100.89	100.14	100.53	99.74	99.27	99.88
wt.% oxides (normalized to 100%)																		
SiO_2	30.71	30.71	30.29	30.80	30.35	30.37	31.13	30.60	31.07	30.99	30.88	30.99	30.83	30.74	30.76	30.64	31.69	30.88
TiO_2	29.51	29.51	29.65	29.26	30.28	27.93	26.64	28.50	26.48	26.36	26.02	26.40	26.32	26.14	26.26	25.00	23.98	25.32
Al_2O_3	7.55	7.55	7.30	7.40	7.18	8.94	9.16	8.62	9.40	9.19	9.92	9.81	9.75	9.64	9.89	10.54	11.03	10.30
CaO*	29.58	29.58	30.11	29.91	29.57	29.78	29.95	29.58	29.69	30.19	29.72	29.68	29.69	29.96	29.93	29.91	29.25	29.73
F	2.65	2.65	2.65	2.62	2.62	2.98	3.11	2.70	3.37	3.27	3.47	3.11	3.41	3.53	3.16	3.91	4.04	3.77
sum	100	100	100	100	100	100	100	100	100	100	100	100	100	100	100	100	100	100
(*:based on mole CaO + CaF2)																		
stoichiometry based on 3 cations																		
Si	0.986	0.986	0.972	0.988	0.976	0.971	0.993	0.978	0.993	0.989	0.986	0.987	0.985	0.983	0.979	0.979	1.011	0.986
Ti	0.712	0.712	0.716	0.706	0.732	0.672	0.639	0.685	0.637	0.633	0.625	0.632	0.632	0.628	0.629	0.601	0.575	0.608
Al	0.285	0.285	0.276	0.280	0.272	0.337	0.344	0.325	0.354	0.346	0.373	0.368	0.367	0.363	0.371	0.397	0.415	0.388
Ca	1.017	1.017	1.036	1.027	1.019	1.020	1.024	1.013	1.016	1.032	1.016	1.013	1.016	1.026	1.021	1.024	0.999	1.018
F	0.269	0.269	0.269	0.266	0.266	0.301	0.314	0.273	0.340	0.330	0.350	0.313	0.344	0.357	0.318	0.395	0.407	0.381
O	4.769	4.769	4.829	4.699	4.783	4.726	4.714	4.663	4.759	4.805	4.742	4.711	4.701	4.640	4.662	4.636	4.628	4.644
Al+Ti	0.998	0.998	0.992	0.985	1.005	1.009	0.983	1.010	0.991	0.979	0.998	1.001	0.999	0.991	1.000	0.997	0.990	0.996
sum an	5.039	5.039	5.098	4.965	5.049	5.026	5.028	4.936	5.099	5.135	5.092	5.024	5.045	4.997	4.980	5.031	5.035	5.026
X_{Al}	0.286	0.286	0.278	0.284	0.271	0.334	0.350	0.322	0.357	0.353	0.374	0.368	0.367	0.366	0.371	0.398	0.419	0.389

Electron microprobe analyses (representative selection): Titanite

exp. no	G-400	G-400	G-383	G-383	G-383	G-383	G-383	G-404	G-404	G-404	G-404	G-404	G-388	G-388	G-388	G-388	G-388	G-397
phase	titanite	titanite	titanite	titanite	titanite	titanite	titanite	titanite	titanite	titanite	titanite	titanite	titanite	titanite	titanite	titanite	titanite	titanite
wt.% atoms																		
Si	14.57	14.58	15.03	14.99	14.96	14.92	15.10	14.61	14.58	14.78	14.53	14.58	14.85	14.65	14.75	15.03	14.78	15.25
Ti	15.23	15.71	13.61	13.27	13.34	13.53	13.51	14.52	14.56	14.63	15.68	14.60	14.78	14.93	15.12	14.46	14.99	13.28
Al	5.64	5.53	6.72	6.91	6.83	6.57	6.74	6.00	6.01	5.91	5.42	5.80	6.16	6.05	6.10	6.68	5.89	7.24
Ca	21.61	21.81	20.52	20.87	21.20	20.71	20.97	21.50	21.85	21.69	21.52	21.42	21.52	21.75	21.73	21.32	21.87	20.57
F	3.95	3.80	4.84	5.05	4.91	4.90	4.92	3.64	4.19	3.84	3.73	3.78	3.56	3.64	3.88	4.21	3.78	4.18
O	39.61	39.34	38.37	38.84	38.76	38.85	38.96	39.03	39.88	39.25	39.68	39.81	39.18	39.43	39.71	40.16	39.30	38.54
total	100.61	100.77	99.09	99.93	100.00	99.48	100.20	99.30	101.07	100.10	100.56	99.99	100.05	100.45	101.29	101.86	100.61	99.06
wt.% oxides (normalized to 100%)																		
SiO_2	30.73	30.53	31.80	31.59	31.46	31.67	31.74	31.10	30.71	31.19	30.69	31.12	31.22	30.79	30.77	31.25	30.94	32.18
TiO_2	25.05	25.65	22.44	21.79	21.88	22.39	22.13	24.07	23.90	24.06	25.79	24.30	24.24	24.49	24.59	23.42	24.48	21.83
Al_2O_3	10.51	10.21	12.57	12.86	12.68	12.33	12.49	11.28	11.17	11.02	10.12	10.94	11.43	11.24	11.23	12.26	10.91	13.48
CaO*	29.81	29.88	28.39	28.78	29.15	28.75	28.80	29.92	30.09	29.94	29.73	29.88	29.61	29.91	29.64	28.98	29.96	28.38
F	3.89	3.73	4.79	4.98	4.83	4.87	4.83	3.62	4.13	3.79	3.68	3.77	3.50	3.58	3.78	4.09	3.71	4.12
sum	100	100	100	100	100	100	100	100	100	100	100	100	100	100	100	100	100	100
(*:based on mole CaO + CaF2)																		
stoichiometry based on 3 cations																		
Si	0.982	0.976	1.016	1.009	1.003	1.012	1.013	0.987	0.979	0.992	0.981	0.990	0.990	0.977	0.979	0.994	0.984	1.017
Ti	0.602	0.617	0.539	0.523	0.525	0.538	0.531	0.574	0.573	0.576	0.620	0.581	0.578	0.585	0.589	0.560	0.586	0.519
Al	0.396	0.385	0.473	0.484	0.477	0.464	0.470	0.422	0.420	0.413	0.381	0.410	0.427	0.420	0.421	0.459	0.409	0.502
Ca	1.020	1.023	0.972	0.984	0.996	0.985	0.985	1.017	1.028	1.020	1.018	1.018	1.006	1.017	1.011	0.987	1.021	0.961
F	0.393	0.377	0.484	0.502	0.487	0.492	0.488	0.364	0.417	0.381	0.372	0.379	0.351	0.359	0.380	0.411	0.373	0.412
O	4.686	4.622	4.553	4.587	4.562	4.628	4.587	4.626	4.702	4.623	4.702	4.743	4.586	4.620	4.628	4.659	4.597	4.512
Al+Ti	0.998	1.001	1.013	1.007	1.001	1.003	1.001	0.996	0.993	0.989	1.001	0.992	1.005	1.005	1.010	1.019	0.995	1.021
sum an	5.080	4.999	5.036	5.089	5.049	5.120	5.075	4.989	5.118	5.004	5.074	5.122	4.937	4.979	5.009	5.070	4.970	4.924
X_{Al}	0.397	0.384	0.467	0.480	0.476	0.463	0.469	0.423	0.423	0.418	0.381	0.414	0.425	0.418	0.417	0.451	0.411	0.492

Electron microprobe analyses (representative selection): Titanite

exp. no	G-397	G-397	G-397	G-397	G-395	G-395	G-395	G-395	G-395	G-386	G-386	G-386	G-386	G-386	G-403	G-403	G-403	G-403
phase	titanite	titanite	titanite	titanite	titanite	titanite	titanite	titanite	titanite	titanite	titanite	titanite	titanite	titanite	titanite	titanite	titanite	titanite
wt.% atoms																		
Si	14.55	14.74	14.65	14.56	14.86	14.89	14.70	14.62	14.69	14.94	14.68	14.80	14.81	14.81	14.88	14.89	14.85	14.97
Ti	14.67	14.99	14.70	14.71	13.87	13.57	13.71	13.14	13.49	13.32	13.09	13.78	13.05	13.27	9.58	9.40	9.93	9.86
Al	5.99	6.04	5.98	6.02	6.72	6.62	6.77	6.86	6.74	6.98	7.07	6.83	7.10	7.15	9.05	9.32	8.91	8.94
Ca	21.52	21.59	21.56	21.38	21.56	21.87	21.54	21.92	21.61	21.72	21.70	21.71	22.01	21.72	21.80	22.14	21.81	21.91
F	3.87	4.19	3.87	4.25	4.48	4.20	4.19	4.70	4.45	4.44	4.71	4.38	4.48	4.73	6.26	6.38	6.01	6.16
O	39.74	39.95	39.57	39.63	39.80	39.82	40.06	39.45	39.65	38.99	39.00	39.62	39.09	39.39	38.71	38.60	38.23	38.84
total	100.34	101.50	100.33	100.55	101.29	100.97	100.97	100.69	100.63	100.39	100.25	101.12	100.54	101.07	100.28	100.73	99.74	100.68
wt.% oxides (normalized to 100%)																		
SiO_2	30.85	30.82	30.97	30.77	31.09	31.29	31.01	30.80	31.02	31.28	30.88	30.95	31.02	30.92	31.29	31.09	31.24	31.35
TiO_2	24.25	24.43	24.21	24.24	22.63	22.24	22.54	21.60	22.20	21.75	21.47	22.48	21.31	21.60	15.72	15.30	16.28	16.09
Al_2O_3	11.22	11.16	11.18	11.24	12.41	12.29	12.62	12.77	12.56	12.90	13.15	12.60	13.13	13.18	16.83	17.18	16.55	16.53
CaO*	29.84	29.50	29.81	29.55	29.49	30.06	29.71	30.20	29.83	29.74	29.87	29.69	30.16	29.67	30.00	30.21	30.02	30.00
F	3.84	4.10	3.83	4.21	4.38	4.12	4.13	4.63	4.39	4.34	4.63	4.28	4.39	4.62	6.16	6.22	5.91	6.03
sum	100	100	100	100	100	100	100	100	100	100	100	100	100	100	100	100	100	100
(*:based on mole CaO + CaF2)																		
stoichiometry based on 3 cations																		
Si	0.982	0.984	0.985	0.983	0.989	0.991	0.983	0.978	0.985	0.991	0.980	0.982	0.981	0.982	0.987	0.980	0.985	0.989
Ti	0.580	0.587	0.579	0.582	0.541	0.530	0.537	0.516	0.530	0.518	0.513	0.537	0.507	0.516	0.373	0.363	0.386	0.382
Al	0.421	0.420	0.419	0.423	0.465	0.459	0.471	0.478	0.470	0.482	0.492	0.471	0.489	0.493	0.626	0.638	0.615	0.615
Ca	1.017	1.009	1.016	1.011	1.005	1.020	1.009	1.028	1.015	1.009	1.016	1.010	1.022	1.009	1.014	1.020	1.014	1.014
F	0.386	0.414	0.385	0.425	0.440	0.413	0.414	0.465	0.441	0.435	0.465	0.430	0.439	0.464	0.614	0.620	0.589	0.602
O	4.707	4.680	4.673	4.698	4.650	4.652	4.701	4.635	4.665	4.538	4.571	4.615	4.546	4.583	4.511	4.456	4.451	4.506
Al+Ti	1.001	1.007	0.998	1.006	1.006	0.989	1.009	0.994	1.000	1.000	1.004	1.008	0.997	1.009	0.999	1.001	1.001	0.996
sum an	5.093	5.094	5.058	5.123	5.090	5.065	5.115	5.100	5.106	4.973	5.036	5.045	4.985	5.046	5.126	5.076	5.041	5.107
X_{Al}	0.420	0.417	0.420	0.421	0.462	0.464	0.467	0.481	0.470	0.482	0.490	0.468	0.491	0.489	0.627	0.638	0.614	0.617

Electron microprobe analyses (representative selection): Titanite

exp. no	G-403	G-411	G-411	G-411	G-411	G-411	G-413	G-413	G-413	G-413	G-413	G-412	G-412	G-412	G-412	G-412	G-407	G-407
phase	titanite	titanite	titanite	titanite	titanite	titanite	titanite	titanite	titanite	titanite	titanite	titanite	titanite	titanite	titanite	titanite	titanite	titanite
wt.% atoms																		
Si	14.95	14.86	14.76	14.83	14.55	14.94	15.14	14.84	14.82	14.85	14.95	14.97	14.85	14.85	14.99	15.12	15.14	15.04
Ti	9.60	11.38	11.43	11.30	11.25	11.87	10.15	10.48	9.85	10.37	9.86	10.09	10.35	10.18	9.82	10.01	8.43	7.97
Al	9.17	8.18	8.02	8.17	8.86	7.80	8.71	8.50	8.94	8.77	8.81	8.93	8.85	9.08	9.03	9.05	10.05	10.24
Ca	21.88	21.86	22.17	22.14	21.84	21.67	21.86	21.51	22.16	21.62	21.69	21.71	21.78	21.82	22.14	21.90	22.18	22.37
F	5.80	5.37	5.51	5.38	5.13	5.27	5.66	5.74	5.94	5.67	5.73	5.79	5.95	5.69	6.43	6.02	6.66	6.67
O	38.71	38.15	38.73	38.81	38.58	38.85	38.91	39.51	38.46	39.04	38.68	38.43	38.12	37.63	38.21	39.06	38.20	37.31
total	100.11	99.80	100.62	100.63	100.21	100.40	100.43	100.58	100.17	100.32	99.72	99.92	99.90	99.25	100.62	101.16	100.66	99.60
wt.% oxides (normalized to 100%)																		
SiO_2	31.43	31.10	30.86	31.00	30.43	31.32	31.74	31.39	31.10	31.28	31.62	31.44	31.09	31.13	31.15	31.47	31.40	31.29
TiO_2	15.72	18.58	18.64	18.41	18.33	19.38	16.59	17.29	16.09	17.03	16.26	16.51	16.89	16.61	15.91	16.23	13.63	12.94
Al_2O_3	17.04	15.13	14.80	15.07	16.38	14.44	16.13	15.88	16.57	16.33	16.46	16.55	16.36	16.79	16.58	16.63	18.42	18.83
CaO*	30.10	29.93	30.32	30.26	29.86	29.71	29.99	29.76	30.41	29.77	30.00	29.82	29.83	29.90	30.10	29.81	30.09	30.45
F	5.70	5.26	5.38	5.26	5.01	5.16	5.55	5.67	5.82	5.59	5.67	5.68	5.83	5.57	6.25	5.86	6.45	6.50
sum	100	100	100	100	100	100	100	100	100	100	100	100	100	100	100	100	100	100
(*:based on mole CaO + CaF2)																		
stoichiometry based on 3 cations																		
Si	0.986	0.982	0.976	0.979	0.956	0.992	0.999	0.991	0.979	0.985	0.995	0.990	0.982	0.978	0.985	0.992	0.985	0.979
Ti	0.371	0.442	0.444	0.437	0.433	0.462	0.393	0.411	0.381	0.404	0.385	0.391	0.401	0.393	0.378	0.385	0.322	0.305
Al	0.630	0.563	0.552	0.561	0.606	0.539	0.598	0.591	0.615	0.606	0.610	0.614	0.608	0.622	0.618	0.617	0.681	0.695
Ca	1.012	1.013	1.028	1.024	1.005	1.008	1.011	1.007	1.025	1.005	1.011	1.006	1.009	1.007	1.019	1.006	1.012	1.021
F	0.566	0.525	0.538	0.525	0.497	0.516	0.552	0.567	0.579	0.557	0.564	0.566	0.582	0.554	0.625	0.584	0.640	0.643
O	4.485	4.430	4.498	4.495	4.448	4.526	4.507	4.632	4.457	4.547	4.517	4.460	4.424	4.349	4.407	4.498	4.365	4.268
Al+Ti	1.002	1.005	0.996	0.998	1.039	1.001	0.991	1.002	0.996	1.010	0.995	1.005	1.010	1.015	0.996	1.002	1.003	0.999
sum an	5.051	4.955	5.036	5.021	4.945	5.042	5.059	5.199	5.036	5.104	5.081	5.026	5.006	4.903	5.032	5.081	5.005	4.911
X_{Al}	0.629	0.561	0.554	0.562	0.583	0.539	0.604	0.590	0.617	0.600	0.613	0.611	0.603	0.613	0.620	0.616	0.679	0.695

Electron microprobe analyses (representative selection): Titanite

exp. no	G-407	G-407	G-407
phase	titanite	titanite	titanite

wt.% atoms

Si	15.12	15.18	15.09
Ti	9.01	8.35	8.63
Al	9.74	10.00	9.91
Ca	22.21	22.63	22.38
F	6.29	6.48	6.58
O	37.03	37.29	37.72
total	99.40	99.93	100.31

wt.% oxides (normalized to 100%)

SiO_2	31.36	31.40	31.26
TiO_2	14.58	13.45	13.92
Al_2O_3	17.84	18.26	18.13
CaO*	30.12	30.63	30.31
F	6.10	6.26	6.37
sum	100	100	100

(*:based on mole CaO + CaF2)

stoichiometry based on 3 cations

Si	0.984	0.983	0.981
Ti	0.344	0.317	0.329
Al	0.660	0.673	0.671
Ca	1.012	1.027	1.019
F	0.606	0.620	0.633
O	4.229	4.238	4.306
Al+Ti	1.004	0.990	0.999
sum an	4.835	4.858	4.939
X_{Al}	0.657	0.680	0.671

Electron microprobe analyses (representative selection): Zoisite

| exp. no	G-197	G-197	G-197	G-197	G-197	G-197	G-203	G-268	G-264	G-264	G-276	G-280	G-295
phase	zoisite	zoisite	zoisite	zoisite	zoisite	zoisite	zoisite	zoisite	zoisite	zoisite	zoisite	zoisite	zoisite
wt.% atoms													
Si	18.37	18.62	18.44	18.23	18.22	18.52	18.09	18.46	18.83	18.55	18.33	18.56	18.73
Al	16.58	17.60	17.90	17.15	17.56	17.20	17.50	18.08	16.90	17.74	17.88	17.98	18.25
Ca	18.31	17.85	18.38	18.17	18.47	18.21	18.24	18.34	17.80	17.90	18.17	18.07	18.20
F	1.99	1.38	1.57	1.79	1.42	1.87	1.22	1.41	2.81	2.41	1.79	1.65	1.41
O	43.81	44.27	44.44	44.46	43.76	43.75	44.40	45.46	43.78	43.20	44.32	43.76	45.05
total	99.06	99.72	100.73	99.80	99.43	99.55	99.45	101.75	100.22	99.87	100.49	100.02	101.64
wt.% oxides (normalized to 100%)													
SiO2	39.99	40.06	39.23	39.54	39.20	39.83	39.28	39.21	40.30	39.42	39.13	39.47	39.51
Al2O3	31.89	33.45	33.64	32.86	33.38	32.67	33.57	33.91	31.96	33.31	33.72	33.77	33.99
CaO*	26.08	25.12	25.57	25.79	25.99	25.62	25.91	25.48	24.92	24.87	25.37	25.12	25.11
F	2.03	1.38	1.56	1.81	1.42	1.87	1.24	1.40	2.81	2.40	1.78	1.64	1.39
sum	100	100	100	100	100	100	100	100	100	100	100	100	100
[based on all Ca]													
stoichiometry based on 8 cations													
Si	3.032	3.012	2.953	2.987	2.948	3.012	2.948	2.946	3.081	2.994	2.952	2.974	2.968
Al	2.850	2.964	2.984	2.926	2.958	2.912	2.969	3.003	2.879	2.982	2.998	2.998	3.010
Ca	2.119	2.024	2.063	2.087	2.094	2.076	2.083	2.051	2.041	2.024	2.051	2.028	2.021
F	0.487	0.328	0.371	0.433	0.339	0.448	0.294	0.333	0.680	0.577	0.425	0.391	0.330
O	12.693	12.570	12.492	12.790	12.431	12.489	12.701	12.728	12.571	12.242	12.527	12.306	12.531
sum an	13.180	12.898	12.863	13.223	12.770	12.937	12.995	13.060	13.251	12.818	12.952	12.697	12.860
XF**	0.413	0.366	0.430	0.354	0.440	0.478	0.295	0.314	0.544	0.705	0.447	0.561	0.383
[**calculated as F/(F+O-12)]													

Appendix 2

Problems with calorimetric measurements

The scanning differential calorimeter used for measuring the heat capacities of $CaAlFSiO_4$ and titanite (Chapter 4), had never been utilised before over such a large temperature range. It was mostly run between 50 and 450 K, and primarily used to determine heat capacity anomalies, such as spikes due to melting or phase transitions. Since quantitative measurements performed with this instrument in the past by others were restricted to the determination of reaction energies by integration of the area under a peak, this calorimeter had never been used before to obtain absolute heat capacity data of a substance. Thus, while the accuracy of the temperature readings of the calorimeter, especially between 50 and 450 K, is good and well tested over the years, the accuracy of absolute values of the heat capacity was uncertain.

Before running the $CaAlFSiO_4$ sample with unknown heat capacity, a titanite sample was investigated, in order to test the accuracy and reproducibility of the measurements, and to become familiar with the calibration procedures. These are the data presented in Chapter 4.

At the time of the first experiments I was unaware that the heat capacity of titanite, which was determined and reproduced successfully several times over the last 50 years (King et al, 1954; Zhang et al., 1995; Thiéblot et al., 1999; Figures 4.1 and 4.2, p. 58), was again subject of discussion. In the abstract by Xirouchakis and Tangeman (1998) heat capacity data are reported from a carefully prepared titanite sample, which exceed those of the previous measurements by up to 4 % at high temperatures (Figure A2.1). The difference of the heat capacity could be ascribed to different sample preparation methods, yielding more accurate measurements from samples prepared entirely at subsolidus conditions by Xirouchakis and Tangeman (1998) (Xirouchakis and Lindsley, 1998). All other previously investigated samples had experienced supersolidus conditions, crystallising from glass or melt, and are therefore prone to be non-stiochiometric and contain impurities (wollastonite, quartz, glass, unspecified Ca-Al silicates) according to Xirouchakis et al. (1997b).
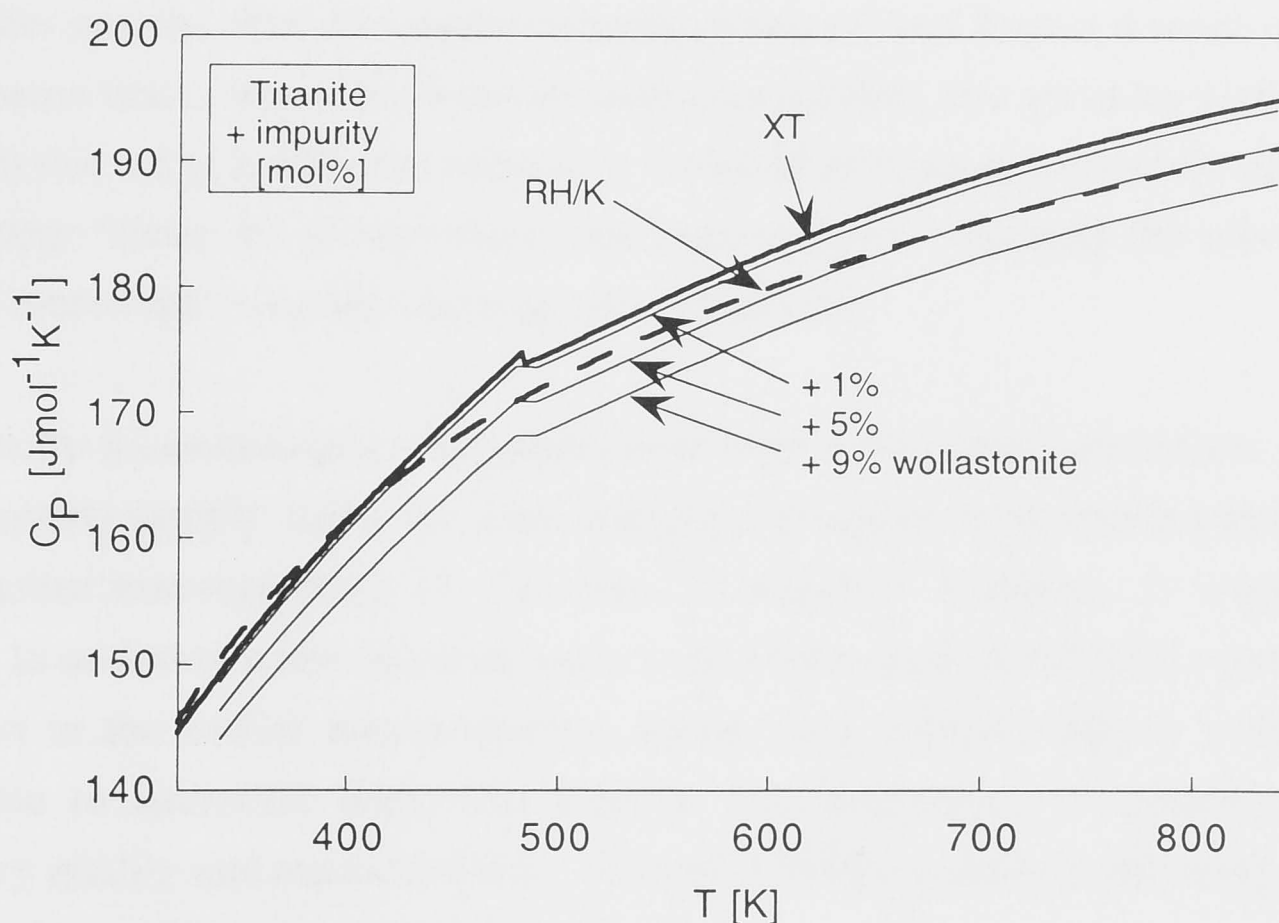
Figure A2.1 Heat capacity of titanite from Xirouchakis and Tangeman (1998) (XT, thick line), recalculated for a fictitious titanite sample with various amounts of wollastonite contamination (thin lines, in mol.%). The data by Robie and Hemingway (1995), that are based on King et al. (1954) (RH/K, dashed line) cut across the contamination contours. Therefore contamination does not seem to be the (only) reason for the difference between the data-bases XT and RH/K.

Figure A2.1 illustrates that the effect of impurities (using wollastonite as example) on the heat capacity of titanite would lower the heat capacity at all temperatures. Since significant differences between the earlier studies and that of Xirouchakis and Tangeman (1998) only exist at high temperatures (Figure A2.1), non-stoichiometry of the sample cannot account for the differences in heat capacity between the studies, and alternative, or additional causes have to be sought.

Whatever the reason might be, in the light of this recent study by Xirouchakis and Tangeman (1999), titanite is clearly not suitable to test the quality of the heat capacity measurements performed in this study. If the hypothesis of a link between impurities/non-stoichiometry and heat capacity data was true, then all other previous studies have errors attached to them, as does the present study, rendering any comparison between the data meaningless. This is because the exact amount and nature of impurities, and thus their quantitative effect on the heat capacity can never be determined. Even if the above hypothesis was not true, and other reasons for the differences in heat capacity data between the various studies would have to be sought, any comparison of titanite data with respect to the present study, again, is fraught with doubt, until alternative explanations would be found.

Thus, a few months after the measurements presented in Chapter 4 were completed, I became aware that it would be better to re-test, or confirm, the accuracy and precision of the instrument, using a different substance. I should have been warned by the tongue-in-cheek saying: 'Never try to reproduce your own analyses.' Opening the calorimetric cell 'only one more time' was like opening a can of worms.

Heat capacity measurements were performed with a powdered corundum standard, as well as a quartz sample, using the same sample preparation and experimental procedures as the earlier measurements (1. baseline, 2. sapphire standard, 3. empty pans, 4. samples). In addition, a few measurements with titanite and $CaAlFSiO_4$ were performed. In contrast to the earlier measurements, which were reproducible to within 2%, and comparable to literature data, this time it was impossible to obtain analyses of satisfactory quality and reproducibility. Several different problems occurred, which may or may not have affected earlier analyses.

The first heat capacity measurement of a sample after the base-line, standard, and empty-pans runs, resulted in good data only at low temperatures. Figure A2.2, which shows three measurements of corundum compared to literature data, demonstrates that the error increases, about linearly, with increasing temperature. At 850 K, the measured heat capacity is about $4 \pm 1\%$ smaller than the literature values.
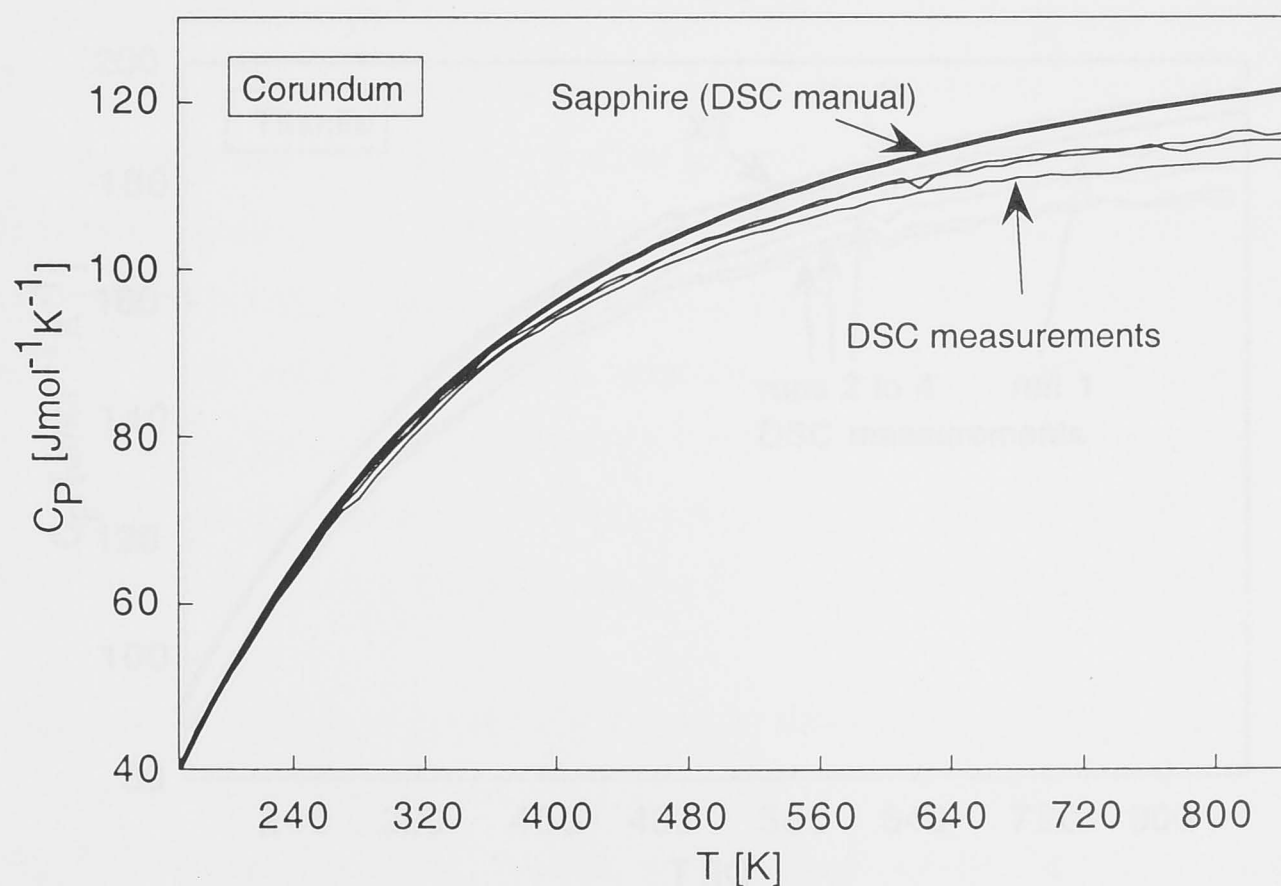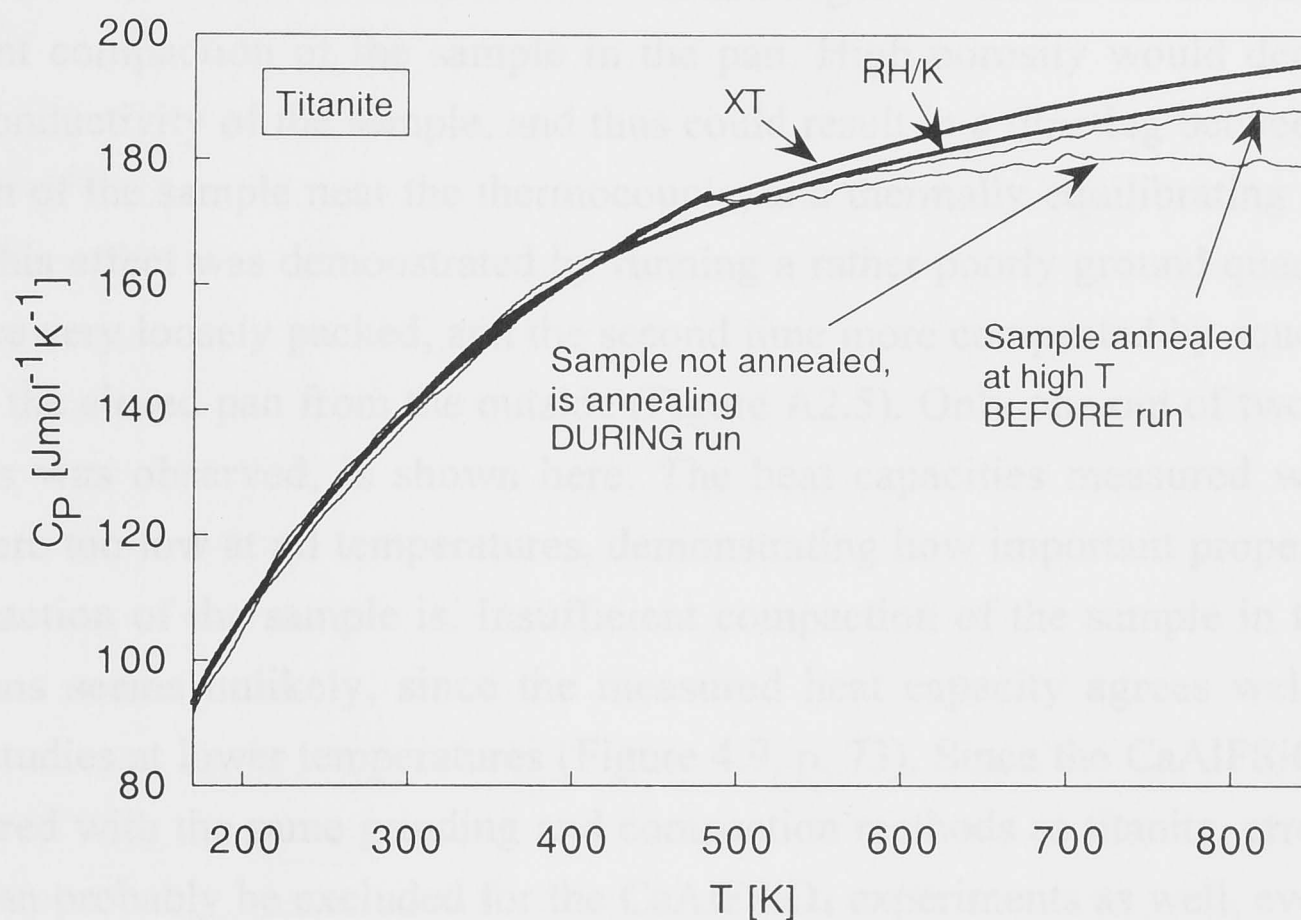

Figure A2.2 Three heat capacity measurements of corundum compared to the data provided for the sapphire standard. All measurements were taken during the first sample run after the calibration runs (baseline, sapphire disk, empty pans).

If a sample was run several times in a row, allowing about half an hour of temperature adjustment at room temperature in between, only the first run would show the behaviour seen in Figure A2.2. Every subsequent run would have a more constant error, comparable to the maximum deviation of the first run (Figure A2.3). Similar deviations as those shown in Figures A2.2 and A2.3 were observed with two more Al_2O_3 samples, which are not shown here. Multiple runs were also performed with titanite (Figure A2.3b). While the later runs clearly show a constant error as observed with corundum, the temperature dependent error of the first run can neither be confirmed nor rejected based on these data.
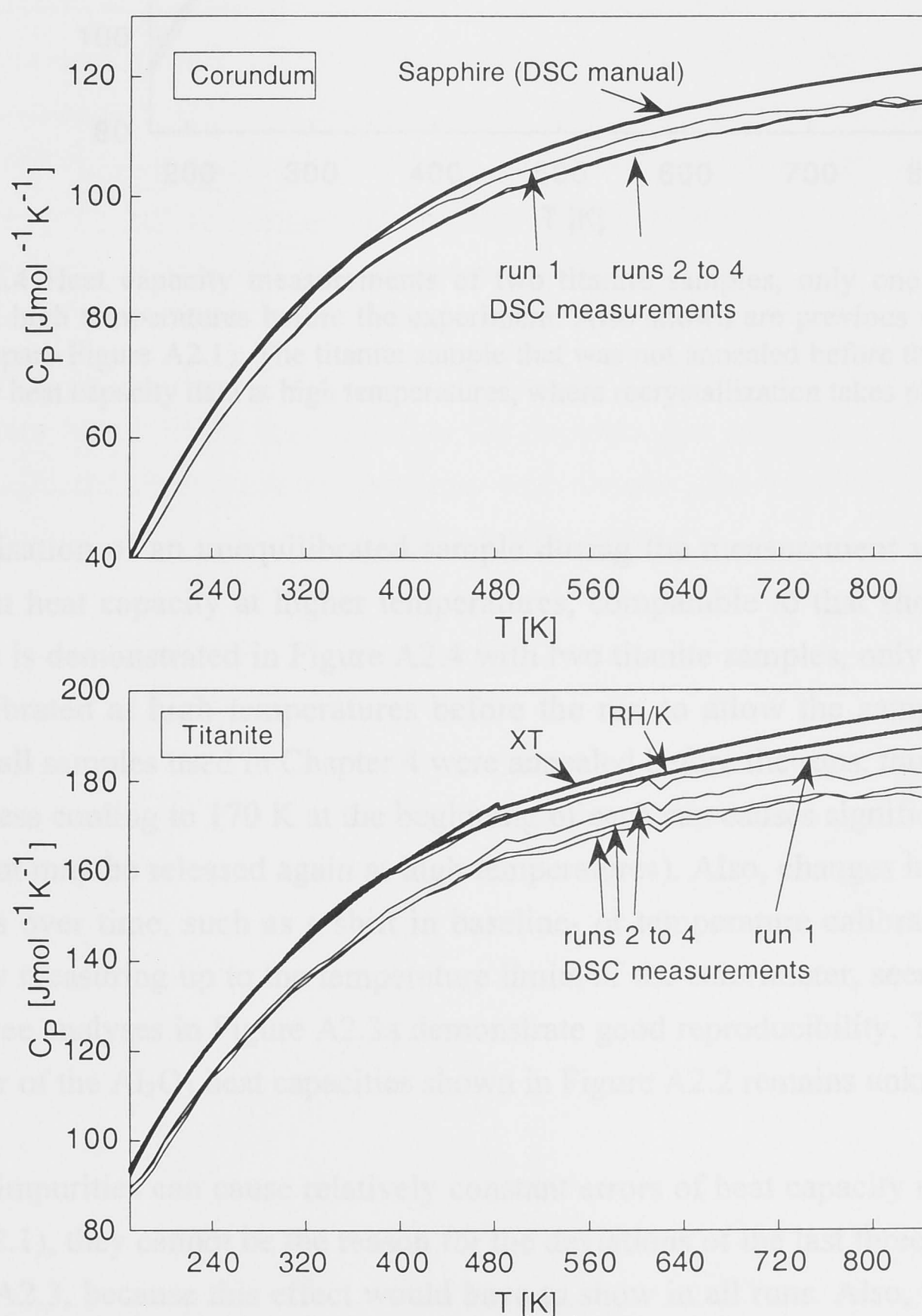
Figure A2.3 Results of four subsequent sample runs for corundum and titanite, compared to the respective literature values (Sapphire: DSC manual; titanite: XT and RH/K, as in Figure A2.1). In each case, the deviation of the measurements of the first run from the literature data increases with temperature, whereas the subsequent runs have a more constant error attached to them.
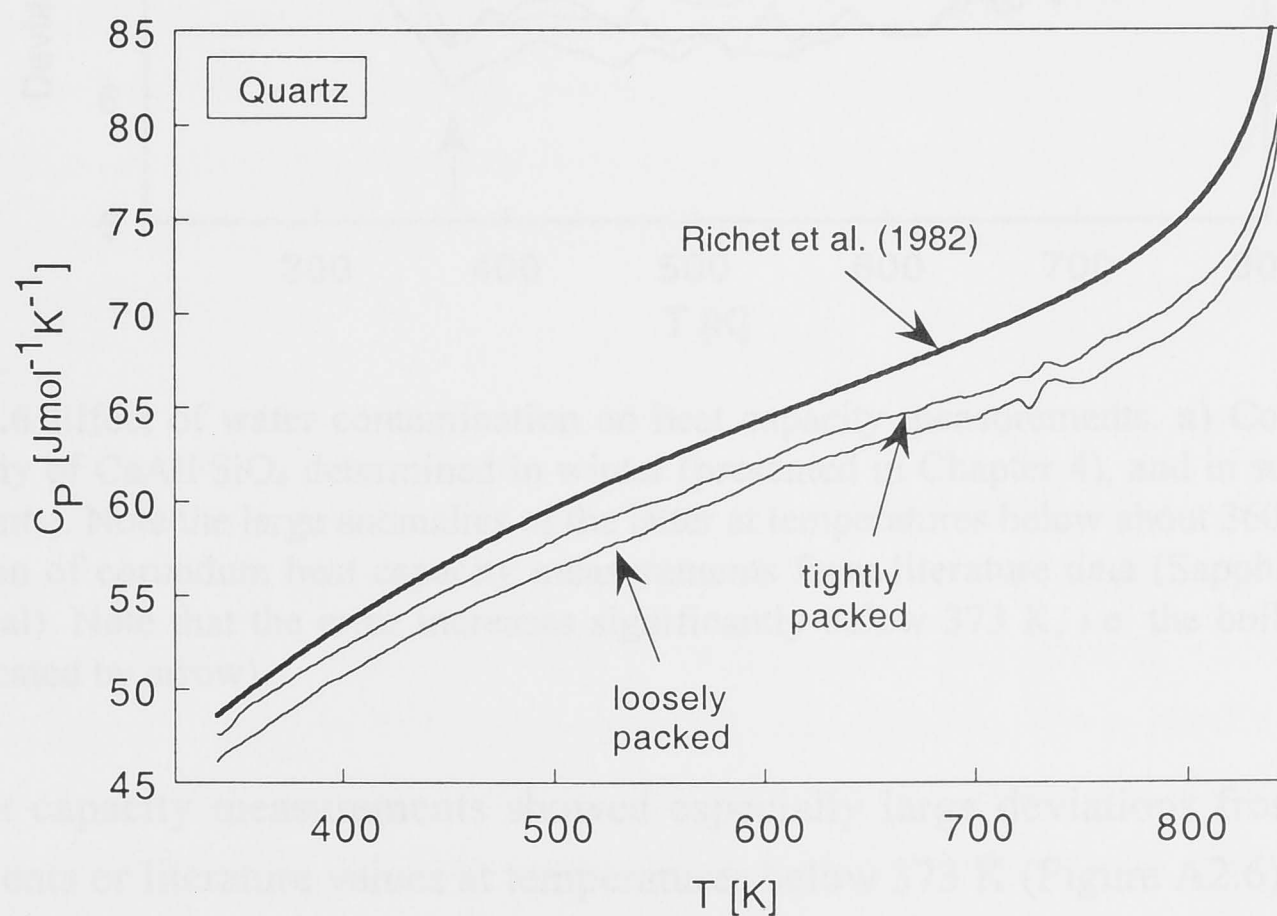
Figure A2.4 Heat capacity measurements of two titanite samples, only one of which was annealed at high temperatures before the experiment. Also shown are previous studies XT and RH/K (compare Figure A2.1). The titanite sample that was not annealed before the run results in much lower heat capacity data at high temperatures, where recrystallization takes place.

Recrystallisation of an unequilibrated sample during the measurement would cause a decrease in heat capacity at higher temperatures, comparable to that shown in Figure A2.2. This is demonstrated in Figure A2.4 with two titanite samples, only one of which was equilibrated at high temperatures before the run to allow the sample to anneal. However, all samples used in Chapter 4 were annealed before the runs, thus limiting this effect (unless cooling to 170 K at the beginning of each run causes significant structural stresses that may be released again at high temperatures). Also, changes in instrumental parameters over time, such as a shift in baseline- or temperature calibration, possibly induced by measuring up to the temperature limits of the calorimeter, seem unlikely, as the last three analyses in Figure A2.3a demonstrate good reproducibility. Thus the cause of the error of the Al_2O_3 heat capacities shown in Figure A2.2 remains unknown.

Although impurities can cause relatively constant errors of heat capacity measurements (Figure A2.1), they cannot be the reason for the deviations of the last three traces shown in Figure A2.3, because this effect would have to show in all runs. Also, the corundum was commercial high purity grade, ruling out significant contamination.

Another factor that could result in a more constant negative error in the measurements is insufficient compaction of the sample in the pan. High porosity would decrease the thermal conductivity of the sample, and thus could result in a time lag between heating the bottom of the sample near the thermocouple, and thermally equilibrating the whole sample. This effect was demonstrated by running a rather poorly ground quartz sample twice, once very loosely packed, and the second time more compacted by squeezing the sample in the closed pan from the outside (Figure A2.5). Only one out of two samples, where this was observed, is shown here. The heat capacities measured with either sample were too low at all temperatures, demonstrating how important proper grinding and compaction of the sample is. Insufficient compaction of the sample in the earlier titanite runs seems unlikely, since the measured heat capacity agrees well with all previous studies at lower temperatures (Figure 4.9, p. 73). Since the CaAlFSiO$_4$ sample was prepared with the same grinding and compaction methods as titanite, errors due to porosity can probably be excluded for the CaAlFSiO$_4$ experiments as well, even though no literature data are available for comparison in this case.

If the reasons for the more constant deviations, observed in subsequent runs of the same sample, were based on the instrument or the experimental procedure, this error would not have affected the earlier experiments with titanite and CaAlFSiO$_4$ (Chapter 4), because only the first traces of these substances were used.

Figure A2.5 Two heat capacity measurements of the same powdered quartz sample, before and after compaction of the latter. Comparison with the quartz data by Richet et al. (1982) demonstrates that significant errors can be introduced by poor sample compaction.
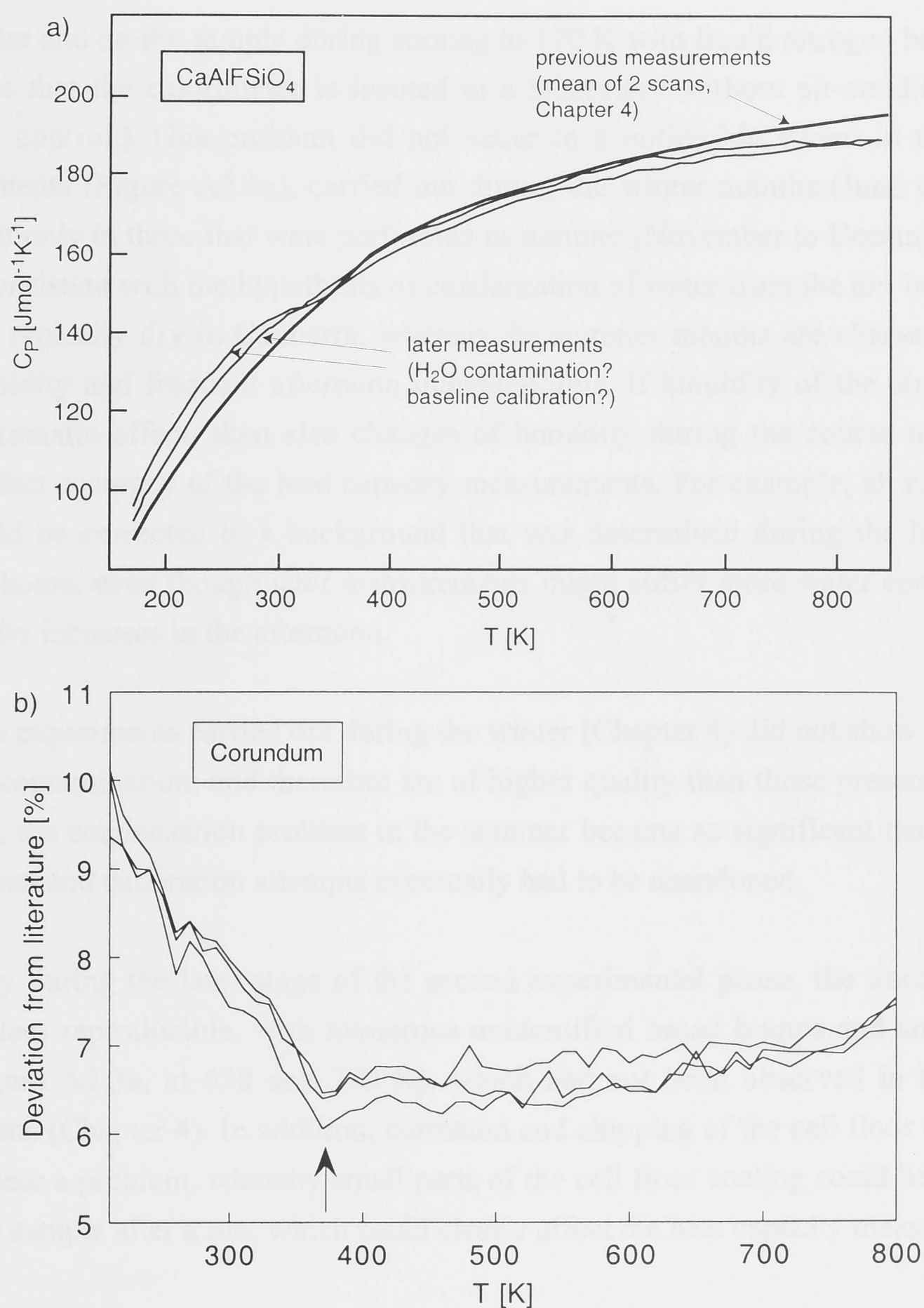
Figure A2.6 Effect of water contamination on heat capacity measurements. **a)** Comparison of heat capacity of CaAlFSiO$_4$ determined in winter (presented in Chapter 4), and in summer (later measurements). Note the large anomalies of the latter at temperatures below about 360 K.
b) Deviation of corundum heat capacity measurements from literature data (Sapphire standard, DSC manual). Note that the error increases significantly below 373 K, i.e. the boiling point of water (indicated by arrow).

Some heat capacity measurements showed especially large deviations from previous measurements or literature values at temperatures below 373 K (Figure A2.6). Since this effect stops at or just below the evaporation temperature of water, it is probably the result of water contamination of the samples or the calorimeter cell. Even thorough drying of the samples could not eliminate this problem. Since this effect also showed in the baseline runs of the empty cell, it is probably due to air humidity condensing in the

calorimeter and on the sample during cooling to 170 K with liquid nitrogen before each run (Note that the calorimeter is located in a laboratory without air-conditioning or humidity control.) This problem did not occur to a noticeable extent in the earlier measurements (Figure A2.6a), carried out during the winter months (June to August, 1999), but only in those that were performed in summer (November to December 1999). This is consistent with the hypothesis of condensation of water from the air, because the winter is typically dry in Canberra, whereas the summer months are characterised by high humidity and frequent afternoon thunderstorms. If humidity of the air can have such a dramatic effect, then also changes of humidity during the course of one day would affect accuracy of the heat capacity measurements. For example, all runs of one day would be corrected to a background that was determined during the less humid morning hours, even though later measurements might suffer more water condensation as humidity increases in the afternoon.

While the experiments carried out during the winter (Chapter 4) did not show any effect of water contamination, and therefore are of higher quality than those presented in this appendix, the condensation problem in the summer became so significant that the DSC experiments and calibration attempts eventually had to be abandoned.

Especially during the later stage of the second experimental phase, the traces became less and less reproducible, with numerous unidentified broad bumps and small peaks (e.g., Figure A2.3a, at 620 and 780 K), which had not been observed in the earlier experiments (Chapter 4). In addition, corrosion and chipping of the cell floor during the runs became a problem, whereby small parts of the cell floor coating could be found on top of the sample after a run, which could clearly affect the heat capacity measurements.

Conclusions

The sheer number of explained and unexplained problems during the second experimental phase compared to the earlier measurements, suggest that the first experiments (Chapter 4), which resulted in reproducible and smooth traces, are more reliable. However, it is not clear which problems discussed in this appendix would also have affected the earlier measurements, the accuracy of which can therefore not be guaranteed. Unfortunately, the time frame of this doctoral study did not allow a thorough investigation of each individual problem of the heat capacity measurements, which would have to include systematic variation of the heating rate, sample material, sample size, sample compaction, etc.. It is strongly recommended by this study that the heat capacity measurements are repeated with a different instrument.

Among the many encountered problems, the temperature dependent error of every first sample run (Figure A2.2) is the most likely error to have affected the earlier measurements. If the heat capacities of titanite and $CaAlFSiO_4$ presented in Chapter 4 have such an error, amounting to up to 4% at high temperatures for corundum, then the interpretations in Chapter 4 would have to be modified. For example, if the heat capacity of titanite was "corrected", or modified, by that amount (increasing linearly from 0% error at 170 K to 4% error at 850 K), the heat capacity determined in this study would match the data by Xirouchakis and Tangeman (1998), and not those of the previous studies (King et al.,1954; Zhang et al., 1995), as suggested in Chapter 4 (Figure A2.7a).
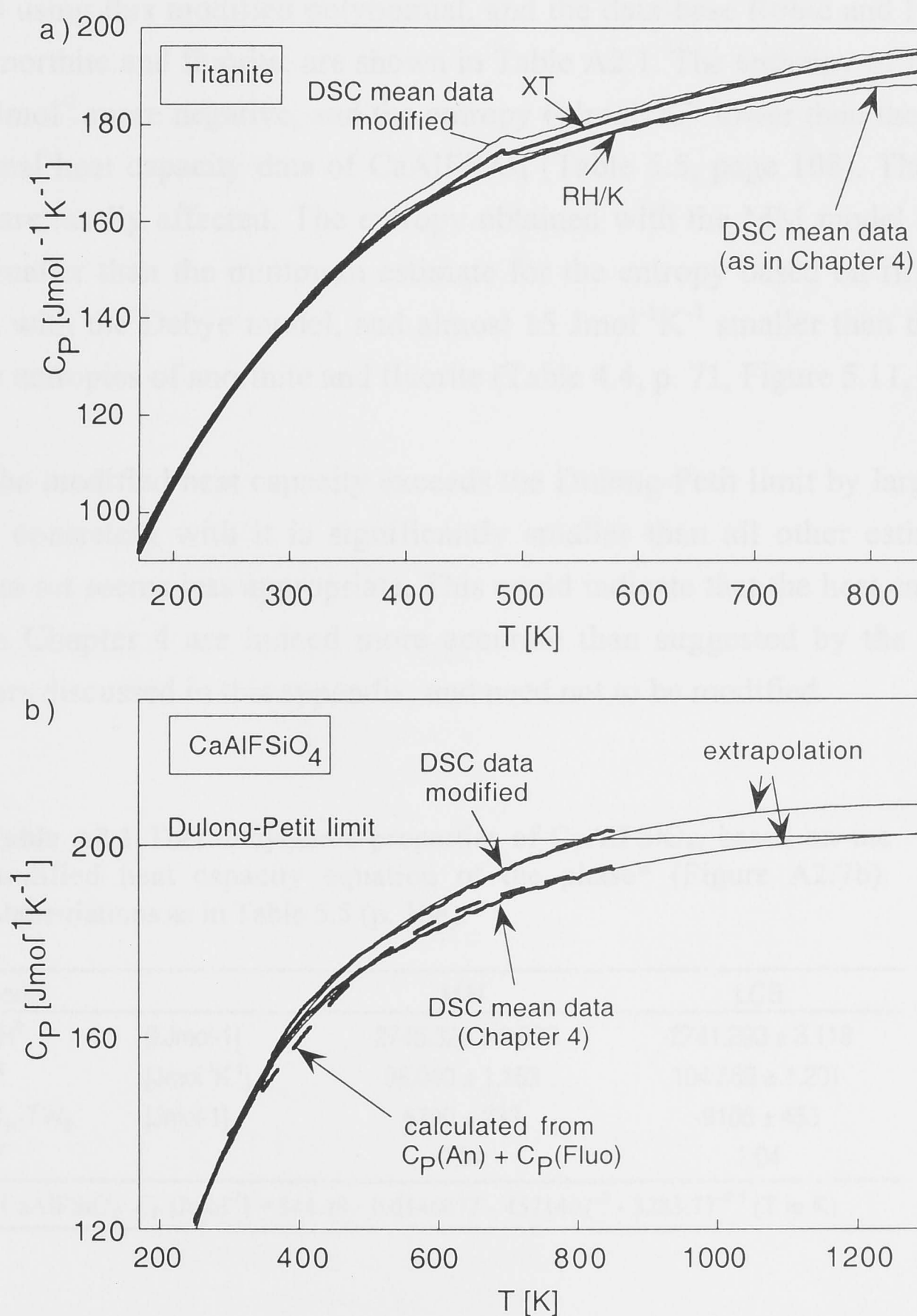
Figure A2.7 Heat capacity data of titanite and $CaAlFSiO_4$ as presented in Chapter 4, and modified according to a potential error (see text). Also shown in a) are previous titanite studies XT and RH/K (compare Figure A2.1). b) Heat capacity data are extrapolated to 1300 K with two dummy points on the Dulong-Petit limit at 1500 and 1800 K (compare Chapter 4). The polynomial coefficients of the modified data are given in Table A2.1.

The modification of the $CaAlFSiO_4$ heat capacity would result in data that are significantly higher than the heat capacity estimate based on fluorite and anorthite (Figure A2.7b). Moreover, these data would exceed the Dulong-Petit limit. Figure A2.7b also shows the extrapolation of this modified data set to 1300 K, using the Haas and Fisher (1976) equation with four terms. Although dummy points at 1500 and 1800 K of the Dulong-Petit limit were included in the refinement, the heat capacity exceeds the limit significantly, by 5.3 Jmol-1K-1 at 1300 K (Figure A2.7b).

The thermodynamic data of $CaAlFSiO_4$, which were obtained from the piston cylinder experiments using this modified polynomial, and the data-base Robie and Hemingway (1995) for anorthite and fluorite, are shown in Table A2.1. The enthalpy of formation is about 4.5 kJmol^{-1} more negative, and the entropy 6 Jmol^{-1}K^{-1} lower than the data based on the original heat capacity data of $CaAlFSiO_4$ (Table 5.5, page 108). The Margules parameters are hardly affected. The entropy obtained with the MM model is almost 7 Jmol^{-1}K^{-1} smaller than the minimum estimate for the entropy based on first principle calculations with the Debye model, and almost 15 Jmol^{-1}K^{-1} smaller than the estimate based on the entropies of anorthite and fluorite (Table 4.4, p. 71, Figure 5.11, p. 111).

Given that the modified heat capacity exceeds the Dulong-Petit limit by large, and that the entropy consistent with it is significantly smaller than all other estimates, this modified data set seems less appropriate. This could indicate that the heat capacity data presented in Chapter 4 are indeed more accurate than suggested by the number of possible errors discussed in this appendix, and need not to be modified.

Table A2.1 Thermodynamic properties of $CaAlFSiO_4$, based on the modified heat capacity equation of the phase* (Figure A2.7b). Abbreviations as in Table 5.5 (p. 108).

model		MM	LCB
d_fH^0	[kJmol-1]	-2748.329 ± 3.067	-2741.290 ± 3.118
S^0	[Jmol^{-1}K^{-1}]	98.040 ± 1.163	104.556 ± 1.201
W_H-TW_S	[Jmol-1]	6790 ± 233	-9106 ± 455
χ^2		0.64	1.04

* $CaAlFSiO_4$: C_P [Jmol^{-1}] = 344.49 - 0.034607T - 457140T^{-2} - 3283.7$T^{-0.5}$ (T in K)

Appendix 3
Abbreviations and symbols

Phase names

AlF	CaAlFSiO$_4$
Als	Aluminosilicate
An	Anorthite
Cc	Calcite
Fa	Fayalite
Fluo	Fluorite
Gro	Grossular
Ha	Halite
Hd	Hedenbergite
Ky	Kyanite
Law	Lawsonite
M	Magnetite
Mar	Margarite
Ru	Rutile
Sill	Sillimanite
Ttn	Titanite
Q	Quartz
Woll	Wollastonite
Zoi, Zoi-F, Zoi-OH	Zoisite, F and OH end-members
V	Vapour, H$_2$O

Constants, coefficients, variables, abbreviations

a^i_j	Activity of component j in phase i
a, b, c, d, β, V	Unit-cell dimensions
α	Thermal expansion
a, b, c, d, e, f	Polynomial coefficients of various equations, including heat capacity, Debye temperature, etc.
AV	Angular variance
B	Data base (Berman, 1988)
B$_{iso}$	Isotropic thermal parameter
BB	Heat capacity equation (Berman and Brown, 1985)
BVS	Bond valence sum
β	Isothermal compressibility
C$_P$	Heat capacity at constant pressure
C$_V$	Heat capacity at constant volume
DSC	Differential scanning calorimetry
fo$_2$, fF$_2$	Oxygen and fluorine fugacity
g(v)	Frequency distribution
G	Gibbs free energy
γ	Grüneisen parameter
γ_j	Activity coefficient of component j
h	Boltzman constant
hkl	Miller indices

H	Enthalpy
HF 4	Heat capacity equation (Haas and Fisher, 1976), 4 coefficients
HF 5	Heat capacity equation (Haas and Fisher, 1976), 5 coefficients
HP	Data base (Holland and Powell, 1998)
k	Planck constant
K	Equilibrium constant, activity ratio
LCB model	Local charge balance model (= molecular mixing model)
M_x	Polynomial coefficients for unit-cell dimensions
MK	Heat capacity equation (Maier and Kelley, 1932)
MM model	Multi-site mixing model (= ionic mixing model)
n, m	Stoichiometric coefficients
oct	Octahedral position in titanite structure
O1, O2, O3	Anion positions in titanite structure
P	Pressure
θ_D	Debye temperature
QE	Quadratic elongation
R	Gas constant
RH	Data base (Robie and Hemingway, 1995)
S	Entropy
SEM	Scanning electron microscopy
SUP94/98	Data base (SUPCRT, Johnson et al., 1991)
t	Time
T	Temperature
TEM	Transmission electron microscopy
V	Volume
v_D	Debye frequency
v_x	Compressibility and expansion coefficients (Berman, 1988)
W_G, W_H, W_S, W_V	Margules parameters ($W_G = W_H - TW_S + PW_V$)
X_j	Molar fraction of component j
x, y, z	Atom coordinates
XRD	X-ray diffraction

Subscripts

ss	Solid-solution
f	... of formation
P,T	... at given pressure and temperature
1,298	... at standard state conditions (1 bar, 298.15 K)
r	... at reference state (1 bar, 298.15 K)
3rd-law	referring to 3rd law of thermodynamics

Superscripts

0	... at standard state conditions (1 bar, 298.15 K)
exc	excess quantity of mixing

Crystal structural changes in titanite along the join TiO-AlF

ULRIKE TROITZSCH *[1], DAVID J. ELLIS [1], JOHN THOMPSON [2]
and JOHN FITZ-GERALD [3]

[1] Department of Geology, Faculty of Science,
[2] Research School of Chemistry,
[3] Research School of Earth Sciences,
at the Australian National University, Canberra, A.C.T. 0200, Australia

Abstract: We investigated the crystal structural changes in titanite solid-solution $Ca(Ti,Al)(O,F)SiO_4$ along the binary join TiO-AlF, on the basis of X-ray powder data and Rietveld refinement of seven synthetic titanites of intermediate compositions. Investigations with the transmission electron microscope allow us to narrow down the space group transition from $P2_1/a$ to $A2/a$ to compositions between $X_{Al} = 0.09$ and $X_{Al} = 0.18$ $[X_{Al} = Al/(Al+Ti)]$. The changes in most of the unit-cell dimensions along the binary join are non-linear, resulting in a small excess volume of mixing with a maximum at $X_{Al} = 0.54$. The commonly observed trend of positive deviation of the excess volume of mixing near the large end-member, and negative deviation towards the small end-member seems to be reversed in this case. At AlF-contents larger than $X_{Al} = 0.6$ the Ca-site and the O1-site in the titanite structure become increasingly overbonded with Al-F substitution. At about $X_{Al} = 0.4$ the octahedral cation-oxygen distances change significantly, indicating that the titanite structure undergoes a major atomic rearrangement at high AlF-contents in order to accommodate the increasingly different ionic size and charge. Generally, with increasing AlF content the polyhedra are being deformed rather than rotated. The changes in unit-cell dimensions, bond lengths and bond valence sums along the binary join suggest the presence of structural strain in AlF-rich titanite, especially at Al-F contents exceeding $X_{Al} = 0.4$. The structural problems are obviously not significant enough to prevent the formation of Al-rich titanite in simple chemical systems as in our experiments. However, the structural strain may be significant enough to decrease the thermodynamic stability of Al-rich titanite in natural rocks compared to other Al- and F-bearing phases. This could partly explain the rare natural occurrence of titanite with $X_{Al} > 0.54$.

Key-words: titanite, solid solution, crystal structure, crystal chemistry, Rietveld refinement.

Introduction

The mineral titanite $CaTiOSiO_4$ is a common accessory phase in a broad range of igneous, metamorphic, and even some sedimentary rocks. The composition of titanite is variable, depending on bulk-rock and fluid composition, pressure and temperature. The Al-content in titanite was the focus of numerous previous studies (*e.g.*, Smith,

1981; Enami *et al.*, 1993) because the two coupled exchange reactions

$$Ti^{4+} + O^{2-} = Al^{3+} + F^-$$
$$Ti^{4+} + O^{2-} = Al^{3+} + OH^-$$
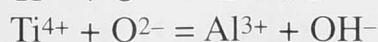
are very sensitive to pressure and temperature, and thus could be of interest for geothermobarometry. Many Al-rich titanites were reported from high-

* E-mail: ulrike@geology.anu.edu.au

pressure terrains (Smith, 1980; Krogh *et al.*, 1990; Carswell *et al.*, 1996), and from low-temperature rocks (Enami *et al.*, 1993), which is consistent with the smaller ionic radii of the substituents Al and F compared to Ti and O. However, other studies point out that also the bulk-rock or fluid composition can influence the Al-content in titanite (Markl & Piazolo, 1999).

Although one sample of titanite with Al contents of X_{Al} = 0.62 has been found (Franz, 1987), the amount of Al in natural titanite is mostly restricted to contents of X_{Al} < 0.54 (Franz & Spear, 1985; Markl & Piazolo, 1999). Because the experimental study of AlF-bearing titanite of Smith (1981) reported the same maximum possible Al-content (X_{Al} = 0.54) from a titanite synthesised at high pressures (35 kbar), it was suggested that a crystal structural constraint might exist which prevents the formation of titanite with X_{Al} > 0.5. Oberti *et al.* (1991) investigated the crystal structures of natural Al-rich titanites, and discussed this possibility in detail, but could not identify the potential structural problems in titanite with increasing Al-content.

In contrast to the previous studies, the experimental re-investigation of this system by Troitzsch & Ellis (1999) demonstrated that complete solid solution does exist between the end-members $CaTiOSiO_4$ and $CaAlFSiO_4$. Thus, while there is obviously no crystal structural limit preventing the formation of Al-rich titanite in these experiments, the question arises as to why there is such a discrepancy between the composition of natural and synthetic titanite.

The pioneering study by Oberti *et al.* (1991) used natural samples for a crystal structural analysis of titanite, and thus was restricted to lower Al-contents (0.0 < X_{Al} < 0.36). Here we present crystal structure data from synthetic samples covering the entire range of compositions of binary titanite solid solution $Ca(Ti,Al)(O,F)SiO_4$. The samples with X_{Al} = 0.09, 0.18, 0.29, 0.37, 0.49, 0.67, 0.75, 0.82, 1.00 are named AlF09, AlF18, AlF29, *etc*.

Crystal structure

The titanite structure (Fig. 1) is composed of kinked chains of edge-sharing octahedra parallel to *a*, which are interlinked by isolated SiO_4-tetrahedra (Speer & Gibbs, 1976). This network encloses the $Ca^{[7]}$-sites, which form chains of edge-sharing polyhedra interlacing with the octahedral chain (Kunz *et al.*, 1997). Along the binary

join TiO-AlF the titanium in the octahedron together with the oxygen occupying the O1-site are replaced by aluminium and fluorine, respectively.

Experimental details

Synthesis

Since the substitution of Al and F in the titanite structure is facilitated by high pressures, the titanite samples used in this study were synthesised in the piston cylinder apparatus at various pressures ranging from 5 to 35 kbar, depending on the Al-content of each sample. Temperatures were chosen to lie below the solidus, and ranged from 1000°C to 1100°C. Individual run conditions are listed in Appendix 1. The starting mixes were composed of synthetic anorthite, fluorite (Specpure), and either synthetic wollastonite and TiO_2 (Degussa), or synthetic titanite. The preparation of anorthite and titanite from glasses is described in Troitzsch & Ellis (1999). The glass for wollastonite synthesis was prepared from $CaCO_3$ (Specpure) and SiO_2 (Aerosil, Degussa), which were dried prior to weighing at 400°C for 4 h, and 1000°C for 18 h, respectively. The mix was ground in acetone in an agate mortar for 2 h. It was then heated from 800°C to 1600°C over the course of 8 h, held at 1600°C for 1 h, and then quenched in water. Wollastonite was then crystallised from the glass at 1100°C for 13 h. Examination of the
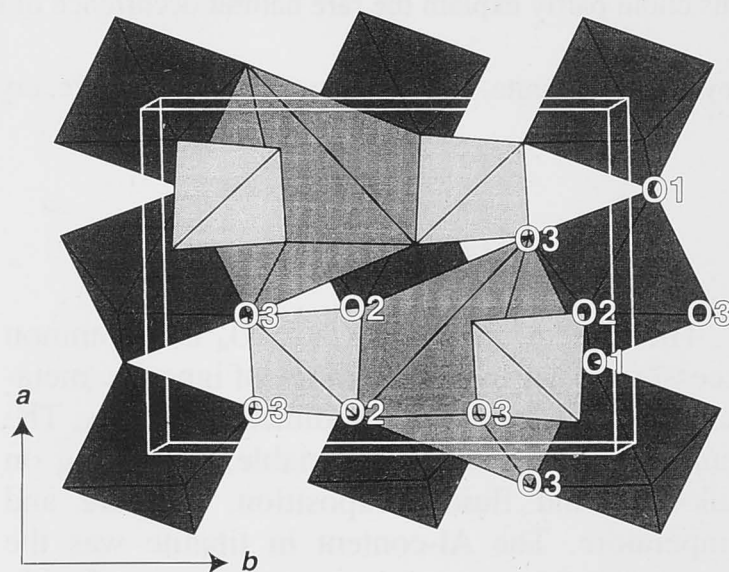

Fig. 1. Polyhedral representation of a section of the titanite structure showing the geometrical relationship between the Al/Ti-octahedra, Si-tetrahedra and $Ca^{[7]}$-polyhedra. O1 is occupied by oxygen and fluorine.

result with optical microscopy and X-ray diffraction confirmed that only wollastonite was present, and no glass remained.

Xirouchakis *et al.* (1997) pointed out that titanite prepared from glass has the potential to be non-stoichiometric due to Ca- and Si-vacancies together with Si-rich and Ca-Si-rich phase impurities, and could yield unit-cell dimensions larger than those of the ideal crystal. However, their unit-cell data for titanite synthesised at sub-solidus conditions ($a = 7.062(1)$, $b = 8.716(2)$, $c = 6.559(1)$, $\beta = 113.802(9)$, $V = 369.4(3)$, Xirouchakis *et al.*, 1997) are in very good agreement with those obtained from the glass-derived titanite that was used for starting mixes in this study ($a = 7.0613(3)$, $b = 8.7158(2)$, $c = 6.5588(2)$, $\beta = 113.809(2)$, $V = 369.31(2)$; determined from powder X-ray diffraction pattern with the computer program RIETAN (Izumi, 1993; Kim & Izumi, 1994)). This shows that titanite prepared from a glass can yield accurate unit-cell data, and that the titanite used as starting mix in this study is close to ideal stoichiometry. Since all Al-bearing titanite samples of this study were synthesised at sub-solidus conditions, their unit-cell volumes should be reliable, unless there is a significant effect of the potential non-stoichiometry of the glass-derived starting mix components anorthite and wollastonite on the titanite unit-cell dimensions.

The starting mixes for the titanite syntheses were ground in acetone, and about 15 mg or 150 mg of mix were filled in silver-palladium capsules ($Ag_{0.75}Pd_{0.25}$) with a diameter of either 2 or 3 mm. The capsules were then dried at 110°C for at least 1 h before welding shut. The pressure medium enclosing the capsule was boron-nitride and a surrounding salt- or salt-pyrex sleeve, with zero friction correction. The pressure readings during the experiments are precise within 2%. The temperature was monitored by a $Pt-Pt_{90}Rh_{10}$ thermocouple, and was regulated automatically by a EUROTHERM controller. The accuracy of the temperature measurements was 5°C. The synthesis of sample AlF100 is described in Troitzsch & Ellis (1999, sample G-297).

Samples AlF09 and AlF75 were crushed and re-run at the same synthesis conditions more than once (Appendix 1) because of chemical inhomogeneity of the first run products. Generally, starting mixes containing wollastonite and TiO_2 resulted in chemically more homogeneous run products, compared to mixes containing titanite. Titanite from the starting mix tended to be preserved as Ti-rich cores in an otherwise Al-rich solid solution.

The grain size of the run products ranged from 5 to 20 μm. Apart from titanite solid solution, all run products contained a certain amount of additional phases, including fluorite, silver-palladium, F-bearing zoisite, kyanite, quartz and halite (Table 1). The formation of fluorite and kyanite is due to slight deviations of the starting mix from the binary join. F-bearing zoisite forms from anorthite and fluorite, and its presence in these types of experiments is discussed in Troitzsch & Ellis (1999). Contamination with the capsule material silver-palladium can occur both during the run as well as afterwards, when recovering the sample by cutting open the capsule. Contamination of the sample by diffusion during the run is suggested by

Table 1. Rietveld refinement results and unit-cell dimensions of synthetic titanite solid solution.

sample	AlF-content [X_{Al}]	other phases	ttn wt%	R_{wp}	R_{Bragg}	a [Å]	b [Å]	c [Å]	β [°]	V [Å³]
AlF09	0.099(40)	AgPd qtz	95	10.27	4.88	7.0541(3)	8.6925(2)	6.5445(2)	113.903(2)	366.88(2)
AlF18	0.182(4)	AgPd fl	98	9.42	3.71	7.0511(2)	8.6722(2)	6.5325(2)	114.026(2)	364.84(2)
AlF29	0.291(12)	AgPd	99	10.03	4.23	7.0462(3)	8.6529(2)	6.5231(2)	114.143(1)	362.92(2)
AlF37	0.372(4)	fl ha	96	9.47	2.97	7.0368(2)	8.6360(2)	6.5135(2)	114.232(2)	360.95(2)
AlF49	0.489(7)	fl	99	9.00	3.58	7.0229(3)	8.6130(2)	6.5023(2)	114.344(2)	358.34(2)
AlF67	0.672(18)	fl qtz	97	9.46	3.84	6.9904(3)	8.5759(2)	6.4798(2)	114.480(2)	353.54(2)
AlF75	0.753(19)	fl qtz zoi	76	10.77	3.93	6.9734(3)	8.5586(2)	6.4704(3)	114.539(2)	351.29(2)
AlF82	0.819(22)	fl zoi	96	11.30	5.11	6.9580(3)	8.5445(2)	6.4612(3)	114.585(3)	349.35(2)
AlF100	1.000(0)	fl qtz zoi ky	84	10.05	3.66	6.9157(2)	8.5076(1)	6.4391(1)	114.683(2)	344.24(1)

Standard deviations of chemical analyses in column 2 are given in brackets. Third column specifies impurity phases which were considered in the refinement (qtz - quartz, fl - fluorite, ha - halite, zoi - F-bearing zoisite, ky - kyanite).

the presence of small interstitial particles of silver-palladium which occur in the vicinity of the capsule-wall, but are clearly detached from it. Small amounts of quartz were detected with X-ray diffraction, but could not be confirmed with scanning electron microscopy. It is therefore likely that quartz contamination occurred during grinding of the samples in an agate mortar when preparing for X-ray diffraction. One sample contained a small amount of halite, which probably represents salt-sleeve material entering the sample through a rupture in the capsule wall. Since the titanite in this sample does not contain any sodium or chlorine, the sample was used for refinement. Sample AlF75 contained almost 20 wt% zoisite, which made the crystal structure refinement of the titanite component difficult. Therefore this sample was only used to determine unit-cell parameters.

Scanning electron microscopy (SEM)

Quantitative analyses were obtained with a JEOL JSM-6400 scanning electron microscope, Link ISIS EDS, at 15 kV and 1 nA, at the Electron Microscopy Unit, Australian National University. Analyses were calculated using ZAF-correction. Analysed elements were silicon, titanium, aluminium, calcium, fluorine and oxygen. The samples were mounted in raisin, polished and carbon-coated. Between 15 and 25 titanite grains were analysed per sample. All analyses were stoichiometric binary titanite solid solution $Ca(Ti,Al)(O,F)SiO_4$ within a precision of 5 mol%.

Transmission electron microscopy (TEM)

Diffraction patterns of sample AlF18 were investigated at 300 kV using a Philips EM 430T at the Electron Microscopy Unit, Australian National University. The camera constant was calibrated against thallium chloride, the uncertainty of the measurements is 1%. The sample was finely ground, dispersed on a carbon-coated copper grid, and mounted on a tilt-rotate holder.

X-ray diffraction (XRD)

Powder diffraction data were collected at room temperature with a Siemens D501 diffractometer at the Geology Department, Australian National University. The diffractometer was equipped with a curved graphite monochromator, a scintillation detector, and $CuK\alpha$ radiation was used. The diffraction data were recorded in four

or five passes over a range of 17 to 95°2-theta, using a step width of 0.02° at a scan speed of 0.5° per minute.

Due to the small amount of material the samples had to be dispersed with acetone onto a low-background holder (oriented quartz single crystal) with a pipette. This technique has the disadvantage of increasing the effect of preferred orientation in the mounted sample.

For the sample AlF82 diffraction data were also collected using a Guinier-Hägg Camera XDC-700 (Junger Instrument Sweden), with Cu $K\alpha_1$ radiation, at 40 kV, 25 mA and 30 min exposure time. The sample was pressed down onto a sticky tape to enhance preferred orientation (see discussion below).

Rietveld refinement

The refinement of the crystal structures using the Rietveld method was carried out with the computer program RIETAN (Izumi, 1993; Kim & Izumi, 1994), using a pseudo-Voigt profile-shape function, and the "International Tables for Crystallography" (Wilson et al., 1992) as the data base. Neutral-atom scattering factors were chosen for all sites. All phases shown in Table 1 were included in the profile fitting. Refined non-atomic parameters include one for specimen displacement, eight background parameters, scale factors, up to 6 peak shape parameters per phase, preferred orientation, and the unit-cell parameters of titanite and silver-palladium. The occupation factors of all sites were set to 1, with the mixed occupation of the octahedral and the O1-site fixed to values obtained from the chemical analyses. Fixing the occupations is justified given that chemical analyses with the microprobe yield more reliable data compared to occupation factors refined from a complex multi-phase powder pattern. Due to significant peak overlap at high 2-theta angles, the background was fixed before the isotropic thermal parameters were refined in order to avoid correlation problems. One global isotropic thermal parameter was refined for all anions.

If no preferred orientation (March-Dollase function) was applied in the refinement, peak intensities could not be matched well in some of the samples (e.g. AlF09 and AlF82). In order to confirm that the intensity mismatch was related to preferred orientation of the sample on the low background holder, a Guinier experiment was carried out with sample AlF82, and the relative peak intensities of both patterns compared. While the reflection geometry in the X-ray diffractometer

leads to preferred diffraction of those planes which are about parallel to the preferred cleavage plane, the transmission geometry of the Guinier Camera will result in preferred diffraction of those lattice planes that are oriented perpendicular to the cleavage.

The comparison of the relative peak intensities of the Guinier pattern with those obtained with Bragg-Brentano geometry showed that in the Guinier pattern peaks $\overline{2}11$ and $\overline{2}02$, for example, were significantly smaller, while reflection 140 was stronger. The fact that plane 140 is about perpendicular to $\overline{2}11$ and $\overline{2}02$ is consistent with the hypothesis that the intensity difference between the two patterns is indeed due to preferred orientation of the crystallites in the sample, with a cleavage plane sub-parallel to reflections $\overline{2}11$ and $\overline{2}02$. The prominent cleavage plane of titanite is $\overline{1}11$ (Deer et al., 1962). Since this plane has a similar orientation to $\overline{2}11$ and $\overline{2}02$, $\overline{1}11$ was chosen to represent the preferred orientation plane in the Rietveld refinement. The application of this preferred orientation correction improved the overall fit of the refinement of AlF82 significantly (R_{wp} decreased from 12.29 to 11.30, and R_{Bragg} of titanite from 7.16 to 5.11), and peak intensities of the main peaks could now be matched well. Preferred orientation correction was applied only to those other samples which showed an intensity mismatch of the same peaks compared to those observed in AlF82 before the correction.

It should be pointed out that the oxygen positions O2 and O3 in sample AlF82 correlated strongly with the preferred orientation correction. Especially the resulting Si-O bonds were sensitive to preferred orientation, resulting in uneven tetrahedral Si-O bonds (1.620(7) Å and 1.660(8) Å) without correction, and more reasonable bond lengths (1.636(6) Å and 1.621(7) Å) when the correction was applied.

Sample AlF100, which was previously investigated by Troitzsch & Ellis (1999), was refined again for this study, this time with the preferred orientation correction for $\overline{1}11$, which probably represents an improved model for this sample. The application of preferred orientation correction lowered the isotropic thermal parameters, and changed the Si-O2 and Si-O3 bonds from 1.603(4) Å and 1.653(4) Å to 1.605(4) Å and 1.642(5) Å, respectively. Thus the tetrahedral distortion in $CaAlFSiO_4$ is slightly less pronounced than described in Troitzsch & Ellis (1999).

Results and discussion

Space group

The well known and intensely studied change in space group from $P2_1/a$ to $A2/a$ in the titanite structure can be induced by chemical substitution (Higgins & Ribbe, 1976; Speer & Gibbs, 1976), temperature (Taylor & Brown, 1976; Kek et al., 1997) and pressure (Kunz et al., 1996). The reason for the gain in symmetry lies in the position of the octahedral atom. At room temperature octahedrally
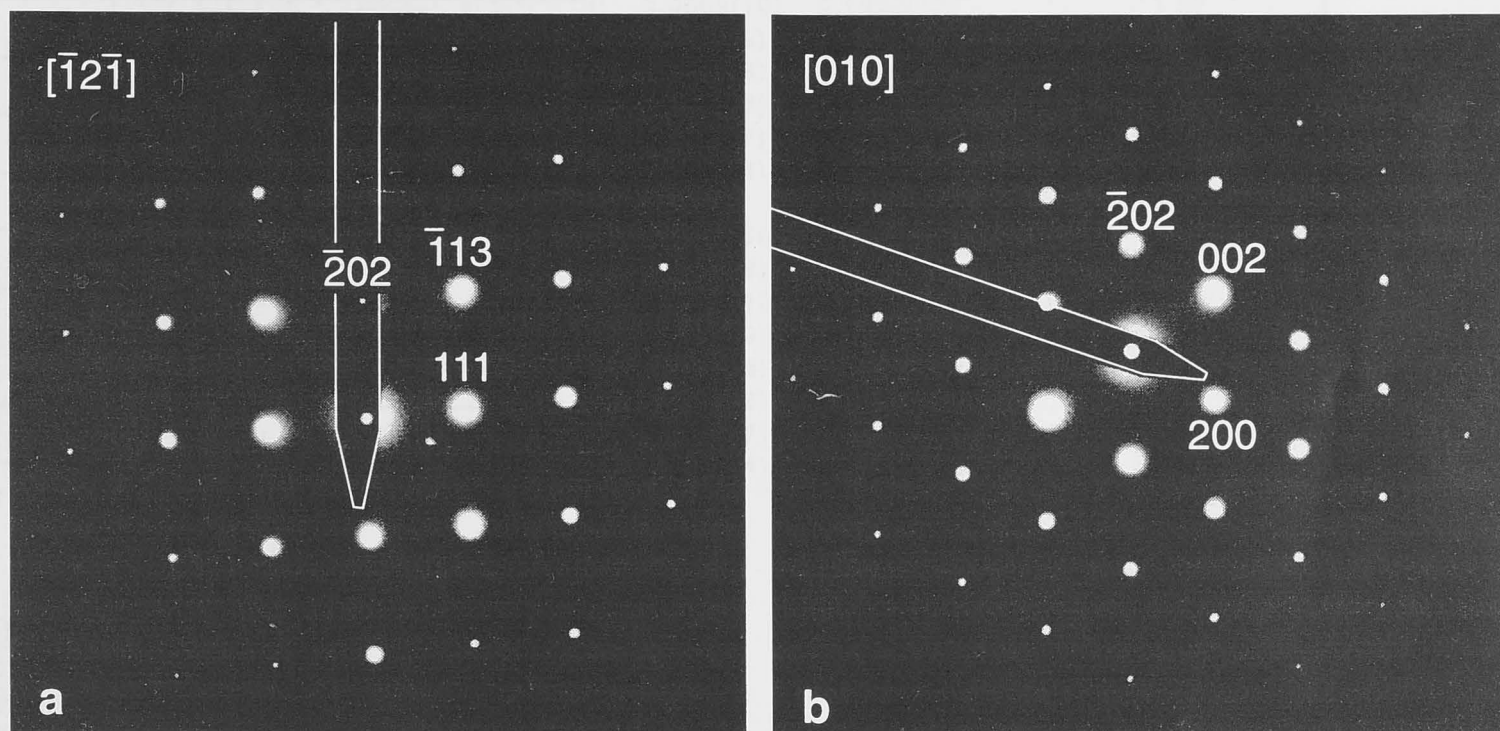

Fig. 2. Diffraction patterns of titanite with $X_{Al} = 0.182$ (sample AlF18) viewed along [$\overline{1}2\overline{1}$] (a) and along [010] (b).
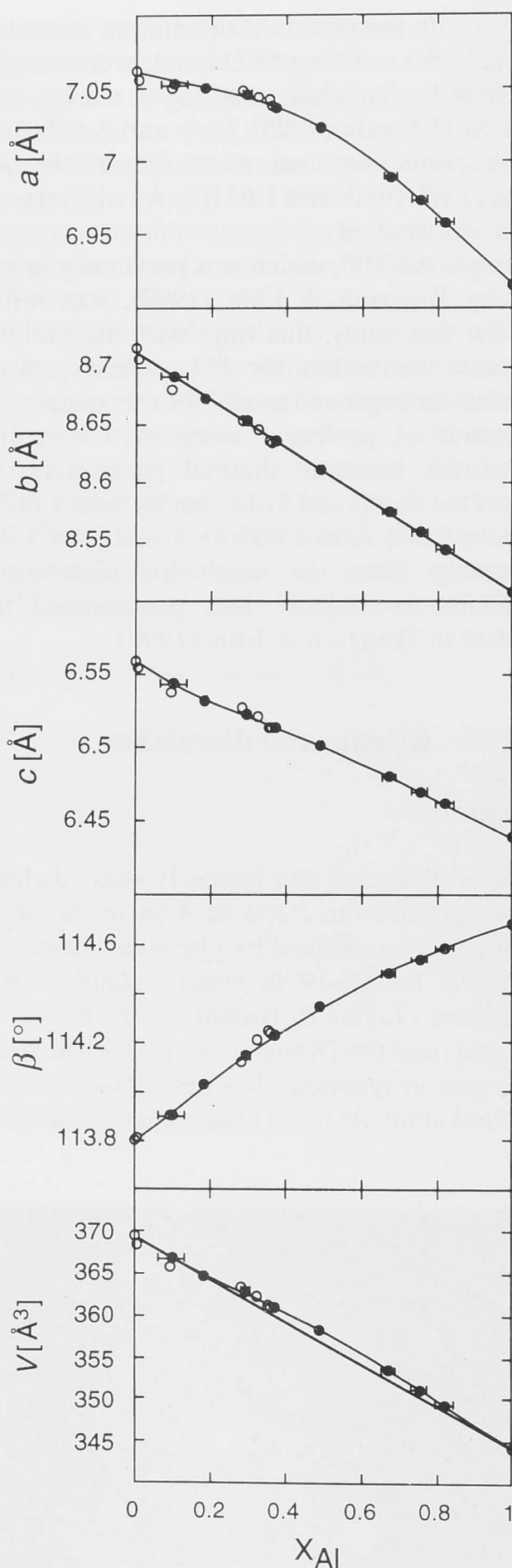
Fig. 3. Unit-cell dimensions of binary titanite solid solution $Ca(Ti,Al)(O,F)SiO_4$. Full symbols, this study; open symbols, previous studies by Xirouchakis *et al.* (1997), Hollabaugh & Foit (1984) and Oberti *et al.* (1991).

tion, but in opposite direction in the neighbouring chains, resulting in symmetry $P2_1/a$. The symmetry can be raised to $A2/a$ by two processes: 1) the Ti atom is shifted to the center of the octahedron, as reported from titanites at very high pressures (Kunz *et al.*, 1996), and 2) the loss of short range order of the Ti off-centring direction within one octahedral chain, resulting in domains of $P2_1/a$ symmetry on the unit-cell scale, but an overall, average symmetry of $A2/a$ on the long-range scale. The latter process can be observed along the binary join TiO-AlF in titanite investigated in this study, because the formation of domains with opposite Ti-displacement is enhanced by chemical substitution of the octahedral cation and the O1 site, since this weakens the interaction between the off-centred Ti atoms within the octahedral chain (Higgins & Ribbe, 1976; Speer & Gibbs, 1976; Kunz *et al.*, 1997).

Sample AlF18 was investigated by TEM in order to narrow down the change in space group from $P2_1/a$ to $A2/a$ with increasing content in Al and F in binary titanite solid solution. In all diffraction patterns, *e.g.* that viewed along the $[\bar{1}21]$ zone axis, reflections hkl, $k+l = 2n+1$ are absent, indicating that the space group is A-centered (Fig. 2 a). Further, the existence of the *a*-glide is seen in the [010] diffraction pattern, where only the $h0l$, $h = 2n$ reflections are present (Fig. 2 b). Note that there is no trace even of diffuse diffraction $k+l = 2n+1$ positions in either Fig. 2 (a) or (b).
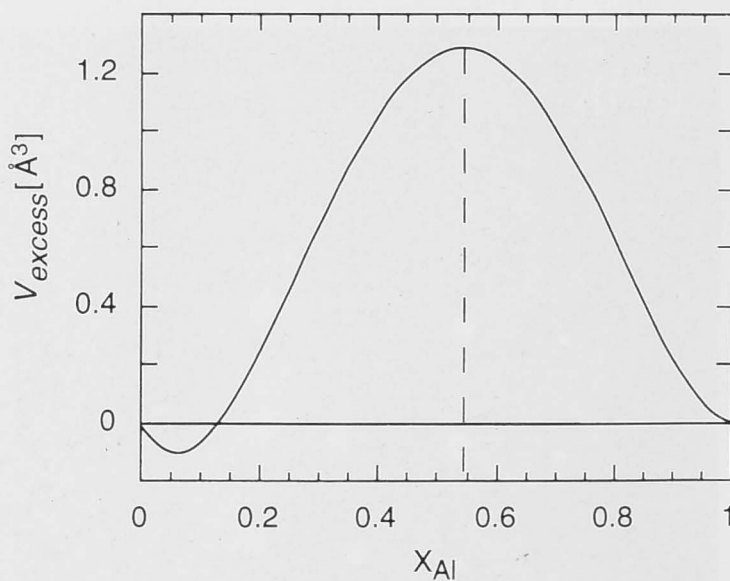

Fig. 4. Excess volume of mixing calculated as the difference between function V (Appendix Table 2) and linear interpolation between the end-member volumes of titanite (Xirouchakis *et al.*, 1997) and $CaAlFSiO_4$. Dashed line shows position of maximum, horizontal bar shows ideal volume.

coordinated Ti is typically displaced off the center of the octahedron. In titanite, all Ti atoms in one octahedral chain are off-centred in the same direc-

Table 2. Atom positions, isotropic thermal parameters and bond valence sums of synthetic titanite solid solution.

	sample	x	y	z	B_{iso} [Å²]	BVS
Ca	AlF09	0.25	0.1666(6)	0.00	1.94(18)	2.00
	AlF18	0.25	0.1659(5)	0.00	1.77(15)	2.05
	AlF29	0.25	0.1652(7)	0.00	1.85(19)	2.03
	AlF37	0.25	0.1651(6)	0.00	1.28(15)	2.13
	AlF49	0.25	0.1639(5)	0.00	1.64(14)	2.03
	AlF67	0.25	0.1632(5)	0.00	1.66(13)	2.09
	AlF82	0.25	0.1623(4)	0.00	1.87(11)	2.17
	AlF100	0.25	0.1642(2)	0.00	1.34(7)	2.18
oct	AlF09	0.50	0.00	0.50	1.98(13)	4.06
	AlF18	0.50	0.00	0.50	1.64(12)	3.91
	AlF29	0.50	0.00	0.50	1.75(14)	3.68
	AlF37	0.50	0.00	0.50	1.59(13)	3.56
	AlF49	0.50	0.00	0.50	1.52(12)	3.55
	AlF67	0.50	0.00	0.50	1.70(12)	3.35
	AlF82	0.50	0.00	0.50	2.20(11)	3.23
	AlF100	0.50	0.00	0.50	1.40(7)	2.99
Si	AlF09	0.75	0.1846(10)	0.00	1.62(21)	3.93
	AlF18	0.75	0.1833(8)	0.00	0.93(16)	3.83
	AlF29	0.75	0.1834(10)	0.00	1.59(21)	4.04
	AlF37	0.75	0.1837(9)	0.00	0.83(17)	4.00
	AlF49	0.75	0.1848(8)	0.00	1.19(16)	3.98
	AlF67	0.75	0.1856(8)	0.00	1.22(15)	4.00
	AlF82	0.75	0.1865(7)	0.00	1.45(13)	3.95
	AlF100	0.75	0.1867(4)	0.00	1.03(7)	4.01
O1	AlF09	0.75	0.0666(14)	0.5	0.65(14)	2.04
	AlF18	0.75	0.0689(11)	0.5	0.09(11)	1.93
	AlF29	0.75	0.0674(13)	0.5	0.49(14)	1.80
	AlF37	0.75	0.0698(12)	0.5	0.38(12)	1.72
	AlF49	0.75	0.0674(11)	0.5	0.50(11)	1.61
	AlF67	0.75	0.0684(10)	0.5	0.81(11)	1.46
	AlF82	0.75	0.0698(9)	0.5	0.95(9)	1.35
	AlF100	0.75	0.0694(5)	0.5	0.56(6)	1.25
O2	AlF09	0.9070(14)	0.0670(9)	0.1832(13)	as O1	1.95
	AlF18	0.9096(11)	0.0664(8)	0.1849(11)	-	1.95
	AlF29	0.9071(13)	0.0669(10)	0.1852(13)	-	1.97
	AlF37	0.9030(11)	0.0654(9)	0.1850(12)	-	2.00
	AlF49	0.9052(10)	0.0673(8)	0.1885(10)	-	1.97
	AlF67	0.9036(9)	0.0650(8)	0.1893(10)	-	1.97
	AlF82	0.9028(8)	0.0624(7)	0.1901(8)	-	1.97
	AlF100	0.9048(5)	0.0662(4)	0.1877(5)	-	1.96
O3	AlF09	0.3842(15)	0.2086(10)	0.4001(15)	as O1	2.02
	AlF18	0.3853(12)	0.2088(8)	0.3989(13)	-	1.98
	AlF29	0.3821(14)	0.2103(10)	0.3993(15)	-	2.00
	AlF37	0.3796(12)	0.2083(9)	0.3948(13)	-	1.98
	AlF49	0.3838(10)	0.2057(8)	0.4017(11)	-	2.00
	AlF67	0.3850(10)	0.2049(8)	0.4045(11)	-	2.02
	AlF82	0.3845(8)	0.2028(7)	0.4049(9)	-	2.03
	AlF100	0.3898(5)	0.2020(4)	0.4054(6)	-	2.01

Thus the change in space group in binary titanite $Ca(Ti,Al)(O,F)SiO_4$ has to occur between $X_{Al} = 0.0$ and $X_{Al} = 0.18$. This is in agreement with previous studies based on natural titanite, containing substituents Fe and OH in addition to Al and F. Higgins & Ribbe (1976) reported the disappear-

ance of diffuse $k+l = 2n+1$ reflections in titanite solid solution between $X_{Al+Fe} = 0.08$ and $X_{Al+Fe} = 0.21$. Hollabaugh & Foit (1984) investigated a titanite in which the Ti-substitution was dominated by Al ($X_{Al} = 0.09$, $X_{Fe} = 0.01$). Diffraction patterns of this specimen still showed diffuse

reflections belonging to space group $P2_1/a$. In contrast to this, the high-Al titanites ($X_{Al} > 0.25$) investigated by Oberti *et al.* (1991) did not produce $k+l = 2n+1$ reflections. Combination of the data of Hollabaugh & Foit (1984) and this study points to the P ↔ A transition occurring between $X_{Al} = 0.09$ and $X_{Al} = 0.18$.

Sample AlF09 of this study was unsuitable for space group investigations because of the large chemical variation this sample displays (Table 1). It probably covers the entire compositional range over which the space group conversion occurs, and contains both titanites belonging to space group $P2_1/a$ as well as those having $A2/a$ symmetry. We chose to refine the structure of this sample in space group $A2/a$, noting that this is possibly a simplification for some of the crystallites in the sample. While the unit-cell parameters resulting from this refinement should represent valid data corresponding to the average composition of the sample, it has to be born in mind that the atom positions and resulting bond lengths of sample AlF09 might only be an approximation.

Unit-cell dimensions

The changes in unit-cell dimensions along the binary join TiO-AlF (Table 1), and the good agreement of our data with those from the literature are shown in Fig. 3. The linear and polynomial functions which were fitted to the data of this study and those of Xirouchakis *et al.* (1997) for pure titanite are given in Appendix 2. Except for unit-cell length *b*, all dimensions change non-linearly, resulting in a small excess volume of mixing. Thus this binary titanite represents a non-ideal solid solution. The excess volume of mixing is shown in Fig. 4. Even though excess volumes of mixing have been reported from many solid solutions, it should be noted that in this case the usual trend of positive deviation near the large end-member, and negative deviation towards the small end-member (Newton & Wood, 1980), seems to be reversed. The negative deviation, however, is small and within error range. Note that the excess volume of mixing reaches its maximum at $X_{Al} = 0.54$ (± 0.11). It might just be coincidence that this value also represents the maximum Al-content in titanite reported in many previous studies (Smith, 1981; Franz & Speer, 1985; Markl & Piazolo, 1999). However, it could also indicate that at this point along the binary join the crystal structure is undergoing major changes in order to accommodate an increasing amount of Al and F.

Bond valence sums

The atom positions, bond valence sums and bond lengths are listed in Tables 2 and 3. The bond valence sums, which were calculated with the computer program EUTAX (based on the idea of Brese & O'Keeffe, 1991), are close to ideal values

Table 3. Selected bond lengths, bond angles and polyhedral volumes of titanite solid solution.

		AlF09	AlF18	AlF29	AlF37	AlF49	AlF67	AlF82	AlF100
Ca-O1	[Å]	2.320(13)	2.300(11)	2.314(13)	2.290(12)	2.314(11)	2.301(10)	2.289(9)	2.267(5)
Ca-O2	[Å]	2.390(9)	2.383(7)	2.371(9)	2.347(8)	2.357(7)	2.323(7)	2.289(6)	2.317(4)
Ca-O3A	[Å]	2.424(9)	2.411(8)	2.412(9)	2.379(8)	2.410(7)	2.416(7)	2.409(5)	2.397(3)
Ca-O3B	[Å]	2.626(10)	2.617(8)	2.63(1)	2.644(9)	2.632(8)	2.620(7)	2.621(6)	2.570(4)
Ca-O mean	[Å]	2.457	2.446	2.449	2.433	2.445	2.431	2.418	2.405
V	[Å³]	19.737	19.382	19.648	19.263	19.502	19.233	18.902	18.401
oct-O1	[Å]	1.856(4)	1.861(3)	1.856(4)	1.860(3)	1.849(3)	1.844(3)	1.839(2)	1.827(1)
oct-O2	[Å]	1.991(8)	1.977(7)	1.970(8)	1.961(7)	1.942(6)	1.922(6)	1.904(5)	1.920(3)
oct-O3	[Å]	1.988(8)	1.983(7)	1.997(8)	1.986(8)	1.945(7)	1.925(7)	1.901(6)	1.876(4)
oct-O mean	[Å]	1.945	1.941	1.941	1.936	1.912	1.897	1.881	1.874
V	[Å³]	9.792	9.723	9.730	9.652	9.309	9.089	8.872	8.767
Si-O2	[Å]	1.623(9)	1.627(8)	1.615(9)	1.609(8)	1.617(7)	1.624(7)	1.636(6)	1.605(4)
Si-O3	[Å]	1.639(12)	1.654(10)	1.627(11)	1.639(10)	1.636(9)	1.625(9)	1.621(7)	1.642(5)
Si-O mean	[Å]	1.631	1.640	1.621	1.624	1.626	1.624	1.629	1.623
V	[Å³]	2.210	2.250	2.172	2.183	2.195	2.182	2.194	2.175
oct-O1-oct	[°]	143.7	142.5	143.4	142.2	143.4	142.9	142.2	142.3

bonds. Although the contribution to the bond valence sum from the Ca-O1 bond decreases with increasing occupation of O1 by F, this effect is more than compensated by the shortening of the two Ca-O2 bonds. The overbonding of the O1-site is caused by an increasing contribution to the bond valence sum from the Ca-O1 bond. While the Ca-site only becomes significantly overbonded at high Al-contents, the O1-site is overbonded at all compositions. Fig. 5 shows that with increasing Al-content the overbonding at the O1-site decreases initially, reaches a minimum at about $X_{Al} = 0.40$, and then increases until it reaches its maximum at the end-member $CaAlFSiO_4$. The curved shape is due to the competing effects of the decrease in average valences of the octahedral and O1-sites along the join TiO-AlF, and the changing bond lengths, which both contribute to the bond valence sums.

Overbonding of the O1-site was suggested by Oberti et al. (1991) to be a potential structural problem in very Al-rich titanite. Their hypothesis, which was based on extrapolation from samples with Al-contents below $X_{Al} = 0.36$, is thus confirmed by the Al-rich samples of this study.

Cation polyhedra

The decrease in unit-cell volume with increasing X_{Al} (Fig. 3) is mainly caused by the decreasing size of the $(Ti,Al)(O,F)_2O_4$ octahedron and the $Ca^{[7]}$ polyhedron (Table 3). In contrast to this the SiO_4 tetrahedron remains constant in volume. The correlation between the octahedral- and Ca-sites in titanite solid solution was pointed out by Oberti et al. (1991) and Kunz et al. (1997). Since the Ca-polyhedron is closely interlinked with the octahedral chain (Fig. 1), it has to change shape and size together with the octahedron when this is occupied by ions of different size. With a remarkably constant oct-O1-oct angle of about $143°$ ($\pm 1°$) (Table 3) the kinked oct-O1 chain is acting as a shrinking, but rigid skeleton which forces the rest of the structure to adjust. Since the SiO_4-tetrahedra represent fairly incompressible structural units, it is the large Ca-polyhedron which is forced to change shape and decrease in size, even though its occupying cation remains the same. This is the reason for the large bond valence sums of Ca at high Al-contents. The competing relationship between the chain of corner-sharing octahedra and that of edge-sharing Ca-polyhedra in the titanite structure was demonstrated for the structurally related titanite-malayaite solid solution by Kunz et al. (1997).

Fig. 5. Bond valence sums (BVS) of the Ca-site, the octahedral cation and the O1-site. Symbols as in Fig. 3. Lines show the ideal valence sums for each site. The deviation from ideality of BVS of O1 was calculated as the difference between function BVS (Appendix Table 2) and the ideal bond valence sum.

for the octahedral site (Fig. 5), Si, O2 and O3. However, those for Ca and the O1 site clearly deviate from ideality (Fig. 5), indicating which parts of the titanite structure seem to have difficulties in adjusting to the increasing amount of the substituting ions Al and F.

The overbonding of the Ca-site at high Al-contents is mainly due to shortening of the two Ca-O2
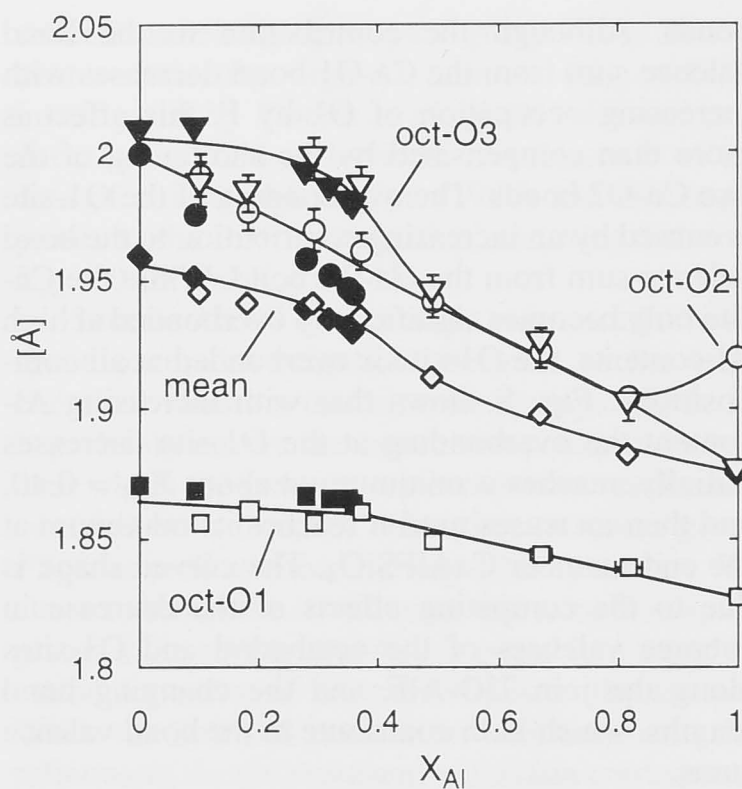
Fig. 6. Bond lengths from the octahedral cation to the coordinating anions O1, O2 and O3. Open symbols, this study; full symbols, previous studies by Xirouchakis *et al.* (1997), Hollabaugh & Foit (1984) and Oberti *et al.* (1991).

Fig. 6 shows the variation with Al-content of the bond-lengths from the octahedral cation to the coordinating anions. All bond lengths decrease in a non-linear way, with a major inflection of bonds oct-O1 and oct-O3 at about $X_{Al} = 0.4$. Beyond this point the oct-O1 distance decreases more rapidly, which can be correlated to the increasing overbonded character of the O1-site (Fig. 5d). The oct-O3 distance decreases significantly at this point until it equals oct-O2. In the end-member $CaAlFSiO_4$ the oct-O2 distance is larger than oct-O3, which is reversed compared to lower Al-contents. Note that the natural samples used by Oberti *et al.* (1991) were restricted to Al-contents just below the inflection point at $X_{Al} = 0.4$, and therefore could not indicate the changes in crystal structural trends shown here.

Conclusions

The crystal structure of titanite accommodates the increasing amount of Al and F by changing the size and shape of all the cation polyhedra, rather than simply by polyhedral rotation. This is in agreement with the study by Hammonds *et al.* (1998) which predicted that due to the absence of rigid unit modes from the titanite structure, polyhedral distortion is to be expected upon chemical substitution in titanite, rather than polyhedral tilting.

The decrease in size of the octahedra forces the closely connected Ca-polyhedron to shrink, resulting in overbonding of both the Ca- and the O1-sites at high Al-contents. The abrupt changes in some of the octahedral bond lengths indicate that a certain atomic rearrangement takes place in titanite at $X_{Al} > 0.4$ in order to accommodate more Al and F. The combination of the non-linear crystal structural changes reported here indicates that the titanite structure is not well suited for Al-contents exceeding $X_{Al} = 0.4$, and that structural strain and lattice energy will increase beyond this point. This could have a negative effect on the thermodynamic stability of titanite. Thus, while titanite with very high Al-contents is stable in simple chemical systems such as those simulated in our experiments, it might be metastable in multi-component systems like natural rocks. Here, other phases such as amphiboles, micas, epidote minerals and garnets might be more suited to accommodate Al and F. This would explain the rare occurrence of titanite with $X_{Al} > 0.54$ in real rocks.

References

Brese, N.E. & O'Keeffe, M. (1991): Bond-valence parameters for solids. *Acta Cryst.*, **B47**, 192-197.

Carswell, D.A., Wilson, R.N., Zhai, M. (1996): Ultra-high pressure aluminous titanites in carbonate-bearing eclogites at Shuanghe in Dabieshan, Central China. *Mineral. Mag.*, **60**, 461-471.

Deer, W.A., Howie, R.A., Zussman, J. (1962): Rock-forming minerals, Orthosilicates, **1A**. John Wiley & Sons, Inc., New York.

Enami, M., Suzuki, K., Liou, J.G., Bird, D.K. (1993): Al-Fe^{3+} and F-OH substitutions in titanite and constraints on their P-T dependence. *Eur. J. Mineral.*, **5**, 219-231.

Franz, G. (1987): Breakdown of amphibole and the formation of Al-titanite - an example from the polymetamorphic "Chephren-Diorite" (Gebl el Asr, SW Egypt). Publication occasionnelle, Centre International pour la formation et les échanges géologiques, Paris, 14th Colloquium African Geology, TU Berlin.

Franz, G. & Spear, F.S. (1985): Aluminous titanite (sphene) from the Eclogite Zone, south-central Tauern Window, Austria. *Chemical Geol.*, **50**, 33-46.

Hammonds, K.D., Bosenick, A., Dove, M.T., Heine, V. (1998): Rigid unit modes in crystal structures with octahedrally coordinated atoms. *Am. Mineral.*, **83**, 476-479.

Higgins, J.B. & Ribbe, P.H. (1976): The crystal chemistry and space groups of natural and synthetic titanites. *Am. Mineral.*, **61**, 878-888.

Hollabaugh, C.L. & Foit, F.F. (1984): The crystal structure of an Al-rich titanite from Grisons, Switzerland. *Am. Mineral.*, **69**, 725-732.

Izumi, F. (1993): Rietveld analysis programs RIETAN and PREMOS and special applications. *in* R.A. Young (Editor), The Rietveld Method. Oxford University Press, Oxford.

Kek, S., Aroyo, M., Bismayer, U., Schmidt, C., Eichhorn, K., Krane, H.G. (1997): The two-step phase transition of titanite, $CaTiSiO_5$: a synchrotron radiation study. *Zeitschr. Kristallog.*, **212**, 9-19.

Kim, Y.-I. & Izumi, F. (1994): Structure refinement with a new version of the Rietveld-refinement program RIETAN. *J. Ceram. Soc. Jpn.*, **102**, 401-404.

Krogh, E.J., Andresen, A., Bryhni, I., Broks, T.M., Kristensen, S.E. (1990): Eclogites and polyphase P-T cycling in the Caledonian Uppermost Allochthon in Troms, northern Norway. *J. metamorphic Geol.*, **8**, 289-309.

Kunz, M., Xirouchakis, D., Lindsley, D.H., Häusermann, D. (1996): High-pressure phase transition in titanite ($CaTiOSiO_4$). *Am. Mineral.*, **81**, 1527-1530.

Kunz, M., Xirouchakis, D., Wang, Y., Parise, J.B., Lindsley, D.H. (1997): Structural investigations along the join $CaTiOSiO_4$-$CaSnOSiO_4$. *Schweiz. Mineral. Petrogr. Mitt.*, **77**, 1-11.

Markl, G. & Piazolo, S. (1999): Stability of high-Al titanite from low-pressure calcsilicates in light of fluid and host-rock composition. *Am. Mineral.*, **84**, 37-47.

Newton, R.C. & Wood, B.J. (1980): Volume behavior of silicate solid solutions. *Am. Mineral.*, **65**, 733-745.

Oberti, R., Smith, D.C., Rossi, G., Caucia, F. (1991): The crystal-chemistry of high-aluminium titanites. *Eur. J. Mineral.*, **3**, 777-792.

Smith, D.C. (1980): Highly aluminous sphene (titanite) in natural high-pressure hydrous-eclogite-facies rocks from Norway and Italy, and in experimental runs at high pressure. 26th Int. Geol. Congr., Paris, France (abs), section **02.3.1**, 145.

— (1981): The pressure and temperature dependence of Al-solubility in sphene in the system Ti-Al-Ca-Si-O-F. *Progr. Experim. Petrol. N.E.R.C. Publication Series*, **D-18**, 193-197.

Speer, J.A. & Gibbs, G.V. (1976): The crystal structure of synthetic titanite $CaTiOSiO_4$, and the domain textures of natural titanites. *Am. Mineral.*, **61**, 238-247.

Taylor, M. & Brown, G.E. (1976): High-temperature structural study of the $P2_1/a \leftrightarrow A2/a$ phase transition in synthetic titanite, $CaTiSiO_5$. *Am. Mineral.*, **61**, 435-447.

Troitzsch, U. & Ellis, D.J. (1999): The synthesis and crystal structure of $CaAlFSiO_4$, the Al-F analog of titanite. *Am. Mineral.*, **84**, (in press).

Wilson, A.J.C., Shmuelli, U., Hahn, T. (1992): International Tables for Crystallography. D. Reidel Pub. Co., Dordrecht.

Xirouchakis, D., Kunz, M., Parise, J.B., Lindsley, D.H. (1997): Synthesis method and unit-cell volume of end-member titanite ($CaTiOSiO_4$). *Am. Mineral.*, **82**, 748-753.

Appendix Table 1. Synthesis conditions. Abbreviations: ttn - titanite, an - anorthite, woll - wollastonite, ru - rutile, and as in Table 1.

sample	no. of runs	starting components	P [kbar]	T [°C]	t [h]	result
AlF09	4	ttn, an, fl	5	1075	24+33+10+24	ttn
AlF18	1	an, fl, woll, ru	7	1000	46	ttn fl
AlF29	1	an, fl, woll, ru	7	1000	46	ttn
AlF37	1	an, fl, woll, ru	13	1000	27	ttn fl ±ha
AlF49	1	an, fl, woll, ru	15	1000	46	ttn fl
AlF67	1	ttn, an, fl	23	1030	24	ttn fl
AlF75	2	ttn, an, fl	24	1000	28+41	ttn fl zoi
AlF82	1	an, fl, woll, ru	30	1000	68	ttn fl zoi
AlF100	1	an, fl, seeds	35	1100	23	ttn, fl, zoi, ky

Appendix Table 2. Curve fit polynomials for Fig. 3 and 5, where $Y_{a,b,c,\beta,V,BVS} = \sum (M_n)_{a,b,c,\beta,V,BVS} X^n$ with $n = 0,1,...,4$. In all polynomials X represents the independent variable X_{Al}, Y is the dependent variable a, b, c, β, V or BVS, and M_n are the polynomial coefficients.

	a	b	c	β	V	BVS O1
M0	7.0614	8.713	6.5591	113.79	369.39	0.17007
M1	-0.07342	-0.20545	-0.17531	1.3305	-28.557	-0.41705
M2	0.17429		0.25563	-0.44351	33.569	0.58867
M3	-0.49918		-0.35437		-56.501	-0.091903
M4	0.25272		0.15414		26.341	
R	0.99985	0.99973	0.99985	0.99967	0.99994	0.99998

The synthesis and crystal structure of CaAlFSiO₄, the Al-F analog of titanite

ULRIKE TROITZSCH AND DAVID J. ELLIS

Department of Geology, Faculty of Science, Australian National University, Canberra, A.C.T., 0200, Australia

ABSTRACT

Aluminum-rich titanites [$Ca(Ti,Al)(O,F)SiO_4$] with $X_{Al} > 0.53$ [$X_{Al} = Al/(Al+Ti)$], including the pure end-member $CaAlFSiO_4$, were synthesized for the first time in a high-pressure experimental study. The crystal structure of $CaAlFSiO_4$ was determined by Rietveld analysis of an X-ray powder diffraction pattern. $CaAlFSiO_4$ is monoclinic, belongs to the space group $A2/a$, and has the unit-cell dimensions $a = 6.9149(2)$ Å, $b = 8.5064(1)$ Å, $c = 6.4384(2)$ Å, and $\beta = 114.684(2)°$. The unit-cell volume is less than 93% of $CaTiOSiO_4$, which is consistent with the natural occurrence of Al-rich titanite in high-P rocks. Although previous studies suggested that titanite with $X_{Al} > 0.5$ is possibly not stable, this study demonstrates that complete solid solution occurs between $CaTiOSiO_4$ and $CaAlFSiO_4$. The similarity of the crystal structures of titanite and $CaAlFSiO_4$ explains why in natural Al-rich titanite the end-member $CaAlFSiO_4$ generally dominates over the hypothetical end-member $CaAlOHSiO_4$, which under geological conditions is stable in a different crystal structure.

INTRODUCTION

Al-rich titanite [$Ca(Ti,Al)(O,F,OH)SiO_4$] has been the focus of many previous mineralogical studies (Higgins and Ribbe 1976; Smith 1981; Oberti et al. 1991) because Al is one of the most common and abundant substituents for Ti in natural titanite (Franz and Spear 1985; Sobolev and Shatsky 1990; Krogh et al. 1990; Carswell et al. 1996). Moreover, the substitution appeared to be pressure and temperature dependent and thus could be of interest for geothermobarometry (Smith 1981; Enami et al. 1993). The two coupled substitution reactions that account for the formation of Al-bearing titanite are $Ti^{4+} + O^{2-} = Al^{3+} + F^-$ and $Ti^{4+} + O^{2-} = Al^{3+} + OH^-$. Hence Al-rich titanite is made up of the three end-members $CaTiOSiO_4$ [titanite], $CaAlFSiO_4$, and $CaAlOHSiO_4$. Although the end-member titanite occurs in nature and its crystal structure is known (Speer and Gibbs 1976), to our knowledge $CaAlFSiO_4$ has never been found or synthesized before, and neither has the pure $CaAlOHSiO_4$ end-member been reported. The mineral vuagnatite [$CaAlOHSiO_4$] is chemically equivalent to the AlOH end-member of Al-rich titanite, but its crystal structure (McNear et al. 1976) is different to that of titanite and thus it does not represent the AlOH-component of titanite solid solution.

The extent of solid solution between these end-members was previously discussed. Because the maximum amount of Al-substitution ($X_{Al} \approx 0.5$) reported from natural titanite (Franz and Spear 1985) is comparable to that of the first and only high-PT experimental investigation of Al- and F-bearing titanite with $X_{Al} = 0.53$ (Smith 1981), previous studies (Franz and Spear 1985; Oberti et al. 1991) pointed out that the Al-content in titanite appears to be restricted to $X_{Al} < 0.5$ (note that earlier studies usually did not distinguish between the two aluminum-end-members due to lack of OH- and F-analyses). Oberti et al. (1991)

investigated several natural Al-rich titanites ($X_{Al} < 0.37$), documenting changes in the crystal structure with increasing X_{Al}. They discussed various crystal structural features that might be responsible for the apparent mixing gap at $X_{Al} > 0.5$, but clear evidence for a crystal structural constraint was still missing.

The present study extends the information on Al-rich titanite summarized by Oberti et al. (1991) by providing crystal structural data for the end-member $CaAlFSiO_4$. Results from high-PT experiments in the binary system $CaTiOSiO_4$-$CaAlFSiO_4$ are reported that show complete solid solution.

EXPERIMENTAL METHODS

Synthesis of CaAlFSiO₄

The synthesis of $CaAlFSiO_4$ was carried out at 35 to 38 kbar and 1100 °C using the piston cylinder apparatus at the Geology Department, Australian National University. Run times varied from 21 to 24 h (see Table 1 for individual run conditions; samples G-295, G-296, G-297). The starting material was a powder of synthetic fluorite (Specpure) and anorthite in equal molar proportions, seeded with about 10 wt% $CaAlFSiO_4$. $CaAlFSiO_4$ does not nucleate without the presence of seeds. Thus $CaAlFSiO_4$ seeds had to be prepared in several cycles from titanite, anorthite and fluorite. In the first cycle, a mix of fluorite and anorthite (1:1) and about 1 wt% titanite seeds was run at 35 kbar and 1100 °C for 24 h, resulting in titanite solid solution with about 99 mol% of the $CaAlFSiO_4$ end-member, besides smaller amounts of zoisite, fluorite, and kyanite (G-274, Table 1). This product was then used as seed material for subsequent cycles. After three cycles, titanium could no longer be detected using scanning electron microscopy, and the material was used as seeds for $CaAlFSiO_4$ synthesis. The anorthite of the starting mix was crystallized from glass at 1000 °C, 1 atm for 24 h with several cycles of crushing and heating. The glass was prepared by melting Al_2O_3, SiO_2, and $CaCO_3$ at 1600 °C and 1 atm, with subsequent quenching in water.

---

*E-mail: ulrike@geology.anu.edu.au

TABLE 1. Experimental details

Expt. no.	T (°)	P (kbar)	t* (h)	Mix†	Run result	X$_{Al}$-range in Tnt	Comments
G-312	1100	15	22	1:9	Tnt	0.01–0.24	Tnt zoned, X$_{Al}$ from core to rim
G-183	1100	30	21	1:1	Tnt	0.43–0.56	
G-184	1000	30	30	1:1	Tnt	0.44–0.50	
G-185	1200	30	22	1:1	Tnt	0.39–0.50	
G-186	1300	30	22	1:1	Tnt Melt	0.25–0.67	Tnt zoned, X$_{Al}$ from core to rim
G-187	1100	25	36	1:1	Tnt	0.46–0.47	
G-194	1100	25	25	2:1	Tnt	0.50–0.69	
G-313	1100	25	23	3:1	Tnt Zoi Fluo	0.05–0.88	Tnt zoned, X$_{Al}$ from core to rim
G-198	1100	10	23	10:1	Tnt An Fluo Sill	0.34–0.36	
G-199	1100	25	26	10:1	Tnt Zoi Fluo Ky	0.85	
G-200	1100	25	21	20:1	Tnt Zoi Fluo Ky	0.87–0.90	
G-201	1100	25	20	99:1	Tnt Zoi Fluo Ky	0.90–0.95	
G-203	1100	25	80	99:1	Tnt Zoi Fluo Ky	0.85–0.90	
G-264	1100	22	21	99:1	Tnt Zoi Fluo Ky	0.87–0.96	
G-265	1100	15	23	99:1	Tnt An Fluo	0.54–0.57	
G-266	1100	35	20	99:1	Tnt Zoi Fluo Ky	0.97–1.00	
G-268	1050	35	47	99:1	Tnt Zoi Fluo Ky	0.95–1.00	
G-274	1100	35	16	99:1	Tnt Zoi Fluo Ky	0.97–1.00	
G-275	1100	35	22	99:1	Tnt Zoi Fluo Ky	0.96–0.99	starting material was G-274
G-276	1100	35	24	999:1	Tnt Zoi Fluo Ky	0.98–0.99	seed material was G-275
G-278	1100	35	21	1:0	Tnt Zoi Fluo Ky	0.98–1.00	seed material was G-276
G-280	1100	35	23	1:0	Tnt Zoi Fluo Ky	0.99–1.00	seed material was G-278
G-282	1100	35	39	1:0	Tnt Zoi Fluo Ky	0.98–1.00	seed material was G-280
G-295	1100	35	24	1:0	Tnt Zoi Fluo Ky	1.00	seed material was G-280
G-296	1100	38	21	1:0	Tnt Zoi Fluo Ky	1.00	seed material was G-280
G-297	1100	35	23	1:0	Tnt Zoi Fluo Ky	1.00	seed material was G-278 and G-280

Notes: Tnt = titanite; An = anorthite; Zoi = F-rich zoisite; Fluo = fluorite; Sill = sillimanite; Ky = kyanite.
* Run Duration.
† Ratio of CaAlFSiO$_4$ to CaTiOSiO$_4$.

For each CaAlFSiO$_4$ synthesis run about 140 mg of mix was filled in 3 mm diameter silver-palladium capsules (Ag$_{75}$Pd$_{25}$), which were then dried at 110 °C for 1 h before welding shut. The pressure medium enclosing the capsule was boron-nitride and a surrounding salt-sleeve with zero friction correction. The pressure readings during the experiments are precise within 1%. The temperature was monitored by a Pt-Pt$_{90}$Rh$_{10}$ thermocouple and was regulated automatically by a EUROTHERM controller. The accuracy of the temperature measurements was ±5 °C. The grain size of all run products was <10 μm.

Synthesis of titanite solid solution Ca(Ti,Al)(O,F)SiO$_4$

Titanite solid solution over a range of compositions was synthesized under various pressures and temperatures (Table 1) from two different starting mixes: Anorthite + fluorite (molar proportion 1:1) and grossular + quartz + kyanite + fluorite (molar proportion 1:1:2:3), both mixed with various amounts of titanite. The preparation of anorthite is described above. Synthetic fluorite (Specpure), SiO$_2$ (Aerosil, Degussa), natural kyanite (Northern Territory, Australia, Fe$_2$O$_3$ < 0.4 wt%) and synthetic grossular and titanite were used. Grossular was made from glass at 1200 °C, 25 kbar for 26 h using the piston cylinder apparatus. Titanite was crystallized from glass at 1100 °C, 1 atm for four weeks with several cycles of heating and crushing. Both the grossular and titanite glass were prepared from the oxides and CaCO$_3$ at 1450 °C and 1 atm, and quenched in water.

Silver-palladium capsules (Ag$_{75}$Pd$_{25}$) of 2 mm diameter were filled with about 10 mg mix and dried at 110 °C before welding shut. Salt or salt and pyrex-sleeves were used as outer pressure media. The grain size of all run products was <10 μm.

SEM

Quantitative analyses were obtained with a JEOL JSM-6400 scanning electron microscope, Link ISIS EDS, at 15 kV and 1 nA, at the Electron Microscopy Unit, Australian National University. Analyses were calculated using ZAF-correction. Analyzed elements were silicon, titanium, aluminum, calcium, fluorine, and oxygen.

TEM

Diffraction patterns of CaAlF SiO$_4$ were investigated at 300 kV using a Philips EM 430T at the Research School of Earth Sciences, Australian National University. The camera constant was calibrated against thallium chloride, the uncertainty of the measurements is 1%. The sample (G-297) was finely ground, dispersed on a carbon-coated copper grid, and mounted on a tilt-rotate holder.

XRD

Powder-diffraction data were collected at room temperature with a Siemens D501 diffractometer at the Geology Department, Australian National University. The diffractometer was equipped with a curved graphite monochromator, a scintillation detector, and CuKα radiation was used. The diffraction data were recorded in four passes over a range of 10 to 100°2θ, using a step width of 0.02° at a scan speed of 0.5° per minute.

IR

Infra-red spectra were recorded using a Bruker IFS 28 FT-IR spectrometer and microscope. Single grains of sample material were investigated individually. KRr pellets were not used.

Raman

The LaserRaman specrtra were recorded on a Dilor SuperLabram spectrometer equipped with a holographic notch filler, 600 and 1800 g/mm gratings, and a liquid N2 cooled, 2000 × 450 pixel CCD detector. The sample was illuminated with 514.5 nm laser excitation from a Spectra Physics model 2017 argon ion laser, using 5 mW power at the samples, and a single second accumulation. A 100× microscope objective was used to focus the laser beam and collect the scattered light. The focused laser spot on the samples was approximately 1 mm in diameter. Wavenumbers are accurate to * 1 cm-1 as determined by plasma and neon emission lines.

Structure refinement

Rietveld refinement using up to 50 parameters was performed on sample G-297 (Table 1) with the computer program RIETAN-94 (Izumi 1993), which uses the pseudo-Voigt function as profile-shape function, and the *International Tables for Crystallography* (Wilson et al. 1992) as the database. All four phases present in the sample (85 wt% CaAlFSiO$_4$, 10 wt% zoisite, 2 wt% fluorite, and 3 wt% kyanite) were accounted for in the refinement. Refined non-atomic parameters included scale factors (4), specimen-displacement (1), background (8), profile-shape parameters (12), preferred orientation (3), and unit-cell parameters (7). Neutral atom scattering factors were chosen for all atoms. The unit-cell parameters of kyanite and fluorite were fixed.

RESULTS

Titanite solid solution

The results of 19 experiments synthesizing titanite solid solution over a range of compositions span the entire spectrum of possible Ti-Al exchange including the end-members titanite and CaAlFSiO$_4$ (Fig. 1; Table 1). This is the first time that titanite is reported with $X_{Al} \gg 0.53$. Moreover, complete solid solution between CaTiOSiO$_4$ and CaAlFSiO$_4$ is observed, showing that there is no crystal structural constraint in the titanite structure that precludes the occupation of the octahedral sites with more than 50% Al.

CaAlFSiO$_4$ synthesis

The results of three experiments carried out under comparable run conditions (G-295 to G-297, Table 1) are identical. They consist of a mixture of CaAlFSiO$_4$ (>70 wt%), F-rich zoisite (<20 wt%), fluorite (<10 wt%), and traces of kyanite.

The formation of CaAlFSiO$_4$ and F-rich zoisite in the experiments from fluorite and anorthite can be described by the reactions

$$CaF_2 + CaAl_2Si_2O_8 = 2 \ CaAlFSiO_4 \qquad (1)$$

and

$$CaF_2 + 3 \ CaAl_2Si_2O_8 = 2 \ Ca_2Al_3Si_3O_{12}(F). \qquad (2)$$

The composition of the synthetic CaAlFSiO$_4$ is close to ideal with a deviation of less than 0.05 apfu of all analyses from the end-member composition. The average chemical formula from 26 SEM analyses of CaAlFSiO$_4$ calculated on the basis of three cations is Ca$_{1.012}$Al$_{0.991}$F$_{0.991}$Si$_{0.997}$O$_{3.998}$.
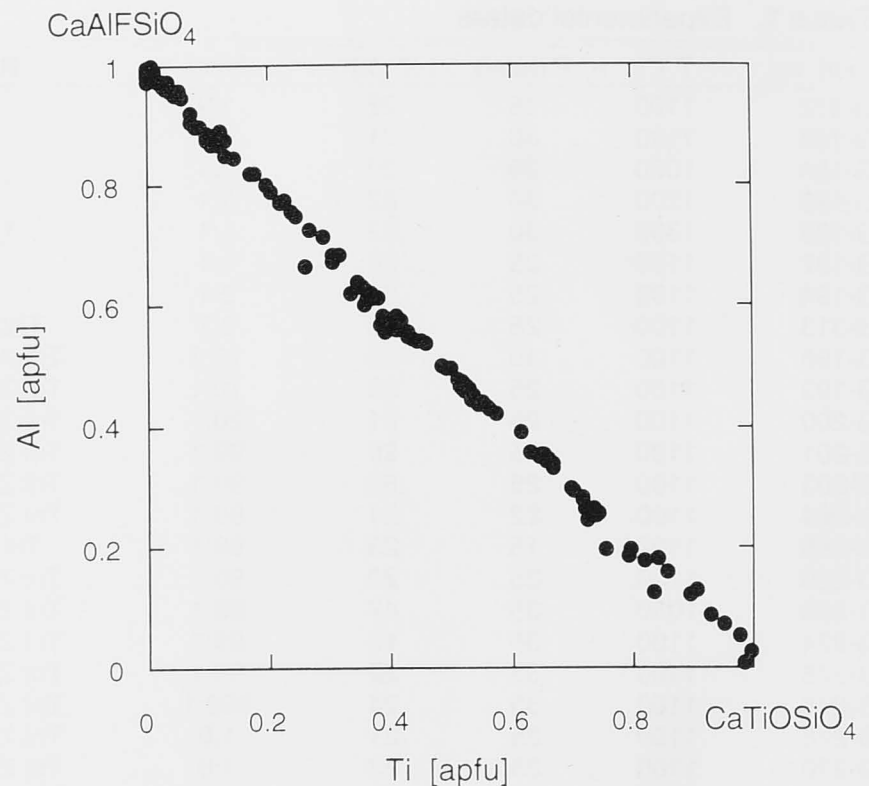

FIGURE 1. Al vs. Ti atoms per formula unit in synthetic binary titanite solid solution Ca(Ti,Al)(O,F)SiO$_4$ from various experiments carried out under a range of pressures and temperatures (see Table 1).

The formation of zoisite under anhydrous conditions was unexpected, because to the authors knowledge the existence of F-rich zoisite has never been reported in the literature before. The average structural formula for zoisite synthesized in this study is Ca$_{2.06}$Al$_{2.94}$Si$_{3.00}$O$_{12.48}$F$_{0.43}$. It was calculated from 17 SEM analyses on the basis of 8 cations. The surplus of O^{2-} and deficiency of F$^-$ compared to the ideal formula as used in reaction 2, together with a charge unbalance of -0.46 for this chemical formula, suggests the presence of about 0.46 apfu H$^+$ in the form of OH$^-$. This changes the above formula to Ca$_{2.06}$Al$_{2.94}$Si$_{3.00}$O$_{12.02}$F$_{0.43}$(OH)$_{0.46}$. The presence of structurally bound OH in zoisite in sample G-297 was confirmed with IR and Raman spectroscopy. Water contamination of the supposedly dry experiments is possible. Even though the starting mix was dried inside the open capsules at 110 °C before welding, water contamination cannot be excluded entirely during the subsequent welding process that involves cooling of the capsule using water-soaked sleeves. Note that for 140 mg sample it requires only 0.00014 g of water contamination to account for 10% of the product to be the above zoisite composition. The formation of F-rich zoisite (reaction 2) instead of CaAlFSiO$_4$ (reaction 1) accounts for the presence of "left-over" fluorite in the run product. The presence of kyanite in the reaction products indicates slight deviation of the starting mix from ideal composition.

It is most likely that F-rich zoisite and fluorite in these experiments are metastable, and only persist because of nucleation problems of CaAlFSiO$_4$ or incomplete reaction due to slow diffusion rates. A high activation energy for nucleation is suggested by the fact that mixes without seeds react to form F-rich zoisite and fluorite, whereas seeded mixes react to form up to 100% CaAlFSiO$_4$. Incomplete reaction is indicated by the textures of the reaction products. Fluorite and F-rich zoisite are typically preserved as isolated grains surrounded by CaAlFSiO$_4$.
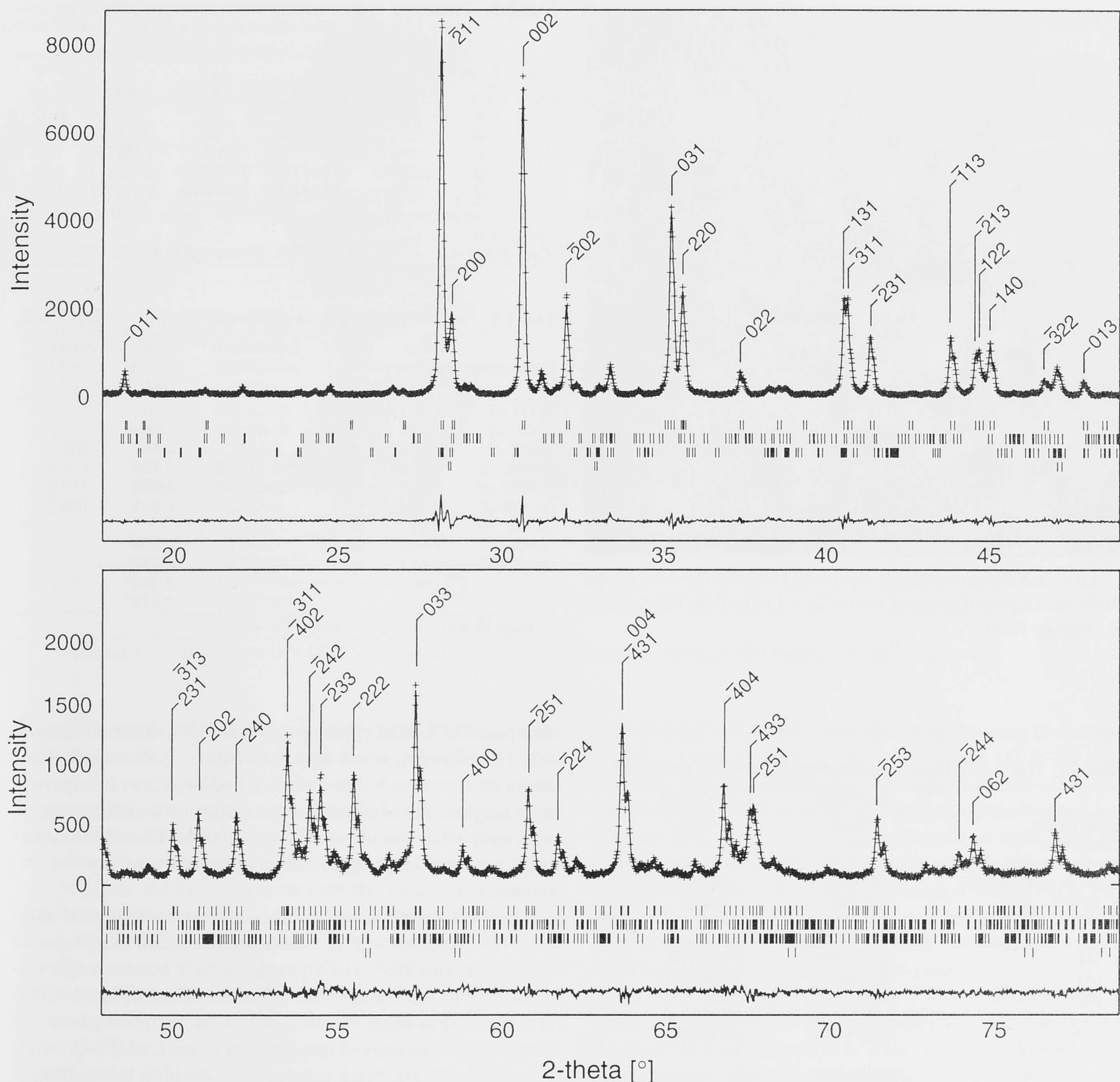
FIGURE 2. X-ray powder diffraction pattern and Rietveld refinement result of CaAlFSiO$_4$ with traces of zoisite, kyanite, and fluorite (sample G-297). Crosses represent the raw diffraction data, the upper solid curve is the calculated trace, and the lower solid curve shows the difference between the two. Positions of all *hkl* reflections are indicated by vertical bars (four rows from top to bottom: CaAlFSiO$_4$, Zoisite, Kyanite, Fluorite), major reflections of CaAlFSiO$_4$ are indexed. Note the difference in scale between the two parts of the figure.

Determination of the crystal structure

The X-ray powder-diffraction pattern of CaAlFSiO$_4$ (Fig. 2) is comparable to that of titanite (space group $P2_1/a$) and Al-rich titanite (space group $A2/a$; Higgins and Ribbe 1976). The space group $A2/a$ was confirmed for CaAlFSiO$_4$ by the absence of k + $l = 2n + 1$ reflections from the diffraction pattern of zone [102] (Fig. 3) (Higgins and Ribbe 1976; Speer and Gibbs 1976). The starting coordinates for the refinement process were those of a titanite with $X_{Al} = 0.09$ in space group $A2/a$ (Hollabaugh and Foit 1984). For the CaAlFSiO$_4$ refinement the octahedral site was fully occupied with Al, and the O1-site with F. Occupancies

of all sites were fixed at 1.0 assuming ideal composition. The refinement result is shown in Figure 2, with R_{wp} = 9.99, R_e = 6.62, S = 1.51, and R_B = 3.42, as defined in Young (1993). The unit-cell dimensions of CaAlFSiO$_4$, atom coordinates, bond-lengths and bond-angles and other structural information are summarized in Tables 2 to 4.

DESCRIPTION AND DISCUSSION OF THE CRYSTAL STRUCTURE

CaAlFSiO$_4$ is isostructural with titanite as determined by Speer and Gibbs (1976). The CaAlFSiO$_4$ structure (Fig. 4) is
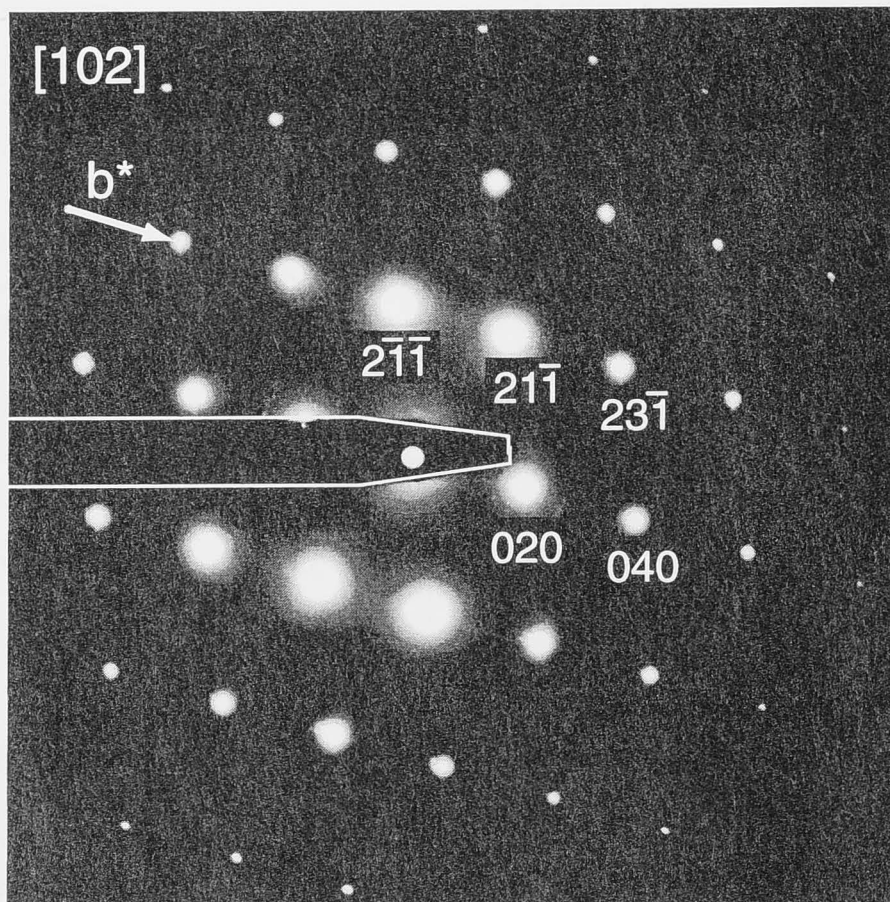
FIGURE 3. Electron diffraction pattern of CaAlFSiO$_4$ viewed along [102], showing the absence of $k + l = 2n + 1$ reflections belonging to space group $P2_1/a$.

TABLE 3. Fractional atomic coordinates, isotropic thermal parameters (Å^2) and bond-valence sums (BVS) of synthetic CaAlFSiO$_4$

Site	Atom	x	y	z	B_{iso}	BVS*
Ca	Ca	1/4	0.1637(2)	0	1.50(7)	2.20
Al	Al	1/2	0	1/2	1.75(7)	3.03
Si	Si	3/4	0.1860(4)	0	1.21(8)	3.97
O1	F	3/4	0.0709(5)	1/2	1.15(12)	1.25
O2	O	0.9031(5)	0.0667(4)	0.1904(5)	0.80(11)	1.98
O3	O	0.3887(6)	0.2011(4)	0.4031(6)	0.79(10)	1.99

Note: Errors as given by the program RIETAN (Izumi 1993), see discussion in text.
*Calculated with the program EUTAX (Brese and O'Keeffe 1991).

TABLE 4. Selected bond lengths and angles of synthetic CaAlFSiO$_4$

Octahedron	Bond lengths (Å)	Angles on Al (°)	Tetrahedron or Ca[7]-site	Bond lengths (Å)	Angles on Si (°)
Al-O1 ×2	1.831		Si-O2 ×2	1.603	
Al-O2 ×2	1.905		Si-O3 ×2	1.653	
Al-O3 ×2	1.873		O2-O2'	2.482	101.4
O1-O2 ×2	2.619	89.0	O2'-O3 ×2	2.706	112.4
O1-O2' ×2	2.665	91.0	O2-O3' ×2	2.680	110.8
O1-O3 ×2	2.560	87.5	O3-O3'	2.691	109.0
O1-O3' ×2	2.677	92.5			
O2-O3 ×2	2.662	89.6	Ca-O1	2.258*	
O2-O3' ×2	2.681	90.4	Ca-O2 ×2	2.319*	
			Ca-O3 ×2	2.383*	
			Ca-O3' ×2	2.579*	

* These four entries pertain to the Ca[7]-site.

TABLE 2. The crystal structures of synthetic CaAlFSiO$_4$ and titanite*

	CaAlFSiO$_4$	CaTiOSiO$_4$*
space group	A2/a	P2$_1$/a
unique axis	b†	b
unit cell content	Z = 4	Z = 4
molar weight (g/mol)	178.14	196.02
D (g/cm^3)	3.439	3.517
Unit cell dimensions		
a (Å)	6.9149(2)	7.0697(3)
b (Å)	8.5064(1)	8.7223(4)
c (Å)	6.4384(2)	6.5654(4)
β (°)	114.684(2)	113.853(4)
V (Å^3)	344.11(2)	370.27(3)
Octahedron		
mean oct-O bond (Å)	1.870	1.959
mean O-O bond (Å)	2.644	2.768
V (Å^3)	8.699	9.971
quadratic elongation	1.0013	1.0058
angle variance	2.773	–
oct-O1-oct angle (°)	141.5	141.8‡
Tetrahedron		
mean Si-O bond (Å)	1.628	1.647
mean O-O bond (Å)	2.658	2.688
V (Å^3)	2.198	2.282
quadratic elongation	1.0053	1.0033
angle variance	17.077	12.566
Ca[7]-site		
mean Ca-O bond	2.403	2.457

Notes: Sites occupied by fluorine or oxygen are represented by "O," the octahedral cation by "oct." Bond lengths, angles, polyhedral volumes, quadratic elongation and angle variance were calculated with the program VOLCAL (Hazen and Finger 1982). Errors of unit cell parameters of CaAlFSiO$_4$ as given by the program RIETAN (Izumi 1993).
* Refined by Kek et al. 1997.
† Non-standard setting was chosen for comparison with titanite.
‡ Speer and Gibbs (1976).

composed of kinked chains parallel to [100] of corner-sharing AlF$_2$O$_4$ octahedra, which are interlinked by isolated SiO$_4$ tetrahedra in a way such that each tetrahedron shares two corners with neighboring octahedra of one chain and the other two corners with octahedra of two different chains. This AlFSiO$_4$-network contains large sevenfold-coordinated sites that accommodate Ca.

The bridging atom occupying site O1 in the octahedral chain is F. This position for F in titanite solid solution was proposed by Higgins and Ribbe (1976) on the basis of bond-strength calculations. In the CaAlFSiO$_4$, refinement F was placed exclusively on this bridging site, which is justified given the overbonded character of this position in the CaAlFSiO$_4$ structure (Table 3). The bond valence sums for most other sites are close to ideal values, which supports our structural model. The Ca-site is slightly overbonded mainly due to shortening of the Ca-O2 bond (Table 4) by about 0.1 Å compared to those in titanite (Table 11 in Kek et al. 1997).

Thermal parameters

The large absolute values of all thermal parameters (Table 3) are unrealistic. For comparison, isotropic atomic displacement parameters determined with single-crystal X-ray diffractometry for an Al-rich titanite $X_{Al} = 0.36$ by Oberti et al. (1991, sample HEL697) are 1.15 (Ca), 1.00 (oct), 0.41 (Si), 0.66 (O1), 0.66 (O2), and 0.59 (O3). Note that the errors obtained from the Rietveld refinement (Table 3) are probably underestimated, which is a problem previously recognized by, for example, Sakata and Cooper (1979) and Scott (1983). Because temperature factors correlate strongly with other 2θ-dependent refinable parameters, they can act as a sink for sys-
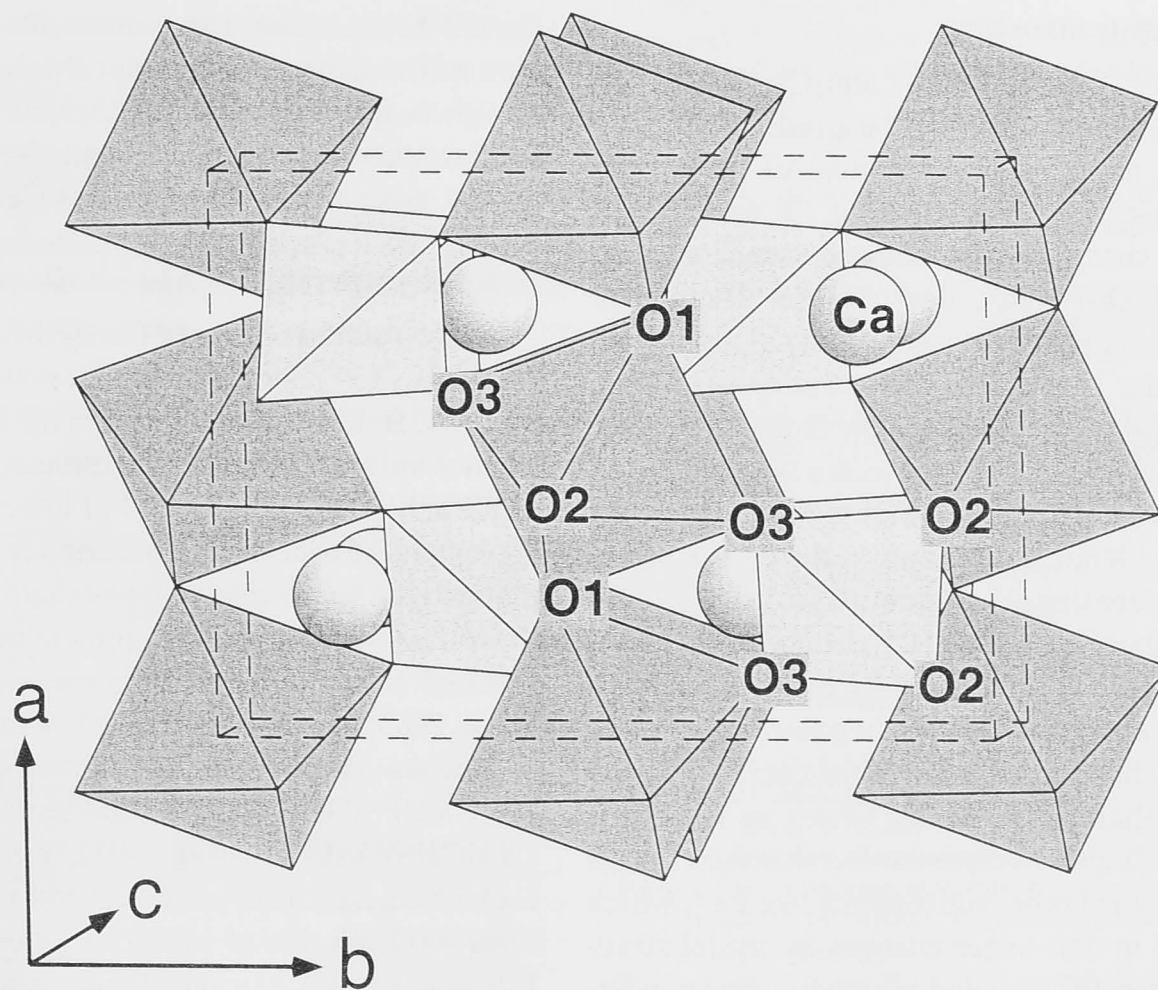
FIGURE 4. Crystal structure of CaAlFSiO$_4$ (ATOMS, Dowty 1993). Stippled lines represent the unit-cell boundaries.

tematic errors in the modeling of the profile. In this case the definition of the background at high angle was difficult due to strong peak overlap (Fig. 2). If the background was chosen too high, the large thermal parameters could represent the compensation for this mismatch.

Although the absolute values of thermal parameters might be erroneous, their relative values are significant. Whereas the relative magnitudes of the thermal parameters of Ca, O2, and O3 in CaAlFSiO$_4$ are comparable to titanite, those of Al, Si, and O1 seem too high. The high thermal parameter observed for the O1-site could be partly explained if the assumption of full occupancy by F was wrong, and trace amounts of F (<0.05 apfu) are replaced by OH in the sample. Trace amounts of structurally bound OH in one phase other than zoisite were detected with IR spectroscopy in the bulk sample (single grains of CaAlFSiO$_4$ large enough to be analyzed individually could not be separated). Disordering of F and O, which could also account for high thermal parameters, is unlikely given the already large bond valence sum for the O1-site (Table 3). High thermal parameters for Al and Si could be caused by some disordering in the octahedral and tetrahedral sites, resulting in local distortion of the crystal lattice. Diffuse scattering in the electron diffraction patterns which could indicate such disorder, however, could not be observed. A single-crystal diffraction study is necessary to obtain more reliable information about the thermal motion of the atoms and possible chemical and displacive disorder in the structure of CaAlFSiO$_4$.

Polyhedral distortion

Whereas the AlF$_2$O$_4$ octahedron in CaAlFSiO$_4$ is quite regular, the SiO$_4$ tetrahedron is very distorted. It has one very short

edge (O2-O2 = 2.482 Å), two short and two long Si-O bonds (Si-O2 = 1.603 Å, Si-O3 = 1.653 Å), a small O2-Si-O2 angle (101.4°), and large angle variance and quadratic elongation values (Hazen and Finger 1982) (Table 2). This is surprising, because SiO$_4$ tetrahedra generally behave as rigid units that hardly deviate from ideal bond lengths and angles, whereas octahedra deform more easily. Although a short O2-O2 edge and a small O2-Si-O2 angle of the tetrahedron is typical for most minerals in the titanite structure, uneven Si-O bonds as described above are unusual for this group.

To double-check the coordinates of our structure model, the refinement was repeated with hard constraints on the Si-O (1.624 Å) and O-O bond lengths (2.652 Å) of the tetrahedron. When the constraints were softened at the end of the refinement process, all atoms moved back to the positions forming the distorted tetrahedron. Because the overall fit (R_{wp}) improved by several percent after releasing the constraints, the distortion of the tetrahedron in CaAlFSiO$_4$ at room pressure and temperature seems to be real. Bond valence sums calculated for the same structure, but with Si located at the equidistant point of the tetrahedron, are 2.13 (Ca), 3.94 (Si), 1.88 (O2), and 2.05 (O3), (those of the Al- and O1-site remain unchanged, Table 2). This shows that off-centering of Si improves the bond-valence sums of all tetrahedral atoms, but slightly worsens that of Ca.

Hammonds et al. (1998) suggest that due to the absence of rigid-unit modes from the titanite structure, formation of solid solutions in this structure requires distortion of the polyhedra to accommodate cations of different size. This is consistent with the distortion of the tetrahedron in CaAlFSiO$_4$ but does not explain why in this case only the tetrahedra appear to take up the strain.

Comparison with titanite structure

The crystallographic data of titanite and CaAlFSiO$_4$ are compared in Table 2. Due to the smaller ionic radii of Al and F compared to Ti and O, all unit-cell dimensions of CaAlFSiO$_4$ are shorter, and its unit-cell volume is at least 7% smaller than that of titanite. This is consistent with the occurrence of natural Al-rich titanite in high-P and/or low-T rocks. The crystal lattice of CaAlFSiO$_4$ is more compact especially along the octahedral chain, resulting in smaller octahedral and Ca-sites, whereas the tetrahedral volume is comparable to that of titanite. Even though the major difference between the two end-members lies in the octahedral chains, their kinking angle (oct-O1-oct, Table 2) is almost identical. Changes in the crystal structure of titanite with increasing Al-content ($0.00 < X_{Al} < 0.37$) were investigated by Oberti et al. (1991). Extrapolation of their crystal structure data to $X_{Al} = 1.0$, especially the trends in site-volumes and the stable kinking-angle, are in general agreement with this study. The slight underestimate of the decrease in unit cell and polyhedral volume with X_{Al} by Oberti et al. (1991) compared to this study is either due to the fact that the crystals analyzed by them contained other substituents like Fe^{3+}, which dilate the structure, or to non-linear changes in crystal structure dimensions between the two end-members. The polyhedral geometry they reported is comparable to that found in CaAlFSiO$_4$ in that the tetrahedra are more distorted with larger quadratic elongation and angle variance values compared to the octahedra. The Si-O distances determined for Al-rich titanite by Oberti et al. (1991), however, only vary over a narrow range (1.633 to 1.640 Å) unlike those in CaAlFSiO$_4$. This does not necessarily mean that the distortion of the Si-O bonds is restricted to $X_{Al} > 0.37$ also in the pure binary system CaTiOSiO$_4$–CaAlFSiO$_4$. It has to be considered that the tetrahedral geometry in the natural crystals examined by Oberti et al. (1991) might be influenced by the presence of hydrogen bonds.

One of the major differences between CaAlFSiO$_4$ and titanite is in the geometry of the octahedron, which influences the space group. In CaAlFSiO$_4$, as in malayaite [CaSnOSiO$_4$] (Higgins and Ribbe 1977; Groat et al. 1996), the octahedral cation is located in the center of the octahedron, resulting in three different bonds from the central cation to the coordinating anions. In contrast to this, Ti in titanite is slightly off-set from the octahedron center, resulting in six different oct-O bonds and five different oxygen sites (Speer and Gibbs 1976). In pure titanite all Ti atoms of one octahedral chain are off-set in the same direction, and in opposite direction in the neighboring chains. The off-centering of Ti reduces the symmetry of titanite to space group $P2_1/a$.

If titanite contains small amounts of substituents such as Al and F or OH, the continuous chains of TiO$_6$ octahedra are interrupted, allowing the formation of antiphase domains with an apparent space group $A2/a$ (Speer and Gibbs 1976; Higgins and Ribbe 1976). The most Al-rich titanites ($0.25 \leq X_{Al} \leq 0.37$) which were characterized crystallographically (Oberti et al. 1991) belong to space group $A2/a$, but no evidence for domains was found. The space group of these high-Al titanites is consistent with that of the end-member CaAlFSiO$_4$.

The hypothetical end-member CaAlOHSiO$_4$ in the titanite structure has never been reported. Under geological conditions CaAlOHSiO$_4$ is stable in a different crystal structure and occurs as the mineral vuagnatite (McNear 1976). Note that although vuagnatite cannot represent the end-member of titanite solid solution its unit-cell volume (342.5 Å^3) and density (3.42 g/cm^3) are comparable to those of CaAlFSiO$_4$ (Table 2).

Natural occurrence of Al-rich titanite

The crystal structures of CaAlFSiO$_4$, titanite, and vuagnatite are the key to understanding their natural occurrence and composition. Both CaAlFSiO$_4$ and vuagnatite have a significantly smaller unit cell volume than titanite, and thus they should be stable at higher pressures and/or lower temperatures. This is in agreement with the natural occurrence of vuagnatite in prehnite-pumpellyite facies assemblages (Sarp et al. 1976; Pabst 1977), as well as with the high Al-content of titanites predominantly reported from eclogite facies rocks (Smith 1980; Franz and Spear 1985; Krogh et al. 1990; Carswell et al. 1996).

Because vuagnatite has a different crystal structure to titanite and CaAlFSiO$_4$ its composition seems to be restricted to pure CaAlOHSiO$_4$ (Oberti et al. 1991). In contrast to this CaTiOSiO$_4$, CaAlFSiO$_4$ and the hypothetical end-member CaAlOHSiO$_4$ can form solid solution to various degrees in the titanite structure. Whereas natural Al-rich titanite is reported to contain up to about 53 mol% CaAlFSiO$_4$, this experimental study has shown that even complete solid solution is possible under appropriate PT-conditions (Fig. 1). However, the solubility of the CaAlOHSiO$_4$ component in the titanite structure seems to be restricted to values less than about 30 mol% in nature as well as in the experiment (e.g., Enami et al. 1993; Franz and Spear 1985; Hellman and Green 1979). The general dominance of F over OH in very Al-rich titanite ($X_{Al} > 0.4$) from high-pressure rocks (Sobolev and Shatsky 1990; Carswell et al. 1996) and low-temperature rocks (Enami et al. 1993) is therefore due to the fact that only a few percent of Al coupled to OH seem to be able to enter the titanite structure, whereas the amount of Al coupled to F is not restricted by the crystal lattice. However, it is possible that OH dominates F in titanite with lower Al-content ($X_{Al} < 0.4$) as observed by Enami et al. (1993). The present study agrees with Enami et al. (1993) and Carswell et al. (1996) that the two Al-end-members in Al-bearing titanite have to be treated as individual phases with different mixing properties and PT-dependencies.

Previous studies (e.g., Smith 1981) pointed out that the different structures of vuagnatite and titanite might be the reason for natural high-Al titanite to be restricted to $X_{Al} < 0.50$. Oberti et al. (1991) discussed several possibilities of a crystal structural limit for Al-rich titanite and "provisionally attributed [the structural limit] either to difficulties in matching the different parts of the structure or to difficulties in local charge balance at O1 at higher Al contents." Although the present study confirms that there is indeed a local charge balance problem at the O1-site in CaAlFSiO$_4$ as indicated by overbonded F (Table 3), it does not appear to be significant enough to destabilize the structure of CaAlFSiO$_4$.

The only natural titanite with an Al-content exceeding $X_{Al} = 0.5$ significantly ($X_A \approx 0.65$) was reported by Franz (1987). One possible reason for the rarity of natural titanites with $X_{Al} \gg 0.50$ and absence in nature of the end-member CaAlFSiO$_4$ is that the equilib-

rium *PTX*-conditions are not expected in nature. Even though the synthesis conditions for CaAlFSiO$_4$ in this study (35 kbar and 1100 °C) can be reached in the mantle, the complete absence of titanium from a real rock may never be realized. The stability of CaAlFSiO$_4$ in Ti-bearing systems, like natural rocks, might be restricted to significantly higher pressures and lower temperatures not found in nature. Alternatively, titanite with $X_{Al} > 0.50$ might form in the lower crust or upper mantle, but decomposes during uplift, due to drop in pressure or change in F fugacity. In this case one would expect to find retrograde phases like anorthite, which was reported by Carswell et al. (1996) to have partly replaced titanite with $X_{Al} < 0.48$.

It could be speculated that the high degree of distortion of the tetrahedra in CaAlFSiO$_4$ has a negative effect on its stability over geological time, because small changes in pressure, temperature, or composition will shift it into stability fields of much less distorted, and thus more stable phases like for example zoisite, grossular, or kyanite.

REFERENCES CITED

Brese, N.E. and O'Keeffe, M. (1991) Bond-valence parameters for solids. Acta Crystallographica, B47, 192–197.

Carswell, D.A., Wilson, R.N., and Zhai, M. (1996) Ultra-high pressure aluminous titanites in carbonate-bearing eclogites at Shuanghe in Dabieshan, central China. Mineralogical Magazine, 60, 461–471.

Dowty, E. (1993) ATOMS. A computer program for displaying atomic structures, Kingsport, Tennessee.

Enami, M., Suzuki, K., Liou, J.G., and Bird, D.K. (1993) Al-Fe^{3+} and F-OH substitutions in titanite and constraints on their *P-T* dependence. European Journal of Mineralogy, 5, 219–231.

Franz, G. (1987) Breakdown of amphibole and the formation of Al-titanite—an example from the polymetamorphic "Chephren-Diorite" (Gebl el Asr, SW Egypt). Publication Occasionelle, Centre International pour le formation et les échanges géologiques, Paris, 14th Colloquium African Geology, TU Berlin.

Franz, G. and Spear, F.S. (1985) Aluminous titanite (sphene) from the Eclogite Zone, south-central Tauern Window, Austria. Chemical Geology, 50, 33–46.

Groat, L.A., Kek, S., Bismayer, U., Schmidt, C., Krane, H.G., Meyer, H., Nistor, L., and Van Tendeloo, G. (1996) A synchrotron radiation, HRTEM, X-ray powder diffraction, and Raman spectroscopic study of malayaite, CaSnSiO$_5$. American Mineralogist, 81, 595–602.

Hammonds, K.D., Bosenick, A., Dove, M.T., and Heine, V. (1998) Rigid unit modes in crystal structures with octahedrally coordinated atoms. American Mineralogist, 83, 476–479.

Hazen, R.M. and Finger, L.W. (1982) Comparative Crystal Chemistry. Wiley, New York.

Hellman, P.L. and Green, T.H. (1979) The role of sphene as an accessory phase in high-pressure partial melting of hydrous mafic compositions. Earth and Planetary Science Letters, 42, 191–201.

Higgins, J.B. and Ribbe, P.H. (1976) The crystal chemistry and space groups of natural and synthetic titanites. American Mineralogist, 61, 878–888.

———(1977) The structure of malayaite, CaSnOSiO$_4$, a tin analog of titanite. American Mineralogist, 62, 801–806.

Hollabaugh, C.L. and Foit, F. F., Jr. (1984) The crystal structure of an Al-rich titanite from Grisons, Switzerland. American Mineralogist, 69, 725–732.

Izumi, F. (1993) Rietveld analysis programs RIETAN and PREMOS and special applications. In R.A. Young, Ed., The Rietveld Method. Oxford University Press, Oxford.

Kek, S., Aroyo, M., Bismayer, U., Schmidt, C., Eichhorn, K., and Krane, H.G. (1997) The two-step phase transition of titanite, CaTiSiO$_5$: a synchrotron radiation study. Zeitschrift für Kristallographie, 212, 9–19.

Krogh, E.J., Andresen, A., Bryhni, I., Broks, T.M., and Kristensen, S.E. (1990) Eclogites and polyphase *P-T* cycling in the Caledonian Uppermost Allochthon in Troms, northern Norway. Journal of Metamorphic Geology, 8, 289–309.

McNear, E., Vincent, M.G., and Parthé, E. (1976) The crystal structure of vuagnatite, CaAl(OH)SiO$_4$. American Mineralogist, 61, 831–838.

Oberti, R., Smith, D.C., Rossi, G., and Caucia, F. (1991) The crystal-chemistry of high-aluminium titanites. European Journal of Mineralogy, 3, 777–792.

Pabst, A. (1977) On some especially dense, hydrous Ca- and Ba-silicates from the Franciscan Formation, California. Neues Jahrbuch der Mineralogie, Abhandlungen, 129(1), 1–14.

Sakata, M. and Cooper, M.J. (1979) An analysis of the Rietveld profile refinement method. Journal of Applied Crystallography, 12, 554–563.

Sarp, H., Bertrand, J., and Mc Near, E. (1976) Vuagnatite, CaAl(OH)SiO$_4$, a new natural calcium aluminium nesosilicate. American Mineralogist, 61, 825–830.

Scott, H.G. (1983) The estimation of standard deviations in powder diffraction Rietveld refinements. Journal of Applied Crystallography, 16, 159–163.

Smith, D.C. (1980) Highly aluminous sphene (titanite) in natural high-pressure hydrous-eclogite-facies rocks from Norway and Italy, and in experimental runs at high pressure. 26th International Geological Congress, Paris, France (abstract), section 02.3.1, 145.

———(1981) The pressure and temperature dependence of Al-solubility in sphene in the system Ti-Al-Ca-Si-O-F. Progress in Experimental Petrology N.E.R.C. Publication Series, D-18, 193–197.

Sobolev, N.V. and Shatsky, V.S. (1990) Diamond inclusions in garnets from metamorphic rocks: a new environment for diamond formation. Nature, 343, 742–746.

Speer, J.A. and Gibbs, G.V. (1976) The crystal structure of synthetic titanite CaTiOSiO$_4$, and the domain textures of natural titanites. American Mineralogist, 61, 238–247.

Wilson, A.J.C., Shmuelli, U., and Hahn, T. (1992) International Tables for Crystallography. Reidel, Dodrecht, The Netherlands.

Young, R.A. (1993) Introduction to the Rietveld method. In R.A. Young, Ed., The Rietveld Method, p. 1–38. Oxford University Press. Oxford.